Microbial Activators of the Inflammasome

Anukriti Mathur

January 2021

Supervised by Professor Si Ming Man

Australian National University

A thesis submitted for the Degree of Doctor of Philosophy at The Australian National University

© Copyright by Anukriti Mathur 2021

All Rights Reserved

Statement of Originality

I, Anukriti Mathur, hereby declare that the results presented in this thesis are, unless otherwise acknowledged, my own work.

Student: *Anukriti Mathur*

Signed: ……

Date: ……....

Supervisor: *Professor Si Ming Man*

Signed: ……

Date: ……....

Table of Contents

List of Figures

Appendices of Chapter 3

Appendices of Chapter 4

Appendices of Chapter 5

List of Tables

Dedication

I want to dedicate this thesis to my grandmother (Nani) who left us in 2020 for her journey to the heavens. She was proud that I will be the first family member to hold a PhD degree. I miss her dearly. I also dedicate this research to all the mice which were ethically used in the experiments for the fulfilment of this thesis.

Acknowledgements

My doctoral study was the best chapter of my life, thus far, which was rewarding both at professional and personal levels. Firstly, I'm grateful to the Australian National University for providing me with the Fee Remission Scholarship and COVID-19 Extension Scholarship, and the John Curtin School of Medical Research for funding 3.5 years of my doctoral study with the generous stipend. The immense support which the University provided during the year 2020 was outstanding and I'm proud to be a student of ANU. For accomplishment of this thesis, several people provided their support, and I would like to acknowledge them here.

I wish to express my deepest gratitude to my supervisor, Professor Si Ming Man, for his continued trust, encouragement, and support throughout my PhD study. Being the first PhD student of the lab, I got the lifetime opportunity to learn all the lab work from Si Ming. Because of his guidance, I was able to develop my own ideas and critically analyse my own research and of others as a peer reviewer. His impeccable supervision not only helped me finish three projects to publication but also motivated me to apply for awards and grants. He also provided me with numerous opportunities such as writing review articles and scientific blogs; interacting with media and public; and engaging with the collaborators. I highly appreciate all the time and efforts he has invested to uplift my writing and presentation skills, assuring my holistic development as a scientist. Si Ming's genius and dedication for science truly inspires me to grow as a scientist and I'm lucky to have completed my PhD from his lab.

My sincere thanks to the members of my PhD advisory committee; Dr. Ben Quah and Dr. Gaetan Burgio. They were highly supportive and encouraging throughout the course of my PhD. I'm thankful to them for providing valuable feedback, advice, and motivation during my PhD project.

I would like to recognise the invaluable assistance that all members from the Man lab have provided during my study. I couldn't have managed to achieve all the milestones without the

help of such an amazing team. The fantastic research driven environment of the lab facilitated me to complete all the projects in a timely manner. My most cherished memories were the intense scientific conversations we had over lunch where everyone brainstorm's exciting results from various projects. I'm thankful to Ms Jenni Hayward, Dr. Chinh Ngo, Ms. Shouya Feng, Mr. Daniel Fox, Mr. Wei Hong Tan, Dr. Yansong Xue, Ms. Yunqi Liu, Mr Abhimanu Pandey, Mr. Cheng Shen, Dr. Daniel Enosi Tuipulotu, Mr. Callum Kay, Dr. Weidong Jing and Mr. Jordan Lo Pilato, for their scientific contribution to my research projects. I appreciate everyone mentioned above as well as Ms. Anya Zhao, Mr. Runli Wang, Mr. Max Kirkby and Mr. Alex Qin for their friendship and support.

My sincere thanks to all the collaborators who provided intellectual inputs and reagents for my projects. Special thanks to Dr. Nadeem Kaakoush who not only helped me in completing certain experiments but also guided me as a mentor and friend. To, Dr. Melanie Rug and Ms. Jiwon Lee, thanks for their welcoming nature, excellent training, and advice on performing electron microscopy experiments. My sincere appreciation extends to the animal service staff of the Australian Phenomics Facility, for working tirelessly to ensure smooth running of the facility, which made the work in this thesis achievable. I would like to thank all the academic and professional staff at the John Curtin School of Medical Research for helping me directly or indirectly during my PhD.

My heartfelt thanks to my family and friends who were the pillars of strength during my PhD study. I want to thank Dr. Ankur Sharma for being my first friend in Canberra and helping me get settled in a new country. To my true mate Ms Astha Sharma, I admire the wonderful friendship you have provided me all these years, for being a loyal and faithful friend who supported me on each step. I'm so grateful to Dr. Mahesh Venkataraman and Ms. Preetha Iyer for their friendship, all the nice food they cooked for me and taking care of me as a guardian. My PhD study went smoothly because of the warm friendship I shared with Mr. Navneet Singh, Ms. Sherin, Ms Yoshika Janapala and Ms Poonam Kumari.

Mom, Papa, Pankhuri and Shitanshu, thank you! I was able to achieve everything because of the endless support and unconditional love I get from you all. Words fall short to thank Mr Chirag Ajwani for all his love, care, and support. You held my hand and sailed with me during all ups and downs especially during the thesis writing phase. I would like to pay my special regards to all the elders and relatives of my family for their blessings and love. I would like to reiterate how grateful I am to everyone who helped me get through my doctoral study.

Anukriti Mathur

Australian National University

January 2021

List of Publications

1. Fox, D*, **Mathur, A***, Xue, Y, Liu, Y, Tan, WH, Feng, S, Pandey, A, Ngo, C, Hayward, JA, Atmosukarto, II, Price, JD, Johnson, MD, Jeßberger, N, Robertson, AAB, Burgio, G, Tscharke, DC, Fox, EM, Leyton, DL, Kaakoush, NO, Märtlbauer, E, Leppla, SH, & Man, SM (2020). *Bacillus cereus* non-haemolytic enterotoxin activates the NLRP3 inflammasome. ***Nature Communications***, 11:760. *Co-first authors
2. **Mathur, A**, Feng, S, Hayward, JA, Ngo, C, Fox, D, Atmosukarto, II, Price, JD, Schauer, K, Märtlbauer, E, Robertson, AAB, Burgio, G, Fox, EM, Leppla, SH, Kaakoush, NO, & Man, SM (2019). A multicomponent toxin from *Bacillus cereus* incites inflammation and shapes host outcome via the NLRP3 inflammasome. ***Nature Microbiology***, 4:362–374.
3. Tuipulotu, DE, **Mathur, A**, Ngo, C, and Man, SM (2021). *Bacillus cereus*: epidemiology, virulence factors and host-pathogen interactions. ***Trends in Microbiology***, 29 (5), 458-471.
4. Hayward, J*, **Mathur, A***, Ngo, C and Man, SM (2018). Cytosolic Recognition of Microbes and Pathogens: Inflammasomes in Action. ***Microbiology and Molecular Biology Reviews***, 82(4). * Co-first authors
5. **Mathur, A***, Hayward, JA*, Man, SM (2018). Molecular mechanisms of inflammasome signaling. ***Journal of Leukocyte Biology***, 103:233–257. * Co-first authors

List of Conference Presentations

1. Oral presentation at the Research Symposium of the Australian Society for Biochemistry and Molecular Biology Annual Meeting, 2020.
2. Oral Presentation at the 7th Annual Meeting of the International Cytokine & Interferon Society in Vienna, 2019.
3. Oral presentation at the 14th World Inflammation Congress, Sydney, 2019.
4. Oral presentation and attended the Nancy Millis student/early-career researcher workshop at the Australian Society for Microbiology Annual Conference, Adelaide, 2019.
5. Oral presentation at the Australian Society for Microbiology ACT-NSW Branch meeting at University of Technology Sydney, 2019.

List of Awards

1. **The Australian Society for Biochemistry and Molecular Biology Fellowship 2020**– for outstanding work in the field of biochemistry or molecular biology (awarded up to 5 early-career researchers).
2. **An industrial grant from a Biotech company Beta Therapeutics**- a total funding of $47,497 was awarded to conduct 'Mechanism studies of heparanase inhibition in macrophages' (2020). This project grant is shared with Dr. Chinh Ngo and Prof. Si Ming Man.
3. **The American Association of Immunologists Trainee Poster award 2020**– for exceptional abstract by early career researchers with a travel support to attend the annual meeting.
4. **The ANU Vice-Chancellor's HDR Travel Grant 2020**– of $1,500 to attend the American Association of Immunologists annual meeting 2020.
5. **The International Cytokine & Interferon Society Sidney & Joan Pestka Graduate Award 2019**– awarded to 1 PhD student worldwide who has begun to make an impact in interferon and cytokine research.
6. **The People Choice Award of the Three-minute thesis competition**– hosted by the College of Health and Medicine, ANU (1 awarded annually).
7. **The Gretel and Gordon Bootes Medical Research Foundation grant award**– awarded to 10 early-career researchers annually at JCSMR for an outstanding research proposal. The two research awards were worth $11,250 (CIA on the grant proposal, 2019) and $12,222 (CIB on the grant proposal, 2020).
8. **The Australian Society for Microbiology Nancy Millis student Award 2019**– awarded to 6 graduate students annually for their outstanding work in the field of microbiology.
9. **The International Association of Inflammation Societies Young Investigator Award 2019**– for performing exploratory and applied research in the general area of inflammation (awarded up to 4 early-career researchers).

Abstract

Innate immune recognition of microbial components serves as a cornerstone in mediating an effective immune response. Innate immune sensors and inflammasomes detect both intracellular and extracellular microorganisms. The inflammasome is an intracellular signalling complex comprising of a sensor, an adaptor protein ASC (known as apoptosis-associated speck-like protein containing a caspase activation and recruitment domain) and the cysteine protease caspase-1. Inflammasomes regulate secretion of the pro-inflammatory cytokines, IL-1β and IL-18, and induction of a cell death pathway known as pyroptosis. Certain intracellular bacteria require cytosolic access to activate the inflammasome, however, how extracellular bacteria are sensed by the inflammasome in the cytoplasm remains largely unclear.

To understand the innate immune recognition of extracellular bacteria, a panel of clinically important intracellular and extracellular bacteria were analysed. This analysis led to the identification of an unknown secreted factor from the foodborne bacterium *Bacillus cereus* that activated the inflammasome without gaining cytosolic access. The tripartite enterotoxin called haemolysin BL (HBL) was identified as the novel activator of the NLRP3 inflammasome. I further identified another tripartite toxin called non-haemolytic enterotoxin (NHE), which also activated NLRP3 to induce inflammation and cell death.

Mechanistically, both multi-component toxins assembled in a specific and linear order on the mammalian plasma membrane to form a lytic pore, which induces potassium efflux. Remarkably, HBL and NHE operated synergistically to drive inflammation in a mouse model of *B. cereus* infection. Administration of a small molecule NLRP3 inhibitor MCC950 inhibited inflammation induced by HBL and NHE in vivo and rescued mice from *B. cereus*-induced lethality. These data showcase the ability of a single inflammasome sensor to detect structurally and functionally similar toxins from the same bacterium.

Given that toxins as novel inflammasome activators can be readily identified, I further conducted an unbiased screen of 34 toxins from phylogenetically diverse organisms from different domains of life. This screen revealed that phospholipase C (PLC) from the human bacterial pathogen *Clostridium perfringens* as an activator of the NLRP3 inflammasome. In contrast to the known NLRP3-activating toxins which emanate an inflammasome-activating signal from the plasma membrane, PLC activated the NLRP3 inflammasome intracellularly via the endosome-lysosomal pathway. Mechanistically, PLC caused lysosomal membrane destabilisation which triggered potassium efflux to initiate the assembly of the NLRP3 inflammasome, highlighting a convergence of signals between the lysosome and potassium efflux in initiating cytosolic sensing of a bacterial phospholipase and innate immunity. Overall, this research identified three novel activators of the inflammasome and their molecular mechanisms in activating inflammation and cell death responses. Understanding the molecular basis of host-pathogen interactions has the potential to contribute therapies which target microbial virulence factors and/or the immune system in the treatment of infectious diseases.

Abbreviations

Terms	Abbreviation
1,2-dioleoyl-sn-glycero-3-phosphocholine	DOPC
1,2-dipalmitoyl-sn-glycero-3-phosphocholine	DPPC
1,2-distearoyl-sn-glycero-3-phosphocholine	DSPC
4,6-diamidino-2-phenylindole	DAPI
American Type Culture Collection	ATCC
Ampere	A
Anti-	α-
Absent in melanoma 2	AIM2
Absent in melanoma 2 like receptors	ALRs
Acridine orange	AO
Adenosine triphosphate	ATP
Alexa Fluor 568 labelled PLC	AF568-PLC
Ammonium chloride	NH_4Cl
Analysis of Variance	ANOVA
Apoptosis-associated speck-like protein containing a CARD	ASC
Bacillus cereus	*B. cereus* or *B. cer.*
Bafilomycin A	BafA
Bone marrow-derived macrophages	BMDMs
Bovine serum albumin	BSA
C-type lectin receptors	CLRs
Chinese Hamster Ovary cells	CHO
Citrobacter rodentium	*C. rod.*
Clostridium perfringens	*C. per; C. perfringens*
Caspase activating and recruitment domain	CARD
Caspase-1	Casp-1
Caspase-1 cleavage product p20	p20
Community-acquired respiratory distress syndrome	CARDS
Colony forming units	CFU
Control	CTRL
Corynebacterium diphtheriae	*C. dip*
Cytochalasin B/D	Cyto B/D
Cytotoxin K	CytK
Danger-associated molecular patterns	DAMPs
Dithiothreitol	DTT
Dulbecco's modified eagle medium	DMEM
Enzyme-linked immunosorbent assay	ELISA
Escherichia coli	*E. coli*
Ethylenediaminetetraacetic acid	EDTA
Fetal bovine serum	FBS
Figure	Fig

Fluorescein isothiocyanate	FITC
Francisella novicida	*F. nov.*
Gasdermin D	GSDMD
Gasdermin D cleavage product p20	GSDMD p20
Gasdermin D cleavage product p30	GSDMD p30
Gram	g
Guanosine triphosphate	GTPases
Haemolysin BL	HBL
Horseradish peroxidase	HRP
Hydrochloric acid	HCl
Immunoglobulin G	IgG
Inductively coupled plasma-optical emission spectroscopy	ICP-OES
Interleukin	IL
Intraperitoneal	i.p.
Keratinocyte chemoattractant	KC
Kilo dalton	kDa
Kilogram	kg
Lactate dehydrogenase	LDH
Latrunculin B	Lat B
Lethal factor	LF
Lipopolysaccharide	LPS
Liposome	Lipo.
Listeria monocytogenes	*L. mon.*
Lysosomal-associated membrane protein 1	LAMP1
Macrophage colony-stimulating factor	M-CSF
Media (untreated cells)	Med
Methyl-β-cyclodextrin	MCD
Micro molar	μM
Microgram	μg
Millilitre	mL
Milligram	mg
Molar	M
Multiplicity of infection	MOI
Mutant	Mut
Nano molar	nM
Nanogram	ng
N,N,N',N'-Tetramethylethylethylenediamine	TEMED
Nigericin	Nig
Nitric acid	HNO_3
Non-haemolytic enterotoxin	NHE
Not significant	NS
Nucleotide-binding domain and leucine-rich repeat receptors	NLRs
Nucleotide-binding domain, leucine-rich and pyrin domain-containing protein 3	NLRP3

Nucleotide-binding oligomerisation domain-like receptor family apoptosis inhibitory protein	NAIP
Optical density	OD
P2X purinoreceptor 7	P2X7
Paraformaldehyde	PFA
Pasteurella multocida	*P. mul*
Pathogen-associated molecular patterns	PAMPs
Pattern-recognition receptors	PRRs
Phosphate buffered saline	PBS
Phospholipase C	PLC
Picogram	pg
Polymerase chain reaction	PCR
Potassium chloride	KCl
Potassium ion	K^+
Pore-forming toxins	PFTs
Protective antigen	PA
Pseudomonas aeruginosa	*P. aer; P. aeruginosa*
Pyrin domain	PYD
Quantification- reverse transcriptase polymerase chain reaction	q-RT PCR
Retinoic acid-inducible gene-I like receptors	RLRs
Salmonella enterica serovar Typhimurium	*S.* Typhi or *S.* Tm
Scanning electron microscopy	SEM
Shigella flexneri	*S. flex.*
Shigella dysenteriae	*S. dyx*
Sodium chloride	NaCl
Sodium ion	Na^+
Sodium dodecyl sulphate	SDS
Sodium dodecyl sulphate polyacrylamide gel electrophoresis	SDS-PAGE
Standard error of the mean	s.e.m.
Staphylococcus epidermidis	*S. epi.*
Streptococcus aureus	*S. aur*
Streptococcus pneumoniae	*S. pne.*
Streptococcus pyogenes	*S. pyo.*
Supernatant	Sup
Toll-like receptors	TLRs
Transmission electron microscopy	TEM
Tripartite motif	TRIM
Tumour necrosis factor	TNF
Type III secretion system	T3SS
Untreated	UT
Vibrio cholera	*V. cho*
Volts	V
Wild-type	WT

Chapter 1♦ Introduction

1.1 Preface

Parts of this chapter were taken or adapted from my published review articles. For review articles in which I was the first or co-first author, I generated greater than fifty percent of the content. My contributions to these publications are stated below.

1. **Mathur, A*,** Hayward, JA*, Man, SM (2018). Molecular mechanisms of inflammasome signaling. ***Journal of Leukocyte Biology***, 103:233–257. * Co-first authors.

As an equal first author, I wrote the sections titled “Introduction”, “NLRP1 inflammasome”, “NLRP3 inflammasome”, “Non-canonical NLRP3 inflammasome”, and “Gasdermin”. I edited subsequent versions of the whole manuscript and addressed comments from co-authors and external peer reviewers with assistance from senior author Prof. Si Ming Man.

2. Hayward, J*, **Mathur, A***, Ngo, C and Man, SM (2018). Cytosolic Recognition of Microbes and Pathogens: Inflammasomes in Action. ***Microbiology and Molecular Biology Reviews***, 82(4). * Co-first authors.

As an equal first author, I wrote the sections titled “Introduction” and “Protozoa”. I edited subsequent versions of the whole manuscript and addressed comments from co-authors and external peer reviewers with assistance from senior author Prof. Si Ming Man.

3. Tuipulotu, DE, **Mathur, A**, Ngo, C, and Man, SM (2021). *Bacillus cereus*: epidemiology, virulence factors and host-pathogen interactions. ***Trends in Microbiology***, 29 (5), 458-471,

As the second author, I wrote the sections titled “Virulence factors of *B. cereus*”, “Membrane-bound receptors of HBL in mammalian cells”, “Novel membrane-bound receptor/s of NHE”, and “Immune response to *B. cereus* infection”. I edited subsequent versions of the whole manuscript and helped the first author in addressing comments from co-authors and external peer reviewers with assistance from senior author Prof. Si Ming Man.

1.2 Innate immunity and pattern recognition receptors

The innate immune system is an evolutionarily ancient host defence system, found in plants, invertebrates, and mammals, that can respond to invading microbes and endogenous stress signals. The innate immune system relies on detection of specific and conserved determinants displayed by microbes and endogenous signals, called pathogen-associated molecular patterns (PAMPs) [1] and damage-associated molecular patterns (DAMPs), respectively [2]. Some examples of PAMPs are lipoproteins, flagellin, and toxins; and of DAMPs are ATP, nuclear proteins, chaperon proteins and uric acid crystals [3]. PAMPs and DAMPs are sensed by germline-encoded pattern recognition receptors (PRRs) [1]. PRRs include Toll-like receptors (TLRs) [4], C-type lectin receptors (CLR) [5], Retinoic acid-inducible gene (RIG-1)-like receptors (RLRs) and Nucleotide-binding oligomerisation domain (NOD)-like receptor (NLRs) [6,7]. These PRRs are expressed on immune and non-immune cells, including macrophages, dendritic cells, neutrophils, NK cells, platelets, epithelial and endothelial cells [8]. These PRRs orchestrate host responses through the production of inflammatory cytokines, chemokines, interferons and antimicrobial molecules [1]. In addition, stimulation of PRRs by PAMPs and DAMPs results in initiation of programmed cell death pathways such as apoptosis, pyroptosis and necroptosis [9].

To mediate an effective immune detection of PAMPs and DAMPs, PRRs monitor both extracellular and intracellular spaces [1]. Concerted activation of multiple PRRs enables the host to respond to diverse stimuli and amplify the immune response for rapid clearance of infection or damage [10]. Owing to the central role of PRRs in mediating an innate immune response, PRRs are controlled by transcriptional and post-translational regulation [11]. Dysregulation and dysfunction of PRRs can result in either decrease or increase of the immune response such as inflammation. Indeed, genetic polymorphisms found in several PRR genes are associated with development of inflammatory, metabolic and neurological disorders.

TLRs are found on the surface and endosomal compartment of the cell [4]. TLRs present on the plasma membrane, such as TLR1, TLR2, TLR4, TLR5, TLR6 and TLR10, recognise cell surface-associated microbial antigens [12]. TLR2/1 and TLR2/6 sense bacterial and parasitic lipoproteins and TLR4 and its co-receptors MD2 and CD14 recognise polysaccharide (LPS) of Gram-negative bacteria [13]. In contrast, endosomal TLRs, such as TLR3 and TLR9, recognise nucleic acids [14]. TLR3 senses double stranded RNA, whereas TLR9 binds to single stranded DNA (ssDNA) containing unmethylated CpG. Engagement of the TLRs with their cognate ligand initiates a signal transduction which modulates gene transcription, epigenetic programming, translation of mRNA, metabolism, cytoskeleton activity and cell viability [4]. TLR responses are also associated with production of pro-inflammatory and anti-inflammatory cytokines, interferons (IFNs), anti-microbial products, molecules for tissue repair, and chemokines [4]. The spectrum of biological activities regulated by the TLR network and signalling highlight their importance as key players of innate immunity.

RLRs sense viral infection and launches an anti-viral response by upregulating the transcription of type I IFNs and other interferon-stimulated genes (ISGs) [15]. Members of the RLRs family includes RIG-I, melanoma differentiation-associated protein 5 (MDA5) and laboratory of genetics and physiology 2 (LGP2) [16]. RLRs are localised in the cytosol where they recognise viral RNA [17]. However, recent studies have revealed that RIG-I can detect host RNA which are unusual, mislocalised or misprocessed [15,18,19]. Notably, certain viruses can hijack the host transcriptional machinery leading to mislocalisation of cellular non-coding RNAs, downregulation of RNA binding proteins and unmasking of endogenous retroviral elements [18,19]. The ability of RLRs to mediate detection of viral and host RNA highlights the protective functions of RLRs in infection and sterile pathologies.

Another important class of PRRs are CLRs, which are predominately expressed on immune cells and interact with pathogens that harbour glycan moieties such as mannose, fucose and glucan carbohydrate structures [20]. CLRs exists as both transmembrane and soluble proteins

[21]. CLRs are expressed on both myeloid- and lymphoid- lineage cells. Examples of myeloid-lineage cells include dendritic cells, monocytes, macrophages, and neutrophils, whereas lymphoid-lineage cells include NK cells [20]. The prominent CLRs expressed on myeloid-lineage cells include Dectin -1 and -2, Mincle, and mannose receptor [22]. CLR-mediated recognition can fine-tune the adaptive immune response either by antigen presentation of internalised pathogen or through secretion of pro- or anti- inflammatory cytokines and chemokines [21]. In addition to recognition of microbial ligands containing carbohydrate moieties, CLRs can recognise damage-associated host ligands such as oxidised phospholipids, heat-shock proteins and ribonucleoproteins [23].

A family of PRRs that has gained attention from the scientific community is the cytosolic NLR family of proteins. NLRs are generally defined by a tripartite domain architecture comprising of a C terminal LRR, a middle nucleotide-binding domain (NBD, also known as the NACHT domain) and a variable N-terminal domain [24]. The N-terminal domains include pyrin (PYD; found in NLRP), caspase activation and recruitment domain (CARD; found in NLRC and NOD), baculoviral inhibitory of apoptosis repeat (BIR; found in NAIP), or transactivator domain (found in CIITA) [24]. The NLRs called NOD1 and NOD2 can recognise peptidoglycan derived from bacterial species. NOD1 detects diaminopimelic acid produced primarily by Gram-negative bacteria [25], whereas NOD2 binds to muramyl dipeptide, a component of both Gram-positive and Gram-negative bacteria [25]. Activation of NOD1 and NOD2 results in activation of mitogen-activated protein kinase (MAPK) and nuclear factor-kB (NF-kB) pathways, leading to transcriptional modulation of genes encoding inflammatory cytokines, such as tumour necrosis factor (TNF) [26]. Certain members of the NLR family are known to form a cytosolic signalling hub called the inflammasome [27]. The inflammasomes detect several microbial and endogenous determinants triggering inflammation and a programmed cell death pathway called pyroptosis (discussed in section 1.3).

1.3 Inflammasomes

Inflammasomes are cytosolic multimeric signalling complexes that coordinate host immune responses to invading pathogens and host-derived danger signals. Less than two decades into its discovery, the inflammasome has become one of the centrepieces of immunology and has continued to inspire research into pattern recognition and innate immunity. A central feature of the inflammasome is its ability to respond to pathogens and danger signals from within the host cytoplasm and emanate a rapid inflammatory and cell death response. Binding between a single entity of ligand and an inflammasome sensor can induce a cascade of oligomerisation events, culminating in inflammation and cell death that define the physiological outcomes in the host. These outcomes are either beneficial, such as immunity to infection, or detrimental, including development of inflammatory, metabolic and neurological diseases and cancer.

To achieve a beneficial outcome, the inflammasome induces a protective response, either by induction of inflammation and cellular recruitment via IL-1β and IL-18, or physical destruction or removal of the infected cell via pyroptosis. Enhancement of these protective responses can be achieved by heightening the inflammasome activity through pharmacological modulation, such as anti-viral therapies [28]. However, timely negative regulation of these protective responses helps in the prevention of a hyper-activated inflammasome that, if left uncontrolled, can cause tissue damage and chronic inflammatory disorders. Experimental therapies that are able to attenuate inflammasome hyperactivation have been successful in the treatment of endotoxaemia and autoinflammatory disorders [29], suggesting that immunomodulators of the inflammasome are a promising armamentarium that may be applied more widely in the clinics. For example, inhibition of the inflammasome may be beneficial to curtail overt inflammatory responses in sepsis that often lead to rapid lethality [29].

1.3.1 General mechanisms of inflammasome activation

Formation of the inflammasome is initiated by cytosolic PRRs, capable of recognising PAMPs and DAMPs. In most cases, activated PRRs bind and engage the inflammasome adaptor protein apoptosis-associated speck-like protein containing a caspase activation and recruitment domain (ASC) in order to recruit and activate the cysteine protease caspase-1 [30]. Several families of PRRs known to form inflammasomes include, the nucleotide-binding domain and leucine-rich repeat receptors (NLRs), the absent in melanoma 2-like receptors (ALRs) and tripartite motif (TRIM). NLRP1 was first described to form an inflammasome complex in 2002 [31], sparking interests to determine which other PRRs might also form inflammasome complexes. Since then, NLRP3, NLRC4, AIM2, Caspase-11 and Pyrin have also been shown to initiate formation of an inflammasome complex [32] ; while less thoroughly characterised, there is also evidence that human NLRP2, NLRP7 and IFI16, and mouse NLRP6, NLRP9b and NLRP12 can activate caspase-1 [33-35].

ASC is a bipartite protein consisting of an N-terminal pyrin domain (PYD) and a C-terminal caspase activation and recruitment domain (CARD). Following PRR activation, ASC rapidly oligomerises through homotypic PYD-PYD interactions into a large filamentous scaffold [36,37]. Inactive pro-caspase-1 monomers are recruited to ASC filaments through CARD-CARD interactions and thereby brought into close proximity for optimal self-activation [36,37]. This sensor-ASC-caspase-1 inflammasome complex can be visualised as a distinct ‘speck’ of 0.8 to 1 µm in diameter within the cytoplasm of macrophages and other cell types such as dendritic cells, neutrophils and epithelial cells [38-42]. Inflammasome specks released from pyroptotic cells have even been found to act as DAMPs and amplify the inflammatory response [43,44]. Inflammasomes can be assembled on several organelles, such as the trans Golgi network, perinuclear sites, or the microtubule-organising center (MTOC) [38,45-49].

After recruitment to the inflammasome complex and undergoing self-activation, caspase-1 executes several key cellular functions that are characteristic hallmarks of inflammasome

activation. Caspase-1 proteolytically processes the pro-inflammatory cytokines pro-IL-1β and pro-IL-18 into their biologically active forms. In addition, caspase-1 cleaves the pro-pyroptotic factor gasdermin D (GSDMD) [50-52]. The N-terminal fragment of GSDMD oligomerises and forms pores on the host cell membrane [53-57], leading to cell swelling, lysis and release of cytoplasmic contents in an inflammatory form of cell death called pyroptosis.

Secretion of IL-1β and IL-18 and induction of pyroptosis have an instrumental role in eliciting, magnifying and perpetuating inflammation and, in most cases, reducing overall pathogen burden. Both cytokines serve as a bridge between innate and adaptive immunity: IL-1β is a potent promoter of inflammation, immune cell extravasation and vasodilation with additional capabilities in modulating adaptive immunity [58], while IL-18 triggers local inflammation, IFN-γ production in Natural Killer (NK) cells, $CD4^+$ T_H1 cells and $CD8^+$ cytotoxic T cells, and augments the development of $CD4^+$ T_H2 cells [59]. In addition to promoting the release of cytokines and DAMPs, another overarching function of pyroptosis is to expel an infected cell from the tissue [60,61] or to expel pathogens from infected macrophages [62,63]. Thus, the inflammasome facilitates disruption of the replicative niche exploited by intracellular pathogens and exposes them to potentially less favourable conditions. However, inappropriate IL-1β and IL-18 release can drive sterile inflammation and contribute to the development of autoimmune and inflammatory disease.

While the downstream consequences of activation of inflammasomes are inflammation and cell death, the molecular mechanisms governing the regulation of ligand detection and activation of each inflammasome sensor are distinct, often in nuanced ways. An extensive overview of the unique molecular mechanisms governing the different inflammasome complexes are outlined in the sections below.

1.3.2 NLRP1 inflammasome

Human NLRP1 was the first protein identified to form an inflammasome complex [31]. This inflammasome complex contains NLRP1, ASC, caspase-1 and caspase-5 [31]. The human NLRP1 protein is composed of a PYD domain, a nucleotide-binding domain (NBD), a leucine rich repeat (LRR), a function-to-find (FIIND) domain, and a CARD domain [31]. Unlike human NLRP1, mice carry three NLRP1 paralogs (NLRP1a, NLRP1b and NLRP1c), all of which lack a PYD domain [64]. Mouse NLRP1b and rat NLRP1 are activated by the anthrax lethal toxin secreted by the human bacterial pathogen *Bacillus anthracis* [65,66]. The anthrax lethal toxin is composed of a receptor binding component known as protective antigen and a zinc metalloprotease called lethal factor **(Fig. 1.1)**. The protective antigen binds to two host cell surface receptors; tumour endothelium marker-8 (TEM8 also known as anthrax receptor 1) and capillary morphogenesis protein-2 (CMG2 also known as anthrax receptor 2) [67-70]. Endocytosis of the receptor-toxin complex facilitates the translocation of the lethal toxin from the extracellular space into the cytosol [71,72]. The low pH of endosomes mediates maturation of the protective antigen channel, transferring the lethal factor from the endosome to the cytosol [71,72].

In the cytosol, the lethal factor induces N-terminal proteolytic cleavage of the mouse NLRP1b and rat NLRP1 to catalyse the activation of the NLRP1 inflammasome [66,73-77] **(Fig. 1.1)**. Mice carry a susceptible and resistant form of NLRP1b [64], and those carrying a susceptible variant are protected against *B. anthracis* infection due to the ability of the susceptible variant to respond to the lethal toxin compared to mice harbouring a resistant form [78,79]. Owing to the presence of a CARD domain, mouse NLRP1b binds to and activate caspase-1, and induces the secretion of IL-1β and induction of pyroptosis in murine macrophages stimulated with lethal toxin [80,81]. In this case, ASC is only required to amplify secretion of IL-1β in response to low-dose lethal toxin [80] **(Fig. 1.1)**.

While NLRP1 is best known for its role in sensing *B. anthracis* infection, it has also been implicated in the host response to the protozoan *Toxoplasma gondii*. For instance, mice deficient in NLRP1b and NLRP3 and infected with *T. gondii* produce less IL-1β and IL-18, harbour increased parasitic loads and succumb to the infection [82]. These findings suggest that NLRP1b in association with another NLR can synergistically mount an effective host response.

1.3.2.1 Mechanisms of NLRP1 inflammasome activation

Several studies have unravelled the biochemical mechanisms involved in assembly and activation of the NLRP1 inflammasome. The FIIND domain of human NLRP1 undergoes autoproteolytic cleavage at the Ser1213 residue [83,84]. Further, studies using point mutations and structural analysis revealed that the His1186 residue located within a loop proximal to the cleavage site of the FIIND domain of human NLRP1 is essential for autoproteolytic cleavage [83,84]. Mutagenesis studies targeting several residues within a fragment of mouse NLRP1b revealed that cleavage of the FIIND domain results in recruitment of pro-caspase-1 [85]. Similarly, genetic disruption of the FIIND domain of mouse NLRP1b leads to impairment of self-oligomerisation and activation of pro-caspase-1 [85]. These studies demonstrate that cleavage of the FIIND domain contributes to activation of the mouse NLRP1b inflammasome.

A model of functional degradation of mouse NLRP1b has been described. In this model, autoproteolytic processing of the FIIND domain separates the NLRP1b protein into N-terminal and C-terminal fragments, which remain non-covalently-associated [86,87]. The anthrax lethal factor induces subsequent cleavage of NLRP1b and generates a destabilising neo-N terminus [86,87]. The neo-N-terminal fragment is ubiquitinated by host E3 ligase UBR2, the ubiquitinating protein UBR4, and the ubiquitin-activating enzyme UBA6, marking this fragment for proteasomal degradation [86,88]. Proteasomal degradation of the N-terminal fragment leads to liberation of the C-terminal fragment [86,87]. The CARD-containing C-terminal fragment initiates a self-assembly process to form a functional NLRP1b inflammasome [86,87]. In addition, following autoprocessing of FIIND, the N-terminal fragment can be directly ubiquitinated by ubiquitin E3

ligase IpaH7.8 of *Shigella flexneri*, which leads to the activation of the NLRP1b inflammasome [87].

1.3.2.2 Activators of the human NLRP1 inflammasome

Similar to the murine NLRP1b, human NLRP1 undergoes proteolysis within a specific N-terminal linker region of unknown sequence between the PYD and NBD domains [89]. However, human NLRP1 is unresponsive to the anthrax lethal factor and IpaH7.8 of *S. flexneri* [87]. The microbial activators of human NLRP1 have now been revealed. The rhinovirus C3 protease can cleave human NLRP1 and activate the inflammasome in human immortalised keratinocytes [90]. The cleavage site of the C3 protease is a single site between Glu^{130} and Gly^{131} of human NLRP1 protein. This cleavage site is located after the PYD domain, a region that is not conserved in rodents [90]. Indeed, due to the lack of this region in mice, murine RAW macrophages did not respond to the rhinovirus C3 protease [90]. Mechanistically, both murine NLRP1b and human NLRP1 undergo the N-terminal degradation pathway to liberate the CARD-containing C-terminal fragment [86,87,90]. Indeed, several viral proteases can cleave human NLRP1 and activate the NLRP1 inflammasome [91]. In addition, human NLRP1 binds dsRNA and dsDNA via its LRR domain [92]. However, only dsRNA can initiate assembly of the inflammasome [92]. The mechanisms through which dsRNA liberates the CARD-containing C-terminal fragment remains unknown.

Similar to mouse NLRP1b, autoprocessing of FIIND is the first step in the activation of the human NLRP1 inflammasome [90]. However, due to the generation of an N-terminal glycine in the C3pro-cleaved NLRP1, an alternative ubiquitination pathway called the N-glycine degron pathway was activated [90]. In this pathway, the receptors ER1 and ZYG11B and their partner cullins, CUL2 and CUL5 form a four-component complex termed $cullin^{ZER1/ZYG11B}$ [90]. Ubiquitination of NLRP1 by the $cullin^{ZER1/ZYG11B}$ machinery results in N-terminal degradation of NLRP1 via the proteasome, analogous to NLRP1b degradation. Furthermore, human rhinovirus infection in Hela-Ohio and primary human bronchial epithelial cells caused 3Cpro-

dependent NLRP1 cleavage and activation of the human NLRP1 inflammasome [90]. These findings are important as rhinovirus C3 is the first identified microbial ligand of human NLRP1 inflammasome, paving a way for exploration of other PAMPs and DAMPs capable of activating the human NLRP1 sensor.

Another mechanism through which the NLRP1 inflammasome can be activated is by inhibition of dipeptidyl dipeptidase (DPP)-8 and DDP-9 [93,94]. Inhibition of DPP8/9 by Val-boroPro, a non-selective inhibitor of post-pro-line-cleaving serine proteases, triggered pyroptosis in monocytes and macrophages [93,95]. DPP9 bound to FIIND of NLRP1 to restrain its activity. The mechanism by which Val-boroPro triggers NLRP1 inflammasome activation is yet to be fully understood, however, removal of DPP8/9 may elicit the autoproteolytic processing of FIIND, which is the first step in functional degradation of NLRP1 [86,87,90,94]. Indeed, Val-boroPro-mediated activation of NLRP1 was dependent on proteasomal degradation [95], however, further experiments are required to determine the exact molecular mechanism underpinning the DPP8/9 and NLRP1 interaction. In addition, it may be reasonable to speculate that any microbial factor capable of inhibiting DPP8/9 can potentially activate the NLRP1 inflammasome.

In context of the role of human NLRP1 in combatting infectious diseases, polymorphisms in the genes encoding NLRP1 or IL-1β are associated with a more severe form of *Plasmodium vivax* infection, whereas a polymorphism in the gene encoding IL-18 is associated with protection against *P. vivax*-induced anaemia [96]. Furthermore, genetic analysis of patients with congenital toxoplasmosis further revealed that polymorphisms in the gene encoding NLRP1 is associated with an increased risk to toxoplasmosis [97]. Indeed, knockdown of NLRP1 using RNA interference in the human monocytic leukemia MonoMac6 cell line results in increased parasitic burden in response to *T. gondii* infection [97]. Both NLRP1b and NLRP3 have been found to provide protection against *T. gondii* infection in mice or rats [98-100]; however, the activators triggering either inflammasomes in response to *T. gondii* infection are unknown.

1.3.2.3 NLRP1a inflammasome

There is evidence to indicate that the NLRP1 paralogue NLRP1a has inflammasome functions. A single point mutation causing a glutamine-to-proline substitution at amino acid 593 of NLRP1a (*Nlrp1a*^{Q593P}) induces a systemic inflammatory disease in mice [101]. This inflammatory phenotype is prevented by genetic deletion of caspase-1, IL-1β or IL-1R, but not ASC [101], implicating a role for NLRP1a in assembling an NLRP1a-Caspase-1 complex, driving IL-1β-mediated immunopathology. Spontaneous caspase-1 activation induced by the *Nlrp1a*^{Q593P} mutation results in pyroptosis of myeloid progenitor cells that affects their capacity to differentiate into mature myeloid cells [101]. The physiological relevance of NLRP1a has been examined in the context of infectious disease. The *Nlrp1a*^{Q593P} *Il1r*$^{-/-}$ mouse strain, which does not develop systemic inflammation, suffers from prolonged cytopenia, bone marrow hypoplasia and immunosuppression in response to lymphocytic choriomeningitis virus infection [101]. Further studies are required to decipher the differential roles of the three paralogues of NLRP1 in mice. While there has been progress in dissecting the molecular mechanisms contributing to the activation of the NLRP1 inflammasome, more comprehensive studies are required to fully understand its role in infection and autoinflammatory diseases.

1.3.2.4 Regulation of NLRP1

Given that NLRP1 can respond to a subset of stimuli, post-translational regulation of the NLRP1 may prevent inadvertent activation. As discussed above, a series of proteases and ubiquitinases regulates the activation of the mouse NLRP1b and human NLRP1 in macrophages and monocytes [83,84,86,87], preventing unwanted activation of the NLRP1 inflammasome. However, in certain cell types such as keratinocytes, NLRP1 activation is modulated through the autoinhibitory function of the PYD and LRR domains [102]. Indeed, mutations targeting the PYD domain (Ala54Thr, Ala66Val and Met77Thr), deletion of the PYD domain (aa 93–1474) or deletion of residues in the LRR domain (Phe787 to Arg843) promote increased production of IL-1β in immortalised human keratinocytes [102]. These results suggest that the PYD and LRR domains maintain human NLRP1 in an inactive conformation rather

than facilitating ASC oligomerisation. In humans, germline gain-of-function mutations in the PYD and LRR domains of NLRP1 predispose individuals to the skin diseases called multiple self-healing palmoplantar carcinoma and familial keratosis lichenoides chronica [102]. These findings in humans highlight critical roles of certain domains of NLRP1 in maintaining homeostasis.

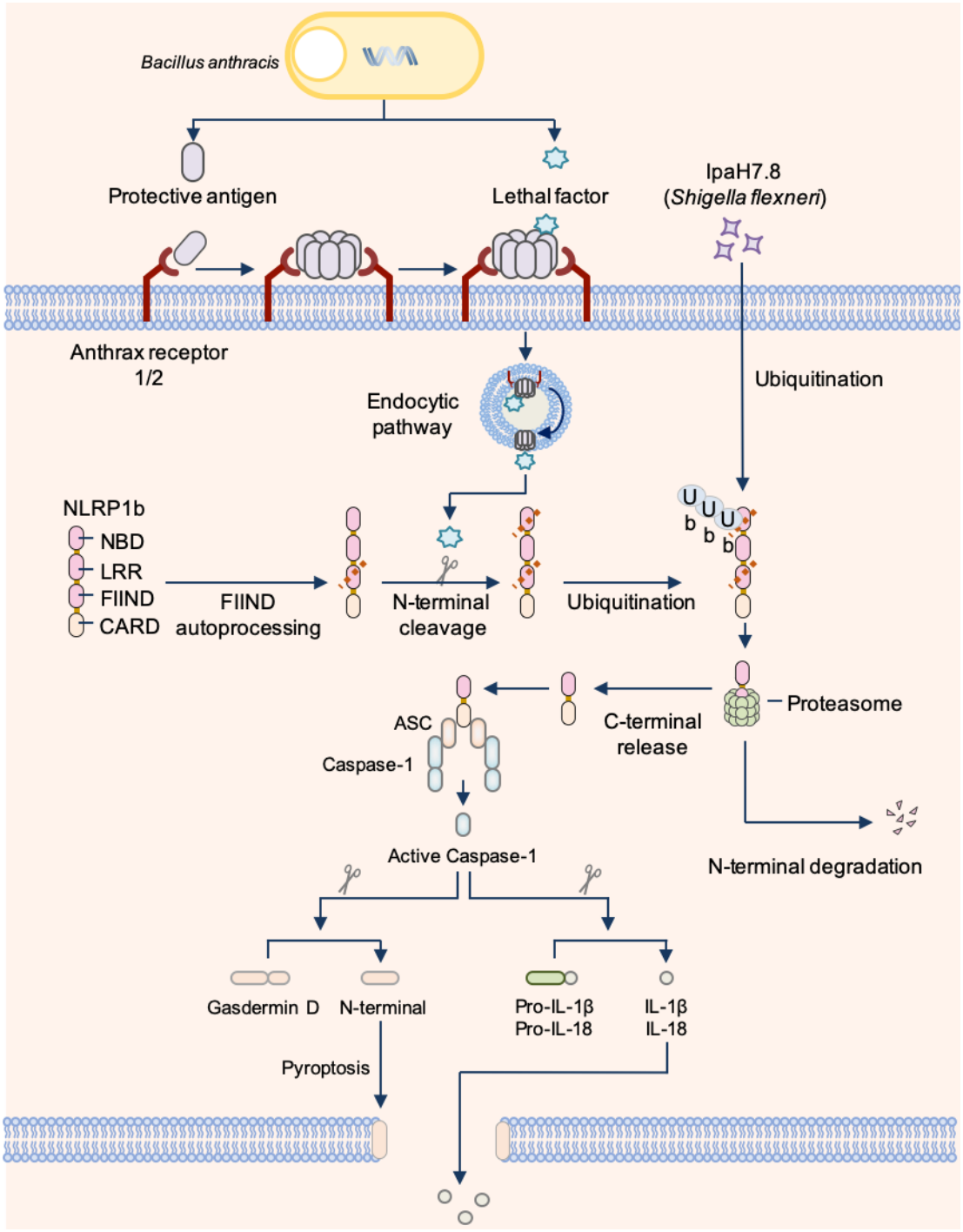

Figure 1.1 | NLRP1 inflammasome.

The NLRP1 inflammasome is activated through a series of proteolytic cleavage events. Firstly, the function-to-find domain (FIIND) undergoes autoproteolytic cleavage generating two fragments: N-terminal and C-terminal fragments. NLRP1b remains in an autoinhibitory state until a stimulus triggers subsequent cleavage and degradation of the inhibitory domain of NLRP1b. The anthrax lethal toxin released by the bacterium *Bacillus anthracis* is a composed of a protective antigen and a lethal factor. The protective antigen binds to its cognate receptors namely tumour endothelial marker-8 (TEM 8 also known as anthrax receptor 1) and capillary morphogenesis protein 2 (CMG2 also known as anthrax receptor 2). Receptor mediated endocytosis of the complex helps in the cytosolic delivery of lethal factor. The lethal factor directly cleaves NLRP1b at the N-terminal domain of the nucleotide-binding domain (NBD)-leucine-rich-repeat domain (LRR)-FIIND fragment. Subsequent ubiquitination by host E3 ligase licenses NLRP1b for proteasomal degradation. *Shigella flexneri* ligase IpaH7.8 can directly ubiquitinate NLRP1b that has undergone FIIND autoprocessing marking it for proteasomal degradation. Proteasomal degradation of the N-terminal fragment of NLRP1b liberates the activate C-terminal fragment (containing a caspase-activation and recruitment domain; CARD) which can initiate assembly of the NLRP1b inflammasome with or without ASC. Activated NLRP1b inflammasome trigger gasdermin D dependent pyroptosis and secretion of pro-inflammatory cytokines interleukin (IL)- 1β and -IL18. In response to a high dose of lethal factor, NLRP1b induces caspase-1-dependent cleavage of pro-IL-1β and pro-IL-18 and pyroptosis independently of ASC or caspase-1 self-proteolysis. In response to a low dose of lethal factor, NLRP1b assembles into an NLRP1b-ASC-Caspase-1 inflammasome complex that contributes to pro-IL-1β and pro-IL-18 processing.

1.3.3 Canonical NLRP3 inflammasome

NLRP3 is a global sensor of PAMPs and DAMPs due to its ability to sense diverse stimuli. NLRP3 is composed of an N-terminal PYD domain, a central NBD domain and a C-terminal LRR domain. The PYD domain of NLRP3 interacts with the PYD domain of ASC, allowing the CARD domain of ASC to recruit and bind to caspase-1 through CARD-CARD interaction [103]. The LRR domain contributes to autoinhibition of NLRP3, whereas the NBD domain is responsible for its oligomerisation [104]. Genome-wide associated studies of human populations have revealed that mutations in the gene encoding NLRP3 are linked to the development of Cryopyrin-associated periodic syndromes (CAPS), a spectrum of clinical manifestations that include muckle-wells syndrome, familial cold auto-inflammatory syndrome and neonatal-onset multisystem inflammatory disease [105-107]. NLRP3 has instrumental roles in the host defence against infection, and contributes to the pathogenesis of rheumatoid arthritis, gout, type 1 diabetes, obesity, cancer and neurodegenerative diseases [108].

1.3.3.1 Mechanisms of NLRP3 inflammasome activation

Activation of the canonical NLRP3 inflammasome normally requires two signals. The first signal, known as priming, upregulates the expression of the NLRP3 protein **(Fig. 1.2a)**. This priming process requires the engagement of TLRs, NOD2 or TNF receptors TNFR1 and TNFR2; all of these pathways initiate NF-kB-mediated expression of NLRP3 [109,110]. However, there is evidence to suggest that activation of the canonical NLRP3 inflammasome can be achieved without extensive priming [111,112]. Simultaneous exposure of unprimed mouse bone-marrow-derived macrophages (BMDMs) to TLRs and NLRP3 activators (LPS plus ATP, LPS plus nigericin or infection with *Listeria monocytogenes*) leads to activation of the NLRP3 inflammasome in 15 or 20 minutes in a manner dependent on the kinases IRAK1 and IRAK4 [111,112]. This rapid mode of activation of the canonical NLRP3 inflammasome allows for instigation of a quick inflammatory response to PAMPs and DAMPs.

The second signal resulting in full activation of the NLRP3 inflammasome is provided by a NLRP3 activator in the form of a PAMP or DAMP. The list of NLRP3 activators is extensive and includes Gram-positive and Gram-negative bacteria, bacterial toxins, DNA and RNA viruses, fungi and protozoa [113-123]. In addition, NLRP3 can sense a variety of DAMPs, including ATP, uric acid crystals, monosodium urate (MSU), silica crystals, saturated fatty acids, asbestos, extracellular histones, lysophosphatidylcholine, aluminium hydroxide and bee venom [110,113,124-130]. It is currently hypothesised that rather than direct binding of NLRP3 to the ligand, these ligands trigger a common set of cellular events that culminate in the activation of NLRP3. There are many proposed molecular mechanisms that lead to activation of the NLRP3 inflammasome **(Fig. 1.2a)**. These molecular mechanisms include potassium efflux via the purinergic receptor P2X7R and TWIK2 [131-135], lysosomal disruption resulting in the leakage of cathepsin B [125], ROS [136,137], oxidised mitochondrial DNA released from the mitochondria [136,138], cardiolipin translocation from the inner to outer membrane of mitochondria [139], recruitment of NLRP3 on dispersed trans-Golgi network [140], calcium influx and reduction in cellular cyclic AMP [141-143], sodium [144] and chloride ion fluxes [145,146], bacteria- or host-induced pores on the cell membrane [147] and modulation in cell volume [148]. Although potassium efflux was proposed to be the converging signal [137], a pathway leading to the activation of the NLRP3 inflammasome that does not require potassium efflux has been observed in response to TLR7 agonists imiquimod and CL097 [137].

Progress has been made to further identify novel components of the NLRP3 inflammasome. The kinase NEK7 is specifically required for the activation of the NLRP3 inflammasome [149-151] **(Fig. 1.2a)**. Phosphorylated NEK7 binds to the LRR domain of NLRP3 [149,151], suggesting that NEK7 may relieve autoinhibition of NLRP3. Overexpression studies revealed that NEK7 binds more strongly to NLRP3 carrying missense mutations associated with neonatal onset multisystem inflammatory disease compared to wild-type NLRP3 [151]. Additionally, NLRP3 can directly interact with the DEAD-box family member and helicase, DDX3X [152]. Under cellular

stress conditions such as exposure to nigericin, NLRP3 associated with DDX3X to initiate the assembly of an inflammasome complex [152].

1.3.3.2 NLRP3 inflammasome and other cell death pathways

Evidence suggest that the NLRP3 inflammasome can interact with inflammatory caspase such as caspase-1 and caspase-11 and apoptotic caspases such as caspase-8 [153]. The activity of the NLRP3 inflammasome can be both positively and negatively regulated by the apoptotic caspase, caspase-8. For example, caspase-8 and its adaptor FADD are required for priming and possibly activation of NLRP3 inflammasome in macrophages and DCs [154-166]. Caspase-8 is recruited to the inflammasome speck, indicating that it is a component of the canonical NLRP3 inflammasome complex [154,160]. Direct activation of caspase-1 by caspase-8 or redundant activation between caspase-1 and caspase-8 leading to the proteolytic processing of pro-IL-1β have also been reported [41,167-182]. By contrast, studies have also shown that caspase-8 suppresses the NLRP3 pathway in DCs [183]. Mouse DCs lacking caspase-8 and treated with LPS in the absence of the activation signal (also known as signal 2) results in the activation of the canonical NLRP3 inflammasome [183]. This effect was mediated by the receptor-interacting protein kinases, RIPK1 and RIPK3, the necroptotic effector MLKL and the phosphatase PGAM5 [183]. A further study has suggested that the caspase-8 inhibitor c-FLIP might form a complex with the NLRP3 inflammasome to mediate caspase-1 activation [184].

A link between the NLRP3 inflammasome and the necroptotic cell death pathway has emerged. In response to necroptotic activators, the kinase RIPK3 and the necroptotic effector MLKL are required to activate the NLRP3 inflammasome and induce IL-1β release [185,186]. In this case, MLKL oligomerises on the cell membrane to induce pore formation, resulting in necroptosis and a reduction in the level of intracellular potassium triggering activation of the NLRP3 inflammasome [185,186]. Of particular interest is that MLKL-dependent secretion of IL-1β does not rely on the pyroptosis executor GSDMD [185,186], suggesting that IL-1β might be

released through MLKL-induced pores instead. These studies further accentuate the complex interplay between the NLRP3 inflammasome and non-pyroptotic cell death pathways.

1.3.3.3 NLRP3 and post-translation modifications

Owing to the large number of stimuli which can activate NLRP3, post-translational modifications exist at multiple levels to modulate and fine-tune NLRP3 inflammasome activation. In resting macrophages NLRP3 is maintained in its inactive form via binding of its LRR domain to the ubiquitin ligase-associated protein SGT1 [187]. Similarly, NLRP3 is ubiquitinated and undergoes proteasomal degradation mediated by ubiquitin ligases SCF, FBXL2, tripartite motif-containing protein 31 (TRIM31), and membrane associated ring-CH-type finger 7 (MARCH7) [188-190]. For example, FBXL2 binds to the W73 residue within the PYD domain and the K689 residue within the LRR domain of NLRP3 and further ubiquitinates at the K689 residue within the LRR domain of NLRP3 [188]. Another E3 ligase called Ariadne homolog 2 (ARIH2) can ubiquitinate the NACHT domain of NLRP3, thereby negatively regulating activation of the NLRP3 inflammasome [191].

In addition to NLRP3 expression being induced by the priming step, NLRP3 is post-translationally activated by several mechanisms. Firstly, by degradation of the inhibitory ubiquitin ligase FBXL2 [188]. Alternatively, ubiquitination of residues, such as the Lys63 residue, within the NLRP3 protein that results in activation of NLRP3 [192]. Deubiquitination of residues within the NLRP3 protein responsible for inhibition of NLRP3 also provides a mechanism through which NLRP3 is activated [193-196]. For example, mouse deubiquitinase enzyme BRCC3 can deubiquitinate the K689 residue within the LRR domain of NLRP3 to switch it to a stimulus-sensing competent state [182]. Additionally, the UAF1/USP1 deubiquitinase complex has been reported to selectively remove K48-linked polyubiquitination of NLRP3 to prevent NLRP3 degradation by the proteasome [197]. Other components of the NLRP3 inflammasome such as ASC are ubiquitinated by the linear ubiquitination assembly complex (LUBAC) to initiate assembly of an inflammasome complex [198].

Another post-translational modification responsible for regulating NLRP3 is phosphorylation. TLR-mediated priming induces phosphorylation of NLRP3 on serine residues (Ser198 in human NLRP3 and Ser194 in mouse NLRP3) by the kinase MAPK8. This process results in self-association of NLRP3 [199]. Phosphorylation of Ser198 in human NLRP3 or Ser194 in mouse NLRP3 promotes binding of mouse deubiquitinase enzyme BRCC3 which promotes activation of NLRP3 as described above [196,199]. Another kinase, Syk, is also known to phosphorylate NLRP3 in response to fungal, malarial and mycobacterial pathogens, however the mechanistic details are not fully elucidated [200-203].

Stimulation with Signal 2 such as ATP and nigericin recruits protein kinase D (PKD) to the Golgi to phosphorylate NLRP3 on Ser295 (in human NLRP3; Ser291 in mouse NLRP3), thereby activating the NLRP3 protein to form an inflammasome complex [204]. Phosphorylation of key residues of mouse NLRP3 involved in NLRP3-ASC interaction are Ser3, Ser157 and Ser725 (human Ser5, Ser161 and Ser728) [205]. Mutagenesis of the human NLRP3 Ser5 residue located in its PYD domain to a phosphomimetic aspartate (Ser5Asp) completely abolishes NLRP3-dependent ASC speck formation [205]. However, mutagenesis of the other two serine sites in human NLRP3 (Ser161 and Ser728) had no effect on its association with ASC [205]. Furthermore, phosphorylation of Ser5 disrupts the electrostatic interaction between the PYD domains of NLRP3 and ASC [205], suggesting that phosphorylation of Ser5 prevents activation of the NLRP3 inflammasome at steady state. Dephosphorylation of Ser5 requires phosphatase 2A, leading to PYD-PYD interaction between NLRP3 and ASC [205].

Both sumoylation and nitrosylation of NLRP3 have been shown to negatively regulate the NLRP3 inflammasome. In steady state, NLRP3 is sumoylated at multiple sites by the E3 SUMO protein ligase MUL1 (also known as MAPL), which restricts activation of the NLRP3 inflammasome [206]. Desumolyation by sentrin-specific protease 6 (SENP6) and SENP7 is responsible for activation of the NLRP3 inflammasome [206]. In addition, NLRP3-mediated IL-1β release and speck formation is inhibited in the presence of NO donor SNAP or GSNO

which stabilises damaged mitochondria and provides protection against endotoxaemia [207]. Further, it was reported that thiol nitrosylation of NLRP3 resulted in inhibition of IL-1-mediated pathology in context of *M. tuberculosis* infection [208]. An inhibitory property of the NO donor, S-nitroso-N-acetylpenicillamine, towards the NLRP3 inflammasome has also been reported [209]. A plethora of other signalling components and cytokines has been shown to negatively regulate the expression or activation of the NLRP3 inflammasome, including CARD9, type I IFNs and IL-10 [210-212]. These diverse yet specific modifications target the NLRP3 inflammasome at various checkpoints, indicating the importance of tightly regulating this sensor of general stress and damage.

1.3.3.4 Therapies targeting NLRP3

Given the versatility of NLRP3 in sensing a multitude of PAMPs and DAMPs, various drug candidates have been developed against NLRP3. These drug candidates include MCC950 [213-215], Tranilast [216], glyburide [217], 16673-34-0 [218,219], JC124 [220], FC11A-2 [221] and OLT1177 [222]. Major caveats in the application of many of these inhibitors are as follows: (i) the largely elusive nature of their mode of action except the reported mechanism of MCC950-mediated inhibition of NLRP3 [213-215]; (ii) unknown target of drugs since many drugs indirectly modulate NLRP3 activity; (iii) potential off-target effects; (iv) lack of clinical evidence of safety and efficacy for majority of the reported inhibitors except MCC950, Inzomelid and Somalix which are under clinical trials for treatment of Parkinson's disease [223]. Therefore, further studies unravelling the molecular basis of inflammasome activation at a structural and biochemical level would inform translational studies.

1.3.4 Non-canonical NLRP3 inflammasome and caspase-11

The non-canonical NLRP3 inflammasome pathway is defined by a requirement for mouse caspase-11 and human caspase4 and caspase-5 in the activation of the NLRP3 inflammasome complex [224] **(Fig. 1.2b)**. Gram-negative bacteria including *Citrobacter rodentium, Escherichia coli, Vibrio cholera, Salmonella enterica* serovar Typhimurium,

Legionella pneumophila and *Yersinia pseudotuberculosis* are the major activators of the non-canonical NLRP3 inflammasome pathway [224-227]. Caspase-11, a murine inflammatory caspase, senses LPS in the cytoplasm [228,229]. The human analogs of caspase-11, caspase-4 and caspase-5, can likewise sense LPS [228] and initiate activation of the NLRP3 inflammasome and secretion of IL-1β and IL-18 [230-232]. Mouse caspase-11, human caspase-4 and human caspase-5 bind to the lipid A portion of LPS with high specificity and affinity via their CARD domain [228,229]. Caspase-11 can also be activated by transfection or electroporation of LPS into macrophages [224-226]. Activated caspase-11 cannot directly proteolytically process pro-IL-1β and pro-IL-18, but can induce pyroptosis without caspase-1 [224]. Pyroptosis mediated by caspase-11 provides effective host defence against cytosolic Gram-negative bacteria *in vivo* [226,233]. The enzymatic activity of caspase-11 along with that of caspase-1 synergistically restricts the growth of intracellular Gram-negative bacteria in macrophages, intestinal epithelial cells and fibroblasts [234-238].

1.3.4.1 Mechanisms of non-canonical NLRP3 inflammasome activation

The mechanisms regulating the activation of the non-canonical NLRP3 inflammasome are still being deciphered. LPS that has gained entry into the cytoplasm activates inflammatory caspases [224-226,239], allow them to directly cleave GSDMD, releasing the N-terminal fragment of GSDMD that drives pyroptosis (further discussed in the section 1.3.4) [50,51] **(Fig. 1.2b)**. Activation of caspase-11 leads to a drop in intracellular potassium levels sufficient to activate NLRP3 [240], highlighting that the non-canonical pathway might also have a dependency on potassium efflux. A further study suggested that LPS-induced activation of caspase-11 leads to caspase-11-dependent cleavage of the large-pore channel pannexin-1 [241], however, another study challenged this result by showcasing no role of pannexin-1 in activation of the non-canonical inflammasome activation [242]. As a result, ATP is released from the cell, activating the purinergic receptor P2X7R to drive pyroptosis [240]. Opening of the pannexin-1 pore also generates potassium efflux that induces IL-1β release [241], providing an explanation for how gasdermin D might activate the NLRP3 inflammasome to mediate secretion of IL-1β.

However, it remains unclear how the Caspase-11–Pannexin-1–P2X7R model leads to pyroptosis and how this pathway amalgamates with the Caspase-11–Gasdermin D model.

Caspase-11 has been proposed to recognise ligands other than LPS. Caspase-11 binds to host-derived oxidised phospholipids (oxPAPC) in activated mouse dendritic cells [243]. LPS and oxPAPC elicited caspase-11-induced inflammasome speck formation and IL-1β release, but not pyroptosis, in dendritic cells [243,244]. In contrast, another study has shown that oxPAPC inhibited the non-canonical inflammasome in mouse macrophages and human macrophages but not in mouse dendritic cells [245]. This study further suggests that, in mouse macrophages, oxPAPC competed with LPS for caspase-11 binding [245]. These studies highlight how different cell types may respond to the same stimulus. In addition, caspase-11 contributes to resistance to the fungal pathogen *Aspergillus fumigatus* in vivo [246], revealing a biological role for caspase-11 in host defence against pathogens other than Gram-negative bacteria. Overall, substantial advances have been made in our understanding of the non-canonical NLRP3 inflammasome. It is likely that caspase-11 has the potential to recognise additional stimuli. Further studies are therefore required to provide a more complete picture of the role of the non-canonical NLRP3 and caspase-11 pathway in infection and sterile inflammation.

1.3.4.2 Regulation of the non-canonical NLRP3 inflammasome

Earlier studies have identified type I IFN signalling as an important signal for the activation of the non-canonical NLRP3 inflammasome [247-249]. The mechanism underlying the essentiality of type I IFN signalling in the activation of the non-canonical NLRP3 inflammasome has been revealed **(Fig. 1.2b)**. Recognition of LPS by TLR4 initiates TRIF-mediated type I IFN signalling, leading to an increased expression of caspase-11 and NLRP3 [247-249]. A further study has shown that the complement-related peptidase, carboxypeptidase B1 induces expression of caspase-4, caspase-5 and caspase-11 downstream of the TLR4 and type I IFN signalling pathway [250]. Type I IFNs induce the expression of IFN-inducible GTPases, including guanylate-binding proteins (GBPs) and Immunity-related GTPases (IRGs). GBPs are 65- to

67-kDa proteins conserved across species, with 7 GBPs in humans and 11 GBPs in mice [251]. In the context of inflammasome biology, GBPs encoded on mouse chromosome 3 (GBP1, 2, 3, 5 and 7) are required for activation of the non-canonical NLRP3 inflammasome induced by *S.* Typhimurium and *L. pneumophila* [252,253]. In addition, human GBP1 was reported to coat the surface of *S.* Typhimurium, leading to the recruitment of GBP2, GBP3 and GBP4 in human HeLa cells [254-256]. GBP1 can also bind the LPS of *Shigella flexneri* to unmask the lipid A moiety for recruitment of caspase-4 [257]. Decoration of GBPs on the bacterial surface induced localisation of caspase-4 on the same protein platform and binding to LPS [258], however, further studies are required to elucidate the structural basis of this GBP-LPS-Caspase-4 complex.

GBPs are also recruited to the vacuole surrounding intracellular bacterial pathogens, where they facilitate lysis of the vacuolar membrane such that LPS is leaked into the cytoplasm for detection by caspase-11 [252]. GBPs also direct IRGB10 to the cell membrane of Gram-negative bacteria to induce bacteriolysis, thereby increasing the cytosolic accessibility of LPS for detection by caspase-11 [259]. In addition to GBP-mediated liberation of LPS from intracellular bacteria, LPS can gain entry into the cytosol through other modes of delivery, such as through LPS-containing outer-membrane vesicles (OMVs) [239] and LPS coated with host high-mobility group box 1 (HMGB1) protein [260]. There is also evidence to suggest that GBPs encoded on mouse chromosome 3 facilitate activation of both non-canonical and canonical inflammasomes in macrophages infected with *Chlamydia muridarum* [261]. In this case, GBPs bound neither the vacuole surrounding *C. muridarum* nor the pathogens [261], suggesting an alternative mechanism of GBPs in the regulation of inflammasome activity.

1.3.5 Gasdermin D

The molecular mechanisms of how pyroptosis is executed following inflammasome activation are being revealed. The current view is that inflammatory caspases cleave the pore-forming protein GSDMD, yielding a 31-kDa N-terminal fragment which drives pyroptosis [50-52] **(Fig. 1.2b)**. The N-terminal fragment also engages activation of the NLRP3 inflammasome via an

undefined mechanism during caspase-11 activated non-canonical NLRP3 inflammasome. Various studies have since identified a capacity for GSDMD to oligomerise on the cell membrane [53-57]. The N-terminal fragment associates with the inner leaflet of the host cell membrane where it forms pores of 10-21 nm in diameter [53-57]. GSDMD-induced pyroptosis allows the passive release of proteolytically processed IL-1β and IL-18 and the cell death marker lactate dehydrogenase enzyme (LDH) into the extracellular space [50-52]. In response to certain activators such platelet-activating factor, silica and MSU, IL-1β is released from the cells independently of GSDMD [262,263]. Further studies are required to comprehensively elucidate the processes by which cytokines can be secreted in a GSDMD-dependent and -independent manner.

The N-terminal fragment of GSDMD also binds to lipids on bacterial cell membranes, creating pores on the bacterial cell membrane as a mechanism to exert antimicrobial activity [53,55,56]. Previous studies have argued that the primary bactericidal mechanism of pyroptosis is its ability to liberate whole bacteria or bacteria entrapped within pore-induced intracellular traps from mouse macrophages, such that these entities are phagocytosed and killed by neutrophils [235,264]. However, in mouse neutrophils, caspase-11 or proteases such as neutrophil elastase can directly cleave GSDMD, leading to cell death and/or release of neutrophil extracellular traps [265,266], suggesting cell-type-specific activity of GSDMD.

It is worthy to note that, in some cases, release of IL-1β could occur prior to pyroptosis or even in the absence of pyroptosis [267]. Formation of low numbers of GSDMD pores function as a conduit for the release of IL-1β, but are unable to induce pyroptosis [244]. In addition, GSDMD pores have been observed to mediate Ca^{2+} influx which signals the recruitment of endosomal sorting complexes required for transport (ESCRT) machinery to initiate repair and restoration of cell membrane integrity in both murine and human cells [268]. In particular, the ESCRT machinery removes GSDMD pores from the plasma membrane [268], highlighting a regulatory mechanism to restrict GSDMD-dependent cell death and cytokine release.

1.3.5.1 GSDMD and other cell death pathways

GSDMD might also have functions in inhibiting apoptosis. Canonical activation of the inflammasome induces apoptosis in the absence of GSDMD [52]. It has also been suggested that in the absence of GSDMD, induction of apoptosis requires caspase-1-mediated activation of caspase-3 and caspase-7 [269]. Site-specific cleavage of GSDMD has been suggested to dictate the functionality of GSDMD in pyroptosis and apoptosis. Inhibition of serine peptidases DPP8 and DPP9 leads to activation of caspase-1, cleavage of GSDMD and pyroptosis [95]. However, in response to classical apoptotic signals, activated caspase-3 and caspase-7 cleave GSDMD at residue Asp87, a different site to that cleaved by inflammatory caspases [269]. The resultant p45 GSDMD fragment is inactive and cannot engage pyroptosis, allowing GSDMD-mediated apoptosis to ensue [269]. In primary mouse macrophages infected with *Yersinia,* GSDMD is cleaved by caspase-8 instead of caspase-1 or caspase-11. *Yersinia* outer protein (YopJ) inhibited kinase TAK1 and IKK which elicited RIPK1- and caspase-8-dependent pyroptosis [270,271], demonstrating a new mechanism of GSDMD processing. Similar results were observed in primary mouse macrophages stimulated with TNF and an antagonist of inhibitor of apoptosis proteins, AZD5582, in which caspase-8 induced GSDMD cleavage and LDH release [272,273]. In the absence of GSDMD, caspase-8-mediated apoptosis or RIPK3-mediated necroptosis was triggered, highlighting the redundancy between different cell death pathways [270]. A related gasdermin member, gasdermin E, has also been reported to mediate cross-regulation between pyroptosis and apoptosis [274], showcasing central roles of gasdermins in controlling cell death.

1.3.5.2 Therapies targeting GSDMD

There is a growing appreciation of the role of GSDMD in infectious and inflammatory diseases. For example, mice deficient in GSDMD had increased susceptibility to infections with either *S. enterica* subsp. *enterica* serovar Typhimurium Δ*SifA* (this mutant is unable to maintain the pathogen-containing vacuole, and therefore, aberrantly enters the cytoplasm to activate caspase-11) or *Brucella abortus* [275,276]. Similarly, mice deficient in GSDMD harbouring the

familial Mediterranean fever (FMF)-associated *Mefv*^{V276A} allele of Pyrin did not develop the autoinflammatory symptoms [277]. In addition, in mice expressing the Asp301Asn gain-of-function mutation of NLRP3, additional deficiency of GSDMD prevented development of the neonatal-onset multisystem inflammatory disease-associated symptoms [278]. The Food and Drug Administration (FDA) approved drug called disulfiram was found to inhibit pyroptosis and cytokine release from primary murine macrophages and protected mice from LPS-induced endotoxaemia [279]. Another study demonstrated that the metabolites dimethyl fumarate (DMF) and endogenous fumarate negatively regulated GSDMD by succination of a critical cysteine residue Cys[192] [280]. Succination of GSDMD restrained the interaction between GSDMD and inflammatory caspases, thereby limiting the ability of GSDMD to induce pyroptosis [280]. Administration of DMF protected mice against endotoxaemia and alleviated FMF and experimental autoimmune encephalitis [280]. These findings highlight the importance of GSDMD in inflammation and immunity, and identified new therapeutic targets for the treatment of inflammasome-associated diseases.

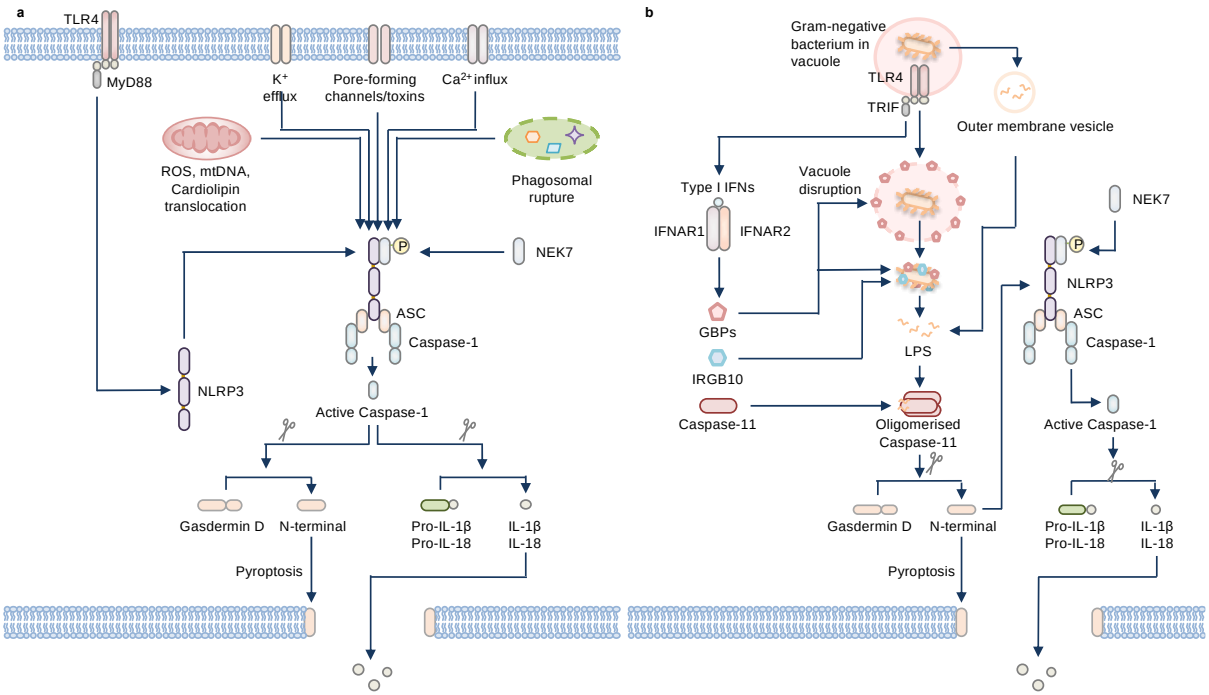

Figure 1.2 | Canonical and non-canonical NLRP3 inflammasomes.

(a) Activation of the canonical NLRP3 inflammasome requires a priming signal (also known as signal 1), often mediated by Toll-like receptors (TLRs) and activation of NF-κB, inducing the expression of NLRP3. An activating signal (also known as signal 2) is provided by pathogen-associated molecular patterns (PAMPs) or danger-associated molecular patterns (DAMPs). PAMPs and DAMPs cause physiological aberrations in the cell, which manifest in the forms of ion efflux and influx, mitochondrial dysfunction or rupture of the phagosome. These physiological alternations are sensed by NLRP3, which induces the assembly of the NLRP3 inflammasome mediated by the kinase NEK7, ASC and caspase-1. Caspase-1 cleaves gasdermin D, releasing the N-terminal fragment of gasdermin D that assembles into pores on the membrane resulting in pyroptosis. Active caspase-1 also cleaves pro-IL-1β and pro-IL-18, which are secreted through the pores formed by gasdermin D. **(b)** The non-canonical NLRP3 inflammasome is specifically activated by Gram-negative bacteria. LPS from Gram-negative bacteria is recognized by TLR4 via the adaptor TRIF, resulting in the production of type I interferons (IFN). Type I IFNs induce the expression of IFN-inducible proteins GBPs and IRGB10, and caspase-11. GBPs rupture the pathogen-containing vacuole causing aberrant release of the bacteria into the cytoplasm, and both GBPs and IRGB10 are recruited to the bacteria to disrupt and the kill the pathogen. LPS can also be released into the cytoplasm via bacterial outer membrane vesicles. Liberated LPS binds to caspase-11, promoting oligomerisation and activation of caspase-11. Active caspase-11 cleaves gasdermin D to induce pyroptosis. The N-terminal fragment of gasdermin D also induces activation of the NLRP3 inflammasome and secretion of IL-1β and IL-18.

1.3.6 NAIP-NLRC4 inflammasome

The NAIP-NLRC4 inflammasome is activated by cytosolic flagellin [281-285] and by both the basal body rod [286,287] and needle [288,289] proteins of the type 3 secretion systems (T3SS) of many Gram-negative bacteria **(Fig. 1.3)**. Further studies have clarified the relationship between NAIP proteins and NLRC4, showing that NAIP proteins dictate the ligand specificity of the NLRC4 inflammasome [290-293]. Indeed, earlier studies have shown that NAIP5 is required in sensing flagellin [284,294-297] and instigating host response to the intracellular pathogen *L. pneumophila* [298-301]. Of the seven NAIP proteins encoded by the mouse genome [302], NAIP1 and NAIP2 recognise the needle and rod protein components of bacterial T3SS, respectively [287-290,293], while both NAIP5 and NAIP6 recognise flagellin [290,293,296]. Analysis of chimeric NAIP proteins mapped the ligand-binding site to the NBD domain [303] rather than the LRR domain which was thought to be responsible for ligand recognition in most NLR family proteins. The functions of the remaining murine NAIP proteins namely NAIP3, NAIP4 and NAIP7 remain uncharacterised.

Interferon regulatory factor 8 (IRF8) was reported to partially regulate transcription of genes encoding NAIPs in mice [304]. Unlike mice, humans encode a single NAIP protein which was initially thought to be functionally similar to murine NAIP1, in that it binds directly to the needle protein of bacterial T3SS to activate the NLRC4 inflammasome [288,289]. However, a later study has shown that human NAIP might also be able to recognise flagellin [305], highlighting the functional versatility of human NAIP compared to its murine counterparts **(Fig. 1.3)**.

The biological effect of NAIP-NLRC4 inflammasome activation varies with cell type. Unlike macrophages, which undergo rapid pyroptosis following activation of the NAIP-NLRC4 inflammasome, neutrophils release IL-1β without undergoing pyroptosis [306]. It is possible that the pyroptosis-resistant phenotype of neutrophils enables sustained killing of bacteria. The interplay between cell types driven by the NAIP-NLRC4 inflammasome can also be observed between DCs and T cells. NLRC4-driven IL-1β and IL-18 production in DCs infected with *S*.

Typhimurium and other Gram-negative bacteria can stimulate the production of IFN-γ in non-cognate memory $CD8^+$ T cells [307].

1.3.6.1 Structural analysis of the NAIP-NLRC4 inflammasome

NLRC4 consists of an N-terminal CARD domain, a centrally located NBD domain and a C-terminal LLR domain [308]. The CARD domain of NLRC4 can directly interact with the CARD domain of procaspase-1, generating a NLRC4-Caspase-1 inflammasome complex that is sufficient to induce pyroptosis and processing of pro-IL-1β and pro-IL-18 in the absence of ASC [40,42,286,309-312]. However, the NLRC4-ASC-Caspase-1 inflammasome has also been observed endogenously in macrophages [41], highlighting the compositional diversity of the NLRC4 inflammasome **(Fig. 1.3)**. In this case, ASC enhances proteolytic cleavage and release of IL-1β and IL-18 [40-42,311-314].

The structures of monomeric or inactive NLRC4 [315] and NLRC4 complexed with either flagellin and NAIP5 [316] or with T3SS rod protein and NAIP2 [317,318] have been determined by crystallography and cryogenic electron microscopy. The crystal structure of inactive mouse NLRC4 showed that the LRR domain sterically occludes the NBD domain [315], revealing an autoinhibitory function of the LRR domain. By contrast, the active structures of NLRC4 in complex with either NAIP2 [317,318] or NAIP5 [316] showed that NLRC4 undergoes a conformational change, exposing an oligomerisation surface to which inactive NLRC4 subunits can be recruited and bind to form a “disc” structure.

1.3.6.2 Regulation of NAIPs and NLRC4

Phosphorylation of NLRC4 at residue Ser533 by the kinase PKCδ was initially found to be critical for activation of the NLRC4 inflammasome in macrophages in response to *S.* Typhimurium infection or flagellin [319] **(Fig. 1.3)**. Further studies found that phosphorylation of NLRC4 at residue Ser533 by PKCδ occurs independently of activation of NAIP5 by flagellin [320,321]. This finding suggests that phosphorylation of NLRC4 at residue Ser533 and binding of

NAIP5 to its cognate ligand are unrelated events. A further study argued that activation of the NAIP-NLRC4 inflammasome in macrophages infected with either *S*. Typhimurium or *S. flexneri* was independent of PKCδ [287]. With identification of leucine-rich repeat kinase 2 (LRRK2) as an additional kinase that can also phosphorylate Ser533 of NLRC4 [321], it is plausible that there is a partial redundancy between the LRRK2 and PKCδ, explaining why activation of the NLRC4 inflammasome can occur independently to PKCδ [287].

The complexity of the mechanisms regulating activation of the NAIP-NLRC4 inflammasome was further addressed. Both NLRC4 and NLRP3 can colocalise within a single inflammasome complex in macrophages infected with *S*. Typhimurium [41,42]. To clarify the relationship between phosphorylation of NLRC4 at residue Ser533 and activation of the inflammasome, Qu and colleagues mutated Ser533 to an alanine (Ser533A) and assessed the effect of this modification on NLRC4 inflammasome activity. The Ser533A mutation abolished phosphorylation of NLRC4 at this residue but only delayed activation of caspase-1 in response to *S*. Typhimurium infection [322]. However, genetic deletion of NLRP3 in macrophages carrying the NLRC4 Ser533A mutation further reduced caspase-1 activation and cleavage of pro-IL-1β in response to infection with *S*. Typhimurium or transfection with flagellin, compared with macrophages carrying the NLRC4 Ser533A mutation alone [322]. These results indicate that recruitment of NLRP3 to the NLRC4 inflammasome might enhance caspase-1 activation, highlighting the dynamic interplay that exists amongst NLRs within the inflammasome.

A later study found no role for phosphorylation of Ser533 of NLRC4 in mediating NLRC4 inflammasome activation and recruitment of NLRP3 to the inflammasome [323]. Nonetheless, the cooperativity between NLRC4 and other NLRs in inflammasome activation has also been observed in contexts other than infection. For instance, mouse macrophages exposed to hyperosmotic stress produce IL-1β in a manner dependent on both NLRC4 and NLRP3 inflammasome activity [324]. Likewise, NLRC4 and NLRP3 mediate sterile inflammasome activation in microglia and astrocytes in response to the DAMP lysophosphatidylcholine [129].

Further, in a rodent model of stroke, the NLRC4 and AIM2 inflammasomes contribute to ischemic brain injury [325].

1.3.6.3 NLRC4 inflammasome and intestinal immunity

In the gastrointestinal tract, activation of the NAIP-NLRC4 inflammasome in intestinal epithelial cells exposed to *S*. Typhimurium or flagellin leads to cell expulsion from the epithelium [60,326]. Selective activation of the NAIP-NLRC4 inflammasome in intestinal epithelial cells stimulated cell expulsion and release of eicosanoids and cytokines in a manner that did not absolutely require caspase-1 or gasdermin D [326]. Instead, caspase-8 was able to compensate in caspase-1-deficient mice and cause cell expulsion of intestinal epithelial cells infected with *S*. Typhimurium [326]. This NLRC4-driven response provides host protection against invading pathogens such as *S*. Typhimurium by shedding infected cells into the intestinal lumen.

NLRC4 has also been shown to facilitate discrimination between commensal and pathogenic bacteria in the intestine by producing IL-1β in response to *S.* Typhimurium and *P. aeruginosa* but not commensal bacteria [327]. Indeed, expression of NLRC4 in the intestinal epithelial cells of mice protects against infection by the enteric pathogen *C. rodentium* [328]. Similarly, NAIP-NLRC4-deficient mice are highly susceptible to oral-gastrointestinal infection of *Shigella flexneri* [329]. A further biological effect of the NAIP-NLRC4 inflammasome is its ability to sustain the level of the growth hormone IGF-1 in white adipose tissue to promote the protective effect of a commensal *E. coli* O21:H+ strain against muscle wasting induced by the pathogenic bacteria *B. thailandensis* [330]. However, uncontrolled activation of the NAIP-NLRC4 inflammasome is detrimental and leads to systemic inflammation and rapid sepsis-like death in mice infected with an *E. coli* pathobiont [331]. Likewise, systemic activation of the NLRC4 inflammasome by flagellin leads to rapid production of inflammatory lipid eicosanoids, loss of vascular fluid and death in mice [332]. Cross-regulation between *S.* Typhimurium and the NLRC4 inflammasome to control the inflammatory response has been reported. During early stages

of infection, the release of lysophospholipids controlled by the NLRC4 inflammasome enhances the expression of flagellin, thereby amplifying the innate immune response [333]. In contrast, at later stages of infection, TRIF-dependent production of type I IFNs represses NLRC4 and lysophospholipid biosynthesis, leading to an indirect down-regulation of flagellin expression by *S.* Typhimurium and dampening of the innate immune response [333]. These studies showcase an immuno-modulatory function of NLRC4 during *S.* Typhimurium infection.

1.3.6.4 Independent functions of NAIPs and NLRC4

Since the NAIP-NLRC4 inflammasome is activated in response to specific bacterial ligands in the context of infection, it is possible that NAIP and NLRC4 may be activated differentially in response to other contextual cues [334-337]. Indeed, mouse NAIPs have been proposed to have NLRC4-independent functions [335]. In this case, NAIPs might suppress the transcription factor STAT3 and cell proliferation in the intestinal epithelium in response to carcinogen exposure [335]. On the other hand, NLRC4 might function independently of NAIPs or the inflammasome during colorectal tumorigenesis through a mechanism that targets inhibition of apoptosis [334]. Furthermore, NLRC4 mediates the production of cytokines and chemokines in tumour-associated macrophages and induces the generation of protective T cell responses independently of the inflammasome in response to melanoma tumour growth [337]. Further, the nucleotide metabolites adenine and N^4-acetylcytidine have been shown to activate the NLRC4 inflammasome in elderly individuals and contribute to the development of arterial hypertension [338]. Additional studies are required to fully understand the distinct molecular mechanisms governing NAIP and NLRC4 activation in conditions other than infectious diseases.

1.3.6.5 NLRC4 and human diseases

Several disease-association mutations of NLRC4 have been identified in humans and mice. Identification of these mutations has contributed to our understanding of the molecular mechanisms regulating activation of the NLRC4 inflammasome. Several gain-of-function

missense mutations in the highly conserved NBD domain of NLRC4 have been observed, including Val341Ala [339], Thr337Ser [340] and His443Pro [341]. Macrophages carrying each of these NLRC4 mutants undergo spontaneous inflammasome formation, constitutive activation of caspase-1 and pyroptosis, and produce increased levels of IL-1β and IL-18 [339-341]. Collectively, these studies highlight the importance of the LRR domain in holding NLRC4 in an autoinhibited state and indicate that mutations in the NBD domain that interrupt LRR domain binding lead to constitutive activation of NLRC4. Further, a study has shown that NLRC4 carrying the His443Pro mutation induces spontaneous caspase-8-dependent apoptosis in human lung epithelial cells [342], confirming a role of NLRC4 in a non-pyroptotic cell death pathway. This finding is in line with an earlier study that identified human proteasome protein Sug1 as a binding partner of NLRC4 that potentiates a caspase-8 dependent cell death pathway by ubiquitinating NLRC4 [343].

Indeed, the NLRC4 mutations mentioned previously cause severe autoinflammatory syndromes when present in humans. Carriers of NLRC4 mutant His443Pro develop familial cold autoinflammatory syndrome [341]. Similarly, two activating missense mutations in NLRC4 (Thr337Ser and Val341Ala) led to the development of severe enterocolitis [339] and recurrent macrophage activation syndrome [340], respectively. All three cases were characterised by constitutive caspase-1 activation and by release of IL-1β and IL-18, indicating that the NLRC4 inflammasome was hyperactive in these patients. Of translational importance is that a patient suffering from life-threatening macrophage activation syndrome caused by NLRC4 mutation Val341Ala was treated with recombinant human IL-18-binding proteins [344]. Within four days of first treatment, the patient's overall demeanour improved, and the patient remained well after 11 months of combined IL-1β and IL-18 blockade [344]. This case report provides an elegant example of how investigations into the molecular mechanisms controlling activation of NLRC4 could lead to therapeutic success in the treatment of human diseases.

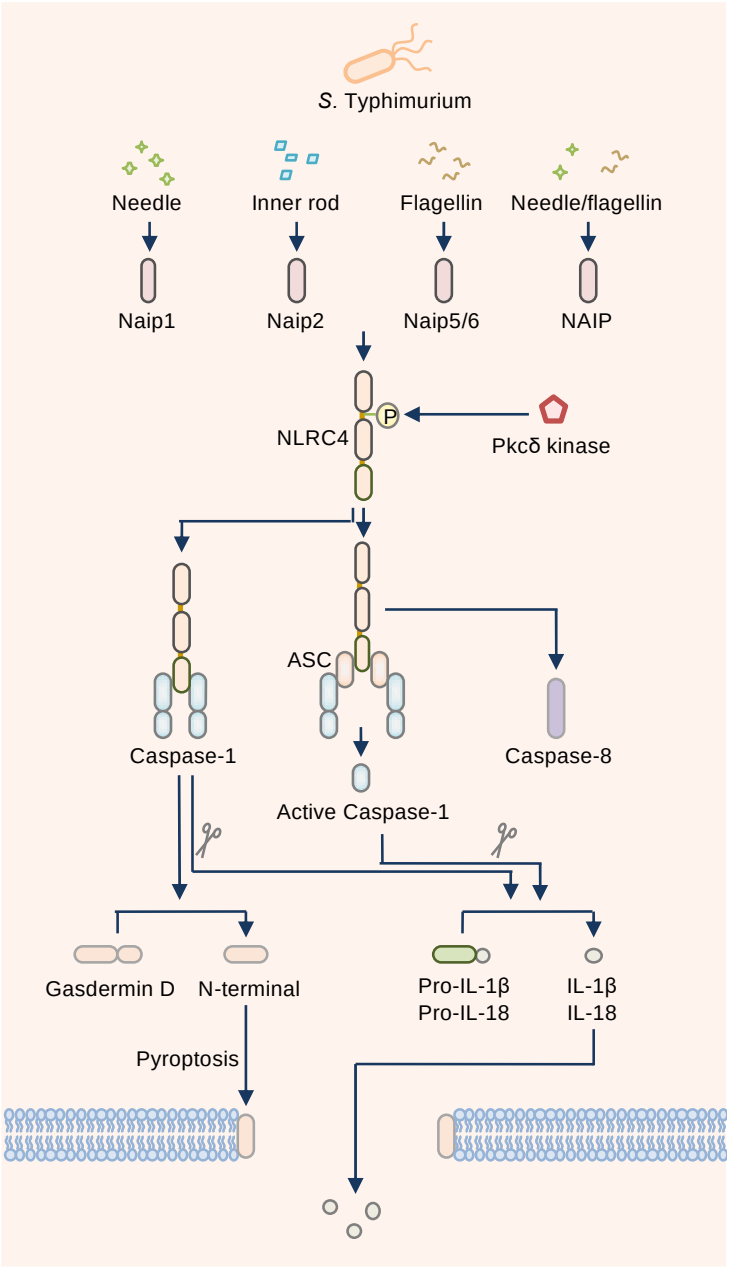

Figure 1.3 | NAIP-NLRC4 inflammasome.

Pathogenic bacteria such as *Salmonella enterica* serovar Typhimurium deliver effector proteins via the Type 3 Secretion System (T3SS). This process leads to the injection of T3SS needle protein, inner rod protein, and flagellin into the cytoplasm for detection by mouse NAIPS or human NAIP. Mouse NAIPS or human NAIP interacts with NLRC4, inducing a conformational change in NLRC4 that catalyzes the recruitment of additional NLRC4 proteins to form a “disc” structure. Phosphorylation of NLRC4 by the kinase Pkcδ downstream of

ligand-NAIP interaction may contribute to full activation of the inflammasome. The NAIP-NLRC4 complex assembles into a NAIP-NLRC4-Caspase-1 inflammasome or a NAIP-NLRC4-ASC-Caspase-1 inflammasome. The NAIP-NLRC4-Caspase-1 inflammasome cleaves gasdermin D, unleashing the N-terminal fragment of gasdermin D that mediates pyroptosis. Both the NAIP-NLRC4-Caspase-1 and NAIP-NLRC4-ASC-Caspase-1 inflammasomes induces caspase-1-dependent proteolytic cleavage of pro-IL-1β and pro-IL-18. The NAIP-NLRC4 inflammasome also induces caspase-8-dependent cell death.

1.3.7 AIM2 inflammasome

AIM2 is a cytoplasmic innate immune sensor of dsDNA capable of forming an inflammasome complex with ASC and pro-caspase-1 [345-348] **(Fig. 1.4)**. AIM2 consists of a C-terminal dsDNA-binding HIN-200 domain and an N-terminal PYD domain [349]. The dsDNA recognised by AIM2 is not sequence-specific but must be at least 80 base pairs in length [350]. In fact, AIM2 binds faster to longer dsDNA (300 bp) compared to 80 bp dsDNA and discerns shorter dsDNA as 'noise', suggesting that the length of dsDNA dictates the formation of AIM2 inflammasome [351]. The crystal structure of AIM2 provides insight into the mechanism of activation of AIM2. In an inactive conformation, the HIN-200 domain of AIM2 interacts with the PYD domain in an autoinhibitory fashion [352]. The release of the AIM2 PYD domain upon binding dsDNA allows for oligomerisation of AIM2 along the DNA [353] and interaction with the PYD domain of ASC [350]. Others have found that the PYD domain facilitates self-oligomerisation of AIM2 and induces activation of the AIM2 inflammasome [354,355].

While AIM2 is constitutively expressed and maintained in an autoinhibitory conformation in resting cells [356], other host-specific mechanisms exist to ensure tight regulation of the AIM2 inflammasome. AIM2 can be tagged for degradation by the regulatory protein TRIM11 and the autophagy-associated protein p62 [357,358]. Furthermore, several proteins that inhibit activation

of the AIM2 inflammasome are also produced by the cell, including the PYD-containing proteins POP1 [359] and POP3 [360] in humans, and the HIN domain-containing protein p202 in mice [348,361-364] **(Fig. 1.4)**.

1.3.7.1 Microbial activators of the AIM2 inflammasome

The AIM2 inflammasome provides immune surveillance for a subset of bacteria – including *Francisella tularensis*, *Francisella novicida, Streptococcus pneumoniae*, *Mycobacterium* species, *L. monocytogenes*, *Chlamydia muridarum*, *Porphyromonas gingivalis*, *Brucella abortus* and *L. pneumophila* [365]. The AIM2 inflammasome is also activated upon infection with the malaria parasite *Plasmodium*, the fungal pathogen *A. fumigatus* and the dsDNA viruses namely cytomegalovirus (CMV) and vaccinia virus [365].

The mechanisms of AIM2 activation and its dependency on type I IFNs differ depending on the pathogen encountered by the cell. Infection by MCMV is sufficient to directly activate the AIM2 inflammasome in macrophages without a requirement for type I IFN signalling, a phenotype which is recapitulated by activation of the AIM2 inflammasome via transfection of naked dsDNA into the cytoplasm of macrophages [366,367]. It is likely that viral DNA is directly exposed to AIM2 in the cytoplasm during infection with MCMV. By contrast, type I IFN signalling is important for AIM2 inflammasome activation in response to intracellular bacterial pathogens [261,366,368-372].

Activation of the AIM2 inflammasome can be inhibited by certain pathogens. For example, the human bacterial pathogen *Mycobacterium tuberculosis*, but not the non-virulent species *Mycobacterium smegmatis*, inhibits the production of IFN-β and thereby prevents activation of the AIM2 inflammasome [371]. *L. pneumophila* encodes the effector protein SdhA, which maintains the integrity of the *Legionella*-containing vacuole [373], and therefore prevents release of PAMPs such as dsDNA into the cytoplasm for sensing by the AIM2 inflammasome. The human viral pathogen HCMV produces a tegument protein pUL83 that directly interacts with AIM2 to prevent inflammasome activation [374]. Interestingly, *F. novicida* encodes a Cas9-

dependent CRISPR-Cas system that enhances envelope integrity [375], thereby promoting evasion of AIM2 inflammasome immune response by potentially resisting GBP- and IRGB10-mediated bacteriolysis. The prevalence of AIM2 inhibitory mechanisms employed by pathogens to escape innate immune recognition highlights the importance of the AIM2 inflammasome in sensing of PAMPs and clearance of pathogens.

1.3.7.2 Regulation of AIM2 inflammasome activation

The molecular mechanisms underlying the differential requirement for IFN signalling between bacteria and viruses has begun to be unravelled **(Fig. 1.4)**. In *Francisella* infection, a small quantity of bacterial DNA is released which is sufficient to activate the DNA sensors cGAS, STING and IFI204 and promote type I IFN production, but not sufficient to activate AIM2 [356,366,376]. Type I IFNs released from cells bind the type I IFN receptor subunits IFNAR1 and IFNAR2 in an autocrine or paracrine manner, promoting signal transduction via the IFN-stimulated gene factor 3 (ISGF3 – which is composed of subunits STAT1, STAT2 and IRF9) to upregulate the production of hundreds of IFN-inducible genes. Of these families of genes, the genes encoding GBP members GBP2, GBP5 and GBP1 and IRG member IRGB10 are upregulated by the type I IFN pathway via the transcription factor IRF1 [256,259,366,372]. GBPs and IRGB10 actively attack and lyse bacterial cells, releasing bacterial DNA into the cytoplasm which activates the AIM2 inflammasome [259,366,372] **(Fig. 1.4)**. It is currently unclear why DNA released upon initial infection can activate the cGAS and STING signalling axis but not AIM2. It is possible that the small amount of DNA released initially is not sufficient to activate AIM2 but is sufficient to upregulate IFN-inducible and host defence proteins to orchestrate cell-autonomous immunity and to avoid premature cell death. However, if a cell is unable to control bacterial replication, a larger amount of DNA is liberated by GBPs and IRGB10 to a level sufficient to trigger activation of the AIM2 inflammasome, resulting in pyroptotic demise of the cell and removal of a replicative niche that would have supported further bacterial growth.

DNA released from damaged or dying cells during infection could also lead to activation of the AIM2 inflammasome. For example, host-derived DNA molecules are liberated from virus-infected cells and accumulate in the lungs following infection by the RNA virus influenza A virus (IAV). A study has shown that that AIM2-deficient mice infected with IAV exhibited attenuated lung injury and significantly improved survival compared to wild-type mice [377]. Another study, however, showed that AIM2-deficient mice had increased susceptibility to IAV infection owing to increased numbers of infiltrating leukocytes and exaggerated immune response [378]. The strikingly different host susceptibility to infection by IAV observed in these two studies could be owing to the different source and infection dose of the virus, as well as differences in the microbiota composition at different animal facilities. Nevertheless, these findings collectively demonstrate that AIM2 can also function as a sensor of DAMPs, in that it activates the inflammasome in response to self-DNA. However, activation of the AIM2 inflammasome in many of these cases leads to excessive cell death and tissue injury rather than a protective inflammatory response.

There is growing evidence supporting the existence of crosstalk between pyroptosis and apoptosis in response to agonists of AIM2. For example, in mice the AIM2 inflammasome recruits both caspase-8 and caspase-1 to induce pyroptosis in response to *A. fumigatus* infection [379]. However, in the absence of caspase-1, AIM2 initiated caspase-8-induced apoptosis in mice infected with *F. novicida* [380,381]. These studies shed light on the complex roles of programmed cell death pathways following AIM2-mediated cytosolic detection of microbial DNA.

1.3.7.3 AIM2 and intestinal homeostasis

Although best known for its function in providing protection against infection, AIM2 also plays a critical role in maintaining intestinal homeostasis. Reduced expression and mutations of the *AIM2* gene in the tumours of colorectal cancer patients has been observed [382-385]. Loss of AIM2 has been implicated in the development of colorectal cancer and is associated with poor

survival in patients with colorectal cancer [382]. Mice deficient in AIM2 are hypersensitive to colorectal cancer in an azoxymethane (causes DNA damage) and DSS (causes inflammation) model as compared to wild-type mice [386,387]. Unlike its role in providing protection against infection, AIM2 suppresses colon tumorigenesis independently of inflammasome activity; instead, AIM2 interferes with DNA-PK-dependent AKT activation in intestinal epithelial cells [386], and prevents Wnt signalling and proliferation of intestinal stem cells [387]. A further study has confirmed a role for AIM2 inhibiting the PI3K-AKT pathway in the human colorectal cancer cell line HCT116 [388]. AIM2-deficient mice are highly susceptible to DSS-induced acute colitis, in a manner that is intricately linked to dysbiosis of the gut microbiota [389,390]. Transfer of gut microbiota from AIM2-deficient mice to wild-type mice conferred higher susceptibility to colitis, while treatment with antibiotics completely attenuated the differences between wild-type and AIM2-deficient mice [389]. It has been proposed that the AIM2-inflammasome-mediated release of IL-18 triggers the upregulation of IL-22 binding protein and antimicrobial peptides by intestinal epithelial cells [389,390], thereby modulating the composition of the gut microbiota. Correspondingly, the AIM2 inflammasome provided protection to mice which underwent bowel laparotomy and suffered from intestinal dysmotility termed as postoperative ileus [391]. This protection was attributed to the gut microbiota of treated mice, which induced secretion of IL-1β via the AIM2 inflammasome resulting in amelioration of postoperative ileus [391].

While AIM2 is beneficial in the context of infection and intestinal homeostasis and protective in colorectal cancer, activation of the AIM2 inflammasome can also cause damage to host cells. A detrimental role of AIM2 in metastatic skin cancer has been proposed. A study has suggested that knockdown of AIM2 resulted in reduced cancer cell viability, suppression of growth and vascularisation of xenografts and the onset of apoptosis [392]. Further, the accumulation of self-DNA in the cytoplasm of keratinocytes in psoriasis lesions [393] or in the joints of chronic polyarthritic mice [394] triggers AIM2 inflammasome activation, leading to the activation of caspase-1, release of proinflammatory cytokines and inflammation. In human monocytic cell line THP1 monocytes, EFLA 945, a mixture of compounds from red grape vine

leaf extracts, mediated inhibition of AIM2 inflammasome [395]. Furthermore, EFLA 945 attenuated imiquimod-induced psoriasis possibly by preventing DNA entry [395]. Furthermore, mice deficient in AIM2 are protected from radiation-induced gastrointestinal syndrome and hematopoietic failure [396]. Importantly, AIM2 relocates to the nucleus where it colocalises with the marker of dsDNA breaks, γ-H2AX, and assembles an inflammasome complex in macrophages exposed to ionising radiation [396] **(Fig. 1.4)**. Andrographolide, an active component extracted from the herbaceous plant *Andrographis paniculata*, suppressed AIM2 inflammasome-mediated pyroptosis of primary murine macrophages in response to radiation or chemotherapeutic agents [397].

Release of self-DNA is a key mechanism driving AIM2-dependent responses. Disruption of the nuclear envelope by an HIV aspartyl protease inhibitor, Nelfinavir, was found to activate the AIM2 inflammasome by releasing DNA into the cytosol [398]. Similarly, loss of mitochondrial membrane integrity facilitated release of mtDNA into the cytosol of murine BMDMs, triggering activation of the AIM2 inflammasome [399]. A further study has shown that dsDNA released from intestinal cells damaged by chemotherapy treatment activates the AIM2 inflammasome in immune cells, leading to production of IL-1β and IL-18 and diarrhoea in mice [400]. In this case, abrogation of AIM2 signalling significantly reduced the incidence of diarrhoea without affecting the anticancer effect of the chemotherapeutic [400].

1.3.7.4 AIM2 and the central nervous system

An emerging role of AIM2 inflammasome in the development and homeostatic maintenance of the central nervous system (CNS) was recently identified. During development of the CNS, a high level of replicative stress and cell death is observed, generating several DAMPs such as damaged DNA, ATP and mitochondrial stress; all of which are capable of activating the inflammasome. At postnatal day 5, AIM2 mediated inflammasome formation in the developing brain [401]. Furthermore, the AIM2 inflammasome facilitated neural cell death via GSDMD to eliminate damaged cells from being incorporated into the mature brain [401]. Indeed, mice

lacking the AIM2 inflammasome had increased accumulation of DNA damage in the brain and displayed global behavioural abnormalities characterised by pronounced anxiety-like behaviours [401].

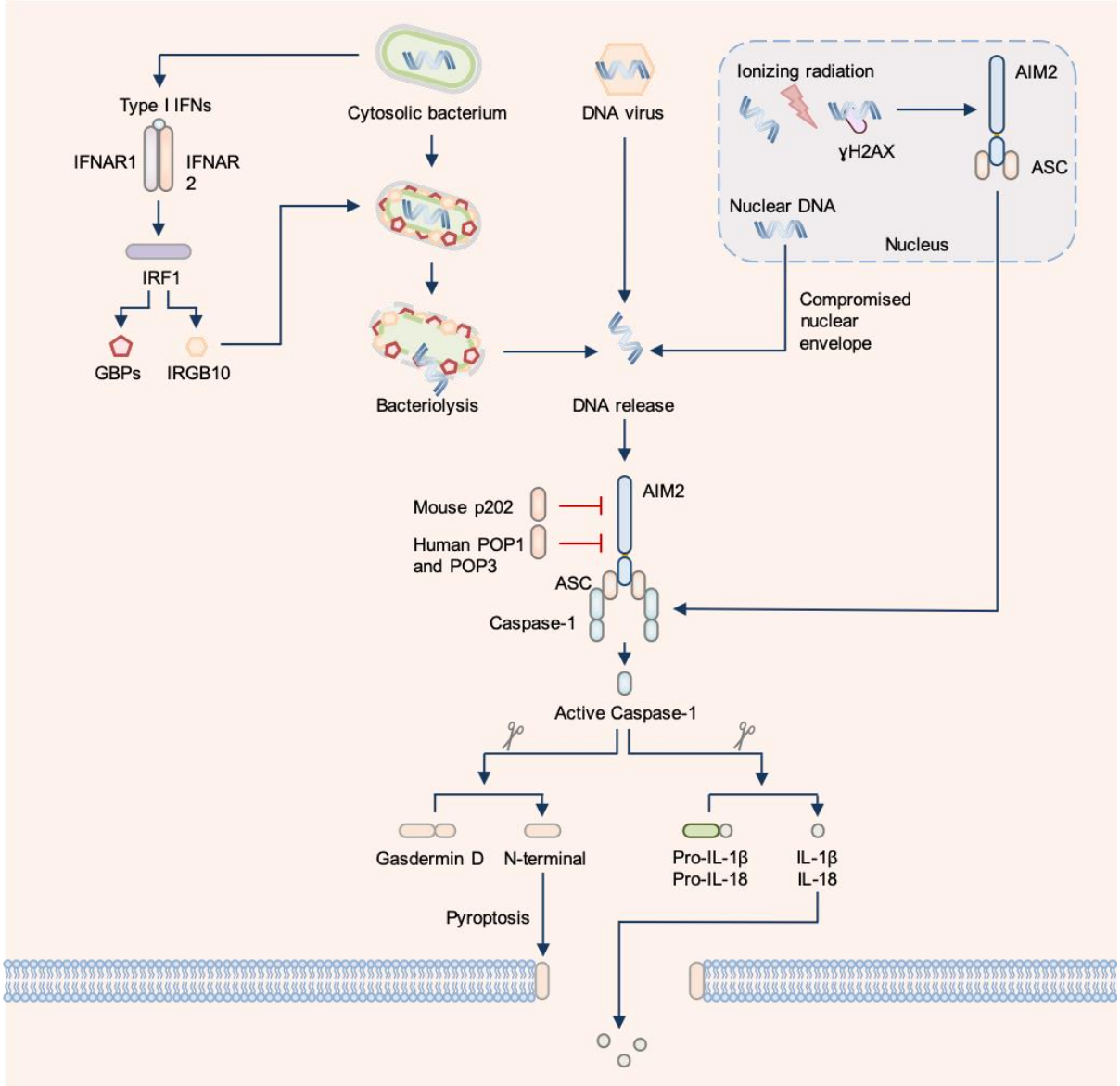

Figure 1.4 | AIM2 inflammasome.

Certain cytosolic bacteria and DNA viruses and mammalian DNA can activate the AIM2 inflammasome. The cytosolic bacterium *Francisella novicida* induces the production of type I IFNs, activating the type I IFN signaling pathway via the transcription factor IRF1. IRF1

induces upregulation of IFN-inducible proteins GBPs and IRGB10, where these proteins directly attack the bacterial membrane of *F. novicida*. The ruptured bacteria release DNA into the cytoplasm. The DNA virus mouse cytomegalovirus activates AIM2 independently of type I IFN signaling. Nuclear DNA from host cells that are exposed to ionizing radiation undergoes dsDNA breakage. AIM2 and ASC redistribute to the nucleus, where the two inflammasome proteins localize to dsDNA breaks and γ-H2AX. The AIM2-ASC complex moves to the cytoplasm to assemble into an inflammasome complex. Damage to the nuclear envelope caused by the HIV-protease inhibitor Nelfinavir mediates the release of nuclear DNA. AIM2 is normally maintained in an autoinhibitory state via interaction between its HIN-200 domain and the PYD domain. On recognition of DNA, AIM2 assembles into an inflammasome complex. AIM2 can be inhibited by a mouse p202, a bipartite protein containing two HIN domains which interact with the HIN domain of AIM2. AIM2 can also be inhibited by human POP1 and POP3.

1.3.8 Pyrin inflammasome

Pyrin, encoded by the *Mefv* gene, is a member of the TRIM family. Missense mutations in MEFV are associated with the development of an autoinflammatory condition in humans known as Familial Mediterranean fever (FMF) [402,403]. Human Pyrin carries a PYD domain, two B-boxes and a coiled-coil domain, and a B30.2 (also known as the SPRY) domain. FMF-associated mutations are frequently found in the C-terminal B30.2 domain of human Pyrin [402,403]. Mouse Pyrin does not have a B30.2 domain. To study the physiological effect of Pyrin and FMF-associated mutations, a mouse model of FMF was generated by knocking-in the B30.2 domain of human Pyrin carrying one of three FMF-associated mutations into mice [404]. Introduction of the B30.2 domain carrying these FMF mutations in mice led to the development of spontaneous inflammation [404]. Importantly, deletion of the gene encoding ASC, GSDMD or IL-1R in these mouse strains abolishes their inflammatory phenotype [404 277], providing robust genetic evidence to suggest that dysregulated Pyrin activity is linked to inflammasome-

mediated pathology. Recently, it was noted that with additional genetic deletion of GSDMD in mice carrying mutations associated with FMF [277], autoinflammatory symptoms were ameliorated, suggesting that pyroptosis associated with GSDMD might be important for disease manifestation.

1.3.8.1 Mechanisms of Pyrin inflammasome activation

Earlier studies had suggested that Pyrin interacts with components of the NLRP3 inflammasome and that Pyrin inhibits the activation of caspase-1, NF-κB and apoptosis [104,405-407]. Further in vitro evidence demonstrates that Pyrin is an inflammasome-activating sensor **(Fig. 1.5)**. Genetic silencing of Pyrin using siRNA reduced inflammasome activation in THP-1 cells infected with *Burkholderia cenocepacia* [408]. Genetic deletion of Pyrin also abolished inflammasome assembly, caspase-1 activation, and IL-1β and IL-18 secretion [409]. The activator of Pyrin was later identified as Rho-inactivating toxins produced by bacteria **(Fig. 1.5)**, including those from *B. cenocepacia*, *Clostridioides difficile*, *Clostridium botulinum*, *Vibrio parahemolyticus*, *Vibrio Cholerae*, *Histophilus somni* and *Yersinia pestis* [409-413]. These toxins inactivate RhoA at the GTPase switch-I region, leading to activation of the Pyrin inflammasome [409].

In contrast to direct modification of RhoA, *Yersinia* outer protein (Yop) effectors impair RhoA activity via stimulation of RhoA GTPase activity and/or sequestration of RhoA in the cytoplasm. YopE functions as a GTPase-activating protein, inactivating RhoA in the host cell [414-416] **(Figure 1.5)**, whereas YopT exhibits a proteinase activity which directly cleaves RhoA at a C-terminal cysteine residue [414,416]. In addition, the pertussis toxin was found to engage activation of the Pyrin inflammasome in a manner dependent on the ADP-ribosyltransferase activity of the toxin [417]. Furthermore, Pyrin contributed to pertussis toxin-induced neutrophil adhesion to cerebral capillaries and the induction of experimental autoimmune encephalomyelitis in mice [417].

The role of Pyrin inflammasome in the host defence against infection has been demonstrated in a mouse model of lethal *B. cenocepacia* infection. Mice lacking Pyrin or ASC develop a milder form of lung inflammation in response to *B. cenocepacia* infection compared with wild-type mice [409]. Further, *B. cenocepacia* lacking the Type VI effector deamidase TecA, and therefore cannot modify Rho GTPases to activate the Pyrin inflammasome, induces lethality in wild-type mice more rapidly than did a wild-type *B. cenocepacia* strain [418]. These findings collectively demonstrate that the Pyrin inflammasome mediates recognition of Rho deamidase activity of TecA in *B. cenocepacia* to drive protective responses in the host.

1.3.8.2 Regulation of Pyrin

The expression of Pyrin is upregulated following TLR priming of mouse BMDMs [419]. While not necessary, TLR-dependent priming enhances activation of the Pyrin inflammasome by the *C. difficile* toxins TcdA and TcdB [419]. TLR-dependent secretion of TNF activated RIPK3 which induced transcriptional upregulation of *Mefv* gene through inhibition of the mechanistic target of rapamycin (mTOR) pathway [420]. Furthermore, inhibition of mTOR promoted *Mefv* expression and activation of the Pyrin inflammasome in primary murine macrophages [420].

Another mechanism to regulate Pyrin inflammasome activation is through the interaction of human Pyrin with the regulatory proteins known as 14-3-3 [421,422]. Phosphorylation of Pyrin at sites Ser208, Ser209, and Ser242 is necessary to mediate interaction with 14-3-3 proteins [421]. Further mechanistic studies have unravelled the biological importance of the interaction between Pyrin and 14-3-3 proteins. A mutation in the *Mefv* gene that causes a Ser242Arg substitution abolishes inhibitory binding of 14-3-3 proteins to Pyrin [423]. This mutation was found in patients with a newly described autoinflammatory condition called Pyrin-associated autoinflammation with neutrophilic dermatosis (PAAND) [423]. The Ser242Arg mutation promotes excessive ASC speck formation and activation of caspase-1 and secretion of IL-1β in 293T cells or in THP-1 monocytic cells [423]. Similarly, monocytes from patients with PAAND

carrying the Ser242Arg mutation undergo spontaneous inflammasome activation in response to LPS stimulation [423].

Studies in the murine system have revealed that mouse Pyrin can be phosphorylated on Ser205 and Ser241, two sites corresponding to Ser208 and Ser242 of human Pyrin, respectively [422] **(Fig. 1.5)**. The two serine residues are dephosphorylated in response to stimulation by Rho-inactivating toxins and infection with *B. cenocepacia*, releasing Pyrin from 14-3-3 proteins [423]. A further study has demonstrated that Pyrin is phosphorylated by the RhoA effector serine-threonine kinases PKN1 and PKN2 [424]. Phosphorylation of human Pyrin at sites Ser208 and Ser242 by PKN1 or PKN2 promotes interaction between Pyrin and 14-3-3ε or 14-3-3τ proteins, thereby, maintaining inhibition of the Pyrin inflammasome in unstimulated cells [424]. The presence of FMF-associated or PAAND-associated mutations in Pyrin impairs binding of Pyrin with 14-3-3 or PKN proteins [423,424]. In monocytes of FMF patients, dephosphorylation of Pyrin was sufficient to trigger activation of the Pyrin inflammasome in response to *C. difficile,* whereas in monocytes from healthy patients, additional control mechanisms existed to regulate activation of the Pyrin inflammasome [425]. These findings provide additional mechanistic insights into why patients carrying these mutations exhibit uncontrolled inflammasome responses.

1.3.8.3 Pyrin and cytoskeleton

Pharmacological drugs that target the microtubule, including colchicine, vinblastine, paclitaxel, BAL27862, nocodazole, ABT-751, CA4P, and CYT997 have all been reported to inhibit assembly and activation of the Pyrin inflammasome induced by TcdA or TcdB [419,422,424]. However, these microtubule inhibitors do not interfere with the dephosphorylation of Pyrin or dissociation of 14-3-3 proteins [422], suggesting that Pyrin dephosphorylation acts upstream of microtubule activities. Human PBMCs carrying FMF-associated mutations in Pyrin secrete IL-1β and IL-18 in response to stimulation with TcdA even in the presence of colchicine treatment

[419], suggesting that Pyrin harbouring FMF-associated mutations bypasses the requirement for microtubules in the activation of the inflammasome.

The role of the cytoskeleton in the activation of the Pyrin inflammasome has also been observed in a mouse model of systemic autoinflammatory disease. Mice carrying an inactivating mutation in the actin-depolymerising cofactor Wdr1 develop systemic autoinflammatory disease that can be delayed by genetic deletion of Pyrin, ASC, caspase-1 or IL-18 [426]. This finding suggests that dysregulated actin dynamics may be sensed by the Pyrin inflammasome, which could lead to inflammation and tissue damage. In support of this idea, a previous study has shown that Pyrin polarises at the leading edge of migrating human monocytes, where it co-localises with polymerising actin [427].

The relationship between Pyrin and other components of the cell has been identified. Human Pyrin was found to associate with the autophagy-related proteins ULK1, Beclin 1, and ATL16L1 [428]. The same study also reported that Pyrin, but not Pyrin carrying FMF-associated mutations on the B30.2 domain, mediates recruitment of ULK1 to the NLRP3 inflammasome, where this complex is degraded by the autophagy machinery [428]. These observations indicate that, under some conditions, Pyrin may negatively regulate activation of other inflammasomes [104,405-407].

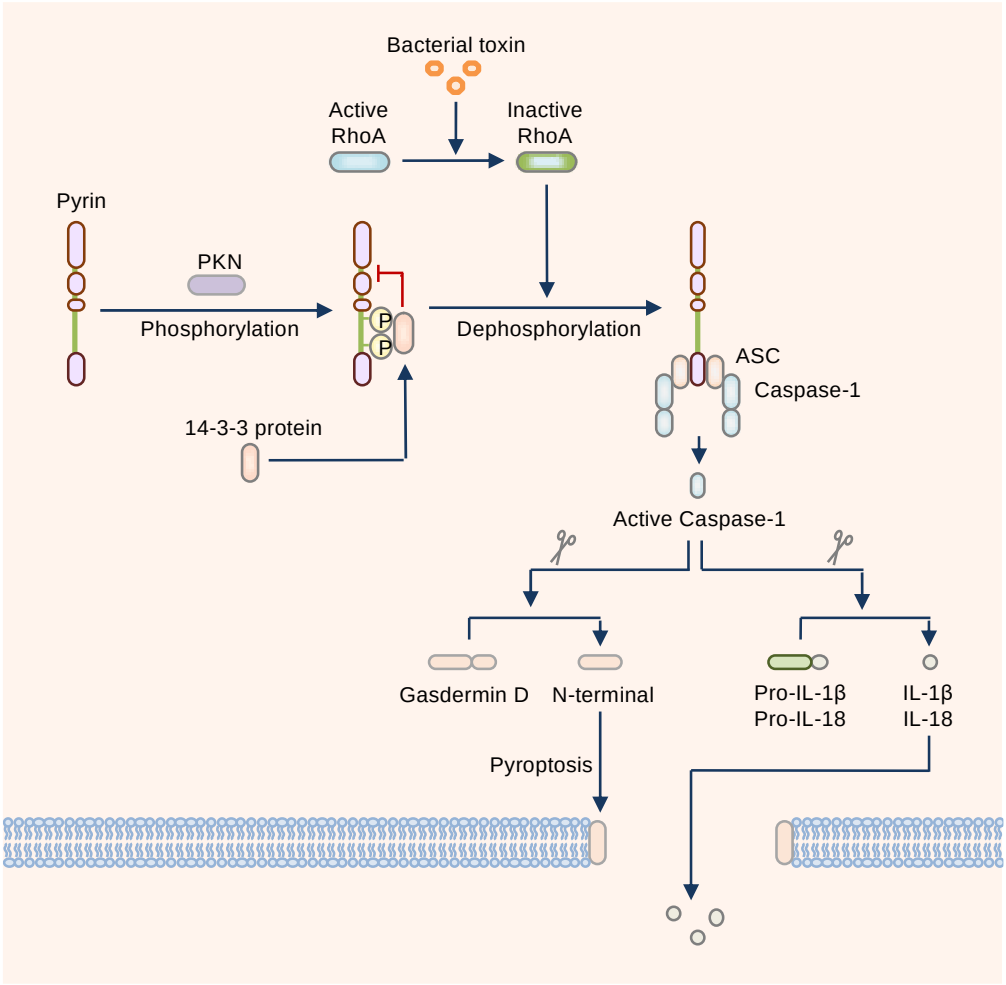

Figure 1.5 | Pyrin inflammasome.

During homeostasis, Pyrin is phosphorylated by RhoA effectors and serine-threonine kinases PKN1 and PKN2. Phosphorylated Pyrin is bound by 14-3-3 proteins, inducing inhibition of Pyrin. Certain bacteria secrete toxins that inactivate RhoA, a process which mediates dephosphorylation of Pyrin. Mutations in certain sites of Pyrin also lead to dephosphorylation of Pyrin. This dephosphorylation event triggers Pyrin dissociation from 14-3-3 proteins, unleashing active Pyrin that is then capable of assembling into an inflammasome complex.

1.3.9 The NLRP6 inflammasome

NLRP6 is highly expressed in the intestine of mice [429-431]. Indeed, deficiency of NLRP6 drives intestinal inflammation and inflammation-induced colorectal cancer in mice [430,432]. In such cases, intestinal immunity required several microbial metabolites which can positively or negatively regulate activation of NLRP6 and IL-18 production [432] (**Fig.1.6**). Metabolites such as bile acid-derived taurine and histamine and polyamine spermine, can positively or negatively dictate activation of NLRP6 [432]. However, the intestinal microbial species producing these metabolites and the precise mechanisms employed by these metabolites in activating NLRP6 are elusive.

In mice, NLRP6 was found to exert a protective role during oral-gastrointestinal infection of encephalomyocarditis virus (EMCV) [433]. Mechanistically, NLRP6 sensed the viral ssRNA via the RNA helicase DEAH box helicase (DHX15) [433]. Binding of ssRNA with DHX15 initiated a signalling cascade to induce type I or III IFNs and ISGs, which exerted an anti-viral response [433]. The NLRP6-driven anti-viral response inhibited viraemia and lethality in EMCV-infected mice [433]. Based on these studies, NLRP6 was proposed to safeguard intestinal homeostasis and immunity. However, two studies using littermate-controlled mice found no role for NLRP6 in maintaining microbiome composition and susceptibility to colitis [434,435]. Further studies are required to clarify the controversial role of NLRP6 in regulating gut homeostasis.

In context of bacterial infection, NLRP6 was found to negatively regulate NF-κB and MAPK-signalling in response to Gram-positive and Gram-negative bacteria [436]. Consistently, a detrimental role of NLRP6 has been suggested in mice infected with either *L. monocytogenes, S. aureus, E. coli* or *S.* Typhimurium [35,436,437]. The cognate ligand of NLRP6 was unknown until a study demonstrating that lipoteichoic acid, a biomolecule derived from the cell wall of Gram-positive bacteria, binds to NLRP6 in murine BMDMs [35]. However, it is unclear what factors from Gram-negative bacteria induced activation of NLRP6. In response to cytosolic

lipoteichoic acid or infection with the Gram-positive bacterium *L. monocytogenes*, NLRP6 formed an inflammasome complex [35].

NLRP6 further promoted dual recruitment of caspase-1 and caspase-11 to the same inflammasome complex which executed maturation of IL-1β and IL-18 [35]. In mice, the NLRP6-Caspase-11 inflammasome response exacerbated *Listeria* infection via secretion of IL-18 but not IL-1β [35]. Further structural analysis revealed that human NLRP6 PYD self-assembled into large filamentous structures and recruit ASC via PYD-PYD interactions [438]. These studies underline a complex role of NLRP6 in host defence and in maintaining intestinal homeostasis.

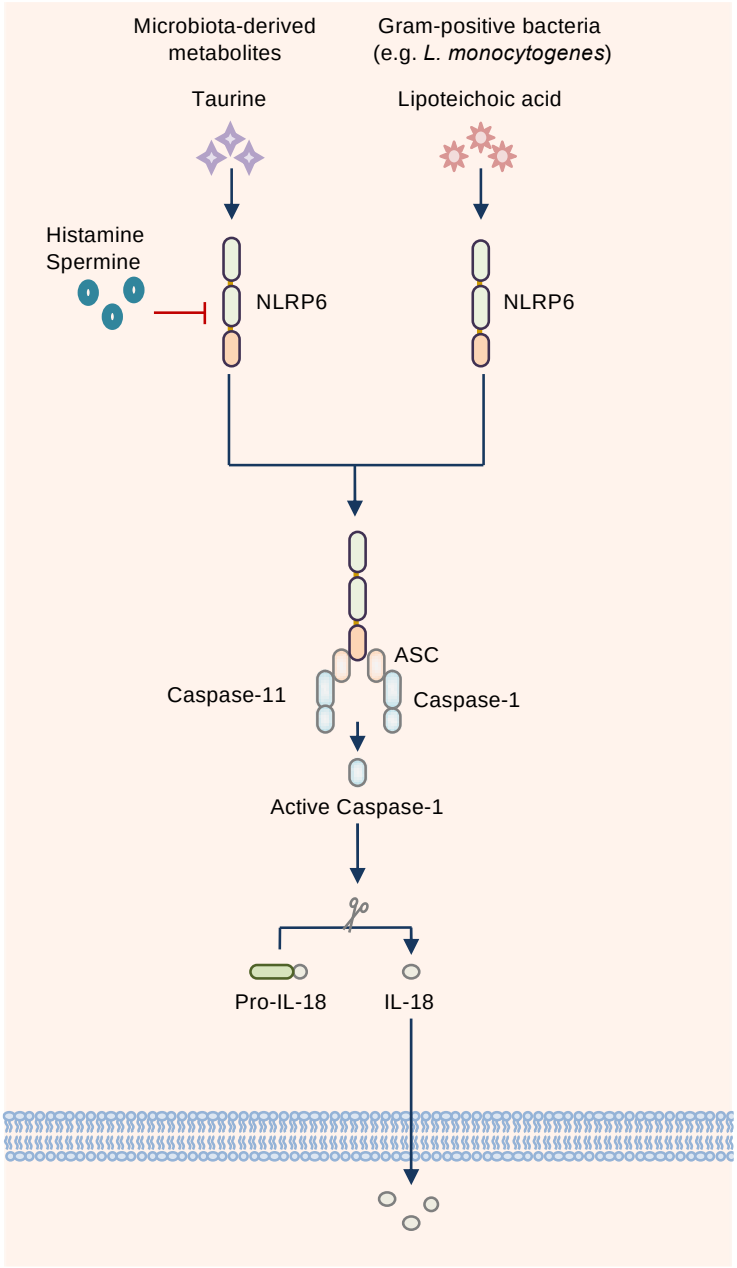

Figure 1.6 | NLRP6 inflammasome.

During healthy or dysbiotic state, microbiota-derived metabolites can either positively or negatively regulate murine NLRP6 activity within the intestine that leads to production of interleukin (IL)-18. NLRP6 can bind to the Gram-positive bacterial cell wall component lipoteichoic acid (LTA). Presence of cytosolic LTA and *L. monocytogenes* activated NLRP6 which recruited ASC, caspase-1 and -11 to form an inflammasome complex. NLRP6 activation

induces processing of caspase-11, which promotes caspase-1 activation and IL-18 secretion; the latter occurring independently of gasdermin D cleavage and pyroptosis.

1.3.10 The NLRP9b inflammasome

Similar to NLRP6, NLRP9b is highly expressed in small and large intestinal epithelial cells of mice [34]. NLRP9b was recognised as the cytosolic inflammasome sensor of Rotavirus infection in murine intestinal epithelial cells [34]. Notably, NLRP9b contributed to inflammasome-dependent responses in intestinal organoids infected with Rotavirus [34] (**Fig. 1.7**). Indeed, mouse intestinal organoids lacking either NLRP9b or DHX9 infected with Rotavirus resulted in reduced secretion of IL-18 and were resistant to pyroptosis, compared to the wild-type organoids [34]. RNA helicase DEAH-box helicase (DHX9), but not NLRP9b, bound short dsRNA stretches, which prompted the formation a DHX9-NLRP9b-ASC-Caspase-1 complex [34]. Mice lacking NLRP9b in all cells or specifically in intestinal epithelial cells had increased susceptibility to Rotavirus infection compared to the wild-type controls [34].

This mechanism of activating NLRP9b is analogous to how NLRC4 [439-443] and NLRP6 [444] are activated. NLRC4 and NLRP6 do not mediate direct ligand binding and that ligand binding is mediated by NAIPs and the RNA helicase DHX15, respectively. NLRP6 also contributed to host defence against Rotavirus, suggesting that NLRP6 and NLRP9b may co-localise to the same inflammasome complex [34]. A similar immune mechanism is noted during *Salmonella* infection where both NLRP3 and NLRC4 sensors are co-activated and recruited to the same inflammasome complex [445].

Human NLRP9 also co-precipitated with both viral dsRNA and DHX9, suggesting functional conservation of the NLRP9 inflammasome across different host species [34]. However, it might be interesting to investigate whether NLRP9b can respond to other activators, such as ssRNA, and whether this recognition is direct or associated with DHX9 or another sensor/s. Owing to

the high similarity in functional and biophysical attributes (requirement of a DHX member) between NLRP9b and NLRP6, it might be worthwhile to evaluate whether NLRP9b can also regulate the gut microbiome composition and intestinal cancer development.

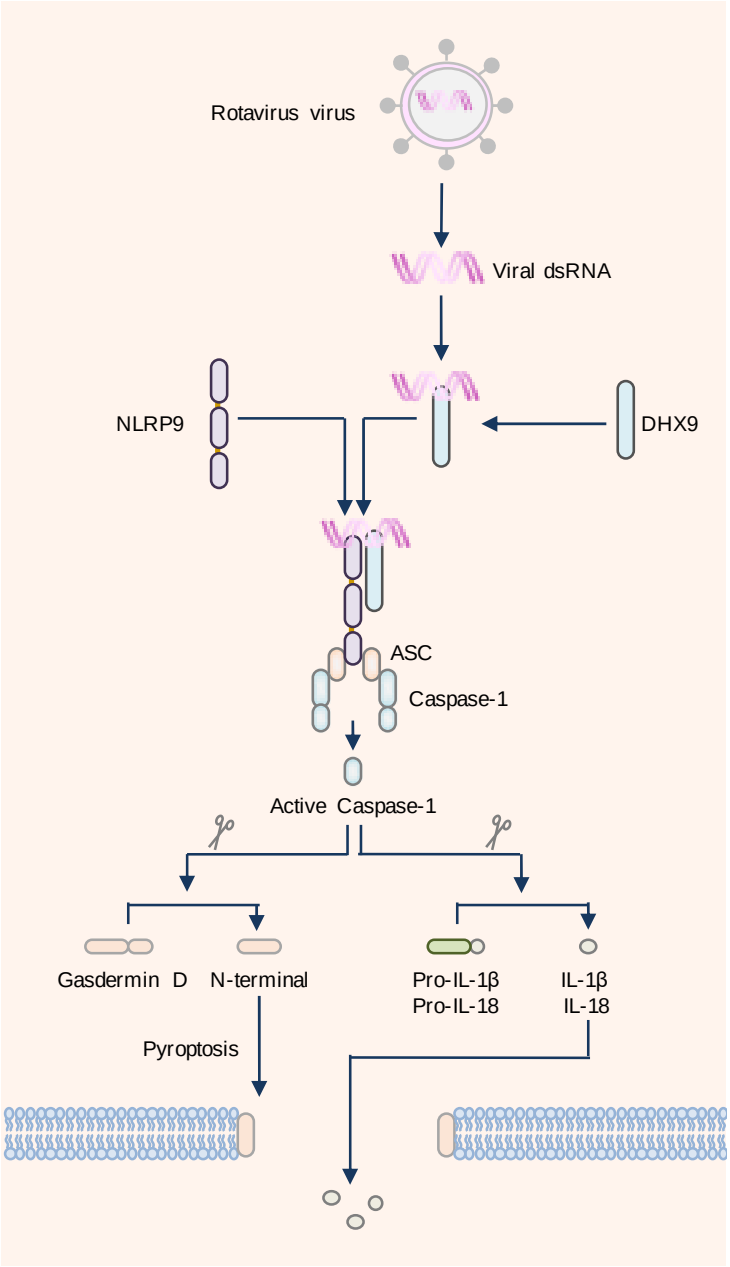

Figure 1.7 | NLRP9b inflammasome.

The NLRP9b inflammasome in murine intestinal epithelial cells is activated by Rotavirus infection. Rotavirus double-stranded RNA (dsRNA) bound an RNA helicase DEAH-box (DHX9) which associated with NLRP9b to form an inflammasome complex. In response to

Rotavirus infection, intestinal cells activated NLRP9b inflammasome which triggered gasdermin D dependent pyroptosis and secretion of IL-18.

1.4 *Bacillus cereus*

Bacillus cereus sensu stricto (herein referred to as *B. cereus*) is an important cause of food poisoning in humans. Isolated in 1887, *B. cereus* was considered a harmless contaminant for almost 80 years before it was widely accepted as a pathogen [446,447]. Since the 1960s, *B. cereus* has gained notoriety as the etiological agent for a variety of intestinal and extra-intestinal diseases [448]. These clinical manifestations include gastroenteritis, vomiting, endophthalmitis, respiratory tract infections or infections similar to gas-gangrene [449] (**Fig. 1.8**).

B. cereus belongs to a bacterial group known as *B. cereus sensu lato* which also includes *B. anthracis*, *B. thuringiensis*, *B. mycoides*, *B. pseudomycoides*, *B. weihenstephanensis*, *B. cytotoxicus*, and *B. toyonensis,* as well as several newly described members identified through more genetic taxonomic analyses, such as *B. gaemokensis*, *B. manliponensis*, and *B. bingmayongensis* [450-454]. These bacteria have a high level of genetic similarity [450,455,456], yet can be classified into unique species based on their morphological and physiological features, and the clinical manifestations resulting from these infections [456]. Of these bacteria, *B. anthracis* is recognised for its ability to cause a lethal anthrax disease in humans [457]. Although *B. cereus* is considered a neglected pathogen, studies are now beginning to unravel its biology and host-pathogen interactions.

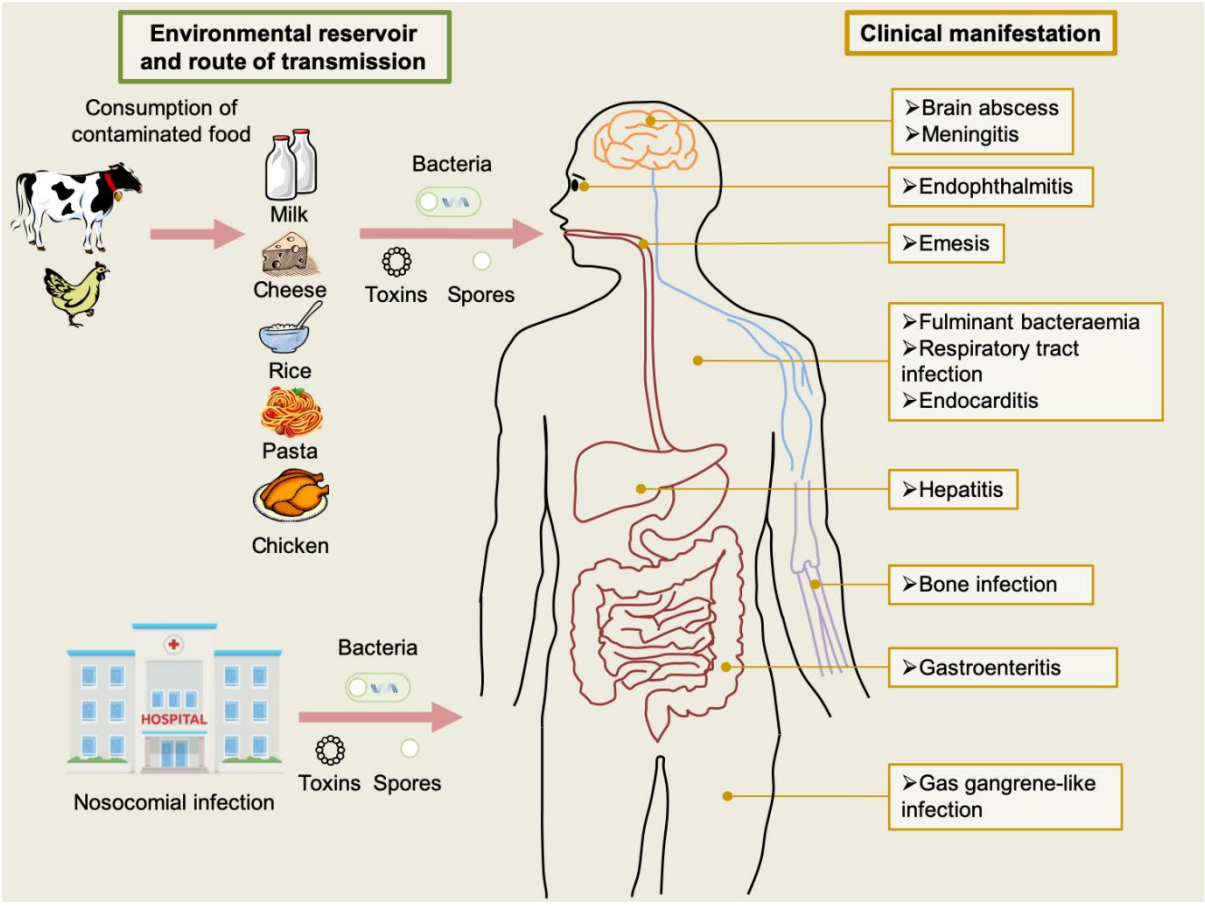

Figure 1.8 | Environmental reservoirs, routes of transmission, and clinical manifestations associated with *Bacillus cereus* infection.

B. cereus can be transmitted to humans through consumption of undercooked or contaminated food via the oral-gastric route. Food contamination caused by *B. cereus* can occur during any stages of food harvesting, processing, storage, preparation and consumption. Nosocomial transmission (also known as hospital-acquired transmission) has been reported to occur due to the formation of *B. cereus* biofilms on items such as catheters and bedsheets. These transmission routes account for the majority of gastrointestinal and/or extra-intestinal manifestations in the hospital setting.

1.4.1 General microbiology of *B. cereus*

B. cereus is a Gram-positive, rod-shaped and spore-forming facultative anaerobe [456] (**Fig. 1.9**). *B. cereus* strains possess peritrichous flagella [458], which are involved in locomotion and/or toxin secretion [458,459]. Further, some strains are encased with a crystalline surface glycoprotein layer (S-layer), covering the cell wall [460,461] (**Fig. 1.9**). Proteins within the S-layer mediate adhesion of *B. cereus* to host cells and provide resistance to gamma-ray radiation [462].

B. cereus strains can vary in their growth and survival characteristics. They are divided into two groups: psychrotrophic and mesophilic. Psychrotrophic strains grow well at temperatures below 10 °C but grow poorly at 37 °C [463]. Psychrotrophic *B. cereus* are generally found in chilled foods and, in some cases, fresh foods [464-466]. In contrast, mesophilic strains grow well at 37 °C and can survive at temperatures below 10 °C [463].

B. cereus can persist and survive in harsh environmental conditions by the production of endospores and formation of biofilms [467-469]. *B. cereus* spores are elongated, characterised by a core surrounded by an inner membrane, peptidoglycan cortex, inner coat and outer coat (**Fig. 1.9**). The bacterial spores have no metabolic activity and are resistant to heating, freezing, drying, and gamma-ray and ultraviolet radiation [462,470]. These spores are extremely resistant to environmental assaults that would normally kill vegetative bacteria, thereby facilitating persistence in the environment until more favourable conditions return. They also facilitate adhesion to human epithelial cells [471,472]. Biofilms of *B. cereus* form on abiotic surfaces and living tissue, but also persist as floating pellicles [469]. These biofilms have been found on central venous catheters and are associated with nosocomial bacteraemia [473,474] (**Fig. 1.8**). Importantly, *B. cereus* in biofilms produce higher amounts of secondary metabolites and enzymes, such as catalase and superoxide dismutases, compared to planktonic cells, contributing to bacterial defence against host responses [475].

Of concern is growing incidence of *B. cereus* isolates expressing a β-lactamase enzyme [476] which can counter the effects of β-lactam antibiotics, such as penicillin, ampicillin, and

cefotaxime [449,477]. The origin of these antibiotic-resistant *B. cereu*s strains can be mapped out to isolates harvested from fresh food products [478-480], dairy products [466,481], agriculture produce [482-484], packaged food products [485-487], and hand or surfaces of commonly used electronic devices such as mobile phones [488]. Numerous investigations have shed light on the reasons pertaining to the observed increase in antibiotic resistance in *B. cereus*. These reasons include: (i) acquisition of antibiotic-resistance genes and/or transposons in either chromosomal or extra-chromosomal genomic locations [483,489-491]; (ii) production of antibiotic-modifying or -inactivating enzymes [492,493]; (iii) alterations in the lipid composition and charge of the cell membrane [494,495]; (iv) presence of multidrug resistance efflux systems [483,496,497]; (v) switching of metabolic state to enhance persistence of infection [498]. A rise in the prevalence of antibiotic resistance amongst pathogenic *B. cereus* isolates threatens our ability to treat severe *B. cereus* infections. Given how the identification, development and approval of novel antibiotics has slowed in recent decades [499], it is imperative that alternative therapies to treat *B. cereus* infections are developed.

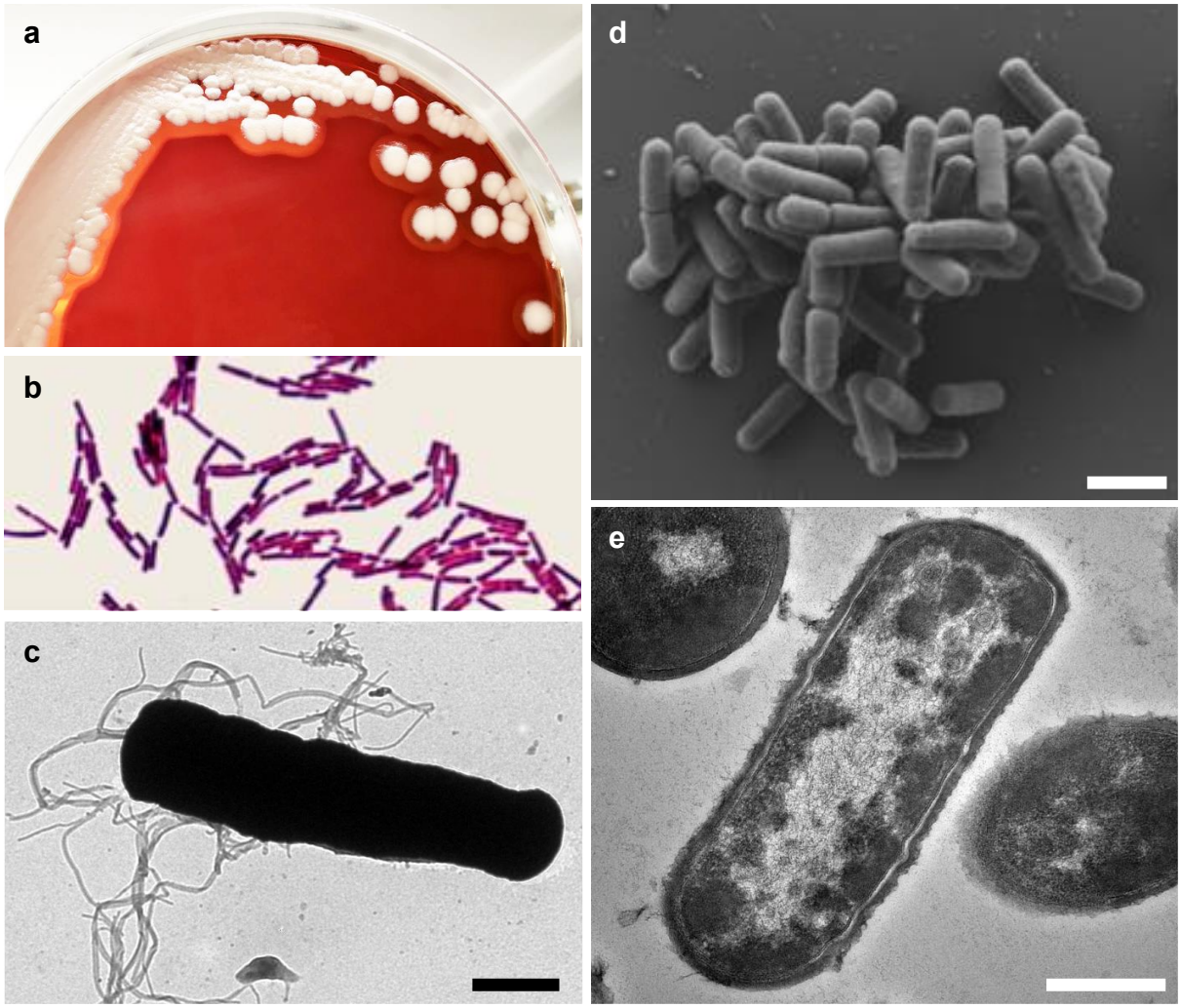

Figure 1.9 | Macroscopic and Microscopic Morphologies of *B. cereus*.

(**a**) Colony morphology of *B. cereus* grown on a blood-agar plate under aerobic conditions at 30°C. *B. cereus* colonies are large, and have a rough surface and irregular edges, often surrounded by a zone of clearing indicating haemolysis. (b) Gram staining reveals that *B. cereus* is a Gram-positive bacterium. (**c**) Transmission electron microscopy and negative staining shows peritrichous flagella protruding from *B. cereus*. Scale bar,1 µm. (**d**) Scanning electron microscopy shows that *B. cereus* is a rod-shaped bacterium. Scale bar, 2 µm. (**e**) Transmission electron microscopy reveals the ultrastructure of *B. cereus*. Scale bar, 0.5 µm

1.4.2 Epidemiological landscape of *B. cereus*

Although *B. cereus* infections have been documented worldwide, the body of literature reporting these infections mainly relates to foodborne outbreaks of gastroenteritis in isolated countries [449,462,500]. The limited global epidemiological data on *B. cereus* infections is attributed to: (i) the mild and short-duration of symptoms and self-limiting nature of most *B. cereus* infections, which means that individuals generally do not seek medical attention; (ii) lack of laboratory testing to confirm whether *B. cereus* is attributed to patient symptoms and/or disease; and (iii) *B. cereus* infections are not notifiable to health authorities in most countries, leading to undocumented cases and/or transmission in the community [449,462,501]. These factors together lead to underreporting and underestimation of the actual incidence of this pathogen in humans. Epidemiological surveillance is further complicated by a lack of testing for other pathogens which can induce symptoms similar to *B. cereus* [501,502]. For example, food poisoning caused by infection with the Gram-positive bacteria *Staphylococcus aureus* and *Clostridium perfringens* leads to emesis and diarrhoea. These infections are largely indistinguishable from *B. cereus* infection [501,502], which further confounds the validity of epidemiological reporting of *B. cereus* in the context of foodborne outbreaks.

Despite the lack of accurate global estimates, several consistent trends have emerged amongst foodborne outbreaks associated with *B. cereus* infection. Epidemiological data have shown that rice, pasta, pastry and noodles are associated with emesis, whereas vegetables, meat products and milk products are associated with diarrhoea [462,500,501,503]. Furthermore, the diarrhoeal-type disease has been reported more frequently in Bulgaria, Finland, Hungary and Norway, whereas the emetic-type disease in Japan and the United Kingdom [462]. These trends might reflect the eating habits of individual countries and suggest that certain food groups act as a vehicle for strains of *B. cereus* harbouring a specific subset of virulence factors that are more likely to cause either emetic or diarrhoeal symptoms. Additional epidemiological analyses of *B. cereus* isolates, including profiling of their genetic markers and virulence factors, in different outbreak settings, would provide insights into the distribution and

transmission of this pathogen. Further, research efforts focusing on improved biosecurity, food safety and methods of detection would further prevent future outbreaks and minimise the health and economic burden of *B. cereus* infection.

1.4.3 Virulence factors of *B. cereus*

B. cereus produces a collection of virulence factors including pore-forming toxins, cereulide, haemolysins, enterotoxins, proteases and phospholipases (**Fig. 1.10**). These virulence factors are discussed in detail below:

1.4.3.1 Pore-forming toxins

B. cereus secretes two three-component pore-forming toxins called haemolysin BL (HBL) and non-haemolytic enterotoxin (NHE), and a single-component toxin called cytotoxin K (CytK, also known as haemolysin IV) (**Fig. 1.10**). These toxins are produced and secreted primarily during the exponential phase of bacterial growth and are regulated by the master transcriptional regulator PlcR [504].

HBL is composed of subunits B, L_1 and L_2 [505], whereas NHE is composed of subunits A, B and C [506]. A previous study found that the subunits of HBL could bind erythrocytes independent of one another [507] whereas, a later study identified HBL-B as the apical subunit mediating assembly of the toxin on host cell membrane [508]. Similarly, previous studies have reported contradicting data regarding the first subunit of NHE to be either B or C [509,510]. Moreover, another study found that subunits of HBL and NHE toxins can form complexes [511,512]. Therefore, further studies are required to decipher the binding order and structure of HBL and NHE subunits.

Indeed, the structures of HBL-B (PDB ID: 2NRJ) and NHE-A (PDB ID: 4K1P) have been solved and were found to be structurally similar to cytolysin A (ClyA) (PDB ID [Monomeric]: 1QOY; PDB ID [Protomeric]: 2WCD) from *Escherichia coli* [513-516]. HBL-B, NHE-A and ClyA are all comprised of two domains; a head domain composed of two α-helices and two β-sheets,

and a tail domain composed of five α-helices [513-515]. However, the head domain of NHE-A was longer and more enlarged than that of HBL-B and ClyA [514]. The similarities in tertiary structures between HBL-B and NHE-A to that of ClyA argue that they should be classified as members of the ClyA superfamily of α-helical pore-forming toxins [517,518].

During an infection, the anaerobic or microaerobic environment of the intestine promotes the production and secretion of HBL and NHE [519-521]. These enterotoxins cause damage to epithelial cells by forming pores leading to microvilli injury, osmotic lysis of intestinal epithelial cells and subsequent diarrhoea [469]. Genomic analysis of clinical, food and environmental strains of *B. cereus* has revealed that HBL, NHE and CytK are highly prevalent, with HBL being present in 40-92% of the isolates, NHE in 95-98% of the isolates, and CytK in 50-80% of the isolates [501,522,523]. The high prevalence of these pore-forming toxins suggests that the probability of a strain carrying at least one of these toxins is very high and that any of these toxin-bearing strains would be capable of causing disease.

1.4.3.2 Cereulide

Consumption of food products contaminated with the emetic toxin, cereulide, leads to emesis in humans (**Fig. 1.10**). Cereulide, a cyclic dodecadepsipeptide, is similar to a potassium ionophore. It is resistant to heat, proteolysis and acidic environments [524]. Cereulide is encoded by a non-ribosomal peptide synthetase gene cluster called ces, located on a mega plasmid called pCER270. This mega plasmid is related to the pXO1 plasmid of *B. anthracis* [525]. It is hypothesised that cereulide biosynthesis follows a canonical non-ribosomal peptide assembly process [526] similar to other well-characterised cyclic antimicrobial peptides, including gramicidin S [527] and surfactin [528]. However, a more recent non-canonical mechanism of non-ribosomal peptide assembly for cereulide biosynthesis has been proposed [317]. In contrast to the canonical pathway where single monomers are building blocks of tetradepsipeptide assembly, the non-canonical pathway utilises dipeptides as building blocks of

tetradepsipeptide assembly [317]. This observation indicates that further structural and functional studies are required to elucidate the complex biosynthesis pathway of cereulide.

Transcription of the cereulide toxin is governed by the nutrient-responsive transcriptional regulator CodY, the sporulation transcription factor Spo0A, and the sporulation-vegetative, transitional-state transcription factor ArbB [456,526,529-531]. The extrinsic environment, and the intrinsic nutritional and developmental cell status collectively dictate CodY- and Spo0A-regulated transcription of cereulide [456,526,530,531]. Furthermore, a putative hydrolase CesH encoded by the cesH gene present in the ces gene cluster was found to be a transcriptional repressor of cereulide [530,532].

Cereulide is secreted predominantly during the stationary phase of bacterial growth. It is found in food products, including rice, pasta, milk and dairy products [462,533]. Following ingestion, cereulide is absorbed in the intestine and distributed throughout the body where it can cross the blood-brain-barrier or accumulate in the liver, kidneys, fat, and muscle tissue [534]. The emetic effect of cereulide is thought to be dependent on its interaction with the serotonin 5-HT3 receptors expressed in the stomach and small intestine, inducing gut-to-brain signalling via the vagus nerve [535] (**Fig. 1.10**). In the house musk shrew, the chemical antagonist of 5-HT3 receptors called ondansetron hydrochloride, or surgical severing of the vagus nerve, inhibited cereulide-induced emesis [535]. These findings suggest an involvement of 5-HT3 receptors in cereulide-induced emesis, however, whether cereulide directly interacts with 5-HT3 receptors at vagal sensory endings or that it indirectly stimulates secretion of serotonin to activate 5-HT3 receptors is not known [535].

1.4.3.3 Haemolysins and enterotoxins

Haemolysis is a key feature of many strains of *B. cereus*. Indeed, HBL, NHE and CytK induce haemolysis in erythrocytes owing to their pore-forming ability, however, *B. cereus* also expresses haemolysin I, haemolysin II and haemolysin III (**Fig. 1.10**). Haemolysin I (also

known as cereolysin O) is a cholesterol-dependent cytolysin similar to perfringolysin O of *Clostridium perfringens*, whereas haemolysin II and haemolysin III are cholesterol-independent cytolysins [523]. Haemolysin II induces apoptosis in mouse macrophages and human monocytes via activation of the apoptotic caspase, caspase-3 [536]. The biochemical properties, structure and mechanism of pore formation of these haemolysins have remained unclear.

Other enterotoxins of *B. cereus* include the lesser characterised enterotoxin T and enterotoxin FM [537,538] (**Fig. 1.10**). Both enterotoxins have been found to be non-cytotoxic to mammalian cells [539] and enterotoxin FM is thought to function as a cell-wall peptidase rather than a functional enterotoxin [540]. The exact role of these toxins in bacterial growth and virulence is unknown and requires further investigation. Given that the production of toxins requires substantial cost to the bacteria in terms of energy and resources, these toxins are probably important at some stage in the lifecycle of *B. cereus*. It is intriguing to speculate that these enterotoxins might be secreted to defend against other competing bacteria or single-cell predatory protozoa in the environment [541,542]. Indeed, an example from another *Bacillus* species is *Bacillus subtilis*, which secretes the tRNase toxin WapA used to extract nutrients from and kill its target prey, *Bacillus megaterium* [543,544].

1.4.3.4 Metalloproteases

In addition to secretion of haemolysins and enterotoxins, spores of *B. cereus* express two metalloproteases called InhA1 and NprA, used for escaping immune surveillance and promote germination leading to establishment of infection in a host [545-547] (**Fig. 1.10**). Genomic analysis has revealed that InhA1 and NprA share 90% nucleotide similarity with proteases found in *B. anthracis* and *B. thuringiensis* [545-547]. In *B. anthracis,* homologues of InhA1 and NprA are thought to degrade host protease inhibitors, extracellular matrix proteins, and epithelial barrier proteins [546,548]. It is possible that InhA1 and NprA of *B. cereus* may have similar functions.

1.4.3.5 Phospholipases

An important class of virulence factors of *B. cereus* used to establish an infection in the host is mammalian membrane-damaging phospholipases. Specifically, *B. cereus* produces a sphingomyelinase (SMase), a phosphatidylinositol-specific phospholipase C (PI-PLC), and a phosphatidylcholine-specific phospholipase C [549] (**Fig. 1.10**).

Previous studies have shown that phospholipases can facilitate haemolysis [550,551]. With the exception of SMase, the role of phospholipases in the pathogenesis of *B. cereus* has remained largely unclear [552]. The presence of SMase is associated with increased severity of *B. cereus* infection in mice, leading to lethality which can be abrogated following pharmacological inhibition of SMase [553,554]. The biochemical properties and pathogenicity of SMase in *B. cereus* infection are discussed further in another review [555]. PI-PLC of *B. cereus* has been shown to complex with Glucosaminyl(α1→6)-d-myo-inositol and facilitates cleavage of membrane-bound GPI-anchored proteins [556-558]. In addition, two synthetic chiral compounds called R-7ABO and S-7ABO were found to be novel inhibitors of *B. cereus* phosphatidylcholine-specific phospholipase C [559], and therefore, these compounds could be further tested in animal models of *B. cereus* infection to validate their potential use as antibacterial therapeutics.

1.4.4 Membrane-bound receptor of HBL in mammalian cells

HBL can form pores in the plasma membrane and exert cytotoxicity on mammalian immune and non-immune. Whether HBL binds to a specific surface receptor to mediate pore formation on mammalian cells was unknown until now. Using a genome-wide CRISPR-Cas9 screen in RAW276.4 mouse macrophages, two mammalian surface receptors called LPS-induced TNF-α factor (LITAF, also known as small integral membrane protein of lysosome/late endosome or SIMPLE) and the LITAF-like protein called Cell Death Inducing P53 Target 1 (CDIP1) were identified as surface receptors of HBL [560] (**Fig. 1.10**). This study demonstrated that primary mouse macrophages or epithelial Chinese Ovary Hamster (CHO) cells lacking LITAF were resistant to HBL-induced cytotoxicity [560]. Further, mice lacking LITAF survived a lethal

challenge of purified HBL [560]. Analysis of truncated variants of LITAF showed that the C-terminal residues of this receptor are critical in mediating HBL binding [560]. In the mouse melanoma cell line B16F10, deletion of CDIP1 in addition to LITAF was required to provide resistance to HBL-mediated cytotoxicity [560]. These results indicate that LITAF functions as the primary receptor of HBL, whereas, in certain cell types, CDIP1 serves as an independent and alternative receptor to LITAF [560]. This finding is analogous to how anthrax toxin utilises a predominant host cell surface receptor CMG2 and an alternate receptor TEM8 [67-70].

It remains unknown how the individual subunits of HBL interact with either of the two receptors and what are the signalling cascades initiated following their engagement. In addition, what might be the physiological advantage of encoding a receptor for HBL which would render a host susceptible to HBL-induced lethality? Earlier studies had shown that LITAF is expressed in multiple tissues and organs in humans, such as peripheral blood leukocytes, lymph nodes, and the spleen [561]. TLRs can induce the expression of LITAF, which then serves as a transcription factor mediating the expression of the pro-inflammatory cytokines, such as TNF and IL-6, in human and mouse macrophages [561,562]. Further, mutations in LITAF, potentially causing impaired endosomal protein trafficking and degradation, are associated with the inherited motor and sensory neuropathies known as Charcot-Marie-Tooth disease [563]. Therefore, LITAF functions as a trigger of inflammation and guardian of fundamental cellular processes. Given its widespread expression and critical functionality in cellular physiology in humans, it is intriguing to speculate that *B. cereus* would strategically use HBL to target LITAF to trigger cell death responses in the mammalian host.

1.4.5 Novel membrane-bound receptor/s of NHE

Identification of LITAF and CDIP1 opens up exciting opportunities to search for other surface receptors of *B. cereus* toxins which are important for pathogenesis. Indeed, isolates of *B. cereus* lacking the HBL toxin can still cause disease in humans [458,564,565]. These strains

probably express NHE and other virulence factors capable of contributing to the infection. It will be interesting to investigate the surface receptor of NHE and other *B. cereus* toxins.

1.4.6 Innate immune recognition of *B. cereus*

PRRs are expressed in immune cells and non-immune cells, including macrophages, dendritic cells, neutrophils, epithelial cells, endothelial cells, and NK cells [4]. Previous studies have shown that macrophages, dendritic cells and neutrophils recognise both vegetative cells and the spore of *B. cereus*, triggering an immune response [566-568].

The innate immune response triggered by TLRs has been predominantly characterised in mouse and rabbit models of endophthalmitis, a severe intraocular infection mostly associated with post-traumatic injury and vision loss [569]. Earlier studies have shown that TLR2 mediated polymorphonuclear leukocytes (PMN) infiltration in the eyes in response to *B. cereus*-induced endophthalmitis in mice [570]. The lack of TLR2 did not affect intraocular growth of *B. cereus,* but reduced the secretion of TNF, IL-6 and IFN-γ in the infected eyes [570] (**Fig. 1.10**). In addition, mice lacking TLR2 exhibited delayed loss of retinal function. However, the inability of TLR2-deficiency to abolish inflammatory cytokine production and provide full protection against loss of retinal function suggests contributions from other innate immune receptors [570].

Subsequent studies revealed that mice lacking either one of the two adaptor proteins of TLRs, called Myeloid differentiation primary response protein MyD88, or TIR domain-containing adapter molecule 1 (also known as TICAM-1 or TRIF) exhibited reduced intraocular inflammation following *B. cereus* infection [571]. TLR4 signals through MyD88 and TRIF, and thus, an involvement of TLR4 might explain the previous observation that mice lacking TLR2 displayed residual intraocular inflammation following *B. cereus* infection [570,571]. Indeed, mice lacking TLR4 exhibited reduced influx of PMN, retinal damage and intraocular inflammation in response to *B. cereus* infection [571]. However, this result was unexpected because *B. cereus* does not encode LPS, a ligand of TLR4-MD2-CD14 receptor complex found in Gram-negative

bacteria. The component/s of *B. cereus* that activate TLR2 are likely to be teichoic and lipoteichoic acid or lipoproteins (**Fig. 1.10**), whereas an unknown virulence factor of *B. cereus* might trigger TLR4 signalling. Previous studies have shown that cholesterol-dependent cytolysins, anthrolysin of *B. anthracis* [572] and pneumolysin of another Gram-positive bacterium *Streptococcus pneumoniae* [573], can induce TLR4-dependent apoptosis in mouse macrophages. The cholesterol-dependent cytolysin of *B. cereus,* cereolysin, could therefore be a putative TLR4 agonist.

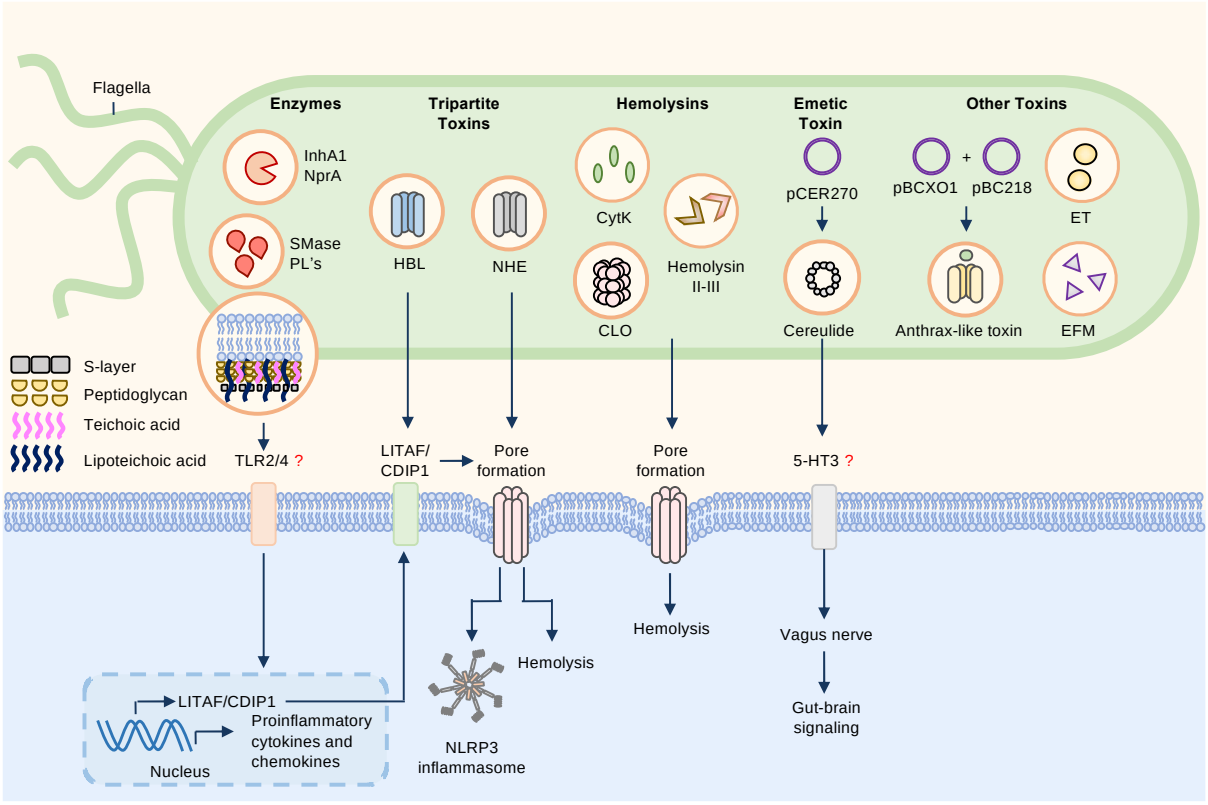

Figure 1.10 | *B. cereus* virulence factors.

The *B. cereus* cell wall comprises an inner lipid bilayer membrane, a peptidoglycan layer, and an outermost crystalline surface glycoprotein layer (S-layer). Interspersed within the cell wall are teichoic and lipoteichoic acid molecules. *B. cereus* infection may involve TLR2 and/or TLR4 activation, however the bacterial ligands for either receptor have remained unknown (indicated by a question mark). *B. cereus* contains several enzymes involved in virulence, including the metalloproteases InhA1 and NprA, sphinogomyelinase (SMase) and several

phospholipases (PL's). Collectively, these enzymes are thought to degrade proteins and lipids within and/or associated with the host cell membrane to establish an infection. Several virulence factors of *B. cereus* are responsible for causing diarrheal symptoms following infection and include the tripartite toxins hemolysin BL (HBL) and non-hemolytic enterotoxin (NHE) as well as cytotoxin K (CytK, also known as hemolysin IV). HBL-induced pore formation occurs after binding to the surface cell receptors LITAF (also known as small integral membrane protein of lysosome/late endosome, or SIMPLE) and the LITAF-like protein called Cell Death Inducing P53 Target 1 (CDIP1). Furthermore, HBL- and NHE-induced pore formation drives activation of the NLRP3 inflammasome. HBL and NHE also possess additional hemolytic activity, along with CytK, cereolysin, (CLO, also known as hemolysin I), hemolysin II and hemolysin III. The emetic toxin, cereulide, is encoded on the plasmid pCER270 and is thought to induce emesis through either a direct or indirect interaction (indicated by a question mark) with 5-HT3 receptors of the stomach and intestine that drive gut-to-brain signaling. Several strains of *B. cereus* have acquired the ability to produce an Anthrax-like toxin, encoded by the plasmids putatively assigned pBCXO1 and pBC218. This toxin is thought to drive a severe anthrax-like infection. Enterotoxin T (ET) and Enterotoxin FM (EFM) are also thought to play an important role in virulence, although their roles as enterotoxins and/or enzymes have remained unclear.

1.5 Rationale of this study

Microorganisms from all domains of life can induce activation of the inflammasome pathway, however, a complete repertoire of microbes that can activate the inflammasome remains unknown. Microbial PAMPs such as lipoproteins, flagella, toxins, nucleic acids and enzymes can activate the inflammasome, suggesting that there is potential to identify new microbial activators of the inflammasome pathway.

1.6 Hypotheses and Aims

1.6.1 Hypotheses

Hypothesis 1: Novel inflammasome activators can be identified from analysis of clinically important intracellular and extracellular bacteria.

Hypothesis 2: Inflammasome sensors can sense toxins from phylogenetically-diverse organisms.

1.6.2 Aims

Aim 1: To identify novel inflammasome activators from clinically important bacteria.

Aim 1.1: To screen a panel of bacteria and bacteria-free culture supernatants to assess their ability to induce inflammasome activation in primary bone-marrow-derived macrophages (BMDMs).

I will investigate whether secreted factors from various intracellular and extracellular bacteria can induce inflammasome activation. Wild-type (WT) BMDMs will be incubated with bacteria-derived culture supernatants for 3-20h. The hallmarks of inflammasome activation will be assessed based on immunoblot analysis of the cleavage of caspase-1, enzyme-linked

immunosorbent assays (ELISA) analysis to measure secretion of inflammasome-dependent pro-inflammatory cytokines IL-1β and IL-18 and lactate dehydrogenase (LDH) analysis to determine the percentage cell death.

Aim 1.2: To identify the inflammasome sensor responsible for recognising the secreted factor/s.

WT BMDMs and BMDMs lacking various inflammasome sensors and components will be incubated with the bacteria-derived supernatant and live bacteria for 3-20h. The hallmarks of inflammasome activation will be assessed as described in Aim 1.1.

Aim 1.3: To characterise the inflammasome activator/s from the bacteria-derived supernatant.

BMDMs will be treated with the bacteria-derived supernatant, and the supernatant that had been treated with heat (37, 50, 75 or 100 °C), proteinase K, RNase and DNase to investigate the nature of the inflammasome-activating ligand. Furthermore, size fractionation of the supernatant will be carried out to determine the size range of the inflammasome-activating activator/s. Screening of >40 environmental and clinical isolates of the inflammasome-activating bacteria will be carried out to facilitate the identification of the inflammasome-activating factor. The results will determine the inflammasome-activating ability of various strains carrying specific virulence factor/s. The hallmarks of inflammasome activation will be assessed as described in Aim 1.1.

Aim 1.4: To delineate the identity of the inflammasome activator/s present in the bacteria-derived supernatant.

BMDMs will be treated with mutant bacteria lacking the activator/s (from Aim 1.3) for 3-20h. The hallmarks of inflammasome activation will be assessed as described in Aim 1.1. For further validation, the purified activator/s will be generated to assess their ability to activate the inflammasome.

Aim 1.5: To investigate the mechanism of inflammasome activation by the activator/s.

Depending on the inflammasome sensor that recognises the bacterial activator/s, experiments will be designed to elucidate the mechanisms of action of how the new activator/s activate the inflammasome. For example, I will investigate whether the activator/s bind to the plasma membrane and remain on the plasma membrane or enter the cytoplasm.

Aim 1.6: To investigate the role of inflammasomes in mediating a host response to the new activator/s.

WT mice and mice lacking the inflammasome sensor and effector caspase-1 will be injected with the activators. Analysis of survival and cytokine production from tissues of mice will be conducted.

Aim 2: To comprehensively analyse inflammasome-activating ability of toxins from phylogenetically diverse organisms.

Aim 2.1: To screen a panel of purified toxins to assess their ability to induce inflammasome activation BMDMs.

Toxins derived from bacteria, fungi, snakes, terrestrial invertebrates or marine organisms will be investigated to assess their ability to induce inflammasome activation. Purified toxins will be added to WT BMDMs and incubated for 3-20h. ELISA assays will be used to measure secretion of the cytokines IL-1β and IL-18.

Aim 2.2: To investigate which inflammasome pathway is responsible for mediating inflammasome activation in response to toxin treatment in BMDMs.

WT BMDMs and BMDMs lacking different inflammasome components will be treated to determine the nature of the inflammasome complexes required to respond to the toxins

identified in Aim 2.1. The hallmarks of inflammasome activation will be assessed as described in Aim 1.1.

Aim 2.3: To investigate the molecular mechanisms by which toxins induce inflammasome activation in BMDMs.

The candidate toxins activating the inflammasome complex will be further investigated for their mechanism of action as described in Aim 1.5.

Aim 2.4: To determine the role of inflammasomes in mediating a host response to the new activator/s.

WT mice and mice lacking the inflammasome sensor and effector caspase-1 will be injected with the purified toxin/s. Analysis of survival and cytokine production from tissues of mice will be conducted.

Chapter 2♦ Materials & Methods

2.1 Mouse strains

WT C57BL/6, *Gsdmd*$^{I105N/I105N}$ [574], *Gsdmd*$^{-/-}$ [574] and *Mefv*$^{-/-}$ were obtained from the Australian Phenomics Facility (APF) at the Australian National University (ANU), Australia. *Casp1/11*$^{-/-}$ [575], *Casp11*$^{-/-}$ [576], *Casp1*$^{-/-}$ [326] and *Nlrp3*$^{-/-}$ [577] mice were obtained from the Jackson Laboratory, USA. *Aim2*$^{-/-}$[356], *Asc*$^{-/-}$ [309] and *Nlrc4*$^{-/-}$ [309] mice were obtained from Genentech, USA. Mice were generated in the C57BL/6 background (*Aim2*$^{-/-}$, *Nlrc4*$^{-/-}$, *Gsdmd*$^{I105N/I105N}$, *Gsdmd*$^{-/-}$ and *Mefv*$^{mut/mut}$) or in the 129 background (*Asc*$^{-/-}$, *Casp1/11*$^{-/-}$, *Casp11*$^{-/-}$ and *Nlrp3*$^{-/-}$) and backcrossed to C57BL/6 for 10 generations. Details of mice strains is listed in **Table 2.5.** Both male and female mice between 6-8 weeks were used in this study. Mice were bred, maintained and caged in specific pathogen-free conditions by Animal Staff Technicians at the APF at the ANU. All experiments were conducted according to the ANU Animal Experimentation Ethics Committee, Protocol number A2020/19.

2.2 Cell culture

2.2.1 Bone-marrow derived macrophages (BMDMs)

To culture primary BMDMs, mice were ethically culled, and the femur and tibia were collected. Both the proximal and distal epiphyses were cut, and the bone marrow was flushed using feeding media [DMEM (D6546, Sigma-Aldrich), 10% (v/v) heat-inactivated FBS (F8192, Sigma-Aldrich), 30% (v/v) L929 conditioned media (source of M-CSF; see below), 1% (v/v) penicillin and streptomycin (11140050, Gibco ThermoFisher Scientific), 1% (v/v) non-essential amino acids (11140050, Gibco ThermoFisher Scientific), 1% (v/v) L-glutamine (25030081, ThermoFisher Scientific)] using a syringe with a 26-gauge needle (NN+2638R, Terumo). An 18-gauge needle (NN+1838R, Terumo) was then used to dissociate and resuspend the cells into solution. The cell suspension was then brought to a final volume of 45 ml with pre-warmed feeding media. The bone marrow obtained from one mouse was split equally between three 150 mm culture dishes (CLS430597-60EA, Sigma-Aldrich).

Bone marrow cells were differentiated into BMDMs by culturing for 5-7 days at 37 °C with 5% CO_2. Cells were fed on days three and five with 5 ml feeding media. Our lab and others have confirmed that 95% to 99% of BMDMs grown using this protocol expressed the myeloid and macrophage surface markers CD11b, CD86, and F4/80 [154,578]. Differentiated BMDMs were washed and scraped from the culture dish in 15 ml of pre-warmed seeding media. Cells were counted using a Cellometer Auto T4 Bright Field Cell Counter. Trypan blue stain (T8154-100ML, Sigma-Aldrich) was used to differentiate between live and dead cells. The BMDM cell suspension was diluted with pre-warmed seeding media to 1×10^6 cells/ml and seeded onto 12-well plates (CLS3513, Corning Costar) at a concentration of 1×10^6 cells/well unless otherwise stated. Experiments were conducted on seeded BMDMs on the following day. Reagents and constitution of solutions used are described in **Tables 2.1 and 2.2** respectively.

2.2.2 L929 fibroblasts

L929 media was generated using the murine L929 fibroblast cell line (ATCC CCL1). L929 cell culture supernatant contains secreted M-CSF which promotes the differentiation of myeloid progenitors in the bone marrow extract into macrophages [579]. L929 fibroblasts were cultured in L929 media [DMEM media + 10% (v/v) FBS + 1% (v/v) penicillin and streptomycin + 1% (v/v) L-glutamine + 1% (v/v) HEPES (11344-041, Gibco)]. 2.4×10^6 cells were seeded in T-175 flasks (159910, ThermoFisher Scientific) with 50 ml of L929 media. Cells were then cultured for 7 days at 37 °C with 5% CO_2, following which the cell culture supernatant was filter-sterilised through a 0.45 µm filter and was used in BMDM feeding and seeding media. Reagents and constitution of solutions used are described in **Tables 2.1 and 2.2** respectively.

2.2.3 THP1 monocytes

To culture human THP-1 monocytes (ATCC® TIB-202™), frozen aliquots of cells [0.9×10^6 cells/ml in 10% (v/v) DMSO)] were thawed and transferred to 25 ml pre-warmed THP-1 media [(RPMI (11875093, Gibco), 10% (v/v) FBS (F8192, Sigma-Aldrich), 1% (v/v) L-glutamine

(25030081, ThermoFisher Scientific), 1% (v/v) penicillin and streptomycin + 1% (v/v)]. Cells were centrifuged for 10 min at 200 *g* at 4 °C. The supernatant containing residual DMSO was removed, and 25 ml THP-1 media were used to resuspend the cell pellet. Cells were then transferred into a T-75 flask and cultured for 2-3 days intervals at 37 °C with 5% CO_2 before being transferred to fresh media. Once cells neared 100% confluency, cell number was determined using a haemocytometer with Trypan blue viability stain to distinguish live or dead cells (T8154-100ML, Sigma-Aldrich). Cells were seeded at a concentration of 5×10^5 cells per well in 24-well plates. Experiments were conducted on THP-1 monocytes the following day. Reagents and constitution of solutions used are described in **Tables 2.1 and 2.2** respectively.

2.2.4 THP1 macrophages

1×10^6 THP1 monocytes were treated with 100nM phorbol 12-myristate 13-acetate (PMA; P8139, Sigma-Aldrich) for 24 hr. After 24 hr of PMA treatment, the cells were cultured in fresh media and allowed to rest for another 24 hr. After resting for 24 hr, the cells were primed with LPS for 3hr followed by various treatments. Cells were seeded at a concentration of 5×10^5 cells per well in 24-well plates. Experiments were conducted on THP-1 macrophages the following day. Reagents and constitution of solutions used are described in **Tables 2.1 and 2.2** respectively.

2.3 Bacterial culture

Salmonella enterica serovar Typhimurium (referred to as *S.* Typhimurium) strain SL3144 were grown in Luria-Bertani (LB) media (244620, BD) overnight under aerobic conditions at 37 °C. *Francisella novicida* were cultured in BBL Trypticase Soy Broth (TSB) (211768, BD) supplemented with 0.2% L-cysteine (BP376-100, ThermoFisher Scientific) overnight under aerobic conditions at 37 °C. *B. cereus* were grown LB media under aerobic conditions at 30 °C. The list of *Bacillus* strains used are shown in Table 2.3. All bacteria were subcultured

(1:10) in fresh media the next day for 3-4 hr under their respective conditions. Details of bacterial strains and composition of media used are shown in **Tables 2.4 and 2.8** respectively.

2.4 Stimulation of cells to activate the inflammasome

2.4.1 Stimulation of BMDMs

To activate the canonical NLRP3 inflammasome, BMDMs in infection media were primed with 0.5 µg/ml ultrapure lipopolysaccharide (LPS) from *E. coli* (ALX-581-014-L002, Enzo Life Sciences) for 3 hr to upregulate the expression of NLRP3 and pro-IL-1β [109]. LPS-primed BMDMs were stimulated with 5 mM ATP for 45 min or 10 µM Nigericin for 30 min. To activate the LPS-sensing non-canonical inflammasome, ultrapure LPS from *Salmonella minnesota* (5 µg/well; tlrl-smlps, InvivoGen) was resuspended in PBS and mixed with 0.3 µl/well of Xfect polymer in Xfect reaction buffer (631318, Clontech Laboratories). After 10 min, the mixture was added to BMDMs in Opti-MEM (31985-070, ThermoFisher Scientific) and left for 5 hr. To activate the AIM2 inflammasome, 2.5 µg of poly(dA:dT) (tlrl-patn, InvivoGen) were resuspended in PBS and mixed with 0.3 µl of Xfect polymer in Xfect reaction buffer (631318, Clontech Laboratories, Inc.). After 30 min, DNA complexes were added to BMDMs in Opti-MEM (31985-070, ThermoFisher Scientific) and stimulated for 4 hr. To activate the NLRC4 inflammasome, BMDMs were infected with *S.* Typhimurium at MOI of 2 for 4 hr. Ultrapure flagellin was mixed with 20 µl of the liposomal transfection reagent DOTAP (11202375001, Sigma-Aldrich) in PBS. After 30 min, the complexes were added to LPS-primed BMDMs in Hank's Balanced Salt Solution (HBSS, H9394, Sigma-Aldrich) and incubated for 3-5 hr.

Details of stimulation of BMDMs with *B. cereus*, supernatant of *B. cereus*, HBL, NHE, and PLC are described in the Materials and Methods section of Chapters 3, 4 and 5. For inhibition studies, 50 µM of cytochalasin B (C6762, Sigma-Aldrich), 50 µM of cytochalasin D (C8273, Sigma-Aldrich), 20 µM of the selective and potent NLRP3 inhibitor, MCC950 [213-215], 50 mM of potassium chloride (KCl) (P9541, Sigma-Aldrich) or 50 mM of sodium chloride (NaCl) (S9888,

Sigma-Aldrich) were added to BMDMs 30 min prior to stimulation. Cell culture supernatants were collected for ELISA and LDH assays. Cell culture supernatants and cell lysates were collected for immunoblot analysis.

2.4.2 Stimulation of THP1 monocytes and macrophages

THP1 monocytes were centrifuged for 10 min at 200 *g* at 4 °C. Cells were resuspended in fresh media containing 0.5 µg/ml ultrapure lipopolysaccharide (LPS) from *E. coli* (ALX-581-014-L002, Enzo Life Sciences) for 3 hr prior to activation. THP-1 macrophages were replaced by fresh media containing 0.5 µg/ml LPS for 3 hr prior to activation. To activate the canonical NLRP3 inflammasome, THP1 monocytes and macrophages in LPS-primed infection media were stimulated with 5 mM ATP for 45 min or 10 µM Nigericin for 30 min. For inhibition experiments, unprimed and LPS-primed THP1 monocytes and macrophages were pre-treated for 30 min with 20 µM of the selective and potent NLRP3 inhibitor, MCC950 [213-215]. Details of bacterial strains and composition of media used are shown in **Tables 2.4 and 2.8** respectively.

2.5 Immunoblotting analyses

BMDMs and cell culture were mixed with 50 µl western blot lysis buffer [10% (v/v) Triton X-100 (T8787, Sigma-Aldrich), 0.01 M DDT (R0862, ThermoFisher Scientific), protease inhibitor cocktail (1183615001, Sigma-Aldrich)] and 120 µl 4x loading dye (8% SDS, 400 mM DDT, 0.4% bromophenol blue, 40% glycerol, 200 mM Tris, pH 6.8). Samples were heated at 100 °C for 20 min before storage at –80°C until required.

Samples were run on 8-12% SDS-PAGE gels (prepared in-house; see **Table 2.8**) at 200 V for 1 hr or until the dye front approaches the bottom of the gel. Gels were then transferred onto PVDF membranes (1PVH00010, Merck) using the Trans-Blot Turbo system (Bio-Rad) at 2.5 A and 25 V for 20 min. Prior to transfer, PVDF membranes were activated with methanol (AJA5005, Ajax Finechem) and then equilibrated with transfer buffer (250 mM Tris, 1.92 M glycine, pH 8.3). Once transferred, the membranes were washed briefly with ddH_2O and then

blocked with 5% skim milk in TBST [5% (w/v) skin milk powder in TBST (200 mM Tris, 1.37 M NaCl, 0.075% (v/v) Tween-20, pH 7.4)] for 1 hr at room temperature with rocking. The membranes were then incubated with primary antibodies against the desired target protein overnight at 4 °C with shaking. A list of primary antibodies can be found in **Table 2.1**.

The following day, membranes were washed 4 times for 10 min with TBST with constant shaking to remove residual/non-specifically bound primary antibody. The membranes were then incubated with 1:5,000 concentration horseradish peroxidase (HRP)-conjugated secondary antibodies in 5% skim milk in TBST for 1 hr at room temperature with rocking (Table 2.1). The type of secondary antibodies used depended on the animal source of the primary antibody. The membranes were then washed 4 times for 10 min with TBST to remove residual secondary antibody. Finally, the membranes were incubated with Clarity Western ECL Substrate (1705061, Bio-Rad) for 1 min and then imaged using the ChemiDoc™ Imaging System (12003153, Bio-Rad). The images were processed using ImgaeLab software (Bio-Rad). Reagents, software and constitution of solutions used are described in **Tables 2.2, 2.6 and 2.8** respectively.

2.6 Enzyme-linked immunosorbent assays (ELISAs)

Murine BMDM and human THP-1 cell culture supernatant (100 µl) from treated and untreated cells and serum and peritoneal fluid from mice were collected into round-bottom 96-well plates (163320, ThermoFisher Scientific). Cytokines were analysed using plate-based ELISAs specific for mouse IL-18 (BMS618-3TEN, ThermoFisher Scientific; or EK-0048, ELISAkit.com) or human IL-1β (BMS224-2TEN, ThermoFisher Scientific) and IL-18 (BMS267-2TEN, ThermoFisher Scientific) or multiplex ELISAs (MCYTOMAG-70K, EMD Millipore) specific for mouse IL-1β, TNF, KC and IL-6. List of commercial kits used are described in **Table 2.3**.

Each well of the primary antibody coated 96-well plates (mouse IL-18 and human IL-1β and IL-18) was washed twice with wash buffer (1% (v/v) Tween-20 in PBS) prior to addition of

samples and standards. Mouse IL-18, human IL-1β or human IL-18 protein standards were serially diluted according to the manufacturers' instructions (2-fold serial dilutions from 2,000 to 31.3 pg/ml) and 50 µl of each dilution was added to the plate. Each sample (25 µl) was then diluted (1:2) in 25 µl of sample diluent in each well. Wells containing only the sample diluent (50 µl) served as a background control. Biotin-conjugated anti-mouse monoclonal detection antibody against IL-18 or biotin-conjugated anti-human monoclonal detection antibody against IL-1β or IL-18 (50 µl) was then added to each well and incubated at room temperature for 2 hr, shaking (400 rpm). Plates were then washed thrice with wash buffer and streptavidin-HRP (100 µl) was added to each well, followed by another incubation period of 1 hr at room temperature with constant agitation. Plates were subsequently washed a further three times with wash buffer. Next, 100 µl of tetramethylbenzidine (TMB; an HRP substrate) substrate solution was added, and the plates were incubated in the dark at room temperature for 10 min or until the most concentrated standard well turned to a dark blue colour. At this point, 100 µl of stop solution was added to each well to inactivate HRP. Absorbance values were read at 450 nm using the Infinite 200 PRO System (Tecan) and the concentration of the relevant cytokine in each sample was calculated based on the standard curve. Finally, values were multiplied by 2 to account for the sample dilution factor.

The protocol for multiplex ELISA kit is as follows; tissue culture samples were diluted in DMEM media (1:10). 25 µl of diluted samples or standard and 25 µl of matrix solution were added to the ELISA plate. 25 µl of mouse cytokine antibody-immobilised magnetic beads were added to the ELISA plate and incubated overnight at 4°C. After washing twice, 25 µl of detection antibody was added and the plate was incubated at room temperature for 1 hr. After incubation, 25 µl of Streptavidin-Phycoerythrin was added and incubated at room temperature for 30 min. After washing twice, 150 µl of Sheath Fluid (or Drive Fluid if using MAGPIX®) was added to all wells and the plate was kept on shaking for 5 min. The Median Fluorescent Intensity (MFI) data was measured by MAGPIX® (Luminex Corporation). Finally, values were multiplied by 10 to account for the sample dilution factor.

2.7 Measurement of intracellular potassium

The supernatant was removed from stimulated and unstimulated BMDMs. BMDMs were washed thrice with PBS to remove dead cells and 70% nitric acid (0.5 ml per 12× 10^6 cells; AJA341-2.5L, Ajax Finechem) was added. Empty 15 ml Falcon tubes were weighed. The cell lysate/nitric acid suspension was then transferred into a 15 ml Falcon tube and the tubes were weighed. The cell lysate/nitric acid suspension was diluted 10 times with MiliQ water followed by weighing of tubes. The concentration of K^+ and Na^+ in each sample was analysed using inductively coupled plasma - optical emission spectroscopy (ICP-OES) on a PerkinElmer OPTIMA 7300 ICP Optical Emission Spectrometer (PerkinElmer, Melbourne, Australia). The intracellular ion concentrations of the treated samples were shown as a percentage relative to the untreated control, set at 100%.

2.8 Immunofluorescence staining of ASC specks

BMDMs were seeded onto coverslips with 18 mm thickness (0111580, Superior Marienfeld) within the wells of 12-well tissue culture plates. BMDMs were left untreated or stimulated with various inflammasome activators. BMDMs were washed thrice with PBS to remove dead. The samples were fixed with 4% paraformaldehyde at room temperature for 15 min. The samples were blocked in 10% normal goat serum (005000121, Jackson ImmunoResearch) supplemented with 0.1% saponin (47036, Sigma-Aldrich) for 1 hr. Cells were incubated with a rabbit anti-ASC antibody (1:500 dilution, clone AL177, AG-25B-0006-C100, AdipoGen) overnight at 4 °C. An anti-rabbit secondary Rhodamine red antibody (111295144, Jackson ImmunoResearch) was used. Cells were counterstained in DAPI mounting medium (H-1200, Vecta Labs). Inflammasome specks and BMDMs were visualised, counted, and imaged using a Leica SP5 confocal microscope.

2.9 Membrane and cytosolic fractionation

The Mem-PER Plus Membrane Protein Extraction Kit (89842, ThermoFisher Scientific) was used to separate the membrane and cytosolic fractions. 12×10^6 cells were used for each sample (2×10^6 cells/well in a 6-well tissue culture plate (CLS3516, Sigma-Aldrich). BMDMs were left untreated or treated for 1 hr. Cells were scraped using a Corning® cell lifter (CLS3008, Sigma-Aldrich) and then centrifuged (500 *g*, 5 min). The supernatant was carefully discarded, and the cells were resuspended in 3 ml of Cell Wash solution. The cell suspension was centrifuged (500 *g*, 5 min) and the supernatant was discarded. The cells were resuspended again in 1.5 ml of Cell Wash solution, centrifuged (500 *g*, 5 min) and the supernatant was carefully discarded. The cell pellet was then resuspended in 750 µl of permeabilisation buffer by vortexing briefly to obtain a homogenous cell suspension. This was then incubated at 4ºC for 10 min with constant mixing.

The permeabilised cells were centrifuged (16,000 *g*, 15 min) to separate the cytosolic and membrane protein fractions. The supernatant containing cytosolic proteins was then carefully transferred into a new tube and 250 µl of 4x loading dye was added. Solubilisation buffer (300 µl; 89842, ThermoFisher Scientific) was added to the remaining pellet and incubated at 4 ºC for 45 min with constant mixing. This solution containing membrane proteins was mixed with 100 µl of 4x loading dye. Both cytosolic and membrane proteins fractions were processed for immunoblotting analysis (See Section 2.5) and detection of membrane protein (Pan-cadherin, 25100, Cell Signaling Technology; CD-14, 17000-1-AP, Proteintech), caspase-1 (control cytosolic protein, AG-20B-0042, Adipogen) as well as toxin components such as HBL -B, -L_1, -L_2 and NHE -C, -B, -A, were performed.

2.10 Lactate dehydrogenase (LDH) assay

LDH is a cytosolic protein that is only released from mammalian cells when the plasma membrane is compromised, which is indicative of lytic cell death [580]. The amount of LDH

released from BMDMs into the cell culture supernatant, which is used to determine the percentage of cell death, was quantified using the CytoTox 96 Non-Radioactive Cytotoxicity Assay (G1780, Promega). Standards were prepared using BMDMs that were seeded at concentrations of 1×10^6, 0.5×10^6, 0.25×10^6, 0.125×10^6, 0.0625×10^6 cells/well. BMDMs were incubated overnight in 5% CO_2 at 37 °C before subjected to three freeze-thaw cycles (-80 °C to 25 °C) to ensure complete lysis. Supernatant (15 µl) from each sample and standards was diluted with 35 µl of PBS (for 50 µl final volume) per well in a 96-well microplate (167008, ThermoFisher Scientific). CytoTox reagent (15 µl; G1780, Promega) was added to each well and incubated in the dark at room temperature for 10 min. Stop solution (15 µl; G1780, Promega) was then added to each well after a change of colour (colourless to dark yellow) in wells containing standards. The plate was read at an absorbance of 490 nm using the Infinite 200 PRO System (Tecan). The percentage LDH release was calculated using a standard curve.

2.11 Liposome Studies

Liposomes were synthesised using cholesterol (23%) and synthetic lipid derivatives DPPC (33%), DOPC (32%) and DSPC (12%), mimicking the mammalian cell membrane [581]. The concentration of liposomes was 7 mM, loaded either with methylene blue dye (75 µg/ml) or saline. Encapsulation of methylene blue dye into the lumen of liposomes allowed us to investigate the ability of toxins to induce pores in the liposomal membrane that would result in leakage of the dye. Liposomes were treated with various toxins for 1 hr at 4 °C. Liposomes that were ruptured by sonication at 100 amplitude for 5 min were used as controls. The released dye was captured by a cation exchanger resin Dowex (10-15 mg per well). The absorbance (OD) of residual dye was measured at a wavelength of 595 nm using the Infinite 200 PRO system (Tecan).

2.12 Real Time qRT-PCR Analysis

RNA was extracted from BMDMs using TRIzol (15596018, ThermoFisher Scientific) and from bacteria using the TRIzol Max Bacterial RNA Isolation kit (16096040, ThermoFisher Scientific). For 1 × 10^6 BMDMs, 500 µl Trizol was added, and samples were vortexed for 1 min to homogenise and incubated at room temperature for 5 min. Then, 100 µl chloroform were added and the mixture was vortexed rigorously for 15 seconds before incubated at room temperature for 15 min. Samples were then centrifuged (12,000 g) at 4°C for 20 min. The aqueous phase was transferred to a fresh Eppendorf tube and 500 µl isopropanol was added before incubation at 80°C for an hour. Samples were thawed at room temperature before being centrifuged (12,000 g) at 4°C for 20 min. The supernatant was discarded, and the remaining pellet was dissolved in the following pre-prepared solution: 500 µl water, 50 µl NaOAc, 500 µl RT isopropanol. Samples were incubated at room temperature for 20 min and washed twice with 75% ethanol. During the washing steps, 500 µl of 75% ethanol were used, and samples were centrifuged (12,000 g) at 4°C for 10 min. The supernatant was discarded, and the pellet was air dried before resuspension in 11.5 µl of water.

In case of RNA extraction from bacteria, overnight cultures of B. cereus were centrifuged (5,000 *g*) at 4°C for 20 min. The supernatant was decanted, and the cell pellet was resuspended in 200 µl of Max Bacterial Enhancement Reagent (16122012, ThermoFisher Scientific) and incubated at 95°C for 4 min. RNA extraction procedures were performed using the TRIzol Max Bacterial RNA Isolation kit (16096040, ThermoFisher Scientific). 1 ml Trizol was added, and the mixture was incubated at room temperature for 5 min. Then, 200 µl chloroform were added and the mixture was vortexed vigorously for 15 s before incubated at room temperature for 15 min. The rest of the steps were followed as listed above.

Reverse transcriptases were used to generate cDNA with the High-Capacity cDNA Reverse Transcription kit (4368813, ThermoFisher Scientific). cDNA was quantified using quantitative PCR with SYBR Green Real-Time PCR Master Mixes (4364346, ThermoFisher Scientific).

Data were analysed using the ddCt method [582]. Real-time qRT-PCR primer sequences are listed in **Table 2.14**.

2.13 Brightfield microscopy

Images of untreated or treated BMDMs were captured with a Leica DMi1 inverted microscope at 40 mm working distance with a Leica HI PLAN I 40x/0.50 PH1 objective lens. Images were captured, cropped and analysed with the LAS AF software version 2.7.3 (Leica; **Table 2.6**).

2.14 Protein production and purification

DNA sequences of the genes encoding the toxin components were acquired from the *B. cereus* strain ATCC 10876 (GenBank: CM000715.1). These nucleotide sequences were translated into peptide sequences using the ExPASy Translate Tool [583]. Predicted hydrophobic transmembrane regions were identified using Membrane Protein Explorer (MPEx) components that searched for regions that are likely to insert into the membrane based upon the free energy of partitioning of amino acids between water and membrane [584]. The amino acids constituting the predicted transmembrane regions were deleted from the protein sequences to yield the following truncated toxin components named accordingly: HBL-B_{Mut}, for the B component of HBL lacking the putative transmembrane domain; and NHE-C_{Mut}, for the C component of NHE lacking the putative transmembrane domain.

2.14.1 Design of the expression construct plasmids

The protein sequences for each wild type and mutant components (HBL-B_{WT}, HBL-B_{mut}, NHE-C_{WT} and NHE-C_{mut}) were submitted to GenScript to design plasmids. Briefly, the synthesised DNA inserts encoding each DNA sequences encoding each HBL component that were codon-optimised for *E. coli* transcription and cloned them into NcoI and XhoI restriction sites of the pET-28a(+)-TEV plasmid. The pET-28a(+)-TEV plasmid is appropriate because it encodes a kanamycin resistance gene for selection and expression of the target gene is under the control

of the T7 promoter. The BL21(DE3) *E. coli* strain (C600003, ThermoFisher Scientific) contains the DE3 lysogen that carries the gene expressing a T7 RNA polymerase under the control of the *lac*UV5 promoter. When BL21(DE3) bacteria are transformed with the pET-28a(+)-TEV plasmid vector, isopropyl β-D-1-thiogalactopyranoside (IPTG; IPTG-RO, Roche) can be used to induce the expression of the T7 RNA polymerase, which is highly specific and only transcribes genes that are downstream of the T7 promoter. Thus, IPTG is used to control the expression of the target genes. The expression constructs produced by GenScript were stored at -20 °C.

2.14.2 Transformation of *E. coli* with plasmid

Chemically-competent *E. coli* strain BL21(DE3) (50 µl; C600003, ThermoFisher Scientific) were gently mixed with 1 µl of each plasmid (1 µg/µl) and incubated on ice for 30-45 min. The plasmids were transformed into chemically-competent *E. coli* strain BL21(DE3) by heat shock in a 42 °C water bath for 45 s. The mixture was then returned to ice and diluted with 450 µl of Luria-Bertani (LB) broth [2.5% (w/v) LB Broth powder (244620, BD Biosciences) in dH_2O]. The transformed bacterial suspension was incubated at 37 °C for 60 min with constant agitation. Thereafter, 100 µl of the bacterial suspension was spread onto LB_{Kan} [LB broth + 1.5% agar (281230, BD Biosciences) + 30 µg/ml kanamycin (10106801001, Roche)]. Plates were incubated under aerobic conditions at 37 °C overnight (16 hr). Single colonies were selected and inoculated into fresh LB_{Kan} broth and incubated with constant agitation (180 rpm) under aerobic conditions at 37 °C overnight. Equal volumes (500 µl) of the bacterial culture and filter-sterilised 40% (v/v) glycerol (GA010, Chem-Supply) in ddH_2O were used to create glycerol stocks and stored at -80 °C. Reagents and consumables used are fully annotated in **Tables 2.2 and 2.7**.

2.14.3 Large-scale expression and culture

Glycerol stocks of transformed bacteria were streaked on LB_{Kan} agar and incubated under aerobic conditions at 37 °C overnight for single colonies. A single colony was picked to inoculate a 20 ml starter culture of LB_{Kan} broth and incubated with constant agitation (180 rpm) under aerobic conditions at 37 ° C overnight. A starter culture (10 ml) was transferred into 1 L of LB_{Kan} broth in a 2 L baffled culture flask (CLS431256, Sigma-Aldrich) and incubated with shaking (180 rpm) at 37 °C for 4 hr until an OD_{600} of 0.6 was obtained. Expression was induced by adding IPTG (1 mM final concentration) and the incubation continued under identical conditions overnight. The culture suspension was centrifuged (5,000 *g*, 20 min, 4 °C) to pellet the bacteria and stored at -80 ^{o}C until required.

2.14.4 Preparation of the soluble fraction

The *E. coli* pellet was resuspended in 15 ml of lysis buffer [50 mM Tris, pH 8.0 (BP152-1, ThermoFisher Scientific); 300 mM NaCl (SA046, Chem-Supply); 5 mM imidazole (I2399, Sigma-Aldrich)] containing egg-white lysozyme (250 µg/ml; 89833, ThermoFisher Scientific). Phenylmethylsulfonyl fluoride (PMSF; 1 mM; 78830, Sigma-Aldrich) were added to inhibit serine proteases. The bacterial suspension was incubated with constant agitation at room temperature for 1 hr. Cells were subsequently disrupted by freeze-thaw cycles (four cycles of freezing at -80 °C until frozen and thawing in a 37 °C water bath until thawed). DNase I (10 µg/ml; 10104159001, Roche) and $MgCl_2$ (5 mM; M2670, Sigma-Aldrich) were then added and incubated with constant agitation at room temperature for 1 hr. The soluble and insoluble fractions were separated by centrifugation (27,000 *g*, 20 min, 4 °C) and the soluble fraction was passed through a 0.22 µm filter (SLGP033RS, Merck) to remove precipitates prior to downstream processing. Constituents of solutions used are described in **Table 2.8**.

2.14.5 Preparation of the insoluble fraction

The pellet containing the insoluble fraction was resuspended in 10 ml of inclusion body wash buffer [50 mM Tris, pH 8.0; 300 mM NaCl; 5 mM imidazole; 0.5% (v/v) Triton X-100 (T8787, Sigma-Aldrich)] and centrifuged (27,000 *g*, 20 min, 4 °C). The pellet was washed using repeated resuspension and centrifuged for at least two cycles until the supernatant became clear. The pellet was then resuspended in 10 ml load/equilibration buffer [50 mM Tris, pH 8.0; 8 M urea (U5128, Sigma-Aldrich); 20 mM imidazole] and incubated with constant agitation at 4 °C overnight to ensure complete denaturation of proteins in the insoluble fraction. The suspension was then centrifuged (27,000 *g*, 20 min, 4 °C) and the supernatant was collected for IMAC Ni-NTA loose resin purification.

The supernatant was mixed with 1 ml of loose HisPur™ Ni-NTA Resin (88221, ThermoFisher Scientific) equilibrated with load/equilibration buffer and incubated with constant agitation at 4 °C for 2 hr. The protein/resin suspension was then centrifuged (2,500 *g*, 10 min, 4 °C) and the supernatant containing contaminants was removed. Contaminants were removed from the resin by washing at least once with 10 ml load/equilibration buffer. The resin was then resuspended with 2 ml of elute buffer (50 mM Tris, pH 8.0; 8 M Urea; 300 mM imidazole) and incubated at 4 °C for 1 hr to elute the target protein. Imidazole competes with the histidine tag of the target protein for binding to the nickel resin [585], thus the target protein is eluted in the presence of high imidazole concentration. The resin suspension was centrifuged (3,300 *g*, 20 min, 4 °C) and the supernatant containing the eluted target protein was collected. The resin was resuspended again in 2 ml elute buffer, centrifuged and the supernatant collected to ensure complete recovery of the target protein.

The target protein was refolded using rapid dilution by slowly adding drops of the eluate into 200 ml of rapid-stirring refolding buffer (50 mM Tris; pH 8.0; 300 mM NaCl). The refolding protein solution was left stirring at 4 °C overnight to allow refolding equilibrium to be reached. The refolded protein solution was passed through a 0.22 µm filter to remove precipitates

before further purification using a HisTrap purification column. Constituents of solutions used are described in **Table 2.8**.

2.14.6 HisTrap purification

The soluble or insoluble preparation of His-tagged recombinant HBL and NHE components was loaded onto 5 ml HisTrap HP histidine-tagged protein purification column at 5 ml/min until 2 sample volumes has been passed through (17524701, GE Healthcare Lifesciences) at 4 °C using the NGC Quest™ 10 Chromatography System (7880001, Bio-Rad) and ChromLab™ software (Bio-Rad). Target proteins were eluted from the HisTrap column using a stepwise gradient of imidazole (10% increments) from Buffer A (50 mM Tris, pH 8.0; 300 mM NaCl; 5 mM imidazole) to Buffer B (50 mM Tris, pH 8.0; 300 mM NaCl; 500 mM imidazole). The presence of protein in the eluate fractions was detected by UV light absorbance at 280 nm. Samples were collected from fractions under the A280 peak, and purity was analysed by SDS-PAGE and Coomassie blue staining. Constituents of solutions used are described in **Table 2.8**.

2.14.7 Coomassie blue staining

Samples were run on 12% SDS-PAGE at 180 V for 45-60 min, or until the dye front approached the bottom of the glass plate. The polyacrylamide gels were placed in ddH_2O and a microwave oven was used to heat the gel until boiling for 30-60 s. The ddH_2O was then discarded and Coomassie blue stain solution [5% (v/v) ethanol; 0.1% (v/v) HCl (20252.324, VWR Chemicals); 0.01% (w/v) Coomassie brilliant blue G-250 (1610406, Bio-Rad)] was added to cover the gels. The gels were boiled again for 30-60 s. The staining solution was discarded, and the gels were washed with ddH_2O overnight until the background was clear. The gels were then imaged using the colorimetric function in the ChemiDoc™ (Bio-Rad). Constituents of solutions used are described in **Table 2.8**.

2.14.8 Concentration and buffer exchange of purified proteins

Eluate fractions determined to have highly purified target proteins were pooled and concentrated using Amicon Ultra-15 Centrifugal Filter Units (UFC903024, Merck) and centrifuged at 4,000 *g* until the final concentrated volume reached 0.5-1.0 ml. The pooled solution was then buffer exchanged with 10 ml storage buffer [0.1 mM PMSF; 0.1 mM EDTA; 10% glycerol in phosphate buffered saline (PBS; 14190-144, ThermoFisher Scientific)]. The concentrated and highly purified protein was then aliquoted and stored at -80 °C. Constituents of solutions used are described in **Table 2.8**.

2.14.9 Analysis of protein purity and concentration

Following the concentration and buffer exchange of the purified protein, the protein purity was evaluated via SDS-PAGE using the Coomassie blue stain. A single band in the lane indicated pure protein. The protein concentration was determined by spectrophotometric measurements of A280 using a NanoDrop™ 2000/2000c spectrophotometer and calculated using the extinction coefficient (ϵ280) of each protein and the pathlength (l).

$$Protein\ molar\ concentration\ = \frac{A_{280}}{\epsilon_{280} \times l}$$

2.15 Scanning electron microscopy

Untreated or treated 1×10^6 BMDMs seeded on coverslips were washed two times with 0.1 M PBS and fixed using a primary fixative [2% (v/v) glutaraldehyde (EMS16400, EMS) in 0.1 M PBS] and incubated in the dark at 4 °C overnight. Cells were then washed three times with 0.1 M PBS for 30 min for each washing step. A secondary fixation [1% osmium tetroxide (75632, Sigma-Aldrich) in dH_2O] was applied and incubated at room temperature for 1 hr. Cells were washed with dH_2O three times for 30 min for each washing step. Cells were dehydrated by stepwise increments of 30%, 50%, 70%, 90%, 100% (v/v) ethanol for 15 min

for each step, followed by another two additional dehydrations with 100% (v/v) ethanol for 15 min each. Cells were then critical-point dried using the liquid CO_2 and Balzers Critical Point Dryer CPD 030. Samples were sputter-coated with platinum at 25 mA for 45 secs using the EMI TECH K550 Sputter coater and visualised under the Zeiss UltraPlus Field emission scanning electron microscope at 5 kV; 30 mm aperture with a below lens secondary electron detector.

2.16 Transmission electron microscopy

Three wells of 2.5×10^6 BMDMs (7.5×10^6 BMDMs total) were seeded into a 6-well plate and left overnight. BMDMs were left untreated or treated for 1-3 hr before each sample was washed with 0.1 M PBS and scraped using a Corning® cell lifter. Cell suspensions were transferred into an Eppendorf tube and centrifuged (300 *g*, 2 min) to pellet the cells. The cell pellet was resuspended and fixed in a primary fixative [2.5% (v/v) glutaraldehyde, 4% (v/v) paraformaldehyde in 0.1 M PBS] and incubated at 4 ºC for 1 hr. Cells were then centrifuged and washed three times with 0.1 M PBS buffer (pH 7.4) with gentle shaking for 10 min. The supernatant was removed, and cells were fixed with a secondary fixative (1% osmium tetroxide in dH_2O) and incubated at room temperature for 1 hr. Cells were washed three times with dH_2O with gentle shaking for 10 min.

Agarose embedding was carried out for samples that have a low cell density determined by cell pellet size of less than 0.5mm in diameter. Cells from these samples were pipetted into an Eppendorf PCR tube (Z316156, Sigma-Aldrich) containing 1.2% DNA-grade low melting agarose (10207, Electron Microscopy Sciences) in ddH_2O. Agarose-embedded samples were then cooled on ice and trimmed to remove excess agarose. All samples were then en-bloc stained with 2% (w/v) uranyl acetate (22400, Electron Microscopy Sciences) in PBS and left at 4 ºC overnight before samples were rinsed three times with dH_2O with gentle shaking for 10 min. Cells were then dehydrated in solutions of ethanol at increasing concentrations of 30%, 50%, 70%. 90%, 100% (v/v) with shaking, each for at least 30 min. Cells were embedded

in LR white resin (C023, ProSciTech) by infiltration with solutions of resin in ethanol at increasing concentrations of 25%, 50%, 75% and 100% (v/v), each for at least 1 hr.

Cells were then washed 3 times with 100% resin with gently shaking for 30 min each. Resin polymerisation was carried out at 60 ºC for 16 hr under vacuum. The Ultramicrotome (UC7, Leica) with glass knives [made with glass knife maker (KMR2, Leica)] was used to create sections of 150 nm thickness, which were placed on silicon wafers (71893-01, Electron Microscopy Sciences). Sections were post-stained with 2% (w/v) uranyl acetate for 10 min and followed by lead citrate for 7 min and washed with ddH_2O. Samples were visualised under the Zeiss UltraPlus Field emission scanning electron microscope at 5 kV; 30 mm aperture with an energy sensitive backscatter detector (EsB).

2.17 IncuCyte analysis

BMDMs were seeded into 24 well tissue culture plates (CLS3524, Sigma-Aldrich) at a density of 0.25×10^6 cells per well. To track the cell viability of BMDMs in response to activators, BMDMs were stimulated with 0.5 nM of HBL combinations in presence of the SYTOX Green nuclear stain (1 µM; S7020, Life Technologies), which is impermeable to live cells but penetrates compromised membrane [586]. SYTOX Green stains nucleic acids and is an indicator of dead cells. Cells were monitored every 10 min over 3 hr using the IncuCyte Zoom "in-incubator" imaging system (Essen Biosciences) with phase-contrast and green fluorescence (dual colour module 4459, Essen Biosciences) microscopy. At the conclusion of the experiment, 0.025% (w/v) saponin (47036-50G-F, Sigma-Aldrich) was added to every well to disrupt the membranes of all cells. A final image of the dead cells was then taken. Images were analysed using the IncuCyte Zoom software (**Table 2.6**), which enumerates the number of dead cells based on the intensity and quantity of green objects ("dead cells"). The dead cell counts from the final image was used to normalise the dead cell counts for each time frame.

$$Normalised\ \%\ cell\ death = \frac{Green\ object\ count}{Total\ green\ object\ count\ in\ final\ image} \times 100\%$$

2.18 Animal infection

For survival analysis, sex-matched male or female 8-week-old mice were injected via an intraperitoneal (i.p.) route with *B. cereus* or PLC (details in the following sections: 3.317 and 4.3.20 (*B. cereus*) and 5.3.15 (PLC)). To investigate the effects of MCC950 [213-215], mice were injected, via an i.p. route, with 50 mg/kg of MCC950 dissolved in PBS or with vehicle control PBS. 1 hr later, mice were injected, via an i.p. route, with *B. cereus* and supernatant of *B. cereus* along with a second dose of 50 mg/kg of MCC950 or a second dose of PBS. The monitoring of mice was done according to the ANU Animal Experimentation Ethics Committee, Protocol number A2020/19. The scoring parameters were body weight, consciousness and general appearance. Based on the score, mice were ethically culled upon reaching the humane endpoint. For cytokine measurement, mice were injected, via an i.p. route, with *B. cereus*, supernatant of *B. cereus*, or PLC for 3-12h before collection of blood and peritoneal samples (details in the following sections: 3.317 and 4.3.20 (*B. cereus*) and 5.3.15 (PLC)). Mice were euthanised using CO_2. 29 ½ G insulin syringes were used for cardiac puncture and blood collection. Blood samples were centrifuged at 13,000 *g* for 10 min and supernatant containing the serum was isolated. To harvest the peritoneal fluid, 2-3 ml of 3% FBS containing PBS were injected into the peritoneum of mice using 26 ½ G needle syringe. The peritoneal fluid was withdrawn using 18 ½ G needle syringes and samples were centrifuged at 200 *g* at 4 °C to remove the cell pellet. The supernatant was collected. Serum and peritoneal fluid were analysis for cytokines production by ELISA.

2.19 Statistical analyses

Data analysis was performed using the GraphPad Prism 6.0 software package (**Table 2.6**). For ELISA, LDH and IncuCyte results, a normal distribution cannot be assumed. Thus, statistical significance between 3 or more groups were calculated via a One-way analysis of variance (ANOVA) with a Tukey's multiple comparison test. The statistical tests between 2

groups were calculated via a Two-tailed t-test. Data are presented as the mean ± the standard error of the mean (s.e.m.) of three independent repeats. Significance was defined as NS, not statically significant and $P > 0.05$; * $P < 0.05$; ** $P < 0.01$; *** $P < 0.001$; and **** $P < 0.0001$. In this study, no statistical methods were used to predetermine the sample size. The experiments were not randomised, and the investigators were not blinded to allocation during the experiments and outcome assessments.

Table 2.1 | List of Antibodies

Reagent or Resource	Source	Identifier
Mouse monoclonal anti-caspase-1	Adipogen	#AG-20B-0042; RRID:AB_2490248
Rabbit monoclonal anti-Phospho- pIκBα	Cell Signaling Technology	#2859; RRID:AB_561111
Rabbit polyclonal anti-IκB	Cell Signaling Technology	#9242; RRID: AB_823540
Rabbit polyclonal anti-Phospho-Erk	Cell Signaling Technology	#9101; RRID:AB_331646
Rabbit polyclonal anti-Erk	Cell Signaling Technology	#9102; RRID:AB_330744
Mouse monoclonal anti-NLRP3	Adipogen	#AG-20B-0014; RRID:AB_2490202
Rabbit monoclonal anti-GAPDH	Cell Signaling Technology	#5174; RRID:AB_10622025
Rabbit polyclonal anti-ASC antibody	AdipoGen	#AG-25B-0006; RRID:AB_2490440
Rabbit monoclonal [EPR19828] anti-Gasdermin-D	Abcam	#ab209845; RRID:AB_2783550
Mouse anti-HBL-B serum	[508]	N/A
Mouse anti-HBL-L_1 serum	[508]	N/A
Mouse anti-HBL-L_2 serum	[508]	N/A
Mouse anti-NHE-B IgG1	[565]	N/A
Mouse anti-NHE-A IgG1	[565]	N/A
Mouse anti-NHE-C IgG1	[565]	N/A
Rabbit polyclonal anti-Pan-cadherin	Cell Signaling Technology	#25100; RRID:AB_2158565
Rabbit polyclonal anti-CD14	Proteintech	#17000-1-AP; RRID:AB_2883746
Rat monoclonal FITC-anti-CD11b	BioLegend	#101205; RRID: AB_312788
Rat monoclonal [1D4B] to LAMP1	Abcam	#ab25245, RRID: AB_449893
Goat anti- Rabbit IgG (H+L) Secondary Antibody Rhodamine Red™-X conjugate	Jackson ImmunoResearch	#111-295-144; RRID:AB_2338028
Goat anti-Mouse IgG (H+L) Secondary Antibody, Rhodamine Red™-X conjugate	Jackson ImmunoResearch	#115-295-146; RRID:AB_2338766

Table 2.2 | List of Chemicals and Reagents

Reagent or Resource	Source	Identifier
DMEM	ThermoFisher Scientific	#11995073
Fetal bovine serum	Sigma-Aldrich	# F8192
Penicillin and streptomycin	Gibco ThermoFisher	#10378016
Difco™ LB Broth, Miller (Luria-Bertani)	BD	#244620
BBL™ Trypticase™ Soy Broth (TSB)	BD	#211768
L-cysteine	ThermoFisher Scientific	#BP376-100
Gentamicin	ThermoFisher Scientific	#15750-060
Lipopolysaccharide (LPS) from E. coli, Serotype J5 (Rc)	Enzo Life Sciences	# ALX-581-014-L002
ATP	Roche	#10127531001
Poly(dA:dT)	InvivoGen	#tlrl-patn
Opti-MEM	ThermoFisher Scientific	#31985-070
Ultrapure flagellin from *Salmonella enterica* serovar Typhimurium	InvivoGen	# tlrl-epstfla-5
DOTAP	Sigma-Aldrich	#11202375001
Hank's Balanced Salt Solution	Sigma-Aldrich	# H9394
Super Signal Femto substrate	ThermoFisher Scientific	#34095
Normal goat serum	Jackson ImmunoResearch	#005000121
Saponin	Sigma-Aldrich	#47036
DAPI mounting medium	Vecta Labs	#H-1200
Potassium chloride (KCl)	Sigma-Aldrich	#P9541
Protease Inhibitor Cocktail Tablets	Roche	#11697498001
Saponin	Sigma-Aldrich	#47036-50G-F
Sodium Chloride (NaCl)	Chem-Supply	#SA046
Sodium Dodecyl Sulfate	Astral Scientific	#S-2066
Super Signal Femto Substrate	ThermoFisher Scientific	#34095
TEMED	Sigma-Aldrich	#T9281
Tris Base	ThermoFisher Scientific	#BP152-1
Triton X-100	Sigma-Aldrich	#T8787
DAPI Mounting Medium	Vecta Labs	#H-1200
Dithiothreitol	ThermoFisher Scientific	#R0862

Dulbecco's Modified Eagle Medium	Sigma-Aldrich	#D6546
Ethanol	Ajax Finechem	#AJA214-2.5LPL
Ethylenediaminetetraacetic Acid	Sigma-Aldrich	#F8192
Foetal Bovine Serum	Sigma-Aldrich	#F8192
Glutaraldehyde	EMS	#EMS16400
Glycerol	Chem-Supply	#GA010
Glycine	Bio-Rad	#1610724
HEPES	Gibco ThermoFisher Scientific	#11344-041
Hydrochloric acid (HCl)	VWR Chemicals	#20252.324
L-Glutamine	ThermoFisher Scientific	#25030081
MEM Non-Essential Amino Acids	Gibco ThermoFisher Scientific	#11140-050
Methanol	Ajax Finechem	#AJA5005
Nitric acid	Ajax Finechem	#AJA341-2.5L
Opti-MEM	ThermoFisher Scientific	#31985-070
Osmium Tetroxide	Sigma-Aldrich	#75632
Penicillin + Streptomycin antibiotics	Gibco ThermoFisher Scientific	#10378016
Normal goat serum	Jackson ImmunoResearch	#005000121
Agarose SFR™ Super Fine Resolution	Electron Microscopy Sciences	#10207
ATP	Roche	#10127531001
Bafilomycin A1 from *Streptomyces griseus*	Sigma-Aldrich	#B1793-2UG
Bromophenol Blue	Sigma-Aldrich	#B-8026
Cytochalasin D from *Zygosporium mansonii*	Sigma-Aldrich	#C8273-5MG
Sodium Chloride (NaCl)	Chem-Supply	#SA046
16% Paraformaldehyde (methanol free)	ThermoFisher Scientific	#28908
16% Paraformaldehyde EM Grade	EMS	#C004
Glutaraldehyde	EMS	#EMS16400
LR Resin, medium & hard grade	ProSciTech	#C023
Bovine serum albumin	Jackson ImmunoResearch	#001000173
Uranyl acetate	Electron Microscopy Sciences	#22400

TRIzol	ThermoFisher Scientific	#15596018
Tween-20	Sigma-Aldrich	#P1379
SYBR Green Real-Time PCR Master Mixes	ThermoFisher Scientific	#4364346
Protease inhibitor	Roche	#11697498001
Phosphatase inhibitor	Roche	#04906837001
SYTOX™ Green Nucleic Acid Stain	ThermoFisher Scientific	#S7020
MCC950	[213]	N/A
1,2-dipalmitoyl-sn-glycero-3-phosphocholine (DPPC)	Avanti Lipids	#850355
1,2-dioleoyl-sn-glycero-3-phosphocholine (DOPC)	Avanti Lipids	#850375
1,2-distearoyl-sn-glycero-3-phosphocholine (DSPC)	Avanti Lipids	#850365
Cholesterol	Avanti Lipids	#700000

Table 2.3 | List of Critical Commercial Assays

Reagent or Resource	Source	Identifier
Xfect transfection kit	Clontech Laboratories, Inc.	#631318
Pierce™ Silver Stain Kit	ThermoFisher Scientific	#24612
CytoTox 96 Non-Radioactive Cytotoxicity Assay	Promega	#G1780
High-capacity cDNA Reverse Transcription kit	ThermoFisher Scientific	#4368813
Mouse Multiplex ELISA kit	Millipore	#MCYTOMAG-70K
Mouse IL-18 ELISA kit	ELISAkit.com	# EK-0048
Mouse IL-18 Platinum ELISA Kit	ThermoFisher Scientific	#BMS618-3TEN
Human IL-1 beta ELISA Kit	ThermoFisher Scientific	#BMS224-2TEN
Human IL-18 ELISA Kit	ThermoFisher Scientific	#BMS267-2TEN
TRIzol Max Bacterial RNA Isolation kit	ThermoFisher Scientific	#16096040
Duopath® Cereus Enterotoxins	Merck	#1041460001
Mem-PER Plus Membrane Protein Extraction Kit	ThermoFisher Scientific	#89842
Alexa Fluor ™ 568 Protein Labeling Kit	ThermoFisher Scientific	#A10238

Pierce ™ BCA Protein Assay Kit	ThermoFisher Scientific	#23225

Table 2.4 | List of bacteria

Strain ID	Reagent or Resource	Source	Identifier
C. rod.	*Citrobacter rodentium*	American Type Culture Collection	#51459
E. coli	*Escherichia coli*	American Type Culture Collection	#11775
P. aer.	*Pseudomonas aeruginosa*	This study	N/A
S. Typhi or *S. Tm*	*Salmonella enterica* serovar Typhimurium	[587]	N/A
S. flex.	*Shigella flexneri*	American Type Culture Collection	#700930
S. epi.	*Staphylococcus epidermidis*	American Type Culture Collection	#14990
S. pneu.	*Streptococcus pneumoniae*	This study	N/A
S. pyo.	*Streptococcus pyogenes*	This study	N/A
F. nov.	*Francisella novicida*	This study	N/A
L. mono.	*Listeria monocytogenes*	American Type Culture Collection (ATCC)	#15313
***B. cereus* strains**			
B. cer. or ATCC	ATCC 14579	Air	ATCC
01	17/0409	Human Blood	This study
02	17/1400	Human Blood	This study
03	56A	Human (no further information)	This study
04	ATCC 10876	Contaminated Flask	[508]
05	A1A1-77	Human (no further information)	This study
06	A1C1-9	Human (no further information)	This study
07	A1C1-11	Human (no further information)	This study
08	Bc13-001	Soil	[588]
09	Bc13-003	Bovine Feces	[588]
10	Bc13-004	Soil	[588]
11	Bc13-005	Soil	[588]
12	Bc13-006	Bovine Feces	[588]
13	Bc13-007	Soil	[588]
14	Bc13-008	Soil	[588]

15	Bc13-009	Soil	[588]
16	Bc13-010	Soil	[588]
17	Bc13-011	Caprine Feces	[588]
18	Bc13-012	Caprine Feces	[588]
19	Bc13-013	Soil	[588]
20	Bc13-015	Soil	[588]
21	Bc14-001	Bovine Feces	[588]
22	Bc14-002	Bovine Feces	[588]
23	Bc14-003	Soil	[588]
24	Bc14-004	Soil	[588]
25	Bc14-005	Milk Filter	[588]
26	Bc14-007	Bovine Feces	[588]
27	Bc14-008	Bovine Feces	[588]
28	Bc14-010	Bovine Feces	[588]
29	Bc14-013	Soil	[588]
30	Bc14-015	Caprine Feces	[588]
31	Bc14-016	Soil	[588]
32	Bc14-017	Soil	[588]
33	Bc14-019	Feed (grain)	[588]
34	F837/76	Human (postoperative infection)	[589]
35	Bc14-021	Soil	[588]
36	Bc14-022	Soil	[588]
37	Bc14-023	Soil	[588]
38	Bc14-024	Soil	[588]
39	Bc14-025	Feed (grain)	[588]
40	Bc14-028	Milk Filter	[588]
41	Bc14-029	Soil	[588]
42	Bc14-030	Soil	[588]
43	C1A1-39	Human (no further information)	This study
44	M015777	Human (thigh)	This study
45	M3-5-63	Human (leg wound)	This study
N/A	Δ*hbl*	ATCC 10876	[508]
N/A	Δ*nhe*	F837/76	[512]

Table 2.5 | List of Experimental Models: Organisms/Strains

Reagent or Resource	Source	Identifier
Nlrp3$^{-/-}$ mice	[577]	N/A
Nlrc4$^{-/-}$ mice	[309]	N/A
Aim2$^{-/-}$ mice	[356]	N/A
Asc$^{-/-}$ mice	[309]	N/A

Mefv$^{K112X/K112X}$ mice (referred as: *Mefv*$^{mut/mut}$)	Australian Phenomics Facility, ANU, Australia	N/A
Gsdmd$^{I105N/I105N}$ mice	[574]	N/A
Gsdmd$^{-/-}$ mice	[574]	N/A
Casp1/11$^{-/-}$ mice	[575]	N/A
Casp11$^{-/-}$ mice	[576]	N/A
Casp1$^{-/-}$ mice	[326]	
THP-1	ATCC	#TIB-202
Nlrp3$^{-/-}$ THP1	Invivogen	thp-konlrp3z
CaCo-2	ATCC	#HTB-37
CT26	ATCC	#CRL-2638
Jurkat	ATCC	#TIB-152
HEK293T	ATCC	#CRL-11268
HT-29	ATCC	#HTB-38
K-562	ATCC	#CCL-243
L-929	ATCC	#CCL-1
LS 174T	ATCC	#CL-188
MC-38	Kerafast	#ENH204-FP
MDCK	ATCC	#CCL-34
U266B1	ATCC	#TIB-196
Vero	ATCC	#CCL-81
RMA-S	Human lymphoma	In this study

Table 2.6 | List of Software and Algorithms

Reagent or Resource	Source	Identifier
GraphPad Prism 6.0	GraphPad Software, Inc.	http://www.graphpad.com
LAS AF version 2.7.3.	Leica Microsystems	https://www.leica-microsystems.com/products/microscope-software/details/product/leica-las-x-ls/
Image Lab Software 6.0	Biorad	https://www.bio-rad.com/en-au/product/image-lab-software?ID=KRE6P5E8Z/
IncuCyte Zoom 2016A	Essen Biosciences	https://www.essenbioscience.com/en/products/software/incucyte-base-software/
MPEx	[590]	http://blanco.biomol.uci.edu/mpex/
HELIQUEST	[591]	http://heliquest.ipmc.cnrs.fr/

Table 2.7 | List of consumables

Reagent or Resource	Source	Identifier
PVDF membrane	Millipore	#IPVH00010
4-20% Mini-Protean TGX Precast Gel	Biorad	#456-1096
Pierce Concentrator 9KMWCO	ThermoFisher Scientific	#89884A
Amicon Ultra-4 Centrifugal Filter Unit	Millipore	# UFC803096
Amicon Ultra-15 Centrifugal Filter Unit	Millipore	# UFC905096
0.45 µm Filter	ThermoFisher Scientific	#NAL295-4545
Cell Scraper 39cm	Sarstedt	#83.1831
Corning Costar Tc-Treated Multiple (12) Well Plates	Sigma-Aldrich	#CLS3513
Corning Costar Tc-Treated Multiple (24) Well Plates	Sigma-Aldrich	#CLS3524
Corning Costar Tc-Treated Multiple (6) Well Plates	Sigma-Aldrich	#CLS3516
Corning® 150 mm Not TC-treated Culture Dish	Sigma-Aldrich	#CLS430597-60EA
Corning® cell lifter	Sigma-Aldrich	#CLS3008
Corning® Erlenmeyer baffled cell culture flasks	Sigma-Aldrich	#CLS431256
Cover glasses, thickness No. 1, circular	Superior Marienfeld	#0111580
Eppendorf® PCR tube	Sigma-Aldrich	#Z316156
Falcon™ 15mL Conical Centrifuge Tubes	ThermoFisher Scientific	#352095
Falcon™ 50mL Conical Centrifuge Tubes	ThermoFisher Scientific	#352070
Glass Knifemaker Leica EM KMR3	Leica Microsystems	#KMR2
Hypodermic 18-guage needle	Terumo	#NN+1838R
Hypodermic 26-guage needle	Terumo	#NN+2638R
HisPur™ Ni-NTA Resin	ThermoFisher Scientific	#88221
Infinite 200 PRO System	Tecan	
Nunc™ MicroWell™ 96-well flat bottom microplates	ThermoFisher Scientific	#167008
Nunc™ MicroWell™ 96-well round bottom microplates	ThermoFisher Scientific	#163320
Standard 90mm Petri Dishes	ThermoFisher Scientific	#101RTIRR
Superfrost™ Plus 1 mm microscope slide	LabServe	#LBS4951
T-175 Flasks	ThermoFisher Scientific	#159910

Ultra-Flat Silicon Wafers	Electron Microscopy Sciences	#71893-01
Ultramicrotome Leica EM UC7	Leica Microsystems	#UC7

Table 2.8 | List of Constituents of solutions

Solution	Constituents	Concentrations
10 × Running Buffer	- Tris (60.6 g) - Glycine (288 g) - SDS (20 g) - dH20 (2000 ml)	- 0.025 M Tris - 0.192 M Glycine - 0.1% (w/v) SDS
10 × TBS	- Tris (121.12 g) - NaCl (400.31 g) - dH2O (5000 ml)	- 200 mM Tris-HCl, pH 7.4 - 1.37 M NaCl
10 × Transfer Buffer	- Tris (60.6 g) - Glycine (288.3 g) - dH2O (2000 ml) - 20% Methanol (only added to 1 × solution)	- 250 mM Tris-HCl, pH 8.3 - 1.92 M glycine
4 × Loading Dye	- Tris (0.97 g) - DTT (2.47 g) - MilliQ H2O (24 ml) - SDS (3.2 g) - Bromophenol blue (0.16 g) - Glycerol (16 ml) pH 6.8	- 200 mM Tris-HCl, pH 6.8 - 400 mM DTT - 8% (w/v) SDS - 0.4% (w/v) bromophenol blue - 40% (v/v) glycerol
4 × Resolving Gel Buffer	- Tris (90.8 g) - SDS (2 g) - dH20 (500 ml)	- 1.5 M Tris-HCl, pH 8.8 - 0.4% (w/v) SDS
4 × Stacking Gel Buffer	- Tris (30.3 g) - SDS (2 g) - dH20 (500 ml)	- 0.5 M Tris-HCl, pH 6.8 - 0.4% (w/v) SDS
5% Skim Milk Blocking Buffer	- Skim milk powder (20 g) - TBST (400 ml)	- 5% (w/v) skim milk
Cell Lysis Buffer	- Triton X-100 (4 ml) - DTT (400 µl from 1M stock) - MilliQ H2O (36 ml) - Protease inhibitor cocktail (4 tablets)	- 4% (v/v) Triton X-100 - 10 mM DTT

Feeding media	- DMEM (300 ml) - L929 conditioned media (150 ml) - FBS (50 ml) - Non-essential amino acids (5 ml) - L-glutamine (5 ml) - Penicillin-streptomycin (5 ml)	- 30% (v/v) L929 conditioned media - 10% (v/v) FBS - 1% (v/v) non-essential amino acids - 1% (v/v) L-glutamine - 1% (v/v) penicillin and streptomycin
Infection media	- DMEM (450 ml) - FBS (50 ml)	- 10% (v/v) FBS
L929 media	- DMEM (300 ml) - FBS (50 ml) - L-glutamine (5 ml) - Penicillin-streptomycin (5 ml)	- 10% (v/v) FBS - 1% (v/v) L-glutamine - 1% (v/v) penicillin and streptomycin - 1% (v/v) HEPES
Resolving Gel Composition (12%)	- dH2O (11.2 ml) - 4 × Resolving buffer (8 ml) - Acrylamide (12.8 ml) - 10% APS (120 µl) - TEMED (40 µl)	- 0.375 M Tris, pH 8.8 - 0.1% (w/v) SDS
Seeding media	- DMEM (300 ml) - L929 conditioned media (150 ml) - FBS (50 ml) - Non-essential amino acids (5 ml) - L-glutamine (5 ml)	- 30% (v/v) L929 conditioned media - 10% (v/v) FBS - 1% (v/v) non-essential amino acids - 1% (v/v) L-glutamine
Stacking Gel Composition (4%)	- dH2O (15.25 ml) - 4 × Stacking buffer (6.5 ml) - Acrylamide (3.25 ml) - 10% APS (125 µl) - TEMED (37.5 µl)	- 0.125 M Tris, pH 6.8 - 0.1% (w/v) SDS
TBST	- 1 × TBS (2,000 ml) - Tween-20 (1.5 ml)	- 200 mM Tris-HCl, pH 7.4 - 1.37 M NaCl - 0.075% (v/v) Tween-20
0.5M EDTA	- 29.224 g EDTA - 200 ml dH2O	- 0.5 M EDTA
10 mM PMSF in isopropanol	- 0.01742 g PMSF - 10 ml Isopropanol	- 10 mM PMSF

Bacterial Lysis Buffer/ HisTrap Buffer A	- 6.057 g Tris - 17.532 g NaCl - 0.340385 g Imidazole -dH2O (up to 1L)	- 50 mM Tris-HCl, pH 8.0 - 300 mM NaCl - 5 mM Imidazole
Cell Lysis Buffer	- Triton X-100 (4 ml) - DTT (400 µl from 1M stock) - MilliQ H2O (36 ml) - Protease inhibitor (4 tablets)	- 4% (v/v) Triton X-100 - 10 mM DTT
Coomassie Blue Stain	40 mg Coomassie brilliant blue R-250 26.7 ml 95% ethanol 1.5 ml HCl add dH2O up to 500 ml	- 5% (v/v) Ethanol - 0.1% (v/v) HCl - 0.01 (w/v) Coomassie brilliant blue G-250
Elute Buffer	- 1.2114 g Tris - 96.096 g Urea - 4.08462 g Imidazole - dH2O (up to 200 ml)	- 50 mM Tris-HCl; pH 8.0 - 8 M Urea - 300 mM Imidazole
HisTrap Buffer B	- 6.057 g Tris - 17.532 g NaCl - 20.4231 g Imidazole - dH2O (up to 1L)	- 50 mM Tris, pH 8.0 - 300 mM NaCl - 300 mM Imidazole
Infection media	- DMEM (450 ml) - FBS (50 ml)	- 10% (v/v) FBS
LB agar	- 6.25 g LB broth powder - 3.75 g agar powder - dH2O (up to 250 ml)	- 2.5% (w/v) LB - 1.5% (w/v) agar
LB broth	- 6.25 g LB broth powder - dH2O (up to 250 ml)	- 2.5% (w/v) LB
Load/Equilibration Buffer	- 1.2114 g Tris - 96.096 g Urea - 0.272308 g Imidazole - dH2O (up to 200 ml)	- 50 mM Tris-HCl, pH 8.0 - 8 M Urea - 20 mM Imidazole
Protein Storage Buffer	- 100 µl 10 mM PMSF in isopropanol - 2 µl 0.5 M EDTA - 1 ml Glycerol - PBS (up to 10 ml)	- 0.1 mM PMSF - 0.1 mM EDTA - 10% (v/v) Glycerol

Table 2.9 | List of Bacterial toxins

Toxin name	Final concentration	Mechanism of action	Source	Identifier
B. cereus HBL-B, -L_1 and -L_2	5 nM of each component	Pore forming toxins	[508]	N/A
B. cereus NHE-C, -B and -A	100 nM of each component	Pore forming toxins	[508]	N/A
C. perf. Phospholipase C	1.5 or 0.625 Units/ml	Phospholipase and sphingomyelinase; degrades eukaryotic cell membranes [592]	Sigma-Aldrich	P7633-500UN
C. dip toxin	0.28 µg/ml	Inhibits eukaryotic translation [593]	Sigma-Aldrich	D0564-1MG
P. aer ETA	0.04 µg/ml	Inhibits eukaryotic translation [594]	Sigma-Aldrich	P0184-.5MG
P. mul toxin	0.014 µg/ml	G protein deaminase [595]	Sigma-Aldrich	P5806-1VL
S. aur α-toxin	0.08 µg/ml	Pore-forming toxin [596]	Sigma-Aldrich	H9395-.5MG
S. aur entA	0.12 µg/ml	T-lymphocyte superantigen [597]	Sigma-Aldrich	S9399-.1MG
S. aur entB	0.12 µg/ml	T-lymphocyte superantigen [597]	Sigma-Aldrich	S4881-1MG
S. dys StxB	0.16 µg/ml	B subunit binds at membrane, allowing A subunit to enter cell and inhibit translation [598]	Sigma-Aldrich	SML0562-.5MG
V. cho toxin	0.16 µg/ml	B subunit binds at membrane, allowing A subunit to enter and target G proteins [599]. B subunit can also transport LPS into cytoplasm [600,601]	Sigma-Aldrich	C8052-.5MG

Abbreviations: *C. dip, Corynebacterium diphtheriae; C. per, Clostridium perfringens; P. aer, Pseudomonas aeruginosa; P. mul, Pasteurella multocida; S. aur, Streptococcus aureus; S. dyx, Shigella dysenteriae; V. cho, Vibrio cholera.*

Table 2.10 | List of Fungal toxins

Toxin name	Final concentration	Mechanism of action	Source	Identifier
α-amanitin	0.2 µg/ml	Transcriptional inhibitor; inhibits RNA polymerase II [602]	Sigma-Aldrich	A2263-1MG
β-amanitin	0.2 µg/ml	Transcriptional inhibitor; inhibits RNA polymerase II [602]	Sigma-Aldrich	A1304-1MG
γ-amanitin	0.2 µg/ml	Transcriptional inhibitor; inhibits RNA polymerase II [602]	Abcam	Ab144514
AAL toxin	0.8 µg/ml	Inhibits ceramide and sphingolipid synthesis [603]	Sigma-Aldrich	A4707-1MG
Gliotoxin	0.4 µg/ml, chloroform	Immunosuppressant [604]	Sigma-Aldrich	G9893-5MG
HC toxin	0.4 µg/ml, methanol	Inhibits histone deacetylases [605]	Sigma-Aldrich	H7270-1MG
Ochratoxin A	0.2 µg/ml, DMSO	Diverse: protein synthesis inhibitor, genotoxic stressor, oxidative stress [606]	Sigma-Aldrich	O1877-1MG
Tentoxin	0.1 µg/ml	Chloroplast ATP synthesis inhibitor [607]	Sigma-Aldrich	T8019-250UG
α-amanitin	0.2 µg/ml	Transcriptional inhibitor; inhibits RNA polymerase II [602]	Sigma-Aldrich	A2263-1MG

Table 2.11 | List of Snake toxins

Toxin name	Final concentration	Mechanism of action	Source	Identifier
α-Bungarotoxin-tetramethylrhodamine (α-BTPR)	0.1 µM	Neurotoxin, binds to acetylcholine receptors [608]	Sigma-Aldrich	T0195 - .5MG
Crotaline	1 mg/ml, DMSO	Pulmonary vascular syndrome [609]	Sigma-Aldrich	C2401-500MG

Sarafotoxin	0.06 µg/ml	Vasoconstrictor [610]	Sigma-Aldrich	S1522-50UG

Table 2.12 | List of Terrestrial invertebrate toxins

Toxin name	Final concentration	Mechanism of action	Source	Identifier
α-Pompilidotoxin	0.04 µM	Slows inactivation of Na^+ channels [611]	Sigma-Aldrich	P6237-.1MG
Charybdotoxin	0.08 µg/ml	Voltage-gated K^+ channel inhibitor [612]	Sigma-Aldrich	C7802-.1MG
Kurtoxin	0.006 µM	Voltage-gated Ca^{2+} channel inhibitor [613]	Sigma-Aldrich	K1514-100UG
Margatoxin	0.0004 µM	Voltage-gated K^+ channel inhibitor [614]	Sigma-Aldrich	M8437-10UG
Mastoparan	0.04 µM	G protein agonist [615]	Sigma-Aldrich	M5280-1MG
Maurotoxin	0.0006 µM	Ca^{2+}-activated K^+ channel inhibitor [616]	Sigma-Aldrich	M7444-10UG
ω-agatoxin IVA	0.05 µg/ml	P-type Ca^{2+} channel agonist [617]	Sigma-Aldrich	A6719-.1MG
Phospholipase A2	0.1 µg/ml	Hydrolyses membrane phospholipids	Sigma-Aldrich	P9279-1MG
Pandinotoxin-Kα (PiTX-Kα)	0.001 µM	Voltage-gated K^+ channel inhibitor [618]	Sigma-Aldrich	P222-10UG
SNX-482	0.0004 µM	Inhibits class E Ca^{2+} channels [619]	Sigma-Aldrich	SML1150-5UG
Tamapin	0.001 µM	Ca^{2+} activated K^+ channel inhibitor [620]	Sigma-Aldrich	T3326-10UG

Table 2.13 | List of Marine organism toxins

Toxin name	Final concentration	Mechanism of action	Source	Identifier
Domoic acid	0.8 µg/ml	Multiple mechanisms, including neurotoxicity and hepatotoxicity [621]	Sigma-Aldrich	D6152-1MG

Microcystin YR	2 µg/ml, DMSO	Hepatotoxin; protein phosphatase inhibitor [622]	Sigma-Aldrich	M4069-100UG
Calyculin A	0.04 µg/ml	Protein phosphatase inhibitor [623]	Sigma-Aldrich	C5552-10UG
Conantokin G	0.016 µM	N-methyl-D-aspartate (NDMR) receptor agonist [624]	Sigma-Aldrich	C4311-.1MG
ω -conotoxin GVIA	0.12 µg/ml	Ca^{2+} channel inhibitor [625]	Sigma-Aldrich	C9915-.1MG

Table 2.14 | List of RT-PCR primers

Gene	Primer	Sequence	Reference
16S rRNA	16S-F	5'-CGCAATTGACGAAAGTCTG-3'	[626]
	16S-R	5'-TAATTCCGGATAACGCTTGC-3'	
hblA	hblA-F	5'CCTTGCAAAAGGCTGGATTA-3'	[626]
	hblA-R	5'-TCGTGTCCCAAGTAACAGC-3'	
hblC	hblC-F	5'-TGGCAGCGTATAACAAAGG-3'	[626]
	hblC-R	5'-GCAAAAACGCCAAATGTTTT-3'	
hblD	hblD-F	5'-AGTTATTGCAGCTATTGGAGG-3'	[627]
	hblD-R	5'-GTCCATATGCTTAGATGCTGTGA-3'	
nheB	nheB-F	5'-GTGAAACAAGCTCCAGTTC-3'	[628]
	nheB-R	5'-AAAGCGTACAGATCCATTACT-3'	
nheA	nheA-F	5'-TTTAATTGCGGGGTTATTGG-3'	[626]
	nheA-R	5'-ACTACTCATCGCGCTCACC-3'	
nheC	nheC-F	5'-CAGCACCAAAGAGATGCAAA-3'	[626]
	nheC-R	5'-CGCGAAAAGCTTTCAAATTC-3'	
CytK	CytK-F	5'-GCTTTGTATAAGCAACTTGGATAG-3'	[626]
	CytK-R	5'-AGCCTCTGTAACACCAAGC-3'	
Gapdh	Gapdh-F	5'-CGT CCC GTA GAC AAA ATG GT-3'	[259]
	Gapdh-R	5'-TTG ATG GCA ACA ATC TCC AC-3'	
Cxcl1	mKc-F	5'-CAA TGA GCT GCG CTG TCA GTG-3'	[387]
	mKc-R	5'-CTT GGG GAC ACC TTT TAG CAT C-3'	
Il1b	mIl1b-F	5'-GAC CTT CCA GGA TGA GGA CA-3'	[259]
	mIl1b-R	5'-AGC TCA TAT GGG TCC GAC AG-3'	
Tnf	mTnf-F	5'-CAT CTT CTC AAA ATT CGA GTG ACA A-3'	[259]
	mTnf-R	5'-TGG GAG TAG ACA AGG TAC AAC CC-3'	

Chapter 3♦ A multicomponent toxin from *Bacillus cereus* incites inflammation and shapes host outcome via the NLRP3 inflammasome

3.1 Preface

This chapter consists primarily of a publication in ***Nature Microbiology***, of which I was the first author.

Mathur, A, Feng, S, Hayward, JA, Ngo, C, Fox, D, Atmosukarto, II, Price, JD, Schauer, K, Märtlbauer, E, Robertson, AAB, Burgio, G, Fox, EM, Leppla, SH, Kaakoush, NO, & Man, SM (2019). A multicomponent toxin from *Bacillus cereus* incites inflammation and shapes host outcome via the NLRP3 inflammasome. ***Nature Microbiology****,* 4:362–374.

As the nominal first author, I generated greater than fifty percent of the content. My contributions to the publication was as follows:

- Planning, design and execution of experiments outlined in Main figures: 3.1a-f; 3.2a-e; 3.4a-c,e-i, k; 3.5a,f,h; 3.6a-e; 3.7a-i; and Appendices chapter 3 figures: 3.1a-f; 3.4c; 3.5a-d; 3.6a-c; 3.7; 3.8b; 3.9a,b; 3.10a-g; 3.11. Curated the Appendices chapter 3 figure 3.6a-c and 3.11.
- Interpretation and analysis of results and compilation of figures listed above.
- Wrote the first draft of the manuscript.
- Edited subsequent versions of the manuscript and addressed comments from co-authors and external peer reviewers with assistance from senior author Prof. Si Ming Man.

I would like to take this opportunity to thank my co-authors on this publication, whose contributions are as follows:

Author initials	Figure	Contribution
S.F.	Main figures: 3.3a-f; 3.4d,j Appendices chapter 3 figures: 3.2a,b; 3.3 a-e; 3.4a,b	Executed experiments, performed analysis and compilation of listed figures. Assisted in collection of serum and peritoneal fluid from mice (Fig. 3.7).
J.A.H.	Appendices chapter 3 figures: 3.6a-c; 3.8a	Designed and executed experiments, performed analysis and generated data for the listed figures. Compilation of listed figures was done by me. Assisted with collection of serum and peritoneal fluid from mice (Fig. 3.7).
C.N.	Main figures: 3.3d; 3.4e,k Appendices chapter 3 figures: 3.1e; 3.3c,d	Executed isolation of RNA and qRT-PCR experiments, generated data for the listed figures. Interpretation and compilation of the listed figures was done by me. Assisted in collection of serum and peritoneal fluid from mice (Fig. 3.7).
D.F.	Main figures: 3.5b-e,g	Executed experiments, performed analysis and compilation of the listed figures.
N.O.K.	Appendices chapter 3 figures: 3.10a,e	Designed and executed experiments, performed analysis and generated data for the listed figures. Interpretation and compilation of the listed figures was done by me.
I.I.A. and J.D.P.	Main figure: 3.6a-c	Synthesised liposomes for the listed figures.
K.S., E.M., A.A.B.R., G.B., E.M.F. and S.H.L.		Provided resources and intellectual input.
S.M.		Overall supervision and conceptualisation of the study. Drew the Appendices chapter 3 Figure 3.11.

3.2 Introduction

Inflammasomes are innate immune signalling complexes capable of responding to a variety of pathogens and danger signals [629,630]. Recognition of PAMPs and DAMPs by inflammasome sensors requires cytosolic exposure of microbial or danger signals. Cytosolic bacterial invasion is central to drive activation of the DNA-sensing AIM2 inflammasome and the LPS-sensing non-canonical inflammasome. This process is initiated by host defense proteins, guanylate-binding proteins and Immunity-related GTPases, mediating a rupture of the pathogen-containing vacuole and liberating bacterial ligands in the cytoplasm [27,259,587,631]. Certain pathogens inject virulence factors into the cytoplasm, such as flagellin delivered by the type III secretion system of *Salmonella enterica* serovar Typhimurium (*S.* Typhimurium), which induces activation of the NAIP-NLRC4 inflammasome [281-283,290,293,309]. However, the mechanisms underpinning how microbial ligands from extracellular bacteria are detected by cytosolic innate immune sensors have remained unclear.

Toxins are critical tools in the arsenal of bacterial virulence factors which can modify the function, metabolism and physiology of the host cell to favour bacterial replication and transmission [632,633]. Previous studies have shown that hemolysins and β-barrel pore-forming toxins secreted by *Staphylococcus aureus* induce activation of the NLRP3 inflammasome in monocytes and macrophages [634-637]. Similarly, hemolysins secreted by *Escherichia coli* [638,639], *Streptococcus pneumoniae* [640-644], *Listeria monocytogenes* [634,645,646] and certain *Vibrio* species [647-649] can activate the NLRP3 inflammasome. The mechanisms governing how inflammasome sensors recognise cellular perturbations induced by structurally and mechanistically diverse virulence factors are unclear.

In this chapter, I analysed a panel of extracellular and cytosolic bacterial pathogens and identified an activator of the inflammasome secreted by the foodborne pathogen *Bacillus cereus*. I showed that the secreted factor is a tripartite toxin called haemolysin BL (HBL). HBL assembled in a highly sequential manner to drive activation of the NLRP3 inflammasome. The

study also demonstrated that the HBL toxin is inserted into the mammalian cell membrane to form a pore, mediating cellular leakage and lysis. Overt activation of the HBL-responsive NLRP3 inflammasome drives rapid death of the host, which can be prevented by pharmacological inhibition of NLRP3. My results revealed that cytosolic sensing of an inflammasome-activating toxin is central to the immune recognition of *B. cereus* infection.

3.3 Materials and Methods

3.3.1 Bacterial culture

Citrobacter rodentium, *Escherichia coli, Pseudomonas aeruginosa*, *Salmonella enterica serovar* Typhimurium strain SL3144, *Shigella flexneri*, *Staphylococcus epidermidis*, *Streptococcus pneumoniae*, and *Streptococcus pyogenes* were grown in Luria-Bertani (LB) media (244620, BD) overnight under aerobic conditions at 37 °C. *Francisella novicida* were cultured in BBL Trypticase Soy Broth (TSB) (211768, BD) supplemented with 0.2% L-cysteine (BP376-100, ThermoFisher Scientific) overnight under aerobic conditions at 37 °C. *Listeria monocytogenes* was grown in Brain heart infusion (BHI) media (211059, BD) overnight under aerobic conditions at 37 °C. *B. cereus* were grown LB media under aerobic conditions at 30 °C. The list of *Bacillus* strains used are mentioned in **(Table 2.4)**. All bacteria were subcultured (1:10) in fresh media the next day for 3-4 hr under their respective conditions.

3.3.2 Stimulation of BMDMs with Bacterial Supernatant

To prepare the bacterial supernatant, bacteria were grown in media under their respective conditions as described above. The overnight bacterial culture was centrifuged at 5000 *g* for 10 min. The supernatant was filter-sterilised using low-protein-binding 0.45 µm filters (SLHV033RS, Merck). For size-fractionation, the supernatant of *B. cereus* was fractionated using spin-filter columns of the 9 kDa (89884A, ThermoFisher Scientific), 30 kDa (UFC803096,

Millipore), or 50 kDa range (UFC905096, Millipore). For heat inactivation, the supernatant of *B. cereus* was heated to 50 °C, 75 °C or 100 °C for 10 min. To remove proteins, DNA or RNA, the supernatant of *B. cereus* was treated with Proteinase K (1 mg/ml, 19133, Qiagen), DNase1 (1 mg/ml, Roche), or RNase A (1 mg/ml, Qiagen) for 1 hr. 50-150 µl of bacterial supernatant were added to BMDMs for 3-4 hr.

For neutralisation studies, the supernatant of *B. cereus* was treated with antibodies against HBL (3 µl), individual components of HBL (1 µl), or NHE-B (3 µl) for 1 hr before addition to LPS-primed BMDMs. Antibodies against HBL and NHE were generated as described previously [508,565]. For controls, mouse serum and isotype IgG1 were used.

3.3.3 Stimulation of BMDMs with Recombinant HBL

Purified recombinant HBL components B, L_1 and L_2 were generated as described previously [508]. LPS-primed BMDMs were stimulated with all three components or with B, L_1 or L_2 individually or in various combinations (5 nM of each components: B, L_1 and L_2 and 3 hr for caspase-1 activation). HBL components were also pre-incubated with either Proteinase K (1 mg/ml, 19133, Qiagen), DNase1 (1 mg/ml, Roche), or RNase A (1 mg/ml, Qiagen) for 1 hr, or heated to 100 °C for 10 min. For binding order studies, LPS-primed BMDMs were stimulated with a single HBL component (5 nM of either B, or L_1, or L_2) for 30 min. This step was followed by extensive washing with PBS three times to remove unbound toxin. The two remaining components were added in concert, or the second individual component was added for 30 min followed by the third individual component, with washing steps in between. The plus symbol indicates ‘added in concert’. The arrow symbol indicates ‘extensive washing’. For transfection of HBL, each reaction consisted of individual HBL components (1.5 µM each) or combination of two components (0.75 µM each) mixed with 10 µl of the liposomal transfection reagent DOTAP (11202375001, Sigma-Aldrich). After 30 min, the complexes were added to LPS-primed BMDMs in Hank’s Balanced Salt Solution (H9394, Sigma-Aldrich) and stimulated for 3-5 hr.

3.3.4 Liposome Studies

Liposomes were synthesised using cholesterol (23%) and synthetic lipid derivatives DPPC (33%), DOPC (32%) and DSPC (12%), mimicking the mammalian cell membrane [581]. The concentration of liposomes was 7 mM, loaded either with methylene blue dye (75 µg/ml) or saline. Encapsulation of methylene blue dye into the lumen of liposomes allowed to investigate the ability of HBL to induce pores in the liposomal membrane that would result in leakage of the dye. Liposomes were treated with HBL (0.5 µM of each component), individual HBL components (0.5 µM of each component), heat-inactivated HBL, a buffer used to carry HBL [10 mM Tris HCl, 0.5 mM EDTA (pH 8.0)], or BSA (1 µg/ml; 001000173, Jackson ImmunoResearch). The liposomes were sonicated at 100 amplitude for 5 mins as control (CTRL). The released dye was captured by a cation exchanger resin Dowex (10-15 mg per well). The absorbance (OD) of residual dye was measured at a wavelength of 595 nm using the Infinite 200 PRO system (Tecan). To investigate the capacity of liposomes to inhibit HBL-induced activation of the inflammasome, recombinant HBL (5 nM of each component) was left untreated or treated with liposomes (7 mM) for 1 hr, prior to addition to LPS-primed BMDMs.

3.3.5 Immunoblotting Analysis

For caspase-1 immunoblotting, BMDMs and supernatant were lysed in RIPA buffer and sample loading buffer containing SDS and 100 mM DTT. For immunoblotting of pIκB, IκB, pERK, ERK, NLRP3 and GAPDH, the supernatant was removed and BMDMs washed once with PBS, followed by lysis in RIPA buffer and sample loading buffer containing SDS and 100 mM DTT. Proteins were separated on 8-12% polyacrylamide gels. Following electrophoretic transfer of proteins onto PVDF membranes (IPVH00010, Millipore), membranes were blocked in 5% skim milk and incubated overnight with primary antibodies against caspase-1 (1:1,000 dilution, #AG-20B-0042, Adipogen), pIκB (1:1,000 dilution, #2859, Cell Signaling Technologies), IκB (1:1,000 dilution, #9242, Cell Signaling Technologies), pERK (1:1,000 dilution, #9101, Cell Signaling Technologies), ERK (1:1,000 dilution, #9102, Cell Signaling

Technologies), NLRP3 (1:1,000 dilution, #AG-20B-0014, Adipogen), GAPDH (1:10,000 dilution, #5174, Cell Signaling Technologies), or Pan-cadherin (1:1,000 dilution, #4068, Cell Signaling Technologies), Gasdermin D (1:1,000 dilution, #ab209845, Abcam), or IL-1β (1:1,000 dilution, #RDSAF401NA, R&D Systems). PVDF membranes were then incubated with HRP-conjugated secondary antibody for 1 hr and proteins were visualised using the Super Signal Femto substrate (34095, ThermoFisher Scientific) and the ChemiDoc™Touch Imaging System (BioRad).

For detection of toxin components, 300 µl of the supernatant of *B. cereus* were mixed with 100 µl of sample loading buffer. Primary antibodies against HBL components B, L_1 and L_2 (1:1,000 dilution) [508], or against NHE-B (1:1,000 dilution) [565] were used. Silver staining was performed for total protein loading controls in accordance with the manufacturer's instructions (24612, Thermo Scientific).

3.3.6 Immunofluorescence Staining

For visualisation of inflammasomes, untreated or treated BMDMs were washed three times with PBS and fixed with 4% paraformaldehyde at room temperature for 15 min, followed by blocking in 10% normal goat serum (005000121, Jackson ImmunoResearch) supplemented with 0.1% saponin (47036, Sigma-Aldrich) for 1 hr. Cells were incubated with a rabbit anti-ASC antibody (1:500 dilution, clone AL177, AG-25B-0006-C100, AdipoGen) overnight at 4 °C. An anti-rabbit secondary Rhodamine red antibody (111295144, Jackson ImmunoResearch) was used. Cells were counterstained in DAPI mounting medium (H-1200, Vecta Labs). Inflammasome specks and BMDMs were visualised, counted, and imaged using a Leica SP5 confocal microscope. For visualisation of HBL and cell membrane, BMDMs were stimulated with HBL component B (5 µg/ml) for 1 hr, washed three times with PBS and fixed with 4% paraformaldehyde at room temperature for 15 min, followed by blocking in 1% BSA in PBS for 1 hr. Cells were incubated with a mouse anti-HBL-B antibody (1:200 dilution in 1% BSA) [508] and a rat FITC-conjugated anti-CD11b antibody (1:200 dilution in 1% BSA, 101205,

BioLegend) overnight at 4 °C. PBS containing 0.05% Tween-20 was used to wash between incubation steps. An anti-mouse secondary Rhodamine red antibody (115295146, Jackson ImmunoResearch) was used. BMDMs were analysed using a Leica SP5 confocal microscope.

3.3.7 Immunological Lateral Flow Tests

The antibody-based assay Duopath Cereus Enterotoxins (1041460001, Merck) detects the presence of the HBL component L_2 and NHE-B in the supernatant of *B. cereus*. The supernatant of *B. cereus* was applied to the Duopath cassette according to the manufacturer's instructions. Sterile LB broth and filter-sterilised supernatant from an overnight culture of *S.* Typhimurium were used as negative controls.

3.3.8 Cryo-Electron Microscopy

Liposomes left untreated or treated with recombinant HBL (0.5 µM) for 1 hr were applied on a holey carbon 400 mesh grid and left to adhere for 30 s. Grids were then blotted for 10 s to remove excess liposomes before plunge frozen using liquid ethane surrounded by a bath of liquid nitrogen. Samples were visualised under Hitachi 7100 TEM at 100kv with a Cryo-TEM holder.

3.3.9 Scanning Electron Microscopy

BMDMs were washed with PBS and post-fixed with 2.5% glutaraldehyde in 0.1 M phosphate buffer overnight and further washed with PBS. Cells were fixed in 1% osmium tetroxide in double distilled water for 1 hr and dehydrated in a series of alcohol. Dehydrated samples were dried using liquid carbon dioxide using critical point drying. Samples were then sputter-coated with platinum (3 nm thickness) at 15 mA for 2 min using the EMI TECH K550 Sputter coater and visualised under a Zeiss UltraPlus Field emission scanning electron microscope at 5 kV.

3.3.10 Transmission Electron Microscopy

BMDMs were washed with PBS and post-fixed with 2.5% glutaraldehyde in 0.1 M phosphate buffer overnight and further washed with PBS. Cells were fixed in 1% osmium tetroxide in

double distilled water for 1 hr and dehydrated in a series of alcohol, and embedded in LR white resin (C023, ProSciTech). Samples were polymerised in a 60 °C oven overnight. Thin sections were cut at 80 nm and viewed using a Hitachi HA7100 transmission electron microscope at 100 kV.

3.3.11 Separation of Membrane and Cytosolic Compartments

BMDMs were stimulated with either purified recombinant HBL protein (5 nM of each component) or the supernatant of *B. cereus* (50 µl) for 45 min, washed three times with PBS followed by separation of membrane and cytosolic fractions using the Mem-PER Plus Membrane Protein Extraction Kit according to the manufacturer's instructions (89842, Thermo Scientific).

3.3.12 Lactate Dehydrogenase Assay

Levels of lactate dehydrogenase released by cells were determined using the CytoTox 96 Non-Radioactive Cytotoxicity Assay according to the manufacturer's instructions (G1780, Promega).

3.3.13 IncuCyte Analysis

To track the viability of BMDMs in response to HBL, BMDMs were stimulated with a high concentration of HBL (0.5 µM of each component) or a low concentration of HBL (5 nM of each component) in presence of the SYTOX Green nuclear stain that penetrates compromised membranes (1 µM; S7020; Life Technologies). Cells were monitored over 3 hr using the IncuCyte Zoom "in-incubator" imaging system (Essen Biosciences).

3.3.14 Real Time qRT-PCR Analysis

RNA was extracted from BMDMs using TRIzol (15596018, ThermoFisher Scientific) and from bacteria using the TRIzol Max Bacterial RNA Isolation kit (16096040, ThermoFisher Scientific). The isolated RNA was converted into cDNA using the High-Capacity cDNA

Reverse Transcription Kit (4368813, ThermoFisher Scientific). Real-time qPCR was performed on an ABI StepOnePlus System PCR instrument with SYBR Green Real-Time PCR Master Mixes (4364346, ThermoFisher Scientific). Real time qRT-PCR sequences can be found in **Table 2.14**.

3.3.15 Cytokine Analysis

Cytokine levels were determined using a multiplex ELISA (MCYTOMAG-70K, EMD Millipore) or IL-18 ELISA (EK-0048, ELISAkit.com) according to the manufacturers' instructions.

3.3.16 Amino Acid Sequence Analysis

Putative transmembrane regions in individual components of HBL were predicted using the software Membrane Protein Explorer server, also known as MPEx [590]. Helical wheel diagrams were constructed using the HELIQUEST server [591].

3.3.17 Animal Infection

B. cereus strains were grown as described above. For survival analysis, 8-week-old mice were injected via an intraperitoneal (i.p.) route with 5×10^6 colony-forming units (CFUs) of *B. cereus*. For cytokine measurement in the serum, mice were injected, via an i.p. route, with 7.5×10^6 CFUs of an overnight culture of *B. cereus* or 200 µl of filter-sterilised supernatant of *B. cereus*. For cytokine measurement in the peritoneal fluid, mice were injected, via an i.p. route, with 7.5×10^6 CFUs of *B. cereus*. The peritoneal fluid and serum were collected after 3-20 hr for analysis by ELISA. To investigate the effects of MCC950 [213-215], mice were injected, via an i.p. route, with 50 mg/kg of MCC950 dissolved in PBS or with vehicle control PBS. 1 hr later, mice were injected, via an i.p. route, with 5×10^6 CFUs of *B. cereus* along with a second dose of 50 mg/kg of MCC950 or a second dose of PBS.

3.3.18 Statistical Analysis

The GraphPad Prism 6.0 software was used for data analysis. Data are shown as mean ± s.e.m. Statistical significance was determined by *t* tests (two-tailed) for two groups or One-way ANOVA (with Dunnett's or Tukey's multiple comparisons tests) for three or more groups. Survival curves were compared using the log-rank test. $P<0.05$ was considered statistically significant. In this study, no statistical methods were used to predetermine the sample size. The experiments were not randomised, and the investigators were not blinded to allocation during the experiments and outcome assessment.

3.4 Results

3.4.1 A secreted bacterial factor induces activation of the inflammasome

Previous studies have demonstrated that certain intracellular and cytosolic bacteria must secure entry into the host cytoplasm such that bacterial ligands are liberated via a host-mediated process for innate immune recognition by inflammasome sensors [27,259,587,631]. In these cases, bacterial ligands enter the cytoplasm following a rupture of the pathogen-containing vacuole and/or the bacterial cell membrane by interferon-inducible GTPases [27,259,587,631]. Indeed, wild-type (WT) bone-marrow-derived macrophages (BMDMs) infected with a range of clinically important bacterial pathogens undergo activation of caspase-1, secretion of IL-1β and IL-18, and induction of pyroptosis (**Fig. 3.1a,b**). Following filter-sterilisation of the bacterial cultures to remove bacteria, the cell-free supernatant from most bacteria was unable to induce activation the inflammasome (**Fig. 3.1a,b**). Remarkably, the cell-free supernatant derived from the foodborne pathogen *B. cereus* potently induced activation of caspase-1, secretion of IL-1β and IL-18, and pyroptosis (**Fig. 3.1a,b**).

To identify the inflammasome sensor required to activate the inflammasome in response to the secreted factor of *B. cereus*, I stimulated LPS-primed WT, *Nlrp3*$^{-/-}$, *Nlrc4*$^{-/-}$, *Aim2*$^{-/-}$, *Asc*$^{-/-}$, *Casp1/11*$^{-/-}$, and *Casp11*$^{-/-}$ BMDMs with the supernatant of *B. cereus*. Activation of caspase-1, the release of IL-1β and IL-18, and induction of cell death were impaired in *Nlrp3*$^{-/-}$ and Asc$^{-/-}$ BMDMs stimulated with the supernatant of *B. cereus* compared with WT, *Nlrc4*$^{-/-}$, *Aim2*$^{-/-}$, and *Casp11*$^{-/-}$ BMDMs (**Fig. 3.1c–e and Appendices for Chapter 3 Fig. 3.1a**). The supernatant of *B. cereus* similarly induced activation of the NLRP3 inflammasome in unprimed BMDMs (**Appendices for Chapter 3 Fig. 3.1b**), suggesting that Signal 1 (priming) and Signal 2 (activation) were both provided by the supernatant of *B. cereus*.

I further found that live *B. cereus* bacteria activated the inflammasome in a manner dependent on NLRP3 (**Fig. 3.1c–e**), consistent with the results obtained using cell-free supernatant. The levels of the pro-inflammatory cytokines tumour-necrosis factor (TNF) and Keratinocyte chemoattractant (KC, also known as CXCL1) secreted by WT and *Nlrp3*$^{-/-}$ BMDMs infected with *B. cereus* were similar (**Appendices for Chapter 3 Fig. 3.1c**). Furthermore, the gene or protein expression of TNF, KC and pro-IL-1β, and the phosphorylation status of IκB and ERK between WT and *Nlrp3*$^{-/-}$ BMDMs infected with *B. cereus* were similar (**Appendices for Chapter 3 Fig. 3.1d,e**), confirming that the production of inflammasome-independent cytokines was not affected by the absence of NLRP3. Further, pharmacological blockade of NLRP3 using the small molecule inhibitor MCC950 [213], impaired activation of caspase-1, secretion of IL-1β and IL-18, and pyroptosis in WT BMDMs infected with *B. cereus* or stimulated with LPS plus ATP (**Appendices for Chapter 3 Fig. 3.1f**).

Formation of the ASC speck is a hallmark of inflammasome activation [27]. Indeed, I found that *Nlrp3*$^{-/-}$ BMDMs had an impaired ability to generate ASC specks in response to stimulation with the supernatant of *B. cereus* or infection with live *B. cereus* bacteria, but not in response to transfected dsDNA poly(dA:dT) (**Fig. 3.1f**). These results collectively suggested that a new

secreted factor produced by the foodborne pathogen *B. cereus* induces activation of the NLRP3 inflammasome.

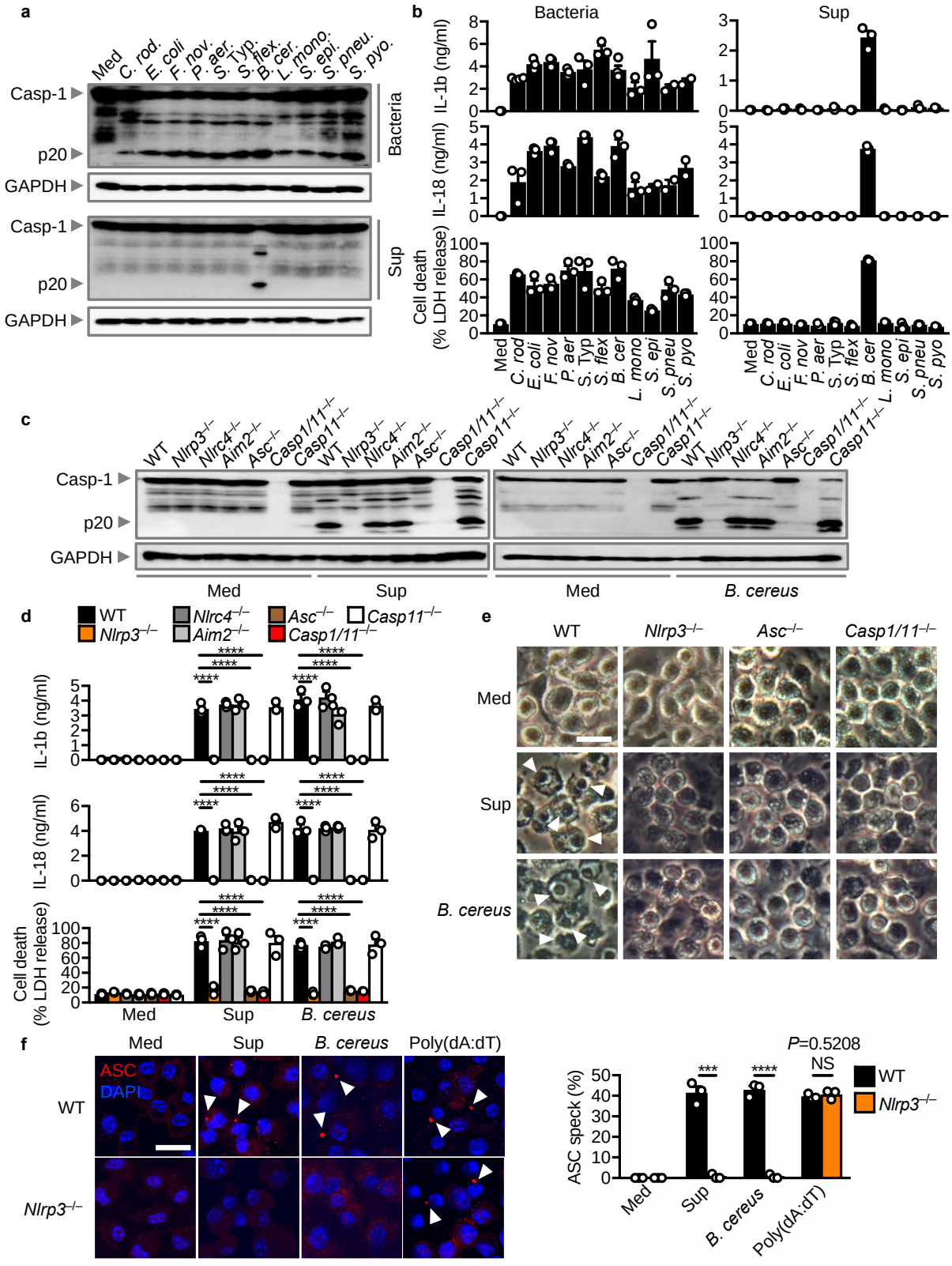

Figure 3.1 | A secreted factor of *B. cereus* activates the NLRP3 inflammasome. (**a**) Immunoblot analysis of pro-caspase-1 (Casp-1) and the caspase-1 subunit p20 (p20) and GAPDH (loading control) in wild-type (WT) BMDMs left untreated (medium alone [Med]) or assessed at various times after infection with *C. rodentium (C. rod), E. coli, F. novicida (F. nov), P. aeruginosa(P. aer), S. Typhimurium (S. Typ), S. flexneri (S. flex), B. cereus (B. cer), L. monocytogenes (L. mono), S. epidermidis (S. epi), S. pneumoniae (S. pneu), S. pyogenes (S. pyo)* (top) or after stimulation with the supernatant (Sup) of the corresponding bacteria (bottom). (**b**) Release of IL-1β (top) and IL-18 (middle), and death (bottom) of BMDMs after treatment as in (a). (**c**) Immunoblot analysis of caspase-1 and GAPDH in WT or mutant BMDMs left untreated or assessed 2 hr after stimulation with the supernatant of *B. cereus* (Sup) (left) or 3 hr after infection with *B. cereus* (MOI, 5; right). *B. cereus* ATCC 14579 is used throughout unless otherwise stated. (**d**) Release of IL-1β (top) and IL-18 (middle), and death (bottom) of BMDMs after treatment as in (c). (**e**) Microscopy analysis of the death of BMDMs after treatment as in (c). (**f**) Confocal microscopy analysis of ASC (red) in WT and *Nlrp3*$^{-/-}$ BMDMs left untreated or assessed 2 hr after stimulation with the supernatant of *B. cereus* (Sup), 3 hr after infection with *B. cereus* (MOI, 5), or 5 hr after transfection with poly(dA:dT) (left). Quantification of the prevalence of ASC inflammasome speck (right). At least 200 BMDMs from each genotype were analysed. Scale bars, 20 μm (e and f). Arrowheads indicate dead cells (e) or inflammasome specks (f). NS, not statistically significant, ***P < 0.001 and ****P < 0.0001 (one-way analysis of variance [ANOVA] with Dunnett's multiple-comparisons test [d]; two-tailed t-test [f]). Data are representative of three independent experiments (a-f; mean and s.e,m. in b, d and f).

3.4.2 The inflammasome-activating secreted factor is a heat-sensitive protein of 30-50 kDa in size

To investigate the biological nature of the unknown inflammasome-activating factor, I stimulated WT BMDMs with the supernatant of *B. cereus* treated with 100 °C heat, proteinase K, DNase, or RNase. Treatment with heat or proteinase K, but not with DNase or RNase, abolished the ability of the supernatant of *B. cereus* to engage activation of caspase-1, secretion of IL-1β and IL-18, and cell death in WT BMDMs (**Fig. 3.2a**). Further, treatment of the supernatant with heat revealed that the supernatant heated to 50 °C, but not 75 °C, retained its ability to activate inflammasome responses (**Appendices for Chapter 3 Fig. 3.2a,b**). Consistent with this finding, heat-killed or paraformaldehyde-fixed *B. cereus* bacteria were unable to induce activation of caspase-1, secretion IL-1β and IL-18, and cell death in BMDMs (**Fig. 3.2b**), suggesting that the bacteria must be viable, secreting a heat-sensitive proteinaceous factor that engages activation of the NLRP3 inflammasome.

I used filter-mediated size-fractionation techniques to separate components in the supernatant to further investigate the size-range of the inflammasome-activating factor. The supernatant fraction of >9 kDa, but not <9 kDa, induced activation of caspase-1, secretion of IL-1β and IL-18, and cell death in unprimed or LPS-primed WT BMDMs (**Fig. 3.2c–e**). I found the fraction of >30 kDa, but not <30 kDa, was required to activate the NLRP3 inflammasome (**Fig. 3.2c–e**). Further, the size fraction of <50 kDa, but not >50 kDa, potentiated activation of the NLRP3 inflammasome (**Fig. 3.2c–e**). Collectively, these findings suggested that a heat-sensitive proteinaceous factor of 30-50 kDa secreted by *B. cereus* is a potent activator of the NLRP3 inflammasome.

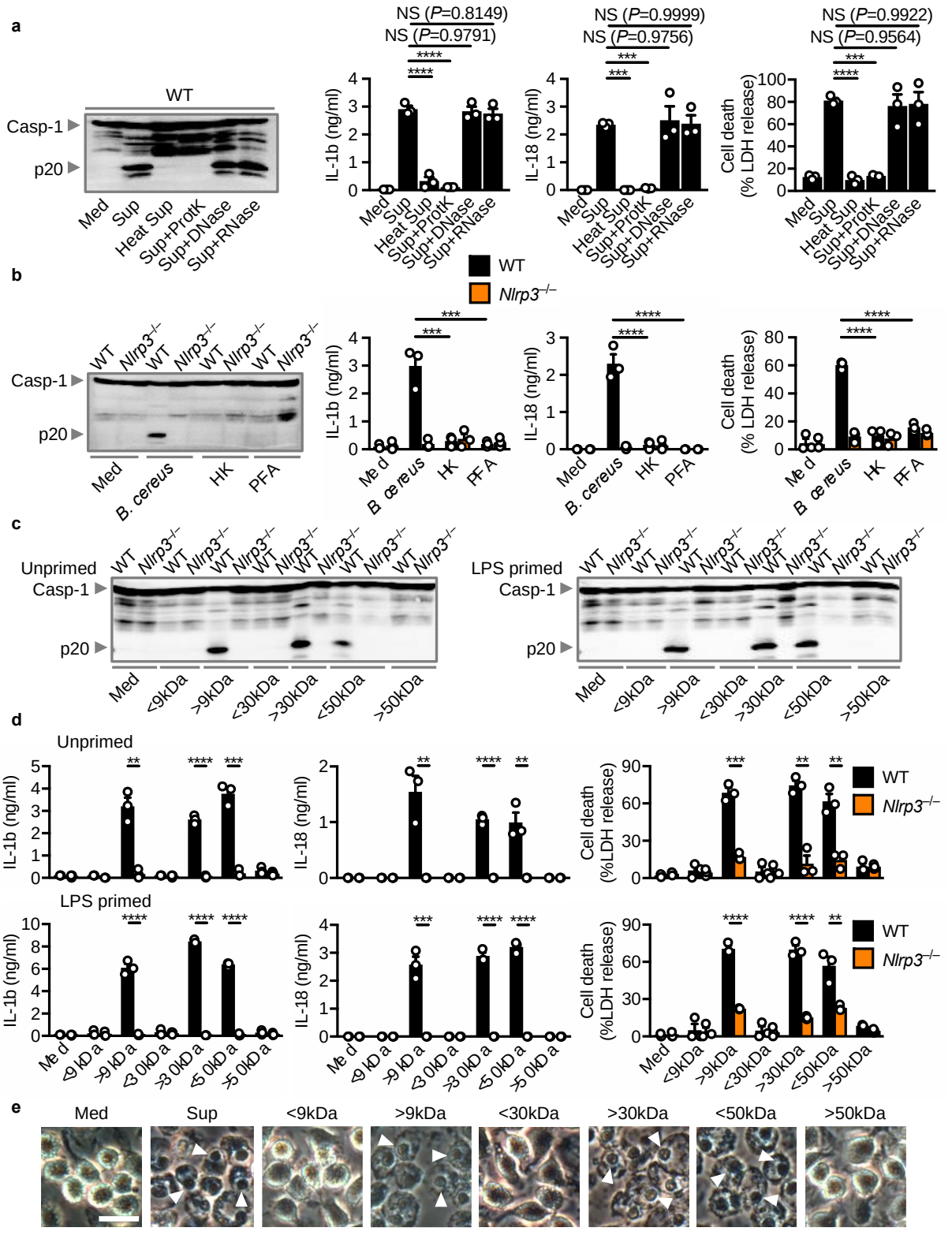

Figure 3.2 | The inflammasome-activating factor is a heat-sensitive protein of 30-50 kDa in size. (**a**) Immunoblot analysis of caspase-1 (left), the release of IL-1β (middle-left) and IL-18 (middle-right), and death (right) of WT BMDMs left untreated (Med) or assessed 2 hr after

stimulation with the supernatant of *B. cereus* (Sup), supernatant heated to 100 °C (Heat Sup), or supernatant treated with Proteinase K (ProtK), DNase or RNase. (**b**) Immunoblot analysis of caspase-1 (left), the release of IL-1β (middle-left) and IL-18 (middle-right), and death (right) of WT or *Nlrp3*$^{-/-}$ BMDMs left untreated or assessed 2 hr after infection of *B. cereus* (MOI, 5), heat-killed *B. cereus* (HK), or paraformaldehyde-fixed *B. cereus* (PFA). (**c**) Immunoblot analysis of caspase-1 of unprimed (left) and LPS-primed (right) WT or *Nlrp3*$^{-/-}$BMDMs left untreated or assessed 2 hr after stimulation with the size-fractionated supernatant. (**d**) Release of IL-1β (left) and IL-18 (middle), and death (right) of unprimed and LPS-primed WT and *Nlrp3*$^{-/-}$ BMDMs after treatment as in (c). (**e**) Microscopy analysis of the death of BMDMs treated as in (c). Scale bar, 20 μm (e). Arrowheads indicate dead cells (e). NS, not statistically significant, *P < 0.05, **P < 0.01, ***P < 0.001 and ****P < 0.0001 (one-way analysis of variance [ANOVA] with Dunnett's multiple-comparisons test [a, b]; two-tailed *t*-test [d]). Data are representative of three independent experiments (a-e; mean and s.e.m. in a, b, d).

3.4.3 The inflammasome-activating secreted factor is highly prevalent in *B. cereus* strains

To unravel the identity of the secreted factor, I comprehensively profiled a collection of 46 strains of *B. cereus,* isolated either from human or environmental sources, for their ability to activate the inflammasome (**Appendices for Chapter 3 Table 1**). The supernatant produced from 91% (42/46) of the strains triggered activation of caspase-1 and secretion of IL-1β and IL-18 in WT BMDMs (**Fig. 3.3a,b**), suggesting that the secreted factor is highly prevalent amongst *B. cereus* isolates. Notably, *Nlrp3*$^{-/-}$ BMDMs did not undergo activation of caspase-1 or release of IL-1β and IL-18 in response to the supernatant of any strains (**Fig. 3. 3a,b**), suggesting that NLRP3 is the cytosolic sensor driving inflammasome-mediated immune detection of this bacterial species. I further confirmed this observation and infected WT and *Nlrp3*$^{-/-}$ BMDMs with all 46 strains of live *B. cereus*. These extensive analyses revealed that

the same 42 strains of *B. cereus* from which the inflammasome-activating supernatant were generated, were capable of inducing activation of the NLRP3 inflammasome (**Appendices for Chapter 3 Fig. 3.3a,b**).

The 4 bacterial strains and their corresponding supernatant that were unable to induce activation of the NLRP3 inflammasome also did not induce pyroptosis but retained the ability to induce secretion of TNF (**Fig. 3.3c and Appendices for Chapter 3 Fig. 3.3c**). These results suggested that the non-activating strains do not have a global defect in eliciting an inflammatory response. The prevalence of a secreted factor amongst *B. cereus* isolates capable of activating the inflammasome suggested that this phenotypic trait is largely conserved across *B. cereus* strains. In addition, the distinction between an "inflammasome-activating" and "non-activating" group of *B. cereus* allows to elucidate key genetic and proteomic differences to facilitate identification of this inflammasome-activating secreted factor.

3.4.4 Identification of the inflammasome-activating factor

B. cereus, a major cause of foodborne diseases, secretes multiple toxins, including the toxins non-haemolytic enterotoxin (NHE), haemolysin BL (HBL), and Cytotoxin K [448]. Individual components of the two tripartite toxins NHE (composed of A, B and C) and HBL (composed of B, L_1 and L_2), and the single-component toxin, Cytotoxin K, are all of 30-50 kDa in size [508,650-653]. Real-time qPCR analysis was used to quantify the expression levels of each of these components and found that inflammasome-activating strains of *B. cereus* expressed high levels of the genes *hblA*, *hblC* and *hblD*, which encode for the HBL components, B, L_2 and L_1 respectively (**Fig. 3.3d**). Remarkably, the non-activating strains did not express these gene products (**Fig. 3.3d**). In addition, I did not observe any association between the expression levels of genes encoding NHE-B and Cytotoxin K and the ability of the strains to activate the

inflammasome (**Appendices for Chapter 3 Fig. 3.3d**). An antibody-mediated immunological lateral flow assay called Duopath was used to further investigate the presence or absence of HBL and NHE in the supernatant of inflammasome-activating and non-activating strains of *B. cereus.* These analyses revealed that the supernatant of 42 inflammasome-activating strains, but not the 4 non-activating strains, were positive for HBL (**Fig. 3.3e and Appendices for Chapter 3 Fig. 3.3e**), whereas NHE was present in the supernatant of all 46 strains (**Fig. 3.3e and Appendices for Chapter 3 Fig. 3.3e**). Indeed, immunoblotting analysis found that the supernatant of inflammasome-activating strains were positive for the HBL components B, L_1 and L_2, whereas none of the non-activating strains were positive for HBL components (**Fig. 3.3f**). These data collectively highlighted that the secretion of the enterotoxin HBL is a feature of inflammasome-activating, but not of non-activating, strains of *B. cereus*.

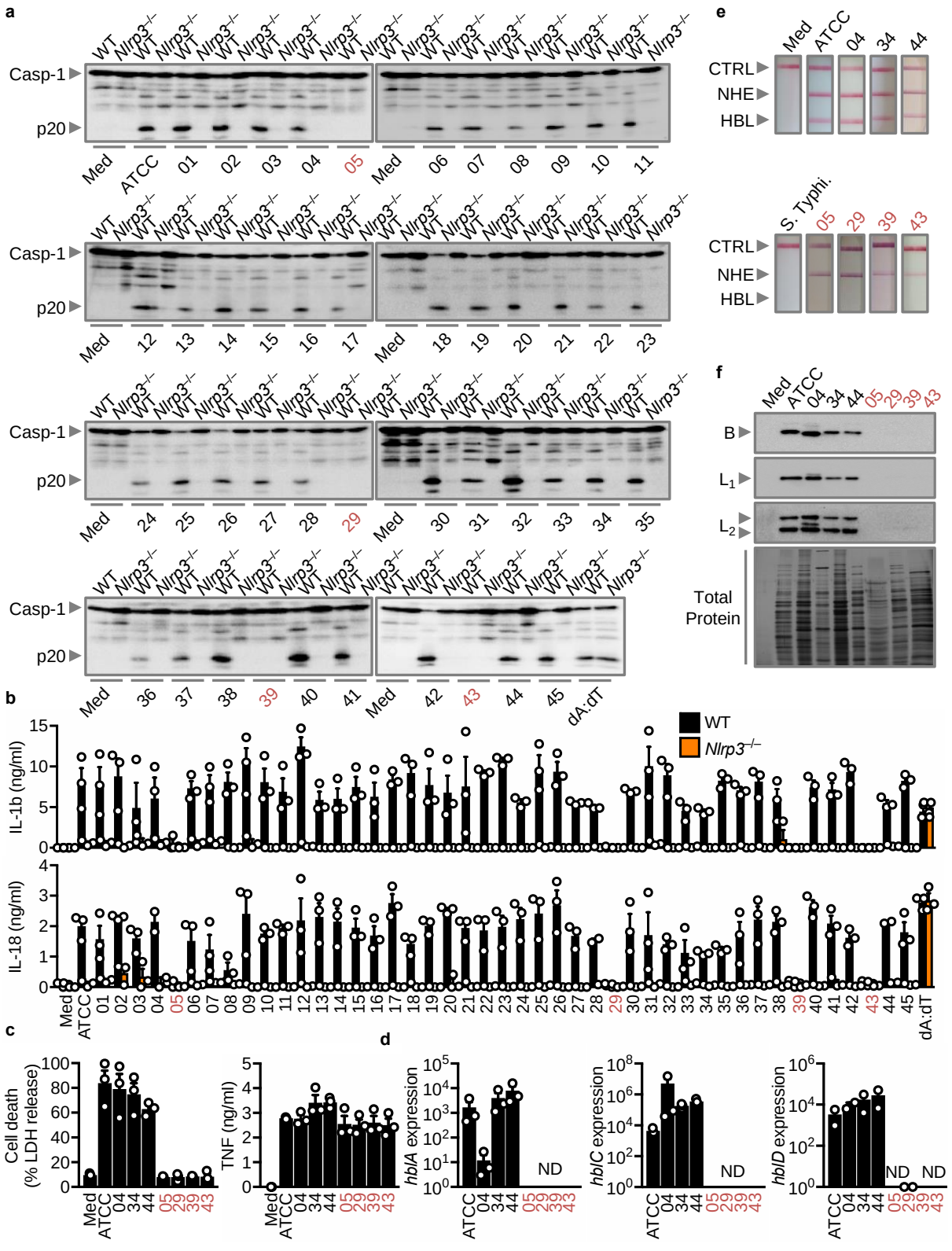

Figure 3.3 | The inflammasome-activating factor is highly prevalent in *B. cereus* isolates and is associated with isolates expressing HBL. (**a**) Immunoblot analysis of caspase-1 of LPS-primed WT or *Nlrp3*$^{-/-}$ BMDMs left untreated (Med) or assessed at

various times after stimulation with filter-sterilised supernatant of overnight cultures of 46 *B. cereus* strains or 5 hr after transfection with poly(dA:dT). The list of strains used is available in Table S1. ATCC refers to ATCC 14579. (**b**) Release of IL-1β (top) and IL-18 (bottom) of LPS-primed WT or *Nlrp3*$^{-/-}$ BMDMs after treatment as in (a). (**c**) Cell death and release of TNF of LPS-primed WT BMDMs after treatment as in (a). (**d**) Real-time quantitative RT-PCR analysis of the gene encoding the HBL components B (*hblA*), L_2 (*hblC*), and L_1 (*hblD*) of overnight culture of *B. cereus*, presented relative to that of the gene encoding 16S rRNA. (**e**) Immunological lateral flow tests (Duopath) of NHE and HBL using LB broth (Med) or filter-sterilised supernatant of overnight cultures of *B. cereus* isolates or *S.* Typhimurium (*S.* Typhi). (**f**) Immunoblot analysis of the HBL components B, L_1, and L_2 in the supernatant of overnight cultures of *B. cereus* and silver stain of the total protein. Numerical IDs of *B. cereus* strains unable to activate caspase-1 are colorised (a-f). CTRL, control (e), NS, not statistically significant, (two-tailed *t*-test; B). Data are representative of three independent experiments (a-f; mean and s.e.m. in b-d).

3.4.5 HBL is the secreted factor engaging activation of the inflammasome

The presence of HBL exclusively in inflammasome-activating but not in non-activating strains suggested that this enterotoxin might be the secreted factor produced by *B. cereus* that led to the activation of the NLRP3 inflammasome. To investigate this possibility, I infected WT and *Nlrp3*$^{-/-}$ BMDMs with a strain of *B. cereus* carrying HBL and its isogenic mutant lacking all three components of the HBL (Δ*hbl B. cereus*). Remarkably, I observed that the parental strain and its supernatant induced activation of caspase-1, secretion IL-1β and IL-18, and pyroptosis in WT BMDMs, whereas the Δ*hbl B. cereus* and its supernatant failed to induce these responses (**Fig. 3.4a,b**). Importantly, *Nlrp3*$^{-/-}$ BMDMs did not undergo activation of caspase-1, secretion of IL-1β and IL-18, and pyroptosis in response to either the bacteria or supernatant from WT or the Δ*hbl B. cereus* strain (**Fig. 3.4a,b**). Indeed, I confirmed that the Δ*hbl B. cereus*

lacked the expression of HBL by Duopath, immunoblotting and real-time qRT-PCR analyses (**Fig. 3.4c–e**). However, the Δ*hbl B. cereus* retained the expression of NHE and Cytotoxin K (**Fig. 3.4c and Appendices for Chapter 3 Fig. 3.4a**). Both the parental and Δ*hbl* strains of *B. cereus* induced similar levels of TNF (**Fig. 3.4b**), confirming that the HBL-dependent response is specific to the NLRP3 inflammasome pathway.

I further neutralised the supernatant of *B. cereus* with antibodies specific to the three components of HBL and assessed the ability of the supernatant to engage activation of the inflammasome. I found that the supernatant treated with anti-HBL antibodies did not induce activation of caspase-1, secretion of IL-1β and IL-18, and pyroptosis in WT BMDMs (**Fig. 3.4f**). In addition, neutralisation of HBL did not impair the ability of the supernatant to stimulate the production of TNF in WT BMDMs (**Fig. 3.4f**).

3.4.6 Deficiency of the related tripartite toxin NHE does not impair activation of the NLRP3 inflammasome

To investigate potential functional redundancies between HBL and NHE in the activation of the inflammasome, I infected WT and *Nlrp3*$^{-/-}$ BMDMs with *B. cereus* and its isogenic mutant lacking NHE (Δ*nhe B. cereus*). I found that Δ*nhe B. cereus* or its supernatant retained the ability to engage activation of the NLRP3 inflammasome (**Fig. 3.4g–k**). Indeed, Δ*nhe B. cereus* expressed HBL and Cytotoxin K (**Appendices for Chapter 3 Fig. 3.4b**). Further, treatment of the supernatant with anti-NHE neutralising antibody did not impair activation of the inflammasome (**Fig. 3.4l**). However, addition of a neutralising antibody against HBL abolished the ability of the supernatant from Δ*nhe B. cereus* to elicit inflammasome responses (**Appendices for Chapter 3 Fig. 3.4c**). These studies collectively suggested that HBL, but not NHE, is the secreted factor of *B. cereus* engaging activation of the NLRP3 inflammasome.

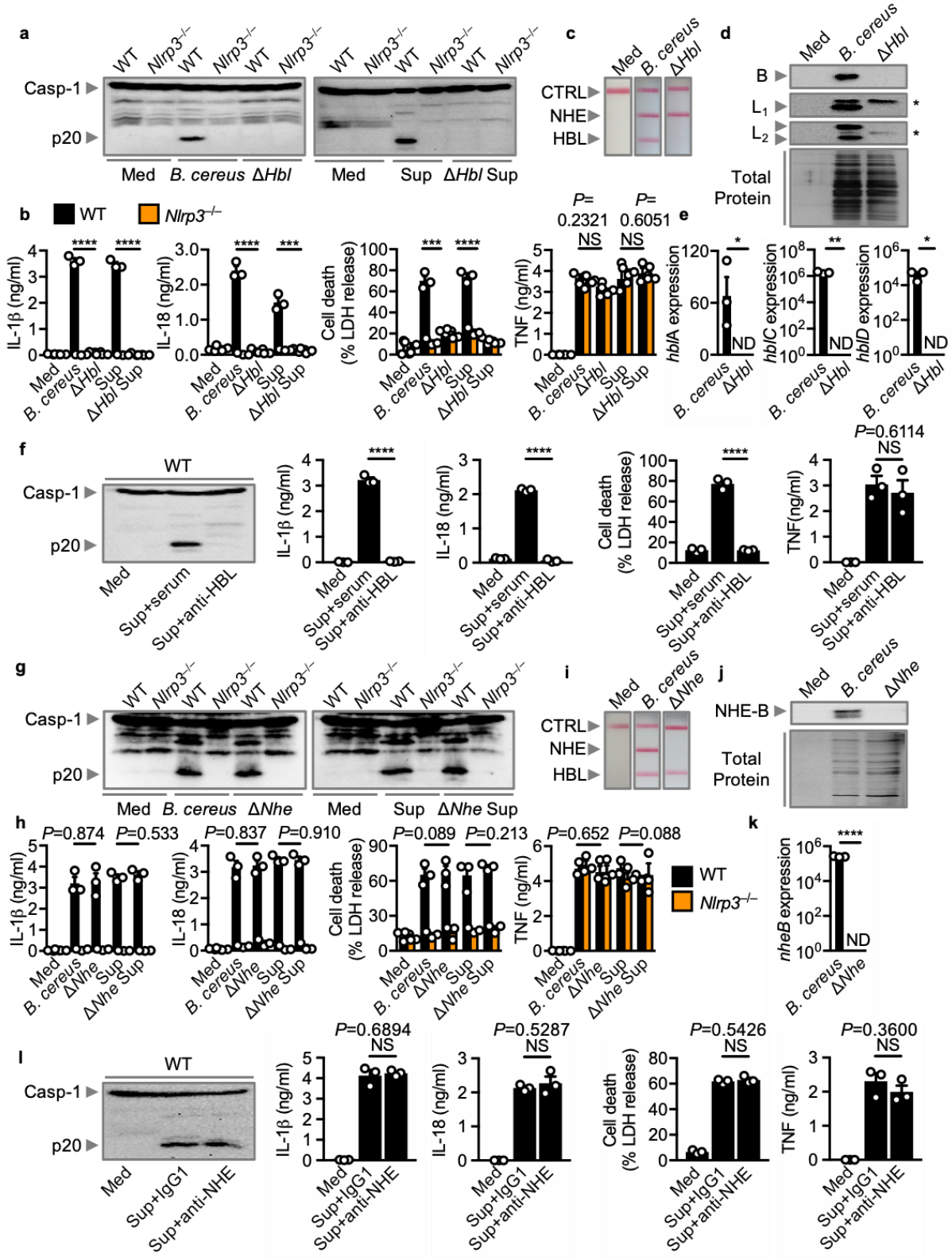

Figure 3.4 | HBL triggers activation of the NLRP3 inflammasome. (**a**) Immunoblot analysis of caspase-1 of unprimed WT or *Nlrp3*$^{-/-}$ BMDMs left untreated (Med) or assessed 3 hr after infection with *B. cereus* ATCC 10876 (MOI, 5) or its isogenic mutant lacking HBL (Δ*hbl*;

[MOI, 5]) (left). Immunoblot analysis of caspase-1 of LPS-primed WT or *Nlrp3*$^{-/-}$ BMDMs left untreated or assessed 2 hr after stimulation with the supernatant of *B. cereus* (Sup) or Δ*hbl B. cereus* supernatant (Δ*hbl* Sup) (right). (**b**) Release of IL-1β (left) and IL-18 (middle-left), death (middle-right), and release of TNF (right) of WT and *Nlrp3*$^{-/-}$ BMDMs after treatment as in (a). (**c**) Immunological lateral flow tests (Duopath) of NHE and HBL using LB broth (Med) or filter-sterilized supernatant of overnight cultures of *B. cereus* or Δ*hbl B. cereus*. (**d**) Immunoblot analysis of the HBL components B, L_1 and L_2 in the supernatant of overnight cultures of *B. cereus* or Δ*hbl B. cereus*, and silver stain of the total protein. (**e**) Real-time quantitative RT-PCR analysis of the gene encoding *hblA*, *hblC*, and *hblD* in overnight cultures of *B. cereus* or Δ*hbl B. cereus*, presented relative to that of the gene encoding 16S rRNA. (**f**) Immunoblot analysis of caspase-1 (left), the release of IL-1β (middle-left) and IL-18 (middle), death (middle-right), and release of TNF (right) of LPS-primed WT BMDMs left untreated or assessed 2 hr after stimulation with the supernatant of *B. cereus* (Sup) incubated with mouse serum (serum) or supernatant incubated with anti-HBL antibodies (anti-HBL). (**g**) Immunoblot analysis of caspase-1 of unprimed WT or *Nlrp3*$^{-/-}$ BMDMs left untreated or assessed 3 hr after infection with *B. cereus* F837/76 (MOI, 5) or its isogenic mutant lacking NHE (Δ*nhe*; [MOI, 5]) (left). Immunoblot analysis of caspase-1 of LPS-primed WT or *Nlrp3*$^{-/-}$ BMDMs left untreated or assessed 2 hr after stimulation with the supernatant of *B. cereus* (Sup) or Δ*nhe B. cereus* supernatant (Δ*nhe* Sup) (right). (**h**) Release of IL-1β (left) and IL-18 (middle-left), death (middle-right), and release of TNF (right) of WT and *Nlrp3*$^{-/-}$ BMDMs after treatment as in (g). (**i**) Immunological lateral flow tests (Duopath) of NHE and HBL using LB broth (Med) or filter-sterilized supernatants of overnight cultures of *B. cereus* or Δ*nhe B. cereus*. (**j**) Immunoblot analysis of NHE-B in the supernatant of overnight cultures of *B. cereus* or Δ*nhe B. cereus*, and silver stain of the total protein. (**k**) Real-time quantitative RT-PCR analysis of the gene encoding *nheB* in overnight cultures of *B. cereus* or Δ*nhe B. cereus*, presented relative to that of the gene encoding 16S rRNA. (**l**) Immunoblot analysis of caspase-1 (left), the release of IL-1β (middle-left) and IL-18 (middle), death (middle-right), and release of TNF (right) of LPS-

primed WT BMDMs left untreated or assessed 2 hr after stimulation with the supernatant of *B. cereus* (Sup) incubated with isotype IgG1 or supernatant incubated with anti-NHE antibodies (anti-NHE). Asterisks in (d) indicate non-specific bands. CTRL, control (c and i). Each symbol represents an independent experiment (b, e, f, h, k, l). NS, not statistically significant, **P* < 0.05, ***P* < 0.01, ****P* < 0.001 and *****P* < 0.0001 (two-tailed *t*-test [b, e, f, h, k, l]). Data are representative of three independent experiments (a-l; mean and s.e.m. in b, e, f, h, k, l).

3.4.7 Sequential assembly of HBL components is required to engage activation of the inflammasome

The tripartite enterotoxin HBL is composed of a 37-41 kDa component B, a 38-42 kDa component L_1, and a 43-47 kDa component L_2 [508,650-652]. I synthesized recombinant B, L_1 and L_2 and added these components to WT and *Nlrp3*$^{-/-}$ BMDMs. I found that recombinant HBL induced robust activation of caspase-1, secretion of IL-1β and IL-18, and pyroptosis in WT BMDMs, but not in *Nlrp3*$^{-/-}$ BMDMs (**Fig. 3.5a**). Treatment with heat or proteinase K, but not DNase or RNase, abolished the ability of HBL to induce activation of inflammasome responses (**Appendices for Chapter 3 Fig. 3.5a**), consistent with my findings that treatment with heat or proteinase K abolished the ability of the supernatant of *B. cereus* to induce activation of the NLRP3 inflammasome (**Fig. 3.2a and Appendices for Chapter 3 Fig. 3.2a,b**).

Importantly, individual components of HBL were unable to engage activation of the NLRP3 inflammasome (**Fig. 3.5a**). Addition of two of the three components in all possible combinations was also unable to induce activation of the inflammasome (**Fig. 3.5b**). Further, neutralisation of a single component, either B, L_1 or L_2, using antibodies impaired activation of the NLRP3 inflammasome induced by *B. cereus* supernatant (**Fig. 3.5c**). These results

suggested that all three components of HBL were necessary to drive activation of the NLRP3 inflammasome.

A previous study has shown that B, L_1 and L_2 can bind sheep red blood cells independently of one another [507], whereas another study has found that B, L_1 and L_2 assemble on Chinese Hamster Ovary cells in a sequential manner [508]. To investigate whether a specific order of toxin component assembly is required to trigger activation of the NLRP3 inflammasome in BMDMs, I added to BMDMs either with B, L_1 or L_2 for 30 min, followed by extensive washing prior to addition of the remaining components. It was found that addition of B, followed by L_1+L_2 (B→L_1+L_2, where the arrow symbol indicates the washing step and the plus symbol indicates 'added in concert') induced robust activation of caspase-1, secretion of IL-1β and IL-18, and pyroptosis (**Fig. 3.5d**). However, the order of L_1→B+L_2 or L_2→B+L_1 did not engage activation of inflammasome responses (**Fig. 3.5d**). These findings indicated that component B is the apical component required to initiate the assembly cascade of HBL and activation of the NLRP3 inflammasome.

To identify the precise order of toxin assembly required to induce activation of the NLRP3 inflammasome, each component in the order of B→L_1→L_2 or B→L_2→L_1 were added to BMDMs. Of the two orders, only B→L_1→L_2 was identified to trigger activation of the inflammasome (**Fig. 3.5e**). Therefore, a highly specific and linear order of HBL assembly is required for successful engagement of the NLRP3 inflammasome.

3.4.8 Cytosolic access of HBL components is not required to engage activation of the inflammasome

Previous studies demonstrated that the anthrax lethal toxin of *Bacillus anthracis,* a phylogenetic neighbour of *B. cereus,* can activate the NLRP1 inflammasome [66,75,654]. The anthrax lethal toxin is composed of a protective antigen and lethal factor, whereby the

protective antigen generates pores on the host cell membrane, through which the lethal factor enters the cell cytoplasm, subsequently cleaving NLRP1b in mice and NLRP1 in rats to induce activation of the inflammasome [66,75,654]. To investigate whether activation of the NLRP3 inflammasome is mechanistically dependent on cytosolic access of HBL components, I inhibited phagocytosis of macrophages using the actin-polymerisation inhibitor cytochalasin B or cytochalasin D. Treatment of WT BMDMs with cytochalasin B or cytochalasin D did not impair the ability of HBL, the supernatant of *B. cereus*, or live *B. cereus* to induce activation of the inflammasome (**Appendices for Chapter 3 Fig. 3.5b,c**). In contrast, treatment of WT BMDMs with cytochalasin B or cytochalasin D impaired activation of the inflammasome by *S.* Typhimurium (**Appendices for Chapter 3 Fig. 3.5b,c**), consistent with my previous findings [655]. Further, I transfected B, L_1, L_2, or L_1+L_2 into BMDMs and assessed the ability of these components to induce activation of the inflammasome. Transfection of any of these toxin components was unable to induce activation of caspase-1, secretion of IL-1β and IL-18, and pyroptosis, whereas transfection of flagellin sufficiently activated inflammasome responses (**Fig. 3.5f**). These findings suggested that, unlike anthrax lethal toxin, cytosolic entry of HBL components is not necessary to engage activation of the NLRP3 inflammasome.

To investigate whether HBL might transport LPS from the cell culture media into the cytoplasm of BMDMs to activate caspase-11 when LPS was used as a priming agent in my experiments, I stimulated LPS-primed WT and *Casp11*$^{-/-}$ BMDMs with HBL and found that both WT and *Casp11*$^{-/-}$ BMDMs underwent similar levels of caspase-1 activation, IL-1β and IL-18 secretion, and pyroptosis (**Appendices for Chapter 3 Fig. 3.5d**), confirming that HBL-induced activation of the NLRP3 inflammasome is not owing to HBL-mediated transportation of LPS to activate caspase-11 and the non-canonical inflammasome.

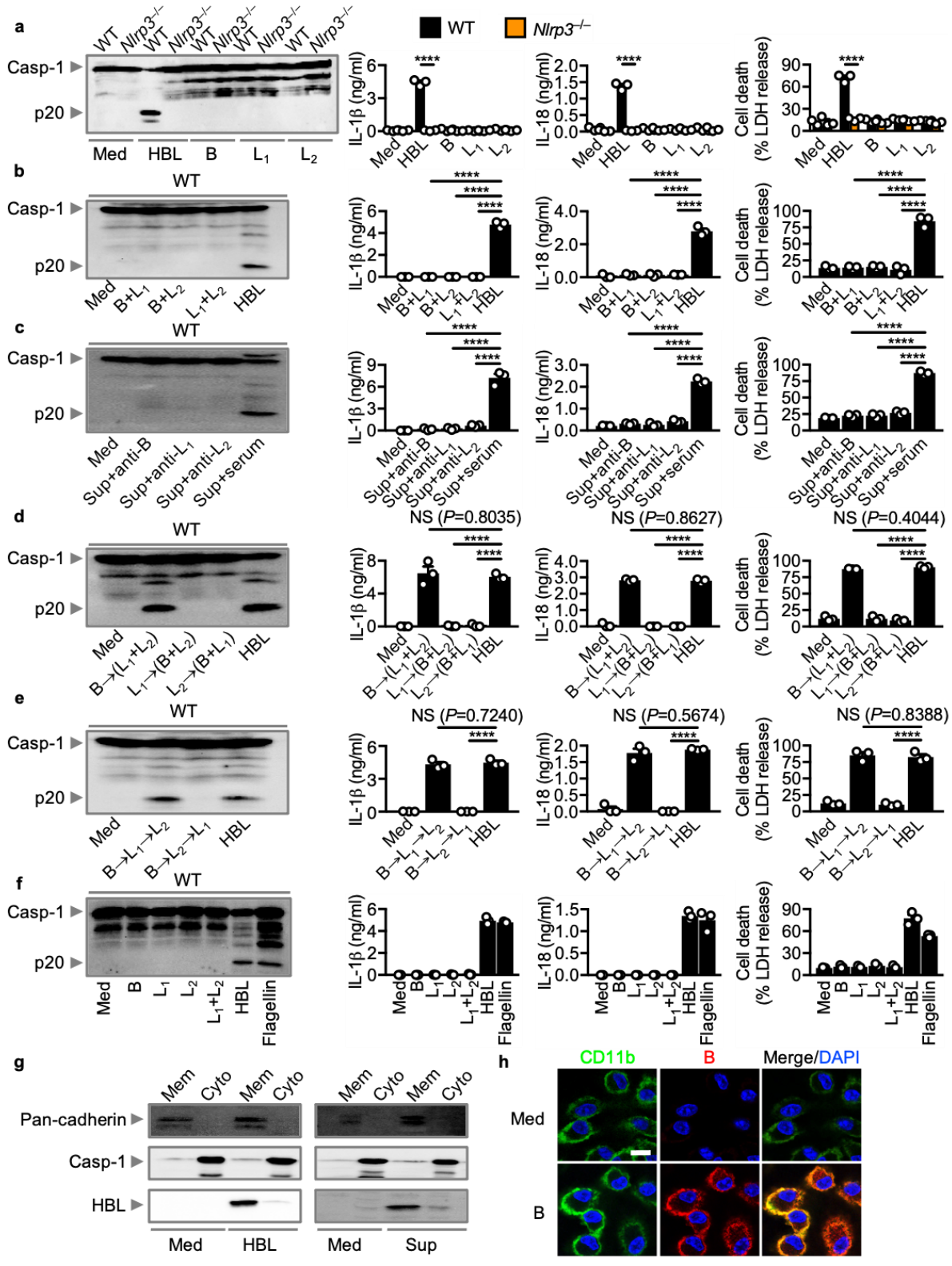

Figure 3.5 | Recombinant HBL components assemble sequentially to induce activation of the NLRP3 inflammasome. (**a**) Immunoblot analysis of caspase-1 (left), the release of IL-1β (middle-left) and IL-18 (middle-right), and death (right) of LPS-primed WT or *Nlrp3*$^{-/-}$

BMDMs left untreated (Med) or assessed 3 hr after stimulation with recombinant HBL or individual HBL components B, L_1 or L_2. (**b**) Immunoblot analysis of caspase-1 (left), the release of IL-1β (middle-left) and IL-18 (middle-right), and death (right) of LPS-primed WT BMDMs left untreated or assessed 3 hr after stimulation with two components of HBL. (**c**) Immunoblot analysis of caspase-1 (left), the release of IL-1β (middle-left) and IL-18 (middle-right), and death (right) of LPS-primed WT BMDMs left untreated or assessed 2 hr after stimulation with the supernatant of *B. cereus* (Sup) incubated with an antibody against either B, L_1 or L_2, or with mouse serum (serum). (**d**) Immunoblot analysis of caspase-1 (left), the release of IL-1β (middle-left) and IL-18 (middle-right), and death (right) of LPS-primed WT BMDMs left untreated or treated with either B, L_1 or L_2 for 30 min, followed by extensive washing (indicated by the arrow symbol), and assessed 3 hr after addition of the remaining components. The plus symbol indicates 'added in concert'. (**e**) Immunoblot analysis of caspase-1 (left), the release of IL-1β (middle-left) and IL-18 (middle-right), and death (right) of LPS-primed WT BMDMs left untreated or treated with the indicated HBL components for 30 min, followed by extensive washing in between (indicated by the arrow symbol), and assessed 3 hr after addition of the last component. (**f**) Immunoblot analysis of caspase-1 (left), the release of IL-1β (middle-left) and IL-18 (middle-right), and death (right) of LPS-primed WT BMDMs left untreated or assessed 2 hr after transfection with one or two components of HBL, or after stimulation with recombinant HBL, or after transfection with flagellin of *S.* Typhimurium. (**g**) Immunoblot analysis of pan-cadherin, caspase-1 and HBL of unprimed WT BMDMs left untreated (Med) or assessed 1 hr after stimulation with recombinant HBL or the supernatant of *B. cereus* (Sup). Mem, membrane fraction; Cyto, cytosolic fraction. (**h**) Confocal microscopy analysis of CD11b (green) and HBL-B (red) in unprimed WT BMDMs left untreated or assessed 1 hr after stimulation with the individual component HBL-B. Scale bar, 10 μm (h); NS, not statistically significant, $^{**}P < 0.01$, $^{***}P < 0.001$ and $^{****}P < 0.0001$ (two-tailed *t*-test [a] or one-way analysis of variance [ANOVA] with Dunnett's multiple-comparisons test [b-e]). Data are representative of three independent experiments (a-h; mean and s.e.m. in a-f).

3.4.9 HBL components assemble on the macrophage cell membrane to induce pores and cell lysis

My size-fractionation studies revealed that only the supernatant fraction carrying proteins of 30-50 kDa in size was capable of inducing activation of the NLRP3 inflammasome (**Fig. 3.2c–e**). This important observation excluded the possibility that HBL forms a bipartite or tripartite toxin complex in solution, resulting in a complex greater than 50 kDa in size, which subsequently binds to the plasma membrane of BMDMs (**Fig. 3.2c–e**). Binding studies further supported the idea that an apical component must bind to the plasma membrane prior to the next component being recruited (**Fig. 3.5d,e**). Indeed, the cell-membrane and cytosolic fractions were separated from BMDMs stimulated with HBL or the supernatant of *B. cereus* and found that HBL components remained in the cell-membrane fraction (**Fig. 3.5g**). Further, confocal microscopy and immunofluorescence staining revealed that HBL and the cell surface marker CD11b co-localised on the membrane of BMDMs (**Fig. 3.5h**).

To identify the mechanisms of action for HBL on the cell membrane, liposomes composed of cholesterol and the lipid species DPPC, DSPC and DOPC were synthesised, mimicking the mammalian cell membrane [581]. Encapsulation of methylene blue dye into the lumen of liposomes, helped to investigate the ability of HBL to induce pores in the liposomal membrane that would result in leakage of the dye (**Fig. 3.6a**). Remarkably, addition of HBL induced robust leakage of the liposome-encapsulated dye. The liberated dye can be captured by dye-capturing resins, removing free-floating dye in the solution (**Fig. 3.6a**). Sonication of the liposome (control) resulted in a similar level of leakage of the dye compared with liposomes treated with HBL (**Fig. 3.6a**). Importantly, heat-inactivated HBL, individual components of HBL, or bovine serum albumin (BSA) did not induce release of the dye from the liposome (**Fig. 3.6a**). Addition of liposomes to HBL sequestered the toxin and completely abolished the ability of HBL to induce activation of caspase-1, secretion of IL-1β and IL-18, and pyroptosis in WT BMDMs (**Fig. 3.6b**).

The observations that HBL has the capacity to insert into liposomal membranes led me to use bioinformatic tools to search for transmembrane regions in HBL components, which might provide insights into their ability to target the cell membrane. A putative transmembrane region corresponding to residues 232 to 250 was found in the protein sequence of component B (**Appendices for Chapter 3 Fig. 3.6a,b**). This analysis is consistent with a previous study reporting the presence of a transmembrane region in component B [513]. Two putative transmembrane regions were identified in component L_1, corresponding to residues 243 to 261, and residues 329 to 347 (**Appendices for Chapter 3 Fig. 3.6a,c**). Of these three transmembrane regions, the transmembrane region of the B component is an amphipathic helix (**Appendices for Chapter 3 Fig. 3.6b**). Indeed, the transmembrane helix of B contains a highly conserved proline residue, which is present in transmembrane α-helices and essential for inducing hinge or distortion in the membrane helix for normal functioning of certain transmembrane channels [656-659]. A signal peptide in the N-terminus of B, L_1 and L_2 was also identified (**Appendices for Chapter 3 Fig. 3.6a**), confirming the secretory nature of these HBL components.

No studies have reported visualisation of a toxin pore induced by HBL. To investigate whether HBL can induce pore formation in cell membrane, I used Cryo-transmission electron microscopy (Cryo-TEM) technique on liposomes treated with recombinant HBL. I found distinct pores in the membrane of liposomes treated with HBL, whereas the membrane of untreated liposomes remained fully intact (**Fig. 3.6c**). To demonstrate HBL-mediated lysis of the cell membrane in macrophages, I stimulated WT BMDMs with HBL or the supernatant of *B. cereus* and visualised the cell membrane using Scanning Electron Microscopy. Untreated BMDMs exhibited a prominent cell body carrying substantial amounts of membrane ruffles and projections (**Fig. 3.6d and Appendices for Chapter 3 Fig. 3.7**). In contrast, BMDMs treated with HBL or the supernatant of *B. cereus* lost their cell shape and membrane ruffles and projections (**Fig. 3.6d and Appendices for Chapter 3 Fig. 3.7**). The morphological features of these cells included cytoplasm flattening and cell rounding, with the corpse of

pyroptotic cells marked by a centralised nucleus in a deflated cell body (**Fig. 3.6d and Appendices for Chapter 3 Fig. 3.7**). Similarly, the membrane integrity and cell shape of BMDMs infected with *B. cereus* were compromised (**Fig. 3.6d and Appendices for Chapter 3 Fig. 3.7**). I also observed phagocytosed bacteria being expelled following membrane rupture (**Fig. 3.6d**), consistent with previous findings [62,660]. Transmission Electron Microscopy further revealed a loss of cytoplasmic content and nuclear condensation in BMDMs stimulated either with HBL or the supernatant of *B. cereus* (**Fig. 3.6e**).

To investigate whether the toxin can directly induce a rupture of the cell membrane, I monitored, using IncuCyte and uptake of SYTOX green nuclear stain that penetrates compromised membranes, the dynamics of the viability of WT and *Nlrp3*$^{-/-}$ BMDMs exposed to a low and high concentration of HBL. A low concentration of 5 nM HBL induced cell death in WT BMDMs, but not in *Nlrp3*$^{-/-}$ BMDMs (**Appendices for Chapter 3 Fig. 3.8a**). This concentration sufficiently triggered activation of caspase-1, cleavage of GSDMD, secretion of IL-1β and IL-18, and pyroptosis in BMDMs (**Appendices for Chapter 3 Fig. 3.8a**). However, a high concentration of 0.5 μM HBL induced very rapid cell death in both WT and *Nlrp3*$^{-/-}$ BMDMs within 20 min (**Appendices for Chapter 3 Fig. 3.8a**). In addition, a high concentration of HBL induced rapid release of LDH without inducing activation of caspase-1 and secretion of IL-1β and IL-18 (**Appendices for Chapter 3 Fig. 3.8b**). In addition, I observed that in response to HBL treatment, BMDMs lacking the full pore-forming ability of the pyroptotic factor gasdermin D (*Gsdmd*$^{I105N/I105N}$) [574,661,662] had an impaired ability to secrete IL-1β and IL-18 and undergo cell death at 1 and 2 hr, compared with WT BMDMs (**Appendices for Chapter 3 Fig. 3.9a,b**). Collectively, these findings indicated that HBL binds and orchestrates disruption of the cell membrane, leading to rapid cell lysis or activation of the NLRP3 inflammasome in a manner dictated by the bioavailability and concentration of HBL.

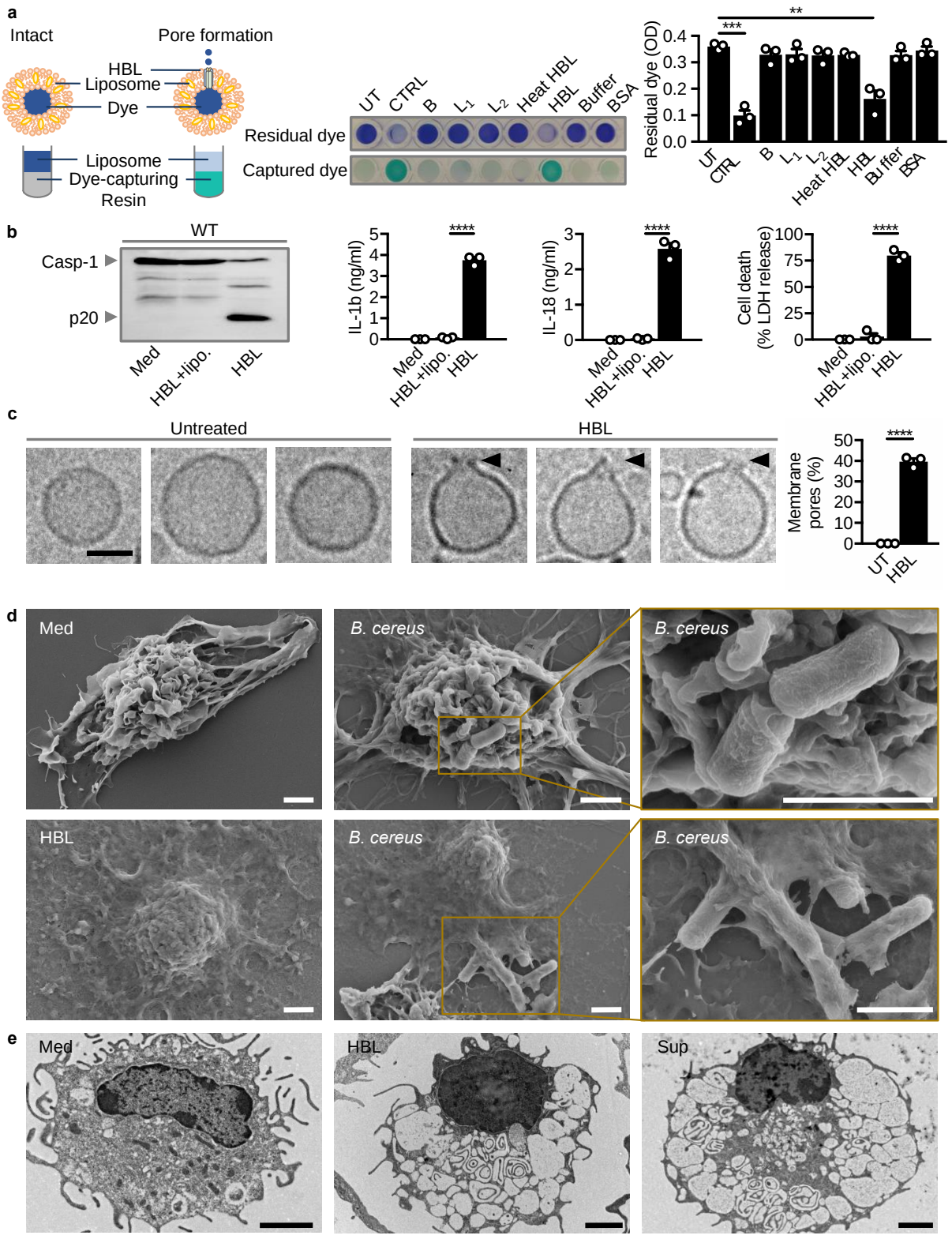

Figure 3.6 | HBL induces pores on the host cell membrane. ((**a**) Colorimetric analysis of liposomes left untreated (UT), sonicated for 5 min at 100 amplitude (CTRL), or assessed 30 min after stimulation with individual HBL components, heat-inactivated HBL, HBL, buffer, or

BSA. The absorbance (OD) of residual dye was measured at 595 nm. (**b**) Immunoblot analysis of caspase-1 (left), the release of IL-1β (middle-left) and IL-18 (middle-right), and death (right) of WT BMDMs left untreated or assessed 3 hr after stimulation with recombinant HBL in presence or absence of liposomes (lipo.). (**c**) Cryo-EM analysis of liposomes left untreated or assessed 1 hr after stimulation with recombinant HBL. Images (left) and quantification of percentages of liposomes (right) exhibiting membrane pores in untreated liposomes (n= 469) and HBL-treated liposomes (n= 814). (**d**) Scanning electron microscopy analysis of WT BMDMs left untreated or assessed 3 hr after infection with *B. cereus* (MOI, 5), showing attachment of *B. cereus* to BMDMs or dead BMDMs. Scanning electron microscopy analysis of LPS-primed WT BMDMs assessed 3 hr after stimulation with HBL. (**e**) Transmission electron microscopy analysis of WT BMDMs left untreated or assessed 3 hr after stimulation with HBL or 2 hr after stimulation with the supernatant of *B. cereus* (Sup). Scale bar, 50 nm (c), 2 μm (d and e). Each symbol represents an independent experiment (a-c). ***P* < 0.01, ****P* < 0.001 and *****P* < 0.0001 (one-way analysis of variance [ANOVA] with Dunnett's multiple-comparisons test [a] or two-tailed *t*-test [b and c]). Data are representative of one (d and e), two (c), or three independent experiments (a and b; mean and s.e.m. in a-c).

3.4.10 HBL-induced activation of the inflammasome requires K^+ efflux

Pore-forming toxins have the capacity to alter intracellular homeostasis. Indeed, efflux of K^+ has been proposed to be a central mechanism by which the NLRP3 inflammasome can be activated [663]. I used Inductively Coupled Plasma-Optical Emission Spectrometry (ICP-OES) to measure intracellular concentration of K^+ in WT BMDMs stimulated with HBL and the supernatant of *B. cereus*. Remarkably, treatment of HBL and the supernatant of *B. cereus* led to significant reduction of cytosolic concentration of K^+ in WT BMDMs similar to that observed in seen in BMDMs treated with the classical NLRP3 activator LPS+ATP (**Appendices for Chapter 3 Fig. 3.10a**). I further observed that addition of extracellular K^+ inhibited activation

of the inflammasome in a dose-dependent manner in response to recombinant HBL, the supernatant of *B. cereus* or *B. cereus* (**Appendices for Chapter 3 Fig. 3.10b,c**). Addition of extracellular K^+ also inhibited activation of the inflammasome by LPS+ATP (**Appendices for Chapter 3 Fig. 3.10b,c**), consistent with previous studies [133,664,665]. To rule out the possibility that addition of extracellular K^+ can interfere with HBL toxin's ability to bind to the membrane and activate the inflammasome, I conducted immunofluorescence analysis of membrane binding ability of the apical subunit HBL-B. Indeed, confocal analysis revealed that addition of extracellular K^+ had no effect on membrane binding ability of subunit B (**Appendices for Chapter 3 Fig. 3.10d**). In contrast, the intracellular concentration of the K^+ counterpart Na^+ was found to be unaltered upon treatment with HBL, the supernatant of *B. cereus* and LPS+ATP, and that addition of extracellular Na^+ did not inhibit activation of the inflammasome in response to HBL or LPS+ATP (**Appendices for Chapter 3 Fig. 3.10e–g)**. These data suggest that HBL induced efflux of K^+ is sufficient to activate the inflammasome.

3.4.11 Pharmacological inhibition of the NLRP3 inflammasome prevents *B. cereus*-induced lethality

I further investigated the role of the NLRP3 inflammasome in host defense against *B. cereus* infection *in vivo.* To this end, WT, *Nlrp3*$^{-/-}$, and *Casp1/11*$^{-/-}$ mice were infected with *B. cereus* via an intraperitoneal (i.p.) route and monitored for their susceptibility to infection. Only 40% (10/25) of the WT mice survived the infection, whereas 92% (12/13) of the *Nlrp3*$^{-/-}$ mice and 81% (13/16) of the *Casp1/11*$^{-/-}$ mice survived (**Fig. 3.7a**). Analysis of the serum showed that *Nlrp3*$^{-/-}$ and *Casp1/11*$^{-/-}$ mice had a reduced level of IL-18 following infection with *B. cereus* compared to infected WT mice (**Fig. 3.7b**). Similarly, administration of the supernatant of *B. cereus* induced IL-18 in the serum of WT mice; levels of IL-18 in *Nlrp3*$^{-/-}$ and *Casp1/11*$^{-/-}$ mice were significantly reduced (**Fig. 3.7c**).

To confirm a role for HBL in the pathogenesis of *B. cereus* infection *in vivo*, I infected WT mice either with WT or Δ*hbl B. cereus*. A higher percentage of WT mice survived when infected with Δ*hbl B. cereus* (87%, 13/15) compared to mice infected with WT *B. cereus* (25%, 4/16) (**Fig. 3.7d**). Further, I observed that WT mice infected with Δ*hbl* produced substantially less IL-18 in the peritoneal fluid and serum compared with WT mice infected with WT *B. cereus* (**Fig. 3.7e,f**).

Given that activation of the NLRP3 inflammasome in response to *B. cereus* infection resulted in rapid lethality in mice (**Fig. 3.7a**), I hypothesised that pharmacological blockade of the NLRP3 inflammasome would yield a beneficial outcome in the host. To this end, I treated WT mice with the small molecule inhibitor MCC950 or with PBS, the first dose administered 1 hr prior to the infection and the second dose administered at the same time as the infection. All (14/14) of the MCC950-treated mice survived the infection, whereas only 23% (3/13) of the PBS-treated mice survived (**Fig. 3.7g**), suggesting that MCC950-mediated inhibition of the NLRP3 inflammasome completely protected WT mice from *B. cereus*-induced lethality. Further, administration of MCC950 to WT mice infected with *B. cereus* attenuated secretion of IL-18 in the peritoneal cavity and circulation, whereas administration of PBS did not (**Fig. 3.7h,i**). This observation is supported by my finding demonstrating the potency of MCC950 in inhibiting activation of the NLRP3 inflammasome in BMDMs infected with *B. cereus* (**Appendices for Chapter 3 Fig. 3. 1f**). Together, these results highlighted that *B. cereus* infection induces activation of the NLRP3 inflammasome *in vivo* and that therapeutic blockade of the NLRP3 inflammasome efficiently rescued mice from *B. cereus*-induced mortality.

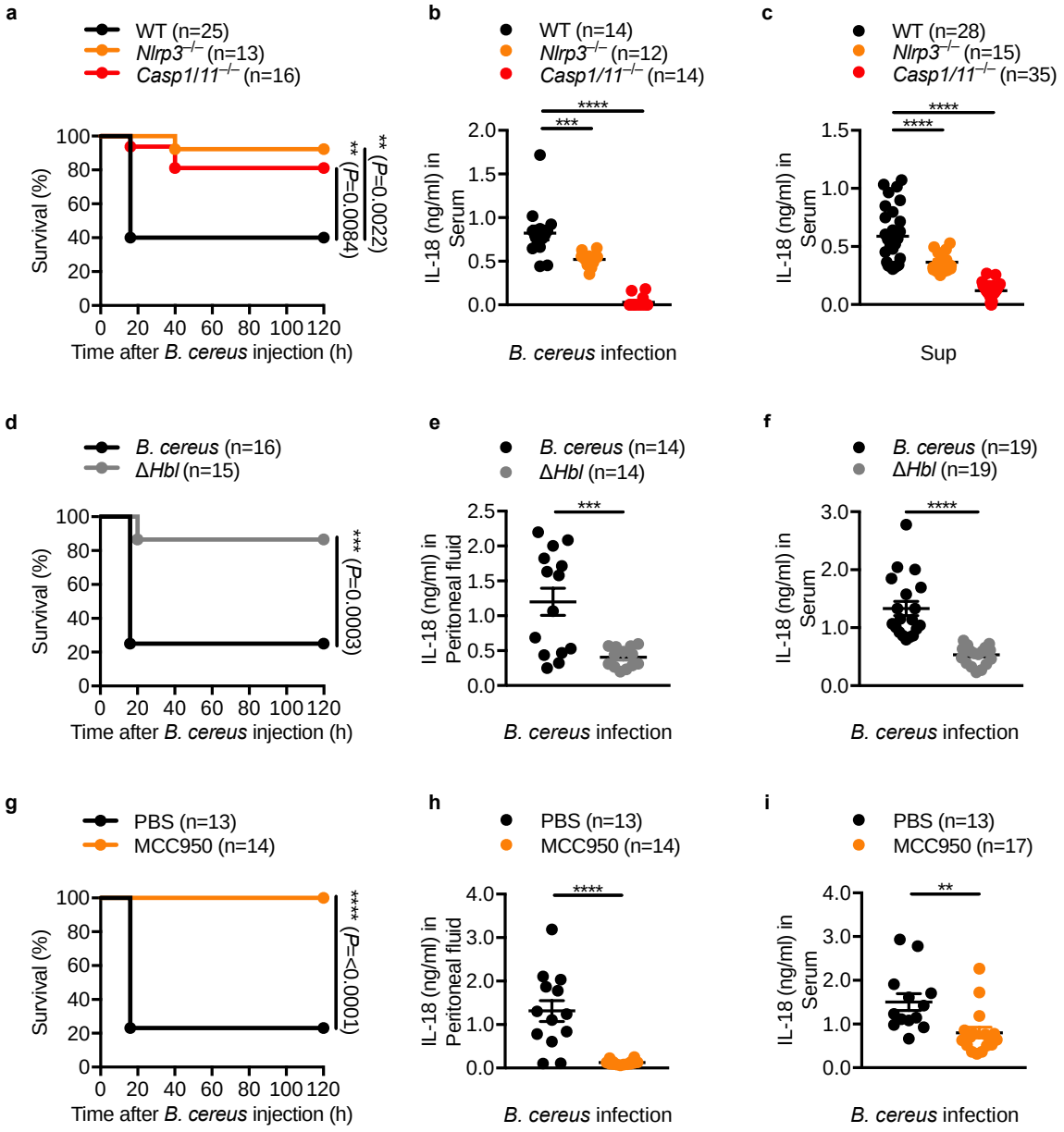

Figure 3.7 | The NLRP3 inflammasome mediates lethality induced by *B. cereus* infection in vivo. (**a**) Survival of 8-week-old WT mice (n = 25), *Nlrp3*$^{-/-}$ mice (n = 13), *Casp1/11*$^{-/-}$ mice (n = 16), after intraperitoneal infection with 5 × 10^6 colony-forming units (CFUs) of *B. cereus*. (**b**) Concentration of IL-18 in the serum of WT mice (n = 14), *Nlrp3*$^{-/-}$ mice (n = 12), *Casp1/11*$^{-/-}$ mice (n = 14), 16 hr after intraperitoneal infection with 7.5 × 10^6 CFUs of *B. cereus*. (**c**) Concentration of IL-18 in the serum of WT mice (n = 28), *Nlrp3*$^{-/-}$ mice (n = 15), *Casp1/11*$^{-/-}$ mice (n = 35), 16 hr after intraperitoneal injection with 200 μl of the

supernatant of *B. cereus* (Sup). (**d**) Survival of 8-week-old WT mice (n = 16) after intraperitoneal injection with 5 × 10^6 CFUs of *B. cereus* ATCC 10876 or of WT mice (n = 15) after intraperitoneal injection with 5 × 10^6 CFUs of the isogenic mutant of *B. cereus* ATCC 10876 lacking HBL (Δ*hbl*). (**e**) Concentration of IL-18 in the peritoneal fluid of WT mice (n = 14), 3 hr after intraperitoneal infection with 7.5 × 10^6 CFUs of *B. cereus* or of WT mice (n = 14), 3 hr after intraperitoneal infection with 7.5 × 10^6 CFUs of Δ*hbl B. cereus*. (**f**) Concentration of IL-18 in the serum of WT mice (n = 10), 16 hr after intraperitoneal infection with 7.5 × 10^6 CFUs of *B. cereus* or of WT mice (n = 15), 16 hr after intraperitoneal infection with 7.5 × 10^6 CFUs of Δ*hbl B. cereus.* (**g**) Survival of 8-week-old WT mice administered with PBS (n = 13) or WT mice administered with 50 mg/kg MCC950 (n = 14), both via an intraperitoneal route, followed by intraperitoneal infection with 5 × 10^6 CFUs of *B. cereus* with a corresponding second dose of PBS or 50 mg/kg MCC950. (**h**) Concentration of IL-18 in the peritoneal fluid of WT mice administered with PBS (n = 13) or WT mice administered with MCC950 (n = 14) as in (g), 3 hr after infection with 7.5 × 10^6 CFUs of *B. cereus*. (**i**) Concentration of IL-18 in the serum of WT mice administered with PBS (n = 13) or WT mice administered with MCC950 (n = 17) as in (g), 6 hr after infection with 7.5 × 10^6 CFUs of *B. cereus*. Each symbol represents an individual mouse (b, c, e, f, h, i). $^{**}P < 0.01$, $^{***}P < 0.001$, and $^{****}P < 0.0001$ (log-rank test [a, d and g] or one-way analysis of variance [ANOVA] with Dunnett's multiple-comparisons test [b and c] or two-tailed *t*-test [e, f, h and i]). Data are pooled from two independent experiments (a, b, and d-i) or from three independent experiments (c, s.e.m. in b, c, e, f, h and i).

3.5 Discussion

Activation of the inflammasome pathway is one of the hallmarks of innate immune recognition of pathogens and danger signals. It has been shown that cytosolic bacteria, such as *F. novicida* and *L. monocytogenes*, must escape the pathogen-containing vacuole to the

cytoplasm of the host cell in order to induce activation of cytosolic inflammasome sensors [27,259,368,666]. However, the mechanisms governing how secreted bacterial factors are detected by innate immune sensors in the cytosol in the absence of bacterial invasion have remained largely unknown.

My studies revealed that the multi-component toxin HBL produced by the foodborne pathogen *B. cereus* is recognised by the cytosolic sensor NLRP3 (**Appendices for Chapter 3 Fig. 3.11**). Identification of a role for the inflammasome in *B. cereus* infection and the specific microbial activator triggering inflammasome responses have several important implications. *B. cereus* is a ubiquitous spore-forming foodborne pathogen of humans. Ingestion of toxins secreted by *B. cereus* is sufficient to result in vomiting and/or diarrhoea [667], suggesting that toxins of *B. cereus* are strong inducers of gastrointestinal inflammation. In addition, *B. cereus* can cause a range of often-lethal extra-gastrointestinal infections, including sepsis, pneumonia, and meningitis [448]. Despite the clinical importance of *B. cereus* in humans, little is known about the role of the immune system in host defense against this pathogen.

In addition to inflammasome inhibition, administration of small-molecule inhibitors or antibody-mediated neutralisation against HBL of *B. cereus* might prevent lethality. Indeed, previous studies have shown that pharmacological inhibition or antibody-mediated neutralisation against the anthrax toxin can prevent lethal infection by *B. anthracis* [668,669]. These studies would suggest that targeting bacterial toxins could be a highly effective and universal strategy in the prevention and treatment of infection by toxin-producing bacteria.

My studies revealed that component B of HBL is the apical subunit initiating assembly of the HBL pore on cell membrane, followed by recruitment of L_1 and L_2. I hypothesise that attachment of B on the macrophage cell membrane induces a conformation change that enables recruitment of L_1. Indeed, a previous study have suggested that B can oligomerise on the cell membrane [513]. L_1 might also anchor to the cell membrane owing to its two putative

transmembrane helices, forming a stable B-L_1 platform mediating the recruitment of the final component, L_2.

Previous studies have shown that both HBL and NHE are tripartite pore-forming toxins [506,507]. The structure of HBL-B [513] and NHE-A [514] have been elucidated, showing that both are α-pore-forming toxins. My data revealed that HBL-induced activation of the NLRP3 inflammasome requires K^+ efflux. A previous study has shown that the NHE pore is also permeable to K^+ [670]. The NHE pore has a predicted diameter of 5 nm [670] whereas the HBL pore has a diameter of 1.2 nm [507]. The different diameters of the pores between HBL and NHE might affect their overall ion selectivity, and therefore, their ability to induce activation of the inflammasome.

In conclusion, this study identified NLRP3 as the cytosolic innate immune sensor of the human foodborne pathogen *B. cereus*. This study also identified the multi-component toxin HBL as an activator of the NLRP3 inflammasome and a virulence factor which drives inflammasome-mediated lethality *in vivo*. My results further highlight that pharmacological inhibition of inflammasomes is a highly effective therapeutic option in potentially lethal bacterial infections.

Chapter 4♦ *Bacillus cereus* non-haemolytic enterotoxin activates the NLRP3 inflammasome

4.1 Preface

This chapter consists primarily of a publication in ***Nature Communications***, of which I was the co-first author with Daniel Fox (PhD student) from the lab.

Fox, D*, **Mathur, A***, Xue, Y, Liu, Y, Tan, WH, Feng, S, Pandey, A, Ngo, C, Hayward, JA, Atmosukarto, II, Price, JD, Johnson, MD, Jeßberger, N, Robertson, AAB, Burgio, G, Tscharke, DC, Fox, EM, Leyton, DL, Kaakoush, NO, Märtlbauer, E, Leppla, SH, & Man, SM (2020). *Bacillus cereus* non-haemolytic enterotoxin activates the NLRP3 inflammasome. ***Nature Communications***, 11:760. *Co-first authors

As the nominal first author, I generated greater than fifty percent of the content. My contributions to the publication was as follows:

- Planning, design and execution of experiments outlined in Main figures: 4.1d,e; 4.2b,d; 4.3b,c,e-h; 4.4a-e; 4.5b,c,e,g,h,i; 4.6a-h; and Appendices chapter 4 figures: 4.1a,b,g,h; 4.2a-e; 4.3a-e; 4.4a-c; 4.5e,f; 4.6c-e; 4.7a-c; 4.9a,b.
- Interpretation and analysis of results and compilation of figures listed above.
- Wrote the first draft of the manuscript.
- Edited subsequent versions of the manuscript and addressed comments from co-authors and external peer reviewers with assistance from senior author Prof. Si Ming Man.

I would like to take this opportunity to thank my co-authors on this publication, whose contributions are as follows:

Author initials	Figure	Contribution
D.F. (Co-first author)	Main figures: 4.1a-c; 4.2a-c,e; 4.3a,d,h; 4.4f,g; 4.5f; 4.6a-h Appendices chapter 4 figures: 4.1a,c,e,f; 4.3f; 4.4d; 4.5a-d; 4.6a,b; 4.8 (figure compilation); 4.11	Executed experiments, performed analysis and compilation of listed figures. Wrote the abstract, introduction, materials and methods sections of the manuscript.
Y.X. and Y.L.	Main figures: 4.3e,f; 4.5a,f; Appendices chapter 4 figures: 4.8a-c	Executed experiments, performed analysis and generated data for the listed figures under my mentorship.
W.H.T.	Main figures: 4.3c; 4.5c-e; Appendices chapter 4 figures: 4.8a-c, 4.10a-d	Prepare SEM and TEM samples post fixing of samples by me. Visualisation and compilation of listed figures was done by me. Assisted with protein production of NHE (4.8a-c). Executed experiments, performed analysis and compilation of Fig. 4.10a-d.
C.N.	Appendices chapter 4 figures: 4.1d; 4.8a	Executed isolation of RNA and qRT-PCR experiments, generated data, interpretation and compilation of the listed figures. Bioinformatics analysis was conducted for 4.8a. Assisted in collection of serum and peritoneal fluid from mice.
S.F.	Appendices chapter 4 figures: 4.3f	Executed experiments, performed analysis and compilation of the listed figures. Assisted in collection of serum and peritoneal fluid from mice.
A.P.	Main figure: 4.4g	Assisted in image acquisition.
J.A.H.	Appendices chapter 4 figures: 4.8a; 4.10a	Designed the plasmids for the study.
N.O.K.	Main figures: 4.3g, 4.5b Appendices chapter 4 figures: 4.10c	Designed and executed experiments, performed analysis and generated data for the listed figures. Interpretation and compilation of the listed figures was done by me.
I.I.A. and J.D.P.	Main figures: 4.4a-e; 4.5h,i	Synthesised liposomes for the listed figures.
M.D.J., D.L.L., N.J., E.M., A.A.B.R., G.B., D.C.T., E.M.F. and S.H.L.		Provided resources and intellectual input.
S.M.	Drew the Appendices chapter 4 Figure 4.11 (assisted by D.F.)	Overall supervision and conceptualisation of the study.

4.2 Introduction

Bacillus cereus is a clinically important human foodborne pathogen. This Gram-positive and rod-shaped bacterium is found ubiquitously in the environment and in undercooked and processed food products [448]. Ingestion of *B. cereus* endospores often leads to germination and propagation of viable vegetative cells in the human gastrointestinal tract, which may lead to emetic and diarrhoeal syndromes largely depending on the production of enterotoxins [500,501]. Of concern is the potential for *B. cereus* to cause often-fatal extra-gastrointestinal disease in immune-compromised patients, including systemic bacterial septicaemia, ocular infections, anthrax-like pneumonia, cutaneous gas-gangrene like infections, and infections of the central nervous system [448].

Of particular interest is that *B. cereus* isolates which lack HBL can cause inflammation and disease in humans [506,671,672], suggesting that other non-redundant virulence factors are critical in the pathogenesis of this pathogen. I have previously shown that a multicomponent toxin of *B. cereus* called haemolysin BL (HBL) can induce activation of the NLRP3 inflammasome via a mechanism independent of entry to the host cell cytoplasm [673]. Here, non-haemolytic enterotoxin (NHE) of *B. cereus* was identified to induce activation of the NLRP3 inflammasome and pyroptosis via a mechanism targeting the plasma membrane of host cells. This study also demonstrates that NHE subunits assembled to form a functional pore, driving efflux of cytosolic potassium. This toxin kills cell types from multiple lineages and host origin, highlighting its functional repertoire in different host species. My results reveal that multiple functionally conserved toxins from *B. cereus* are targeted by a single inflammasome to initiate inflammation and cell death in the host. This host strategy offers a single pathogen sensor the flexibility to mediate the recognition of functionally conserved toxins, often produced by phylogenetically diverse bacterial species or even within different strains of a single bacterial species.

4.3 Material and Methods

4.3.1 Cell Lines

CaCo-2 cells were cultured for 3 days in EMEM (670086, ThermoFisher Scientific) supplemented with 20% FBS, and 1% penicillin and streptomycin. CT26, Jurkat, RMA-S, and THP-1 cells were cultured for 3 days in RPMI-1640 (11875093, ThermoFisher Scientific) supplemented with 10% FBS, and 1% penicillin and streptomycin. HEK293T and HT-29 cells were cultured for 3 days in DMEM supplemented with 10% FBS, and 1% penicillin and streptomycin. L-929, LS 174T, MDCK and Vero cells were cultured for 3 days in EMEM supplemented with 10% FBS, and 1% penicillin and streptomycin. K-562 cells were cultured for 3 days in IMDM (12440053, ThermoFisher Scientific) supplemented with 10% FBS, and 1% penicillin and streptomycin. MC-38 cells were cultured for 3 days in DMEM supplemented with 10% FBS, 1% non-essential amino acids (11140050, Gibco ThermoFisher Scientific), 1% HEPES (15630080, Gibco ThermoFisher Scientific), and 1% penicillin and streptomycin. MutuDCs were cultured for 3 days in IMDM supplemented with 10% FBS, 1% sodium bicarbonate (25080094, Gibco ThermoFisher Scientific), 1% HEPES, and 1% penicillin and streptomycin. U266B1 cells were cultured for 3 days in RPMI supplemented with 15% FBS, and 1% penicillin and streptomycin. Cells were seeded in antibiotic-free media at a concentration of 0.5 x 10^6 cells per well in 24-well plates.

4.3.2 Bacterial Culture

B. cereus was grown in Luria-Bertani (LB) media (244620, BD) overnight under aerobic conditions at 30 °C [673]. The *Bacillus* strains used in this study are listed in **(Table 2.4)**. *Salmonella enterica* serovar Typhimurium was grown in LB media overnight under aerobic conditions at 37 °C. The next day, all bacteria were subcultured (1:10) in fresh media for 3-4 hr.

4.3.3 Stimulation of BMDMs with Bacteria and Inflammasome Activators

Unprimed BMDMs were infected with WT or Δ*hbl B. cereus* at multiplicity of infection (MOI) of 2-5 for 3-20 hr for inflammasome activation; BMDMs were infected with Δ*hbl B. cereus* at MOI of 2 for 0-60 min for pIκB, IkB, pERK, ERK, NLRP3 and GAPDH protein levels. To activate the canonical NLRP3 inflammasome, BMDMs were primed with 500 ng/ml ultrapure LPS from *E. coli* (ALX-581-014-L002, Enzo Life Sciences) for 4 hr and stimulated with 5 mM ATP (10127531001, Roche) for 45 min. To activate the NLRC4 inflammasome, BMDMs were infected with *S.* Typhimurium at MOI of 2 for 4 hr. Ultrapure flagellin was mixed with 20 µl of the liposomal transfection reagent DOTAP (11202375001, Sigma-Aldrich) in PBS. After 30 min, the complexes were added to LPS-primed BMDMs in Hank's Balanced Salt Solution (HBSS, H9394, Sigma-Aldrich) and incubated for 3-5 hr. To activate the AIM2 inflammasome, 2.5 µg of poly(dA:dT) (tlrl-patn, InvivoGen) were resuspended in PBS and mixed with 0.3 µl of Xfect polymer in Xfect reaction buffer (631318, Clontech Laboratories, Inc.). After 30 min, DNA complexes were added to BMDMs in Opti-MEM (31985-070, ThermoFisher Scientific) and left stimulated for 4 hr. To activate caspase-11, 5 µg of LPS was transfected as described for poly(dA:dT) transfection. For inhibition studies, 50 µM of cytochalasin B (C6762, Sigma-Aldrich), 50 µM of cytochalasin D (C8273, Sigma-Aldrich), 20 µM of the selective and potent NLRP3 inhibitor, MCC950 [213-215], 50 mM of potassium chloride (KCl) (P9541, Sigma-Aldrich) or 50 mM of sodium chloride (NaCl) (S9888, Sigma-Aldrich) were added to BMDMs 30 min prior to stimulation. Cell culture supernatants were collected for ELISA and LDH assays. Cell culture supernatants and cell lysates were collected for immunoblot analysis.

4.3.4 Stimulation of BMDMs with Bacterial Supernatant

The overnight bacterial culture was centrifuged at 4,000 x g for 10 min. The supernatant was filter-sterilised using low-protein-binding 0.45 µm filter (SLHV033RS, Merck). For size-fractionation, the supernatant of Δ*hbl B. cereus* was fractionated using spin-filter columns of the 9 kDa (89884A, ThermoFisher Scientific), 30 kDa (UFC803096, Millipore), or 50 kDa range

(UFC905096, Millipore). For heat inactivation, the supernatant of Δ*hbl B. cereus* was heated to 50 °C, 75 °C or 100 °C for 10 min. To remove proteins, DNA or RNA, the supernatant of Δhbl *B. cereus* was pre-treated with Proteinase K (1 mg/ml, 19133, Qiagen), DNase I (1 mg/ml, Roche), or RNase A (1 mg/ml, Qiagen), respectively, for 1 hr. 50-150 µl of bacterial supernatant were added to LPS-primed BMDMs.

For neutralisation studies, the supernatant from various *B. cereus* strains was treated with antibodies against NHE (2 µl of 0.8 mg/ml α-NHE-B), HBL (2 µl 0.8 mg/ml α-HBL-L2), or combination of NHE (2 µl of 0.8 mg/ml α-NHE-B) and HBL (2 µl 0.8 mg/ml α-HBL-L2) for 1 hr before addition to LPS-primed BMDMs [508,565]. For controls, mouse isotype IgG1 (2 µl, 5415, Cell Signaling Technologies) was used.

4.3.5 Cloning, Protein Expression and Purification

Putative transmembrane regions in individual component of NHE were predicted using the software Membrane Protein Explorer server, also known as MPEx [590]. Helical wheel diagrams were constructed using the HELIQUEST server [591]. DNA sequences of the gene encoding NHE-C and HBL-B were acquired from the genome of *B. cereus* NVH 1230-88 (GenBank: CAB53340.2) and *B. cereus* strain ATCC 10876 (GenBank: CM000715.1) respectively, and were submitted to GenScript for cloning. DNA sequences encoding NHE-C and HBL-B with and without their putative transmembrane region were cloned into NcoI and XhoI restriction sites of the pET-28a(+)-TEV plasmid containing kanamycin resistance. The BL21(DE3) *E. coli* strain (C600003, ThermoFisher Scientific) was transformed with the pET-28a(+)-TEV plasmid vector. A single colony was picked to inoculate a starter culture of 10 mL LB_{Kan} broth (LB broth + 30 µg/ml kanamycin (10106801001, Roche) which was incubated at 37 °C, shaking (180 rpm) overnight. After overnight incubation, 10 mL of starter culture was transferred into 1 L of LB_{Kan} broth and incubated at 37 °C, shaking (180 rpm) for 4 hr until an OD_{600} of 0.6 was obtained. Expression was induced by adding isopropyl β-D-1-thiogalactopyranoside (1 mM; IPTG, Roche) and the incubation continued under identical conditions overnight. The culture

suspension was centrifuged (5,000 g, 20 min, 4 °C) to pellet the bacteria and stored at -80 °C until required. The cell pellet was resuspended in lysis buffer (50 mM Tris, pH 8.0 (BP152-1, ThermoFisher Scientific); 300 mM NaCl (SA046, Chem-Supply); 5 mM imidazole (I2399, Sigma-Aldrich); 250 µg/ml lysozyme (89833, ThermoFisher Scientific); and 1 mM phenylmethylsulfonyl fluoride (78830, Sigma-Aldrich)). Cells were subsequently disrupted by sonication and centrifuged (27,000 x g, 20 min, 4 °C). The supernatant was passed through a 0.22 µm filter (SLGP033RS, Merck). The C-terminal hexa-His-tagged proteins were purified by using HisTrap HP histidine-tagged protein purification column (17524701, GE Healthcare Lifesciences) at 4 °C using the NGC Quest™ 10 Chromatography System (7880001, Bio-Rad) and ChromLab™ software (Bio-Rad). The target proteins were eluted from the HisTrap column using a stepwise gradient of imidazole (10% increments) from Buffer A (50 mM Tris, pH 8.0; 300 mM NaCl; 5 mM imidazole) to Buffer B (50 mM Tris, pH 8.0; 300 mM NaCl; 500 mM imidazole). Purity of the eluted proteins was analysed by SDS-PAGE and Coomassie blue staining. The protein concentration was determined by spectrophotometric measurements of A280 using a NanoDrop™ 2000/2000c spectrophotometer.

4.3.6 Circular dichroism measurement

Circular dichroism (CD) is valuable tool for rapid determination of the secondary structure of purified proteins and is often used to determine if mutations affect the conformation or stability of the protein [674]. HBL protein samples (0.2-0.5 mg/ml; 2.53-2.67 µM) in PBS were filtered into 1 mm path-length quartz cuvettes using a 0.22 µm filter. The CD spectrum (θ) was recorded at 2 nm/s scanning speed on a Chirascan™ V100 Circular Dichroism Spectrometer from 200-260 nm at 25 °C. The mean residue ellipticity was calculated using the formula to account for the differences in molecular weight between the protein. The spectra are shown as an average of three scans.

$$Mean\ residue\ ellipticity\ (cm^2 dmol^{-1}) = \frac{100 \times \theta}{C \times N \times l}$$

θ = degree of ellipticity, C = protein concentration (in M), N = number of amino acids, l = pathlength (in cm)

4.3.7 Stimulation of BMDMs with Recombinant NHE and HBL

LPS-primed BMDMs were stimulated with all three NHE or HBL components, individually or in various combinations (NHE: 100 nM of each component, HBL: 5nM of each component and 1-3 hr for caspase-1 activation). For binding order studies, LPS-primed BMDMs were stimulated with a single NHE component (either A, or B, or C) for 1 hr. This step was followed by extensive washing (denoted by: $\rightarrow$) with PBS three times to remove unbound toxin. The two remaining components were added in concert (denoted by: +), or the second individual component was added for 1 hr followed by the third individual component, with washing steps in between. For transfection of NHE, each reaction consisted of individual NHE components (100 nM each) or a combination of two components (50 nM each) mixed with 10 µl of the liposomal transfection reagent DOTAP. After 30 min the complexes were added to LPS-primed BMDMs in HBSS and left for 3 hr.

4.3.8 Liposome Studies

Liposomes were synthesised [673] and treated with NHE (30 nM of each component), individual NHE component (30 nM), heat-inactivated NHE, HBL (0.5 µM), a protein buffer used to carry NHE and HBL [10 mM Tris HCl, 0.5 mM EDTA (pH 8.0)], or BSA (1 µg/ml; 001000173, Jackson ImmunoResearch) or $NHE_{mut.}$ (30 nM). The liposomes were sonicated at 100 amplitude for 5 min as control (CTRL). The released dye was captured by a cation exchanger resin Dowex (10-15 mg per well). The absorbance (OD) of residual dye was measured at a wavelength of 595 nm using the Infinite 200 PRO system (Tecan). To investigate the capacity of liposomes to inhibit NHE-induced activation of the inflammasome, recombinant NHE (100 nM) was left untreated or treated with liposomes (7 mM) for 1 hr, prior to addition to LPS-primed BMDMs.

4.3.9 Immunoblotting Analysis

For caspase-1 immunoblotting, BMDMs and supernatant were lysed in lysis buffer and sample loading buffer containing SDS and 100 mM DTT. For immunoblotting of pIκB, IκB, pERK, ERK, NLRP3 and GAPDH, the supernatant was removed and BMDMs were washed once with PBS, followed by lysis in RIPA buffer and sample loading buffer containing SDS and 100 mM DTT. Proteins were separated on 8-12% polyacrylamide gels. Following electrophoretic transfer of proteins onto PVDF membranes (IPVH00010, Millipore), membranes were blocked in 5% skim milk in TBST and incubated overnight with primary antibodies against caspase-1 (1:1,000 dilution, AG-20B-0042, Adipogen), pIκB (1:1,000 dilution, 2859, Cell Signaling Technologies), IκB (1:1,000 dilution, 9242, Cell Signaling Technologies), pERK (1:1,000 dilution, 9101, Cell Signaling Technologies), ERK (1:1,000 dilution, 9102, Cell Signaling Technologies), NLRP3 (1:1,000 dilution, AG-20B-0014, Adipogen), GAPDH (1:10,000 dilution, 5174, Cell Signaling Technologies), CD14 (1:1,000 dilution, 17000-1-AP, Proteintech), gasdermin D (1:1,000 dilution, ab209845, Abcam), IL-1β (1:1,000 dilution, RDSAF401NA, R&D Systems), NHE-C (1:200 dilution, NHE-C rabbit antisera), NHE-B (1:1,000 dilution, 1E11, 0.8 mg/ml), NHE-A (1:1,000 dilution, 1G4, 0.8 mg/ml) or HBL-B (1:1,000 dilution, HBL-B mouse antisera)[508,565]. PVDF membranes were then incubated with HRP-conjugated secondary antibody (1:5,000) for 1 hr and proteins were visualised using the Super Signal Femto substrate (34095, ThermoFisher Scientific) and the ChemiDoc™Touch Imaging System (BioRad). Uncropped full length immunoblots are provided in the Source Data file.

For detection of toxin components, 300 µl of the supernatant of *B. cereus* were mixed with 100 µl of sample loading buffer. Primary antibodies against HBL components B, L_1 and L_2 (1:1,000 dilution) [508], or against NHE-B, NHE-A, NHE-C (1:1,000 dilution) [565] were used. Silver staining was performed for total protein loading controls in accordance with the manufacturer's instructions (24612, Thermo Scientific).

4.3.10 Immunofluorescence Staining

Immunofluorescence staining for visualisation of inflammasomes were described in my previous publication [673]. For visualisation of NHE and cell membrane, BMDMs were stimulated with NHE component C_{WT} or $C_{mut.}$ or C+B for 1 hr, or C+B+A for 30 min, washed three times with PBS and fixed with 4% paraformaldehyde at room temperature for 15 min, followed by blocking in 1% BSA in PBS for 1 hr. Cells were incubated with a rabbit sera anti-NHE-C (1:200 dilution in 1% BSA) [565], a mouse anti-NHE-B, or -A (1:200 dilution in 1% BSA) [565], an mouse anti-Histidine antibody (1:200 dilution in 1% BSA, ab18184, Abcam), and a rat FITC-conjugated anti-CD11b antibody (1:200 dilution in 1% BSA, 101205, BioLegend) overnight at 4 °C. PBS containing 0.05% Tween-20 was used to wash between incubation steps. An anti-mouse secondary Rhodamine red antibody (115295146, Jackson ImmunoResearch) or rabbit secondary Rhodamine red antibody (111295144, Jackson ImmunoResearch) were used. The samples were mounted with VECTASHIELD® Hardset™ Mounting Medium with DAPI (H-1500, Vector Laboratories, Inc.) and analysed using a Leica SP5 confocal microscope.

4.3.11 Scanning Electron Microscopy

BMDMs were washed with PBS and post-fixed with 2.5% glutaraldehyde in 0.1 M phosphate buffer overnight and further washed with PBS. Cells were fixed in 1% osmium tetroxide in double distilled water for 1 hr and dehydrated in a series of alcohol. Dehydrated samples were dried using liquid carbon dioxide using critical point drying. Samples were then sputter-coated with platinum (3 nm thickness) at 15 mA for 2 min using the EMI TECH K550 Sputter coater and visualised under a Zeiss UltraPlus Field emission scanning electron microscope at 5 kV.

4.3.12 Transmission Electron Microscopy

BMDMs were washed with PBS and post-fixed with 2.5% glutaraldehyde in 0.1 M phosphate buffer overnight and further washed with PBS. Cells were fixed in 1% osmium tetroxide in double distilled water for 1 hr and dehydrated in a series of alcohol, and embedded in LR white

resin (C023, ProSciTech). Samples were polymerised in a 60 °C oven overnight. Thin sections were cut at 80 nm and viewed using a Hitachi HA7100 transmission electron microscope at 100 kV.

4.3.13 Cryo-Transmission Electron Microscopy

Liposomes left untreated or treated with recombinant NHE_{WT} or $NHE_{mut.}$ (30 nM) for 1 hr were applied on a holey carbon 400 mesh grid and left to adhere for 30 s. Grids were then blotted for 10 s to remove excess liposomes before plunge frozen using liquid ethane surrounded by a bath of liquid nitrogen. Samples were visualised under Hitachi 7100 TEM at 100 kv with a Cryo-TEM holder.

4.3.14 Separation of Membrane and Cytosolic Compartments

BMDMs were stimulated with the supernatant of Δ*hbl B. cereus* (50 µl), recombinant NHE_{WT} or $NHE_{mut.}$ (100 nM), and HBL-BWT or HBL-$B_{mut.}$ (5 nM) for 1 hr, washed three times with PBS followed by separation of membrane and cytosolic fractions using the Mem-PER Plus Membrane Protein Extraction Kit according to the manufacturer's instructions (89842, ThermoFisher Scientific).

4.3.15 Lactate Dehydrogenase Assay

Levels of lactate dehydrogenase released by cells were determined using the CytoTox 96 Non-Radioactive Cytotoxicity Assay according to the manufacturer's instructions (G1780, Promega).

4.3.16 IncuCyte and Cytotoxicity Analysis

To track viability, BMDMs or various cell types were stimulated with 0.5 µM NHE (high) or 100 nM NHE (low), LPS+ATP, or with 100nM NHE_{WT} or $NHE_{mut.}$, in presence of the SYTOX Green nuclear stain that penetrates compromised membranes (1 µM; S7020; Life Technologies). Cell death was monitored over 3 hr using the IncuCyte Zoom imaging system (Essen

Biosciences) or fluorescence was assessed using a Zeiss Axio Observer Fluorescent/Brightfield microscope.

4.3.17 Real Time PCR analysis

RNA was extracted from BMDMs using TRIzol (15596018, ThermoFisher Scientific). The isolated RNA was converted into cDNA using the High-Capacity cDNA Reverse Transcription Kit (4368813, ThermoFisher Scientific). RT-PCR was performed on an ABI StepOnePlus System PCR instrument with SYBR Green Real-Time PCR Master Mixes (4364346, ThermoFisher Scientific). Primer sequences can be found in Supplementary Table 2.

4.3.18 Cytokine Analysis

Cytokine concentrations from BMDMs were calculated using a multiplex ELISA (MCYTOMAG-70K, EMD Millipore) or IL-18 ELISA (BMS618-3TEN, ThermoFisher Scientific) according to the manufacturers' instructions. Cytokine levels from THP-1 cells were calculated using a human IL-1β ELISA (BMS224-2TEN, ThermoFisher Scientific) or human IL-18 ELISA (BMS267-2TEN, ThermoFisher Scientific) according to the manufacturer's instructions.

4.3.19 ICP-OES analysis

The intracellular concentrations of K^+ and Na^+ ions were determined by inductively coupled plasma-optical emission spectroscopy (ICP-OES) analysis. BMDMs were stimulated with recombinant WT or mutant NHE for 2 hr, washed three times with PBS followed by lysis with concentrated nitric acid (HNO_3). The cell lysates were analysed for K^+ and Na^+ ions performed through ICP-OES using a PerkinElmer OPTIMA 7300 ICP Optical Emission Spectrometer (PerkinElmer).

4.3.20 Animal Infection

To investigate the role of NHE in inflammasome activation in vivo, WT mice were injected intraperitoneally with 200 µl of supernatant of WT or Δ*hbl B. cereus* which had been treated with either isotype control, anti-HBL neutralising antibodies, anti-NHE neutralising antibodies or both anti-HBL neutralising antibodies and anti-NHE neutralising antibodies. To investigate contributions from the NLRP3 inflammasome, mice were injected, via an i.p. route, with 5×10^6 colony forming units (CFUs) of culture of Δ*hbl B. cereus*. To investigate the effects of MCC950 [213-215], mice were intraperitoneally injected with 50 mg per kg of MCC950 dissolved in PBS or with an equal amount of the vehicle control PBS. One hour later, mice were intraperitoneally injected with 5×10^6 CFU of Δ*hbl B. cereus* along with a second dose of 50 mg per kg of MCC950 or a second dose of PBS. For cytokine measurement serum and peritoneal fluid were collected after 1-16 hr for analysis by ELISA.

4.4 Results

4.4.1 A non-redundant factor of *B. cereus* activates the inflammasome independently of HBL

I have previously demonstrated that innate immune recognition of *Bacillus cereus* infection requires inflammasome-mediated sensing of a toxin known as HBL [673]. Stimulation of primary wild-type (WT) bone-marrow-derived macrophages (BMDMs) with the supernatant of WT *B. cereus* led to activation of caspase-1, cleavage of gasdermin D, secretion of IL-1β and IL-18, and pyroptosis within 3 hr, whereas stimulation of WT BMDMs with the supernatant of an isogenic mutant of *B. cereus* lacking HBL (Δ*hbl B. cereus*) did not (**Fig. 4.1a**), consistent with my previous findings [673]. Surprisingly, WT BMDMs treated overnight with the supernatant of Δ*hbl B. cereus* underwent robust activation of caspase-1, cleavage of gasdermin D, secretion of IL-1β and IL-18, and induction of cell death (**Fig. 4.1a;** top panel). Similarly, live Δ*hbl B. cereus* bacteria also induced activation of the inflammasome in WT BMDMs following overnight stimulation (**Fig. 4.1a;** bottom panel). Furthermore, the unknown factor activated the inflammasome after 6h of incubation with the supernatant of Δ*hbl B. cereus* by inducing activation of caspase-1, secretion of IL-1β and IL-18, and induction of cell death (**Appendices for Chapter 4 Fig. 4.2a,b**). These findings suggest that an additional non-redundant secreted factor of *B. cereus* might be sensed by the inflammasome.

To elucidate the identity of the inflammasome sensor responsible for the recognition of the secreted factor, LPS-primed primary WT, *Nlrp3*$^{-/-}$, *Nlrc4*$^{-/-}$, *Aim2*$^{-/-}$, *Asc*$^{-/-}$, *Casp1/11*$^{-/-}$, and *Casp11*$^{-/-}$ BMDMs were stimulated with the supernatant of Δ*hbl B. cereus*. The supernatant of Δ*hbl B. cereus* induced caspase-1 activation, cleavage of gasdermin D, secretion of IL-1β and IL-18, and cell death in WT, *Nlrc4*$^{-/-}$, *Aim2*$^{-/-}$, and *Casp11*$^{-/-}$ BMDMs (**Fig. 4.1b–d**). In contrast, the supernatant of Δ*hbl B. cereus* did not induce activation of the inflammasome and cell death in *Nlrp3*$^{-/-}$ and *Asc*$^{-/-}$ BMDMs (**Fig. 4.1b–d**), indicating that NLRP3 is the cytosolic sensor of the secreted factor of *B. cereus*. Consistent with the results obtained using cell-free

supernatant, live Δ*hbl B. cereus* bacteria activated the NLRP3 inflammasome at this later time point (**Fig. 4.1b,c and Appendices for Chapter 4 Fig. 4.1a**). Further, pharmacological inhibition of NLRP3 using the small molecule inhibitor MCC950 [213-215] abrogated caspase-1 activation, secretion of IL-1β and IL-18, and cell death in WT BMDMs stimulated with the supernatant or live bacteria of Δ*hbl B. cereus* (**Appendices for Chapter 4 Fig. 4.1f**).

It was further confirmed that assembly of the inflammasome complex, which can be visualised by immunostaining of the ASC speck [27], occurred in WT BMDMs treated with the supernatant from either WT *B. cereus* or Δ*hbl B. cereus* or infected with either WT *B. cereus* or Δ*hbl B. cereus* (**Fig. 4.1e and Appendices for Chapter 4 Fig. 4.1e**). Indeed, *Nlrp3*$^{-/-}$ BMDMs had an impaired ability to generate ASC specks in response to either strain of *B. cereus* (**Fig. 4.1e and Appendices for Chapter 4 Fig. 4.1e**).

The gene and protein expression analysis of pro-inflammatory cytokines tumour-necrosis factor (TNF) (**Fig. 4.1c**), keratinocyte chemoattractant (KC, also known as CXCL1) and pro-IL-1β, and the phosphorylation status of IκB and ERK between WT and *Nlrp3*$^{-/-}$ BMDMs following stimulation by the supernatant or live bacteria of Δ*hbl B. cereus* were similar (**Appendices for Chapter 4 Fig. 4.1b–d**). These data confirm that the production of inflammasome-independent cytokines was not affected by the genetic deletion of NLRP3, and that the unknown secreted factor did not affect priming of the inflammasome. Collectively, these data suggest that a putative secreted factor of *B. cereus* activates the NLRP3 inflammasome.

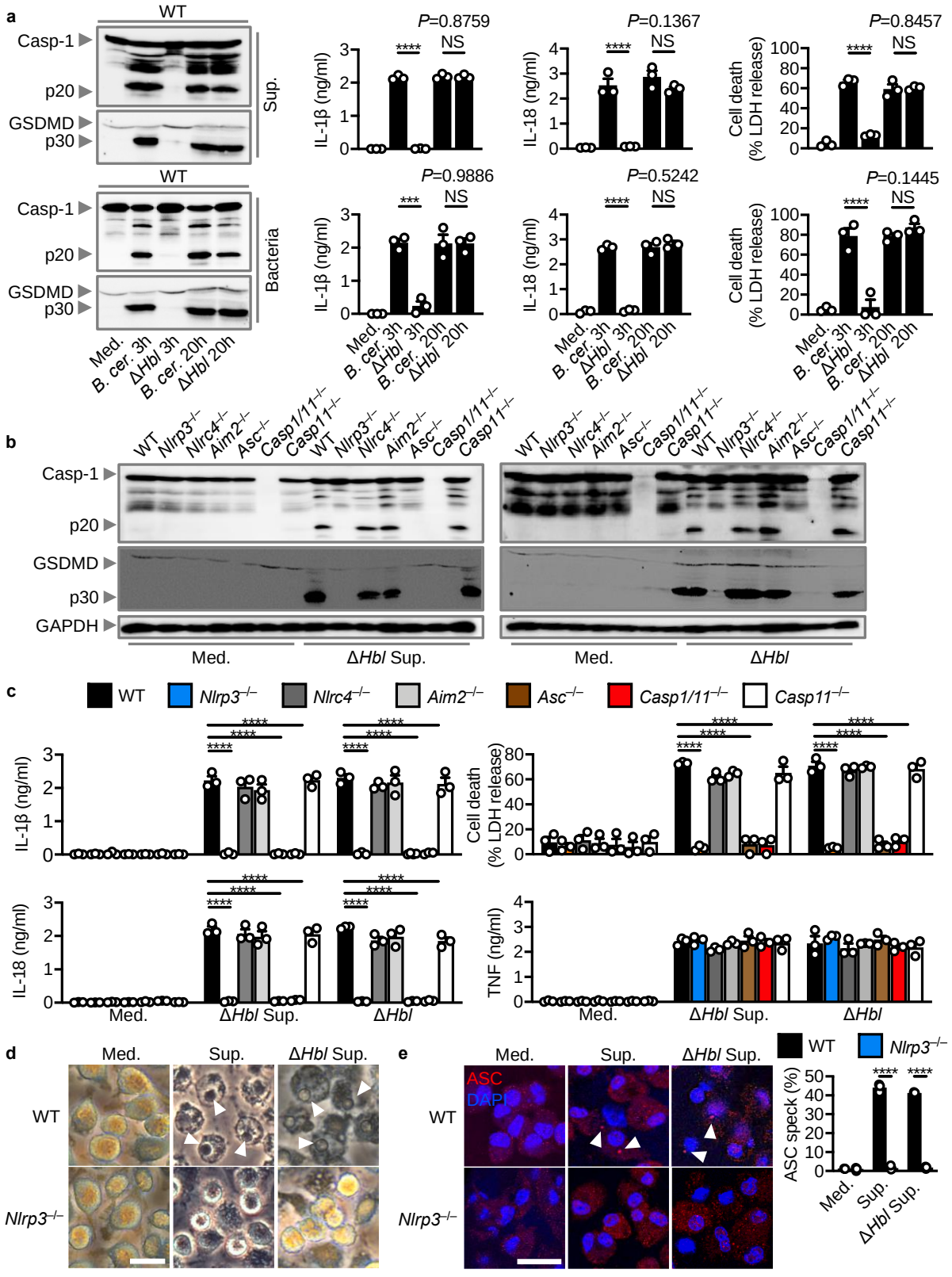

Figure 4.1 | A non-redundant secreted factor of *B. cereus* activates the NLRP3 inflammasome independently of HBL. (**a**) Immunoblot analysis of pro-caspase-1 (Casp-1), the active caspase-1 p20 subunit, pro-pyroptotic effector protein gasdermin D (GSDMD), the

active GSDMD p30 subunit and release of IL-1β and IL-18 and death of WT BMDMs left untreated [Medium alone (Med.)] or LPS-primed and assessed either 3 hr or 20 hr after stimulation with the supernatant of WT *B. cereus* (*B. cer.*) or Δ*hbl B. cereus* (Δ*hbl*) (top; Sup.) or infection with *B. cer.* or Δ*hbl* (bottom; MOI of 5). (**b**) Immunoblot analysis of caspase-1, gasdermin D and GAPDH (loading control) in WT or mutant BMDMs left untreated or LPS-primed and assessed 20 hr after stimulation with Δ*hbl* supernatant, or after infection with Δ*hbl* (MOI of 5). (**c**) Release of IL-1β, IL-18 and TNF and death of BMDMs after treatment as in (b). (**d**) Brightfield microscopy analysis of BMDMs 8 hr after stimulation as in (b). (**e**) Immunofluorescent analysis of ASC speck formation (red) in BMDMs after treatment as in (b). Quantification of the prevalence of ASC specks is shown on the right as a percentage of total cells (DAPI). At least 200 cells from each genotype were assessed. Scale bar, 25 μm (d, e). Arrowheads indicate pyroptotic cells (d) or ASC specks (e). NS, not significant, *** $P<0.001$ and **** $P<0.0001$ (one-way analysis of variance [ANOVA] with Dunnett's multiple-comparisons test (c) or student's unpaired *t*-test (a, e). Each symbol represents an independent experiment (a, c and e). Data are representative of three independent experiments (a-e; mean and s.e.m. in a, c and e).

4.4.2 The inflammasome-activating secreted factor is a heat-sensitive protein of 30-50 kDa in size

To decipher the biological identity of the putative secreted inflammasome-activating factor, WT BMDMs were stimulated overnight with the supernatant of Δ*hbl B. cereus* which had been heat-treated or treated with proteinase K, DNase, or RNase. It was found that the supernatant heated to 50 °C, but not 75 °C and 100 °C, retained its ability to induce cleavage of caspase-1 and gasdermin D, secretion of IL-1β and IL-18, and cell death in WT BMDMs (**Fig. 4.2a**). Further, the supernatant treated with proteinase K did not lead to activation of caspase-1, cleavage of gasdermin D, secretion of IL-1β and IL-18, and cell death in WT BMDMs, whereas

treatment of DNase or RNase did not affect the ability of the supernatant to induce inflammasome responses (**Fig. 4.2b**). To deduce the molecular size of the secreted factor, filter-mediated size-fractionation techniques was used to separate the supernatant of Δ*hbl B. cereus* into different molecular-sized fractions. It was found that the supernatant fractions of >9 kDa, >30 kDa and <50 kDa, but not fractions of <9 kDa, <30 kDa and >50 kDa, potentiated activation of the inflammasome (**Fig. 4.2c**). These findings indicate that a heat-labile proteinaceous factor of 30-50 kDa secreted by *B. cereus* is a potent activator of the inflammasome.

4.4.3 NHE is a non-redundant toxin driving the activation of the NLRP3 inflammasome

I previously excluded a contribution from Non-Haemolytic Enterotoxin (NHE) in driving the early inflammasome response owing to a role for HBL [673]. However, toxins have different kinetics and assembly processes which determine their activity [633]. Therefore, I reasoned that NHE could have been overlooked as a potential candidate [506]. This idea is supported by my finding that another 30-50 kDa secreted factor is acting in a non-redundant manner in the activation of the NLRP3 inflammasome during *B. cereus* infection (**Fig. 4.2c**), and that NHE is comprised of three subunits, called A, B and C, all of which are of 30-50 kDa in size [508-510,675].

To this end, the supernatant of WT *B. cereus* was neutralised with antibodies against NHE and/or HBL and stimulated WT BMDMs with the supernatant overnight. It was found that neutralisation of both NHE and HBL, but not NHE or HBL alone, abolished the ability of the supernatant to induce activation of caspase-1, cleavage of gasdermin D, secretion of IL-1β and IL-18, and pyroptosis in WT BMDMs (**Fig. 4.2d**). Further, neutralisation of NHE abrogated the ability of the supernatant of Δ*hbl B. cereus* to induce activation of caspase-1, cleavage of gasdermin D, secretion of IL-1β and IL-18, and pyroptosis in WT BMDMs (**Fig. 4.2e**), Conversely, neutralisation of HBL abolished the ability of Δ*nhe B. cereus* to elicit

inflammasome responses in WT BMDMs (**Fig. 4.2e**). Neutralisation of the supernatant with antibodies against either or both NHE and HBL did not affect the secretion of TNF and KC in BMDMs (**Fig. 4.2d,e and Appendices for Chapter 4 Fig. 4.1g,h**), suggesting that secretion of inflammasome-independent cytokines was not compromised in response to supernatant treated with neutralising antibodies. To dissect the kinetics between HBL and NHE toxins we utilised antibody mediated neutralisation of the two toxins in the supernatant of *B. cereus* from various strains namely, ATCC 14579, ATCC 10876, and F837/76. It was found that with neutralisation of HBL, NHE was found to be associated with inflammasome activation after 6h of stimulation whereas HBL activated in 3h (**Appendices for Chapter 4 Fig. 4.2c–e**). These data revealed that, in addition to blockade of HBL, abrogation of NHE by means of neutralisation or genetic deletion prevented cytosolic inflammasome sensing of *B. cereus* infection.

To investigate further, three recombinant subunits which comprise NHE: subunit A (41 kDa), subunit B (40 kDa), and subunit C (37 kDa) were expressed [508]. Treatment with recombinant NHE resulted in robust activation of inflammasome responses in LPS-primed WT BMDMs but not in LPS-primed *Nlrp3*$^{-/-}$ BMDMs (**Fig. 4.3a**). Importantly, treatment of LPS-primed WT and *Casp11*$^{-/-}$ BMDMs with NHE resulted in inflammasome activation (**Appendices for Chapter 4 Fig. 4.3a**), indicating that NHE-induced inflammasome responses were not due to NHE-mediated translocation of extracellular LPS into the cytoplasm to activate the caspase-11-NLRP3 pathway. Further, NHE induced ASC speck formation in WT BMDMs but not in *Nlrp3*$^{-/-}$ BMDMs, whereas dsDNA poly(dA:dT) induced ASC speck formation in both WT and *Nlrp3*$^{-/-}$ BMDMs (**Fig. 4.3b**). In addition, it was observed that in response to NHE, BMDMs lacking the full pore-forming ability of the pyroptotic factor gasdermin D (*Gsdmd*$^{I105N/I105N}$) [574,661,662] had an impaired ability to secrete IL-1β and IL-18 and undergo cell death at 1 and 2 hr, compared with WT BMDMs (**Appendices for Chapter 4 Fig. 4.3c,d**). Electron microscopy analyses revealed that stimulation with NHE led to a disruption of cellular morphology and architecture in BMDMs **(Fig. 4.3c and Appendices for Chapter 4 Fig. 4.3e**). Further, it was found that

NHE induced secretion of IL-1β and IL-18 and led to cell death in human THP-1 monocytes, and that this response was impaired following inhibition of NLRP3 by MCC950 (**Appendices for Chapter 4 Fig. 4.3f**). These findings highlight that NHE is a non-redundant toxin driving activation of the NLRP3 inflammasome during *B. cereus* infection, and that innate immune recognition of NHE by the NLRP3 inflammasome is functionally conserved between mice and humans.

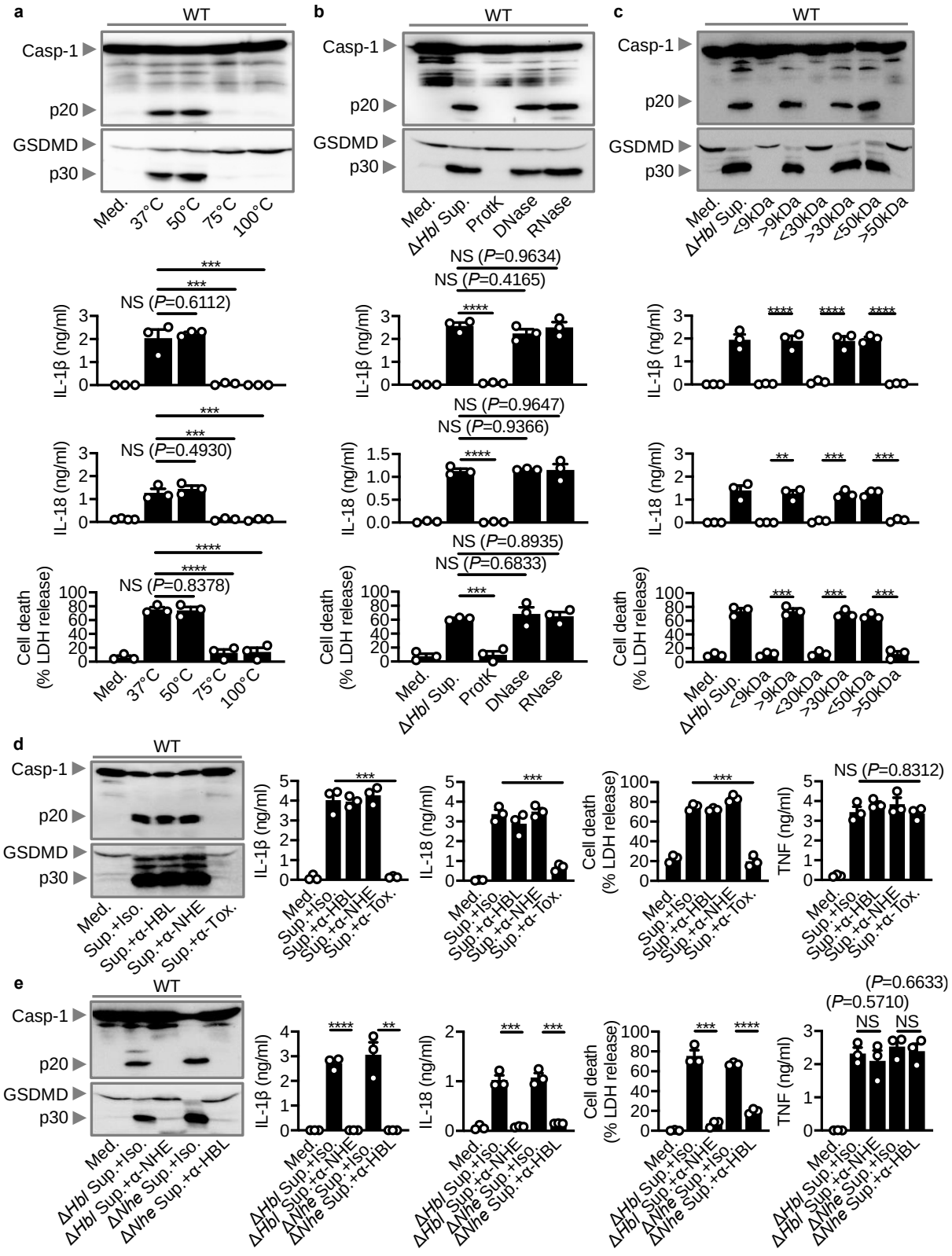

Figure 4.2 | NHE is an activator of the NLRP3 inflammasome. (**a**) Immunoblot analysis of caspase-1 and gasdermin D, release of IL-1β and IL-18, and death of BMDMs left untreated (Med.) or LPS-primed and assessed 20 hr after treatment with the supernatant of Δ*hbl* (Δ*hbl*

Sup.) which had been treated with the indicated temperatures; (**b**) Immunoblot analysis of caspase-1 and gasdermin D, release of IL-1β and IL-18, and death of BMDMs left untreated or LPS-primed and assessed 20 hr after treatment with the supernatant of Δ*hbl* which had been treated with proteinase K (ProtK), DNase or RNase; (**c**) Immunoblot analysis of caspase-1 and gasdermin D, release of IL-1β and IL-18, and death of BMDMs left untreated or LPS-primed and assessed 20 hr after treatment with the size-fractionated supernatant of Δ*hbl*. (**d**) Immunoblot analysis of caspase-1 and gasdermin D, release of IL-1β, IL-18 and TNF, and death of BMDMs left untreated or LPS-primed and assessed 20 hr after treatment with the supernatant of WT *B. cereus* (Sup.) treated with an isotype control (Iso.), anti-HBL neutralising antibodies (α-HBL), anti-NHE neutralising antibodies (α-NHE) or with both anti-HBL and anti-NHE neutralising antibodies (α-Tox.). (**e**) Immunoblot analysis of caspase-1 and gasdermin D, release of IL-1β, IL-18 and TNF, and death of BMDMs left untreated or LPS-primed and assessed 20 hr after treatment with the supernatant of Δ*hbl* treated with an isotype control or anti-NHE neutralising antibodies or assessed 20 hr after treatment with the supernatant of Δ*nhe B. cereus* (Δ*nhe* Sup.) treated with an isotype control or anti-HBL neutralising antibodies. NS, not significant, ** $P<0.01$, *** $P<0.001$ and **** $P<0.0001$ (one-way analysis of variance [ANOVA] with Dunnett's multiple-comparisons test (a, b and d) or student's unpaired *t*-test (c, e). Each symbol represents an independent experiment (a-e). Data are representative of three independent experiments (a-e; mean and s.e.m. in a-e).

4.4.4 A specified order of assembly by NHE subunits on the plasma membrane is essential

The tripartite composition of NHE suggests that an important assembly process must occur in order to exert the full activity of this toxin. Indeed, neither the individual components of NHE nor all possible combinations of two of the three components of NHE trigger activation of the NLRP3 inflammasome (**Fig. 4. 3a** and **3d**), suggesting that all the three subunits of NHE are

essential in eliciting activation of the NLRP3 inflammasome. An earlier study reported that the B subunit is the binding component of the NHE complex on Vero cells [509]. A later study found that both the B and C subunits can bind to Vero cells, whereas the A subunit exerts cytotoxic effects in these cells [510]. A further study revealed that the C subunit initiates binding on Chinese Hamster Ovary cells [508].

To investigate whether a specified order of assembly of NHE components leads to activation of the NLRP3 inflammasome in BMDMs, WT BMDMs were stimulated either with A, B or C for 30 min, followed by extensive washing to remove unbound subunits prior to addition of the remaining subunits. It was observed that C→A+B (where the arrow symbol indicates a washing step and the plus symbol indicates 'added in concert') induced activation of caspase-1, secretion of IL-1β and IL-18, and pyroptosis (**Fig. 4.3e**). The order of A→B+C or B→A+C did not trigger inflammasome responses (**Fig. 4.3e**). These data suggest that C is the apical binding subunit. To elucidate the precise order of subunit assembly leading to inflammasome activation, the WT BMDMs were treated with individual components in the order of C→A→B or C→B→A. It was identified that the order of C→B→A led to activation of caspase-1, secretion of IL-1β and IL-18, and pyroptosis (**Fig. 4.3f**). These findings demonstrate that individual subunits of NHE follow a specific and linear order of NHE complex assembly to induce effective engagement of the NLRP3 inflammasome.

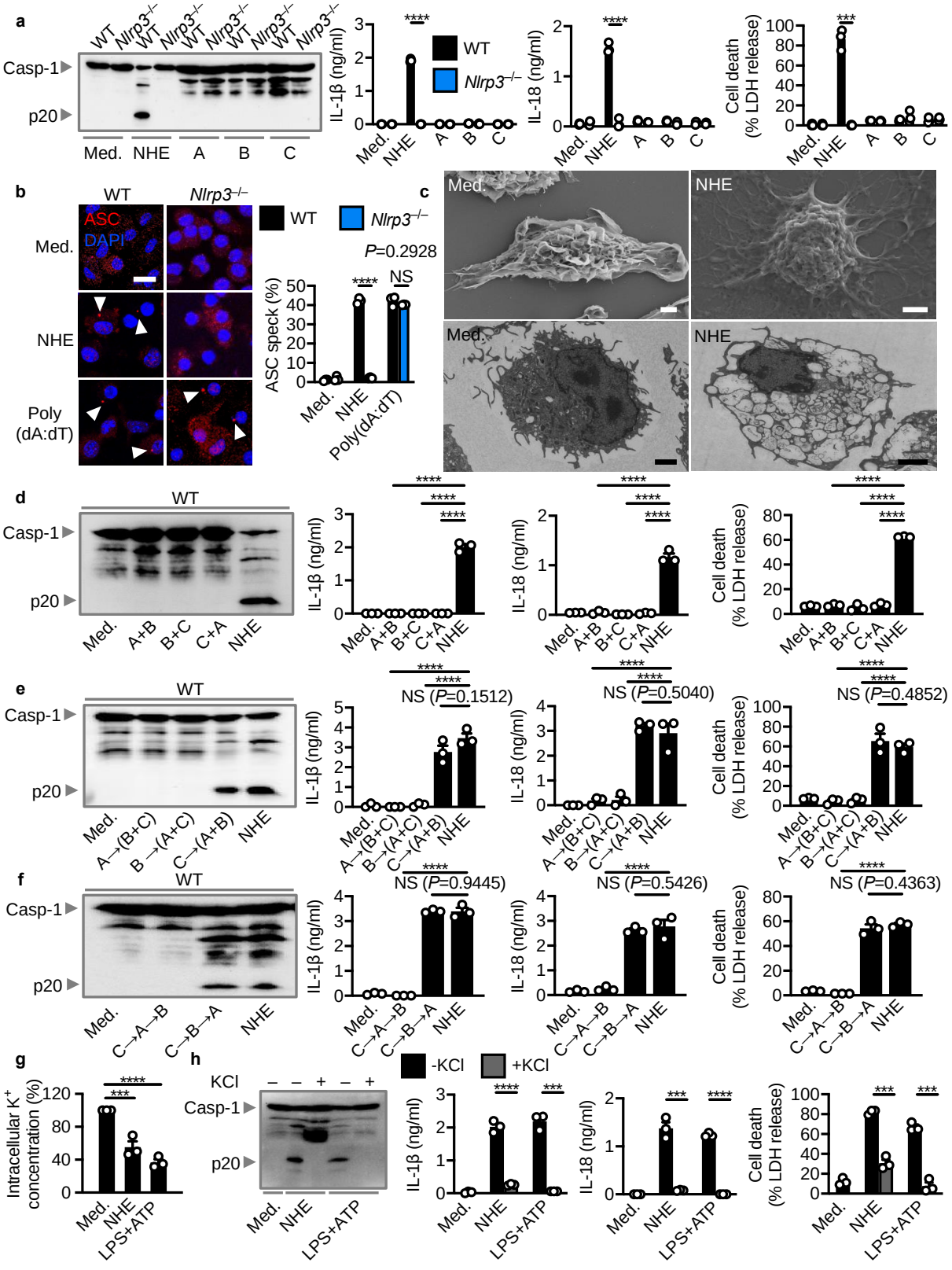

Figure 4.3 | NHE assembles in a linear order to induce K^+ efflux and trigger activation of the NLRP3 inflammasome. (**a**) Immunoblot analysis of caspase-1, release of IL-1β and IL-18, and death of WT or *Nlrp3*$^{-/-}$ BMDMs left untreated (Med.) or LPS-primed and assessed

3 hr after treatment with recombinant NHE, or with the individual NHE subunits A, B or C. (**b**) Immunofluorescent analysis of ASC speck formation (red) in WT or *Nlrp3*$^{-/-}$ BMDMs left untreated or LPS-primed and assessed 3 hr after stimulation with NHE or 5 hr after transfection with poly(dA:dT). Quantification of the prevalence of ASC specks as a percentage of total cells (DAPI). At least 200 cells from each genotype were assessed. Arrowheads indicate ASC specks. (**c**) Scanning electron microscopy analysis (top) or transmission electron microscopy analysis (bottom) of WT BMDMs left untreated or LPS-primed and assessed 3 hr after treatment with NHE. (**d**) Immunoblot analysis of caspase-1, release of IL-1β and IL-18, and death of WT BMDMs left untreated or LPS-primed and assessed 3 hr after treatment with binary combinations of NHE, or after treatment with tripartite NHE. (**e**) Immunoblot analysis of caspase-1, release of IL-1β and IL-18, and death of WT BMDMs left untreated or LPS-primed and assessed 3 hr after treatment with A→(B+C), B→(A+C) or C→(A+B) or after treatment with tripartite NHE; where "→" indicates 3 wash steps and "+" indicates addition of subunits in concert. (**f**) Immunoblot analysis of caspase-1, release of IL-1β and IL-18, and death of WT BMDMs left untreated or LPS-primed and assessed 3 hr after treatment with C→A→B or C→B→A or after treatment with tripartite NHE; where "→" indicates 3 wash steps. (**g**) Inductively coupled plasma-optical emission spectrometry analysis of intracellular concentrations of K^+ of BMDMs left untreated or assessed 2 hr after treatment with NHE, or 30 mins after treatment with LPS+ATP. (**h**) Immunoblot analysis of caspase-1, release of IL-1β and IL-18, and death of WT BMDMs left untreated or LPS-primed and assessed 3 hr after treatment with NHE, or 30 mins after treatment with LPS+ATP, in the absence (-) or presence (+; 50 mM) of extracellular KCl. Scale bar, 12 μm (b), 2 μm (c). NS, not significant, *** P<0.001 and **** P<0.0001 (one-way analysis of variance [ANOVA] with Dunnett's multiple-comparisons test (d-g) or student's unpaired *t*-test (a, b and h). Each symbol represents an independent experiment (a, d, e, f, g and h). Data are representative of three independent experiments (a-h; mean and s.e.m. in a, b, d, e, f, g and h).

4.4.5 NHE induces K^+ efflux from the plasma membrane to activate NLRP3

To assess whether NHE is maintained on the plasma membrane leading to activation of the NLRP3 inflammasome, WT BMDMs were treated with NHE and performed immunofluorescence staining using antibodies against individual subunits of NHE. Immunofluorescence staining techniques revealed that all three subunits of NHE co-localised with the cell-surface marker CD11b of BMDMs, suggesting that NHE localises on the plasma membrane (**Appendices for Chapter 4 Fig. 4.4a–c**). Further, the cell-membrane and cytosolic fractions were separated from BMDMs stimulated with the supernatant of Δ*hbl B. cereus* and found all three subunits of NHE in the membrane fraction (**Appendices for Chapter 4 Fig. 4.4d**). In addition, inhibition of phagocytosis using the inhibitor cytochalasin B or cytochalasin D did not impede the ability of NHE, the supernatant of Δ*hbl B. cereus*, or live Δ*hbl B. cereus* to induce activation of the inflammasome in WT BMDMs (**Appendices for Chapter 4 Fig. 4.5a–d**). These results indicate that internalisation of NHE into BMDMs is not required to drive inflammasome activation. Indeed, transfection of NHE subunits into WT BMDMs did not trigger inflammasome activation, whereas transfection of flagellin triggered activation of the inflammasome (**Appendices for Chapter 4 Fig. 4.5e,f**). These data suggest that localisation of NHE on the plasma membrane is sufficient to induce activation of the inflammasome.

The localisation of NHE implies that the mechanism driving activation of the NLRP3 inflammasome might emanate from the plasma membrane. NLRP3 is activated by membrane-induced cellular perturbations via pathways dependent on K^+ efflux or independent of K^+ efflux [133,140,664,665,676]. To investigate the role of K^+ efflux in NHE-induced activation of the inflammasome, Inductively Coupled Plasma-Optical Emission Spectrometry (ICP-OES) was used to measure the cytosolic concentration of K^+ in WT BMDMs stimulated with NHE. The level of cytosolic concentration of K^+ in BMDMs treated with NHE decreased substantially compared with untreated BMDMs, a reduction which is similar to that seen in BMDMs treated

with the classical NLRP3 activator LPS+ATP (**Fig. 4.3g**). To confirm this observation, KCl was added into the cell culture media prior to addition of NHE. It was observed that addition of extracellular K^+ inhibited activation of the inflammasome in response to NHE, the supernatant of Δ*hbl B. cereus*, Δ*hbl B. cereus*, or LPS+ATP (**Fig. 4.3h and Appendices for Chapter 4 Fig. 4.6a,b**). Further, no difference in the cytosolic concentration of Na^+ was observed in BMDMs treated with NHE or LPS+ATP compared with untreated BMDMs, and that addition of extracellular Na^+ did not inhibit activation of the inflammasome in response to NHE or LPS+ATP (**Appendices for Chapter 4 Fig. 4.6c–e**). These data suggest that localisation of NHE on the plasma membrane is sufficient to induce activation of the inflammasome via efflux of K^+.

4.4.6 NHE induces pore formation in the lipid bilayer of mammalian plasma membranes and causes cytotoxicity in multiple cell types

Given that NHE subunits localises on the mammalian plasma membrane and induce K^+ efflux, I hypothesised that NHE might be able to create a membrane pore, destabilising the plasma membrane of BMDMs. To test this possibility, liposomes composed of the lipid species DPPC, DSPC and DOPC and cholesterol were synthesised, which mimic the mammalian plasma membrane [581]. These liposomes contain an internal aqueous methylene blue dye, which when released can be captured by dye-capturing resins (**Fig. 4.4a**). Addition of NHE, but not individual components of NHE, heat-inactivated NHE, or bovine serum albumin resulted in the release of dye from the liposomes (**Fig. 4.4b,c**). The level of dye leakage induced by NHE was similar to that of HBL or sonication of the liposomes (**Fig. 4.4b,c**). Further, incubation of NHE with liposomes inhibited the ability of NHE to induce inflammasome responses in BMDMs (**Fig. 4.4d**), suggesting potential sequestration of NHE on the membrane of the liposome.

Under Cryo-transmission electron microscopy (Cryo-TEM), I observed distinct pores in the membrane of liposomes treated with NHE (**Fig. 4.4e**). The ability of NHE to insert into the membrane suggests that this toxin could kill different cell types from different host species. To this end, immune and non-immune cells were treated with NHE and found that NHE induced cell death in all cell types tested, including those from humans, mice, monkeys and dogs (**Fig. 4.4f,g**). To further explore the dynamics of NHE-induced cell death, BMDMs were treated with NHE and examined cell viability kinetics using IncuCyte assays. A lower concentration of 100 nM NHE induced activation of caspase-1, cleavage of gasdermin D and pro-IL-1β, secretion of IL-1β and IL-18, and cell death in WT BMDMs, but not in *Nlrp3*$^{-/-}$ BMDMs (**Appendices for Chapter 4 Fig. 4.7a–c**). However, a higher concentration of 500 nM NHE induced rapid cell death in both WT and *Nlrp3*$^{-/-}$ BMDMs within 20 min but was unable to induce inflammasome responses (**Appendices for Chapter 4 Fig. 4.7a–c**). Accumulation of NHE pores on the plasma membrane of BMDMs would mediate membrane rupture independently of the inflammasome, which provides an explanation for the mechanism of cell death in cell types which do not express inflammasome components (**Fig. 4.4f,g**). Taken together, these findings indicate that NHE induces pore formation in the cell membrane and can induce cytotoxic effects across multiple cell types and host species dictated by the bioavailability of the toxin.

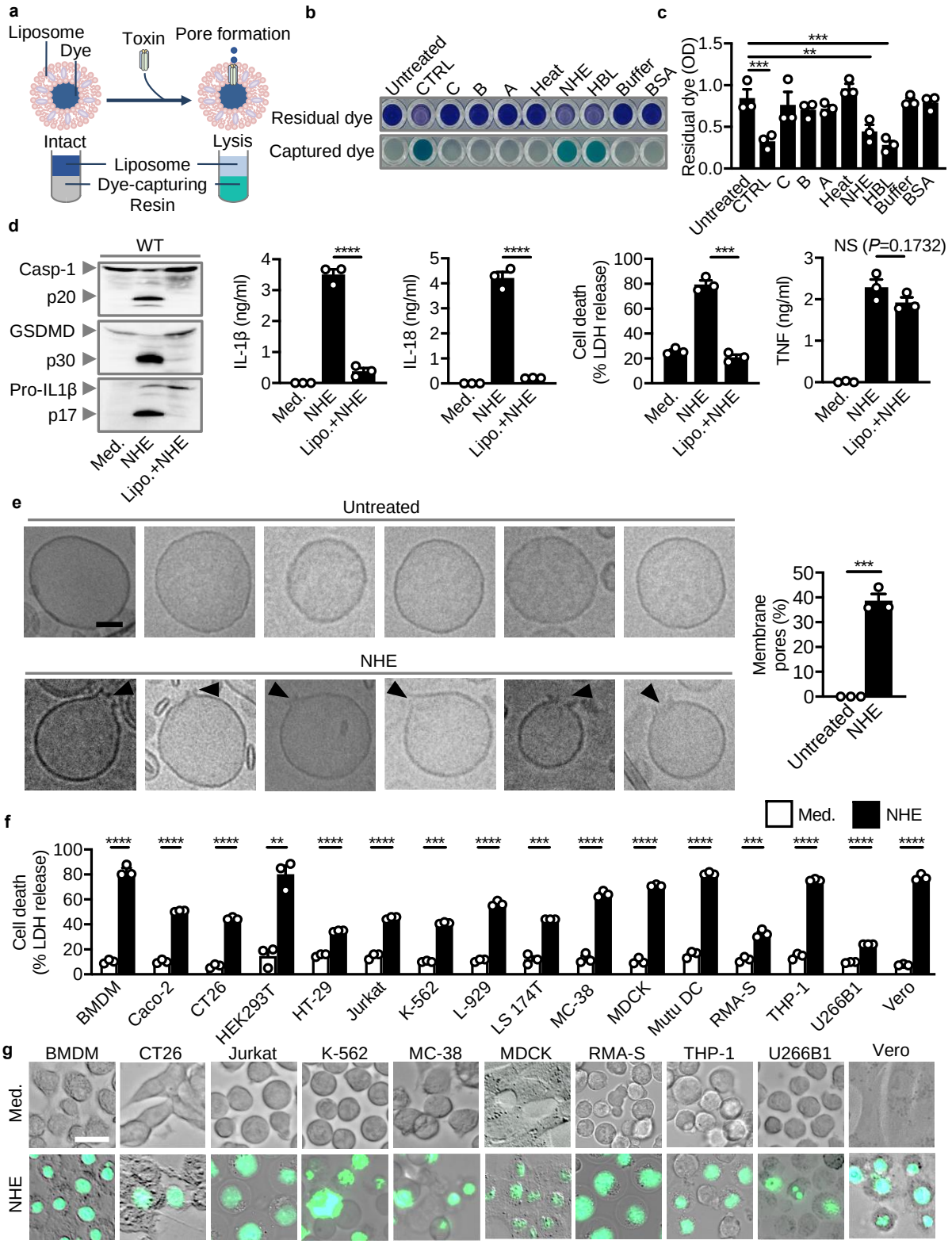

Figure 4.4 | NHE forms pores in the cell membrane and elicits cytotoxicity in multiple cell types. (**a**) Schematic of toxin-induced liposomal rupture and leakage of dye. (**b**) Colorimetric analysis of liposomes left untreated, sonicated for 5 mins at 100 amplitude

(CTRL) or assessed 30 mins after treatment with individual NHE subunits (C, B, or A), heat-inactivated NHE (Heat), NHE, HBL, buffer or BSA. (**c**) The absorbance (OD) of residual dye following treatment as in (b). (**d**) Immunoblot analysis of caspase-1, gasdermin D and IL-1β, release of IL-1β, IL-18 and TNF, and death of WT BMDMs left untreated or LPS-primed and assessed 3 hr after treatment with NHE in the absence or presence of liposomes (Lipo.). (**e**) Cryo-transmission electron microscopy analysis of liposomes left untreated or assessed 1 hr after treatment with NHE (left). Quantification of membrane pores of liposomes (right). (**f**) Death of various cell types left untreated or assessed 3 hr after treatment with NHE. (**g**) Brightfield and fluorescent (SYTOX) images of cell lines left untreated or assessed 3 hr after treatment with NHE. Arrowheads indicate pores (e). Green indicates dead cells (g). Scale bar, 50 nm (e), 20 μm (g). Each symbol represents an independent experiment (c-f). NS, not significant, ** P<0.01, *** P<0.001 and **** P<0.0001 (one-way analysis of variance [ANOVA] with Dunnett's multiple-comparisons test [c] or student's unpaired *t*-test [d, f]). Data are representative of three independent experiments (b-g; mean and s.e.m. in c-f).

4.4.8 The putative transmembrane region of the C subunit is essential for membrane binding, pore formation and inflammasome activation

My data suggested that NHE is localised to the plasma membrane of macrophages and that the C subunit of NHE is the apical subunit binding the plasma membrane. Bioinformatic analysis of the protein sequence of the C subunit of NHE revealed the presence of a putative transmembrane region between amino acid positions 228 and 250 (**Appendices for Chapter 4 Fig. 4.8a,b**), consistent with previous studies [514,518]. I hypothesised that deletion of the putative transmembrane region in this subunit would abolish the ability of NHE to bind the plasma membrane and induce activation of the inflammasome. To address this hypothesis, I expressed the C subunit with and without the putative transmembrane region (**Appendices for Chapter 4 Fig. 4.8c**). Next, WT BMDMs were treated with WT NHE (designated as NHE_{WT},

carrying all the three WT subunits) or mutant NHE (designated as $NHE_{mut.}$, where the WT C subunit is replaced with the mutant C subunit). It was found that NHE_{WT} induced K^+ efflux, activation of caspase-1, secretion of IL-1β and IL-18, and pyroptosis, whereas $NHE_{mut.}$ did not (**Fig. 4.5a,b**). This observation was not due to differences in secondary structures between the WT C subunit and mutant C subunit as shown by circular dichroism analysis (**Fig. 4.5c**). Further, IncuCyte, scanning electron microscopy and transmission electron microscopy analyses collectively revealed that BMDMs treated with NHE_{WT}, but not $NHE_{mut.}$, underwent cell death (**Fig. 4.5d,e and Appendices for Chapter 4 Fig. 4.9a,b**).

To assess the membrane-binding ability of the mutant C subunit, WT BMDMs were treated either with NHE_{WT} or $NHE_{mut.}$ followed by fractionation of the membrane and cytosolic compartments. All the three subunits of NHE were found in the membrane fraction of BMDMs treated with NHE_{WT}, whereas none of the NHE subunits were detected in the membrane fraction of BMDMs treated with $NHE_{mut.}$ (**Fig. 4.5f**). Confocal microscopy techniques revealed that while the WT C subunit co-localised with CD11b on the plasma membrane, the mutant C subunit was unable to do so (**Fig. 4.5g**). Furthermore, liposomes treated with NHE_{WT} underwent leakage of the dye, whereas liposomes treated with $NHE_{mut.}$ did not (**Fig. 4.5h**). Cryo-TEM analysis confirmed that liposomes treated with NHE_{WT} had membrane pores, whereas liposomes treated with $NHE_{mut.}$ were largely intact (**Fig. 4.5i**). Like NHE-C, the apical binding subunit of HBL, HBL-B, also carries a corresponding putative transmembrane region [513,673]. Importantly, deletion of the putative transmembrane region of HBL-B did not affect the secondary structure or the ability of this subunit to bind to the cell membrane of BMDMs (**Appendices for Chapter 4 Fig. 4.10a–d**), suggesting a functional divergence of these putative transmembrane regions between the two toxins. These data collectively suggest that the putative transmembrane region of the C subunit of NHE might be important in mediating membrane binding and pore formation, leading to activation of the inflammasome.

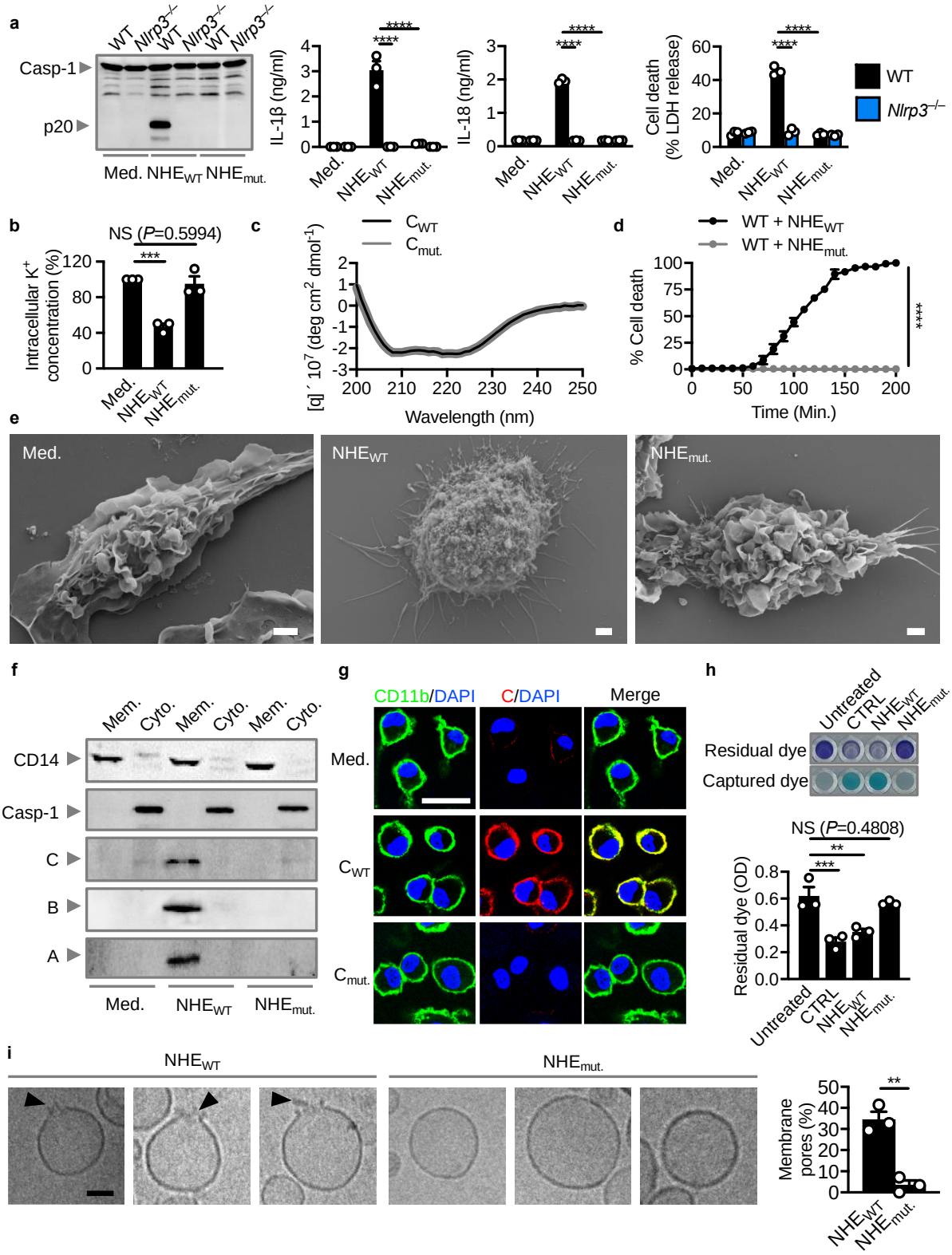

Figure 4.5 | A putative transmembrane domain in the C subunit of NHE is essential for membrane binding, activation of the NLRP3 inflammasome and pore formation.

(**a**) Immunoblot analysis of caspase-1, release of IL-1β and IL-18, and death of WT or *Nlrp3*$^{-/-}$ BMDMs left untreated (Med.) or LPS-primed and assessed 3 hr after treatment with C+B+A (NHE_{WT}) or C_{mut}+B+A ($NHE_{mut.}$). (**b**) Inductively coupled plasma-optical emission spectrometry analysis of intracellular concentrations of K^+ of BMDMs left untreated or assessed 3 hr after treatment with NHE_{WT} or NHE_{mut}. (**c**) Circular dichroism analysis of the secondary structures of C_{WT} or C_{mut}. (**d**) IncuCyte live-imaging analysis of the viability of WT BMDMs left untreated or LPS-primed and assessed after treatment with NHE_{WT} or NHE_{mut}. (**e**) Scanning electron microscopy analysis of WT BMDMs left untreated or LPS-primed and assessed 3 hr after treatment NHE_{WT} or NHE_{mut}. (**f**) Immunoblot analysis of CD14, caspase-1, C, B and A of unprimed WT BMDMs left untreated or assessed 1 hr after treatment with NHE_{WT} or NHE_{mut}. Mem, membrane fraction; Cyto, cytosolic fraction. (**g**) Immunofluorescent analysis of CD11b (green) and C (red) in unprimed WT BMDMs left untreated or assessed 1 hr after treatment with C_{WT} or C_{mut}. (**h**) Colorimetric analysis (top) and the absorbance (OD, bottom) of liposomes left untreated, sonicated for 5 mins at 100 amplitude (CTRL) or assessed 30 mins after treatment with NHE_{WT} or NHE_{mut}. (**i**) Cryo-transmission electron microscopy analysis of liposomes left untreated or assessed 1 hr after treatment with NHE_{WT} or $NHE_{mut.}$ (left). Quantification of membrane pores of liposomes (right). Arrowheads indicate pores (**i**). Scale bar, 2 μm (e, f), 25 μm (h), 50 nm (i). Each symbol represents an independent experiment (a, b, h and i). NS, not significant, ** P<0.01, *** P<0.001 and **** P<0.0001 (one-way analysis of variance [ANOVA] with Dunnett's multiple-comparisons test [a, b and i] or student's unpaired *t*-test [c]). Data are representative of one independent experiment (c) or three independent experiments (a, b, d-i; mean and s.e.m. in a, b, d, h and i).

4.4.9 NHE induces inflammasome-mediated inflammation in the host

Given that NHE induces activation of the NLRP3 inflammasome in primary macrophages, I speculated that this toxin might induce activation of the NLRP3 inflammasome in the host. To

test this idea, WT mice were administered with the supernatant of *B. cereus* or supernatant which had been neutralised against NHE, HBL or both NHE and HBL. It was observed that neutralisation of both NHE and HBL abolished the ability of the supernatant to induce elevated amounts of IL-18 in the serum and peritoneal fluid of WT mice (**Fig. 4.6a,b**). Neutralisation of either NHE or HBL alone led to some reduction in the secretion of IL-18 compared to isotype-treated controls; however, this reduction was less substantial compared to neutralisation of both NHE and HBL (**Fig. 4.6a,b**). This finding suggests a potential synergistic effect of the two toxins in driving inflammasome responses. To validate that secretion of IL-18 was specific to NHE, WT mice were administered with the supernatant of Δ*hbl B. cereus* which had been neutralised with antibodies against NHE or with an IgG isotype. Indeed, neutralisation of NHE impaired the ability of the supernatant of Δ*hbl B. cereus* to induce secretion of IL-18 in WT mice compared to the corresponding control-treated supernatant (**Fig. 4.6c,d**). To confirm a role for the NLRP3 inflammasome, WT, *Nlrp3*$^{-/-}$, *Casp1/11*$^{-/-}$ and *Gsdmd*$^{I105N/I105N}$ mice were infected with Δ*hbl B. cereus* and analysed the levels of IL-18 in the circulation and peritoneal cavity. These analyses revealed that WT mice had elevated levels of IL-18, whereas *Nlrp3*$^{-/-}$, *Casp1/11*$^{-/-}$ and *Gsdmd*$^{I105N/I105N}$ mice had reduced levels of IL-18 in response to Δ*hbl B. cereus* infection (**Fig. 4.6e,f**). Furthermore, pharmacological inhibition of the NLRP3 inflammasome with MCC950 attenuated secretion of IL-18 in the circulation and the peritoneal cavity of mice infected with Δ*hbl B. cereus* (**Fig. 4.6g,h**). Together, these data indicate that recognition of NHE via the NLRP3 inflammasome provides another layer of innate immune mechanism in triggering inflammation in the host in response to *B. cereus* infection. The functional conservation between the mechanism of action of NHE and HBL is exploited by NLRP3 to ensure effective host recognition of the genetically-diverse family of *B. cereus* strains which express either one or both toxins.

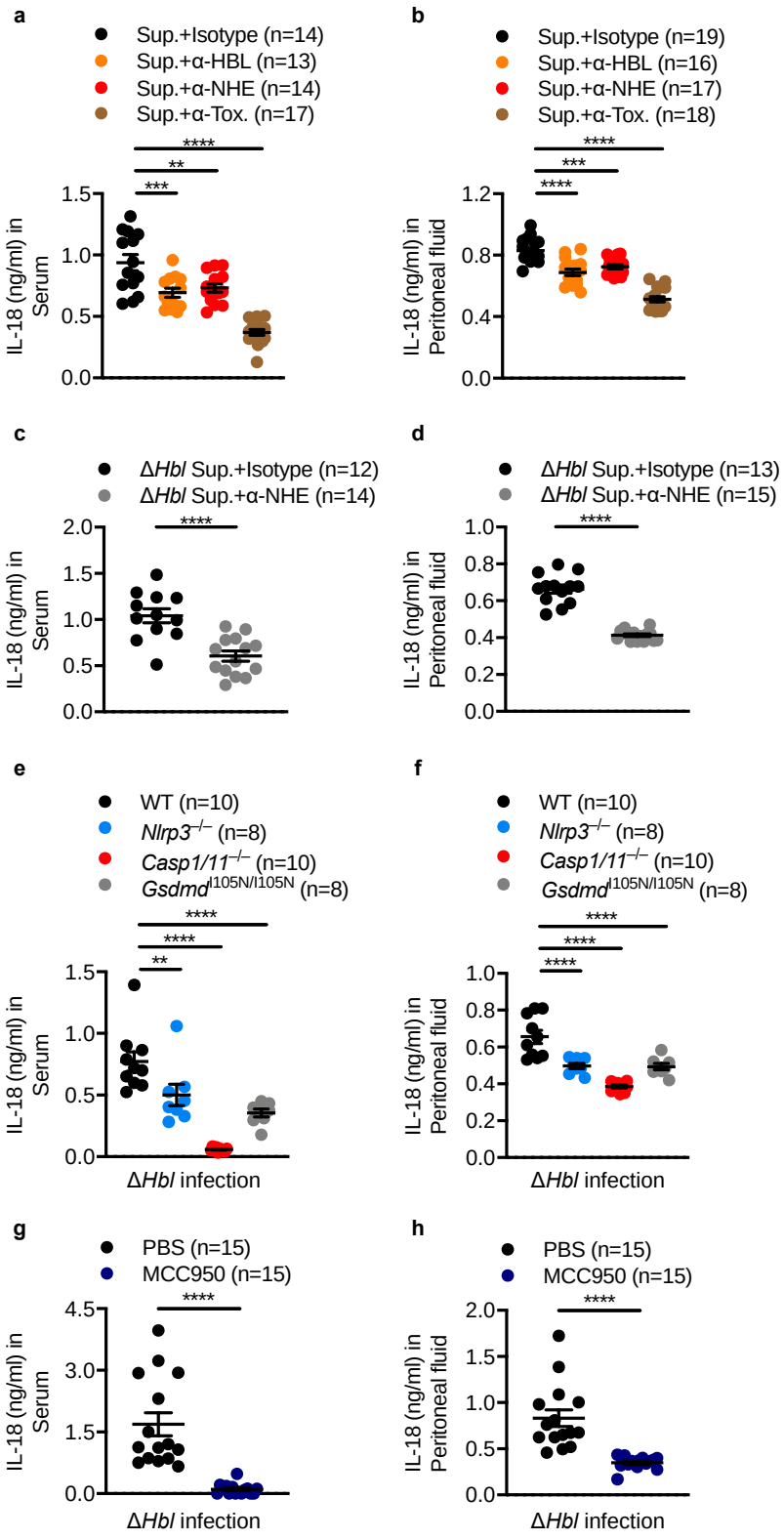

Figure 4.6 | NHE induces activation of the NLRP3 inflammasome in the host. a) Concentration of IL-18 in the serum of WT mice assessed 16 hr after intraperitoneal injection with 200 µl of supernatant of WT *B. cereus* (Sup.) which had been treated with either an

isotype control, anti-HBL neutralising antibodies (α-HBL), anti-NHE neutralising antibodies (α-NHE) or both (α-Tox.). (**b**) Concentration of IL-18 in the peritoneal fluid of WT mice assessed 1 hr after intraperitoneal injection with treatment as in (a). (**c**) Concentration of IL-18 in the serum of WT mice assessed 16 hr after intraperitoneal injection with 200 µl Δ*hbl B. cereus* supernatant which had been treated with either an isotype control or anti-NHE neutralising antibodies (α-NHE). (**d**) Concentration of IL-18 in the peritoneal fluid of WT mice assessed 1 hr after intraperitoneal injection with treatment as in (c). (**e**) Concentration of IL-18 in the serum of WT, *Nlrp3*$^{-/-}$, *Casp1/11*$^{-/-}$ or *Gsdmd*$^{I105N/I105N}$ mice assessed 6 hr after intraperitoneal injection with 5 × 10^6 CFU of Δ*hbl B. cereus* (Δ*hbl*). (**f**) Concentration of IL-18 in the peritoneal fluid of WT, *Nlrp3*$^{-/-}$, *Casp1/11*$^{-/-}$ or *Gsdmd*$^{I105N/I105N}$ mice assessed 6 hr after intraperitoneal injection with treatment as in (e). (**g**) Concentration of IL-18 in the serum of WT mice administered with either PBS or MCC950, both intraperitoneally, followed by intraperitoneal infection with 5 × 10^6 CFU of Δ*hbl* with a corresponding second dose of PBS or MCC950, 6 hr after infection. (**h**) Concentration of IL-18 in the peritoneal fluid of WT mice administered with either PBS or MCC950 (as in g), 6 hr after infection with 5 × 10^6 CFU of Δ*hbl*. Each symbol represents an individual mouse (a-h). ** P<0.01, *** P<0.001 and **** P<0.0001 (one-way analysis of variance [ANOVA] with Dunnett's multiple-comparisons test [a, b, e and f] or student's unpaired *t*-test [c, d, g and h]). Data are pooled from two independent experiments (a-h; mean and s.e.m. in a-h).

4.5 Discussion

B. cereus is a Gram-positive bacterium which causes gastrointestinal and extra-gastrointestinal pathologies in humans [448]. This study revealed that cytosolic recognition of *B. cereus* infection by the host relies on exploitation of the conserved mechanism of action of two different toxins produced by the same bacterium (**Appendices for Chapter 4 Fig. 4.11a**). Importantly, my results further suggest that NLRP3 might potentially exploit the functional and structural similarity of many other PAMPs. Studies have reported that NHE is found in 95-98% of the clinical, food and environmental isolates of *B. cereus* [565,673,677], and that HBL is found in 40-92% of the isolates [458,564,565,673]. The prevalence of NHE and HBL suggests that both toxins are key virulence factors important for the pathogenesis of *B. cereus* infection. Further, these epidemiological data give rise to scenarios that some strains might express NHE or HBL, or both NHE and HBL. I reasoned that the ability of macrophages to detect both toxins allow the host to respond to any naturally-occurring pathogenic variants and that a single NLR protein is able to sense any variants expressing at least one of the two toxins or to sense strains which have phase-variable expression of the two toxins.

The functional and structural similarity of NHE and HBL exploited by NLRP3 is based on pore formation and the permissiveness of the pore to K^+ efflux. The ability of NHE to induce K^+ efflux aligned with previous findings suggesting that NHE induces the formation of large conducting openings which are permeable to cations [518,670]. Previous studies have classified NHE as a member of the α-helical pore-forming toxin family; members of which are characterised by the presence of an α-helical hydrophobic membrane-integrative region [514,518]. It was observed that deletion of this hydrophobic region impairs the ability of subunit C to bind to membrane (**Appendices for Chapter 4 Fig. 4.11b,c**), highlighting that the hydrophobic region in subunit C might be responsible for anchoring to the host membrane, similar to that observed in cytolysin A of the α-helical pore-forming toxin family [515,516]. These findings are consistent with a previous study reporting that deletion of the same hydrophobic region in

subunit C leads to a loss of cytotoxicity of NHE on Vero cells [510]. I postulate that the anchorage mediated by the hydrophobic region in subunit C can also function to initiate a series of conformational changes in subunit C, triggering recruitment of subunit B and subunit A for the final construction of the NHE pore complex. Although the NHE and HBL pores are both permissive to efflux of K^+, subtle differences in the mechanism of action between the two toxins have been observed. Unlike subunit C of NHE, it was found that deletion of the corresponding hydrophobic region of HBL-B, which is the apical subunit of HBL [673], does not impair the ability of the subunit to bind the plasma membrane. It is possible that the hydrophobic region of HBL-B is not essential for membrane binding and that deletion of this region exposes the bona fide binding region/s of HBL-B, enhancing binding of HBL-B to the plasma membrane.

Targeting the conserved activity of bacterial pore-forming toxins might be efficacious against certain bacterial infections. For example, neutralisation of the activity of the pore-forming toxin haemolysin A of *Staphylococcus aureus* [678,679] and the anthrax toxin of *B. anthracis* [668,669], have been effective. These findings are of clinical importance given the increasing incidence of antibiotic-resistant bacteria, including *B. cereus* [448,449]. Therefore, a better understanding of the host defence strategy against *B. cereus* infection will be beneficial and neutralisation of toxins might complement current therapies against infection caused by toxin-producing bacteria. In conclusion, this study identified that the functional similarity and conserved mechanism of action of two multicomponent toxins of *B. cereus* is exploited for innate immune sensing by an inflammasome sensor protein. Further studies are required to understand whether NHE and HBL might target any cell surface receptor/s for binding to the plasma membrane.

Chapter 5♦ Phospholipase C of *Clostridium perfringens* disrupts lysosomal integrity and activates the NLRP3 inflammasome and pyroptosis

5.1 Preface

This chapter consists of unpublished data generated by Callum Kay (former Honours student and current Medical Project student in the lab) and myself. I generated greater than fifty percent of the content. My contribution to the Chapter is as follows:

- Planning, design and execution of experiments except mentioned below.
- Interpretation and analysis of results and compilation of figures except mentioned below.

I would like to take this opportunity to thank Callum Kay for initiating this project during his Honours in the lab. He was involved in the planning, designing and execution of experiments; interpretation and analysis of results; and compilation of below mentioned figures in this chapter:

- Main Figures: 5.1a,c-e,g,h; 5.2a, 5.4a,e; 5.5a,b,e; 5.6a-c
- Appendices Chapter 5 figures: 5.1a-d; 5.2a-e; 5.3a; 5.7

5.2 Introduction

Bacteria encode an arsenal of toxins that modify the function, metabolism and physiology of the host cell to favour bacterial infection. The host immune system can sense certain bacterial toxins and activate the inflammasome in response to bacterial infection. Inflammasome activation by bacterial toxins is generally achieved through the pore-forming and/or enzymatic activity of the toxin.

Many bacterial toxins function by forming pores in the host cell membrane. Certain pore-forming toxins produced by both Gram-positive and Gram-negative bacteria are indirectly sensed by the NLRP3 inflammasome [680]. Mechanistically, toxin-induced pore formation in the host cell membrane can cause potassium efflux [665], which in turn activates the NLRP3 inflammasome **(Figure 1.2a)**. Indeed, potassium efflux has been proposed as a common upstream activator of the NLRP3 inflammasome in response to bacterial toxins [665]. However, the presence of other bacterial PAMPs in concert with potassium efflux appears to be important for NLRP3 inflammasome activation by some pore-forming toxins. For instance, the Gram-negative pathogenic bacteria *V. cholerae* and *Vibrio vulnificus* [647] and the Gram-positive bacterium *S. aureus* [681] produce haemolysin toxins that induce potassium efflux in macrophages. The culture supernatants derived from *V. cholerae* can trigger potassium efflux and activation of caspase-1 via the NLRP3 inflammasome in macrophages; however, purified haemolysin induces substantially less caspase-1 activation [647]. It is possible that other bacterial PAMPs, such as peptidoglycan, may provide a priming signal (Signal 1) to upregulate inflammasome components, while toxin-induced potassium efflux acts as the inflammasome activating signal (Signal 2). In this way, haemolysins may function in concert with other bacterial virulence factors to maximally activate the NLRP3 inflammasome. Other examples of bacterial toxins capable of activating the NLRP3 inflammasome via the K^+ efflux are: perfringolysin O from *Clostridium perfringens* [682], listeriolysin O from *L. monocytogenes* [683], Shiga toxin from *Shigella dysenteriae* [684,685], streptolysin O from *Streptococcus pyogenes* [643],

and pneumolysin from *Streptococcus pneumoniae* [686]. Certain toxins such as Panton-Valentine leucocidin (PVL) of *S. aureus* [687-689] and pneumolysin of *S. pneumoniae* [686] induce K^+ efflux associated with phagosomal rupture, showcasing how different cellular perturbations converge at triggering K^+ efflux to activate the inflammasome.

Introducing pores into the pathogen-containing vacuole membrane can also permit bacterial escape, and subsequent release of PAMPs, into the cytoplasm for innate immune sensing. For instance, the *L. monocytogenes* toxin listeriolysin O is required for bacterial invasion of the cytoplasm from the pathogen-containing vacuole [282]. A mutant strain of *L. monocytogenes* lacking listeriolysin O fails to induce IL-1β secretion in macrophages [282], likely due to inflammasome-activating PAMPs remaining sequestered in the pathogen-containing vacuole. A further study implicated listeriolysin O-mediated rupture of phagosomes and release of cathepsin B as the main mechanism by which NLRP3 is activated upon *L. monocytogenes* infection of human peripheral blood mononuclear cells [683]. Similarly, *Streptococcus agalactiae* produces a β-haemolysin toxin which forms pores in the pathogen-containing vacuole and presumably releases RNA and lysosomal components into the cytoplasm for sensing by the NLRP3 inflammasome [642].

The lethal toxin produced by *B. anthracis* carries both a pore-forming and enzymatic activity that leads to activation of the NLRP1 inflammasome. The lethal toxin is a two-component toxin comprising a pore-forming protective antigen and an enzymatically-active lethal factor [632]. The protective antigen facilitates lethal factor entry into the host cell cytoplasm, where the lethal factor cleaves mouse NLRP1b in the N-terminal region to liberate the CARD-containing C-terminal fragment [66,74-76,690] **(Figure 1.1)**. The mechanisms of NLRP1b activation are discussed in Section 1.3.1.

Post-translational modifications induced by enzymatically-active toxins represent an additional mechanism by which the inflammasome can be activated. For instance, *Mycoplasma pneumoniae* encodes an ADP-ribosylating and vacuolating toxin, designated community-

acquired respiratory distress syndrome (CARDS) toxin [691], which activates the NLRP3 inflammasome by direct ADP-ribosylation of NLRP3 [691]. Similarly, certain bacterial toxins post-translationally modify Rho family GTPases to relieve inhibition of Pyrin and licensing activation of the Pyrin inflammasome [410,692,693] **(Figure 1.5)**. Specifically, the *Clostridioides difficile* cytotoxins TcdA and TcdB monoglucosylate RhoA; the *Clostridium botulinum* toxin C3 ADP-ribosylates RhoA; and the *Vibrio parahemolyticus* toxin VopS, the *Histophilus somni* toxin IbpA adenylates RhoA and Yop of *Yersinia* impairs RhoA activity through either direct cleavage or indirect inhibition of RhoA [410,414-416,693-695] **(Figure 1.5)**. Taken together, these studies demonstrate the various mechanisms utilised by inflammasome sensors to detect structurally and functionally diverse bacterial toxins.

Systematic identification of new activators of the inflammasome is critical in unveiling new innate immune sensing pathways or mechanisms resulting in inflammation and cell death, leading to the development of novel therapeutics. The inflammasome-toxin axis is important in host immunity and the resulting inflammasome-driven responses can promote either host survival and protection, or disease and mortality. Whilst inflammasomes are critical in responding to pathogens and their toxins, a complete atlas of toxins capable of activating the inflammasome remains unknown.

In this chapter, a panel of 34 toxins from phylogenetically diverse organisms were screened and phospholipase C (PLC) from the human bacterial pathogen *Clostridium perfringens* was identified as an activator of the NLRP3 inflammasome. Unlike the majority of toxins leading to the activation of NLRP3 via signals emanating from the plasma membrane, PLC requires endosomal uptake and is trafficked to the lysosome, where it causes lysosomal membrane destabilisation, triggering K^+ efflux and promotes NLRP3 inflammasome assembly. This data identified PLC as a new activator of the NLRP3 inflammasome and highlights a convergence of signals between the lysosome and K^+ efflux in triggering cytosolic sensing of a bacterial phospholipase and innate immunity.

5.3 Material and Methods

5.3.1 Toxin reconstitution

Purified toxins in lyophilised powders were reconstituted in solvent to a concentration recommended by the manufacturer. Information describing the toxins, including working concentration, solvent, proposed mechanisms of action and identifier can be found in **Tables 2.9-2.13**.

5.3.2 Stimulation of BMDMs with Toxins and Inflammasome Activators

For stimulation of BMDMs in the toxin screening experiment, reconstituted toxins were added gradually to LPS-primed BMDMs until the final concentration described in Tables **2.9-2.13** was reached, then left overnight. For specific toxins, LPS-primed BMDMs were treated with 1.5 Units/ml of PLC (P7633, Sigma-Aldrich) for 3 hr, 50 ng/ml of α-toxin of *C. septicum* (1161A1, List biological laboratories) for 3 hr, or 0.6 mg/ml of perfringolysin O (RPC2043, Biomatik) for 3 hr. For stimulation of inflammasome with lysosomal destabilising agent Leu-Leu-OMe (LLOMe), LPS-primed BMDMs were treated with 1mM of LLOMe for 2 hr. To activate the canonical NLRP3 inflammasome, LPS-primed BMDMs were stimulated with 5 mM ATP (10127531001, Roche) for 45 min or 10 µM Nigericin (Nig., N7143, Sigma-Aldrich) for 30 min. To activate caspase-11, 5 µg of LPS (tlrl-smlps, InvivoGen) were resuspended in PBS and mixed with 0.3 µl of Xfect polymer in Xfect reaction buffer (631318, Clontech Laboratories, Inc.). After 30 min, LPS complexes were added to BMDMs in Opti-MEM (31985-070, ThermoFisher Scientific) and left stimulated for 16 hr. To activate the NLRC4 inflammasome, BMDMs were infected with *S.* Typhimurium at MOI of 2 for 4 hr. To activate the AIM2 inflammasome, BMDMs were infected with *Francisella novicida* at MOI of 100 for 16 hr.

For inhibition experiments, BMDMs were pre-treated for 30 mins with the following inhibitors; 20 µM of the selective and potent NLRP3 inhibitor, MCC950 [213-215], 5 mM, 25 mM, 50 mM or 75 mM of potassium chloride (KCl, P9541, Sigma-Aldrich), 50 µM of cytochalasin D (cytoD,

C8273, Sigma-Aldrich), 1µg/ml Of Latrunculin B (Lat B, ab144291, abcam), 5 mM of methyl-β-cyclodextrin (MCD, C4555, Sigma-Aldrich), 0.05 U/ml of Phosphatidylinositol-specific Phospholipase C from *B. cereus* (PI-PLC, P5542, Sigma-Aldrich), 100 nM of bafilomycin A (Baf A, B1793, Sigma-Aldrich), 10 µM of ammonium chloride (NH_4Cl, A9434, Sigma-Aldrich), or 100 µM of CA-074-Me (a cathepsin B-specific inhibitor [696], C5732, Sigma-Aldrich). Cell culture supernatants were collected for ELISA and LDH assays. Cell culture supernatants and cell lysates were collected for immunoblot analysis.

5.3.3 Stimulation of THP1 cells with Inflammasome Activators

LPS-primed THP1 monocytes and macrophages were treated with 1.5 Units/ml of PLC or 10 µM nigericin. For inhibition experiments THP1 monocytes were pre-treated for 30 mins with 20 µM of the selective and potent NLRP3 inhibitor, MCC950 [213-215]. Cell culture supernatant was collected 4 hr later for cytokine analysis.

5.3.4 Immunoblotting Analysis

For caspase-1 immunoblotting, BMDMs and supernatant were lysed in lysis buffer and sample loading buffer containing SDS and 100 mM DTT. Proteins were separated on 8-12% polyacrylamide gels. Following electrophoretic transfer of proteins onto PVDF membranes (IPVH00010, Millipore), membranes were blocked in 5% skim milk in TBST and incubated overnight with primary antibodies against caspase-1 (1:1,000 dilution, AG-20B-0042, Adipogen), gasdermin D (1:1,000 dilution, ab209845, Abcam), and GAPDH (1:10,000 dilution, 5174, Cell Signaling Technologies). PVDF membranes were then incubated with HRP-conjugated secondary antibody (1:5,000; Jackson ImmunoResearch) for 1 hr and proteins were visualised using the Super Signal Femto substrate (34095, ThermoFisher Scientific) and the ChemiDoc™Touch Imaging System (BioRad).

5.3.5 Fluorescent labelling of PLC

Alexa Fluor 568 Protein Labelling Kit (#A10238, Invitrogen) was used to label PLC for immunofluorescence studies. The concentration of PLC was determined using the Pierce BCA Protein Assay Kit (#23225, ThermoFisher Scientific), and an aliquot of PLC was diluted to 2 mg per ml in 500 µl ddH_2O. 1 M bicarbonate (50 µl) was added to give an optimal pH (~8.3) for labelling. This 550 µl reaction volume was added to a vial of Alexa Fluor 568 reactive dye and incubated at room temperature for 1 hr with gentle rotation. The reactive dye contains a succinimidyl ester moiety that reacts with primary amines of proteins, producing stable protein-dye conjugates. Excess dye was separated from labelled protein by gel filtration using a Bio-Rad BioGel P-30 Fine size exclusion resin. The column was assembled by filling a supplied plastic column with resin until ~3 cm from the top and was equilibrated with PBS to ensure proper flow. Next, the labelled protein mixture was added to the column and allowed to settle into the resin, before elution of the protein with elution buffer (10 mM potassium phosphate, 150 mM NaCl, 0.2 mM sodium azide, pH 7.2). The faster running purple band containing labelled PLC was collected in 1 ml fractions, whilst the slower running, unincorporated dye was not collected.

5.3.6 Immunofluorescence Staining

BMDMs were stimulated with 60 µg/ml of Alexa Fluor 568 labelled PLC for 2 hr with or without inhibitors, 50 µM cytochalasin D or 5 mM methyl-β-cyclodextrin (MCD), washed three times with PBS and fixed with 4% paraformaldehyde at room temperature for 15 min, followed by blocking in 1% BSA in PBS for 1 hr. Cells were incubated with a rat FITC-conjugated anti-CD11b antibody (1:200 dilution in 1% BSA, 101205, BioLegend). The samples were mounted with VECTASHIELD® Hardset™ Mounting Medium with DAPI (H-1500, Vector Laboratories, Inc.) and analysed using a Leica SP5 confocal microscope.

5.3.7 Scanning Electron Microscopy

PLC or ATP treated BMDMs were washed with PBS and post-fixed with 2.5% glutaraldehyde in 0.1 M phosphate buffer overnight and further washed with PBS. Cells were fixed in 1% osmium tetroxide in double distilled water for 1 hr and dehydrated in a series of alcohol. Dehydrated samples were dried using liquid carbon dioxide using critical point drying. Samples were then sputter-coated with platinum (3 nm thickness) at 15 mA for 2 min using the EMI TECH K550 Sputter coater and visualised under a Zeiss UltraPlus Field emission scanning electron microscope at 5 kV.

5.3.8 Transmission Electron Microscopy

PLC or ATP treated BMDMs were washed with PBS and post-fixed with 2.5% glutaraldehyde in 0.1 M phosphate buffer overnight and further washed with PBS. Cells were fixed in 1% osmium tetroxide in double distilled water for 1 hr and dehydrated in a series of alcohol, and embedded in LR white resin (C023, ProSciTech). Samples were polymerised in a 60 °C oven overnight. Thin sections were cut at 80 nm and viewed using a Hitachi HA7100 transmission electron microscope at 100 kV.

5.3.9 Flow cytometry

For evaluation of lysosomal rupture, cells were incubated for 15 min with acridine orange (1 µg/ml), were washed three times and then were stimulated with 1.5 Units/ml PLC or 1mM of LLOMe for 30-60 min. Lysosomal rupture was assessed by flow cytometry as loss of emission at 600–650 nm. An LSRII (BD Biosciences) was used for all flow cytometry. Data were acquired by DIVA (BD Biosciences) and were analysed with FlowJo software (Tree Star).

5.3.10 Liposome Studies

Liposomes were synthesised[673] and left untreated or treated with 1.5 Units/ml of PLC, the solvent containing PLC (ddH2O) or BSA (1 µg/ml) and Alexa Fluor 568 labelled PLC for 1 hr at 4 °C. The liposomes were sonicated at 100 amplitude for 5 mins as control (CTRL). The released dye was captured by a cation exchanger resin Dowex (10-15 mg/well). The

absorbance (OD) of residual dye was measured at a wavelength of 595 nm using the Infinite 200 PRO system (Tecan).

5.3.11 Lactate Dehydrogenase Assay

Levels of lactate dehydrogenase released by cells were determined using the CytoTox 96 Non-Radioactive Cytotoxicity Assay according to the manufacturer's instructions (G1780, Promega).

5.3.12 IncuCyte Analysis

To track viability in real-time, BMDMs were stimulated with either 1.5 Units/ml of PLC for or 5 mM ATP or 5 µg of transfected LPS or infection of *F. novicida* (MOI 100) with or without inhibitors namely, 100 nM of bafilomycin A and 10 µM of ammonium chloride, in presence of the SYTOX Green nuclear stain that penetrates compromised membranes (1 µM; S7020; Life Technologies). Cell death was monitored over 3-16 hr using the IncuCyte Zoom imaging system (Essen Biosciences).

5.3.13 Cytokine Analysis

Cytokine concentrations from BMDMs were calculated using a multiplex ELISA (MCYTOMAG-70K, EMD Millipore) or IL-18 ELISA (BMS618-3TEN, ThermoFisher) according to the manufacturers' instructions. Cytokine levels from THP-1 cells were calculated using a human IL-1β ELISA (BMS224-2TEN, ThermoFisher) or human IL-18 ELISA (BMS267-2TEN, ThermoFisher) according to the manufacturer's instructions.

5.3.14 ICP-OES analysis

The intracellular concentrations of K^+ and Na^+ ions were determined by inductively coupled plasma-optical emission spectroscopy (ICP-OES) analysis. In brief, BMDMs were stimulated with recombinant 1.5 Units/ml of PLC for 2 hr or 5 mM ATP for 30 min or 10 µM nigericin for

30 min in the absence or presence of inhibitors (as described in section 5.3.2), washed three times with PBS followed by lysis with 70% concentrated nitric acid (HNO_3). The cell lysates were analysed for K^+ and Na^+ ions performed through ICP-OES using a PerkinElmer OPTIMA 7300 ICP Optical Emission Spectrometer (PerkinElmer).

5.3.15 Animal studies

To investigate the role of PLC in inflammasome activation in vivo, WT, *Nlrp3*$^{-/-}$ and *Casp1*$^{-/-}$ KO mice were injected intraperitoneally with 0.625 Units/ml of PLC. For cytokine measurement serum and peritoneal fluid were collected after 4 hr for analysis by ELISA.

5.4 Results

5.4.1 An unbiased screen identifies PLC as an activator of the inflammasome

Toxins produced by a range of pathogens and other organisms can elicit rapid inflammation and cell death in the host, which is a hallmark of an innate immune response [697]. To identify potentially new activators of the inflammasome, a panel of 34 toxins derived from bacteria, fungi, snakes, terrestrial invertebrates or marine organisms were screened in wild-type (WT) primary mouse bone marrow-derived macrophages (BMDMs) (**Tables 2.9-2.13**). Of the 34 toxins, phospholipase C (PLC) from the human bacterial pathogen *Clostridium perfringens* and nigericin from the bacterium *Streptomyces hygroscopicus* [309], induced robust secretion of IL-1β and IL-18 in LPS-primed WT BMDMs (**Fig. 5.1a**). Notably, all other candidates tested did not induce secretion of IL-1β and IL-18, suggesting that many toxins, contrary to previous assumptions [113,132,635,697,698], do not readily activate the inflammasome. Further analysis confirmed that PLC and nigericin induced activation and cleavage of caspase-1 and gasdermin D (GSDMD) in WT BMDMs (**Fig. 5.1b**). Therefore, this screening experiment identified PLC as a new activator of the inflammasome.

To elucidate the identity of the inflammasome sensor recognising PLC, LPS-primed WT BMDMs and BMDMs lacking various inflammasome sensors or components were stimulated with PLC. Cleavage of caspase-1 and/or GSDMD, secretion of IL-1β and IL-18, and induction of cell death were impaired in *Nlrp3*$^{-/-}$ and *Asc*$^{-/-}$ and *Casp1/11*$^{-/-}$ BMDMs, whereas these responses were intact in WT, *Nlrc4*$^{-/-}$, *Aim2*$^{-/-}$, *Mefv*$^{-/-}$, and *Casp11*$^{-/-}$ BMDMs (**Fig. 5.1c–f; Appendices for Chapter 5 Fig. 5.1b)**. The observation that inflammasome activation was similar in WT and *Casp11*$^{-/-}$ BMDMs treated with PLC suggest that inflammasome activation was not due to PLC-mediated transport of LPS into the cytoplasm to activate the caspase-11 non-canonical NLRP3 inflammasome [601]. In addition, scanning electron microscopy and transmission electron microscopy techniques revealed substantial plasma membrane damage, cytoplasmic clearance, and architectural collapse in WT BMDMs stimulated with PLC compared to the untreated BMDMs (**Fig. 5.1g,h; Appendices for Chapter 5 Fig. 5.2a–c**). Importantly, I observed that the secretion of tumour necrosis factor (TNF), keratinocyte chemoattractant (KC, also known as CXCL1) and IL-6 was similar in WT BMDMs and BMDMs lacking various inflammasome sensors or components following stimulation with PLC, suggesting that activation of other major pro-inflammatory signalling pathways was not compromised in these cells (**Fig. 5.1d; Appendices for Chapter 5 Fig. 5.1a**).

Notably, in absence of signal 1 (provided by LPS priming), PLC induced cleavage of caspase-1 and GSDMD (**Appendices for Chapter 5 Fig. 5.1c**), suggesting that PLC can act both as signal 1 and 2 in the activation of the NLRP3 inflammasome. Further, pharmacological inhibition of NLRP3 using the small-molecule inhibitor MCC950 impaired inflammasome activation in WT BMDMs and human THP1 cells stimulated with PLC (**Appendices for Chapter 5 Fig. 5.1d, 5.3a**). *Nlrp3*$^{-/-}$ THP1 cells stimulated with PLC also had an impaired ability to induce inflammasome activation compared to WT THP1 cells (**Appendices for Chapter 5 Fig. 5.3b)**. Collectively, these data suggest that PLC induces the activation of the NLRP3 inflammasome and pyroptosis, and that NLRP3-mediated sensing of PLC is functionally conserved between mice and humans.

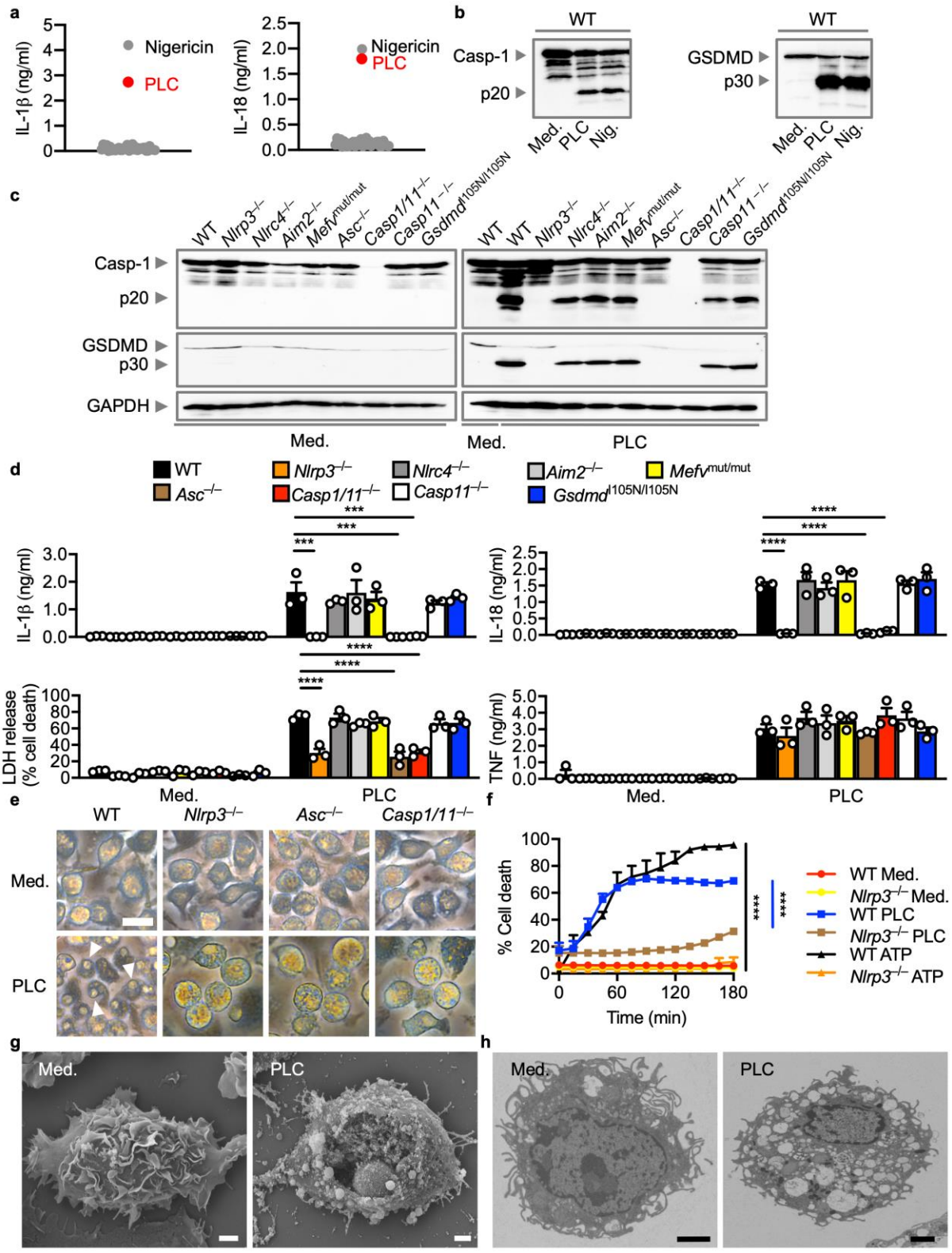

Figure 5.1 | Toxin screen identifies PLC as a novel activator of the NLRP3 inflammasome. (**a**) Release of IL-1β and IL-18 from LPS-primed WT BMDMs after stimulation

with toxins listed in Tables 2.9-2.13. (**b**) Immunoblot analysis of pro-caspase-1 (Casp-1), the active caspase-1 p20 subunit, pro-pyroptotic effector protein gasdermin D (GSDMD), the active GSDMD p30 subunit of WT BMDMs left untreated [Medium alone (Med.)] or LPS-primed and assessed 3 hr after stimulation with PLC or 30 min with nigericin (Nig.). (**c**) Immunoblot analysis of caspase-1, gasdermin D and GAPDH (loading control) in WT or mutant BMDMs left untreated or LPS-primed and assessed 3 hr after stimulation with PLC. (**d**) Release of IL-1β, IL-18 and TNF, and death of BMDMs after treatment as in (c). (**e**) Brightfield microscopy analysis of BMDMs 3 hr after stimulation as in (c). (**f**) IncuCyte live-imaging analysis of the viability of WT or *Nlrp3*$^{-/-}$ BMDMs left untreated or LPS-primed and assessed 3 hr after stimulation with PLC. (**g**) Scanning electron microscopy analysis of WT BMDMs left untreated or LPS-primed and assessed 3 hr after treatment with PLC. (**h**) Transmission electron microscopy analysis of BMDMs after treatment as in (g). Scale bar, 25 μm (e), 2 μm (g,h). Arrowheads indicate pyroptotic cells (e). Each symbol is representative of mean of three experiments (a). Each symbol represents an independent experiment (d,f). NS, not significant, *** P<0.001 and **** P<0.0001 (one-way analysis of variance [ANOVA] with Dunnett's multiple-comparisons test [d,f]). Data are representative of three independent experiments (a-h; mean and s.e.m. in d,f).

5.4.2 GSDMD is not required for PLC-mediated cytokine release and pyroptosis

Caspase-1 or caspase-11 mediates the proteolytic cleavage of GSDMD, liberating the N-terminal domain of GSDMD to oligomerise in the plasma membrane to form membrane pores [574,699,700]. In response to PLC, WT and *Gsdmd*$^{I105N/I105N}$ BMDMs (encoding a mutant GSDMD protein lacking the ability to form pores) [574,661,662] released similar levels of IL-1β, IL-18, and LDH (**Fig. 5.1d**). The similar levels of IL-1β and IL-18 released by WT and *Gsdmd*$^{I105N/I105N}$ BMDMs were surprising because GSDMD pores were thought to be the primary channel through which IL-1β and IL-18 exit pyroptotic cells. However, we and other have previously

shown that GSDMD is largely not required for the release of IL-1β and IL-18 following prolonged stimulation by certain endogenous or exogenous inflammasome activators, such as ATP, flagellin, non-haemolytic enterotoxin of *Bacillus cereus*, and platelet-activating factor [262,574,701]. Time-course experiments revealed that the secretion of IL-1β, IL-18 and LDH was similar between WT and *Gsdmd*$^{I105N/I105N}$ BMDMs stimulated with PLC (**Fig. 5.2a**). Caspase-1 and GSDMD cleavage were similar between WT and *Gsdmd*$^{I105N/I105N}$ BMDMs in response to PLC (**Fig. 5.2b**). Consistent with a previous study [574], *Gsdmd*$^{I105N/I105N}$ BMDMs displayed impaired activation of caspase-1, secretion of IL-1β, IL-18 and LDH in response of transfection of LPS (**Fig. 5.2a,b**).

To further rule out the role of GSDMD, I performed the experiment using WT and *Gsdmd*$^{-/-}$ BMDMs and found that the kinetics of IL-1β and IL-18 secretion and LDH release in these cells were again similar in response to PLC, however, *Gsdmd*$^{-/-}$ BMDMs secreted significantly less amount of IL-1β, IL-18 and LDH compared to WT BMDMs in response to LPS transfection (**Fig. 5.2c**) [574]. Caspase-1 cleavage and activation were similar between WT and *Gsdmd*$^{-/-}$ BMDMs treated with PLC (**Fig. 5.2d**). Cell viability analysis using the IncuCyte real-time imaging system revealed that, in response to PLC treatment, WT, *Gsdmd*$^{I105N/I105N}$ and *Gsdmd*$^{-/-}$ BMDMs underwent death with similar kinetics (**Fig. 5.2e**). In contrast, BMDMs underwent robust cell death, whereas *Gsdmd*$^{I105N/I105N}$ and *Gsdmd*$^{-/-}$ BMDMs did not, in response to LPS transfection (**Fig. 5.2f**). These data suggest that PLC-induced activation of the inflammasome leads to the secretion of inflammasome-associated cytokines and LDH independently of GSDMD.

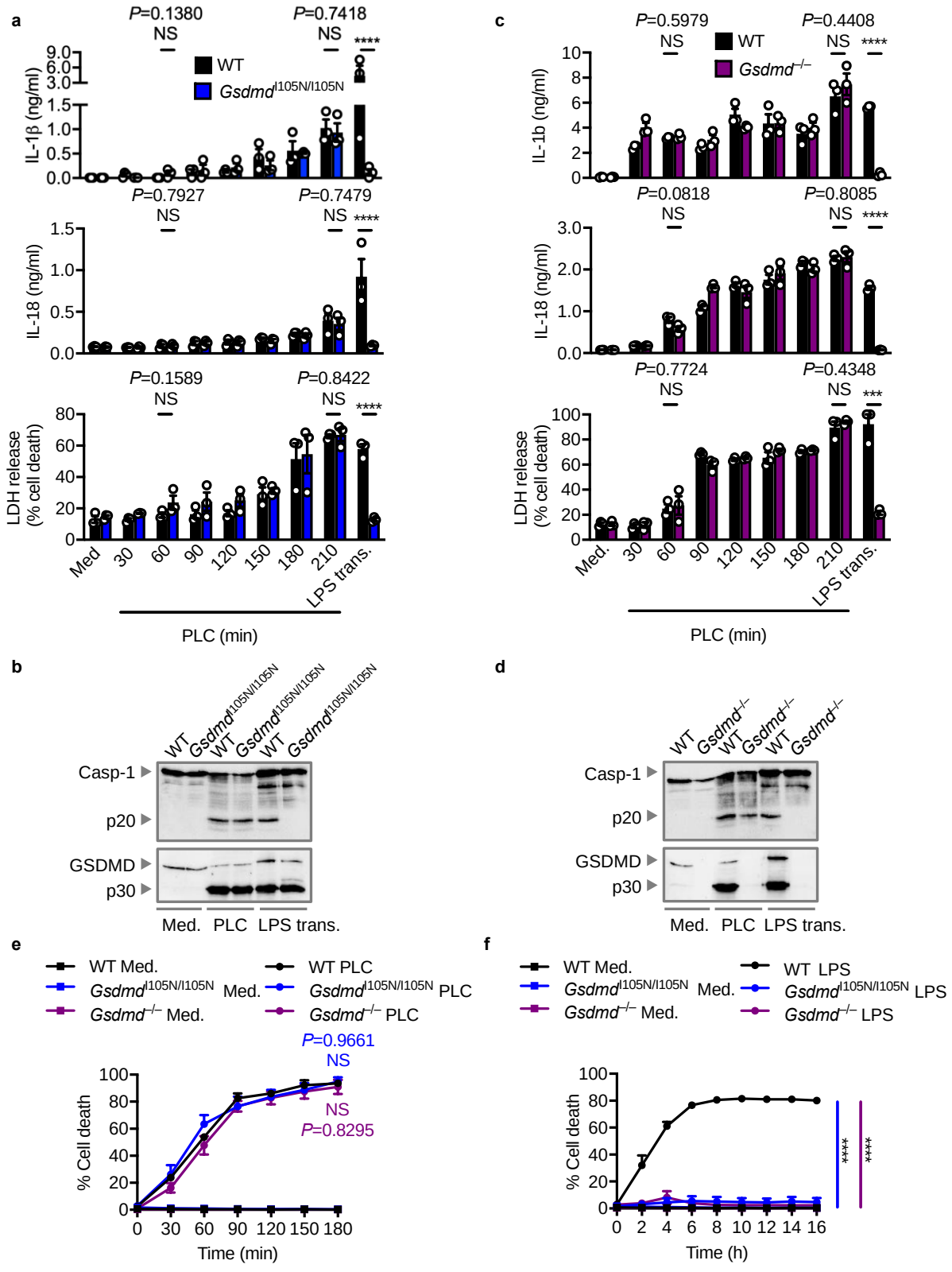

Figure 5.2 | GSDMD is not required for PLC-mediated cytokines and LDH release. (**a**) Release of IL-1β, IL-18, and cell death of WT or *Gsdmd*$^{I105N/I105N}$ BMDMs left untreated [Medium alone (Med.)] or LPS-primed and assessed 3 hr after stimulation with PLC or 16 hr

after transfection with LPS (LPS trans.). (**b**) Release of IL-1β, IL-18 and cell death of WT or *Gsdmd*$^{-/-}$ BMDMs left untreated or LPS-primed and assessed 3 hr after stimulation with PLC or 16 hr after transfection with LPS (LPS trans.). (**c**) Immunoblot analysis of caspase-1 and gasdermin D of BMDMs after treatment as in (a). (**d**) Immunoblot analysis of caspase-1 and gasdermin D of BMDMs after treatment as in (b). (**e**) IncuCyte live-imaging analysis of the viability of BMDMs after treatment as in (a). (**f**) IncuCyte live-imaging analysis of the viability of BMDMs after treatment as in (b). Each symbol represents an independent experiment (a, b, e and f). NS, not significant, *** P<0.001 and **** P<0.0001 (student's unpaired t-test [a and b] or one-way analysis of variance [ANOVA] with Dunnett's multiple-comparisons test [e and f]). Data are representative of three independent experiments (a-f; mean and s.e.m. in a, b, e and f).

5.4.3 Endocytosis of PLC leads to inflammasome activation

The ability of PLC to cleave phospholipid moieties (**Appendices for Chapter 5 Fig. 5.2d**) may suggest that PLC can emanate a signal from the plasma membrane to activate NLRP3 without entering the host cell. The surface receptor of PLC is GM1a ganglioside, which is a type of glycophospholipid [702]. GM1a ganglioside is synthesised by an enzyme called beta-1,4-N-acetyl-galactosaminyl transferase. This enzyme is encoded by *B4galnt1* gene which is transcriptionally upregulated in LPS-primed BMDMs (**Appendices for Chapter 5 Fig. 5.4**). The toxin-ganglioside interaction can form on cholesterol-rich lipid rafts on the plasma membrane [703]. Indeed, depletion of the plasma membrane cholesterol using methyl-β-cyclodextrin (MCD) abrogated inflammasome activation in response to PLC and the cholesterol-dependent cytolysin perfringolysin O, but had no effect on nigericin-mediated inflammasome activation (**Fig. 5.3a,b**).

Glycosylphosphatidylinositol (GPI)-anchored proteins can localise to cholesterol-rich lipid rafts on plasma membrane and were hypothesised to mediate cytotoxicity of PLC in the fibroblast cell line DonQ [704]. However, cleavage of the phosphatidylinositol group from membrane-associated GPI-anchored proteins using phosphatidylinositol (PI)-specific phospholipase C (PI-PLC), did not abrogate the ability of PLC to induce activation of caspase-1, secretion of IL-1β, IL-18 and cell death in BMDMs (**Fig. 5.3c,d**), suggesting that GPI-anchored proteins are not required to drive PLC-induced inflammasome activation and pyroptosis. These data also suggest that membrane attachment mediated by cholesterol is the apical step in PLC-induced activation of the inflammasome.

We next investigated whether internalisation of PLC into BMDMs is required to drive inflammasome activation. Toxins can activate the inflammasome pathway either from the plasma membrane or cytosol. Some examples of toxins capable of engaging in activation of the inflammasome from the plasma membrane are nigericin [309], HBL [673] and NHE [701]. In contrast, certain toxins require cytosolic access to activate the inflammasome such as *B. anthracis* lethal toxin [73] and *C. difficile* TcdB [410]. Unlike the pore-forming toxins HBL and NHE, PLC-induced inflammasome activation was inhibited in BMDMs pre-treated with an inhibitor of actin polymerisation, cytochalasin D, compared to BMDMs not treated with cytochalasin D (**Fig. 5.4a,b**). I observed similar results using an inhibitor of actin-based endocytosis, latrunculin B, (**Fig. 5.4c,d**). Incubation of BMDMs with cytochalasin D, latrunculin B and MCD did not affect the secretion of TNF (**Appendices for Chapter 5 Fig. 5.5a–c**). Consistently, these inhibitors also abrogated inflammasome activation by the intracellular bacterium Salmonella enterica serovar Typhimurium, which requires intracellular invasion of the host cell, but not by nigericin (**Fig. 5.3a–d**) [655].

To further confirm that PLC requires cytosolic access to engage the NLRP3 inflammasome, PLC was fluorescently labelled with Alexa Fluor 568 (designated AF568-PLC) and its localisation in the cell was tracked using confocal microscopy. Labelling of PLC did not affect

its ability to induce inflammasome activation (**Appendices for Chapter 5 Fig. 5.6a**), or its ability to induce lysis of dye-containing liposomes (**Appendices for Chapter 5 Fig. 5.6b**). Confocal microscopy analysis revealed that AF568-PLC localised to punctate structures (**Fig. 5.4e**). Distinct puncta were observed primarily in the cytoplasm, suggesting internalisation of PLC and/or that PLC is localised in the cytosolic endosomal transport pathway. Indeed, cytochalasin D prevented accumulation of AF568-PLC puncta in cytoplasm of BMDMs (**Fig. 5.4e**). Furthermore, MCD also prevented AF568-PLC puncta in cytoplasm of BMDMs (**Appendices for Chapter 5 Fig. 5.7**), suggesting that membrane cholesterol is required for endocytosis of PLC. Taken together, these results suggest that cytosolic access is a requirement for inflammasome activation by PLC.

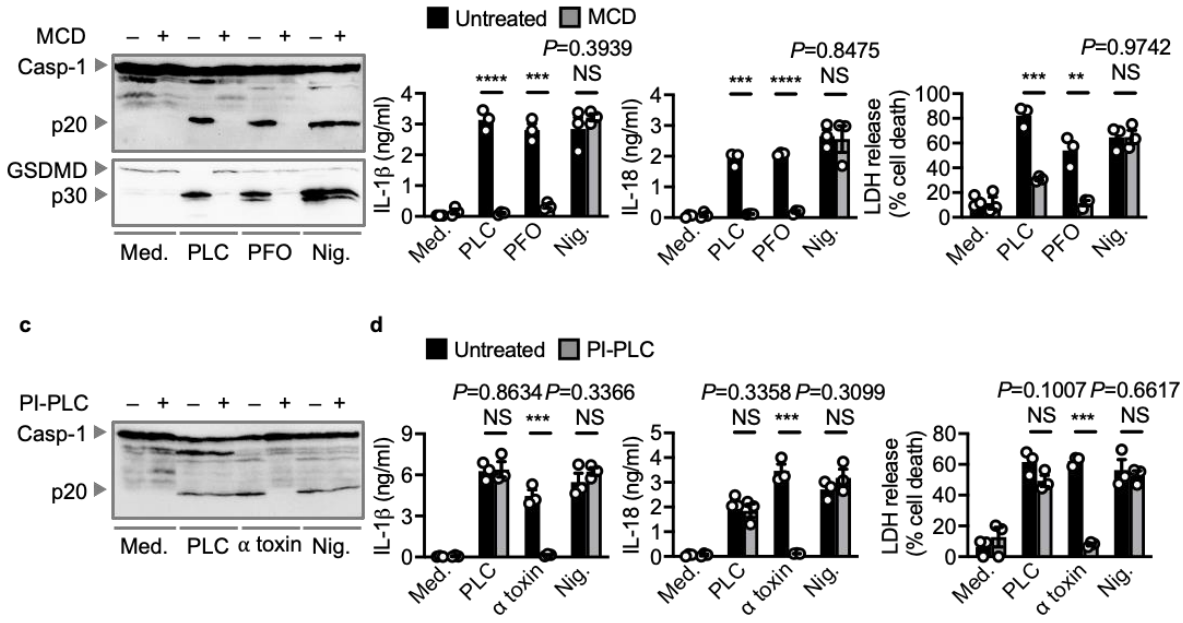

Figure 5.3 | PLC-mediated inflammasome activation requires cholesterol. (a) Immunoblot analysis of caspase-1 and GSDMD of unprimed or LPS-primed WT BMDMs left untreated (Med.) or assessed 3 hr after stimulation with PLC, or 3 hr after stimulation with PFO, or 30 mins after stimulation with nigericin (Nig.) in the absence or presence of methyl-β-cyclodextrin (MCD; 5 mM). (**b**) Release of IL-1β (left) and IL-18 (middle), and death (right) of

WT BMDMs after treatment as in (a). (**c**) Immunoblot analysis of caspase-1 and GSDMD of unprimed or LPS-primed WT BMDMs left untreated or assessed 3 hr after stimulation with PLC, or 3 hr after stimulation with α-toxin of *C. septicum*, or 30 mins after stimulation with nigericin (Nig.) in the absence or presence of phosphatidylinositol (PI)-specific phospholipase C (PI-PLC; 0.05 Units/ml). (**d**) Release of IL-1β (left) and IL-18 (middle), and death (right) of WT BMDMs after treatment as in (c). Each symbol represents an independent experiment (b, d, f). NS, not statistically significant. *$P < 0.05$, **$P < 0.01$, ***$P < 0.001$ and ****$P < 0.0001$ (two-tailed *t*-test [b, d, f]). Data are representative of three independent experiments (a-f; mean and s.e.m. in b, d, f).

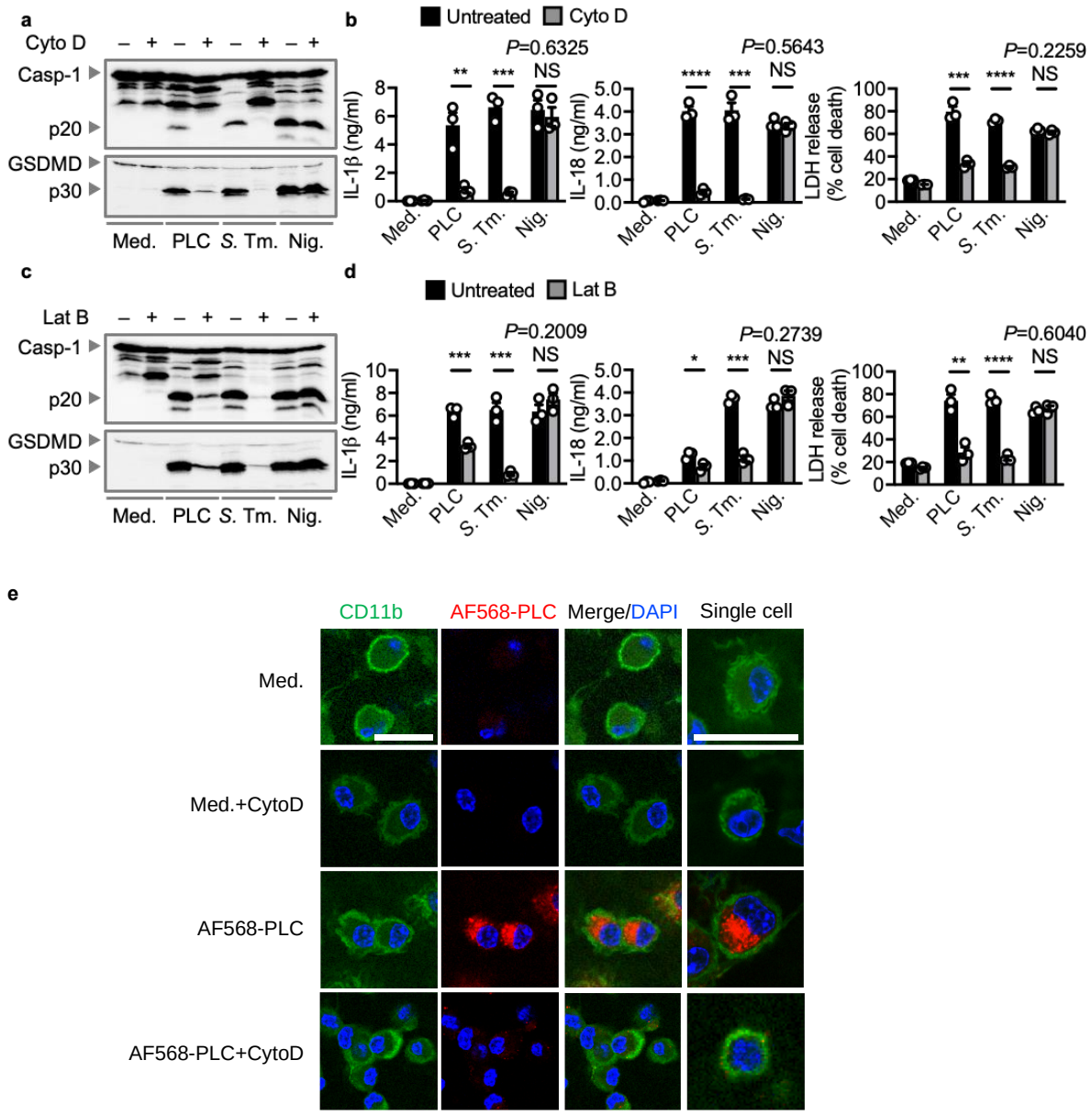

Figure 5.4 | PLC requires phagocytosis to induce inflammasome activation. a) Immunoblot analysis of caspase-1 and GSDMD of unprimed or LPS-primed WT BMDMs left untreated (Med.) or assessed 3 hr after stimulation with PLC, or 4 hr after infection with *S.* Typhimurium (*S.* Tm.; MOI, 5), or 30 mins after stimulation with nigericin (Nig.) in the absence or presence of cytochalasin D (CytoD; 50 μM). (**b**) Release of IL-1β (left) and IL-18 (middle), and death (right) of WT BMDMs after treatment as in (a). (**c**) Immunoblot analysis of caspase-1 and GSDMD of unprimed or LPS-primed WT BMDMs left untreated or assessed 3 hr after stimulation with PLC, or 4 hr after infection with *S.* Typhimurium (*S.* Tm.; MOI, 5), or 30 mins

after stimulation with nigericin (Nig.) in the absence or presence of latrunculin B (Lat B; 1 μg/ml). (**d**) Release of IL-1β (left) and IL-18 (middle), and death (right) of WT BMDMs after treatment as in (c). (**e**) Confocal microscopy analysis of CD11b (green) and PLC (red) in unprimed WT BMDMs left untreated or assessed 1 hr after stimulation with Alexa Fluor 568 PLC (AF568-PLC) in the absence or presence of cytochalasin D (CytoD; 50 μM). Scale bar, 25 μm (e, f). Each symbol represents an independent experiment (b, d, f). NS, not statistically significant. *P < 0.05, **P < 0.01, ***P < 0.001 and ****P < 0.0001 (two-tailed t-test [b, d, e, f]). Data are representative of two (e, f), or three independent experiments (a-d; mean and s.e.m. in b, d, f).

5.4.4 PLC localises to lysosome and induces lysosomal destabilisation to activate the NLRP3 inflammasome

Upon internalisation, endosomal compartments frequently fuse with lysosomes to enable degradation of extracellular molecules and pathogens [705]. Once localised within the lysosome, many molecules can cause damage to the lysosomal membrane. Indeed, lysosomal membrane rupture and release of lysosomal contents is a proposed activation mechanism of the NLRP3 inflammasome [680]. To investigate the dependence of the lysosome in PLC-mediated inflammasome activation, the dual lysosomal H^+ ATPase and phago-lysosomal fusion inhibitor bafilomycin A [706,707] was used. WT BMDMs treated with bafilomycin A did not undergo inflammasome activation in response to PLC (**Fig. 5.5a,b**). In contrast, nigericin-induced inflammasome activation was unaffected (**Fig. 5.5a,b**). Further, I observed that BMDMs treated with the weak base ammonium chloride (NH_4Cl), an inhibitor of phago-lysosomal fusion in macrophages [708], inhibited PLC-mediated inflammasome activation, whereas it had no effect on nigericin-mediated inflammasome activation (**Fig. 5.5c,d)**. Consistent with a previous report, *F. novicida*-induced inflammasome activation was impaired in presence of the ammonium chloride (**Fig. 5.5c,d)** [709]. Production of TNF was unaltered in

the presence of either bafilomycin A or ammonium chloride (**Appendices for Chapter 5 Fig. 5.5d,e**). Kinetic analysis of death of BMDMs caused by PLC was performed using IncuCyte analysis, demonstrating that cell death was impaired in the presence of both bafilomycin A and ammonium chloride (**Fig. 5.5e–g**).

To assess whether PLC induced lysosomal rupture, WT BMDM were loaded with acridine orange, a lysotrophic dye which preferentially accumulates in the acidic environment within the lysosome [710]. When lysosomal integrity is lost, the dye escapes into the cytoplasm which can be quantified via flow cytometry. I observed that WT BMDMs underwent a time-dependent increase in cytoplasmic acridine orange upon treatment with PLC, indicating that PLC causes lysosomal rupture (**Fig. 5.5h,i**; gating strategy represented in **Appendices for Chapter 5 Fig. 5.8c**). An increase in cytoplasmic acridine orange was observed in response to the known lysosomal disrupting agent LLOMe, which is also an activator of the NLRP3 inflammasome [711] (**Fig. 5.5h; Appendices for Chapter 5 Fig. 5.8a**). In addition, I observed similar levels of lysosomal disruption in WT and *Nlrp3*$^{-/-}$ BMDMs stimulated with PLC (**Fig. 5.5h,i; Appendices for Chapter 5 Fig. 5.8b**), demonstrating that lysosomal disruption occurs upstream of the activation of the NLRP3 inflammasome. Furthermore, a cathepsin B-specific inhibitor CA-074-Me [696] did not affect PLC-mediated inflammasome activation (**Appendices for Chapter 5 Fig. 5.8d**), suggesting that release of cathepsin B from the damaged lysosome does not affect PLC-induced inflammasome activation. These findings demonstrate that PLC disrupts the lysosomal integrity to induce activation of the NLRP3 inflammasome.

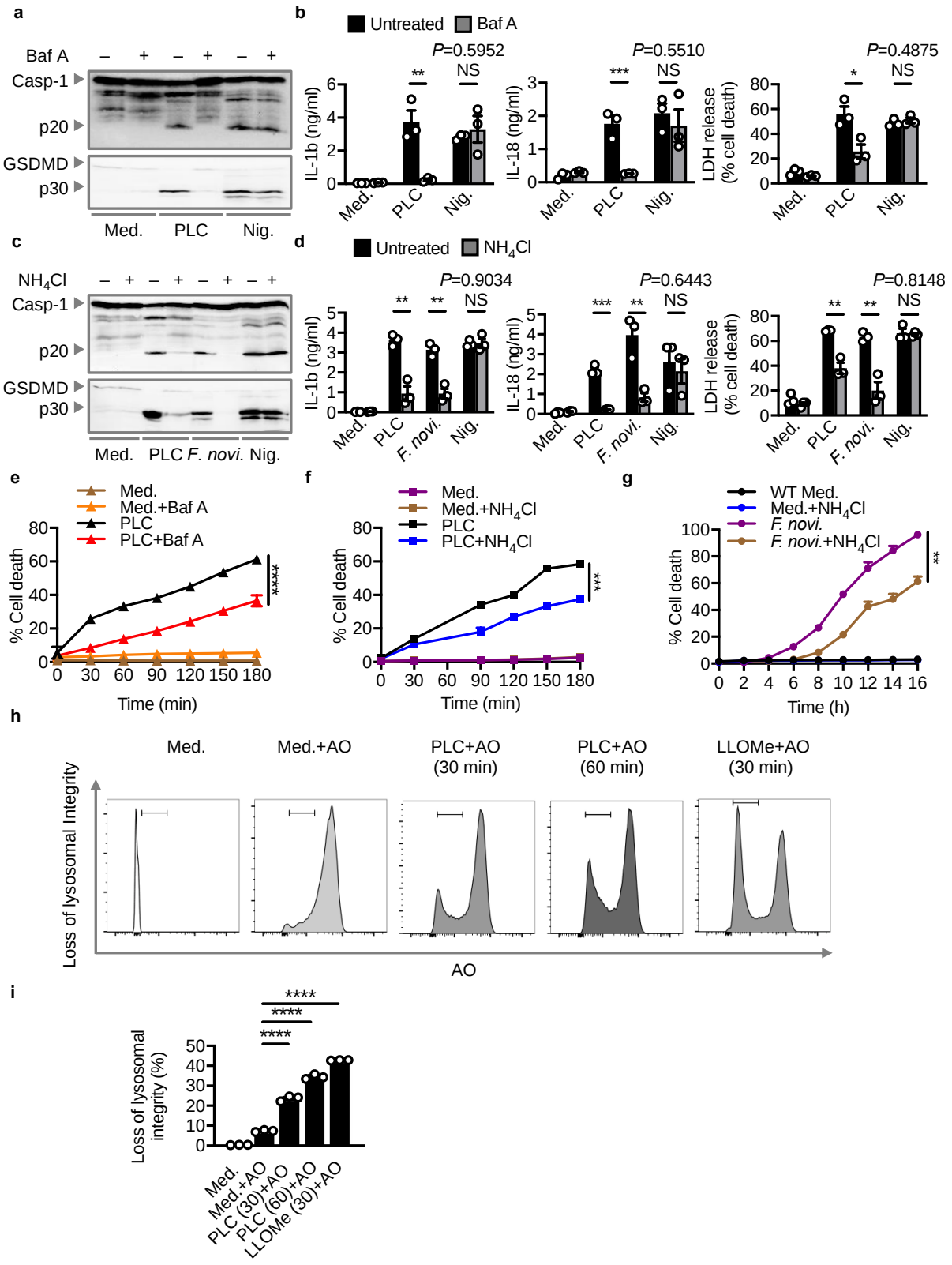

Figure 5.5 | Endo-lysosomal transport of PLC is required for activation of the NLRP3 inflammasome. (**a**) Immunoblot analysis of caspase-1 and GSDMD of unprimed or LPS-primed WT BMDMs left untreated (Med.) or assessed 3 hr after stimulation with PLC, or 30

mins after stimulation with nigericin (Nig.) in the absence or presence of bafilomycin A (Baf A; 100nM). (**b**) Release of IL-1β (left) and IL-18 (middle), and death (right) of WT BMDMs after treatment as in (a). (**c**) Immunoblot analysis of caspase-1 and GSDMD of unprimed or LPS-primed WT BMDMs left untreated or assessed 3 hr after stimulation with PLC, or 16 hr after infection with *F. novicida* (*F. novi.,* MOI 100), or 30 mins after stimulation with nigericin (Nig.) in the absence or presence of ammonium chloride (NH_4Cl; 20 μM). (**d**) Release of IL-1β (left) and IL-18 (middle), and death (right) of WT BMDMs after treatment as in (c). (**e**) IncuCyte live-imaging analysis of the viability of BMDMs after treatment as in (a). (**f,g**) IncuCyte live-imaging analysis of the viability of BMDMs after treatment as in (c). (**h,i**) Flow cytometry analysis of WT BMDMs that are unstained or stained with acridine orange (1μg/ml) and assessed 30 or 60 min after treatment with PLC or 30 min after treatment with LLOMe. Each symbol represents an independent experiment (b, d, e, f, g and i). NS, not statistically significant. *P < 0.05, **P < 0.01, ***P < 0.001 and ****P < 0.0001 (two-tailed *t*-test [b, d, e, f and g] or one-way analysis of variance [ANOVA] with Dunnett's multiple-comparisons test [i]). Data are representative of three independent experiments (a-i; mean and s.e.m. in b, d, e-g, i).

5.4.5 PLC activates the NLRP3 inflammasome via K^+ efflux downstream of lysosomal disruption

Unlike several inflammasome complexes which have a well-defined mechanism of activation, such as direct recognition of dsDNA by AIM2 [345-348] or N-terminal cleavage and degradation of NLRP1b [86,87], there is no consensus on a unified mechanism of activation of NLRP3. A proposed mechanism of NLRP3 activation is via K^+ efflux following plasma membrane disruption [712,713]. To determine whether PLC-mediated inflammasome activation required K^+ efflux, BMDMs were stimulated with PLC or ATP, and the intracellular K^+ concentration of BMDMs was determined using inductively coupled plasma optical emission spectrometry (ICP-OES). The intracellular K^+ concentration of BMDMs treated with either PLC or ATP

decreased to 39% and 47%, respectively, compared to untreated BMDMs set at 100% (**Fig. 5.6c**). Further, supplementation of extracellular KCl in the cell culture media dose-dependently inhibited PLC- or ATP-induced inflammasome activation (**Fig. 5.6a,b**).

To investigate whether K^+ efflux occurred downstream of PLC endocytosis and lysosomal disruption, intracellular K^+ concentration was measured in BMDMs stimulated with PLC in the presence of MCD, cytochalasin D, or bafilomycin A (**Fig. 5.3a,b; 5.4a,b; 5.5a–d**). MCD prevented a loss of intracellular K^+ in BMDMs stimulated with PLC, but not with nigericin (**Fig. 5.6d**). Cytochalasin D and bafilomycin A partially prevented a loss of intracellular K^+ in BMDMs stimulated with PLC (**Fig. 5.6d**). These results may suggest that cholesterol-mediated endocytosis of PLC followed by PLC-induced lysosomal disruption provides a signal leading to efflux of K^+, activating the NLRP3 sensor. The observation that MCD blocked a loss of intracellular K^+ in BMDMs stimulated with PLC is not surprising given that MCD substantially reduced binding of PLC to the plasma membrane. In contrast, cytochalasin D and bafilomycin A did not block attachment of PLC to the plasma membrane. Therefore, it is possible that PLC associated on the plasma membrane may have already caused a level of damage that is sufficient to trigger some K^+ efflux directly from the plasma membrane.

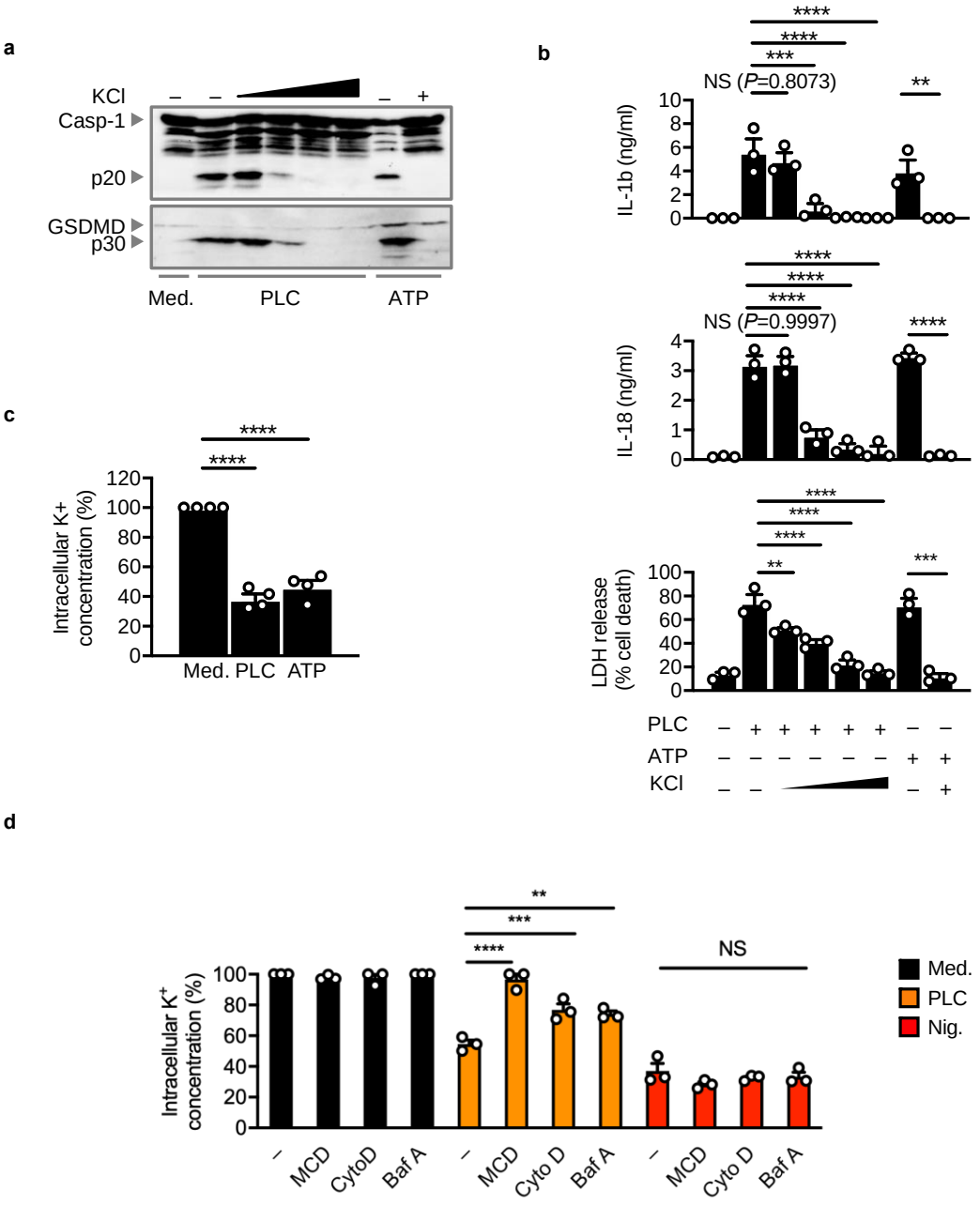

Figure 5.6 | PLC-mediated inflammasome activation is dependent on K^+ efflux. (**a**) Immunoblot analysis of caspase-1 in WT BMDMs left untreated (Med.) or assessed 3 hr after stimulation with PLC or 30 mins after stimulation with ATP in the absence (–) or presence (+ or wedge) of 50 mM KCl (+) or at increasing concentrations of KCl (wedge; 5, 25, 50 and 75 mM). (**b**) Release of IL-1β (top) and IL-18 (middle), and death (bottom) of WT BMDMs after treatment as in (a). (**c**) Inductively coupled plasma-optical emission spectrometry analysis of

intracellular concentrations of K^+ of BMDMs left untreated or assessed 2 hr after treatment with PLC, or 30 mins after treatment with LPS+ATP. (**d**) Inductively coupled plasma-optical emission spectrometry analysis of intracellular concentrations of K^+ of BMDMs left untreated or assessed 2 hr after treatment with PLC, or 30 mins after treatment with nigericin in absence (–) or presence of cytochalasin D (CytoD, 50μM), bafilomycin A (Baf A, 100nM) and methyl-β-cyclodextrin (MCD, 5mM). Each symbol represents an independent experiment (b-d). NS, not statistically significant. $^{**}P < 0.01$, $^{***}P < 0.001$ and $^{****}P < 0.0001$ (one-way analysis of variance [ANOVA] with Dunnett's multiple-comparisons test [b-d]). Data are representative of three independent experiments (a, b, d) or four independent experiments (c; mean and s.e.m. in b-d).

5.4.6 PLC incites inflammation *in vivo* via the NLRP3 inflammasome

The NLRP3 inflammasome is important in detecting toxins *in vivo*, either by exacerbating inflammation and causing lethal septic shock or by promoting host survival [680]. Given that PLC induces activation of the NLRP3 inflammasome in macrophages, I speculated that it might induce activation of the NLRP3 inflammasome in the host. To assess the role of the NLRP3 inflammasome pathway in response to PLC *in vivo*, I intraperitoneally injected PLC into WT, *Nlrp3*$^{-/-}$ and *Casp1*$^{-/-}$ mice. I observed that in response to PLC, WT mice produced elevated level of IL-18 in the serum, which was significantly reduced in *Nlrp3*$^{-/-}$ and *Casp1*$^{-/-}$ mice (**Fig. 5.7a**). Consistently, analysis of peritoneal fluid showed that *Nlrp3*$^{-/-}$ and *Casp1*$^{-/-}$ mice had a reduced level of IL-18 following administration of PLC compared to treated WT mice (**Fig. 5.7b**). These data suggest that PLC is sensed by the NLRP3 inflammasome *in vivo*.

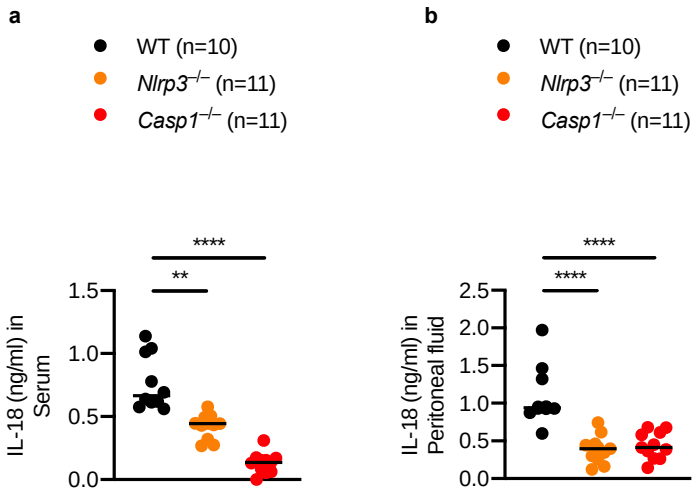

Figure 5.7 | PLC triggers inflammation *in vivo* via the NLRP3 inflammasome. (**a**) Concentration of IL-18 in the serum of WT mice (n = 10), *Nlrp3*$^{-/-}$ mice (n = 11), and *Casp1*$^{-/-}$ mice (n = 11), 4 hr after intraperitoneal administration of 0.625 Units/ml of PLC. (**b**) Concentration of IL-18 in the peritoneal fluid of mice treated as in (a). Each symbol represents an individual mouse (a, b). ***P* < 0.01 and *****P* < 0.0001 (one-way analysis of variance [ANOVA] with Dunnett's multiple-comparisons test [a and b]). Data are pooled from two independent experiments (a, b; mean and s.e.m. in a, b).

5.5 Discussion

Activation of the inflammasome is a key mechanism of host response to pathogens and danger signals. Many pathogens are recognised indirectly through their secreted toxins by inflammasome sensors. Indeed, three dedicated inflammasome sensor proteins, NLRP1b, NLRP3 and Pyrin, can detect the noxious effects of toxins [365,697]. However, despite their key role in innate immune recognition and pathogen dissemination, a complete atlas of toxins capable of driving inflammasome activation has remained elusive.

Following analysis of a panel of toxins from phylogenetically diverse organisms, the phospholipase PLC produced by the human bacterial pathogen *C. perfringens* was identified as an activator of the NLRP3 inflammasome. None of the remaining toxins induced inflammasome activation, challenging the paradigm that toxins can generally be sensed by inflammasome sensors [113,132,635,697,698,714]. Based on this finding, I propose that only a subset of toxins is sensed by inflammasomes in macrophages. Further, only toxins with unique structural and functional composition can elicit inflammasome activation. It is possible that this specificity enables the immune system to respond to the most damaging of toxins, without responding to any noxious insult and becoming overactivated.

The majority of bacterial toxins that activate the NLRP3 inflammasome are pore-forming toxins that bind to the plasma membrane and mediate K^+ efflux [673,697], however several enzymatic toxins which do not induce pore formation, such as *Mycoplasma pneumoniae* CARDS toxin and Shiga toxin, have also been reported to activate NLRP3 [715,716]. The identification of a phospholipase as an activator of the NLRP3 inflammasome represents a substantial departure from the prototypical bacterial pore-forming toxin as an activator of NLRP3.

Phospholipases and related sphingomyelinases are a heterogenous group of virulence factors produced by diverse pathogens, including bacteria, fungi and invertebrates [717-719]. Importantly, they are implicated in diseases caused by many clinically important pathogens, for example *S. aureus* β-toxin, *Listeria ivonovii* SmcL and fungal phospholipase Ds [718,720,721]. The identification of PLC highlights this class of toxins as potentially underappreciated PAMPs. Further work should investigate whether other phospholipases and/or sphingomyelinases can be similarly recognised by inflammasome sensors. This study also delineated a mechanism by which PLC-induced cellular perturbations is sensed by NLRP3. Unlike pore-forming toxins which emanate a signal directly from the plasma membrane to trigger K^+ efflux and subsequent NLRP3 activation, PLC accesses the lysosome to trigger NLRP3 activation. Several activators of NLRP3, such as asbestos and silica crystals [711,722], and endogenous

molecules including protein aggregates like circulating ASC specks or neuronal amyloid-β fibrils [723,724], have been described to follow a similar pathway of internalisation, endo-lysosomal trafficking and lysosomal membrane disruption, highlighting the sensory role of the lysosome in triggering NLRP3 activation.

It has been previously reported that lysosomal disruption occurs prior to K^+ efflux across the plasma membrane [712], a finding supported by this study. However, it remains unclear precisely how lysosomal permeabilisation leads to K^+ efflux and NLRP3 activation. One conceivable explanation is that the activator itself can escape the disrupted lysosome and damage the plasma membrane from the cytoplasmic side, increasing the permeability of the plasma membrane to K^+. Alternatively, lysosomal membrane permeabilisation may induce activation of K^+ channels that mediate K^+ efflux and NLRP3 activation. It is also possible that lysosomal rupture releases a pro-pyroptotic factor from within the lysosome into the cytoplasm and causes plasma membrane damage. These scenarios offer an explanation as to why GSDMD is not required for pyroptosis or IL-1β and IL-18 secretion triggered by PLC and other phagocytosed NLRP3 activators, such as platelet activating factor and silica crystals [262,263]. Future work investigating the link between the lysosomes, K^+ efflux and NLRP3 activation is required, and will deepen our understanding of the pathways that lead to NLRP3 activation, cell death and inflammation.

In conclusion, NLRP3 was identified as the cytosolic innate immune sensor for PLC. My work expands the growing repertoire of PAMPs that can be recognised by inflammasome sensors and defines a mechanism by which a phospholipase can be recognised by the mammalian innate immune system.

Chapter 6♦ Discussion

6.1 The knowns and unknowns about *B. cereus*

B. cereus mostly causes diarrhoea and vomiting owing to the presence of toxins such as HBL, NHE, CytK and cereulide [501]. Since the discovery of *B. cereus* in 1887, researchers have primarily focused on characterisation and detection of these toxins produced by *B. cereus,* which has led to the development of sensitive and rapid diagnostic tools [725]. However, how these toxins interact with the host immune system has remained largely unclear. Furthermore, the contribution of host-pathogen interactions in shaping the disease outcome during *B. cereus* infection, and whether the immune response is protective or detrimental to the host, are also largely elusive. This knowledge is essential because delineation of the molecular mechanisms underpinning host-pathogen interactions might guide the development of novel therapeutics in the treatment of *B. cereus* infection. Indeed, identification of gasdermin D as an executor of inflammasome pathways activated in response to LPS has led to the use of gasdermin D inhibitors against endotoxaemia in pre-clinical models. For example, a study has shown that the FDA-approved chemical inhibitor of gasdermin D called disulfiram, protected mice from LPS-induced lethality [279]. Given the crucial function of inflammasomes in providing immunity against infections, potential therapies that can modulate the activity of inflammasomes may help in the prevention and treatment of infections.

6.1.1 *B. cereus* toxins as activators of the inflammasome

My research identified that in primary mouse macrophages, human THP1 monocytes and mice, *B. cereus* initiated an innate immune response via the NLRP3 inflammasome. This response is triggered by two toxins called HBL and NHE (**Fig. 6.1**). Previous studies have characterised the function and disease-causing potential of HBL and NHE toxins [448,501,505,506,552], however the interaction of these toxins with the immune system has remained elusive until my studies. Previous studies have shown that 40-92% of the *B. cereus* strains were positive for HBL [458,564,565,673]. Indeed, analysis of 46 *B. cereus* strains revealed that the presence of HBL in these strains (42 out of 46 strains) is associated with inflammasome

activation in BMDMs, highlighting the importance of inflammasomes in host defence against prevalent bacterial virulence factors. I also provided genetic evidence to show that a *B. cereus* mutant strain lacking HBL failed to activate the NLRP3 inflammasome. The *B. cereus* mutant strain lacking HBL did not induce inflammation and cell death in macrophages, which is consistent with a previous study [508]. Further, recombinant HBL activated the NLRP3 inflammasome, demonstrating that HBL is a novel activator of the inflammasome.

Surprisingly, I observed that inflammasome activation ensued when BMDMs were infected with the *B. cereus* mutant strain lacking HBL for 20 hr. Using multiple experimental approaches, I found that the other inflammasome-activating factor of *B. cereus* being NHE. Analogous to HBL, recombinant NHE triggered activation of the NLRP3 inflammasome. HBL and NHE share structural functional and biochemical similarities [505,506,508,513,514], a characteristic which is targeted by the inflammasome pathway such that an inflammatory response against the two toxins is triggered.

Inflammasome activation culminates in pyroptosis and inflammation. Indeed, both HBL and NHE induced GSDMD-dependent pyroptosis and inflammation in BMDMs. Owing to the rapid inflammasome-activating potential of HBL, I reasoned that pyroptosis had occurred before the mammalian cells can sense NHE. Indeed, NHE-mediated inflammasome activation was only observed in BMDMs infected with a *B. cereus* strain lacking HBL, the supernatant of a *B. cereus* strain lacking HBL, or the supernatant neutralised with anti-HBL antibodies. Antibody-mediated neutralisation of HBL and NHE has been shown to inhibit cytotoxicity in various cell lines, such as macrophages, Vero monkey kidney epithelial cells, Chinese Hamster Ovary (CHO) epithelial cells, pluripotent stem cell (iPSC)-derived human cardiomyocytes, human epithelial and endothelial cell lines (A549, A204, CaCo-2, and Hep-G2 cells) [508,560,726]. Notably, antibody-mediated neutralisation of both the toxins prevented activation of an inflammasome response, suggesting that in mouse BMDMs, HBL and NHE may be the only activators of the inflammasome (**Fig. 6.1**).

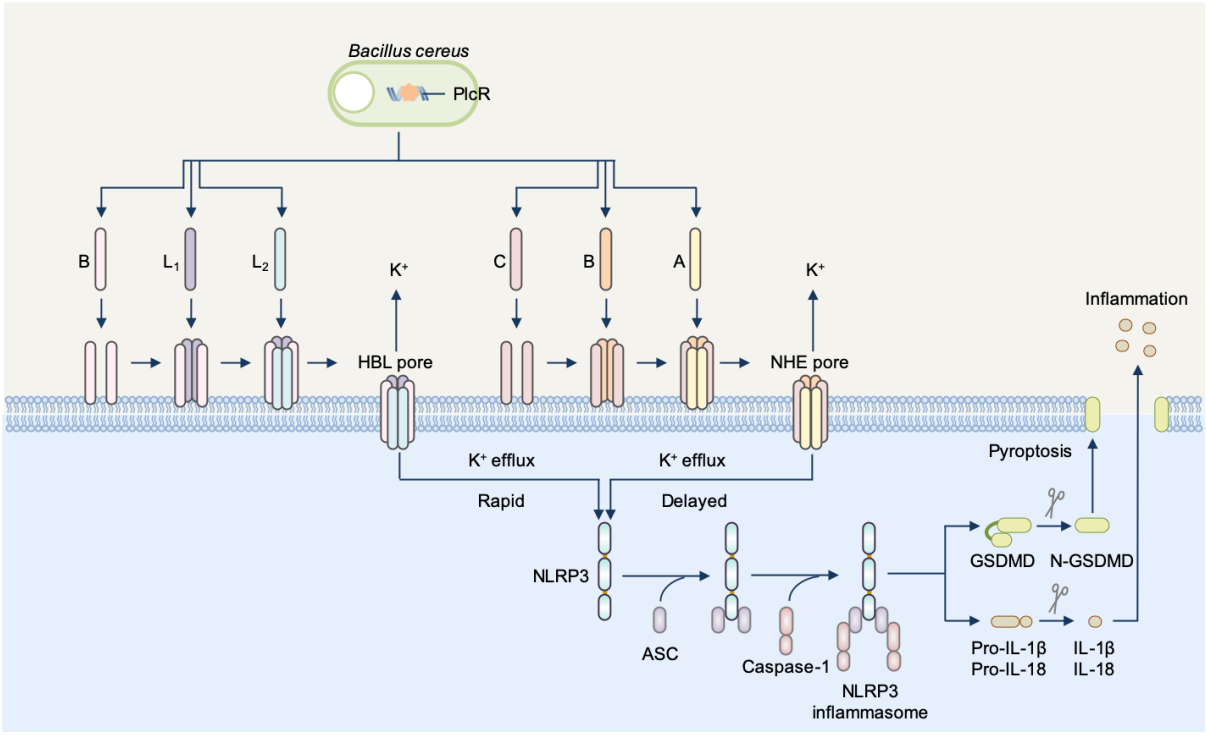

Figure 6.1: *B. cereus* toxins HBL and NHE elicit an immune response via the NLRP3 inflammasome.

6.1.2 Characterisation of HBL and NHE toxins

HBL and NHE belong to the α pore-forming toxin family [633]. Unlike other known members of this family, both HBL and NHE required all three subunits to form a functional pore. This study is the first to delineate the sequence of assembly of the three subunits of HBL and NHE on the plasma membrane of macrophages. The proposed binding sequence of HBL subunits is B, L_1 and L_2, whereas NHE subunits bind in the order of C, B and A (**Fig. 6.1**). Indeed, the proposed binding order of HBL was recently confirmed by another group [727]. These results differed to other studies showing that subunits of HBL and NHE can form complexes in solution [511,512]. The differences between my results and previously published results can be attributed to the variable experimental conditions, such as using different bacteria for protein production i.e., *E. coli* or *B. anthracis*, that may have induced different post-translational modifications and conformational changes in the subunits of HBL and NHE enabling protein-protein interactions in solution [508,510,512,728,729]. In addition, differences in techniques used to generate

recombinant toxins and assays used to determine the binding activity of the toxins may account for the variable results between studies [508,510,512,728,729].

Assembly of the HBL and NHE subunits on plasma membrane of macrophages can emanate signals to activate the NLRP3 inflammasome (**Fig. 6.1**). HBL is known to bind LITAF and CDIP1 on the cell surface [560] (**Fig. 1.10**). However, we and others have shown that HBL can induce pore formation in synthetic liposomes in the absence of cellular proteins, that is, protein receptors [507,670,701,729,730]. These conflicting data suggest that perhaps HBL does not always require a receptor to mediate pore formation and has receptor-dependent and receptor-independent modes of activity. Furthermore, previous studies predicted that both HBL and NHE pores are cation-selective and have a diameter of 1-2 nm and 5 nm, respectively [507,670,729]. Indeed, I found that both HBL and NHE pores were permissive to K^+ ions, leading to the generation of a K^+ efflux which was responsible for activating the NLRP3 inflammasome (**Fig. 6.1**).

6.1.3 Why does HBL activates the NLRP3 inflammasome more rapidly than NHE?

One of the most interesting findings arising from this thesis is the differential activation of the NLRP3 inflammasome by HBL and NHE toxins present in the supernatant of *B. cereus* (**Fig. 6.1**). HBL activates the inflammasome within 3 hr whereas NHE activates in 6 hr (**Appendices for Chapter 4 Fig. 4.2a,b**). Several possible reasons might explain this differential kinetics:

1. Bioavailability of the two toxins in the supernatant of *B. cereus*: It is possible that the bacterium secreted the two toxins in different amount [565]. The kinetics study was conducted in supernatant isolated from three different strains of *B. cereus*; in all three cases, HBL activated the inflammasome more rapidly than NHE (**Appendices for Chapter 4 Fig. 4.2c–e**). This data suggested that species-associated differences would be unlikely responsible for the differential inflammasome activation kinetics observed between HBL and NHE. However, further studies are required to quantify

the concentrations of HBL and NHE to verify whether the bacterium secreted more HBL than NHE.

2. Membrane binding: I attempted to assess whether there is differential kinetics in the membrane-binding ability of the two toxins [731]. I isolated the membrane and cytosolic fractions from BMDMs treated with the supernatant of *B. cereus* and the supernatant which has been neutralised with antibodies specific to HBL and NHE. However, due to the rapid killing activity of HBL, a clean fractionation of the two compartments was not obtained at the later timepoints.
3. Pore formation: Previous studies have estimated that the HBL pore size is 1-2 nm in diameter and the NHE pore size is 5 nm in diameter [507,670]. It is possible that due the large pore size of NHE, assembly of the individual subunits may require additional time and subunits. The smaller pore size of HBL may facilitate quicker assembly of the individual subunits [507,670]. To assess this possibility, a potential experimental setup could be to use liposomes encapsulated with a fluorescent dye or giant unilamellar vesicles and capture real-time loss of fluorescence due to pore formation by the toxins. This experiment will help understand if differences in pore formation between the two toxins is leading to the temporal difference in initiating an inflammasome response.
4. Generation of K^+ efflux: Recombinant HBL and NHE elicited K^+ efflux which triggers assembly of the NLRP3 inflammasome. In primary murine macrophages, HBL induced an average of 65.75% of K^+ efflux compared to untreated cells (**Appendices for Chapter 3 Fig. 3.10a**) whereas NHE induced an average of 44.65% of K^+ efflux compared to untreated cells (**Fig. 4.3g**). The difference in the level of K^+ efflux between HBL and NHE is unlikely to be the reason for the differential activation kinetics, because a baseline of 20-30% efflux of K^+ ions is sufficient to trigger activation of the NLRP3 sensor [665], and that both recombinant toxins were capable of exceeding this baseline to induce activation.
5. Potential structural differences in apical subunits: The HBL-B subunit lacking its hydrophobic transmembrane region (HBL-B_{mut}) exhibited stronger binding to the cell

membrane of primary mouse macrophages than the wildtype HBL-B subunit. A possible explanation is that deletion of this hydrophobic region in HBL-B might have stereochemically uncovered a putative binding site to the HBL receptors, LITAF and CIDP1. Interestingly, HBL-B_{mut} inhibited HBL-induced inflammasome activation. In contrast, NHE-C lacking the hydrophobic transmembrane region neither bound the plasma membrane nor activated the inflammasome. Indeed, a previous study also demonstrated that the C subunit NHE lacking its transmembrane region is unable to induce cell death in mammalian cell lines [510]. This observation highlights potential structural differences between the binding subunits of HBL and NHE, which might lead to differential kinetics of inflammasome activation [510].

6.1.4 Can additional virulence factors of *B. cereus* activate the inflammasome?

The best characterised virulence factors of *B. cereus* are HBL, NHE, CytK, and cereulide [501], however, *B. cereus* also produces a myriad of other virulence factors with poorly characterised or unknown function (**Table 6.1**). It is currently uncertain if or how these factors interact with the mammalian host innate immune system. The inflammasome-activating ability of different fractions of the supernatant of *B. cereus* shed light on the size of virulence factors that possess the potential to engage activation of the inflammasome pathway. Previous studies have reported that virulence factors of *B. cereus* other than HBL and NHE can induce cell death and inflammation [501,534,552,732-734]. In addition, my experiments demonstrated that secretory factors of *B. cereus* that are between 30kDa and 50kDa in size can activate the inflammasome. Based on results from previous studies [501,534,552,732,733] and my size-fractionation experiments, I hypothesise that other virulence factors of *B. cereus* can potentially activate the inflammasome. These virulence factors are as follows: Cytk, haemolysin II and III, phosphatidylinositol phospholipase C (PI-PLC), phospholipase C (PLC), sphingomyelinase, protease NprA, and flagellin (**Table 6.1).**

CytK belongs to the β pore-forming toxins superfamily [501]. Certain members of the β pore-forming cytotoxins, such as α-haemolysin of *S. aureus* [636], aerolysin from *Aeromonas* spp. [735,736], and pneumolysin of *S. pneumoniae* [686], have been shown to activate the NLRP3 inflammasome in mouse and human monocyte-derived cells. Indeed, bioinformatic analysis revealed that CytK bears a 30% amino-acid sequence identity with α-haemolysin of *S. aureus* [634,653], suggesting that CytK may activate the NLRP3 inflammasome.

Additional inflammasome-activating candidates of *B. cereus* which fall in the size range include haemolysin II and III, proteases, phosphatidylinositol phospholipase C, sphingomyelinase and flagellin. Of these virulence factors, a previous study found that haemolysin II can induce caspase-3- and caspase-8-dependent apoptosis in the J774 macrophage cell line. Given that caspase-8 can mediate inflammasome activation [536,737], purified haemolysin II should be tested in mouse primary macrophages and human monocytes to assess its inflammasome-activating ability.

Haemolysin III is the least characterised haemolysin of *B. cereus* and further studies are needed to assess its function in the physiology of the bacterium and its role in interacting with the host. In addition, *B. cereus* also harbours two metalloproteases called InhA1 and NprA which are predicted to bear nucleic acid similarity with proteases from *B. anthracis* and *B. thuringiensis* [545-547]. InhA1 and NprA metalloproteases mediate immune evasion of *B. cereus* spores [545-547]. Due to evolutionary pressure, it is possible that an innate immune response has been developed against these metalloproteases. Indeed, *B. anthracis* lethal factor, a zinc metalloprotease, is an activator of the mouse NLRP1b inflammasome [73], suggesting that proteases of *B. cereus* may also activate the inflammasome. Furthermore, with identification of PLC of *C. perfringens* as a novel activator of inflammasome, it is reasonable to speculate that PLC, PI-PLC and sphingomyelinase of *B. cereus* may be capable of inducing an inflammasome response.

Interestingly, *B. cereus* harbours peritrichous flagella for motility and nutrient acquisition, however, the ability of its flagella to initiate an immune response is disputed. Bacterial flagellin binds TLR5 on the cell surface and the NAIPs in the cytosol. Structural studies have demonstrated that both the D1 and D0 domains of flagellin from *Salmonella* interacted with TLR5 [738-740]; whereas only the D0 domain of flagellin was required to make the first contact with mouse NAIP5 [741]. Crystallographic analysis of the flagellin from *B. cereus* (PDB ID 5Z7Q) has revealed the presence of D0 and D1 domains [742], suggesting the possibility of interactions with TLR5 and mouse NAIP5. Indeed, cytosolic delivery of flagellin from *B. subtilis* can activate the NLRC4 inflammasome in peritoneal macrophages [743]. Therefore, transfection of purified flagellin of *B. cereus* into mouse BMDMs and human monocytes can be conducted to test the hypothesis that flagellin is an activator of the NAIP-NLRC4 inflammasome.

6.1.5 Exploring the physiological relevance of the NLRP3 inflammasome during *B. cereus* infection

My work has shown that *B. cereus* infection induced inflammation and caused lethality in mice via the NLRP3 inflammasome. Furthermore, HBL and NHE synergistically drove inflammasome-dependent inflammation in mice. Inflammation associated with the presence of NHE required NLRP3, Caspase-1 and GSDMD. However, NLRP3-driven lethality by *B. cereus* was predominantly attributed to the presence of HBL. Indeed, administration of the NLRP3 inhibitor MCC950, completely rescued mice from *B. cereus*-mediated lethality and prevented IL-18 release. Similar results were observed in other models of infection, such as influenza A virus [744] and helminth nematode *Trichuris muris* [745], where MCC950 potently inhibited deleterious activation of the NLRP3 inflammasome. In my study, mice were administered with two doses of MCC950; one dose was given before *B. cereus* infection and one dose was given at the same time as the bacterial infection. Another approach would be to administer MCC950 only after the onset of symptoms caused by *B. cereus* infection, to assess whether inhibition of NLRP3 could rescue mice from lethality in this scenario. Previous

studies have reported that during pathogen-driven host lethality, inflammasome-induced inflammation and pyroptosis may exert detrimental or protective effects on host survival [62,233,745-747]. For example, in response to *Salmonella* Typhimurium infection, IL-18-driven overt inflammation resulted in rapid lethality of mice [745]. In contrast, IL-18-driven inflammation resulted in protection of mice from lethality induced by *Burkholderia thailandensis* [233]. Additionally, GSDMD-dependent pyroptosis protected mice from lethality induced by *B. thailandensis* [747]. Given the potentially contrasting functions of inflammation and pyroptosis during infection *in vivo*, it will be interesting to investigate whether *B. cereus*-mediated lethality of mice is driven by IL-1β- and/or IL-18-mediated inflammation or by pyroptosis. This question can be addressed by comparing the susceptibility of WT mice against mice lacking IL-18, IL-1β, and GSDMD to *B. cereus* infection.

B. cereus induces gastroenteritis in humans. To mimic *B. cereus*-induced gastroenteritis, spores and vegetative forms of *B. cereus* can be administered to mice via the oral-gastrointestinal route. This model can be applied to WT mice, mice lacking various components of the NLRP3 inflammasome, or mice lacking IL-1β and/or IL-18 to study the inflammatory and survival outcomes. Notably, in intestinal colonisation of the *S.* Typhimurium, inflammasome responses have led to a reduction in bacterial load and elimination of the infection through secretion of IL-1β and IL-18 [746].

Furthermore, strain-specific inflammasome responses have been shown in mouse models of infection. For example, inflammasome-mediated inflammation can be protective in response to a less virulent strain of influenza A virus [749,750], whereas the inflammation can be deleterious in response to a more pathogenic strain of influenza A virus [751-753]. In my study, two *B. cereus* strains were used (ATCC 14579 and ATCC 10876) to infect mice to ensure that the observed *B. cereus*-induced inflammasome response is not specific to only one strain. Importantly, both strains of *B. cereus* induced overt inflammation through activation of the NLRP3 inflammasome. The *in vivo* results presented in this thesis identified a role of inflammasomes

in shaping the inflammatory landscape during *B. cereus* infection. Also, these findings highlight the advantage of using therapies directed to modulate the host immune system in the prevention and treatment of bacterial infections.

6.2 Comparison between *B. cereus*- and *B. anthracis*-induced inflammasome activation

In contrast to *B. cereus*-induced NLRP3 inflammasome activation, the phylogenetic relative *B. anthracis* activates the NLRP1b inflammasome [73] (**Figs. 1.1 and 6.1**). Despite the phylogenetic similarity between *B. cereus* and *B. anthracis,* both bacteria have diverged in how they use toxins to interact with the host innate immune system. *B. anthracis* deploys a metalloprotease lethal factor in the cytosol to mediate cleavage of NLRP1b, resulting in formation of the NLRP1b inflammasome [65,66]. In contrast, *B. cereus* secretes the pore-forming toxins HBL and NHE to induce potassium efflux to activate the NLRP3 inflammasome without requiring cytosolic entry. The toxins secreted by *B. cereus* and *B. anthracis* ultimately lead to the death of immune cells which could have been evolutionarily selected by the two bacteria for acquiring nutrients and increase bacterial replication. However, we now know that this toxin-associated strategy is counteracted by the potent and robust activation of the inflammasome triggering inflammation as a defence mechanism. Thus, innate immune defence against *B. cereus* and *B. anthracis* requires the innate immune system to recognise unique virulence factors with varied functional and biochemical properties to trigger an inflammasome-dependent inflammatory response against phylogenetically similar pathogens.

6.3 A bacterial phospholipase activates the inflammasome

PLC of *C. perfringens* is one of the primary virulence factors responsible in causing myonecrosis or gas-gangrene disease in humans. However, no studies have investigated the innate immune response generated against PLC. Thus, identification of PLC as an activator of the inflammasome in mouse macrophages, human monocytes and macrophages and in mice, has important biological implications, such as identification of other bacterial phospholipases capable of driving inflammasome activation.

Indeed, another phospholipase named phospholipase A2, a component of bee venom, was used in the screening experiment. Consistent with a previous study [754], phospholipase A2 did not activate the inflammasome, suggesting that key differences between PLC and other phospholipases may be responsible for activation of the inflammasome pathway. Structural analysis has revealed that PLC of *C. perfringens* and γ toxin of *Clostridium novyi* contain two domains whereas PLC of *B. cereus* and *L. monocytogenes* contains one domain [755,756]. PLC and γ toxin contain an extra C-terminal domain which may facilitate membrane binding of these toxins, and hence could enable activation of the inflammasome pathway [757]. Examination of residues in the C-terminal domain of PLC using mutagenesis will provide insights into how PLC of *C. perfringens* induces cytotoxicity and inflammasome responses. This information might inform the development of novel therapeutics to inhibit PLC and restrict the severity of *C. perfringens* infection.

6.3.1 PLC requires cytosolic access and endo-lysosomal rupture to activate the NLRP3 inflammasome

Owing to the phospholipase and sphingomyelinase activity of PLC, I hypothesised that PLC-induced hydrolysis of membrane-bound lipids will lead to a loss of plasma membrane integrity, and thereby, inducing K^+ efflux to activate the NLRP3 inflammasome. Unlike HBL and NHE, PLC required cytosolic access to induce K^+ efflux and activation of the NLRP3 inflammasome.

This observation is unique because the majority of NLRP3-activating toxins assemble on the plasma membrane to induce K^+ efflux. My work in determining the steps involved in the endo-lysosomal pathway uncovered some distinct features of PLC-induced inflammasome activation.

The receptor of PLC is called GM1a ganglioside receptor [702]. The contribution of GM1a in mediating PLC-induced inflammasome activation remains unknown and can be studied by stimulating *GalNAcT*$^{-/-}$ [702] BMDMs with PLC and assessed for hallmarks of inflammasome activation. Based on the mammalian cell type, endocytosis of PLC can occur in a receptor-dependent [702] or -independent manner [758]. Whilst my data indicated that PLC was endocytosed, they did not reveal whether GM1a was required to mediate this process in BMDMs. This question can be answered by testing the cytosolic presence of PLC in *GalNAcT*$^{-/-}$ BMDMs. Mechanistically, endosomes carrying the ligand-receptor complex transits into the sorting stage of the endosome by creating an acidic environment to facilitate dissociation of the ligand from the receptor [759]. Indeed, endosomal acidification was necessary to mediate PLC-induced activation of the inflammasome, suggesting a scenario that receptor-mediated endocytosis of PLC might be occurring in BMDMs. However, further experiments are necessary to dissect the role of GM1a in the endocytosis of PLC and subsequent inflammasome activation.

My results indicated that PLC-induced lysosomal rupture leads to the activation of the NLRP3 inflammasome. Given that the lysosomal membrane is rich in phospholipids, the enzymatic activity of PLC might be responsible for driving the observed lysosomal rupture in BMDMs. The mechanisms through which lysosomal rupture activates the NLRP3 inflammasome remains debatable. However, it is proposed that NLRP3 senses either the release of lysosomal proteins such as cathepsins, or lysosomal rupture-induced K^+ efflux [760]. My data suggest that the latter model is more likely, where lysosomal rupture is in part regulating K^+ efflux. Findings from the use of the cathepsin B-specific inhibitor, CA-074-Me, indicated that

the release of cathepsin B from the damaged lysosomes was dispensable for PLC-induced activation of the NLRP3 inflammasome. Some possible mechanisms through which lysosomal rupture partially regulate PLC-induced K^+ efflux are listed below.

A compelling possibility is that lysosomal membrane damage executed by PLC will facilitate the leakage of PLC from lysosome to cytosol. In the cytosol, PLC can damage the inner leaflet of the plasma membrane [592], leading to membrane lesions that can induce K^+ efflux. Alternatively, PLC can activate specific ion channels associated with either the plasma membrane or lysosome to permeate K^+ ion movement. Indeed, several K^+ channels apart from P2X7 have been implicated in mediating K^+ efflux to trigger activation of the NLRP3 inflammasome, such as TWIK2 [135], P2X4 [761], K^+ voltage-gated channel Kv1.3 [762], KCNB2 [763], K^+ inwardly rectifying channel KCNJ3 [763], K^+-Ca^{2+}-activated channel subfamily M alpha 1 [763], K^+ intermediate/small conductance calcium-activated channel [763], and subfamily N, member 4 (KCNN4) [763]. A suspected crosstalk between TWIK2 and lysosomes has been put forward where recombinant TWIK2 is localised to the lysosome. TWIK2 spawned weak background K^+ currents, which in principle, can initiate movement of K^+ from cytosol to lysosomal lumen that could trigger activation of NLRP3 [764]. In addition, the P2X4 receptor localises on lysosomes [765,766]. Interestingly, P2X4 has been shown to shuttle between the lysosome and plasma membrane to interact with surface P2X7 receptor in rat microglia and mouse BMDMs [765,766]. However, to test the role of these K^+ channels in PLC-mediated inflammasome activation, pharmacological inhibitors and genetic ablation of these channels in human and/or mouse cells may be necessary.

6.3.2 PLC induces GSDMD independent secretion of cytokines and LDH

Another striking finding in this thesis is that PLC-treated BMDMs underwent GSDMD-independent pyroptosis (**Fig 5.2**). Pyroptosis is defined as a sequential process composed of two prominent steps [767]. In the first step, small-size pores (e.g. GSDMD pores) are formed to mediate the secretion of cytokines such as IL-1β and IL-18. In the second step, plasma

membrane rupture is required to release large cytosolic molecules such as LDH, leading to cell lysis. A transmembrane protein called NINJ1 induces plasma membrane rupture in BMDMs in response to cytosolic LPS and nigericin [768]. Therefore, a mechanism in driving the secretion of IL-1β and IL-18 and a mechanism for the release of LDH can now be defined.

Several models might explain the mechanisms of GSDMD-independent secretion of IL-1β and IL-18 from PLC-treated BMDMs. First consideration is that other members of the gasdermin family such as GSDMA or GSDME may get activated in GSDMD-deficient cells to induce the secretion of IL-1β and IL-18 from PLC-treated BMDMs. Previous studies have shown that the N-terminal domains of mouse GSDMA3 and human GSDMA can bind membrane lipids and form gasdermin pores similar to that of GSDMD [769,770]. Indeed, cleavage of GSDMA and GSDME by caspases has been reported [267]. For example, caspase-3 cleaves GSDME [771,772] to induce pyroptosis instead of apoptosis in melanoma cancer cells, breast cancer and colorectal tumours [773]. Further, the pyroptosis-inducing capability of GSDMA3 was used to exert anti-tumour effects in 4T1 mammary tumour [774]. Whether GSDMA and GSDME mediate PLC-induced secretion of IL-1β and IL-18 remains to be determined. Additionally, formation of PIP2 membrane microdomains in GSDMD-deficient BMDMs has been observed to facilitate movement of IL-1β through its polybasic motif [775]. Further investigation is required to assess if this mechanism is functional in response to PLC.

Several models could be considered to explain GSDMD-independent LDH release. Firstly, the role of NINJ1 should be tested in mediating PLC-induced plasma membrane rupture and LDH release. In case NINJ1 is not required for inducing plasma membrane rupture in response to PLC, it might be considered that intracellular PLC can induce plasma membrane rupture through its enzymatic activity [776]. To ascertain whether membrane permeabilisation by PLC is the reason for GSDMD-independent pyroptosis, BMDMs can be treated with PLC in the presence of cytoprotectant glycine followed by quantification of LDH. In addition, a membrane permeabilisation blocker punicalagin has been suggested to inhibit IL-1β and LDH secretion

in response to ATP stimulation [777]. It may be worthwhile to investigate if punicalagin can regulate membrane permeabilisation of BMDMs in response to PLC stimulation.

6.4 Comparison of inflammasome activation induced by pore-forming toxins versus enzymatic toxins

My work has shown that pore-forming toxins HBL and NHE activated the NLRP3 inflammasome in BMDMs. HBL and NHE pores were responsible for outward movement of intracellular K^+ which is sensed by NLRP3 (**Fig. 6.2**). PLC, an enzymatic toxin, induced lysosomal rupture and triggered K^+ efflux to activate the NLRP3 inflammasome (**Fig. 6.2**). Analogous to HBL and NHE, PLC also required binding to the mammalian plasma membrane to induce K^+ efflux, however, subsequent processes of the endo-lysosomal pathway partially contributed to K^+ efflux. A key difference between the two categories of toxins is that HBL and NHE could emanate inflammasome-activating signals from the cell surface, whereas PLC required endocytosis to activate the inflammasome (**Fig. 6.2**).

In addition, all three toxins induced caspase-1-mediated cleavage of GSDMD, however there was a difference in the dependency on GSDMD in inducing pyroptosis. In the case of HBL and NHE, GSDMD was required to mediate extracellular release of IL-1β, IL-18 and LDH, whereas in the case of PLC, GSDMD was not required for this function. Similarly, activators which require the endo-lysosomal pathway to activate NLRP3, such as uric acid crystals, alum, silica and platelet-activating factor, induce the secretion of IL-1β independently of GSDMD [262,263]. These observations suggest that in the case of NLRP3 activators utilising the endo-lysosomal pathway, an unknown substrate associated with either the endosome or lysosome may regulate cell death and inflammation. However, further experiments are required to validate this hypothesis.

This study provided a mechanistic insight into the inflammasome-activating ability of pore-forming and enzymatic toxins (**Fig. 6.2**). Despite the differences in modes of action, both types of toxins induced K^+ efflux. Indeed, K^+ efflux has emerged as the converging signal for activation of the NLRP3 inflammasome [665]. Moreover, my research highlighted the ability of NLRP3 to detect structurally and functionally diverse toxins.

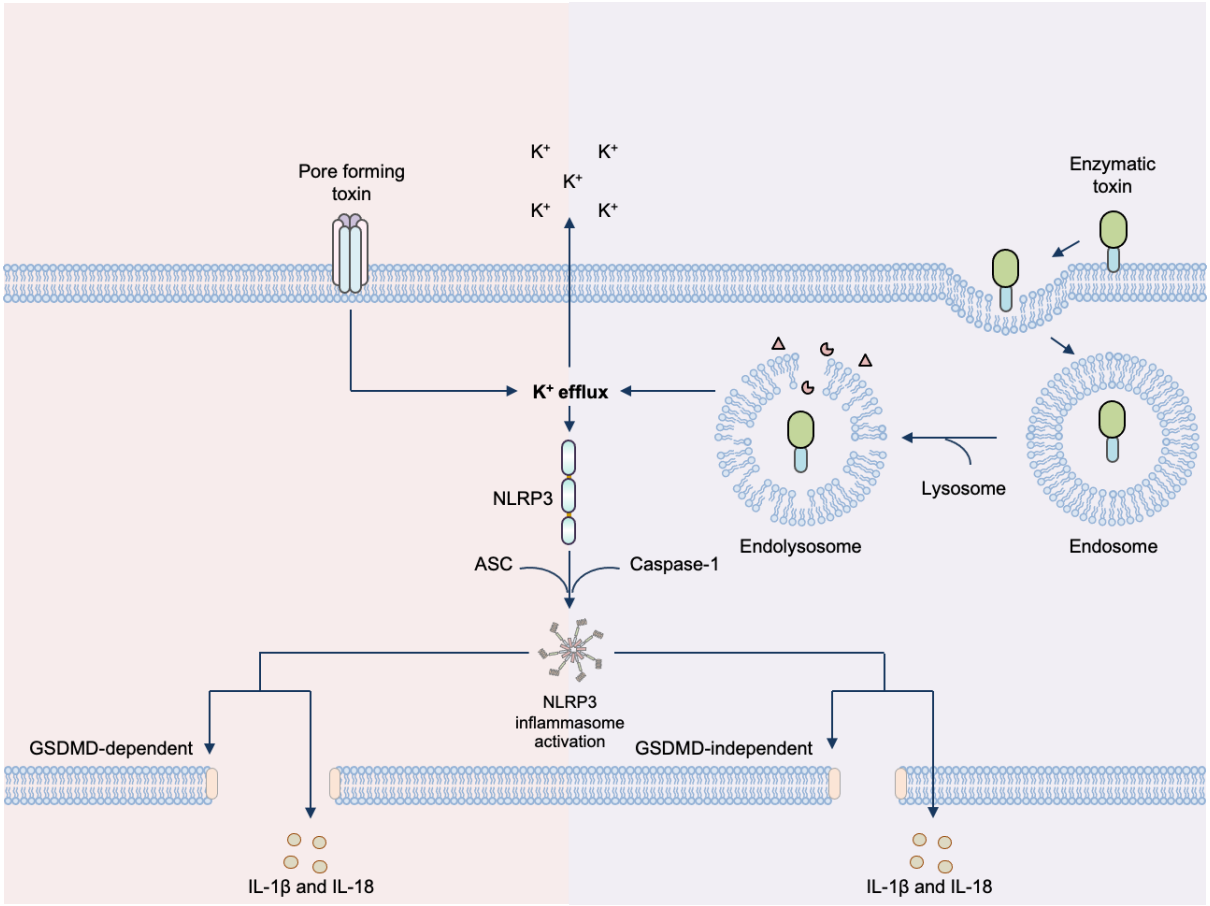

Figure 6.2: Comparison between the mechanisms of NLRP3 inflammasome activation by pore-forming and enzymatic toxins.

6.5 Potential therapeutic relevance

Infectious diseases are a major health burden in many countries. According to the 2020 WHO report, infectious diseases results in 14.2 million deaths each year worldwide [778]. Antibiotics

are the first line of treatment against bacterial infection. However, the misuse of antibiotics in clinical and agricultural practices has resulted in a significant rise in resistance. The United Nations reports that antimicrobial resistance will push 24 million people into extreme poverty by 2030, and that drug-resistant infections will kill 10 million people annually by 2050 if no immediate action is taken.

Indeed, there is a growing incidence of acquisition of antibiotic resistance in *B. cereus*. Studies have shown that multiple *B. cereus* isolates express the β-lactamase enzyme [476] which can counter the effects of β-lactam antibiotics, such as penicillin, ampicillin, and cefotaxime [449,477]. Similarly, the presence of plasmid-derived and mobile antibiotic-resistance elements have been identified from *C. perfringens* isolates [779]. To combat antibiotic-resistant infections, an alternative and exciting avenue is to develop therapies targeting either virulence factor/s such as disease-causing toxins or host processes such as immune responses. Such alternative therapies may complement the current antimicrobials used in the treatment of antibiotic-resistant infections [499].

6.5.1 Anti-toxin directed therapies

My results indicate that HBL, NHE and PLC induce inflammation in mice via the NLRP3 inflammasome. I demonstrated that neutralising antibodies against HBL and NHE led to impairment of inflammation and cytotoxicity induced by these toxins in BMDMs and mice, suggesting that anti-toxin antibodies may also be effective in humans. Indeed, FDA has approved three anti-toxin biologics, including the polyclonal anthrax immune globulin antibody; monoclonal Raxibacumab antibody; and monoclonal ETI-204 antibody [780]. The effectiveness of anti-toxin antibodies in experimental animal models and clinical trials has led to clinical development of multiple biologics. Examples of anti-toxin antibodies which are under clinical trials include antibodies targeting the *S. aureus* alpha-toxin and five leucocidin toxins, Psl and PcrV, and *E. coli* shiga toxin type 2 [781]. Given the disease-causing potential of HBL, NHE and PLC, biologics targeting these toxins could be an avenue for future research.

6.5.2 Host-directed therapies

Toxins usually require one or more surface receptors to initiate attachment to the host cell membrane. The surface receptors of HBL are LITAF and CIDP1 [560], whereas the surface receptor of PLC is GM1a [702]. Indeed, genetic deficiency of these receptors protected mice from toxin-mediated lethality [560,702]. Similarly, genetic deficiency and therapeutic targeting of the anthrax receptors protected rats from rapid mortality induced by lethal toxin [782]. Owing to the success of biologics targeting the anthrax receptors in the resolution of the disease, it is reasonable to hypothesise that antibody-mediated or small molecule-mediated pharmacological blockade of toxin receptors represents an effective treatment strategy.

Due to the important role of inflammasomes in maintaining health and immunity in the mammalian host, therapies targeting the inflammasomes are under development. The first FDA-approved biologic targeting the inflammasome pathway was against the IL-1 family of cytokines and receptors [783]. These biologics are effective in dampening autoinflammatory pathologies, including CAPS, rheumatoid arthritis, and FMF [783]. Following the success of anti-IL-1 biologics, multiple experimental and clinical studies have identified inhibitors targeting inflammasome sensors such as NLRP3 [680], caspase-1 [784] and GSDMD [279,280]. From these NLRP3-inhibitors, MCC950 has emerged as a promising candidate dampening NLRP3-driven chronic inflammatory disorders such as CAPS, Parkinson's disease and diabetes [680]. Owing to the success of using MCC950 in the treatment of different immunopathologies, a phase II clinical trial is ongoing to assess the safety of MCC950 in the treatment of Parkinson's disease [223]. My data contributes to the rising role of MCC950 in the treatment and prevention of NLRP3-driven overt inflammation during bacterial infections.

6.6 Conclusion and Future Directions

This thesis has shown that a single inflammasome sensor is capable of mounting an inflammatory response against structurally and functionally similar or diverse toxins. I also demonstrated that therapeutic modulation of the inflammasome pathway is beneficial in the treatment and prevention of deadly bacterial diseases in mice. Overall, this thesis has: **(i)** enhanced scientific knowledge of clinically important human pathogens; **(ii)** provided insights into the biology of cell-killing toxins; **(iii)** identified toxin components involved in cell death and inflammation; **(iv)** expanded the growing collection of inflammasome activators. Findings from the current study may advance translational research to benefit patients that may be allergic to certain antibiotics, are immunocompromised, or are infected with antibiotic-resistant pathogens. Future studies can investigate the genetic profile of patients suffering from foodborne illness, sepsis, and extra-gastrointestinal infections to understand the genetic correlation of the immune sensors to prognosis of the disease; ultimately improving disease management and treatment options.

Table 6.1 List of virulence factors *B. cereus*

Virulence factor	Size (kDa)	Mechanism	Original Reference
Emetic Toxin			
Cereulide	15	Acts like an ionophore, interrupts mitochondrial oxidative phosphorylation and metabolism of fatty acids.	[524]
Haemolysin			
Haemolysin BL (HBL)	38-49	α-pore-forming tripartite toxin.	[785]
Haemolysin I (Cereolysin O)	50-80	Poorly characterised, cytotoxicity of retinal, cardio and pulmonary tissues have been reported.	[505]
Haemolysin II	42.6	β-pore-forming toxin.	[786]
Haemolysin III	24.4	Poorly characterised, possesses predicted transmembrane regions.	[787]
Haemolysin IV (Cytotoxin K)	34	β-pore-forming toxin.	[653]
Non-haemolytic enterotoxin (NHE)	36-41	α-pore-forming tripartite toxin, may be capable of forming a β-pore.	[506]
Phospholipase			
Phosphatidylcholine-preferring Phospholipase C (PC-PLC)	29.9	Hydrolyses phosphatidylcholine, phosphatidylethanolamine and phosphatidylserine.	[788]
Phosphatidylinositol Phospholipase C (PI-PLC)	37-40	Hydrolyses phosphatidylinositol.	[558]
Sphingomyelinase (SMase)	34.2	Hydrolyses sphingomyelin.	[788]
Protease			
InhA	75	Degrades antimicrobial peptides and host tissue components; are major components of *B. cereus* endospores.	[789]
NprA	35	Degrades host tissue components.	[790]

References

1. Takeuchi, O. & Akira, S. Pattern recognition receptors and inflammation. *Cell* **140**, 805-820 (2010).
2. Cao, X. Self-regulation and cross-regulation of pattern-recognition receptor signalling in health and disease. *Nat Rev Immunol* **16**, 35-50 (2016).
3. Zindel, J. & Kubes, P. DAMPs, PAMPs, and LAMPs in Immunity and Sterile Inflammation. *Annu Rev Pathol* **15**, 493-518 (2020).
4. Fitzgerald, K.A. & Kagan, J.C. Toll-like Receptors and the Control of Immunity. *Cell* **180**, 1044-1066 (2020).
5. Dambuza, I.M. & Brown, G.D. C-type lectins in immunity: recent developments. *Curr Opin Immunol* **32**, 21-27 (2015).
6. Philpott, D.J., Sorbara, M.T., Robertson, S.J., Croitoru, K. & Girardin, S.E. NOD proteins: regulators of inflammation in health and disease. *Nat Rev Immunol* **14**, 9-23 (2014).
7. Jones, J.D., Vance, R.E. & Dangl, J.L. Intracellular innate immune surveillance devices in plants and animals. *Science* **354**(2016).
8. Brubaker, S.W., Bonham, K.S., Zanoni, I. & Kagan, J.C. Innate immune pattern recognition: a cell biological perspective. *Annu Rev Immunol* **33**, 257-290 (2015).
9. Samir, P., Malireddi, R.K.S. & Kanneganti, T.D. The PANoptosome: A Deadly Protein Complex Driving Pyroptosis, Apoptosis, and Necroptosis (PANoptosis). *Front Cell Infect Microbiol* **10**, 238 (2020).
10. Kieser, K.J. & Kagan, J.C. Multi-receptor detection of individual bacterial products by the innate immune system. *Nat Rev Immunol* **17**, 376-390 (2017).
11. Liu, J., Qian, C. & Cao, X. Post-Translational Modification Control of Innate Immunity. *Immunity* **45**, 15-30 (2016).
12. Bryant, C.E.*, et al.* Advances in Toll-like receptor biology: Modes of activation by diverse stimuli. *Crit Rev Biochem Mol Biol* **50**, 359-379 (2015).
13. Kawai, T. & Akira, S. The role of pattern-recognition receptors in innate immunity: update on Toll-like receptors. *Nat Immunol* **11**, 373-384 (2010).
14. Pandey, S., Kawai, T. & Akira, S. Microbial sensing by Toll-like receptors and intracellular nucleic acid sensors. *Cold Spring Harb Perspect Biol* **7**, a016246 (2014).
15. Rehwinkel, J. & Gack, M.U. RIG-I-like receptors: their regulation and roles in RNA sensing. *Nat Rev Immunol* **20**, 537-551 (2020).
16. Yan, N. & Chen, Z.J. Intrinsic antiviral immunity. *Nat Immunol* **13**, 214-222 (2012).
17. Zevini, A., Olagnier, D. & Hiscott, J. Crosstalk between Cytoplasmic RIG-I and STING Sensing Pathways. *Trends Immunol* **38**, 194-205 (2017).
18. Chiang, J.J.*, et al.* Viral unmasking of cellular 5S rRNA pseudogene transcripts induces RIG-I-mediated immunity. *Nat Immunol* **19**, 53-62 (2018).
19. Zhao, Y., Ye, X., Dunker, W., Song, Y. & Karijolich, J. RIG-I like receptor sensing of host RNAs facilitates the cell-intrinsic immune response to KSHV infection. *Nat Commun* **9**, 4841 (2018).
20. Geijtenbeek, T.B. & Gringhuis, S.I. Signalling through C-type lectin receptors: shaping immune responses. *Nat Rev Immunol* **9**, 465-479 (2009).
21. Sancho, D. & Reis e Sousa, C. Signaling by myeloid C-type lectin receptors in immunity and homeostasis. *Annu Rev Immunol* **30**, 491-529 (2012).
22. Hoving, J.C., Wilson, G.J. & Brown, G.D. Signalling C-type lectin receptors, microbial recognition and immunity. *Cell Microbiol* **16**, 185-194 (2014).
23. Del Fresno, C., Cueto, F.J. & Sancho, D. Sensing Tissue Damage by Myeloid C-Type Lectin Receptors. *Curr Top Microbiol Immunol* **429**, 117-145 (2020).
24. Ye, Z. & Ting, J.P. NLR, the nucleotide-binding domain leucine-rich repeat containing gene family. *Curr Opin Immunol* **20**, 3-9 (2008).

25. Shaw, M.H., Reimer, T., Kim, Y.G. & Nunez, G. NOD-like receptors (NLRs): bona fide intracellular microbial sensors. *Curr Opin Immunol* **20**, 377-382 (2008).
26. Kanneganti, T.D., Lamkanfi, M. & Nunez, G. Intracellular NOD-like receptors in host defense and disease. *Immunity* **27**, 549-559 (2007).
27. Man, S.M. & Kanneganti, T.D. Regulation of inflammasome activation. *Immunol Rev* **265**, 6-21 (2015).
28. De Clercq, E. & Li, G. Approved Antiviral Drugs over the Past 50 Years. *Clin Microbiol Rev* **29**, 695-747 (2016).
29. Xue, Y., Enosi Tuipulotu, D., Tan, W.H., Kay, C. & Man, S.M. Emerging Activators and Regulators of Inflammasomes and Pyroptosis. *Trends Immunol* **40**, 1035-1052 (2019).
30. Rathinam, V.A. & Fitzgerald, K.A. Inflammasome Complexes: Emerging Mechanisms and Effector Functions. *Cell* **165**, 792-800 (2016).
31. Martinon, F., Burns, K. & Tschopp, J. The Inflammasome: A Molecular Platform Triggering Activation of Inflammatory Caspases and Processing of proIL-β. *Molecular Cell* **10**, 417-426 (2002).
32. Broz, P. & Dixit, V.M. Inflammasomes: mechanism of assembly, regulation and signalling. *Nat Rev Immunol* **16**, 407-420 (2016).
33. Man, S.M. & Kanneganti, T.-D. Converging roles of caspases in inflammasome activation, cell death and innate immunity. *Nature reviews. Immunology* **16**, 7-21 (2016).
34. Zhu, S.*, et al.* Nlrp9b inflammasome restricts rotavirus infection in intestinal epithelial cells. *Nature* **546**, 667-670 (2017).
35. Hara, H.*, et al.* The NLRP6 inflammasome recognizes lipoteichoic acid and regulates gram-positive pathogen infection. *Cell* **175**, 1651-1664 (2018).
36. Lu, A.*, et al.* Unified Polymerization Mechanism for the Assembly of ASC-dependent Inflammasomes. *Cell* **156**, 1193-1206 (2014).
37. Cai, X.*, et al.* Prion-like Polymerization Underlies Signal Transduction in Antiviral Immune Defense and Inflammasome Activation. *Cell* **156**, 1207-1222 (2014).
38. Fernandes-Alnemri, T.*, et al.* The pyroptosome: a supramolecular assembly of ASC dimers mediating inflammatory cell death via caspase-1 activation. *Cell Death and Differentiation* **14**, 1590-1604 (2007).
39. Huang, J.*, et al.* Activation of antibacterial autophagy by NADPH oxidases. *Proceedings of the National Academy of Sciences of the United States of America* **106**, 6226-6231 (2009).
40. Broz, P., von Moltke, J., Jones, J.W., Vance, R.E. & Monack, D.M. Differential requirement for Caspase-1 autoproteolysis in pathogen-induced cell death and cytokine processing. *Cell Host Microbe* **8**, 471-483 (2010).
41. Man, S.M.*, et al.* Inflammasome activation causes dual recruitment of NLRC4 and NLRP3 to the same macromolecular complex. *Proceedings of the National Academy of Sciences* **111**, 7403-7408 (2014).
42. Broz, P.*, et al.* Redundant roles for inflammasome receptors NLRP3 and NLRC4 in host defense against *Salmonella*. *J Exp Med* **207**, 1745-1755 (2010).
43. Baroja-Mazo, A.*, et al.* The NLRP3 inflammasome is released as a particulate danger signal that amplifies the inflammatory response. *Nat Immunol* **15**, 738-748 (2014).
44. Franklin, B.S.*, et al.* The adaptor ASC has extracellular and 'prionoid' activities that propagate inflammation. *Nat Immunol* **15**, 727-737 (2014).
45. Li, X.*, et al.* MARK4 regulates NLRP3 positioning and inflammasome activation through a microtubule-dependent mechanism. *Nat Commun* **8**, 15986 (2017).
46. Bryan, N.B., Dorfleutner, A., Rojanasakul, Y. & Stehlik, C. Activation of inflammasomes requires intracellular redistribution of the apoptotic speck-like protein containing a caspase recruitment domain. *J Immunol* **182**, 3173-3182 (2009).
47. Hong, S.*, et al.* Brefeldin A-sensitive ER-Golgi vesicle trafficking contributes to NLRP3-dependent caspase-1 activation. *FASEB J* **33**, 4547-4558 (2019).

48. Guo, C.*, et al.* Cholesterol Homeostatic Regulator SCAP-SREBP2 Integrates NLRP3 Inflammasome Activation and Cholesterol Biosynthetic Signaling in Macrophages. *Immunity* **49**, 842-856 e847 (2018).
49. Magupalli, V.G.*, et al.* HDAC6 mediates an aggresome-like mechanism for NLRP3 and pyrin inflammasome activation. *Science* **369** (2020).
50. Shi, J.*, et al.* Cleavage of GSDMD by inflammatory caspases determines pyroptotic cell death. *Nature* **526**, 660-665 (2015).
51. Kayagaki, N.*, et al.* Caspase-11 cleaves gasdermin D for non-canonical inflammasome signalling. *Nature* **526**, 666-671 (2015).
52. He, W.-t.*, et al.* Gasdermin D is an executor of pyroptosis and required for interleukin-1[beta] secretion. *Cell Res* **25**, 1285-1298 (2015).
53. Ding, J.*, et al.* Pore-forming activity and structural autoinhibition of the gasdermin family. *Nature* **535**, 111-116 (2016).
54. Aglietti, R.A.*, et al.* GsdmD p30 elicited by caspase-11 during pyroptosis forms pores in membranes. *Proceedings of the National Academy of Sciences of the United States of America* **113**, 7858-7863 (2016).
55. Liu, X.*, et al.* Inflammasome-activated gasdermin D causes pyroptosis by forming membrane pores. *Nature* **535**, 153-158 (2016).
56. Sborgi, L.*, et al.* GSDMD membrane pore formation constitutes the mechanism of pyroptotic cell death. *The EMBO Journal* **35**, 1766-1778 (2016).
57. Chen, X.*, et al.* Pyroptosis is driven by non-selective gasdermin-D pore and its morphology is different from MLKL channel-mediated necroptosis. *Cell Res* **26**, 1007-1020 (2016).
58. Joosten, L.A., Netea, M.G. & Dinarello, C.A. Interleukin-1beta in innate inflammation, autophagy and immunity. *Seminars in immunology* **25**, 416-424 (2013).
59. Dinarello, C.A., Novick, D., Kim, S. & Kaplanski, G. Interleukin-18 and IL-18 binding protein. *Frontiers in immunology* **4**, 289 (2013).
60. Sellin, M.E.*, et al.* Epithelium-intrinsic NAIP/NLRC4 inflammasome drives infected enterocyte expulsion to restrict *Salmonella* replication in the intestinal mucosa. *Cell Host Microbe* **16**, 237-248 (2014).
61. Knodler, L.A.*, et al.* Noncanonical inflammasome activation of caspase-4/caspase-11 mediates epithelial defenses against enteric bacterial pathogens. *Cell host & microbe* **16**, 249-256 (2014).
62. Miao, E.A.*, et al.* Caspase-1-induced pyroptosis is an innate immune effector mechanism against intracellular bacteria. *Nat Immunol* **11**, 1136-1142 (2010).
63. Man, S.M., Karki, R. & Kanneganti, T.D. Molecular mechanisms and functions of pyroptosis, inflammatory caspases and inflammasomes in infectious diseases. *Immunol Rev* **277**, 61-75 (2017).
64. Boyden, E.D. & Dietrich, W.F. Nalp1b controls mouse macrophage susceptibility to anthrax lethal toxin. *Nat Genet* **38**, 240-244 (2006).
65. Levinsohn, J.L.*, et al.* Anthrax Lethal Factor Cleavage of Nlrp1 Is Required for Activation of the Inflammasome. *PLoS Pathogens* **8**, e1002638 (2012).
66. Hellmich, K.A.*, et al.* Anthrax Lethal Factor Cleaves Mouse Nlrp1b in Both Toxin-Sensitive and Toxin-Resistant Macrophages. *PLoS ONE* **7**, e49741 (2012).
67. Bradley, K.A., Mogridge, J., Mourez, M., Collier, R.J. & Young, J.A. Identification of the cellular receptor for anthrax toxin. *Nature* **414**, 225-229 (2001).
68. Scobie, H.M., Rainey, G.J., Bradley, K.A. & Young, J.A. Human capillary morphogenesis protein 2 functions as an anthrax toxin receptor. *Proc Natl Acad Sci U S A* **100**, 5170-5174 (2003).
69. Liu, S.*, et al.* Capillary morphogenesis protein-2 is the major receptor mediating lethality of anthrax toxin in vivo. *Proc Natl Acad Sci U S A* **106**, 12424-12429 (2009).
70. Liu, S., Zhang, Y., Hoover, B. & Leppla, S.H. The receptors that mediate the direct lethality of anthrax toxin. *Toxins (Basel)* **5**, 1-8 (2012).

71. Lacy, D.B., Wigelsworth, D.J., Melnyk, R.A., Harrison, S.C. & Collier, R.J. Structure of heptameric protective antigen bound to an anthrax toxin receptor: a role for receptor in pH-dependent pore formation. *Proc Natl Acad Sci U S A* **101**, 13147-13151 (2004).
72. Kalu, N.*, et al.* Effect of endosomal acidification on small ion transport through the anthrax toxin PA63 channel. *FEBS Lett* **591**, 3481-3492 (2017).
73. Martinon, F., Burns, K. & Tschopp, J. The inflammasome: a molecular platform triggering activation of inflammatory caspases and processing of proIL-beta. *Mol Cell* **10**, 417-426 (2002).
74. Boyden, E.D. & Dietrich, W.F. Nalp1b controls mouse macrophage susceptibility to anthrax lethal toxin. *Nat Genet* **38**, 240-244 (2006).
75. Levinsohn, J.L.*, et al.* Anthrax lethal factor cleavage of Nlrp1 is required for activation of the inflammasome. *PLoS Pathog* **8**, e1002638 (2012).
76. Chavarria-Smith, J. & Vance, R.E. Direct proteolytic cleavage of NLRP1B is necessary and sufficient for inflammasome activation by anthrax lethal factor. *PLoS Pathog* **9**, e1003452 (2013).
77. Moayeri, M., Leppla, S.H., Vrentas, C., Pomerantsev, A.P. & Liu, S. Anthrax Pathogenesis. *Annu Rev Microbiol* **69**, 185-208 (2015).
78. Terra, J.K.*, et al.* Resistance to *Bacillus anthracis* Infection Mediated by a Lethal Toxin Sensitive Allele of Nalp1b/Nlrp1b. *Journal of immunology (Baltimore, Md. : 1950)* **184**, 17-20 (2010).
79. Moayeri, M.*, et al.* Inflammasome Sensor Nlrp1b-Dependent Resistance to Anthrax Is Mediated by Caspase-1, IL-1 Signaling and Neutrophil Recruitment. *PLoS Pathogens* **6**, e1001222 (2010).
80. Van Opdenbosch, N.*, et al.* Activation of the NLRP1b inflammasome independently of ASC-mediated caspase-1 autoproteolysis and speck formation. *Nature Communications* **5**, 3209 (2014).
81. Guey, B., Bodnar, M., Manié, S.N., Tardivel, A. & Petrilli, V. Caspase-1 autoproteolysis is differentially required for NLRP1b and NLRP3 inflammasome function. *Proceedings of the National Academy of Sciences of the United States of America* **111**, 17254-17259 (2014).
82. Gorfu, G.*, et al.* Dual Role for Inflammasome Sensors NLRP1 and NLRP3 in Murine Resistance to *Toxoplasma gondii*. *mBio* **5**, e01117-01113 (2014).
83. D'Osualdo, A.*, et al.* CARD8 and NLRP1 Undergo Autoproteolytic Processing through a ZU5-Like Domain. *PLoS ONE* **6**, e27396 (2011).
84. Finger, J.N.*, et al.* Autolytic Proteolysis within the Function to Find Domain (FIIND) Is Required for NLRP1 Inflammasome Activity. *The Journal of Biological Chemistry* **287**, 25030-25037 (2012).
85. Frew, B.C., Joag, V.R. & Mogridge, J. Proteolytic Processing of Nlrp1b Is Required for Inflammasome Activity. *PLoS Pathogens* **8**, e1002659 (2012).
86. Chui, A.J.*, et al.* N-terminal degradation activates the NLRP1B inflammasome. *Science* **364**, 82-85 (2019).
87. Sandstrom, A.*, et al.* Functional degradation: A mechanism of NLRP1 inflammasome activation by diverse pathogen enzymes. *Science* **364** (2019).
88. Okondo, M.C.*, et al.* DPP8 and DPP9 inhibition induces pro-caspase-1-dependent monocyte and macrophage pyroptosis. *Nature chemical biology* **13**, 46-53 (2017).
89. Chavarría-Smith, J., Mitchell, P.S., Ho, A.M., Daugherty, M.D. & Vance, R.E. Functional and Evolutionary Analyses Identify Proteolysis as a General Mechanism for NLRP1 Inflammasome Activation. *PLoS Pathogens* **12**, e1006052 (2016).
90. Robinson, K.S.*, et al.* Enteroviral 3C protease activates the human NLRP1 inflammasome in airway epithelia. *Science* **370** (2020).
91. Tsu, B.V.*, et al.* Diverse viral proteases activate the NLRP1 inflammasome. *Elife* **10** (2021).
92. Bauernfried, S., Scherr, M.J., Pichlmair, A., Duderstadt, K.E. & Hornung, V. Human NLRP1 is a sensor for double-stranded RNA. *Science,* **371**, eabd0811 (2020).

93. Okondo, M.C.*, et al.* Inhibition of Dpp8/9 Activates the Nlrp1b Inflammasome. *Cell Chem Biol* **25**, 262-267 e265 (2018).
94. Zhong, F.L.*, et al.* Human DPP9 represses NLRP1 inflammasome and protects against autoinflammatory diseases via both peptidase activity and FIIND domain binding. *J Biol Chem* **293**, 18864-18878 (2018).
95. Okondo, M.C.*, et al.* DPP8 and DPP9 inhibition induces pro-caspase-1-dependent monocyte and macrophage pyroptosis. *Nat Chem Biol* **13**, 46-53 (2017).
96. Santos, M.L.*, et al.* Contribution of inflammasome genetics in *Plasmodium vivax* malaria. *Infection, genetics and evolution: journal of molecular epidemiology and evolutionary genetics in infectious diseases* **40**, 162-166 (2016).
97. Witola, W.H.*, et al.* NALP1 influences susceptibility to human congenital toxoplasmosis, proinflammatory cytokine response, and fate of *Toxoplasma gondii*-infected monocytic cells. *Infection and immunity* **79**, 756-766 (2011).
98. Gorfu, G.*, et al.* Dual role for inflammasome sensors NLRP1 and NLRP3 in murine resistance to *Toxoplasma gondii*. *MBio* **5**, e01117-01113 (2014).
99. Ewald, S.E., Chavarria-Smith, J. & Boothroyd, J.C. NLRP1 is an inflammasome sensor for *Toxoplasma gondii*. *Infection and immunity* **82**, 460-468 (2014).
100. Cirelli, K.M.*, et al.* Inflammasome sensor NLRP1 controls rat macrophage susceptibility to *Toxoplasma gondii*. *PLoS Pathog* **10**, e1003927 (2014).
101. Masters, S.L.*, et al.* NLRP1 inflammasome activation induces pyroptosis of hematopoietic progenitor cells. *Immunity* **37**, 1009-1023 (2012).
102. Zhong, Franklin L.*, et al.* Germline NLRP1 Mutations Cause Skin Inflammatory and Cancer Susceptibility Syndromes via Inflammasome Activation. *Cell* **167**, 187-202.e117 (2016).
103. Agostini, L.*, et al.* NALP3 Forms an IL-1β-Processing Inflammasome with Increased Activity in Muckle-Wells Autoinflammatory Disorder. *Immunity* **20**, 319-325 (2004).
104. Dowds, T.A.*, et al.* Regulation of cryopyrin/Pypaf1 signaling by pyrin, the familial Mediterranean fever gene product. *Biochemical and Biophysical Research Communications* **302**, 575-580 (2003).
105. Hoffman, H.M., Mueller, J.L., Broide, D.H., Wanderer, A.A. & Kolodner, R.D. Mutation of a new gene encoding a putative pyrin-like protein causes familial cold autoinflammatory syndrome and Muckle–Wells syndrome. *Nature genetics* **29**, 301-305 (2001).
106. Feldmann, J.*, et al.* Chronic Infantile Neurological Cutaneous and Articular Syndrome Is Caused by Mutations in CIAS1, a Gene Highly Expressed in Polymorphonuclear Cells and Chondrocytes. *American Journal of Human Genetics* **71**, 198-203 (2002).
107. Neven, B.*, et al.* Molecular Basis of the Spectral Expression of CIAS1 Mutations Associated With Phagocytic Cell-Mediated Autoinflammatory Disorders CINCA/NOMID, MWS, and FCU. *Blood* **103**, 2809 (2004).
108. Man, S.M. & Kanneganti, T.-D. Regulation of inflammasome activation. *Immunological reviews* **265**, 6-21 (2015).
109. Bauernfeind, F.*, et al.* NF-kB activating pattern recognition and cytokine receptors license NLRP3 inflammasome activation by regulating NLRP3 expression. *Journal of immunology (Baltimore, Md. : 1950)* **183**, 787-791 (2009).
110. Franchi, L., Eigenbrod, T. & Núñez, G. TNF-α Mediate Sensitization to ATP and Silica via the NLRP3 Inflammasome in the Absence of Microbial Stimulation. *Journal of immunology (Baltimore, Md. : 1950)* **183**, 792-796 (2009).
111. Lin, K.-M.*, et al.* IRAK-1 bypasses priming and directly links TLRs to rapid NLRP3 inflammasome activation. *Proceedings of the National Academy of Sciences of the United States of America* **111**, 775-780 (2014).
112. Fernandes-Alnemri, T.*, et al.* Toll-Like Receptor Signaling Licenses IRAK1 For Rapid Activation Of The NLRP3 Inflammasome. *Journal of immunology (Baltimore, Md. : 1950)* **191**, 3995-3999 (2013).
113. Mariathasan, S.*, et al.* Cryopyrin activates the inflammasome in response to toxins and ATP. *Nature* **440**, 228-232 (2006).

114. Sander, L.E.*, et al.* Sensing prokaryotic mRNA signifies microbial viability and promotes immunity. *Nature* **474**, 385-389 (2011).
115. Kanneganti, T.-D.*, et al.* Bacterial RNA and small antiviral compounds activate caspase-1 through cryopyrin/Nalp3. *Nature* **440**, 233-236 (2006).
116. Martinon, F., Agostini, L., Meylan, E. & Tschopp, J. Identification of Bacterial Muramyl Dipeptide as Activator of the NALP3/Cryopyrin Inflammasome. *Current Biology* **14**, 1929-1934 (2004).
117. Kailasan Vanaja, S.*, et al.* Bacterial RNA:DNA hybrids are activators of the NLRP3 inflammasome. *Proceedings of the National Academy of Sciences of the United States of America* **111**, 7765-7770 (2014).
118. Sha, W.*, et al.* Human NLRP3 inflammasome senses multiple types of bacterial RNAs. *Proceedings of the National Academy of Sciences of the United States of America* **111**, 16059-16064 (2014).
119. Franchi, L.*, et al.* Cytosolic Double-Stranded RNA Activates the NLRP3 inflammasomevia MAVS-Induced Membrane Permeabilization and K(+) Efflux. *Journal of immunology (Baltimore, Md. : 1950)* **193**, 4214-4222 (2014).
120. Franchi, L., Muñoz-Planillo, R. & Núñez, G. Sensing and Reacting to Microbes via the Inflammasomes. *Nature immunology* **13**, 325-332 (2012).
121. Lupfer, C. & Kanneganti, T.-D. The Expanding Role of NLRs in Antiviral Immunity. *Immunological reviews* **255**, 13-24 (2013).
122. Kanneganti, T.-D. Central roles of NLRs and inflammasomes in viral infection. *Nature reviews. Immunology* **10**, 688-698 (2010).
123. Thomas, P.G.*, et al.* NLRP3 (NALP3/CIAS1/Cryopyrin) mediates key innate and healing responses to influenza A virus via the regulation of caspase-1. *Immunity* **30**, 566-575 (2009).
124. Dostert, C.*, et al.* Innate Immune Activation Through Nalp3 Inflammasome Sensing of Asbestos and Silica. *Science (New York, N.Y.)* **320**, 674-677 (2008).
125. Hornung, V.*, et al.* Silica crystals and aluminum salts mediate NALP-3 inflammasome activation via phagosomal destabilization. *Nature immunology* **9**, 847-856 (2008).
126. Martinon, F., Petrilli, V., Mayor, A., Tardivel, A. & Tschopp, J. Gout-associated uric acid crystals activate the NALP3 inflammasome. *Nature* **440**, 237-241 (2006).
127. Palm, N.W. & Medzhitov, R. Role of the inflammasome in defense against venoms. *Proceedings of the National Academy of Sciences of the United States of America* **110**, 1809-1814 (2013).
128. Allam, R., Darisipudi, M.N., Tschopp, J. & Anders, H.-J. Histones trigger sterile inflammation by activating the NLRP3 inflammasome. *European Journal of Immunology* **43**, 3336-3342 (2013).
129. Freeman, L.*, et al.* NLR members NLRC4 and NLRP3 mediate sterile inflammasome activation in microglia and astrocytes. *The Journal of Experimental Medicine* **214**, 1351 (2017).
130. Duan, N.-N., Liu, X.-J. & Wu, J. Palmitic acid elicits hepatic stellate cell activation through inflammasomes and hedgehog signaling. *Life Sciences* **176**, 42-53 (2017).
131. Perregaux, D. & Gabel, C.A. Interleukin-1 beta maturation and release in response to ATP and nigericin. Evidence that potassium depletion mediated by these agents is a necessary and common feature of their activity. *Journal of Biological Chemistry* **269**, 15195-15203 (1994).
132. Muñoz-Planillo, R.*, et al.* K(+) efflux is the Common Trigger of NLRP3 inflammasome Activation by Bacterial Toxins and Particulate Matter. *Immunity* **38**, 1142-1153 (2013).
133. Petrilli, V.*, et al.* Activation of the NALP3 inflammasome is triggered by low intracellular potassium concentration. *Cell Death Differ* **14**, 1583-1589 (2007).
134. Franchi, L., Kanneganti, T.-D., Dubyak, G.R. & Núñez, G. Differential Requirement of P2X7 Receptor and Intracellular K+ for Caspase-1 Activation Induced by Intracellular and Extracellular Bacteria. *Journal of Biological Chemistry* **282**, 18810-18818 (2007).
135. Di, A.*, et al.* The TWIK2 Potassium Efflux Channel in Macrophages Mediates NLRP3 Inflammasome-Induced Inflammation. *Immunity* **49**, 56-65 e54 (2018).

136. Zhou, R., Yazdi, A.S., Menu, P. & Tschopp, J. A role for mitochondria in NLRP3 inflammasome activation. *Nature* **469**, 221-225 (2011).
137. Groß, Christina J.*, et al.* K(+) Efflux-Independent NLRP3 Inflammasome Activation by Small Molecules Targeting Mitochondria. *Immunity* **45**, 761-773 (2016).
138. Shimada, K.*, et al.* Oxidized Mitochondrial DNA Activates the NLRP3 Inflammasome During Apoptosis. *Immunity* **36**, 401-414 (2012).
139. Iyer, S.S.*, et al.* Mitochondrial cardiolipin is required for Nlrp3 inflammasome activation. *Immunity* **39**, 311-323 (2013).
140. Chen, J. & Chen, Z.J. PtdIns4P on dispersed trans-Golgi network mediates NLRP3 inflammasome activation. *Nature* **564**, 71-76 (2018).
141. Murakami, T.*, et al.* Critical role for calcium mobilization in activation of the NLRP3 inflammasome. *Proceedings of the National Academy of Sciences of the United States of America* **109**, 11282-11287 (2012).
142. Lee, G.-S.*, et al.* The calcium-sensing receptor regulates the NLRP3 inflammasome through Ca(2+) and cAMP. *Nature* **492**, 123-127 (2012).
143. Rossol, M.*, et al.* Extracellular Ca(2+) is a danger signal activating the NLRP3 inflammasome through G protein-coupled calcium sensing receptors. *Nature Communications* **3**, 1329 (2012).
144. Schorn, C.*, et al.* Sodium overload and water influx activate the NALP3 inflammasome. *J Biol Chem* **286**, 35-41 (2011).
145. Verhoef, P.A., Kertesy, S.B., Lundberg, K., Kahlenberg, J.M. & Dubyak, G.R. Inhibitory effects of chloride on the activation of caspase-1, IL-1beta secretion, and cytolysis by the P2X7 receptor. *J Immunol* **175**, 7623-7634 (2005).
146. Tang, T.*, et al.* CLICs-dependent chloride efflux is an essential and proximal upstream event for NLRP3 inflammasome activation. *Nat Commun* **8**, 202 (2017).
147. Gurcel, L., Abrami, L., Girardin, S., Tschopp, J. & van der Goot, F.G. Caspase-1 Activation of Lipid Metabolic Pathways in Response to Bacterial Pore-Forming Toxins Promotes Cell Survival. *Cell* **126**, 1135-1145 (2006).
148. Compan, V.*, et al.* Cell Volume Regulation Modulates NLRP3 Inflammasome Activation. *Immunity* **37**, 487-500 (2012).
149. He, Y., Zeng, M.Y., Yang, D., Motro, B. & Núñez, G. Nek7 is an essential mediator of NLRP3 activation downstream of potassium efflux. *Nature* **530**, 354-357 (2016).
150. Schmid-Burgk, J.L.*, et al.* A Genome-wide CRISPR (Clustered Regularly Interspaced Short Palindromic Repeats) Screen Identifies NEK7 as an Essential Component of NLRP3 Inflammasome Activation. *The Journal of Biological Chemistry* **291**, 103-109 (2016).
151. Shi, H.*, et al.* NLRP3 activation and mitosis are mutually exclusive events coordinated by NEK7, a new inflammasome component. *Nature immunology* **17**, 250-258 (2016).
152. Samir, P.*, et al.* DDX3X acts as a live-or-die checkpoint in stressed cells by regulating NLRP3 inflammasome. *Nature* **573**, 590-594 (2019).
153. Man, S.M. & Kanneganti, T.D. Converging roles of caspases in inflammasome activation, cell death and innate immunity. *Nat Rev Immunol* **16**, 7-21 (2016).
154. Gurung, P.*, et al.* FADD and caspase-8 mediate priming and activation of the canonical and non-canonical Nlrp3 inflammasomes. *Journal of immunology (Baltimore, Md. : 1950)* **192**, 1835-1846 (2014).
155. Allam, R.*, et al.* Mitochondrial apoptosis is dispensable for NLRP3 inflammasome activation but non-apoptotic caspase-8 is required for inflammasome priming. *EMBO Reports* **15**, 982-990 (2014).
156. Vince, James E.*, et al.* Inhibitor of Apoptosis Proteins Limit RIP3 Kinase-Dependent Interleukin-1 Activation. *Immunity* **36**, 215-227 (2012).
157. Su, H.*, et al.* Requirement for Caspase-8 in NF-κB Activation by Antigen Receptor. *Science* **307**, 1465 (2005).
158. Hu, W.-H., Johnson, H. & Shu, H.-B. Activation of NF-κB by FADD, Casper, and Caspase-8. *Journal of Biological Chemistry* **275**, 10838-10844 (2000).

159. Antonopoulos, C.*, et al.* Caspase-8 as an Effector and Regulator of NLRP3 Inflammasome Signaling. *Journal of Biological Chemistry* **290**, 20167-20184 (2015).
160. Man, S.M.*, et al. Salmonella* infection induces recruitment of Caspase-8 to the inflammasome to modulate interleukin-1β production. *Journal of immunology (Baltimore, Md. : 1950)* **191**, 10.4049/jimmunol.1301581 (2013).
161. Kuriakose, T.*, et al.* ZBP1/DAI is an innate sensor of influenza virus triggering the NLRP3 inflammasome and programmed cell death pathways. *Science immunology* **1**, aag2045 (2016).
162. Zhang, X.*, et al.* MLKL and FADD Are Critical for Suppressing Progressive Lymphoproliferative Disease and Activating the NLRP3 Inflammasome. *Cell Reports* **16**, 3247-3259 (2016).
163. Kang, S.*, et al.* Caspase-8 scaffolding function and MLKL regulate NLRP3 inflammasome activation downstream of TLR3. *Nature Communications* **6**, 7515 (2015).
164. Lawlor, K.E.*, et al.* RIPK3 promotes cell death and NLRP3 inflammasome activation in the absence of MLKL. *Nature Communications* **6**, 6282 (2015).
165. Lemmers, B.*, et al.* Essential Role for Caspase-8 in Toll-like Receptors and NFκB Signaling. *Journal of Biological Chemistry* **282**, 7416-7423 (2007).
166. Schroder, K.*, et al.* Acute lipopolysaccharide priming boosts inflammasome activation independently of inflammasome sensor induction. *Immunobiology* **217**, 1325-1329 (2012).
167. Weng, D.*, et al.* Caspase-8 and RIP kinases regulate bacteria-induced innate immune responses and cell death. *Proceedings of the National Academy of Sciences* **111**, 7391-7396 (2014).
168. Philip, N.H.*, et al.* Caspase-8 mediates caspase-1 processing and innate immune defense in response to bacterial blockade of NF-κB and MAPK signaling. *Proceedings of the National Academy of Sciences* **111**, 7385-7390 (2014).
169. Karki, R.*, et al.* Concerted activation of the AIM2 and NLRP3 inflammasomes orchestrates host protection against *Aspergillus* infection. *Cell Host Microbe* **17**, 357-368 (2015).
170. Ganesan, S.*, et al.* Caspase-8 modulates dectin-1 and complement receptor 3-driven IL-1β production in response to β-glucans and the fungal pathogen, *Candida albicans*. *The Journal of Immunology* **193**, 2519 (2014).
171. Lukens, J.R.*, et al.* Dietary modulation of the microbiome affects autoinflammatory disease. *Nature* **516**, 246-249 (2014).
172. Gurung, P., Burton, A. & Kanneganti, T.-D. NLRP3 inflammasome plays a redundant role with caspase 8 to promote IL-1β–mediated osteomyelitis. *Proceedings of the National Academy of Sciences of the United States of America* **113**, 4452-4457 (2016).
173. Uchiyama, R., Yonehara, S. & Tsutsui, H. Fas-mediated inflammatory response in *Listeria monocytogenes* infection. *The Journal of Immunology* **190**, 4245 (2013).
174. Pierini, R.*, et al.* AIM2/ASC triggers caspase-8-dependent apoptosis in *Francisella*-infected caspase-1-deficient macrophages. *Cell Death and Differentiation* **19**, 1709-1721 (2012).
175. Sagulenko, V.*, et al.* AIM2 and NLRP3 inflammasomes activate both apoptotic and pyroptotic death pathways via ASC. *Cell Death Differ* **20**, 1149-1160 (2013).
176. Moriwaki, K., Bertin, J., Gough, P.J. & Chan, F.K.-M. A RIPK3-Caspase 8 complex mediates atypical pro-IL-1β processing. *Journal of immunology (Baltimore, Md. : 1950)* **194**, 1938-1944 (2015).
177. Antonopoulos, C., El Sanadi, C., Kaiser, W.J., Mocarski, E.S. & Dubyak, G.R. Proapoptotic Chemotherapeutic Drugs Induce Non-canonical Processing and Release of IL-1β via Caspase-8 in Dendritic Cells. *Journal of immunology (Baltimore, Md. : 1950)* **191**, 10.4049/jimmunol.1300645 (2013).
178. England, H., Summersgill, H.R., Edye, M.E., Rothwell, N.J. & Brough, D. Release of Interleukin-1α or Interleukin-1β Depends on Mechanism of Cell Death. *Journal of Biological Chemistry* **289**, 15942-15950 (2014).

179. Shenderov, K.*, et al.* Cutting Edge: Endoplasmic Reticulum Stress Licenses Macrophages To Produce Mature IL-1β in Response to TLR4 Stimulation through a Caspase-8– and TRIF-Dependent Pathway. *The Journal of Immunology* **192**, 2029 (2014).
180. Bossaller, L.*, et al.* FAS mediates non-canonical IL-1β and IL-18 maturation via caspase-8 in a Rip3-independent manner(). *Journal of immunology (Baltimore, Md. : 1950)* **189**, 5508-5512 (2012).
181. Gringhuis, S.I.*, et al.* Dectin-1 is an extracellular pathogen sensor for the induction and processing of IL-1[beta] via a noncanonical caspase-8 inflammasome. *Nat Immunol* **13**, 246-254 (2012).
182. Maelfait, J.*, et al.* Stimulation of Toll-like receptor 3 and 4 induces interleukin-1β maturation by caspase-8. *The Journal of Experimental Medicine* **205**, 1967-1973 (2008).
183. Kang, T.-B., Yang, S.-H., Toth, B., Kovalenko, A. & Wallach, D. Caspase-8 Blocks Kinase RIPK3-Mediated Activation of the NLRP3 Inflammasome. *Immunity* **38**, 27-40 (2013).
184. Wu, Y.H.*, et al.* Participation of c-FLIP in NLRP3 and AIM2 inflammasome activation. *Cell Death and Differentiation* **21**, 451-461 (2014).
185. Conos, S.A.*, et al.* Active MLKL triggers the NLRP3 inflammasome in a cell-intrinsic manner. *Proceedings of the National Academy of Sciences* **114**, E961-E969 (2017).
186. Gutierrez, K.D.*, et al.* MLKL Activation Triggers NLRP3-Mediated Processing and Release of IL-1β Independently of Gasdermin-D. *The Journal of Immunology* **198**, 2156 (2017).
187. Mayor, A., Martinon, F., De Smedt, T., Petrilli, V. & Tschopp, J. A crucial function of SGT1 and HSP90 in inflammasome activity links mammalian and plant innate immune responses. *Nat Immunol* **8**, 497-503 (2007).
188. Han, S.*, et al.* Lipopolysaccharide Primes the NALP3 Inflammasome by Inhibiting Its Ubiquitination and Degradation Mediated by the SCF(FBXL2) E3 Ligase. *The Journal of Biological Chemistry* **290**, 18124-18133 (2015).
189. Song, H.*, et al.* The E3 ubiquitin ligase TRIM31 attenuates NLRP3 inflammasome activation by promoting proteasomal degradation of NLRP3. *Nat Commun* **7**, 13727 (2016).
190. Yan, Y.*, et al.* Dopamine controls systemic inflammation through inhibition of NLRP3 inflammasome. *Cell* **160**, 62-73 (2015).
191. Kawashima, A.*, et al.* ARIH2 Ubiquitinates NLRP3 and Negatively Regulates NLRP3 Inflammasome Activation in Macrophages. *J Immunol* **199**, 3614-3622 (2017).
192. Humphries, F.*, et al.* The E3 ubiquitin ligase Pellino2 mediates priming of the NLRP3 inflammasome. *Nat Commun* **9**, 1560 (2018).
193. Juliana, C.*, et al.* Non-transcriptional Priming and Deubiquitination Regulate NLRP3 Inflammasome Activation. *The Journal of Biological Chemistry* **287**, 36617-36622 (2012).
194. Lopez-Castejon, G.*, et al.* Deubiquitinases Regulate the Activity of Caspase-1 and Interleukin-1β Secretion via Assembly of the Inflammasome. *The Journal of Biological Chemistry* **288**, 2721-2733 (2013).
195. Ren, G.*, et al.* ABRO1 promotes NLRP3 inflammasome activation through regulation of NLRP3 deubiquitination. *EMBO J* **38**, e100376 (2019).
196. Py, Bénédicte F., Kim, M.-S., Vakifahmetoglu-Norberg, H. & Yuan, J. Deubiquitination of NLRP3 by BRCC3 Critically Regulates Inflammasome Activity. *Molecular Cell* **49**, 331-338 (2013).
197. Song, H.*, et al.* UAF1 deubiquitinase complexes facilitate NLRP3 inflammasome activation by promoting NLRP3 expression. *Nat Commun* **11**, 6042 (2020).
198. Rodgers, M.A.*, et al.* The linear ubiquitin assembly complex (LUBAC) is essential for NLRP3 inflammasome activation. *The Journal of experimental medicine* **211**, 1333-1347 (2014).

199. Song, N.*, et al.* NLRP3 Phosphorylation Is an Essential Priming Event for Inflammasome Activation. *Mol Cell* **68**, 185-197 e186 (2017).
200. Gross, O.*, et al.* Syk kinase signalling couples to the Nlrp3 inflammasome for anti-fungal host defence. *Nature* **459**, 433-436 (2009).
201. Tiemi Shio, M.*, et al.* Malarial Hemozoin Activates the NLRP3 Inflammasome through Lyn and Syk Kinases. *PLoS Pathogens* **5**, e1000559 (2009).
202. Saïd-Sadier, N., Padilla, E., Langsley, G. & Ojcius, D.M. *Aspergillus fumigatus* Stimulates the NLRP3 Inflammasome through a Pathway Requiring ROS Production and the Syk Tyrosine Kinase. *PLoS ONE* **5**, e10008 (2010).
203. Wong, K.-W. & Jacobs Jr, W.R. Critical role for NLRP3 in necrotic death triggered by *Mycobacterium tuberculosis. Cellular Microbiology* **13**, 1371-1384 (2011).
204. Zhang, Z.*, et al.* Protein kinase D at the Golgi controls NLRP3 inflammasome activation. *The Journal of experimental medicine* **214**, 2671-2693 (2017).
205. Stutz, A.*, et al.* NLRP3 inflammasome assembly is regulated by phosphorylation of the pyrin domain. *The Journal of Experimental Medicine* (2017).
206. Barry, R.*, et al.* SUMO-mediated regulation of NLRP3 modulates inflammasome activity. *Nat Commun* **9**, 3001 (2018).
207. Mao, K.*, et al.* Nitric oxide suppresses NLRP3 inflammasome activation and protects against LPS-induced septic shock. *Cell Research* **23**, 201-212 (2013).
208. Mishra, B.B.*, et al.* Nitric oxide controls tuberculosis immunopathology by inhibiting NLRP3 inflammasome-dependent IL-1β processing. *Nature immunology* **14**, 52-60 (2013).
209. Hernandez-Cuellar, E.*, et al.* Cutting Edge: Nitric Oxide Inhibits the NLRP3 Inflammasome. *The Journal of Immunology* **189**, 5113-5117 (2012).
210. Pereira, M., Tourlomousis, P., Wright, J., P. Monie, T. & Bryant, C.E. CARD9 negatively regulates NLRP3-induced IL-1β production on *Salmonella* infection of macrophages. **7**, 12874 (2016).
211. Guarda, G.*, et al.* Type I Interferon Inhibits Interleukin-1 Production and Inflammasome Activation. *Immunity* **34**, 213-223 (2011).
212. Gurung, P.*, et al.* Chronic TLR Stimulation Controls NLRP3 Inflammasome Activation through IL-10 Mediated Regulation of NLRP3 Expression and Caspase-8 Activation. **5**, 14488 (2015).
213. Coll, R.C.*, et al.* A small-molecule inhibitor of the NLRP3 inflammasome for the treatment of inflammatory diseases. *Nat Med* **21**, 248-255 (2015).
214. Coll, R.C.*, et al.* MCC950 directly targets the NLRP3 ATP-hydrolysis motif for inflammasome inhibition. *Nat Chem Biol* **15**, 556-559 (2019).
215. Tapia-Abellan, A.*, et al.* MCC950 closes the active conformation of NLRP3 to an inactive state. *Nat Chem Biol* **15**, 560-564 (2019).
216. Darakhshan, S. & Pour, A.B. Tranilast: a review of its therapeutic applications. *Pharmacol Res* **91**, 15-28 (2015).
217. Lamkanfi, M.*, et al.* Glyburide inhibits the Cryopyrin/Nalp3 inflammasome. *J Cell Biol* **187**, 61-70 (2009).
218. Marchetti, C.*, et al.* A novel pharmacologic inhibitor of the NLRP3 inflammasome limits myocardial injury after ischemia-reperfusion in the mouse. *J Cardiovasc Pharmacol* **63**, 316-322 (2014).
219. Marchetti, C.*, et al.* Pharmacologic Inhibition of the NLRP3 Inflammasome Preserves Cardiac Function After Ischemic and Nonischemic Injury in the Mouse. *J Cardiovasc Pharmacol* **66**, 1-8 (2015).
220. Kuwar, R.*, et al.* A novel small molecular NLRP3 inflammasome inhibitor alleviates neuroinflammatory response following traumatic brain injury. *J Neuroinflammation* **16**, 81 (2019).
221. Liu, W.*, et al.* A novel benzo[d]imidazole derivate prevents the development of dextran sulfate sodium-induced murine experimental colitis via inhibition of NLRP3 inflammasome. *Biochem Pharmacol* **85**, 1504-1512 (2013).

222. Marchetti, C.*, et al.* OLT1177, a beta-sulfonyl nitrile compound, safe in humans, inhibits the NLRP3 inflammasome and reverses the metabolic cost of inflammation. *Proc Natl Acad Sci U S A* **115**, E1530-E1539 (2018).
223. El-Sharkawy, L.Y., Brough, D. & Freeman, S. Inhibiting the NLRP3 Inflammasome. *Molecules* **25**(2020).
224. Kayagaki, N.*, et al.* Non-canonical inflammasome activation targets caspase-11. *Nature* **479**, 117-121 (2011).
225. Kayagaki, N.*, et al.* Noncanonical Inflammasome Activation by Intracellular LPS Independent of TLR4. *Science* **341**, 1246 (2013).
226. Aachoui, Y.*, et al.* Caspase-11 protects against bacteria that escape the vacuole. *Science (New York, N.Y.)* **339**, 975-978 (2013).
227. Casson, C.N.*, et al.* Caspase-11 Activation in Response to Bacterial Secretion Systems that Access the Host Cytosol. *PLoS Pathogens* **9**, e1003400 (2013).
228. Shi, J.*, et al.* Inflammatory caspases are innate immune receptors for intracellular LPS. *Nature* **514**, 187-192 (2014).
229. Hagar, J.A., Powell, D.A., Aachoui, Y., Ernst, R.K. & Miao, E.A. Cytoplasmic LPS activates caspase-11: implications in TLR4-independent endotoxic shock. *Science (New York, N.Y.)* **341**, 1250-1253 (2013).
230. Casson, C.N.*, et al.* Human caspase-4 mediates noncanonical inflammasome activation against gram-negative bacterial pathogens. *Proceedings of the National Academy of Sciences of the United States of America* **112**, 6688-6693 (2015).
231. Baker, P.J.*, et al.* NLRP3 inflammasome activation downstream of cytoplasmic LPS recognition by both caspase-4 and caspase-5. *European Journal of Immunology* **45**, 2918-2926 (2015).
232. Schmid-Burgk, J.L.*, et al.* Caspase-4 mediates non-canonical activation of the NLRP3 inflammasome in human myeloid cells. *European Journal of Immunology* **45**, 2911-2917 (2015).
233. Aachoui, Y.*, et al.* Canonical inflammasomes drive IFN-γ to prime caspase-11 in defense against a cytosol-invasive bacterium. *Cell host & microbe* **18**, 320-332 (2015).
234. Akhter, A.*, et al.* Caspase-11 promotes the fusion of phagosomes harboring pathogenic bacteria with lysosomes by modulating actin polymerization. *Immunity* **37**, 35-47 (2012).
235. Miao, E.A.*, et al.* Caspase-1-induced pyroptosis is an innate immune effector mechanism against intracellular bacteria. *Nature immunology* **11**, 1136-1142 (2010).
236. Man, S.M.*, et al.* Actin polymerization as a key innate immune effector mechanism to control *Salmonella* infection. *Proceedings of the National Academy of Sciences of the United States of America* **111**, 17588-17593 (2014).
237. Knodler, L.A.*, et al.* Non-canonical inflammasome activation of caspase-4/caspase-11 mediates epithelial defenses against enteric bacterial pathogens. *Cell host & microbe* **16**, 249-256 (2014).
238. Thurston, T.L.M.*, et al.* Growth inhibition of cytosolic *Salmonella* by caspase-1 and caspase-11 precedes host cell death. *Nature Communications* **7**, 13292 (2016).
239. Vanaja, S.K.*, et al.* Bacterial outer membrane vesicles mediate cytosolic localization of LPS and caspase-11 activation. *Cell* **165**, 1106-1119 (2016).
240. Rühl, S. & Broz, P. Caspase-11 activates a canonical NLRP3 inflammasome by promoting K+ efflux. *European Journal of Immunology* **45**, 2927-2936 (2015).
241. Yang, D., He, Y., Muñoz-Planillo, R., Liu, Q. & Núñez, G. Caspase-11 requires the pannexin-1 channel and the purinergic P2X7 pore to mediate pyroptosis and endotoxic shock. *Immunity* **43**, 923-932 (2015).
242. Chen, K.W., Demarco, B. & Broz, P. Pannexin-1 promotes NLRP3 activation during apoptosis but is dispensable for canonical or noncanonical inflammasome activation. *Eur J Immunol* **50**, 170-177 (2020).
243. Zanoni, I.*, et al.* An endogenous caspase-11 ligand elicits interleukin-1 release from living dendritic cells. *Science* (2016).

244. Evavold, C.L.*, et al.* The pore-forming protein gasdermin D regulates interleukin-1 secretion from living macrophages. *Immunity* **48**, 35-44 (2018).
245. Chu, L.H.*, et al.* The oxidized phospholipid oxPAPC protects from septic shock by targeting the non-canonical inflammasome in macrophages. *Nat Commun* **9**, 996 (2018).
246. Man, S.M.*, et al.* Differential roles of caspase-1 and caspase-11 in infection and inflammation. *Scientific Reports* **7**, 45126 (2017).
247. Gurung, P.*, et al.* Toll or Interleukin-1 Receptor (TIR) Domain-containing Adaptor Inducing Interferon-β (TRIF)-mediated Caspase-11 Protease Production Integrates Toll-like Receptor 4 (TLR4) Protein- and Nlrp3 Inflammasome-mediated Host Defense against Enteropathogens. *The Journal of Biological Chemistry* **287**, 34474-34483 (2012).
248. Broz, P.*, et al.* Caspase-11 increases susceptibility to *Salmonella* infection in the absence of caspase-1. *Nature* **490**, 288-291 (2012).
249. Rathinam, V.A.K.*, et al.* TRIF Licenses Caspase-11-Dependent NLRP3 Inflammasome Activation by Gram-Negative Bacteria. *Cell* **150**, 606-619 (2012).
250. Napier, B.A.*, et al.* Complement pathway amplifies caspase-11–dependent cell death and endotoxin-induced sepsis severity. *The Journal of Experimental Medicine* **213**, 2365-2382 (2016).
251. Man, S.M., Place, D.E., Kuriakose, T. & Kanneganti, T.-D. Interferon-inducible guanylate-binding proteins at the interface of cell-autonomous immunity and inflammasome activation. *Journal of Leukocyte Biology* **101**, 143-150 (2017).
252. Meunier, E.*, et al.* Caspase-11 activation requires lysis of pathogen-containing vacuoles by IFN-induced GTPases. *Nature* **509**, 366-370 (2014).
253. Pilla, D.M.*, et al.* Guanylate binding proteins promote caspase-11–dependent pyroptosis in response to cytoplasmic LPS. *Proceedings of the National Academy of Sciences of the United States of America* **111**, 6046-6051 (2014).
254. Wandel, M.P.*, et al.* Guanylate-binding proteins convert cytosolic bacteria into caspase-4 signaling platforms. *Nat Immunol* **21**, 880-891 (2020).
255. Santos, J.C.*, et al.* Human GBP1 binds LPS to initiate assembly of a caspase-4 activating platform on cytosolic bacteria. *Nat Commun* **11**, 3276 (2020).
256. Fisch, D.*, et al.* Human GBP1 is a microbe-specific gatekeeper of macrophage apoptosis and pyroptosis. *EMBO J* **38**, e100926 (2019).
257. Kutsch, M.*, et al.* Direct binding of polymeric GBP1 to LPS disrupts bacterial cell envelope functions. *EMBO J* **39**, e104926 (2020).
258. Feng, S. & Man, S.M. Captain GBP1: inflammasomes assemble, pyroptotic endgame. *Nat Immunol* **21**, 829-830 (2020).
259. Man, S.M.*, et al.* IRGB10 Liberates Bacterial Ligands for Sensing by the AIM2 and Caspase-11-NLRP3 Inflammasomes. *Cell* **167**, 382-396.e317 (2016).
260. Deng, M.*, et al.* The endotoxin delivery protein HMGB1 mediates caspase-11-dependent lethality in sepsis. *Immunity* **49**, 740-753 (2018).
261. Finethy, R.*, et al.* Guanylate Binding Proteins Enable Rapid Activation of Canonical and Noncanonical Inflammasomes in Chlamydia-Infected Macrophages. *Infection and Immunity* **83**, 4740-4749 (2015).
262. Deng, M.*, et al.* Platelet-activating factor (PAF) mediates NLRP3-NEK7 inflammasome induction independently of PAFR. *The Journal of experimental medicine* **216**, 2838-2853 (2019).
263. Rashidi, M.*, et al.* The Pyroptotic Cell Death Effector Gasdermin D Is Activated by Gout-Associated Uric Acid Crystals but Is Dispensable for Cell Death and IL-1beta Release. *J Immunol* **203**, 736-748 (2019).
264. Jorgensen, I., Zhang, Y., Krantz, B.A. & Miao, E.A. Pyroptosis triggers pore-induced intracellular traps (PITs) that capture bacteria and lead to their clearance by efferocytosis. *The Journal of Experimental Medicine* **213**, 2113-2128 (2016).
265. Chen, K.W.*, et al.* Noncanonical inflammasome signaling elicits gasdermin D–dependent neutrophil extracellular traps. *Science immunology* **3**, eaar6676 (2018).

266. Kambara, H.*, et al.* Gasdermin D exerts anti-inflammatory effects by promoting neutrophil death. *Cell reports* **22**, 2924-2936 (2018).
267. Broz, P., Pelegrin, P. & Shao, F. The gasdermins, a protein family executing cell death and inflammation. *Nat Rev Immunol* **20**, 143-157 (2020).
268. Rühl, S.*, et al.* ESCRT-dependent membrane repair negatively regulates pyroptosis downstream of GSDMD activation. *Science* **362**, 956-960 (2018).
269. Taabazuing, C.Y., Okondo, M.C. & Bachovchin, D.A. Pyroptosis and Apoptosis Pathways Engage in Bidirectional Crosstalk in Monocytes and Macrophages. *Cell Chemical Biology* **24**, 507-514.e504 (2017).
270. Orning, P.*, et al.* Pathogen blockade of TAK1 triggers caspase-8-dependent cleavage of gasdermin D and cell death. *Science* **362**, 1064-1069 (2018).
271. Sarhan, J.*, et al.* Caspase-8 induces cleavage of gasdermin D to elicit pyroptosis during *Yersinia* infection. *Proceedings of the National Academy of Sciences* **115**, E10888-E10897 (2018).
272. Taabazuing, C.Y., Okondo, M.C. & Bachovchin, D.A. Pyroptosis and Apoptosis Pathways Engage in Bidirectional Crosstalk in Monocytes and Macrophages. *Cell chemical biology* **24**, 507-514 e504 (2017).
273. Chen, K.W.*, et al.* Extrinsic and intrinsic apoptosis activate pannexin-1 to drive NLRP3 inflammasome assembly. *EMBO J* **38** (2019).
274. Wang, Y.*, et al.* Chemotherapy drugs induce pyroptosis through caspase-3 cleavage of a Gasdermin. *Nature* **547**, 99–103 (2017).
275. Chen, K.W.*, et al.* Noncanonical inflammasome signaling elicits gasdermin D-dependent neutrophil extracellular traps. *Sci Immunol* **3**, eaar6676 (2018).
276. Cerqueira, D.M.*, et al.* Guanylate-binding protein 5 licenses caspase-11 for Gasdermin-D mediated host resistance to *Brucella abortus* infection. *PLoS Pathog* **14**, e1007519 (2018).
277. Kanneganti, A.*, et al.* GSDMD is critical for autoinflammatory pathology in a mouse model of Familial Mediterranean Fever. *The Journal of experimental medicine* **215**, 1519-1529 (2018).
278. Xiao, J.*, et al.* Gasdermin D mediates the pathogenesis of neonatal-onset multisystem inflammatory disease in mice. *PLoS Biol* **16**, e3000047 (2018).
279. Hu, J.J.*, et al.* FDA-approved disulfiram inhibits pyroptosis by blocking gasdermin D pore formation. *Nat Immunol* **21**, 736-745 (2020).
280. Humphries, F.*, et al.* Succination inactivates gasdermin D and blocks pyroptosis. *Science* **369**, 1633-1637 (2020).
281. Amer, A.*, et al.* Regulation of *Legionella* phagosome maturation and infection through flagellin and host Ipaf. *J Biol Chem* **281**, 35217-35223 (2006).
282. Franchi, L.*, et al.* Cytosolic flagellin requires Ipaf for activation of caspase-1 and interleukin 1beta in *Salmonella*-infected macrophages. *Nat Immunol* **7**, 576-582 (2006).
283. Miao, E.A.*, et al.* Cytoplasmic flagellin activates caspase-1 and secretion of interleukin 1beta via Ipaf. *Nat Immunol* **7**, 569-575 (2006).
284. Ren, T., Zamboni, D.S., Roy, C.R., Dietrich, W.F. & Vance, R.E. Flagellin-deficient *Legionella* mutants evade caspase-1- and Naip5-mediated macrophage immunity. *PLoS Pathog* **2**, e18 (2006).
285. Miao, E.A., Ernst, R.K., Dors, M., Mao, D.P. & Aderem, A. *Pseudomonas aeruginosa* activates caspase 1 through Ipaf. *Proc Natl Acad Sci U S A* **105**, 2562-2567 (2008).
286. Miao, E.A.*, et al.* Innate immune detection of the type III secretion apparatus through the NLRC4 inflammasome. *Proc Natl Acad Sci U S A* **107**, 3076-3080 (2010).
287. Suzuki, S.*, et al. Shigella* type III secretion protein MxiI is recognized by Naip2 to induce Nlrc4 inflammasome activation independently of Pkcdelta. *PLoS Pathog* **10**, e1003926 (2014).
288. Yang, J., Zhao, Y., Shi, J. & Shao, F. Human NAIP and mouse NAIP1 recognize bacterial type III secretion needle protein for inflammasome activation. *Proc Natl Acad Sci U S A* **110**, 14408-14413 (2013).

289. Rayamajhi, M., Zak, D.E., Chavarria-Smith, J., Vance, R.E. & Miao, E.A. Cutting edge: Mouse NAIP1 detects the type III secretion system needle protein. *J Immunol* **191**, 3986-3989 (2013).
290. Kofoed, E.M. & Vance, R.E. Innate immune recognition of bacterial ligands by NAIPs determines inflammasome specificity. *Nature* **477**, 592-595 (2011).
291. Rauch, I.*, et al.* NAIP proteins are required for cytosolic detection of specific bacterial ligands in vivo. *J Exp Med* **213**, 657-665 (2016).
292. Zhao, Y.*, et al.* Genetic functions of the NAIP family of inflammasome receptors for bacterial ligands in mice. *J Exp Med* **213**, 647-656 (2016).
293. Zhao, Y.*, et al.* The NLRC4 inflammasome receptors for bacterial flagellin and type III secretion apparatus. *Nature* **477**, 596-600 (2011).
294. Molofsky, A.B.*, et al.* Cytosolic recognition of flagellin by mouse macrophages restricts *Legionella pneumophila* infection. *J Exp Med* **203**, 1093-1104 (2006).
295. Vinzing, M.*, et al.* NAIP and Ipaf control *Legionella pneumophila* replication in human cells. *J Immunol* **180**, 6808-6815 (2008).
296. Lightfield, K.L.*, et al.* Critical function for Naip5 in inflammasome activation by a conserved carboxy-terminal domain of flagellin. *Nat Immunol* **9**, 1171-1178 (2008).
297. Lightfield, K.L.*, et al.* Differential Requirements for NAIP5 in Activation of the NLRC4 Inflammasome. *Infection and Immunity* **79**, 1606-1614 (2011).
298. Wright Jr, E.K.*, et al.* Naip5 Affects Host Susceptibility to the Intracellular Pathogen *Legionella pneumophila*. *Current Biology* **13**, 27-36 (2003).
299. Diez, E.*, et al.* Birc1e is the gene within the Lgn1 locus associated with resistance to *Legionella pneumophila*. *Nat Genet* **33**, 55-60 (2003).
300. Diez, E., Yaraghi, Z., MacKenzie, A. & Gros, P. The Neuronal Apoptosis Inhibitory Protein (Naip) Is Expressed in Macrophages and Is Modulated After Phagocytosis and During Intracellular Infection with *Legionella pneumophila*. *The Journal of Immunology* **164**, 1470 (2000).
301. Zamboni, D.S.*, et al.* The Birc1e cytosolic pattern-recognition receptor contributes to the detection and control of *Legionella pneumophila* infection. *Nat Immunol* **7**, 318-325 (2006).
302. Endrizzi, M.G., Hadinoto, V., Growney, J.D., Miller, W. & Dietrich, W.F. Genomic sequence analysis of the mouse Naip gene array. *Genome research* **10**, 1095-1102 (2000).
303. Tenthorey, J.L., Kofoed, E.M., Daugherty, M.D., Malik, H.S. & Vance, R.E. Molecular basis for specific recognition of bacterial ligands by NAIP/NLRC4 inflammasomes. *Mol Cell* **54**, 17-29 (2014).
304. Karki, R.*, et al.* IRF8 regulates transcription of Naips for NLRC4 inflammasome activation. *Cell* **173**, 920-933 (2018).
305. Kortmann, J., Brubaker, S.W. & Monack, D.M. Cutting Edge: Inflammasome Activation in Primary Human Macrophages Is Dependent on Flagellin. *J Immunol* **195**, 815-819 (2015).
306. Chen, K.W.*, et al.* The neutrophil NLRC4 inflammasome selectively promotes IL-1beta maturation without pyroptosis during acute *Salmonella* challenge. *Cell Rep* **8**, 570-582 (2014).
307. Kupz, A.*, et al.* NLRC4 inflammasomes in dendritic cells regulate noncognate effector function by memory CD8(+) T cells. *Nat Immunol* **13**, 162-169 (2012).
308. Poyet, J.L.*, et al.* Identification of Ipaf, a human caspase-1-activating protein related to Apaf-1. *J Biol Chem* **276**, 28309-28313 (2001).
309. Mariathasan, S.*, et al.* Differential activation of the inflammasome by caspase-1 adaptors ASC and Ipaf. *Nature* **430**, 213-218 (2004).
310. Franchi, L.*, et al.* Critical role for Ipaf in *Pseudomonas aeruginosa*-induced caspase-1 activation. *Eur J Immunol* **37**, 3030-3039 (2007).
311. Sutterwala, F.S.*, et al.* Immune recognition of *Pseudomonas aeruginosa* mediated by the IPAF/NLRC4 inflammasome. *J Exp Med* **204**, 3235-3245 (2007).

312. Case, C.L., Shin, S. & Roy, C.R. Asc and Ipaf Inflammasomes direct distinct pathways for caspase-1 activation in response to *Legionella pneumophila*. *Infect Immun* **77**, 1981-1991 (2009).
313. Suzuki, T.*, et al.* Differential regulation of caspase-1 activation, pyroptosis, and autophagy via Ipaf and ASC in *Shigella*-infected macrophages. *PLoS Pathog* **3**, e111 (2007).
314. Man, S.M.*, et al. Salmonella* infection induces recruitment of Caspase-8 to the inflammasome to modulate IL-1beta production. *J Immunol* **191**, 5239-5246 (2013).
315. Hu, Z.*, et al.* Crystal structure of NLRC4 reveals its autoinhibition mechanism. *Science* **341**, 172-175 (2013).
316. Halff, E.F.*, et al.* Formation and structure of a NAIP5-NLRC4 inflammasome induced by direct interactions with conserved N- and C-terminal regions of flagellin. *J Biol Chem* **287**, 38460-38472 (2012).
317. Marxen, S.*, et al.* Depsipeptide Intermediates Interrogate Proposed Biosynthesis of Cereulide, the Emetic Toxin of *Bacillus cereus*. *Sci Rep* **5**, 10637 (2015).
318. Zhang, L.*, et al.* Cryo-EM structure of the activated NAIP2-NLRC4 inflammasome reveals nucleated polymerization. *Science* **350**, 404-409 (2015).
319. Qu, Y.*, et al.* Phosphorylation of NLRC4 is critical for inflammasome activation. *Nature* **490**, 539-542 (2012).
320. Matusiak, M.*, et al.* Flagellin-induced NLRC4 phosphorylation primes the inflammasome for activation by NAIP5. *Proc Natl Acad Sci U S A* **112**, 1541-1546 (2015).
321. Liu, W.*, et al.* LRRK2 promotes the activation of NLRC4 inflammasome during *Salmonella* Typhimurium infection. *Journal of Experimental Medicine* **214**, 3051-3066 (2017).
322. Qu, Y.*, et al.* NLRP3 recruitment by NLRC4 during *Salmonella* infection. *J Exp Med* **213**, 877-885 (2016).
323. Tenthorey, J.L.*, et al.* NLRC4 inflammasome activation is NLRP3- and phosphorylation-independent during infection and does not protect from melanoma. *The Journal of experimental medicine* **217**, e20191736 (2020).
324. Ip, W.K. & Medzhitov, R. Macrophages monitor tissue osmolarity and induce inflammatory response through NLRP3 and NLRC4 inflammasome activation. *Nat Commun* **6**, 6931 (2015).
325. Denes, A.*, et al.* AIM2 and NLRC4 inflammasomes contribute with ASC to acute brain injury independently of NLRP3. *Proc Natl Acad Sci U S A* **112**, 4050-4055 (2015).
326. Rauch, I.*, et al.* NAIP-NLRC4 Inflammasomes Coordinate Intestinal Epithelial Cell Expulsion with Eicosanoid and IL-18 Release via Activation of Caspase-1 and -8. *Immunity* **46**, 649-659 (2017).
327. Franchi, L.*, et al.* NLRC4-driven production of IL-1beta discriminates between pathogenic and commensal bacteria and promotes host intestinal defense. *Nat Immunol* **13**, 449-456 (2012).
328. Nordlander, S., Pott, J. & Maloy, K.J. NLRC4 expression in intestinal epithelial cells mediates protection against an enteric pathogen. *Mucosal immunology* **7**, 775-785 (2014).
329. Mitchell, P.S.*, et al.* NAIP-NLRC4-deficient mice are susceptible to shigellosis. *Elife* **9**, e59022 (2020).
330. Schieber, A.M.*, et al.* Disease tolerance mediated by microbiome *E. coli* involves inflammasome and IGF-1 signaling. *Science* **350**, 558-563 (2015).
331. Ayres, J.S., Trinidad, N.J. & Vance, R.E. Lethal inflammasome activation by a multi-drug resistant pathobiont upon antibiotic disruption of the microbiota. *Nature medicine* **18**, 799-806 (2012).
332. von Moltke, J.*, et al.* Rapid induction of inflammatory lipid mediators by the inflammasome in vivo. *Nature* **490**, 107-111 (2012).

333. Akhade, A.S.*, et al.* Type 1 interferon-dependent repression of NLRC4 and iPLA2 licenses down-regulation of *Salmonella* flagellin inside macrophages. *Proc Natl Acad Sci U S A* **117**, 29811-29822 (2020).
334. Hu, B.*, et al.* Inflammation-induced tumorigenesis in the colon is regulated by caspase-1 and NLRC4. *Proc Natl Acad Sci U S A* **107**, 21635-21640 (2010).
335. Allam, R.*, et al.* Epithelial NAIPs protect against colonic tumorigenesis. *J Exp Med* **212**, 369-383 (2015).
336. Kolb, R.*, et al.* Obesity-associated NLRC4 inflammasome activation drives breast cancer progression. *Nat Commun* **7**, 13007 (2016).
337. Janowski, A.M.*, et al.* NLRC4 suppresses melanoma tumor progression independently of inflammasome activation. *J Clin Invest* **126**, 3917-3928 (2016).
338. Furman, D.*, et al.* Expression of specific inflammasome gene modules stratifies older individuals into two extreme clinical and immunological states. *Nature medicine* **23**, 174-184 (2017).
339. Romberg, N.*, et al.* Mutation of NLRC4 causes a syndrome of enterocolitis and autoinflammation. *Nat Genet* **46**, 1135-1139 (2014).
340. Canna, S.W.*, et al.* An activating NLRC4 inflammasome mutation causes autoinflammation with recurrent macrophage activation syndrome. *Nat Genet* **46**, 1140-1146 (2014).
341. Kitamura, A., Sasaki, Y., Abe, T., Kano, H. & Yasutomo, K. An inherited mutation in NLRC4 causes autoinflammation in human and mice. *J Exp Med* **211**, 2385-2396 (2014).
342. Raghawan, A.K.*, et al.* A Disease-associated Mutant of NLRC4 Shows Enhanced Interaction with SUG1 Leading to Constitutive FADD-dependent Caspase-8 Activation and Cell Death. *J Biol Chem* **292**, 1218-1230 (2017).
343. Kumar, Y., Radha, V. & Swarup, G. Interaction with Sug1 enables Ipaf ubiquitination leading to caspase 8 activation and cell death. *Biochemical Journal* **427**, 91 (2010).
344. Canna, S.W.*, et al.* Life-threatening NLRC4-associated hyperinflammation successfully treated with IL-18 inhibition. *The Journal of allergy and clinical immunology* **139**, 1698-1701 (2017).
345. Burckstummer, T.*, et al.* An orthogonal proteomic-genomic screen identifies AIM2 as a cytoplasmic DNA sensor for the inflammasome. *Nat Immunol* **10**, 266-272 (2009).
346. Fernandes-Alnemri, T., Yu, J.W., Datta, P., Wu, J. & Alnemri, E.S. AIM2 activates the inflammasome and cell death in response to cytoplasmic DNA. *Nature* **458**, 509-513 (2009).
347. Hornung, V.*, et al.* AIM2 recognizes cytosolic dsDNA and forms a caspase-1-activating inflammasome with ASC. *Nature* **458**, 514-518 (2009).
348. Roberts, T.L.*, et al.* HIN-200 proteins regulate caspase activation in response to foreign cytoplasmic DNA. *Science* **323**, 1057-1060 (2009).
349. Kumari, P., Russo, A.J., Shivcharan, S. & Rathinam, V.A. AIM2 in health and disease: Inflammasome and beyond. *Immunol Rev* **297**, 83-95 (2020).
350. Jin, T.*, et al.* Structures of the HIN domain:DNA complexes reveal ligand binding and activation mechanisms of the AIM2 inflammasome and IFI16 receptor. *Immunity* **36**, 561-571 (2012).
351. Matyszewski, M., Morrone, S.R. & Sohn, J. Digital signaling network drives the assembly of the AIM2-ASC inflammasome. *Proceedings of the National Academy of Sciences* **115**, E1963-E1972 (2018).
352. Jin, T., Perry, A., Smith, P., Jiang, J. & Xiao, T.S. Structure of the absent in melanoma 2 (AIM2) pyrin domain provides insights into the mechanisms of AIM2 autoinhibition and inflammasome assembly. *J Biol Chem* **288**, 13225-13235 (2013).
353. Morrone, S.R.*, et al.* Assembly-driven activation of the AIM2 foreign-dsDNA sensor provides a polymerization template for downstream ASC. *Nat Commun* **6**, 7827 (2015).
354. Lu, A., Kabaleeswaran, V., Fu, T., Magupalli, V.G. & Wu, H. Crystal Structure of the F27G AIM2 PYD Mutant and Similarities of its Self-association to DED/DED Interactions. *Journal of molecular biology* **426**, 1420-1427 (2014).

355. Hou, X. & Niu, X. The NMR solution structure of AIM2 PYD domain from *Mus musculus* reveals a distinct α2–α3 helix conformation from its human homologues. *Biochemical and Biophysical Research Communications* **461**, 396-400 (2015).
356. Jones, J.W.*, et al.* Absent in melanoma 2 is required for innate immune recognition of *Francisella tularensis*. *Proc Natl Acad Sci U S A* **107**, 9771-9776 (2010).
357. Shi, C.S.*, et al.* Activation of autophagy by inflammatory signals limits IL-1beta production by targeting ubiquitinated inflammasomes for destruction. *Nat Immunol* **13**, 255-263 (2012).
358. Liu, T.*, et al.* TRIM11 Suppresses AIM2 Inflammasome by Degrading AIM2 via p62-Dependent Selective Autophagy. *Cell Rep* **16**, 1988-2002 (2016).
359. de Almeida, L.*, et al.* The PYRIN Domain-only Protein POP1 Inhibits Inflammasome Assembly and Ameliorates Inflammatory Disease. *Immunity* **43**, 264-276 (2015).
360. Khare, S.*, et al.* The PYRIN domain-only protein POP3 inhibits ALR inflammasomes and regulates responses to infection with DNA viruses. *Nat Immunol* **15**, 343-353 (2014).
361. Yin, Q.*, et al.* Molecular mechanism for p202-mediated specific inhibition of AIM2 inflammasome activation. *Cell Rep* **4**, 327-339 (2013).
362. Choubey, D., Walter, S., Geng, Y. & Xin, H. Cytoplasmic localization of the interferon-inducible protein that is encoded by the AIM2 (absent in melanoma) gene from the 200-gene family. *FEBS Letters* **474**, 38-42 (2000).
363. Choubey, D. & Panchanathan, R. Interferon-inducible Ifi200-family genes in systemic lupus erythematosus. *Immunology letters* **119**, 32-41 (2008).
364. Sester, D.P.*, et al.* Deficient NLRP3 and AIM2 Inflammasome Function in Autoimmune NZB Mice. *The Journal of Immunology* **195**, 1233 (2015).
365. Hayward, J.A., Mathur, A., Ngo, C. & Man, S.M. Cytosolic Recognition of Microbes and Pathogens: Inflammasomes in Action. *Microbiol Mol Biol Rev* **82**, :e00015-18 (2018).
366. Man, S.M.*, et al.* The transcription factor IRF1 and guanylate-binding proteins target activation of the AIM2 inflammasome by *Francisella* infection. *Nat Immunol* **16**, 467-475 (2015).
367. Muruve, D.A.*, et al.* The inflammasome recognizes cytosolic microbial and host DNA and triggers an innate immune response. *Nature* **452**, 103-107 (2008).
368. Henry, T., Brotcke, A., Weiss, D.S., Thompson, L.J. & Monack, D.M. Type I interferon signaling is required for activation of the inflammasome during *Francisella* infection. *J Exp Med* **204**, 987-994 (2007).
369. Belhocine, K. & Monack, D.M. *Francisella* infection triggers activation of the AIM2 inflammasome in murine dendritic cells. *Cell Microbiol* **14**, 71-80 (2012).
370. Fang, R.*, et al.* Type I interferon signaling regulates activation of the absent in melanoma 2 inflammasome during *Streptococcus pneumoniae* infection. *Infect Immun* **82**, 2310-2317 (2014).
371. Shah, S.*, et al.* Cutting edge: *Mycobacterium tuberculosis* but not nonvirulent mycobacteria inhibits IFN-beta and AIM2 inflammasome-dependent IL-1beta production via its ESX-1 secretion system. *J Immunol* **191**, 3514-3518 (2013).
372. Meunier, E.*, et al.* Guanylate-binding proteins promote activation of the AIM2 inflammasome during infection with *Francisella novicida*. *Nat Immunol* **16**, 476-484 (2015).
373. Ge, J., Gong, Y.N., Xu, Y. & Shao, F. Preventing bacterial DNA release and absent in melanoma 2 inflammasome activation by a *Legionella* effector functioning in membrane trafficking. *Proc Natl Acad Sci U S A* **109**, 6193-6198 (2012).
374. Huang, Y.*, et al.* Interaction between HCMV pUL83 and human AIM2 disrupts the activation of the AIM2 inflammasome. *Virology journal* **14**, 34 (2017).
375. Sampson, T.R.*, et al.* A CRISPR-Cas system enhances envelope integrity mediating antibiotic resistance and inflammasome evasion. *Proc Natl Acad Sci U S A* **111**, 11163-11168 (2014).

376. Storek, K.M., Gertsvolf, N.A., Ohlson, M.B. & Monack, D.M. cGAS and Ifi204 cooperate to produce type I IFNs in response to *Francisella* infection. *J Immunol* **194**, 3236-3245 (2015).
377. Zhang, H.*, et al.* AIM2 Inflammasome Is Critical for Influenza-Induced Lung Injury and Mortality. *J Immunol* **198**, 4383-4393 (2017).
378. Schattgen, S.A., Gao, G., Kurt-Jones, E.A. & Fitzgerald, K.A. Cutting Edge: DNA in the Lung Microenvironment during Influenza Virus Infection Tempers Inflammation by Engaging the DNA Sensor AIM2. *J Immunol* **196**, 29-33 (2016).
379. Karki, R.*, et al.* Concerted activation of the AIM2 and NLRP3 inflammasomes orchestrates host protection against *Aspergillus* infection. *Cell host & microbe* **17**, 357-368 (2015).
380. Pierini, R.*, et al.* AIM2/ASC triggers caspase-8-dependent apoptosis in *Francisella*-infected caspase-1-deficient macrophages. *Cell death and differentiation* **19**, 1709-1721 (2012).
381. Zhu, Q., Man, S.M., Karki, R., Malireddi, R.S. & Kanneganti, T.-D. Detrimental type I interferon signaling dominates protective AIM2 inflammasome responses during *Francisella novicida* infection. *Cell reports* **22**, 3168-3174 (2018).
382. Dihlmann, S.*, et al.* Lack of Absent in Melanoma 2 (AIM2) expression in tumor cells is closely associated with poor survival in colorectal cancer patients. *International journal of cancer* **135**, 2387-2396 (2014).
383. Schulmann, K.*, et al.* HNPCC-associated small bowel cancer: Clinical and molecular characteristics. *Gastroenterology* **128**, 590-599 (2005).
384. Kim, T.-M., Laird, P.W. & Park, P.J. The Landscape of Microsatellite Instability in Colorectal and Endometrial Cancer Genomes. *Cell* **155**, 10.1016/j.cell.2013.1010.1015 (2013).
385. Woerner, S.M.*, et al.* The putative tumor suppressor AIM2 is frequently affected by different genetic alterations in microsatellite unstable colon cancers. *Genes, Chromosomes and Cancer* **46**, 1080-1089 (2007).
386. Wilson, J.E.*, et al.* Inflammasome-independent role of AIM2 in suppressing colon tumorigenesis via DNA-PK and Akt. *Nat Med* **21**, 906-913 (2015).
387. Man, S.M.*, et al.* Critical Role for the DNA Sensor AIM2 in Stem Cell Proliferation and Cancer. *Cell* **162**, 45-58 (2015).
388. Chen, J., Wang, Z. & Yu, S. AIM2 regulates viability and apoptosis in human colorectal cancer cells via the PI3K/Akt pathway. *OncoTargets and therapy* **10**, 811-817 (2017).
389. Hu, S.*, et al.* The DNA Sensor AIM2 Maintains Intestinal Homeostasis via Regulation of Epithelial Antimicrobial Host Defense. *Cell Rep* **13**, 1922-1936 (2015).
390. Ratsimandresey, R.A., Indramohan, M., Dorfleutner, A. & Stehlik, C. The AIM2 inflammasome is a central regulator of intestinal homeostasis through the IL-18/IL-22/STAT3 pathway. *Cellular & molecular immunology* **14**, 127-142 (2017).
391. Hupa, K.J.*, et al.* AIM2 inflammasome-derived IL-1beta induces postoperative ileus in mice. *Sci Rep* **9**, 10602 (2019).
392. Farshchian, M.*, et al.* Tumor cell-specific AIM2 regulates growth and invasion of cutaneous squamous cell carcinoma. *Oncotarget* (2017).
393. Dombrowski, Y.*, et al.* Cytosolic DNA triggers inflammasome activation in keratinocytes in psoriatic lesions. *Science translational medicine* **3**, 82ra38 (2011).
394. Jakobs, C., Perner, S. & Hornung, V. AIM2 Drives Joint Inflammation in a Self-DNA Triggered Model of Chronic Polyarthritis. *PLoS One* **10**, e0131702 (2015).
395. Chung, I.C.*, et al.* EFLA 945 restricts AIM2 inflammasome activation by preventing DNA entry for psoriasis treatment. *Cytokine* **127**, 154951 (2020).
396. Hu, B.*, et al.* The DNA-sensing AIM2 inflammasome controls radiation-induced cell death and tissue injury. *Science* **354**, 765-768 (2016).
397. Gao, J.*, et al.* Inhibition of AIM2 inflammasome-mediated pyroptosis by Andrographolide contributes to amelioration of radiation-induced lung inflammation and fibrosis. *Cell Death Dis* **10**, 957 (2019).

398. Di Micco, A.*, et al.* AIM2 inflammasome is activated by pharmacological disruption of nuclear envelope integrity. *Proceedings of the National Academy of Sciences of the United States of America* **113**, E4671-E4680 (2016).
399. Dang, E.V., McDonald, J.G., Russell, D.W. & Cyster, J.G. Oxysterol restraint of cholesterol synthesis prevents AIM2 inflammasome activation. *Cell* **171**, 1057-1071 (2017).
400. Lian, Q.*, et al.* Chemotherapy-induced intestinal inflammatory responses are mediated by exosome secretion of double-strand DNA via AIM2 inflammasome activation. *Cell Res* **27**, 784-800 (2017).
401. Lammert, C.R.*, et al.* AIM2 inflammasome surveillance of DNA damage shapes neurodevelopment. *Nature* **580**, 647-652 (2020).
402. The International, F.M.F.C. Ancient Missense Mutations in a New Member of the RoRet Gene Family Are Likely to Cause Familial Mediterranean Fever. *Cell* **90**, 797-807 (1997).
403. Consortium., F.F. A candidate gene for familial Mediterranean fever. *Nat Genet* **17**, 25-31 (1997).
404. Chae, J.J.*, et al.* Gain-of-function Pyrin Mutations Induce NLRP3 Protein-Independent Interleukin-1β Activation and Severe Autoinflammation in Mice. *Immunity* **34**, 755-768 (2011).
405. Masumoto, J.*, et al.* ASC is an activating adaptor for NF-κB and caspase-8-dependent apoptosis. *Biochemical and Biophysical Research Communications* **303**, 69-73 (2003).
406. Chae, J.J.*, et al.* The B30.2 domain of pyrin, the familial Mediterranean fever protein, interacts directly with caspase-1 to modulate IL-1β production. *Proceedings of the National Academy of Sciences of the United States of America* **103**, 9982-9987 (2006).
407. Papin, S.*, et al.* The SPRY domain of Pyrin, mutated in familial Mediterranean fever patients, interacts with inflammasome components and inhibits proIL-1[beta] processing. *Cell Death Differ* **14**, 1457-1466 (2007).
408. Gavrilin, M.A.*, et al.* Activation of the Pyrin Inflammasome by Intracellular *Burkholderia cenocepacia*. *Journal of immunology (Baltimore, Md. : 1950)* **188**, 3469-3477 (2012).
409. Xu, H.*, et al.* Innate immune sensing of bacterial modifications of Rho GTPases by the Pyrin inflammasome. *Nature* **513**, 237-241 (2014).
410. Xu, H.*, et al.* Innate immune sensing of bacterial modifications of Rho GTPases by the Pyrin inflammasome. *Nature* **513**, 237-241 (2014).
411. Chung, L.K.*, et al.* The *Yersinia* virulence factor YopM hijacks host kinases to inhibit type III effector-triggered activation of the pyrin inflammasome. *Cell host & microbe* **20**, 296-306 (2016).
412. Ratner, D.*, et al.* The *Yersinia pestis* effector YopM inhibits pyrin inflammasome activation. *PLoS pathogens* **12**, e1006035 (2016).
413. Mamantopoulos, M.*, et al.* El Tor Biotype *Vibrio cholerae* Activates the Caspase-11-Independent Canonical Nlrp3 and Pyrin Inflammasomes. *Frontiers in immunology* **10**, 2463 (2019).
414. Chung, L.K.*, et al.* The *Yersinia* Virulence Factor YopM Hijacks Host Kinases to Inhibit Type III Effector-Triggered Activation of the Pyrin Inflammasome. *Cell Host Microbe* **20**, 296-306 (2016).
415. Brodsky, I.E.*, et al.* The *Yersinia pestis* Effector YopM Inhibits Pyrin Inflammasome Activation. *PLOS Pathogens* **12**, e1006035 (2016).
416. Medici, N.P., Rashid, M. & Bliska, J.B. Characterization of Pyrin Dephosphorylation and Inflammasome Activation in Macrophages as Triggered by the *Yersinia* Effectors YopE and YopT. *Infection and immunity* **87**, e00822-18 (2019).
417. Dumas, A.*, et al.* The Inflammasome Pyrin Contributes to Pertussis Toxin-Induced IL-1β Synthesis, Neutrophil Intravascular Crawling and Autoimmune Encephalomyelitis. *PLoS Pathogens* **10**, e1004150 (2014).
418. Aubert, Daniel F.*, et al.* A *Burkholderia* Type VI Effector Deamidates Rho GTPases to Activate the Pyrin Inflammasome and Trigger Inflammation. *Cell Host & Microbe* **19**, 664-674 (2016).

419. Van Gorp, H.*, et al.* Familial Mediterranean fever mutations lift the obligatory requirement for microtubules in Pyrin inflammasome activation. *Proceedings of the National Academy of Sciences of the United States of America* **113**, 14384-14389 (2016).
420. Sharma, D., Malik, A., Balakrishnan, A., Malireddi, R.K.S. & Kanneganti, T.D. RIPK3 Promotes Mefv Expression and Pyrin Inflammasome Activation via Modulation of mTOR Signaling. *J Immunol* **205**, 2778-2785 (2020).
421. Jéru, I.*, et al.* Interaction of pyrin with 14.3.3 in an Isoform-specific and phosphorylation-dependent manner regulates its translocation to the nucleus. *Arthritis & Rheumatism* **52**, 1848-1857 (2005).
422. Gao, W., Yang, J., Liu, W., Wang, Y. & Shao, F. Site-specific phosphorylation and microtubule dynamics control Pyrin inflammasome activation. *Proceedings of the National Academy of Sciences of the United States of America* **113**, E4857-E4866 (2016).
423. Masters, S.L.*, et al.* Familial autoinflammation with neutrophilic dermatosis reveals a regulatory mechanism of pyrin activation. *Science translational medicine* **8**, 332ra345 (2016).
424. Park, Y.H., Wood, G., Kastner, D.L. & Chae, J.J. Pyrin Inflammasome Activation and RhoA Signaling in the Autoinflammatory Diseases FMF and HIDS. *Nature immunology* **17**, 914-921 (2016).
425. Magnotti, F.*, et al.* Pyrin dephosphorylation is sufficient to trigger inflammasome activation in familial Mediterranean fever patients. *EMBO Mol Med* **11**, e10547 (2019).
426. Kim, M.L.*, et al.* Aberrant actin depolymerization triggers the pyrin inflammasome and autoinflammatory disease that is dependent on IL-18, not IL-1β. *The Journal of Experimental Medicine* **212**, 927-938 (2015).
427. Waite, A.L.*, et al.* Pyrin and ASC Co-Localize to Cellular Sites that Are Rich in Polymerizing Actin. *Experimental Biology and Medicine* **234**, 40-52 (2009).
428. Kimura, T.*, et al.* TRIM-mediated precision autophagy targets cytoplasmic regulators of innate immunity. *The Journal of Cell Biology* **210**, 973-989 (2015).
429. Chen, G.Y., Liu, M., Wang, F., Bertin, J. & Núñez, G. A functional role for Nlrp6 in intestinal inflammation and tumorigenesis. *The Journal of Immunology* **186**, 7187-7194 (2011).
430. Elinav, E.*, et al.* NLRP6 inflammasome regulates colonic microbial ecology and risk for colitis. *Cell* **145**, 745-757 (2011).
431. Normand, S.*, et al.* Nod-like receptor pyrin domain-containing protein 6 (NLRP6) controls epithelial self-renewal and colorectal carcinogenesis upon injury. *Proceedings of the National Academy of Sciences of the United States of America* **108**, 9601-9606 (2011).
432. Levy, M.*, et al.* Microbiota-Modulated Metabolites Shape the Intestinal Microenvironment by Regulating NLRP6 Inflammasome Signaling. *Cell* **163**, 1428-1443 (2015).
433. Wang, P.*, et al.* Nlrp6 regulates intestinal antiviral innate immunity. *Science* **350**, 826-830 (2015).
434. Lemire, P.*, et al.* The NLR protein NLRP6 does not impact gut microbiota composition. *Cell Rep* **21**, 3653-3661 (2017).
435. Mamantopoulos, M.*, et al.* Nlrp6- and ASC-dependent inflammasomes do not shape the commensal gut microbiota composition. *Immunity* **47**, 339-348 (2017).
436. Anand, P.K.*, et al.* NLRP6 negatively regulates innate immunity and host defence against bacterial pathogens. *Nature* **488**, 389-393 (2012).
437. Ghimire, L.*, et al.* NLRP6 negatively regulates pulmonary host defense in Gram-positive bacterial infection through modulating neutrophil recruitment and function. *PLoS Pathog* **14**, e1007308 (2018).
438. Shen, C.*, et al.* Molecular mechanism for NLRP6 inflammasome assembly and activation. *Proceedings of the National Academy of Sciences of the United States of America* **116**, 2052-2057 (2019).

439. Ren, T., Zamboni, D.S., Roy, C.R., Dietrich, W.F. & Vance, R.E. Flagellin-deficient *Legionella* mutants evade caspase-1-and Naip5-mediated macrophage immunity. *PLoS pathogens* **2**, e18 (2006).
440. Zhao, Y.*, et al.* The NLRC4 inflammasome receptors for bacterial flagellin and type III secretion apparatus. *Nature* **477**, 596-600 (2011).
441. Tenthorey, J.L., Kofoed, E.M., Daugherty, M.D., Malik, H.S. & Vance, R.E. Molecular basis for specific recognition of bacterial ligands by NAIP/NLRC4 inflammasomes. *Molecular cell* **54**, 17-29 (2014).
442. Lightfield, K.L.*, et al.* Critical function for Naip5 in inflammasome activation by a conserved carboxy-terminal domain of flagellin. *Nature immunology* **9**, 1171-1178 (2008).
443. Kofoed, E.M. & Vance, R.E. Innate immune recognition of bacterial ligands by NAIPs determines inflammasome specificity. *Nature* **477**, 592-595 (2011).
444. Wang, P.H.*, et al.* Nlrp6 regulates intestinal antiviral innate immunity. *Science* **350**, 826-830 (2015).
445. Man, S.M.*, et al.* Inflammasome activation causes dual recruitment of NLRC4 and NLRP3 to the same macromolecular complex. *Proc Natl Acad Sci U S A* **111**, 7403-7408 (2014).
446. Frankland, G.C. & Frankland, P.F. XI. Studies on some new micro-organisms obtained from air. *Philosophical Transactions of the Royal Society of London.(B.)*, 257-287 (1887).
447. Farrar, W.E., Jr. Serious infections due to "non-pathogenic" organisms of the genus *Bacillus*. Review of their status as pathogens. *Am J Med* **34**, 134-141 (1963).
448. Bottone, E.J. *Bacillus cereus*, a volatile human pathogen. *Clin Microbiol Rev* **23**, 382-398 (2010).
449. Glasset, B.*, et al. Bacillus cereus*, a serious cause of nosocomial infections: Epidemiologic and genetic survey. *PLoS One* **13**, e0194346 (2018).
450. Liu, Y.*, et al.* Genomic insights into the taxonomic status of the *Bacillus cereus* group. *Sci Rep* **5**, 14082 (2015).
451. Jung, M.Y.*, et al. Bacillus gaemokensis* sp. nov., isolated from foreshore tidal flat sediment from the Yellow Sea. *J Microbiol* **48**, 867-871 (2010).
452. Jimenez, G.*, et al.* Description of *Bacillus toyonensis* sp. nov., a novel species of the *Bacillus cereus* group, and pairwise genome comparisons of the species of the group by means of ANI calculations. *Syst Appl Microbiol* **36**, 383-391 (2013).
453. Jung, M.Y.*, et al. Bacillus manliponensis* sp. nov., a new member of the *Bacillus cereus* group isolated from foreshore tidal flat sediment. *J Microbiol* **49**, 1027-1032 (2011).
454. Liu, B.*, et al. Bacillus bingmayongensis* sp. nov., isolated from the pit soil of Emperor Qin's Terra-cotta warriors in China. *Antonie Van Leeuwenhoek* **105**, 501-510 (2014).
455. Carroll, L.M., Wiedmann, M. & Kovac, J. Proposal of a Taxonomic Nomenclature for the *Bacillus cereus* Group Which Reconciles Genomic Definitions of Bacterial Species with Clinical and Industrial Phenotypes. *mBio* **11**(2020).
456. Ehling-Schulz, M., Frenzel, E. & Gohar, M. Food-bacteria interplay: pathometabolism of emetic *Bacillus cereus*. *Front Microbiol* **6**, 704 (2015).
457. Mock, M. & Fouet, A. Anthrax. *Annu Rev Microbiol* **55**, 647-671 (2001).
458. Senesi, S. & Ghelardi, E. Production, secretion and biological activity of *Bacillus cereus* enterotoxins. *Toxins (Basel)* **2**, 1690-1703 (2010).
459. Mazzantini, D.*, et al.* GTP-Dependent FlhF Homodimer Supports Secretion of a Hemolysin in *Bacillus cereus*. *Front Microbiol* **11**, 879 (2020).
460. Kotiranta, A.*, et al.* Surface structure, hydrophobicity, phagocytosis, and adherence to matrix proteins of *Bacillus cereus* cells with and without the crystalline surface protein layer. *Infection and immunity* **66**, 4895-4902 (1998).
461. Mignot, T.*, et al.* Distribution of S-layers on the surface of *Bacillus cereus* strains: phylogenetic origin and ecological pressure. *Environ Microbiol* **3**, 493-501 (2001).
462. Kotiranta, A., Lounatmaa, K. & Haapasalo, M. Epidemiology and pathogenesis of *Bacillus cereus* infections. *Microbes Infect* **2**, 189-198 (2000).

463. Wijnands, L.M., Dufrenne, J.B., Zwietering, M.H. & van Leusden, F.M. Spores from mesophilic *Bacillus cereus* strains germinate better and grow faster in simulated gastro-intestinal conditions than spores from psychrotrophic strains. *Int J Food Microbiol* **112**, 120-128 (2006).
464. Webb, M.D., Barker, G.C., Goodburn, K.E. & Peck, M.W. Risk presented to minimally processed chilled foods by psychrotrophic *Bacillus cereus*. *Trends Food Sci Technol* **93**, 94-105 (2019).
465. Altayar, M. & Sutherland, A.D. *Bacillus cereus* is common in the environment but emetic toxin producing isolates are rare. *J Appl Microbiol* **100**, 7-14 (2006).
466. Owusu-Kwarteng, J., Wuni, A., Akabanda, F., Tano-Debrah, K. & Jespersen, L. Prevalence, virulence factor genes and antibiotic resistance of *Bacillus cereus sensu lato* isolated from dairy farms and traditional dairy products. *BMC Microbiol* **17**, 65 (2017).
467. Bressuire-Isoard, C., Broussolle, V. & Carlin, F. Sporulation environment influences spore properties in *Bacillus*: evidence and insights on underlying molecular and physiological mechanisms. *FEMS Microbiol Rev* **42**, 614-626 (2018).
468. Kailas, L.*, et al.* Surface architecture of endospores of the *Bacillus cereus*/*anthracis*/*thuringiensis* family at the subnanometer scale. *Proc Natl Acad Sci U S A* **108**, 16014-16019 (2011).
469. Duport, C., Jobin, M. & Schmitt, P. Adaptation in *Bacillus cereus*: From Stress to Disease. *Front Microbiol* **7**, 1550 (2016).
470. Vidic, J., Chaix, C., Manzano, M. & Heyndrickx, M. Food Sensing: Detection of *Bacillus cereus* Spores in Dairy Products. *Biosensors (Basel)* **10** (3), 15 (2020).
471. Hornstra, L.M., van der Voort, M., Wijnands, L.M., Roubos-van den Hil, P.J. & Abee, T. Role of germinant receptors in Caco-2 cell-initiated germination of *Bacillus cereus* ATCC 14579 endospores. *Appl Environ Microbiol* **75**, 1201-1203 (2009).
472. Wijnands, L.M., Dufrenne, J.B., van Leusden, F.M. & Abee, T. Germination of *Bacillus cereus* spores is induced by germinants from differentiated Caco-2 Cells, a human cell line mimicking the epithelial cells of the small intestine. *Appl Environ Microbiol* **73**, 5052-5054 (2007).
473. Kuroki, R.*, et al.* Nosocomial bacteremia caused by biofilm-forming *Bacillus cereus* and *Bacillus thuringiensis*. *Intern Med* **48**, 791-796 (2009).
474. Ikram, S.*, et al. Bacillus cereus* biofilm formation on central venous catheters of hospitalised cardiac patients. *Biofouling* **35**, 204-216 (2019).
475. Caro-Astorga, J.*, et al.* Two genomic regions encoding exopolysaccharide production systems have complementary functions in *B. cereus* multicellularity and host interaction. *Sci Rep* **10**, 1000 (2020).
476. Karsisiotis, A.I., Damblon, C.F. & Roberts, G.C. Solution structures of the *Bacillus cereus* metallo-beta-lactamase BcII and its complex with the broad spectrum inhibitor R-thiomandelic acid. *Biochem J* **456**, 397-407 (2013).
477. Ikeda, M.*, et al.* Clinical characteristics and antimicrobial susceptibility of *Bacillus cereus* blood stream infections. *Ann Clin Microbiol Antimicrob* **14**, 43 (2015).
478. Fiedler, G.*, et al.* Antibiotics resistance and toxin profiles of *Bacillus cereus*-group isolates from fresh vegetables from German retail markets. *BMC Microbiol* **19**, 250 (2019).
479. Park, K.M., Jeong, M., Park, K.J. & Koo, M. Prevalence, Enterotoxin Genes, and Antibiotic Resistance of *Bacillus cereus* Isolated from Raw Vegetables in Korea. *J Food Prot* **81**, 1590-1597 (2018).
480. Zhang, Y.*, et al.* Prevalence, Virulence Feature, Antibiotic Resistance and MLST Typing of B*acillus cereus* Isolated From Retail Aquatic Products in China. *Front Microbiol* **11**, 1513 (2020).
481. Gao, T.*, et al.* Prevalence, Virulence Genes, Antimicrobial Susceptibility, and Genetic Diversity of *Bacillus cereus* Isolated From Pasteurized Milk in China. *Front Microbiol* **9**, 533 (2018).

482. Halverson, L.J., Clayton, M.K. & Handelsman, J. Variable stability of antibiotic-resistance markers in *Bacillus cereus* UW85 in the soybean rhizosphere in the field. *Mol Ecol* **2**, 65-78 (1993).
483. Fernandez-Fuentes, M.A., Abriouel, H., Ortega Morente, E., Perez Pulido, R. & Galvez, A. Genetic determinants of antimicrobial resistance in Gram positive bacteria from organic foods. *Int J Food Microbiol* **172**, 49-56 (2014).
484. Jensen, L.B., Baloda, S., Boye, M. & Aarestrup, F.M. Antimicrobial resistance among *Pseudomonas* spp. and the *Bacillus cereus* group isolated from Danish agricultural soil. *Environ Int* **26**, 581-587 (2001).
485. Chon, J.W., Kim, J.H., Lee, S.J., Hyeon, J.Y. & Seo, K.H. Toxin profile, antibiotic resistance, and phenotypic and molecular characterization of *Bacillus cereus* in Sunsik. *Food Microbiol* **32**, 217-222 (2012).
486. Yu, S.*, et al.* A Study on Prevalence and Characterization of *Bacillus cereus* in Ready-to-Eat Foods in China. *Front Microbiol* **10**, 3043 (2019).
487. Rosenquist, H., Smidt, L., Andersen, S.R., Jensen, G.B. & Wilcks, A. Occurrence and significance of *Bacillus cereus* and *Bacillus thuringiensis* in ready-to-eat food. *FEMS Microbiol Lett* **250**, 129-136 (2005).
488. Al Momani, W., Khatatbeh, M. & Altaany, Z. Antibiotic susceptibility of bacterial pathogens recovered from the hand and mobile phones of university students. *Germs* **9**, 9-16 (2019).
489. Spanogiannopoulos, P., Waglechner, N., Koteva, K. & Wright, G.D. A rifamycin inactivating phosphotransferase family shared by environmental and pathogenic bacteria. *Proc Natl Acad Sci U S A* **111**, 7102-7107 (2014).
490. Bernhard, K., Schrempf, H. & Goebel, W. Bacteriocin and antibiotic resistance plasmids in *Bacillus cereus* and *Bacillus subtilis*. *J Bacteriol* **133**, 897-903 (1978).
491. Glenwright, H.*, et al.* The Identification of Intrinsic Chloramphenicol and Tetracycline Resistance Genes in Members of the *Bacillus cereus* Group (*sensu lato*). *Front Microbiol* **7**, 2122 (2016).
492. Thompson, M.K.*, et al.* Structural and chemical aspects of resistance to the antibiotic fosfomycin conferred by FosB from *Bacillus cereus*. *Biochemistry* **52**, 7350-7362 (2013).
493. Fenselau, C.*, et al.* Identification of beta-lactamase in antibiotic-resistant *Bacillus cereus* spores. *Appl Environ Microbiol* **74**, 904-906 (2008).
494. Meena, S., Mehla, J., Kumar, R. & Sood, S.K. Common Mechanism of Cross-Resistance Development in Pathogenic Bacteria *Bacillus cereus* Against Alamethicin and Pediocin Involves Alteration in Lipid Composition. *Curr Microbiol* **73**, 534-541 (2016).
495. Abi Khattar, Z.*, et al.* The dlt operon of *Bacillus cereus* is required for resistance to cationic antimicrobial peptides and for virulence in insects. *J Bacteriol* **191**, 7063-7073 (2009).
496. Simm, R.*, et al.* BC4707 is a major facilitator superfamily multidrug resistance transport protein from *Bacillus cereus* implicated in fluoroquinolone tolerance. *PLoS One* **7**, e36720 (2012).
497. Hassan, K.A.*, et al.* The putative drug efflux systems of the *Bacillus cereus* group. *PLoS One* **12**, e0176188 (2017).
498. Frenzel, E., Kranzler, M., Stark, T.D., Hofmann, T. & Ehling-Schulz, M. The Endospore-Forming Pathogen *Bacillus cereus* Exploits a Small Colony Variant-Based Diversification Strategy in Response to Aminoglycoside Exposure. *mBio* **6**, e01172-01115 (2015).
499. Chiang, C.Y.*, et al.* Mitigating the Impact of Antibacterial Drug Resistance through Host-Directed Therapies: Current Progress, Outlook, and Challenges. *mBio* **9**(2018).
500. Granum, P.E. & Lund, T. *Bacillus cereus* and its food poisoning toxins. *FEMS Microbiol Lett* **157**, 223-228 (1997).
501. Stenfors Arnesen, L.P., Fagerlund, A. & Granum, P.E. From soil to gut: *Bacillus cereus* and its food poisoning toxins. *FEMS Microbiol Rev* **32**, 579-606 (2008).

502. Glasset, B.*, et al. Bacillus cereus*-induced food-borne outbreaks in France, 2007 to 2014: epidemiology and genetic characterisation. *Euro Surveill* **21**, 30413 (2016).
503. Drobniewski, F.A. *Bacillus cereus* and related species. *Clin Microbiol Rev* **6**, 324-338 (1993).
504. Fermanian, C., Lapeyre, C., Fremy, J.M. & Claisse, M. Production of diarrheal toxin by selected strains of *Bacillus cereus*. *Int J Food Microbiol* **30**, 345-358 (1996).
505. Beecher, D.J. & Wong, A.C. Identification of hemolysin BL-producing *Bacillus cereus* isolates by a discontinuous hemolytic pattern in blood agar. *Appl Environ Microbiol* **60**, 1646-1651 (1994).
506. Lund, T. & Granum, P.E. Characterisation of a non-haemolytic enterotoxin complex from *Bacillus cereus* isolated after a foodborne outbreak. *FEMS Microbiol Lett* **141**, 151-156 (1996).
507. Beecher, D.J. & Wong, A.C. Tripartite hemolysin BL from *Bacillus cereus*. Hemolytic analysis of component interactions and a model for its characteristic paradoxical zone phenomenon. *J Biol Chem* **272**, 233-239 (1997).
508. Sastalla, I.*, et al.* The *Bacillus cereus* Hbl and Nhe tripartite enterotoxin components assemble sequentially on the surface of target cells and are not interchangeable. *PLoS One* **8**, e76955 (2013).
509. Lindback, T., Fagerlund, A., Rodland, M.S. & Granum, P.E. Characterization of the *Bacillus cereus* Nhe enterotoxin. *Microbiology* **150**, 3959-3967 (2004).
510. Lindback, T.*, et al.* Cytotoxicity of the *Bacillus cereus* Nhe enterotoxin requires specific binding order of its three exoprotein components. *Infect Immun* **78**, 3813-3821 (2010).
511. Heilkenbrinker, U.*, et al.* Complex formation between NheB and NheC is necessary to induce cytotoxic activity by the three-component *Bacillus cereus* Nhe enterotoxin. *PLoS One* **8**, e63104 (2013).
512. Tausch, F.*, et al.* Evidence for Complex Formation of the *Bacillus cereus* Haemolysin BL Components in Solution. *Toxins (Basel)* **9**(2017).
513. Madegowda, M., Eswaramoorthy, S., Burley, S.K. & Swaminathan, S. X-ray crystal structure of the B component of Hemolysin BL from *Bacillus cereus*. *Proteins* **71**, 534-540 (2008).
514. Ganash, M.*, et al.* Structure of the NheA component of the Nhe toxin from *Bacillus cereus*: implications for function. *PLoS One* **8**, e74748 (2013).
515. Wallace, A.J.*, et al. E. coli* hemolysin E (HlyE, ClyA, SheA): X-ray crystal structure of the toxin and observation of membrane pores by electron microscopy. *Cell* **100**, 265-276 (2000).
516. Mueller, M., Grauschopf, U., Maier, T., Glockshuber, R. & Ban, N. The structure of a cytolytic alpha-helical toxin pore reveals its assembly mechanism. *Nature* **459**, 726-730 (2009).
517. Brauning, B. & Groll, M. Structural and Mechanistic Features of ClyA-Like alpha-Pore-Forming Toxins. *Toxins (Basel)* **10**(2018).
518. Fagerlund, A., Lindback, T., Storset, A.K., Granum, P.E. & Hardy, S.P. *Bacillus cereus* Nhe is a pore-forming toxin with structural and functional properties similar to the ClyA (HlyE, SheA) family of haemolysins, able to induce osmotic lysis in epithelia. *Microbiology* **154**, 693-704 (2008).
519. Jessberger, N.*, et al.* Simulating Intestinal Growth Conditions Enhances Toxin Production of Enteropathogenic *Bacillus cereus*. *Front Microbiol* **8**, 627 (2017).
520. Ceuppens, S.*, et al.* Enterotoxin production by *Bacillus cereus* under gastrointestinal conditions and their immunological detection by commercially available kits. *Foodborne Pathog Dis* **9**, 1130-1136 (2012).
521. Zigha, A., Rosenfeld, E., Schmitt, P. & Duport, C. Anaerobic cells of *Bacillus cereus* F4430/73 respond to low oxidoreduction potential by metabolic readjustments and activation of enterotoxin expression. *Arch Microbiol* **185**, 222-233 (2006).
522. Cui, Y.*, et al.* Multifaceted toxin profile, an approach toward a better understanding of probiotic *Bacillus cereus*. *Crit Rev Toxicol* **49**, 342-356 (2019).

523. Ramarao, N. & Sanchis, V. The pore-forming haemolysins of *Bacillus cereus*: a review. *Toxins (Basel)* **5**, 1119-1139 (2013).
524. Agata, N.*, et al.* A novel dodecadepsipeptide, cereulide, isolated from *Bacillus cereus* causes vacuole formation in HEp-2 cells. *FEMS Microbiol Lett* **121**, 31-34 (1994).
525. Rasko, D.A.*, et al.* Complete sequence analysis of novel plasmids from emetic and periodontal *Bacillus cereus* isolates reveals a common evolutionary history among the *B. cereus*-group plasmids, including *Bacillus anthracis* pXO1. *J Bacteriol* **189**, 52-64 (2007).
526. Alonzo, D.A., Magarvey, N.A. & Schmeing, T.M. Characterization of cereulide synthetase, a toxin-producing macromolecular machine. *PLoS One* **10**, e0128569 (2015).
527. Hoyer, K.M., Mahlert, C. & Marahiel, M.A. The iterative gramicidin s thioesterase catalyzes peptide ligation and cyclization. *Chem Biol* **14**, 13-22 (2007).
528. Bruner, S.D.*, et al.* Structural basis for the cyclization of the lipopeptide antibiotic surfactin by the thioesterase domain SrfTE. *Structure* **10**, 301-310 (2002).
529. Lucking, G., Dommel, M.K., Scherer, S., Fouet, A. & Ehling-Schulz, M. Cereulide synthesis in emetic *Bacillus cereus* is controlled by the transition state regulator AbrB, but not by the virulence regulator PlcR. *Microbiology* **155**, 922-931 (2009).
530. Lucking, G.*, et al.* Ces locus embedded proteins control the non-ribosomal synthesis of the cereulide toxin in emetic *Bacillus cereus* on multiple levels. *Front Microbiol* **6**, 1101 (2015).
531. Kranzler, M.*, et al.* Temperature Exerts Control of *Bacillus cereus* Emetic Toxin Production on Post-transcriptional Levels. *Front Microbiol* **7**, 1640 (2016).
532. Tian, S., Xiong, H., Geng, P., Yuan, Z. & Hu, X. CesH Represses Cereulide Synthesis as an Alpha/Beta Fold Hydrolase in *Bacillus cereus*. *Toxins (Basel)* **11**(2019).
533. Agata, N., Ohta, M. & Yokoyama, K. Production of *Bacillus cereus* emetic toxin (cereulide) in various foods. *Int J Food Microbiol* **73**, 23-27 (2002).
534. Bauer, T.*, et al.* First Insights Into Within Host Translocation of the *Bacillus cereus* Toxin Cereulide Using a Porcine Model. *Front Microbiol* **9**, 2652 (2018).
535. Agata, N., Ohta, M., Mori, M. & Isobe, M. A novel dodecadepsipeptide, cereulide, is an emetic toxin of *Bacillus cereus*. *FEMS Microbiol Lett* **129**, 17-20 (1995).
536. Tran, S.L.*, et al.* Haemolysin II is a *Bacillus cereus* virulence factor that induces apoptosis of macrophages. *Cell Microbiol* **13**, 92-108 (2011).
537. Asano, S.I., Nukumizu, Y., Bando, H., Iizuka, T. & Yamamoto, T. Cloning of novel enterotoxin genes from *Bacillus cereus* and *Bacillus thuringiensis*. *Appl Environ Microbiol* **63**, 1054-1057 (1997).
538. Agata, N., Ohta, M., Arakawa, Y. & Mori, M. The bceT gene of *Bacillus cereus* encodes an enterotoxic protein. *Microbiology* **141 (Pt 4)**, 983-988 (1995).
539. Choma, C. & Granum, P.E. The enterotoxin T (BcET) from *Bacillus cereus* can probably not contribute to food poisoning. *FEMS Microbiol Lett* **217**, 115-119 (2002).
540. Tran, S.L., Guillemet, E., Gohar, M., Lereclus, D. & Ramarao, N. CwpFM (EntFM) is a *Bacillus cereus* potential cell wall peptidase implicated in adhesion, biofilm formation, and virulence. *J Bacteriol* **192**, 2638-2642 (2010).
541. Jamet, A., Charbit, A. & Nassif, X. Antibacterial Toxins: Gram-Positive Bacteria Strike Back! *Trends Microbiol* **26**, 89-91 (2018).
542. Gonzalez, D. & Mavridou, D.A.I. Making the Best of Aggression: The Many Dimensions of Bacterial Toxin Regulation. *Trends Microbiol* **27**, 897-905 (2019).
543. Koskiniemi, S.*, et al.* Rhs proteins from diverse bacteria mediate intercellular competition. *Proc Natl Acad Sci U S A* **110**, 7032-7037 (2013).
544. Stempler, O.*, et al.* Interspecies nutrient extraction and toxin delivery between bacteria. *Nat Commun* **8**, 315 (2017).
545. Charlton, S., Moir, A.J., Baillie, L. & Moir, A. Characterization of the exosporium of *Bacillus cereus*. *J Appl Microbiol* **87**, 241-245 (1999).
546. Chung, M.C.*, et al.* Secreted neutral metalloproteases of *Bacillus anthracis* as candidate pathogenic factors. *J Biol Chem* **281**, 31408-31418 (2006).

547. Ivanova, N.*, et al.* Genome sequence of *Bacillus cereus* and comparative analysis with *Bacillus anthracis*. *Nature* **423**, 87-91 (2003).
548. Chitlaru, T., Gat, O., Gozlan, Y., Ariel, N. & Shafferman, A. Differential proteomic analysis of the *Bacillus anthracis* secretome: distinct plasmid and chromosome CO2-dependent cross talk mechanisms modulate extracellular proteolytic activities. *J Bacteriol* **188**, 3551-3571 (2006).
549. Lyu, Y.*, et al.* Recent research progress with phospholipase C from *Bacillus cereus*. *Biotechnol Lett* **38**, 23-31 (2016).
550. Pomerantsev, A.P., Kalnin, K.V., Osorio, M. & Leppla, S.H. Phosphatidylcholine-specific phospholipase C and sphingomyelinase activities in bacteria of the *Bacillus cereus* group. *Infect Immun* **71**, 6591-6606 (2003).
551. Beecher, D.J. & Wong, A.C. Cooperative, synergistic and antagonistic haemolytic interactions between haemolysin BL, phosphatidylcholine phospholipase C and sphingomyelinase from *Bacillus cereus*. *Microbiology* **146 Pt 12**, 3033-3039 (2000).
552. Beecher, D.J., Olsen, T.W., Somers, E.B. & Wong, A.C. Evidence for contribution of tripartite hemolysin BL, phosphatidylcholine-preferring phospholipase C, and collagenase to virulence of *Bacillus cereus* endophthalmitis. *Infection and immunity* **68**, 5269-5276 (2000).
553. Oda, M.*, et al.* Role of sphingomyelinase in infectious diseases caused by *Bacillus cereus*. *PLoS One* **7**, e38054 (2012).
554. Oda, M.*, et al.* Novel inhibitor of bacterial sphingomyelinase, SMY-540, developed based on three-dimensional structure analysis. *J Enzyme Inhib Med Chem* **29**, 303-310 (2014).
555. Oda, M., Yokotani, A., Hayashi, N. & Kamoshida, G. Role of Sphingomyelinase in the Pathogenesis of *Bacillus cereus* Infection. *Biol Pharm Bull* **43**, 250-253 (2020).
556. Bullock, T.L., Ryan, M., Kim, S.L., Remington, S.J. & Griffith, O.H. Crystallization of phosphatidylinositol-specific phospholipase C from *Bacillus cereus*. *Biophys J* **64**, 784-791 (1993).
557. Heinz, D.W.*, et al.* Crystal structure of phosphatidylinositol-specific phospholipase C from *Bacillus cereus* in complex with glucosaminyl(alpha 1-->6)-D-myo-inositol, an essential fragment of GPI anchors. *Biochemistry* **35**, 9496-9504 (1996).
558. Volwerk, J.J., Koke, J.A., Wetherwax, P.B. & Griffith, O.H. Functional characteristics of phosphatidylinositol-specific phospholipases C from *Bacillus cereus* and *Bacillus thuringiensis*. *FEMS Microbiol Lett* **52**, 237-241 (1989).
559. Zhao, Y., Su, L., Li, K. & Zhao, B. Discovery of novel PC-PLC activity inhibitors. *Chem Biol Drug Des* **95**, 380-387 (2020).
560. Liu, J.*, et al.* Sequential CRISPR-Based Screens Identify LITAF and CDIP1 as the *Bacillus cereus* Hemolysin BL Toxin Host Receptors. *Cell host & microbe* (2020).
561. Myokai, F., Takashiba, S., Lebo, R. & Amar, S. A novel lipopolysaccharide-induced transcription factor regulating tumor necrosis factor alpha gene expression: molecular cloning, sequencing, characterization, and chromosomal assignment. *Proc Natl Acad Sci U S A* **96**, 4518-4523 (1999).
562. Tang, X., Metzger, D., Leeman, S. & Amar, S. LPS-induced TNF-alpha factor (LITAF)-deficient mice express reduced LPS-induced cytokine: Evidence for LITAF-dependent LPS signaling pathways. *Proc Natl Acad Sci U S A* **103**, 13777-13782 (2006).
563. Saifi, G.M.*, et al.* SIMPLE mutations in Charcot-Marie-Tooth disease and the potential role of its protein product in protein degradation. *Hum Mutat* **25**, 372-383 (2005).
564. Guinebretiere, M.H., Broussolle, V. & Nguyen-The, C. Enterotoxigenic profiles of food-poisoning and food-borne *Bacillus cereus* strains. *J Clin Microbiol* **40**, 3053-3056 (2002).
565. Dietrich, R., Moravek, M., Burk, C., Granum, P.E. & Martlbauer, E. Production and characterization of antibodies against each of the three subunits of the *Bacillus cereus* nonhemolytic enterotoxin complex. *Appl Environ Microbiol* **71**, 8214-8220 (2005).
566. Tran, S.L. & Ramarao, N. *Bacillus cereus* immune escape: a journey within macrophages. *FEMS Microbiol Lett* **347**, 1-6 (2013).

567. Livingston, E.T., Mursalin, M.H. & Callegan, M.C. A Pyrrhic Victory: The PMN Response to Ocular Bacterial Infections. *Microorganisms* **7**(2019).
568. Stewart, G.C. The Exosporium Layer of Bacterial Spores: a Connection to the Environment and the Infected Host. *Microbiol Mol Biol Rev* **79**, 437-457 (2015).
569. Mursalin, M.H., Livingston, E.T. & Callegan, M.C. The cereus matter of *Bacillus* endophthalmitis. *Exp Eye Res* **193**, 107959 (2020).
570. Novosad, B.D., Astley, R.A. & Callegan, M.C. Role of Toll-like receptor (TLR) 2 in experimental *Bacillus cereus* endophthalmitis. *PLoS One* **6**, e28619 (2011).
571. Parkunan, S.M.*, et al.* Unexpected Roles for Toll-Like Receptor 4 and TRIF in Intraocular Infection with Gram-Positive Bacteria. *Infect Immun* **83**, 3926-3936 (2015).
572. Park, J.M., Ng, V.H., Maeda, S., Rest, R.F. & Karin, M. Anthrolysin O and other gram-positive cytolysins are toll-like receptor 4 agonists. *J Exp Med* **200**, 1647-1655 (2004).
573. Srivastava, A.*, et al.* The apoptotic response to pneumolysin is Toll-like receptor 4 dependent and protects against pneumococcal disease. *Infect Immun* **73**, 6479-6487 (2005).
574. Kayagaki, N.*, et al.* Caspase-11 cleaves gasdermin D for non-canonical inflammasome signalling. *Nature* **526**, 666-671 (2015).
575. Kuida, K.*, et al.* Altered cytokine export and apoptosis in mice deficient in interleukin-1 beta converting enzyme. *Science* **267**, 2000-2003 (1995).
576. Wang, S.Y.*, et al.* Murine caspase-11, an ICE-interacting protease, is essential for the activation of ICE. *Cell* **92**, 501-509 (1998).
577. Kovarova, M.*, et al.* NLRP1-dependent pyroptosis leads to acute lung injury and morbidity in mice. *J Immunol* **189**, 2006-2016 (2012).
578. Ying, W., Cheruku, P.S., Bazer, F.W., Safe, S.H. & Zhou, B. Investigation of macrophage polarization using bone marrow derived macrophages. *J Vis Exp* (2013).
579. Englen, M.D., Valdez, Y.E., Lehnert, N.M. & Lehnert, B.E. Granulocyte/Macrophage Colony-Stimulating Factor Is Expressed and Secreted in Cultures of Murine L929 Cells. *J Immunol Methods* **184**, 281-283 (1995).
580. Kumar, P., Nagarajan, A. & Uchil, P.D. Analysis of Cell Viability by the Lactate Dehydrogenase Assay. *Cold Spring Harbor Protocols* **2018**, pdb. prot095497 (2018).
581. van Meer, G., Voelker, D.R. & Feigenson, G.W. Membrane lipids: where they are and how they behave. *Nat Rev Mol Cell Biol* **9**, 112-124 (2008).
582. Livak, K.J. & Schmittgen, T.D. Analysis of relative gene expression data using real-time quantitative PCR and the 2(-Delta Delta C(T)) Method. *Methods* **25**, 402-408 (2001).
583. Gasteiger, E.*, et al.* ExPASy: the proteomics server for in-depth protein knowledge and analysis. *Nucleic Acids Research* **31**, 3784-3788 (2003).
584. Snider, C., Jayasinghe, S., Hristova, K. & White, S.H. MPEx: A tool for exploring membrane proteins. *Protein Science : A Publication of the Protein Society* **18**, 2624-2628 (2009).
585. Porath, J. Immobilized metal ion affinity chromatography. *Protein Expression and Purification* **3**, 263-281 (1992).
586. Roth, B.L., Poot, M., Yue, S.T. & Millard, P.J. Bacterial viability and antibiotic susceptibility testing with SYTOX green nucleic acid stain. *Appl Environ Microbiol* **63**, 2421-2431 (1997).
587. Meunier, E.*, et al.* Caspase-11 activation requires lysis of pathogen-containing vacuoles by IFN-induced GTPases. *Nature* **509**, 366-370 (2014).
588. Drean, P., McAuley, C.M., Moore, S.C., Fegan, N. & Fox, E.M. Characterization of the spore-forming *Bacillus cereus sensu lato* group and *Clostridium perfringens* bacteria isolated from the Australian dairy farm environment. *BMC Microbiol* **15**, 38 (2015).
589. Turnbull, P.C., Nottingham, J.F. & Ghosh, A.C. A severe necrotic enterotoxin produced by certain food, food poisoning and other clinical isolates of *Bacillus cereus*. *Br J Exp Pathol* **58**, 273-280 (1977).
590. Snider, C., Jayasinghe, S., Hristova, K. & White, S.H. MPEx: a tool for exploring membrane proteins. *Protein Sci* **18**, 2624-2628 (2009).

591. Gautier, R., Douguet, D., Antonny, B. & Drin, G. HELIQUEST: a web server to screen sequences with specific alpha-helical properties. *Bioinformatics* **24**, 2101-2102 (2008).
592. Sakurai, J., Nagahama, M. & Oda, M. *Clostridium perfringens* alpha-toxin: characterization and mode of action. *J Biochem* **136**, 569-574 (2004).
593. Bell, C.E. & Eisenberg, D. Crystal structure of diphtheria toxin bound to nicotinamide adenine dinucleotide. *Biochemistry* **35**, 1137-1149 (1996).
594. Jorgensen, R.*, et al.* Exotoxin A-eEF2 complex structure indicates ADP ribosylation by ribosome mimicry. *Nature* **436**, 979-984 (2005).
595. Wilson, B.A. & Ho, M. *Pasteurella multocida* toxin interaction with host cells: entry and cellular effects. *Curr Top Microbiol Immunol* **361**, 93-111 (2012).
596. Bhakdi, S. & Tranum-Jensen, J. Alpha-toxin of *Staphylococcus aureus*. *Microbiol Rev* **55**, 733-751 (1991).
597. Pinchuk, I.V., Beswick, E.J. & Reyes, V.E. Staphylococcal enterotoxins. *Toxins (Basel)* **2**, 2177-2197 (2010).
598. Melton-Celsa, A.R. Shiga Toxin (Stx) Classification, Structure, and Function. *Microbiol Spectr* **2**, EHEC-0024-2013 (2014).
599. Spangler, B.D. Structure and function of cholera toxin and the related *Escherichia coli* heat-labile enterotoxin. *Microbiol Rev* **56**, 622-647 (1992).
600. Kayagaki, N.*, et al.* Non-canonical inflammasome activation targets caspase-11. *Nature* **479**, 117-121 (2011).
601. Kayagaki, N.*, et al.* Noncanonical inflammasome activation by intracellular LPS independent of TLR4. *Science* **341**, 1246-1249 (2013).
602. Baumann, K., Munter, K. & Faulstich, H. Identification of structural features involved in binding of alpha-amanitin to a monoclonal antibody. *Biochemistry* **32**, 4043-4050 (1993).
603. Abbas, H.K.*, et al.* Fumonisin- and AAL-Toxin-Induced Disruption of Sphingolipid Metabolism with Accumulation of Free Sphingoid Bases. *Plant Physiol* **106**, 1085-1093 (1994).
604. Schlam, D.*, et al.* Gliotoxin Suppresses Macrophage Immune Function by Subverting Phosphatidylinositol 3,4,5-Trisphosphate Homeostasis. *MBio* **7**, e02242 (2016).
605. Walton, J.D. HC-toxin. *Phytochemistry* **67**, 1406-1413 (2006).
606. Koszegi, T. & Poor, M. Ochratoxin A: Molecular Interactions, Mechanisms of Toxicity and Prevention at the Molecular Level. *Toxins (Basel)* **8**, 111 (2016).
607. Tucker, W.C., Du, Z., Hein, R., Gromet-Elhanan, Z. & Richter, M.L. Role of the ATP synthase alpha-subunit in conferring sensitivity to tentoxin. *Biochemistry* **40**, 7542-7548 (2001).
608. Young, H.S., Herbette, L.G. & Skita, V. Alpha-bungarotoxin binding to acetylcholine receptor membranes studied by low angle X-ray diffraction. *Biophys J* **85**, 943-953 (2003).
609. Wilson, D.W.*, et al.* Mechanisms and pathology of monocrotaline pulmonary toxicity. *Crit Rev Toxicol* **22**, 307-325 (1992).
610. Kloog, Y.*, et al.* Sarafotoxin, a novel vasoconstrictor peptide: phosphoinositide hydrolysis in rat heart and brain. *Science* **242**, 268-270 (1988).
611. Sahara, Y.*, et al.* A new class of neurotoxin from wasp venom slows inactivation of sodium current. *Eur J Neurosci* **12**, 1961-1970 (2000).
612. Banerjee, A., Lee, A., Campbell, E. & Mackinnon, R. Structure of a pore-blocking toxin in complex with a eukaryotic voltage-dependent K(+) channel. *Elife* **2**, e00594 (2013).
613. Chuang, R.S., Jaffe, H., Cribbs, L., Perez-Reyes, E. & Swartz, K.J. Inhibition of T-type voltage-gated calcium channels by a new scorpion toxin. *Nat Neurosci* **1**, 668-674 (1998).
614. Garcia-Calvo, M.*, et al.* Purification, characterization, and biosynthesis of margatoxin, a component of *Centruroides margaritatus* venom that selectively inhibits voltage-dependent potassium channels. *J Biol Chem* **268**, 18866-18874 (1993).

615. Higashijima, T., Uzu, S., Nakajima, T. & Ross, E.M. Mastoparan, a peptide toxin from wasp venom, mimics receptors by activating GTP-binding regulatory proteins (G proteins). *J Biol Chem* **263**, 6491-6494 (1988).
616. Castle, N.A.*, et al.* Maurotoxin: a potent inhibitor of intermediate conductance Ca2+-activated potassium channels. *Mol Pharmacol* **63**, 409-418 (2003).
617. Nebe, J., Vanegas, H., Neugebauer, V. & Schaible, H.G. Omega-agatoxin IVA, a P-type calcium channel antagonist, reduces nociceptive processing in spinal cord neurons with input from the inflamed but not from the normal knee joint--an electrophysiological study in the rat in vivo. *Eur J Neurosci* **9**, 2193-2201 (1997).
618. Rogowski, R.S.*, et al.* Three new toxins from the scorpion *Pandinus imperator* selectively block certain voltage-gated K+ channels. *Mol Pharmacol* **50**, 1167-1177 (1996).
619. Newcomb, R.*, et al.* Selective peptide antagonist of the class E calcium channel from the venom of the tarantula Hysterocrates gigas. *Biochemistry* **37**, 15353-15362 (1998).
620. Pedarzani, P.*, et al.* Tamapin, a venom peptide from the Indian red scorpion (*Mesobuthus tamulus*) that targets small conductance Ca2+-activated K+ channels and afterhyperpolarization currents in central neurons. *J Biol Chem* **277**, 46101-46109 (2002).
621. Pulido, O.M. Domoic acid toxicologic pathology: a review. *Mar Drugs* **6**, 180-219 (2008).
622. Campos, A. & Vasconcelos, V. Molecular mechanisms of microcystin toxicity in animal cells. *Int J Mol Sci* **11**, 268-287 (2010).
623. Suganuma, M.*, et al.* Calyculin A, an inhibitor of protein phosphatases, a potent tumor promoter on CD-1 mouse skin. *Cancer Res* **50**, 3521-3525 (1990).
624. Donevan, S.D. & McCabe, R.T. Conantokin G is an NR2B-selective competitive antagonist of N-methyl-D-aspartate receptors. *Mol Pharmacol* **58**, 614-623 (2000).
625. Stocker, J.W., Nadasdi, L., Aldrich, R.W. & Tsien, R.W. Preferential interaction of omega-conotoxins with inactivated N-type Ca2+ channels. *J Neurosci* **17**, 3002-3013 (1997).
626. Melnick, R.L., Testen, A.L., Poleatewich, A.M., Backman, P.A. & Bailey, B.A. Detection and expression of enterotoxin genes in endophytic strains of *Bacillus cereus*. *Lett Appl Microbiol* **54**, 468-474 (2012).
627. Wehrle, E., Didier, A., Moravek, M., Dietrich, R. & Martlbauer, E. Detection of *Bacillus cereus* with enteropathogenic potential by multiplex real-time PCR based on SYBR Green I. *Mol Cell Probes* **24**, 124-130 (2010).
628. Jessberger, N.*, et al.* From genome to toxicity: a combinatory approach highlights the complexity of enterotoxin production in *Bacillus cereus*. *Front Microbiol* **6**, 560 (2015).
629. Schroder, K. & Tschopp, J. The inflammasomes. *Cell* **140**, 821-832 (2010).
630. Lamkanfi, M. & Dixit, V.M. Mechanisms and functions of inflammasomes. *Cell* **157**, 1013-1022 (2014).
631. Meunier, E.*, et al.* Guanylate-binding proteins promote activation of the AIM2 inflammasome during infection with Francisella novicida. *Nat Immunol* **16**, 476-484 (2015).
632. Liu, S., Moayeri, M. & Leppla, S.H. Anthrax lethal and edema toxins in anthrax pathogenesis. *Trends Microbiol* **22**, 317-325 (2014).
633. Dal Peraro, M. & van der Goot, F.G. Pore-forming toxins: ancient, but never really out of fashion. *Nat Rev Microbiol* **14**, 77-92 (2016).
634. Mariathasan, S.*, et al.* Cryopyrin activates the inflammasome in response to toxins and ATP. *Nature* **440**, 228-232 (2006).
635. Muñoz-Planillo, R., Franchi, L., Miller, L.S. & Núñez, G. A Critical Role for Hemolysins and Bacterial Lipoproteins in *Staphylococcus aureus*-Induced Activation of the Nlrp3 Inflammasome. *Journal of immunology (Baltimore, Md. : 1950)* **183**, 3942-3948 (2009).
636. Craven, R.R.*, et al. Staphylococcus aureus* alpha-hemolysin activates the NLRP3-inflammasome in human and mouse monocytic cells. *PLoS One* **4**, e7446 (2009).

637. Kebaier, C*., et al. Staphylococcus aureus* alpha-hemolysin mediates virulence in a murine model of severe pneumonia through activation of the NLRP3 inflammasome. *J Infect Dis* **205**, 807-817 (2012).
638. Zhang, X*., et al.* Enterohemorrhagic *Escherichia coli* specific enterohemolysin induced IL-1beta in human macrophages and EHEC-induced IL-1beta required activation of NLRP3 inflammasome. *PLoS One* **7**, e50288 (2012).
639. Schaale, K*., et al.* Strain- and host species-specific inflammasome activation, IL-1β release, and cell death in macrophages infected with uropathogenic *Escherichia coli*. *Mucosal Immunology* **9**, 124 (2015).
640. Costa, A*., et al.* Activation of the NLRP3 inflammasome by group B streptococci. *J Immunol* **188**, 1953-1960 (2012).
641. Whidbey, C*., et al.* A streptococcal lipid toxin induces membrane permeabilization and pyroptosis leading to fetal injury. *EMBO Mol Med* **7**, 488-505 (2015).
642. Gupta, R*., et al.* RNA and beta-hemolysin of group B *Streptococcus* induce interleukin-1beta (IL-1beta) by activating NLRP3 inflammasomes in mouse macrophages. *J Biol Chem* **289**, 13701-13705 (2014).
643. Harder, J*., et al.* Activation of the Nlrp3 inflammasome by *Streptococcus pyogenes* requires streptolysin O and NF-kappa B activation but proceeds independently of TLR signaling and P2X7 receptor. *J Immunol* **183**, 5823-5829 (2009).
644. Keyel, P.A., Roth, R., Yokoyama, W.M., Heuser, J.E. & Salter, R.D. Reduction of streptolysin O (SLO) pore-forming activity enhances inflammasome activation. *Toxins (Basel)* **5**, 1105-1118 (2013).
645. Ozoren, N*., et al.* Distinct roles of TLR2 and the adaptor ASC in IL-1beta/IL-18 secretion in response to *Listeria monocytogenes*. *J Immunol* **176**, 4337-4342 (2006).
646. Hamon, M.A. & Cossart, P. K+ efflux is required for histone H3 dephosphorylation by *Listeria monocytogenes* listeriolysin O and other pore-forming toxins. *Infection and immunity* **79**, 2839-2846 (2011).
647. Toma, C*., et al.* Pathogenic *Vibrio* activate NLRP3 inflammasome via cytotoxins and TLR/nucleotide-binding oligomerization domain-mediated NF-kappa B signaling. *J Immunol* **184**, 5287-5297 (2010).
648. Higa, N*., et al. Vibrio parahaemolyticus* effector proteins suppress inflammasome activation by interfering with host autophagy signaling. *PLoS Pathog* **9**, e1003142 (2013).
649. Song, L*., et al.* A critical role for hemolysin in *Vibrio fluvialis*-induced IL-1beta secretion mediated by the NLRP3 inflammasome in macrophages. *Front Microbiol* **6**, 510 (2015).
650. Beecher, D.J. & Wong, A.C. Improved purification and characterization of hemolysin BL, a hemolytic dermonecrotic vascular permeability factor from *Bacillus cereus*. *Infection and immunity* **62**, 980-986 (1994).
651. Heinrichs, J.H., Beecher, D.J., MacMillan, J.D. & Zilinskas, B.A. Molecular cloning and characterization of the *hblA* gene encoding the B component of hemolysin BL from *Bacillus cereus*. *J Bacteriol* **175**, 6760-6766 (1993).
652. Ryan, P.A., Macmillan, J.D. & Zilinskas, B.A. Molecular cloning and characterization of the genes encoding the L1 and L2 components of hemolysin BL from *Bacillus cereus*. *J Bacteriol* **179**, 2551-2556 (1997).
653. Lund, T., De Buyser, M.L. & Granum, P.E. A new cytotoxin from *Bacillus cereus* that may cause necrotic enteritis. *Mol Microbiol* **38**, 254-261 (2000).
654. Moayeri, M*., et al.* Inflammasome sensor Nlrp1b-dependent resistance to anthrax is mediated by caspase-1, IL-1 signaling and neutrophil recruitment. *PLoS Pathog* **6**, e1001222 (2010).
655. Man, S.M*., et al.* Actin polymerization as a key innate immune effector mechanism to control Salmonella infection. *Proc Natl Acad Sci U S A* **111**, 17588-17593 (2014).
656. Yohannan, S., Faham, S., Yang, D., Whitelegge, J.P. & Bowie, J.U. The evolution of transmembrane helix kinks and the structural diversity of G protein-coupled receptors. *Proc Natl Acad Sci U S A* **101**, 959-963 (2004).

657. Cordes, F.S., Bright, J.N. & Sansom, M.S. Proline-induced distortions of transmembrane helices. *J Mol Biol* **323**, 951-960 (2002).
658. Jin, T.*, et al.* The (beta)gamma subunits of G proteins gate a K(+) channel by pivoted bending of a transmembrane segment. *Mol Cell* **10**, 469-481 (2002).
659. Tieleman, D.P., Shrivastava, I.H., Ulmschneider, M.R. & Sansom, M.S. Proline-induced hinges in transmembrane helices: possible roles in ion channel gating. *Proteins* **44**, 63-72 (2001).
660. Jorgensen, I., Zhang, Y., Krantz, B.A. & Miao, E.A. Pyroptosis triggers pore-induced intracellular traps (PITs) that capture bacteria and lead to their clearance by efferocytosis. *J Exp Med* **213**, 2113-2128 (2016).
661. Aglietti, R.A.*, et al.* GsdmD p30 elicited by caspase-11 during pyroptosis forms pores in membranes. *Proc Natl Acad Sci U S A* **113**, 7858-7863 (2016).
662. Sborgi, L.*, et al.* GSDMD membrane pore formation constitutes the mechanism of pyroptotic cell death. *EMBO J* **35**, 1766-1778 (2016).
663. Hayward, J.A., Mathur, A., Ngo, C. & Man, S.M. Cytosolic Recognition of Microbes and Pathogens: Inflammasomes in Action. *Microbiology and Molecular Biology Reviews* **82** (2018).
664. Perregaux, D. & Gabel, C.A. Interleukin-1 beta maturation and release in response to ATP and nigericin. Evidence that potassium depletion mediated by these agents is a necessary and common feature of their activity. *J Biol Chem* **269**, 15195-15203 (1994).
665. Munoz-Planillo, R.*, et al.* K(+) efflux is the common trigger of NLRP3 inflammasome activation by bacterial toxins and particulate matter. *Immunity* **38**, 1142-1153 (2013).
666. Hara, H.*, et al.* Dependency of caspase-1 activation induced in macrophages by *Listeria monocytogenes* on cytolysin, listeriolysin O, after evasion from phagosome into the cytoplasm. *J Immunol* **180**, 7859-7868 (2008).
667. Ehling-Schulz, M., Fricker, M. & Scherer, S. *Bacillus cereus,* the causative agent of an emetic type of food-borne illness. *Mol Nutr Food Res* **48**, 479-487 (2004).
668. Moayeri, M.*, et al.* Small-molecule inhibitors of lethal factor protease activity protect against anthrax infection. *Antimicrob Agents Chemother* **57**, 4139-4145 (2013).
669. Leysath, C.E.*, et al.* Mouse monoclonal antibodies to anthrax edema factor protect against infection. *Infect Immun* **79**, 4609-4616 (2011).
670. Haug, T.M.*, et al.* Formation of very large conductance channels by *Bacillus cereus* Nhe in Vero and GH(4) cells identifies NheA + B as the inherent pore-forming structure. *J Membr Biol* **237**, 1-11 (2010).
671. Granum, P.E.*, et al.* Evidence for a further enterotoxin complex produced by *Bacillus cereus*. *FEMS Microbiol Lett* **141**, 145-149 (1996).
672. Lund, T. & Granum, P.E. Comparison of biological effect of the two different enterotoxin complexes isolated from three different strains of *Bacillus cereus*. *Microbiology* **143 (Pt 10)**, 3329-3336 (1997).
673. Mathur, A.*, et al.* A multicomponent toxin from *Bacillus cereus* incites inflammation and shapes host outcome via the NLRP3 inflammasome. *Nat Microbiol* **4**, 362-374 (2019).
674. Greenfield, N.J. Using circular dichroism spectra to estimate protein secondary structure. *Nature Protocols* **1**, 2876 (2007).
675. Granum, P.E., O'Sullivan, K. & Lund, T. The sequence of the non-haemolytic enterotoxin operon from *Bacillus cereus*. *FEMS Microbiol Lett* **177**, 225-229 (1999).
676. Gross, C.J.*, et al.* K(+) Efflux-Independent NLRP3 Inflammasome Activation by Small Molecules Targeting Mitochondria. *Immunity* **45**, 761-773 (2016).
677. Moravek, M.*, et al.* Determination of the toxic potential of *Bacillus cereus* isolates by quantitative enterotoxin analyses. *FEMS Microbiol Lett* **257**, 293-298 (2006).
678. Dong, J.*, et al.* Oroxylin A inhibits hemolysis via hindering the self-assembly of alpha-hemolysin heptameric transmembrane pore. *PLoS Comput Biol* **9**, e1002869 (2013).
679. Qiu, J.*, et al.* Molecular modeling reveals the novel inhibition mechanism and binding mode of three natural compounds to *staphylococcal* alpha-hemolysin. *PLoS One* **8**, e80197 (2013).

680. Swanson, K.V., Deng, M. & Ting, J.P. The NLRP3 inflammasome: molecular activation and regulation to therapeutics. *Nat Rev Immunol* **19**, 477-489 (2019).
681. Munoz-Planillo, R., Franchi, L., Miller, L.S. & Nunez, G. A critical role for hemolysins and bacterial lipoproteins in Staphylococcus aureus-induced activation of the Nlrp3 inflammasome. *J Immunol* **183**, 3942-3948 (2009).
682. Yamamura, K.*, et al.* Inflammasome Activation Induced by Perfringolysin O of *Clostridium perfringens* and Its Involvement in the Progression of Gas Gangrene. *Front Microbiol* **10**, 2406 (2019).
683. Meixenberger, K.*, et al. Listeria monocytogenes*-infected human peripheral blood mononuclear cells produce IL-1beta, depending on listeriolysin O and NLRP3. *J Immunol* **184**, 922-930 (2010).
684. Johannes, L. & Romer, W. Shiga toxins--from cell biology to biomedical applications. *Nat Rev Microbiol* **8**, 105-116 (2010).
685. Krishnan, M., Kannan, T.R. & Baseman, J.B. *Mycoplasma pneumoniae* CARDS toxin is internalized via clathrin-mediated endocytosis. *PLoS One* **8**, e62706 (2013).
686. McNeela, E.A.*, et al.* Pneumolysin activates the NLRP3 inflammasome and promotes proinflammatory cytokines independently of TLR4. *PLoS Pathog* **6**, e1001191 (2010).
687. Holzinger, D.*, et al. Staphylococcus aureus* Panton-Valentine leukocidin induces an inflammatory response in human phagocytes via the NLRP3 inflammasome. *J Leukoc Biol* **92**, 1069-1081 (2012).
688. Spaan, A.N.*, et al.* The staphylococcal toxin Panton-Valentine Leukocidin targets human C5a receptors. *Cell host & microbe* **13**, 584-594 (2013).
689. Tromp, A.T.*, et al.* Human CD45 is an F-component-specific receptor for the staphylococcal toxin Panton-Valentine leukocidin. *Nat Microbiol* **3**, 708-717 (2018).
690. Frew, B.C., Joag, V.R. & Mogridge, J. Proteolytic processing of Nlrp1b is required for inflammasome activity. *PLoS Pathog* **8**, e1002659 (2012).
691. Bose, S.*, et al.* ADP-ribosylation of NLRP3 by *Mycoplasma pneumoniae* CARDS toxin regulates inflammasome activity. *MBio* **5**, e02186-02114 (2014).
692. Gao, W., Yang, J., Liu, W., Wang, Y. & Shao, F. Site-specific phosphorylation and microtubule dynamics control Pyrin inflammasome activation. *Proceedings of the National Academy of Sciences of the United States of America* **113**, E4857-4866 (2016).
693. Masters, S.L.*, et al.* Familial autoinflammation with neutrophilic dermatosis reveals a regulatory mechanism of pyrin activation. *Science translational medicine* **8**, 332ra345 (2016).
694. Dumas, A.*, et al.* The inflammasome pyrin contributes to pertussis toxin-induced IL-1beta synthesis, neutrophil intravascular crawling and autoimmune encephalomyelitis. *PLoS Pathog* **10**, e1004150 (2014).
695. Van Gorp, H.*, et al.* Familial Mediterranean fever mutations lift the obligatory requirement for microtubules in Pyrin inflammasome activation. *Proc Natl Acad Sci U S A* **113**, 14384-14389 (2016).
696. Buttle, D.J., Murata, M., Knight, C.G. & Barrett, A.J. CA074 methyl ester: a proinhibitor for intracellular cathepsin B. *Arch Biochem Biophys* **299**, 377-380 (1992).
697. Greaney, A.J., Leppla, S.H. & Moayeri, M. Bacterial Exotoxins and the Inflammasome. *Front Immunol* **6**, 570 (2015).
698. Jing, W., Lo Pilato, J., Kay, C. & Man, S.M. Activation mechanisms of inflammasomes by bacterial toxins. *Cell Microbiol* **23**, e13309 (2021).
699. Shi, J.*, et al.* Cleavage of GSDMD by inflammatory caspases determines pyroptotic cell death. *Nature* **526**, 660-665 (2015).
700. He, W.T.*, et al.* Gasdermin D is an executor of pyroptosis and required for interleukin-1beta secretion. *Cell Res* **25**, 1285-1298 (2015).
701. Fox, D.*, et al. Bacillus cereus* non-haemolytic enterotoxin activates the NLRP3 inflammasome. *Nat Commun* **11**, 760 (2020).
702. Oda, M.*, et al. Clostridium perfringens* alpha-toxin recognizes the GM1a-TrkA complex. *J Biol Chem* **287**, 33070-33079 (2012).

703. Ichikawa, N.*, et al.* Binding of laminin-1 to monosialoganglioside GM1 in lipid rafts is crucial for neurite outgrowth. *J Cell Sci* **122**, 289-299 (2009).
704. Monturiol-Gross, L.*, et al.* Internalization of *Clostridium perfringens* alpha-toxin leads to ERK activation and is involved on its cytotoxic effect. *Cell Microbiol* **16**, 535-547 (2014).
705. Luzio, J.P., Pryor, P.R. & Bright, N.A. Lysosomes: fusion and function. *Nat Rev Mol Cell Biol* **8**, 622-632 (2007).
706. Mauvezin, C. & Neufeld, T.P. Bafilomycin A1 disrupts autophagic flux by inhibiting both V-ATPase-dependent acidification and Ca-P60A/SERCA-dependent autophagosome-lysosome fusion. *Autophagy* **11**, 1437-1438 (2015).
707. Yamamoto, A.*, et al.* Bafilomycin A1 prevents maturation of autophagic vacuoles by inhibiting fusion between autophagosomes and lysosomes in rat hepatoma cell line, H-4-II-E cells. *Cell Struct Funct* **23**, 33-42 (1998).
708. Hart, P.D. & Young, M.R. Ammonium chloride, an inhibitor of phagosome-lysosome fusion in macrophages, concurrently induces phagosome-endosome fusion, and opens a novel pathway: studies of a pathogenic *Mycobacterium* and a nonpathogenic yeast. *J Exp Med* **174**, 881-889 (1991).
709. Fernandes-Alnemri, T.*, et al.* The AIM2 inflammasome is critical for innate immunity to *Francisella tularensis*. *Nat Immunol* **11**, 385-393 (2010).
710. Pierzynska-Mach, A., Janowski, P.A. & Dobrucki, J.W. Evaluation of acridine orange, LysoTracker Red, and quinacrine as fluorescent probes for long-term tracking of acidic vesicles. *Cytometry A* **85**, 729-737 (2014).
711. Hornung, V.*, et al.* Silica crystals and aluminum salts activate the NALP3 inflammasome through phagosomal destabilization. *Nat Immunol* **9**, 847-856 (2008).
712. Munoz-Planillo, R.*, et al.* K^+ efflux is the common trigger of NLRP3 inflammasome activation by bacterial toxins and particulate matter. *Immunity* **38**, 1142-1153 (2013).
713. Ruhl, S. & Broz, P. Caspase-11 activates a canonical NLRP3 inflammasome by promoting K(+) efflux. *Eur J Immunol* **45**, 2927-2936 (2015).
714. Bischofberger, M., Iacovache, I. & van der Goot, F.G. Pathogenic pore-forming proteins: function and host response. *Cell host & microbe* **12**, 266-275 (2012).
715. Bose, S.*, et al.* ADP-ribosylation of NLRP3 by Mycoplasma pneumoniae CARDS toxin regulates inflammasome activity. *mBio* **5**(2014).
716. Lee, M.S.*, et al.* Shiga Toxins Activate the NLRP3 Inflammasome Pathway To Promote Both Production of the Proinflammatory Cytokine Interleukin-1beta and Apoptotic Cell Death. *Infection and immunity* **84**, 172-186 (2016).
717. Flores-Diaz, M., Monturiol-Gross, L., Naylor, C., Alape-Giron, A. & Flieger, A. Bacterial Sphingomyelinases and Phospholipases as Virulence Factors. *Microbiol Mol Biol Rev* **80**, 597-628 (2016).
718. Dias-Lopes, C.*, et al.* Identification of new sphingomyelinases D in pathogenic fungi and other pathogenic organisms. *PLoS One* **8**, e79240 (2013).
719. Fernandes Pedrosa Mde, F.*, et al.* Molecular cloning and expression of a functional dermonecrotic and haemolytic factor from Loxosceles laeta venom. *Biochem Biophys Res Commun* **298**, 638-645 (2002).
720. Gonzalez-Zorn, B.*, et al.* The smcL gene of Listeria ivanovii encodes a sphingomyelinase C that mediates bacterial escape from the phagocytic vacuole. *Mol Microbiol* **33**, 510-523 (1999).
721. Walev, I., Weller, U., Strauch, S., Foster, T. & Bhakdi, S. Selective killing of human monocytes and cytokine release provoked by sphingomyelinase (beta-toxin) of Staphylococcus aureus. *Infection and immunity* **64**, 2974-2979 (1996).
722. Dostert, C.*, et al.* Innate immune activation through Nalp3 inflammasome sensing of asbestos and silica. *Science* **320**, 674-677 (2008).
723. Halle, A.*, et al.* The NALP3 inflammasome is involved in the innate immune response to amyloid-beta. *Nat Immunol* **9**, 857-865 (2008).
724. Franklin, B.S.*, et al.* The adaptor ASC has extracellular and 'prionoid' activities that propagate inflammation. *Nat Immunol* **15**, 727-737 (2014).

725. Ramarao, N., Tran, S.L., Marin, M. & Vidic, J. Advanced Methods for Detection of *Bacillus cereus* and Its Pathogenic Factors. *Sensors (Basel)* **20**(2020).
726. Didier, A.*, et al.* Monoclonal antibodies neutralize *Bacillus cereus* Nhe enterotoxin by inhibiting ordered binding of its three exoprotein components. *Infection and immunity* **80**, 832-838 (2012).
727. Jessberger, N.*, et al.* Binding to The Target Cell Surface Is The Crucial Step in Pore Formation of Hemolysin BL from *Bacillus cereus*. *Toxins (Basel)* **11**(2019).
728. Zhu, K.*, et al.* Formation of small transmembrane pores: An intermediate stage on the way to *Bacillus cereus* non-hemolytic enterotoxin (Nhe) full pores in the absence of NheA. *Biochem Biophys Res Commun* **469**, 613-618 (2016).
729. Jessberger, N.*, et al.* Characteristics of the Protein Complexes and Pores Formed by *Bacillus cereus* Hemolysin BL. *Toxins (Basel)* **12**(2020).
730. Mathur, A.*, et al.* A multicomponent toxin from *Bacillus cereus* incites inflammation and shapes host outcome via the NLRP3 inflammasome. *Nature Microbiology* **4**, 362-374 (2019).
731. Fahie, M.A.*, et al.* Disruption of the open conductance in the beta-tongue mutants of Cytolysin A. *Sci Rep* **8**, 3796 (2018).
732. Andreeva, Z.I.*, et al.* Purification and cytotoxic properties of *Bacillus cereus* hemolysin II. *Protein Expr Purif* **47**, 186-193 (2006).
733. Enosi Tuipulotu, D., Mathur, A., Ngo, C. & Man, S.M. *Bacillus cereus*: Epidemiology, Virulence Factors, and Host-Pathogen Interactions. *Trends Microbiol* (2020).
734. Parkunan, S.M., Astley, R. & Callegan, M.C. Role of TLR5 and flagella in *Bacillus* intraocular infection. *PLoS One* **9**, e100543 (2014).
735. McCoy, A.J.*, et al.* Cytotoxins of the human pathogen *Aeromonas hydrophila* trigger, via the NLRP3 inflammasome, caspase-1 activation in macrophages. *Eur J Immunol* **40**, 2797-2803 (2010).
736. McCoy, A.J., Koizumi, Y., Higa, N. & Suzuki, T. Differential regulation of caspase-1 activation via NLRP3/NLRC4 inflammasomes mediated by aerolysin and type III secretion system during *Aeromonas veronii* infection. *J Immunol* **185**, 7077-7084 (2010).
737. Van Opdenbosch, N. & Lamkanfi, M. Caspases in Cell Death, Inflammation, and Disease. *Immunity* **50**, 1352-1364 (2019).
738. Song, W.S., Jeon, Y.J., Namgung, B., Hong, M. & Yoon, S.I. A conserved TLR5 binding and activation hot spot on flagellin. *Sci Rep* **7**, 40878 (2017).
739. Yoon, S.I.*, et al.* Structural basis of TLR5-flagellin recognition and signaling. *Science* **335**, 859-864 (2012).
740. Hong, M., Yoon, S.I. & Wilson, I.A. Recombinant expression of TLR5 proteins by ligand supplementation and a leucine-rich repeat hybrid technique. *Biochem Biophys Res Commun* **427**, 119-124 (2012).
741. Tenthorey, J.L.*, et al.* The structural basis of flagellin detection by NAIP5: A strategy to limit pathogen immune evasion. *Science* **358**, 888-893 (2017).
742. Il Kim, M., Lee, C., Park, J., Jeon, B.Y. & Hong, M. Crystal structure of *Bacillus cereus* flagellin and structure-guided fusion-protein designs. *Sci Rep* **8**, 5814 (2018).
743. Lage, S.L.*, et al.* Cytosolic flagellin-induced lysosomal pathway regulates inflammasome-dependent and -independent macrophage responses. *Proc Natl Acad Sci U S A* **110**, E3321-3330 (2013).
744. Coates, B.M.*, et al.* Inhibition of the NOD-Like Receptor Protein 3 Inflammasome Is Protective in Juvenile Influenza A Virus Infection. *Front Immunol* **8**, 782 (2017).
745. Alhallaf, R.*, et al.* The NLRP3 Inflammasome Suppresses Protective Immunity to Gastrointestinal Helminth Infection. *Cell Rep* **23**, 1085-1098 (2018).
746. Raupach, B., Peuschel, S.K., Monack, D.M. & Zychlinsky, A. Caspase-1-mediated activation of interleukin-1beta (IL-1beta) and IL-18 contributes to innate immune defenses against *Salmonella enterica* serovar Typhimurium infection. *Infect Immun* **74**, 4922-4926 (2006).

747. Schneider, B.E.*, et al.* A role for IL-18 in protective immunity against *Mycobacterium tuberculosis*. *Eur J Immunol* **40**, 396-405 (2010).
748. Wang, J., Deobald, K. & Re, F. Gasdermin D Protects from Melioidosis through Pyroptosis and Direct Killing of Bacteria. *J Immunol* **202**, 3468-3473 (2019).
749. Thomas, P.G.*, et al.* The intracellular sensor NLRP3 mediates key innate and healing responses to influenza A virus via the regulation of caspase-1. *Immunity* **30**, 566-575 (2009).
750. Allen, I.C.*, et al.* The NLRP3 inflammasome mediates in vivo innate immunity to influenza A virus through recognition of viral RNA. *Immunity* **30**, 556-565 (2009).
751. Tate, M.D.*, et al.* Reassessing the role of the NLRP3 inflammasome during pathogenic influenza A virus infection via temporal inhibition. *Sci Rep* **6**, 27912 (2016).
752. Pinar, A.*, et al.* PB1-F2 Peptide Derived from Avian Influenza A Virus H7N9 Induces Inflammation via Activation of the NLRP3 Inflammasome. *J Biol Chem* **292**, 826-836 (2017).
753. McAuley, J.L.*, et al.* Activation of the NLRP3 inflammasome by IAV virulence protein PB1-F2 contributes to severe pathophysiology and disease. *PLoS Pathog* **9**, e1003392 (2013).
754. Palm, N.W. & Medzhitov, R. Role of the inflammasome in defense against venoms. *P Natl Acad Sci USA* **110**, 1809-1814 (2013).
755. Naylor, C.E.*, et al.* Structure of the key toxin in gas gangrene. *Nat Struct Biol* **5**, 738-746 (1998).
756. Hough, E.*, et al.* High-resolution (1.5 A) crystal structure of phospholipase C from *Bacillus cereus*. *Nature* **338**, 357-360 (1989).
757. Nagahama, M., Mukai, M., Morimitsu, S., Ochi, S. & Sakurai, J. Role of the C-domain in the biological activities of *Clostridium perfringens* alpha-toxin. *Microbiol Immunol* **46**, 647-655 (2002).
758. Flores-Diaz, M.*, et al.* A cellular deficiency of gangliosides causes hypersensitivity to *Clostridium perfringens* phospholipase C. *J Biol Chem* **280**, 26680-26689 (2005).
759. Kaksonen, M. & Roux, A. Mechanisms of clathrin-mediated endocytosis. *Nat Rev Mol Cell Biol* **19**, 313-326 (2018).
760. Mathur, A., Hayward, J.A. & Man, S.M. Molecular mechanisms of inflammasome signaling. *J Leukoc Biol* **103**, 233-257 (2018).
761. Hafner-Bratkovic, I. & Pelegrin, P. Ion homeostasis and ion channels in NLRP3 inflammasome activation and regulation. *Curr Opin Immunol* **52**, 8-17 (2018).
762. Zhu, J.*, et al.* T-lymphocyte Kv1.3 channel activation triggers the NLRP3 inflammasome signaling pathway in hypertensive patients. *Exp Ther Med* **14**, 147-154 (2017).
763. Marie, C., Verkerke, H.P., Theodorescu, D. & Petri, W.A. A whole-genome RNAi screen uncovers a novel role for human potassium channels in cell killing by the parasite Entamoeba histolytica. *Sci Rep* **5**, 13613 (2015).
764. Bobak, N.*, et al.* Recombinant tandem of pore-domains in a Weakly Inward rectifying K(+) channel 2 (TWIK2) forms active lysosomal channels. *Sci Rep* **7**, 649 (2017).
765. Qureshi, O.S., Paramasivam, A., Yu, J.C. & Murrell-Lagnado, R.D. Regulation of P2X4 receptors by lysosomal targeting, glycan protection and exocytosis. *J Cell Sci* **120**, 3838-3849 (2007).
766. Boumechache, M., Masin, M., Edwardson, J.M., Gorecki, D.C. & Murrell-Lagnado, R. Analysis of assembly and trafficking of native P2X4 and P2X7 receptor complexes in rodent immune cells. *J Biol Chem* **284**, 13446-13454 (2009).
767. Fink, S.L. & Cookson, B.T. Caspase-1-dependent pore formation during pyroptosis leads to osmotic lysis of infected host macrophages. *Cell Microbiol* **8**, 1812-1825 (2006).
768. Kayagaki, N.*, et al.* NINJ1 mediates plasma membrane rupture during lytic cell death. *Nature* **591**, 131–136 (2021).
769. Ding, J.*, et al.* Pore-forming activity and structural autoinhibition of the gasdermin family. *Nature* **535**, 111-116 (2016).

770. Ruan, J., Xia, S., Liu, X., Lieberman, J. & Wu, H. Cryo-EM structure of the gasdermin A3 membrane pore. *Nature* **557**, 62-67 (2018).
771. Rogers, C.*, et al.* Cleavage of DFNA5 by caspase-3 during apoptosis mediates progression to secondary necrotic/pyroptotic cell death. *Nat Commun* **8**, 14128 (2017).
772. Wang, Y.*, et al.* Chemotherapy drugs induce pyroptosis through caspase-3 cleavage of a gasdermin. *Nature* **547**, 99-103 (2017).
773. Zhang, Z.*, et al.* Gasdermin E suppresses tumour growth by activating anti-tumour immunity. *Nature* **579**, 415-420 (2020).
774. Wang, Q.*, et al.* A bioorthogonal system reveals antitumour immune function of pyroptosis. *Nature* **579**, 421-426 (2020).
775. Monteleone, M.*, et al.* Interleukin-1beta Maturation Triggers Its Relocation to the Plasma Membrane for Gasdermin-D-Dependent and -Independent Secretion. *Cell Rep* **24**, 1425-1433 (2018).
776. Ingolfsson, H.I.*, et al.* Lipid organization of the plasma membrane. *J Am Chem Soc* **136**, 14554-14559 (2014).
777. Martin-Sanchez, F.*, et al.* Inflammasome-dependent IL-1beta release depends upon membrane permeabilisation. *Cell Death Differ* **23**, 1219-1231 (2016).
778. R Bonita, R.B.a.T.K. Basic epidemiology in *World Health Organization*, Vol. 2nd edition (2020).
779. Adams, V., Han, X., Lyras, D. & Rood, J.I. Antibiotic resistance plasmids and mobile genetic elements of *Clostridium perfringens*. *Plasmid* **99**, 32-39 (2018).
780. Chen, Z., Moayeri, M. & Purcell, R. Monoclonal antibody therapies against anthrax. *Toxins (Basel)* **3**, 1004-1019 (2011).
781. Morrison, C. Antibacterial antibodies gain traction. *Nat Rev Drug Discov* **14**, 737-738 (2015).
782. Scobie, H.M.*, et al.* A soluble receptor decoy protects rats against anthrax lethal toxin challenge. *J Infect Dis* **192**, 1047-1051 (2005).
783. Dinarello, C.A., Simon, A. & van der Meer, J.W. Treating inflammation by blocking interleukin-1 in a broad spectrum of diseases. *Nat Rev Drug Discov* **11**, 633-652 (2012).
784. Boxer, M.B.*, et al.* A highly potent and selective caspase 1 inhibitor that utilizes a key 3-cyanopropanoic acid moiety. *ChemMedChem* **5**, 730-738 (2010).
785. Beecher, D.J. & Macmillan, J.D. Characterization of the components of hemolysin BL from *Bacillus cereus*. *Infection and immunity* **59**, 1778-1784 (1991).
786. Baida, G., Budarina, Z.I., Kuzmin, N.P. & Solonin, A.S. Complete nucleotide sequence and molecular characterization of hemolysin II gene from *Bacillus cereus*. *FEMS Microbiol Lett* **180**, 7-14 (1999).
787. Baida, G.E. & Kuzmin, N.P. Mechanism of action of hemolysin III from *Bacillus cereus*. *Biochim Biophys Acta* **1284**, 122-124 (1996).
788. Kuppe, A., Evans, L.M., McMillen, D.A. & Griffith, O.H. Phosphatidylinositol-specific phospholipase C of *Bacillus cereus*: cloning, sequencing, and relationship to other phospholipases. *J Bacteriol* **171**, 6077-6083 (1989).
789. Fedhila, S., Daou, N., Lereclus, D. & Nielsen-LeRoux, C. Identification of *Bacillus cereus* internalin and other candidate virulence genes specifically induced during oral infection in insects. *Mol Microbiol* **62**, 339-355 (2006).
790. Madeira, J.P., Alpha-Bazin, B., Armengaud, J. & Duport, C. Time dynamics of the *Bacillus cereus* exoproteome are shaped by cellular oxidation. *Front Microbiol* **6**, 342 (2015).
791. Ringwald, M., Wu, C. & Su, A.I. BioGPS and GXD: mouse gene expression data-the benefits and challenges of data integration. *Mamm Genome* **23**, 550-558 (2012).
792. Lattin, J.E.*, et al.* Expression analysis of G Protein-Coupled Receptors in mouse macrophages. *Immunome Res* **4**, 5 (2008).

Appendices

Appendices for Chapter 3: A multicomponent toxin from *Bacillus cereus* incites inflammation and shapes host outcome via the NLRP3 inflammasome

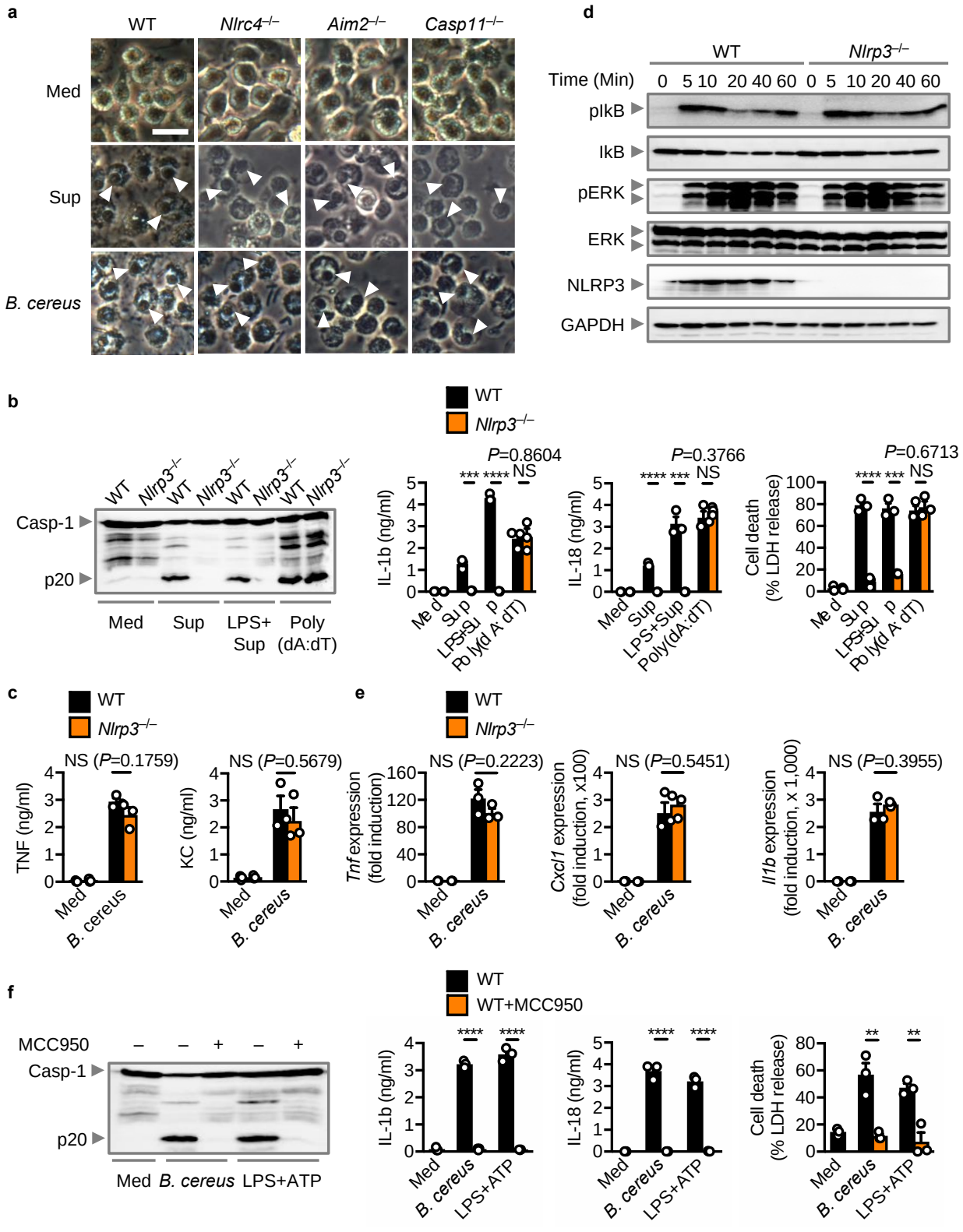
a
WT
Nlrc4−/−
Aim2−/−
Casp11−/−
Med
Sup
B. cereus
d
WT
Nlrp3−/−
Time (Min)
0 5 10 20 40 60 0 5 10 20 40 60
pIkB
IkB
pERK
ERK
NLRP3
GAPDH
b
WT
Nlrp3−/−
Casp-1
p20
Med
Sup
LPS+ Sup
Poly (dA:dT)
P=0.8604
P=0.3766
P=0.6713
NS
IL-1b (ng/ml)
IL-18 (ng/ml)
Cell death (% LDH release)
Poly(dA:dT)
c
TNF (ng/ml)
KC (ng/ml)
NS (P=0.1759)
NS (P=0.5679)
e
Tnf expression (fold induction)
Cxcl1 expression (fold induction, x100)
Il1b expression (fold induction, x 1,000)
NS (P=0.2223)
NS (P=0.5451)
NS (P=0.3955)
f
WT+MCC950
MCC950
LPS+ATP

Figure 3.1 | Production of other pro-inflammatory cytokines in response to *B. cereus* and its secreted factor is not affected by the absence of NLRP3. (**a**) Microscopy analysis of the death of WT or mutant BMDMs left untreated (Med, top) or assessed 2 hr after stimulation with the supernatant of *B. cereus* (Sup, middle) or 3 hr after infection with *B. cereus* (MOI, 5; bottom). (**b**) Immunoblot analysis of caspase-1 (left), the release of IL-1β (middle-left) and IL-18 (middle-right), and death (right) of WT or *Nlrp3*$^{-/-}$ BMDMs left untreated (Med) or assessed 2 hr after stimulation with the supernatant of *B. cereus* (Sup) or 5 hr after transfection with poly(dA:dT). (**c**) Release of TNF (left) and Keratinocyte chemoattractant (KC) (right) in WT or *Nlrp3*$^{-/-}$ BMDMs left untreated or assessed 3 hr after infection with *B. cereus* (MOI, 5). (**d**) Immunoblot analysis of phospho-IκB (pIκB), IκB, phospho-ERK (pERK), ERK, NLRP3 and GAPDH (loading control) of unprimed WT or *Nlrp3*$^{-/-}$ BMDMs 0-60 min after infection with *B. cereus* (MOI, 2). (**e**) Real-time quantitative RT-PCR analysis of the gene encoding TNF (left), Keratinocyte chemoattractant (*Cxcl1*, middle) and IL-1β (right) in WT or *Nlrp3*$^{-/-}$ BMDMs 3 hr after infection with *B. cereus*, presented relative to that of the gene encoding GAPDH. (**f**) Immunoblot analysis of caspase-1 (left), the release of IL-1β (middle-left) and IL-18 (middle-right), and death (right) of unprimed or LPS-primed WT BMDMs left untreated or assessed 3 hr after infection with *B. cereus* (MOI, 5) or 30 min after stimulation with ATP in absence or presence of the NLRP3 inhibitor MCC950 (20 μM). Scale bar, 20 μm (a). Arrowheads indicate dead cells (a). Each symbol represents an independent experiment (b, c, e, and f). NS, not statistically significant. ***P* < 0.01, ****P* < 0.001, and *****P* < 0.0001 (two-tailed *t*-test [b, c, e and f]). Data are representative three independent experiments (a-f; mean and s.e.m. in b, c, e and f).

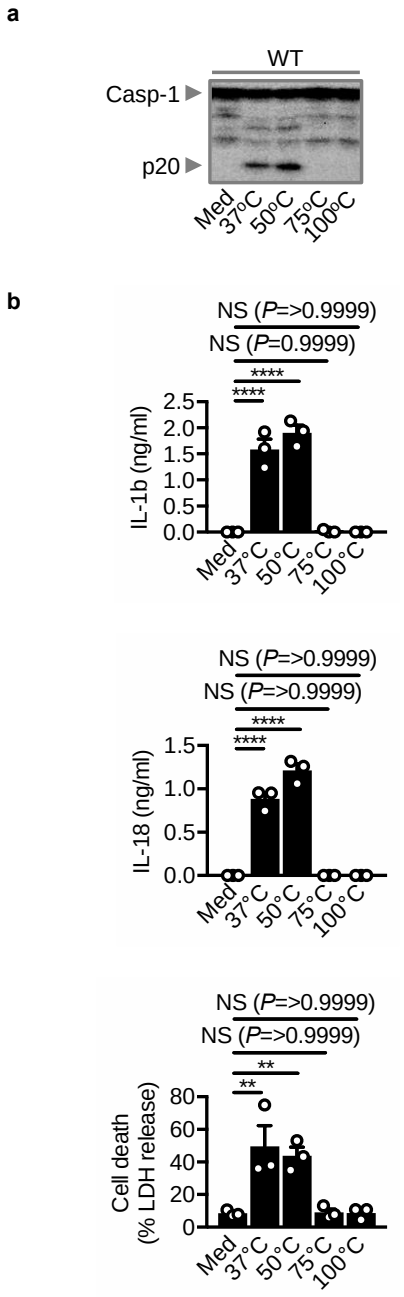

Figure 3.2 | The secreted factor of *B. cereus* is sensitive to heat. (**a**) Immunoblot analysis of caspase-1 in LPS-primed WT BMDMs left untreated (Med) or assessed 2 hr after stimulation with the supernatant of *B. cereus* heated to 37 °C, 50 °C, 75 °C or 100 °C. (**b**) Release of IL-1β (top) and IL-18 (middle) and death (bottom) of WT BMDMs analysed as in (a). Each symbol represents an independent experiment (b). NS, not statistically significant. $^{**}P < 0.01$ and $^{****}P < 0.0001$ (one-way analysis of variance [ANOVA] with Dunnett's multiple-comparisons [b]). Data are representative of three independent experiments (a and b; mean and s.e.m. in b).

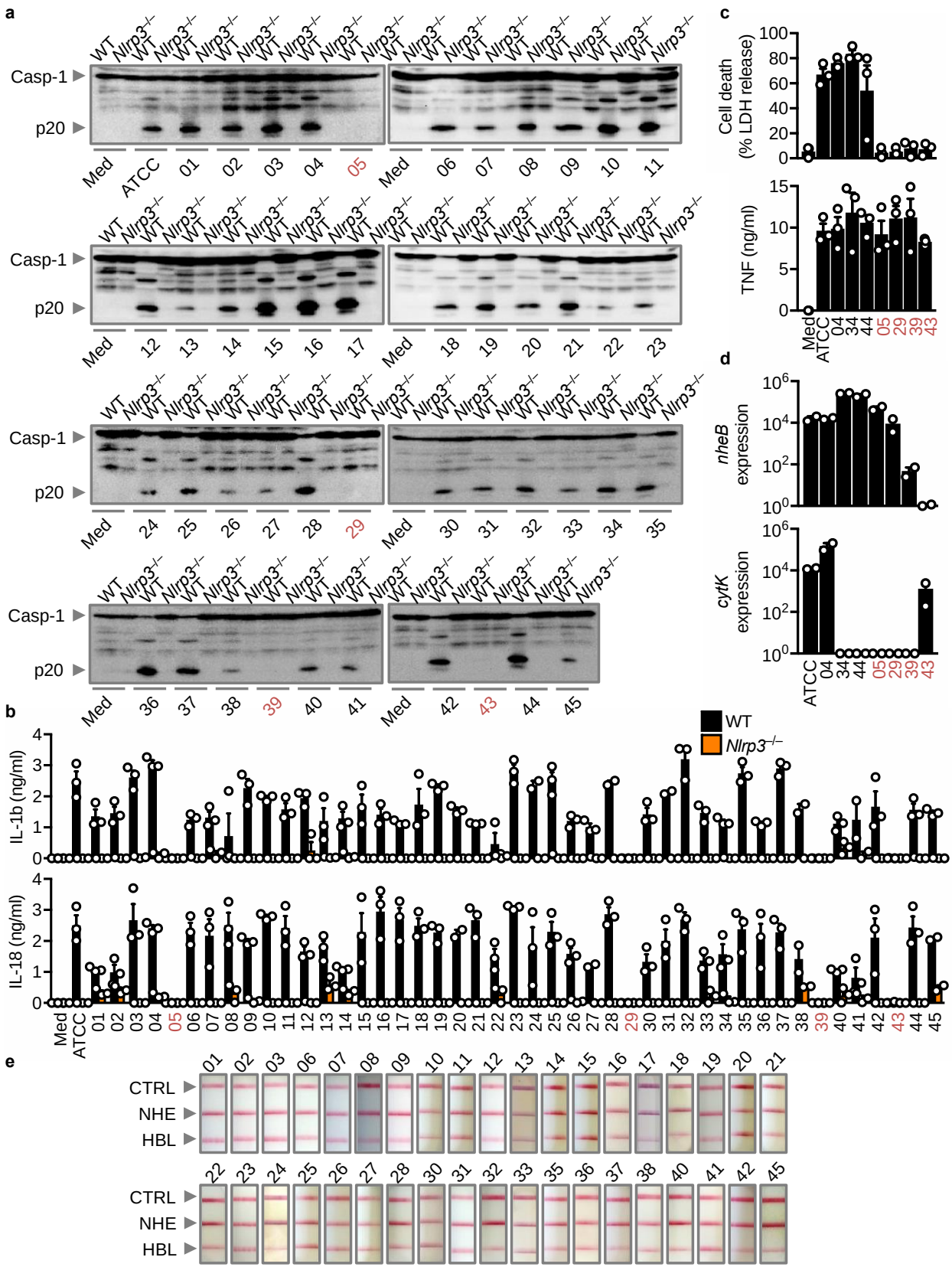
a
Casp-1
p20
WT
Nlrp3−/−
Med
ATCC
01 02 03 04 05 06 07 08 09 10 11
12 13 14 15 16 17 18 19 20 21 22 23
24 25 26 27 28 29 30 31 32 33 34 35
36 37 38 39 40 41 42 43 44 45
c
Cell death (% LDH release)
TNF (ng/ml)
d
nheB expression
cytK expression
b
IL-1b (ng/ml)
IL-18 (ng/ml)
e
CTRL
NHE
HBL

Figure 3.3 | The inflammasome-activating factor is highly prevalent in *B. cereus* isolates and is not associated with isolates expressing of NHE or Cytotoxin K. (**a**) Immunoblot analysis of caspase-1 in unprimed WT or *Nlrp3*$^{-/-}$ BMDMs left untreated (Med) or assessed at various times after infection with *B. cereus* (MOI, 2-50). (**b**) Release of IL-1β (top) and IL-18 (bottom) of WT or *Nlrp3*$^{-/-}$ BMDMs after treatment as in (a). (**c**) Cell death (top) and release of TNF (bottom) of WT BMDMs after treatment as in (a). (**d**) Real-time quantitative RT-PCR analysis of the gene encoding NHE-B (*nheB*, top) and Cytotoxin K (*cytK,* bottom) of overnight cultures of *B. cereus*, presented relative to that of the gene encoding 16S rRNA. (**e**) Immunological lateral flow tests (Duopath) of NHE and HBL using the supernatant of overnight cultures of *B. cereus*. Numerical IDs of *B. cereus* strains unable to activate caspase-1 are colorized (a-d). Each symbol represents an independent experiment (b-d). Data are representative of at least two independent experiments (n=3 in a, c-e, n=2-3 in b; mean and s.e.m. in b-d)

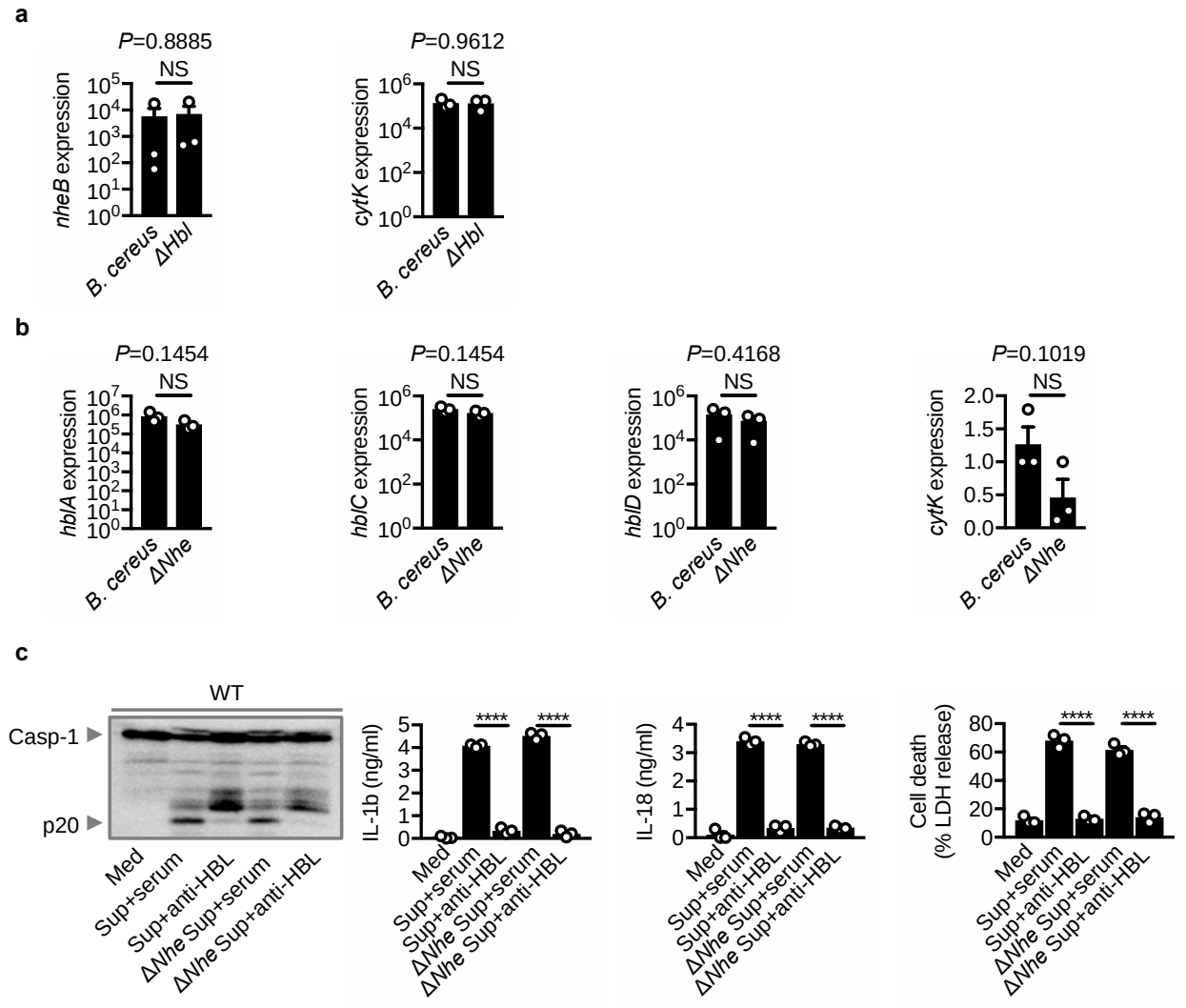
a
P=0.8885
NS
nheB expression
B. cereus
ΔHbl
P=0.9612
NS
cytK expression
B. cereus
ΔHbl
b
P=0.1454
NS
hblA expression
B. cereus
ΔNhe
P=0.1454
NS
hblC expression
B. cereus
ΔNhe
P=0.4168
NS
hblD expression
B. cereus
ΔNhe
P=0.1019
NS
cytK expression
B. cereus
ΔNhe
c
WT
Casp-1
p20
Med
Sup+serum
Sup+anti-HBL
ΔNhe Sup+serum
ΔNhe Sup+anti-HBL
IL-1b (ng/ml)
****
IL-18 (ng/ml)
****
Cell death (% LDH release)
****

Figure 3.4 | NHE and Cytotoxin K are not associated with activation of the inflammasome. (**a**) Real-time quantitative RT-PCR analysis of the gene encoding NHE-B (*nheB*, left) and Cytotoxin K (*cytK,* right) of overnight cultures of *B. cereus* ATCC 10876 or its isogenic mutant lacking HBL (Δ*hbl*) presented relative to that of the gene encoding 16S rRNA. (**b**) Real-time quantitative RT-PCR analysis of the gene encoding HBL (*hblA*, *hblC*, and *hblD*; left) and Cytotoxin K (*cytK,* right) of overnight cultures of *B. cereus* F837/76 or its isogenic mutant lacking NHE (Δ*nhe*), presented relative to that of the gene encoding 16S rRNA. (**c**) Immunoblot analysis of caspase-1 (left), the release of IL-1β (middle-left) and IL-18 (middle-right), and death (right) of unprimed or LPS-primed WT BMDMs left untreated (Med) or 2 hr after stimulation with the supernatant of *B. cereus* (Sup) or supernatant of Δ*nhe B. cereus* (Δ*nhe* Sup) treated with mouse serum (serum) or anti-HBL antibodies (anti-HBL). Each symbol represents an independent experiment (a-c). NS, not statistically significant. ****$P < 0.0001$ (two-tailed *t*-test [a-c]). Data are representative of three independent experiments (a-c; mean and s.e.m. in a-c).

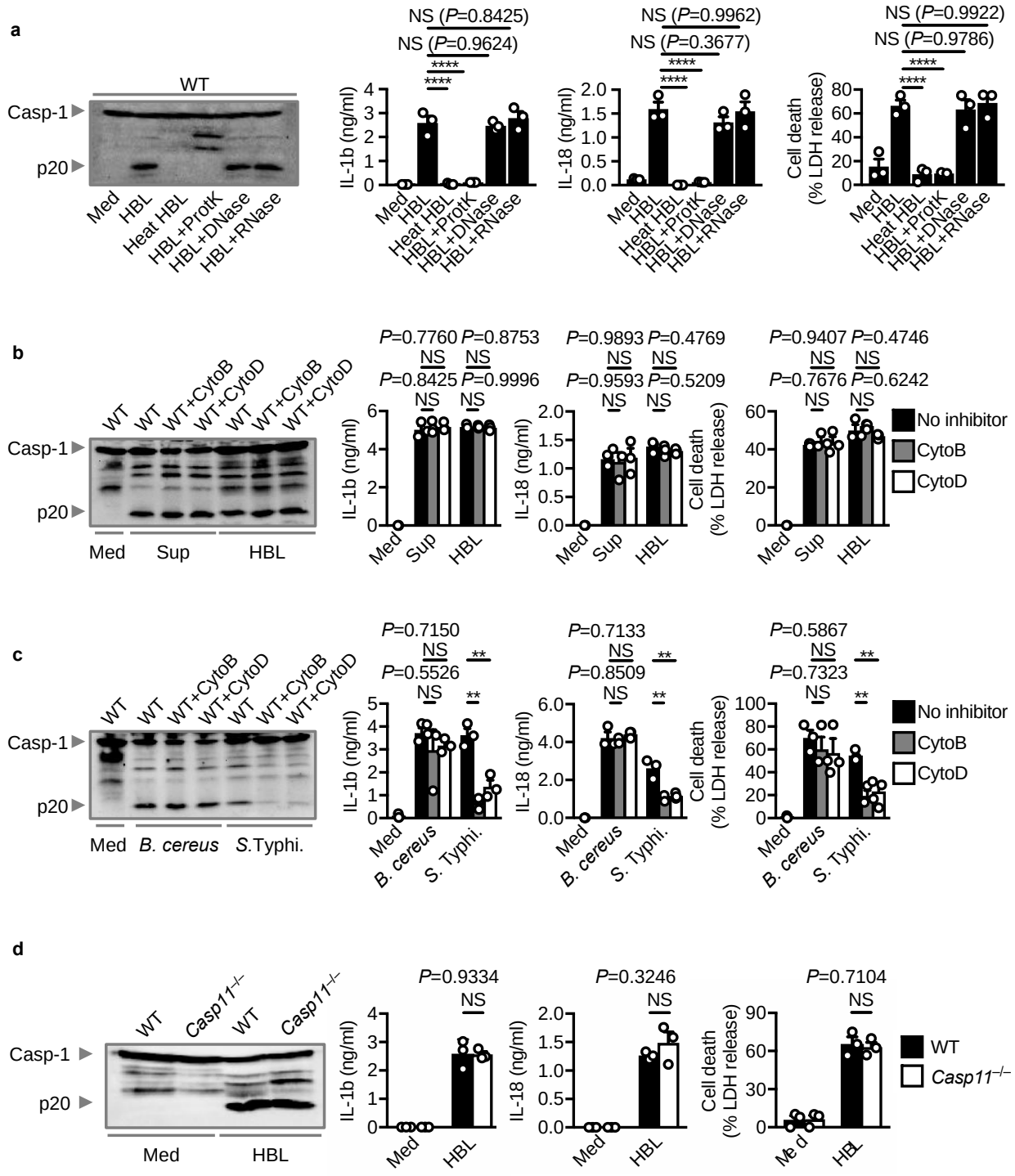
a
WT
Casp-1
p20
Med
HBL
Heat HBL
HBL+ProtK
HBL+DNase
HBL+RNase
NS (P=0.8425)
NS (P=0.9624)
****
****
IL-1b (ng/ml)
NS (P=0.9962)
NS (P=0.3677)
****
****
IL-18 (ng/ml)
NS (P=0.9922)
NS (P=0.9786)
****
****
Cell death (% LDH release)
b
WT
WT
WT+CytoB
WT+CytoD
WT
WT+CytoB
WT+CytoD
Casp-1
p20
Med
Sup
HBL
P=0.7760 P=0.8753
NS NS
P=0.8425 P=0.9996
NS NS
IL-1b (ng/ml)
P=0.9893 P=0.4769
NS NS
P=0.9593 P=0.5209
NS NS
IL-18 (ng/ml)
P=0.9407 P=0.4746
NS NS
P=0.7676 P=0.6242
NS NS
Cell death (% LDH release)
No inhibitor
CytoB
CytoD
c
WT
WT
WT+CytoB
WT+CytoD
WT
WT+CytoB
WT+CytoD
Casp-1
p20
Med
B. cereus
S.Typhi.
P=0.7150
NS **
P=0.5526
NS **
IL-1b (ng/ml)
P=0.7133
NS **
P=0.8509
NS **
IL-18 (ng/ml)
P=0.5867
NS **
P=0.7323
NS **
Cell death (% LDH release)
No inhibitor
CytoB
CytoD
d
WT
Casp11−/−
WT
Casp11−/−
Casp-1
p20
Med
HBL
P=0.9334
NS
IL-1b (ng/ml)
P=0.3246
NS
IL-18 (ng/ml)
P=0.7104
NS
Cell death (% LDH release)
WT
Casp11−/−

Figure 3.5 | Cytosolic entry of HBL is not required for activation of the NLRP3 inflammasome. (**a**) Immunoblot analysis of caspase-1 (left), the release of IL-1β (middle-left) and IL-18 (middle-right), and death (right) of unprimed or LPS-primed WT BMDMs left untreated (Med) or assessed 3 hr after stimulation with recombinant HBL, HBL heated to 100 °C (Heat HBL), or HBL treated with Proteinase K (ProtK), DNase or RNase. (**b**) Immunoblot analysis of caspase-1 (left), the release of IL-1β (middle-left) and IL-18 (middle-right), and death (right) of unprimed or LPS-primed WT BMDMs left untreated (Med) or 2 hr after stimulation with the supernatant of *B. cereus* (Sup) or 3 hr after stimulation with recombinant HBL, in the absence or presence of cytochalasin B (CytoB; 50 μM) or cytochalasin D (CytoD; 50 μM). (**c**) Immunoblot analysis of caspase-1 (left), the release of IL-1β (middle-left) and IL-18 (middle-right), and death (right) of WT BMDMs left untreated or assessed 3 hr after infection with *B. cereus* (MOI, 2) or 4 hr after infection with *S.* Typhimurium (*S.* Typhi.; MOI, 5), in the presence or absence of cytochalasin B (CytoB; 50 μM) or cytochalasin D (CytoD; 50 μM). (**d**) Immunoblot analysis of caspase-1 (left), the release of IL-1β (middle-left) and IL-18 (middle-right), and death (right) of unprimed or LPS-primed WT or *Casp11*$^{-/-}$ BMDMs left untreated or assessed 3 hr after stimulation with recombinant HBL. Each symbol represents an independent experiment (a-d). NS, not statistically significant. ***P* < 0.01, ****P* < 0.001 and *****P* < 0.0001 (one-way analysis of variance [ANOVA] with Dunnett's multiple-comparisons [a-c] or two-tailed *t*-test [d]). Data are representative of three independent experiments (a-d; mean and s.e.m. in a-d).

a

B protein sequence

MIKKIPYKLLAVSTLLTITTANVVSPVTTFA SEIEQTNNGDTALSANEARMKETLQKAGLFAKSMNAYSYMLIKN
PDVNFEGITINGYVDLPGRIVQDQKNARAHAVTWDTKVKKQLLDTLNGIVEYDTTFDNYYETMVEAINTGDGETL
KEGITDLRGEIQQNQKYAQQLIEELTKLRDSIGHDVRAFGSNKELLQSILKNQGADVDADQKRLEEVLGSVNYYK
QLESDG**FNVMKGAILGLPIIGGIIV** GVARDNLGKLEPLLAELRQTVDYKVTLNRVVGVAYSNINEMHKALDDAIN
ALTYMSTQWHDLDSQYSGVLGHIENAAQKADQNKFKFLKPNLNAAKDSWKTLRTDAVTLKEGIKELKVETVTPQK

L_1 protein sequence

MKKFPFKVLTLATLATVITATTGNTIHA FAQETTAQEQKVGNYALGPEGLKKALAETGSHILVMDLYAKTMIKQP
NVNLSNIDLGSEGGELLKNIHLNQELSRINANYWLDTAKPQIQKTARNIVNYDEQFQNYYDTLVETVQKKDKAGL
KEGINDLITTINTNSKEVTDVIKMLQDFKGKLYQNSTDFKNNVGGPDGKGGLTAILAGQQATIPQLQAEIEQLRS
TQKKHFDDVLAWSIGGG**LGAAILVIAAIGGAVVIVV** TGGTATPAVVGGLSALGAAGIGLGTAAGVTASKHMDSYN
EISNKIGELSMKADRANQAVLSLTNAKE **TLAYLYQTVDQAILSLTNI** QKQWNTMGANYTDLLDNIDSMEDHKFSL
IPDDLKAAKESWNDIHKDAEFISKDIAFKQE

L_2 protein sequence

MKNKIMTGFLITSIVTGATIPINTLATPIVQA ETPQESIDISSSLRKLGAQSKLIQTYIDQSLMSPNVQLEEVPA
LHSNQSLIQQDMKEWSSELYPQLILLNSKSKGFVTKFNSYYPTLKAFVDTKEDKEGFLDRLEVLQDMATTNQENV
QRQINELTDLKSQLDNKLKNLDTDVTKAQVALSSDGTGKIDQLKNELLNTQKSIQNDLQQIALLPGALNEQGFVI
FKEVYNLSKDIIEPAAQTAVAAYNKGKEINNSILEAEKKAEKEATEKGKSALEIEAAKKAAREEIEKSKQAEIAA
AAVTKTKEYDLTKVIDPEKIKKTYSAFAEVNKLTAEQRAHLADLEVQNQKFYDLTKNLAVADLQKSMLLIMQNDL
HTFANQVDVELDLLKRYKEDLNLIKNNITKLSTNVDTTDQQSQKDTLRQLKNISSYLEEQVYKF

b

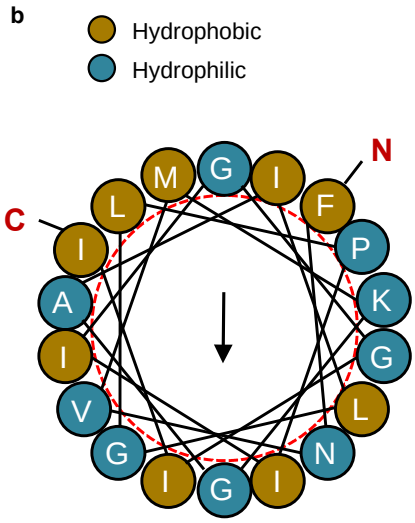

c

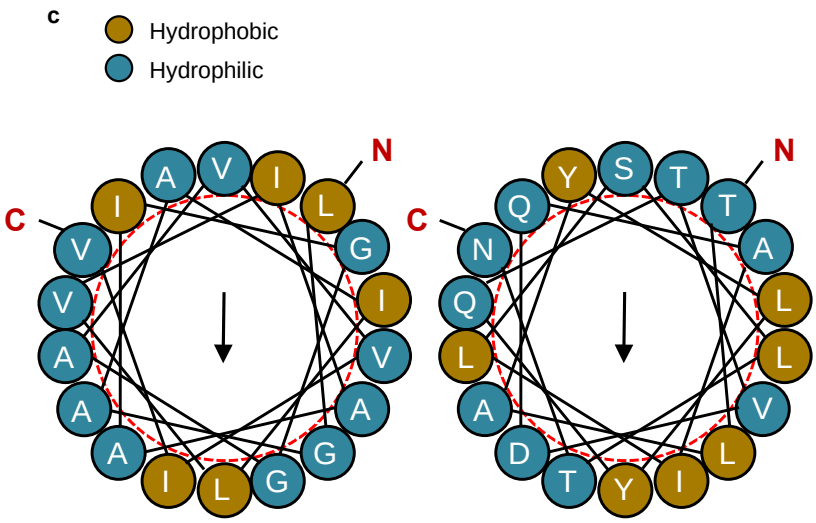

Figure 3.6 | Putative transmembrane regions of HBL. (**a**) Full-length amino acid sequences of the three components of HBL, B, L_1 and L_2, highlighting the putative signal-peptide sequence (blue) and transmembrane regions (red) based on bioinformatic-assisted analysis using the Membrane Protein Explorer (MPEx) Application. (**b**) A standard helical wheel diagram showing the distribution of hydrophobic versus hydrophilic residues in the transmembrane region of the HBL component B, drawn using the HELIQUEST server. (**c**) Standard helical wheel diagrams showing the distribution of hydrophobic versus hydrophilic residues in the two putative transmembrane regions of the HBL component L_1, drawn using the HELIQUEST server. Arrow in the helical wheel represents the direction of the hydrophobic moment. N, N-terminus of the sequence; C, C-terminus of the sequence (b and c).

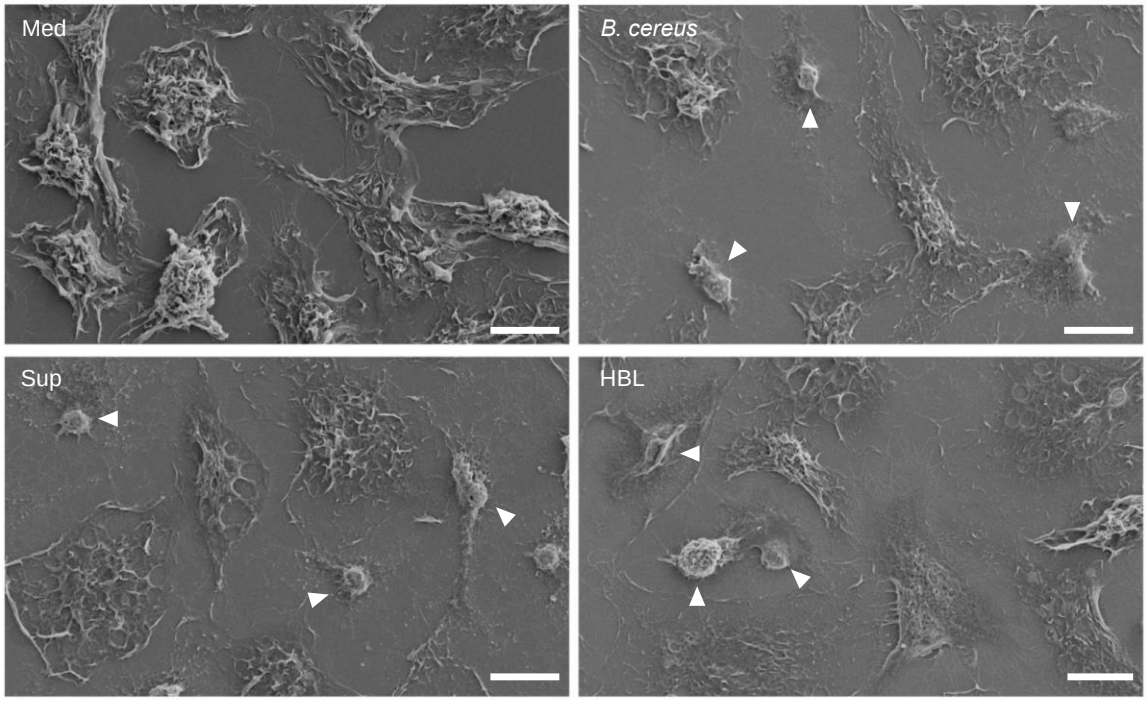

Figure 3.7 | HBL induces morphological changes and cell death in BMDMs. Scanning electron microscopy analysis of WT BMDMs assessed left untreated (Med; top left) or 3 hr after infection with *B. cereus* (MOI, 5; top right), or 2 hr after stimulation with the supernatant of *B. cereus* (Sup; bottom left), or 3 hr after stimulation with recombinant HBL (bottom right). Scale bar, 10 µm. Arrowheads indicate dead cells. Data are representative of one independent experiment.

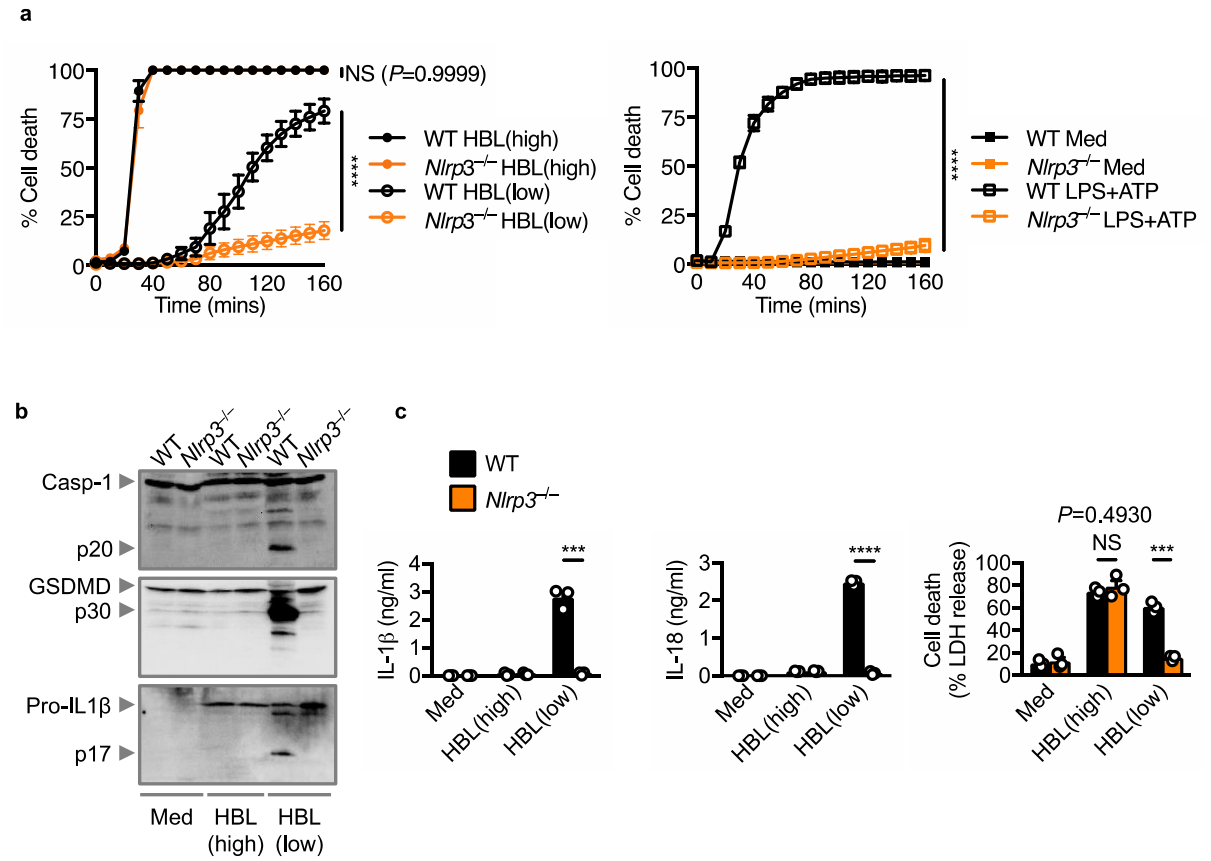

Figure 3.8 | HBL mediates activation of the NLRP3 inflammasome is dependent on its concentration. (**a**) The viability of LPS-primed WT or *Nlrp3*$^{-/-}$ BMDMs left untreated (Med) or after stimulation with a high dose of recombinant HBL (0.5 μM) or a low dose of recombinant HBL (5 nM) or with ATP (control), as determined by the IncuCyte live-imaging system. (**b**) Immunoblot analysis of caspase-1 (top), Gasdermin D (middle) and IL-1β (bottom) of unprimed or LPS-primed WT or *Nlrp3*$^{-/-}$ BMDMs left untreated or assessed 3 hr after stimulation with a high dose of recombinant HBL (0.5 μM) or a low dose of recombinant HBL (5 nM). (**c**) Release of IL-1β (left) and IL-18 (middle), and death (right) of WT BMDMs after treatment as in (b). Each symbol represents an independent experiment (c). NS, not statistically significant. ***P < 0.001 and ****P < 0.0001 (two-tailed t-test [a and c]). Data are representative of three independent experiments (a-c; mean and s.e.m. in a and c).

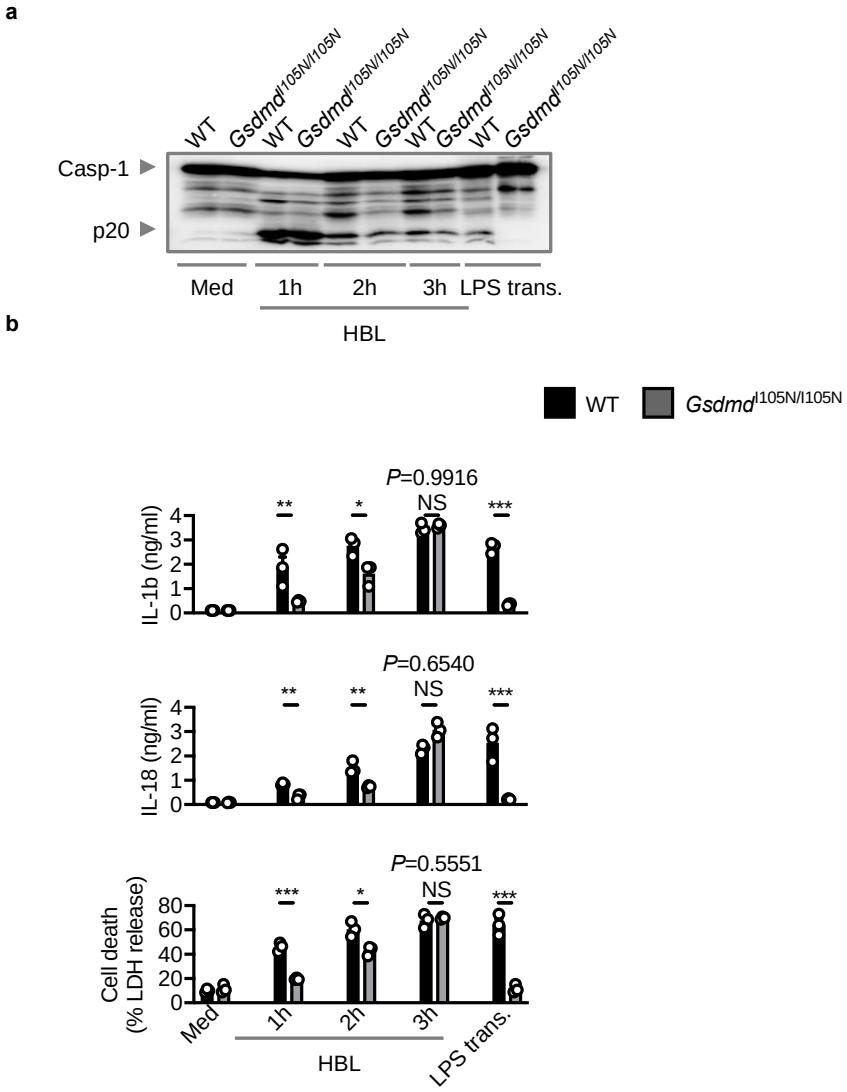

Figure 3.9 | HBL induced Gasdermin D dependent cytokine release and cell death. (**a**) Immunoblot analysis of caspase-1 of WT and *Gsdmd*$^{I105N/I105N}$ BMDMs left untreated (Med) or assessed at either 1, 2 or 3 hr after stimulation with recombinant HBL, or 16h after transfection of LPS with ATP; (**b**) Release of IL-1β and IL-18, and cell death of BMDMs as treated in (a). Each symbol represents an independent experiment (b). NS, not statistically significant, *P < 0.05, **P < 0.01 and ***P < 0.001 (student's unpaired t-test [b]). Data are representative of three independent experiments (a,b; mean and s.e.m. in b).

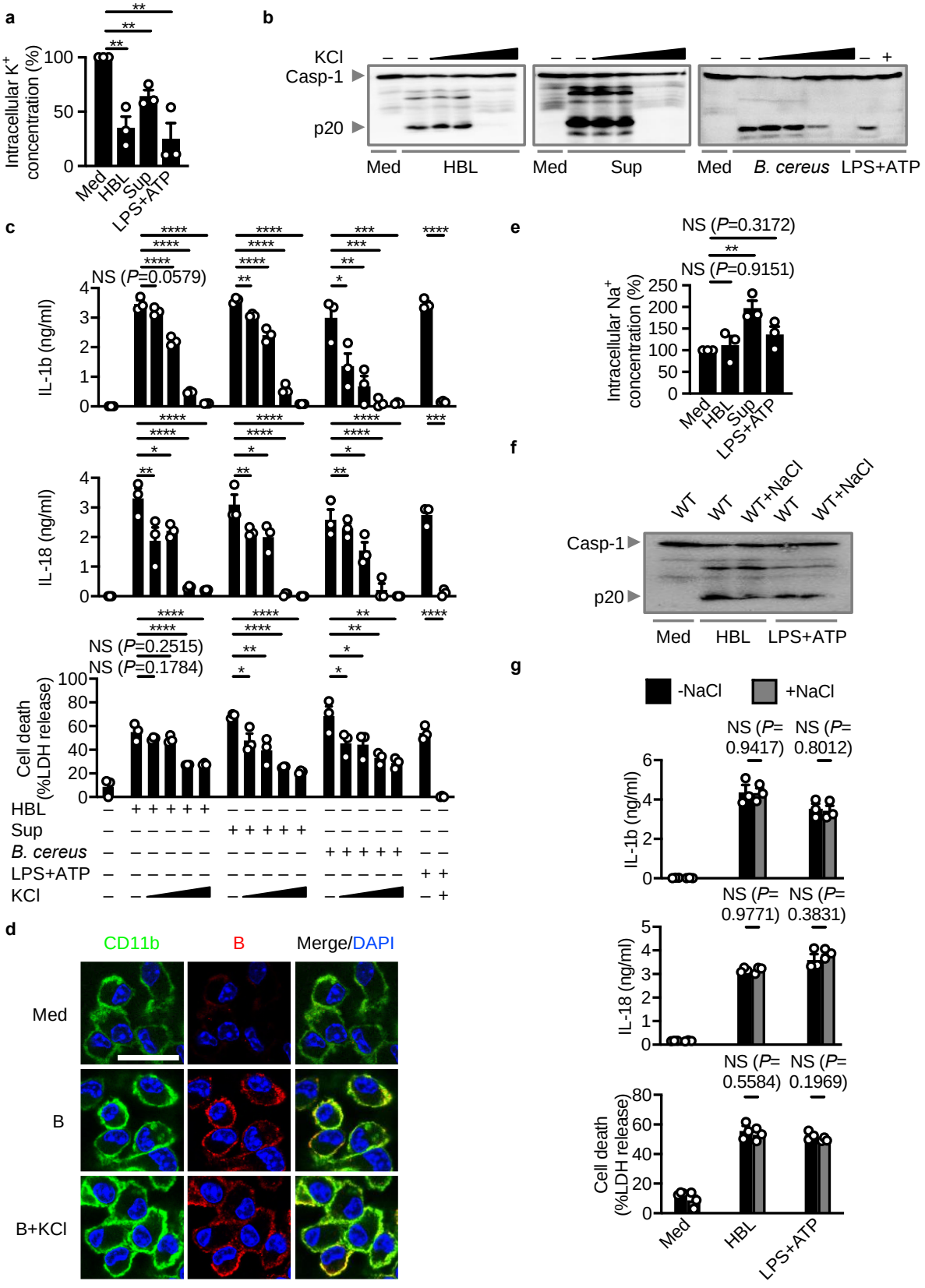
a
Intracellular K+ concentration (%)
Med
HBL
Sup
LPS+ATP
b
KCl
Casp-1
p20
Med
HBL
Med
Sup
Med
B. cereus
LPS+ATP
c
IL-1b (ng/ml)
NS (P=0.0579)
IL-18 (ng/ml)
Cell death (%LDH release)
NS (P=0.2515)
NS (P=0.1784)
HBL
Sup
B. cereus
LPS+ATP
KCl
d
CD11b
B
Merge/DAPI
Med
B
B+KCl
e
NS (P=0.3172)
NS (P=0.9151)
Intracellular Na+ concentration (%)
Med
HBL
Sup
LPS+ATP
f
WT
WT
WT+NaCl
WT
WT+NaCl
Casp-1
p20
Med
HBL
LPS+ATP
g
-NaCl
+NaCl
NS (P= 0.9417)
NS (P= 0.8012)
IL-1b (ng/ml)
NS (P= 0.9771)
NS (P= 0.3831)
IL-18 (ng/ml)
NS (P= 0.5584)
NS (P= 0.1969)
Cell death (%LDH release)
Med
HBL
LPS+ATP

Figure 3.10 | HBL induced activation of the NLRP3 inflammasome via K^+ efflux. (**a**) Inductively coupled plasma-optical emission spectrometry analysis of intracellular concentrations of K^+ of BMDMs left untreated or assessed 2 hr after treatment with either HBL or with the supernatant of *B. cereus* (Sup), or 30 mins after treatment with LPS+ATP. (**b**) Immunoblot analysis of caspase-1 in WT BMDMs left untreated (Med) or assessed 3 hr after stimulation with recombinant HBL (left), or 2 hr after stimulation with the supernatant of *B. cereus* (Sup; middle), or 3 hr after infection with *B. cereus* (MOI, 5; right) or 30 mins after stimulation with ATP (right) in the absence (–) or presence (+ or wedge) of 50 mM KCl (+) or at increasing concentrations of KCl (wedge; 5, 25, 50 and 75 mM). (**c**) Release of IL-1β (top) and IL-18 (middle), and death (bottom) of WT BMDMs after treatment as in (a). (**d**) Confocal microscopy analysis of CD11b (green) and HBL-B (red) in unprimed WT BMDMs left untreated or assessed 1 hr after stimulation with the individual component HBL-B in the absence or presence of 50 mM of KCl. (**e**) Inductively coupled plasma-optical emission spectrometry analysis of intracellular concentrations of Na^+ of BMDMs left untreated or assessed 2 hr after treatment with either HBL or with the supernatant of *B. cereus* (Sup), or 30 mins after treatment with LPS+ATP. **f**) Immunoblot analysis of caspase-1 in WT BMDMs left untreated (Med) or assessed 3 hr after stimulation with recombinant HBL, or 2 hr after stimulation with the supernatant of *B. cereus* (Sup), in the absence or presence of 50 mM NaCl. (**g**) Release of IL-1β (top) and lL-18 (middle), and death (bottom) of WT BMDMs after treatment as in (f). Scale bar, 25 μm. Each symbol represents an independent experiment (a, b, d, and f). NS, not statistically significant. **P* < 0.05, ***P* < 0.01, ****P* < 0.001 and *****P* < 0.0001 (one-way analysis of variance [ANOVA] with Dunnett's multiple-comparisons [a and d] or two-tailed *t*-test [d, for LPS+ATP only and f]). Data are representative of three independent experiments (a-g; mean and s.e.m. in a, b, d, and f).

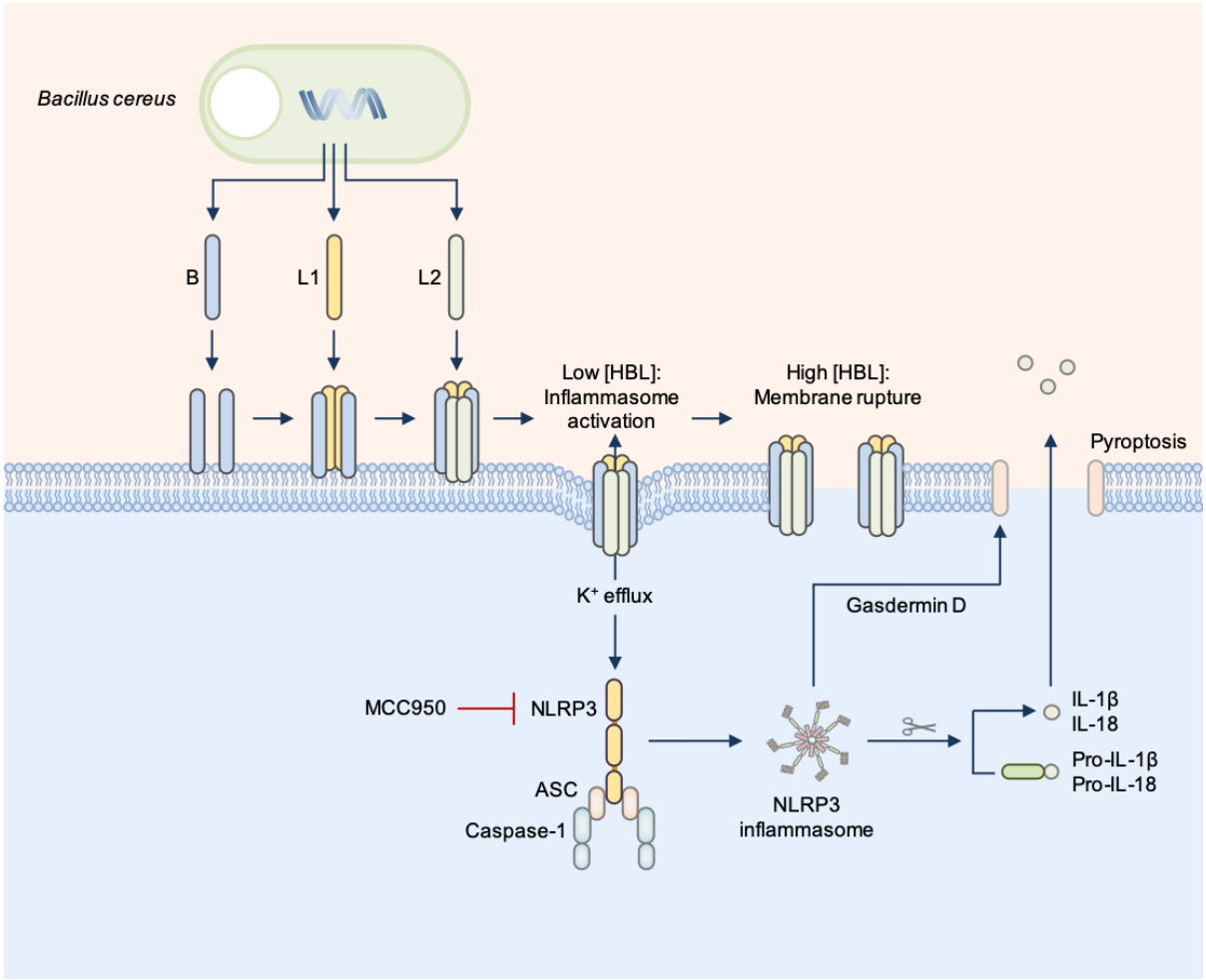

Figure 3.11 | Model of HBL-induced activation of the NLRP3 inflammasome.

Appendices of Chapter 4: *Bacillus cereus* non-haemolytic enterotoxin activates the NLRP3 inflammasome

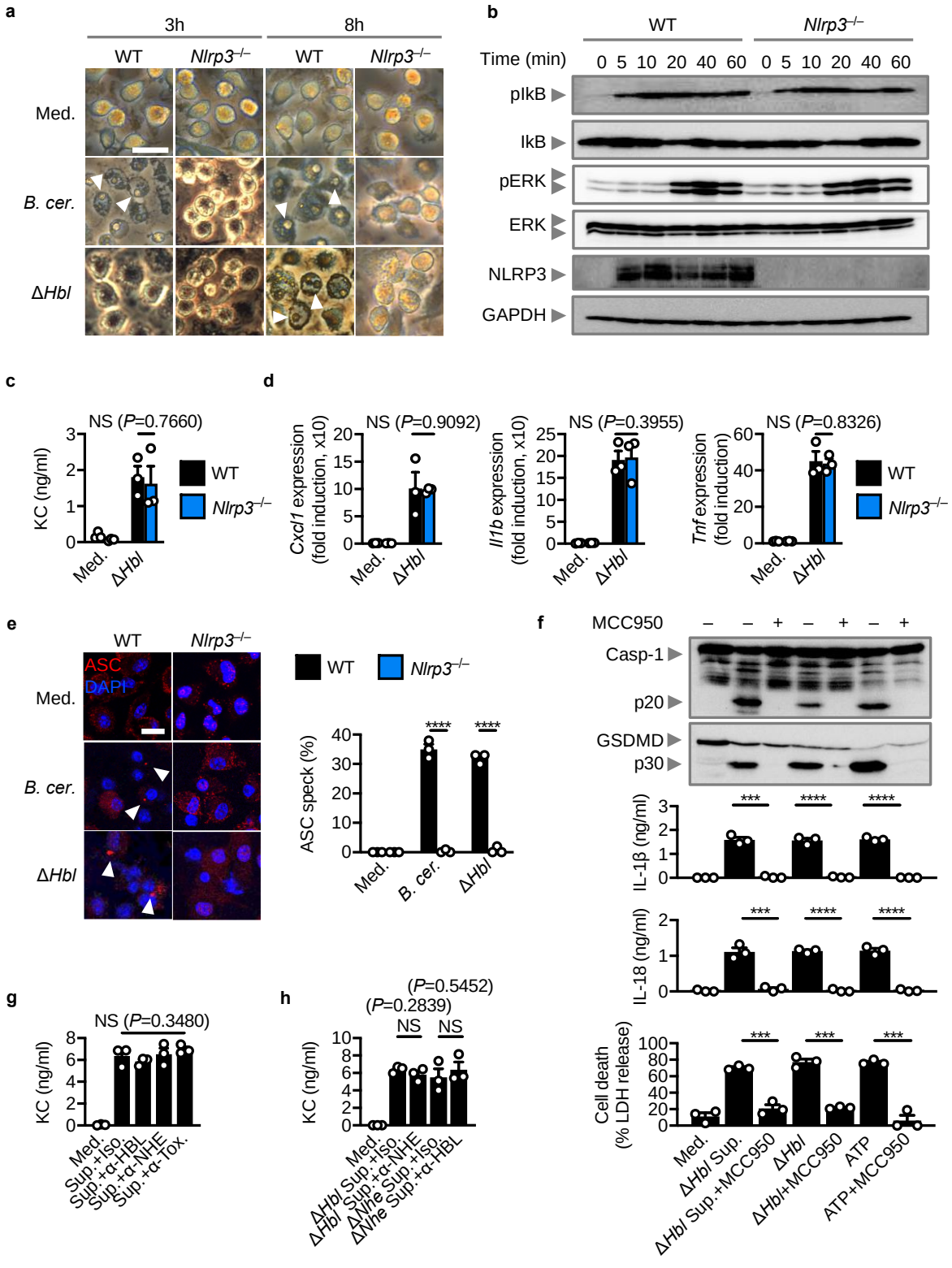
a
3h
8h
WT
Nlrp3−/−
WT
Nlrp3−/−
Med.
B. cer.
ΔHbl
b
WT
Nlrp3−/−
Time (min)
0 5 10 20 40 60 0 5 10 20 40 60
pIkB
IkB
pERK
ERK
NLRP3
GAPDH
c
NS (P=0.7660)
KC (ng/ml)
WT
Nlrp3−/−
Med.
ΔHbl
d
NS (P=0.9092)
Cxcl1 expression (fold induction, x10)
NS (P=0.3955)
Il1b expression (fold induction, x10)
NS (P=0.8326)
Tnf expression (fold induction)
e
WT
Nlrp3−/−
ASC
DAPI
Med.
B. cer.
ΔHbl
ASC speck (%)
****
f
MCC950
Casp-1
p20
GSDMD
p30
IL-1β (ng/ml)
IL-18 (ng/ml)
Cell death (% LDH release)
***
****
Med.
ΔHbl Sup.
ΔHbl Sup.+MCC950
ΔHbl
ΔHbl+MCC950
ATP
ATP+MCC950
g
NS (P=0.3480)
KC (ng/ml)
Med.
Sup.+Iso.
Sup.+α-HBL
Sup.+α-NHE
Sup.+α-Tox.
h
(P=0.5452)
(P=0.2839)
NS
NS
KC (ng/ml)
Med.
ΔHbl Sup.+Iso.
ΔHbl Sup.+α-NHE
ΔNhe Sup.+Iso.
ΔNhe Sup.+α-HBL

Figure 4.1 | Production of other pro-inflammatory cytokines is not affected by the absence of NLRP3. (**a**) Microscopy analysis of death of WT or *Nlrp3*$^{-/-}$ BMDMs left untreated (Med.) or assessed 3 hr or 8 hr after infection with WT (*B. cer.*, m.o.i. of 5) or Δ*hbl B. cereus* (Δ*hbl*, m.o.i. of 5) (**b**) Immunoblot analysis of phospho- IκB (pIκB), pIκB, phospho-ERK (pERK), ERK, NLRP3 and GAPDH of unprimed WT or *Nlrp3*$^{-/-}$ BMDMs 0-60 min after infection with Δ*hbl B. cereus* (m.o.i. of 2). (**c**) Release of KC in WT or *Nlrp3*$^{-/-}$ BMDMs left untreated or assessed 20 hr after infection with Δ*hbl B. cereus*. (**d**) RT-PCR analysis of the gene encoding KC (*Cxcl1*), IL-1β and TNF in WT or *Nlrp3*$^{-/-}$ BMDMs 3 hr after infection with Δ*hbl B. cereus*, relative to *Gapdh*. (**e**) Confocal microscopy analysis and quantification of ASC specks (red) in WT or *Nlrp3*$^{-/-}$ BMDMs left untreated or assessed 8 hr after infection as in (a). At least 200 BMDMs from each genotype were analysed. (**f**) Immunoblot analysis of caspase-1 and gasdermin D, release of IL-1β and IL-18, and death of BMDMs left untreated or LPS-primed and assessed 20 hr after treatment with the supernatant of Δ*hbl B. cereus* or 20 hr after infection with Δ*hbl B. cereus* (m.o.i. of 5) or 30 min after stimulation with ATP in absence or presence of MCC950 (20 μM). (**g**) Release of KC in WT BMDMs left untreated or LPS-primed and assessed 20 hr after treatment with the supernatant of WT *B. cereus* (Sup.) treated with an isotype control (Iso.), or with neutralising antibodies against HBL (α-HBL), NHE (α-NHE), or both (α-Tox.). (**h**) Release of KC in WT BMDMs left untreated or LPS-primed and assessed 20 hr after treatment with the supernatant of Δ*hbl* treated with an isotype control or α-NHE or assessed 20 hr after treatment with the supernatant of Δ*nhe B. cereus* (Δ*nhe* Sup.) treated with an isotype control or α-HBL. Scale bars, 25 μm (a), 12 μm (e). Arrowheads indicate dead cells (a) or inflammasome specks (e). Each symbol represents an independent experiment (c-h). NS, not statistically significant, ***$P < 0.001$ and ****$P < 0.0001$ [student's unpaired *t*-test (c, d, e, f, g and h)]. Data are representative of three independent experiments (a-h; mean and s.e.m. in c-h).

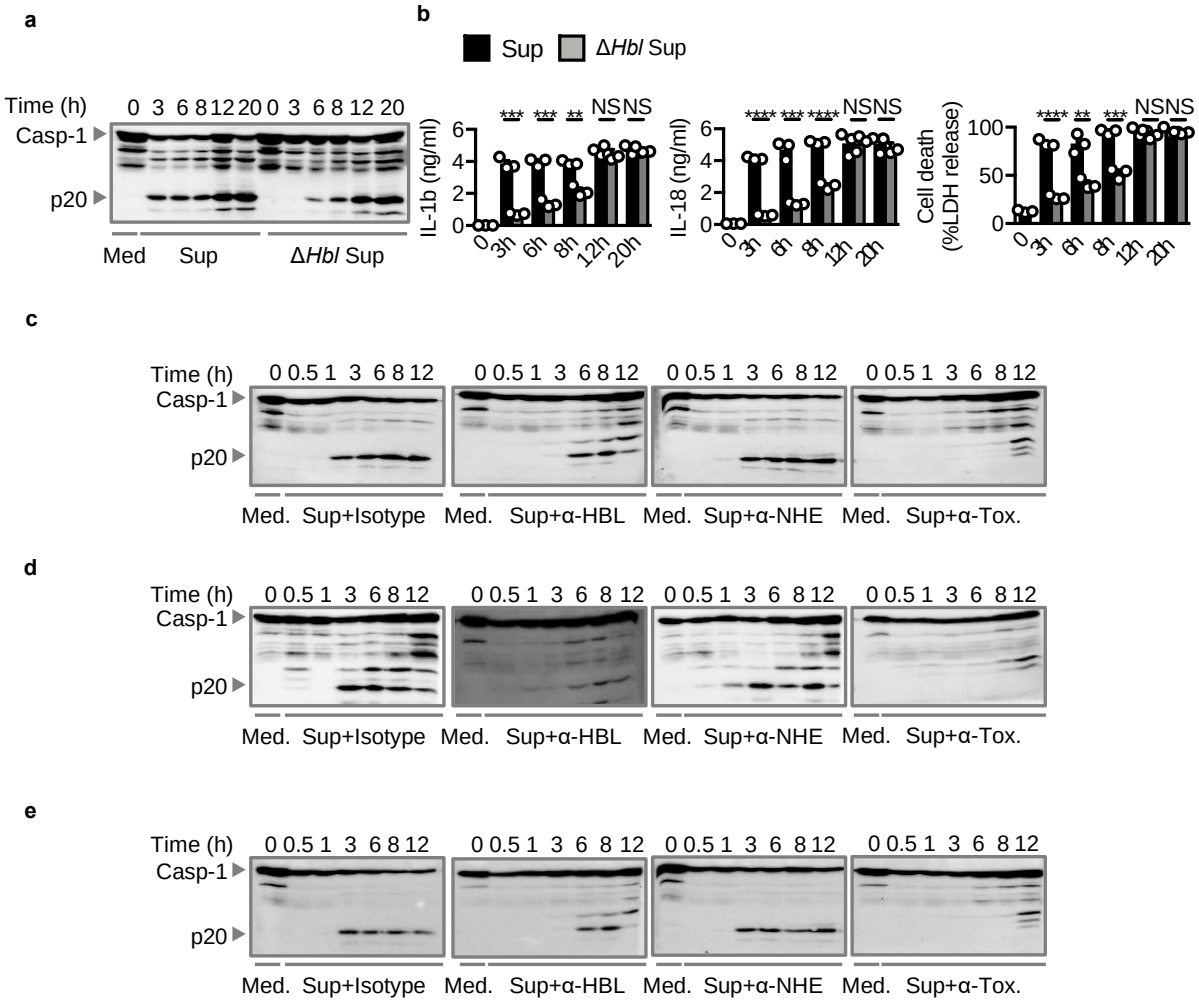
a
b
Sup
ΔHbl Sup
Time (h)
0 3 6 8 12 20 0 3 6 8 12 20
Casp-1
p20
Med
Sup
ΔHbl Sup
IL-1b (ng/ml)
IL-18 (ng/ml)
Cell death (%LDH release)
NS
0 3h 6h 8h 12h 20h
c
d
e
Time (h)
0 0.5 1 3 6 8 12
Casp-1
p20
Med. Sup+Isotype Med. Sup+α-HBL Med. Sup+α-NHE Med. Sup+α-Tox.

Figure 4.2 | Kinetics of inflammasome activation between HBL and NHE toxins. ((**a**) Immunoblot analysis of caspase-1 of BMDMs left untreated (Med.) or LPS-primed and assessed after treatment with the supernatant of WT and Δ*hbl B. cereus* (Δ*hbl* Sup.) which had been treated for indicated times in hours (h). (**b**) Release of IL-1β and IL-18, and cell death of BMDMs treated as in (a). (**c-e**) Immunoblot analysis of BMDMs left untreated (Med.) or LPS-primed and assessed for indicated times in hours (h) after treatment with the supernatant of *B. cereus* (Sup.) treated with an isotype control (Iso.), anti-HBL neutralising antibodies (α-HBL), anti-NHE neutralising antibodies (α-NHE) or with both anti-HBL and anti-NHE neutralising antibodies (α-Tox.). Supernatant was harvested from following *B. cereus* isolates: ATCC 14579 (**c**), ATCC 10876 (**d**), and F837/76 (**e**). Each symbol represents an independent experiment (b). NS, not statistically significant, $^{**}P < 0.01$, $^{***}P < 0.001$ and $^{****}P < 0.0001$ [Student's unpaired *t*-test (b)]. Data are representative three independent experiments (a-e; mean and s.e.m. in b).

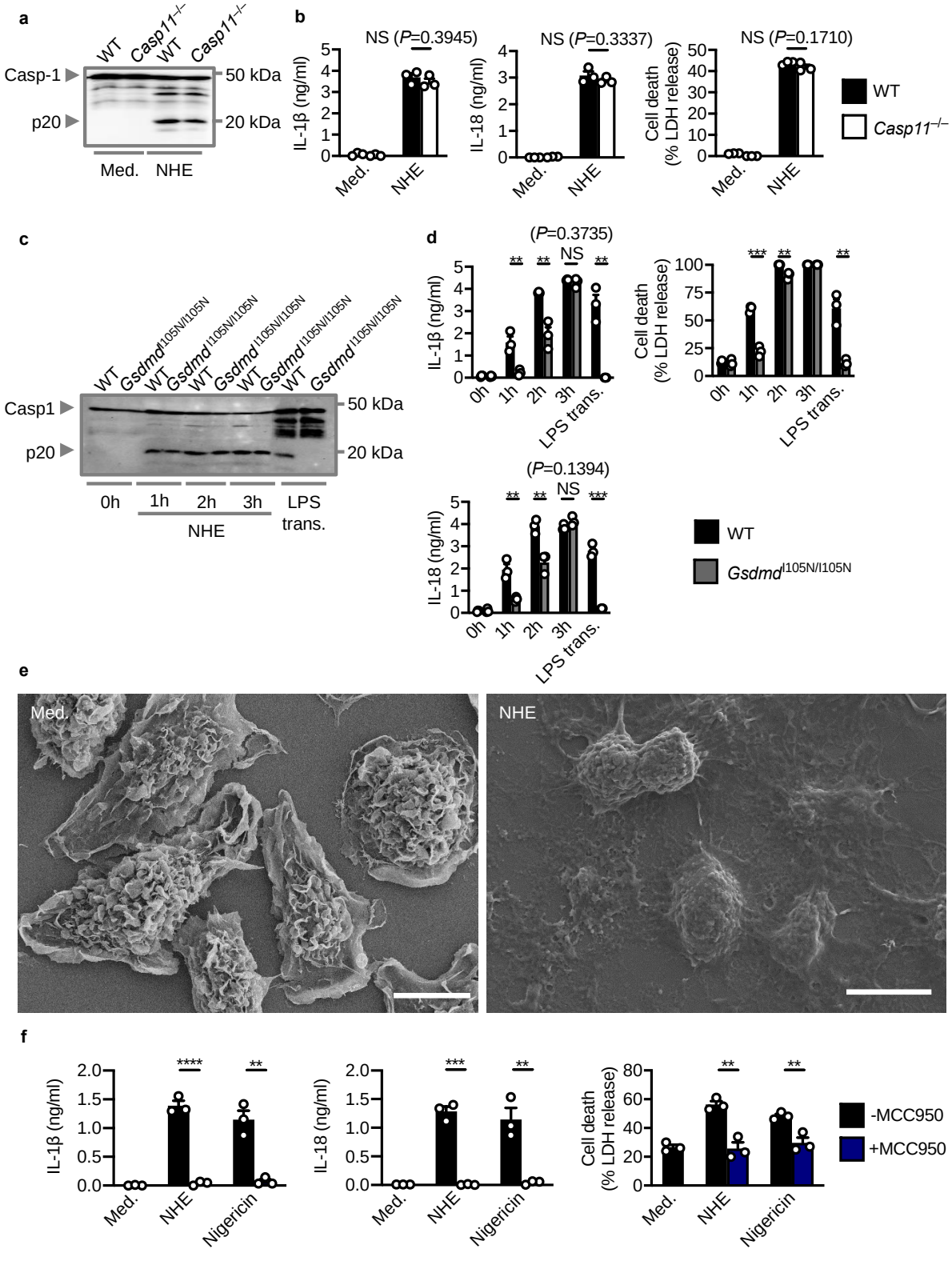
a
WT
Casp11−/−
WT
Casp11−/−
Casp-1
p20
50 kDa
20 kDa
Med.
NHE
b
NS (P=0.3945)
NS (P=0.3337)
NS (P=0.1710)
IL-1β (ng/ml)
IL-18 (ng/ml)
Cell death (% LDH release)
Med.
NHE
WT
Casp11−/−
c
WT
Gsdmd I105N/I105N
Casp1
p20
50 kDa
20 kDa
0h
1h
2h
3h
LPS trans.
NHE
d
(P=0.3735)
(P=0.1394)
NS
IL-1β (ng/ml)
IL-18 (ng/ml)
Cell death (% LDH release)
0h
1h
2h
3h
LPS trans.
WT
Gsdmd I105N/I105N
e
Med.
NHE
f
IL-1β (ng/ml)
IL-18 (ng/ml)
Cell death (% LDH release)
Med.
NHE
Nigericin
-MCC950
+MCC950

Figure 4.3 | NHE induces activation of the inflammasome in both mice and humans. (**a**) Immunoblot analysis of caspase-1 of WT and *Casp11*$^{-/-}$ BMDMs left untreated (Med.) or LPS-primed and assessed 3 hr after treatment with NHE; (**b**) Release of IL-1β and IL-18, and cell death of BMDMs as treated in (a). (**c**) Immunoblot analysis of caspase-1 of WT and *Gsdmd*$^{I105N/I105N}$ BMDMs left untreated or LPS-primed and assessed at either 1, 2 or 3 hr after treatment with NHE; (**d**) Release of IL-1β and IL-18, and cell death of BMDMs as treated in (c). (**e**) Overview of scanning electron microscopy analysis of WT BMDMs left untreated or LPS-primed and assessed 2 hr after stimulation with NHE. (**f**) Release of IL-1β and IL-18, and death of WT THP-1 cells left untreated and assessed 3 hr after treatment with NHE or Nigericin. Scale bars, 10 μm (**e**). Each symbol represents an independent experiment (b, d and f). NS, not statistically significant, $^{**}P < 0.01$ and $^{***}P < 0.001$, $^{****}P < 0.0001$ [student's unpaired *t*-test (b, d and f)]. Data are representative of three independent experiments (a-f; mean and s.e.m. in b, d and f).

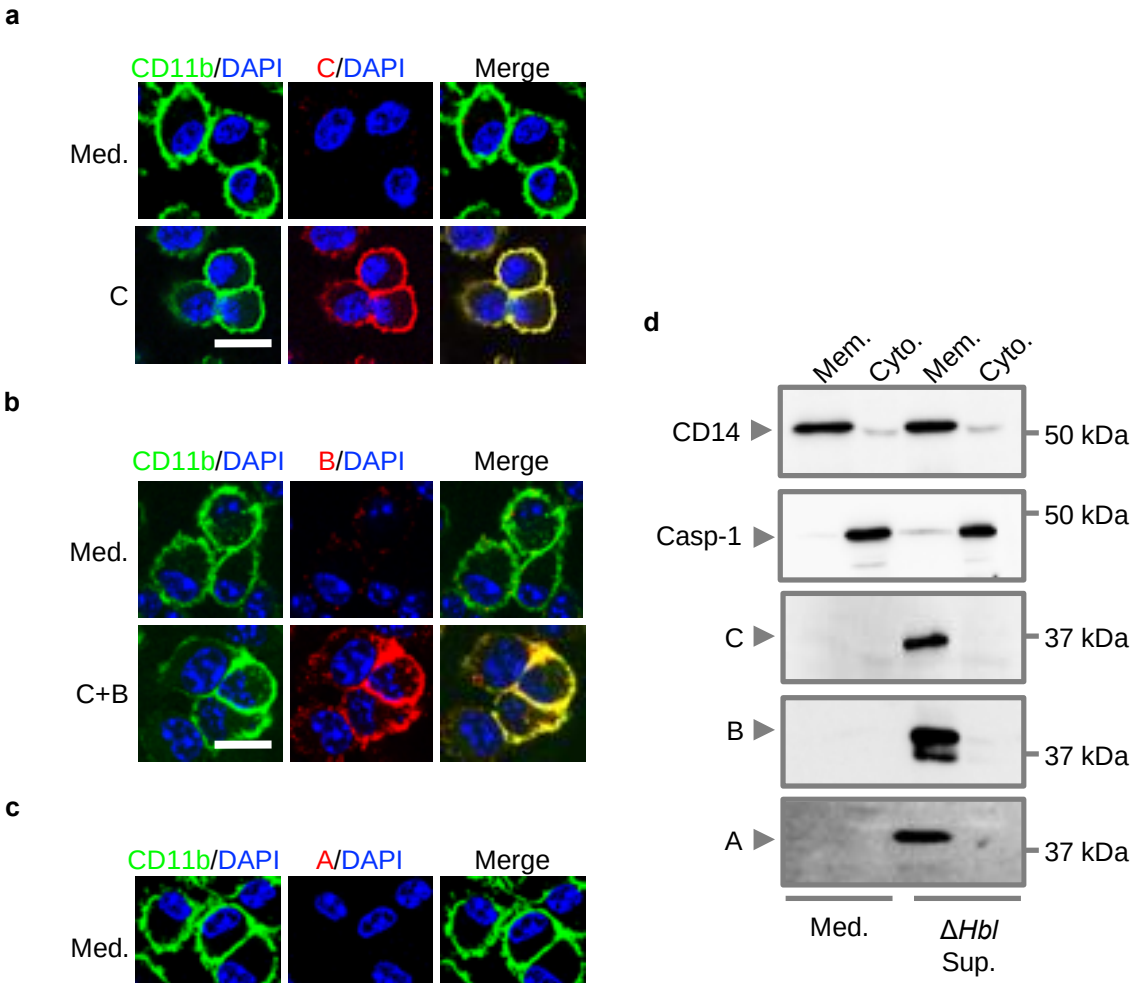
a
CD11b/DAPI
C/DAPI
Merge
Med.
C
b
CD11b/DAPI
B/DAPI
Merge
Med.
C+B
c
CD11b/DAPI
A/DAPI
Merge
Med.
C+B+A
d
Mem.
Cyto.
Mem.
Cyto.
CD14
50 kDa
Casp-1
50 kDa
C
37 kDa
B
37 kDa
A
37 kDa
Med.
ΔHbl
Sup.

Figure 4.4 | NHE co-localises with and is present in the membrane fraction of BMDMs. (**a**) Immunofluorescent analysis of CD11b (green) and NHE-C (red) in WT BMDMs left untreated (Med.) or LPS-primed and assessed 1 hr after treatment with NHE-C. (**b**) Immunofluorescent analysis of CD11b (green) and NHE-B (red) in WT BMDMs left untreated or LPS-primed and assessed 1 hr after treatment with NHE-C and NHE-B. (**c**) Immunofluorescent analysis of CD11b (green) and NHE-A (red) in WT BMDMs left untreated or LPS-primed and assessed 30 min after treatment with NHE-C NHE-B and NHE-A. (**d**) Immunoblot analysis of CD14, caspase-1, C, B and A of WT BMDMs left untreated or assessed 1 hr after treatment with the supernatant of Δ*hbl B. cereus*. Mem, membrane fraction; Cyto, cytosolic fraction. Scale bar, 12 μm (a-c). Data are representative of three independent experiments (a-d).

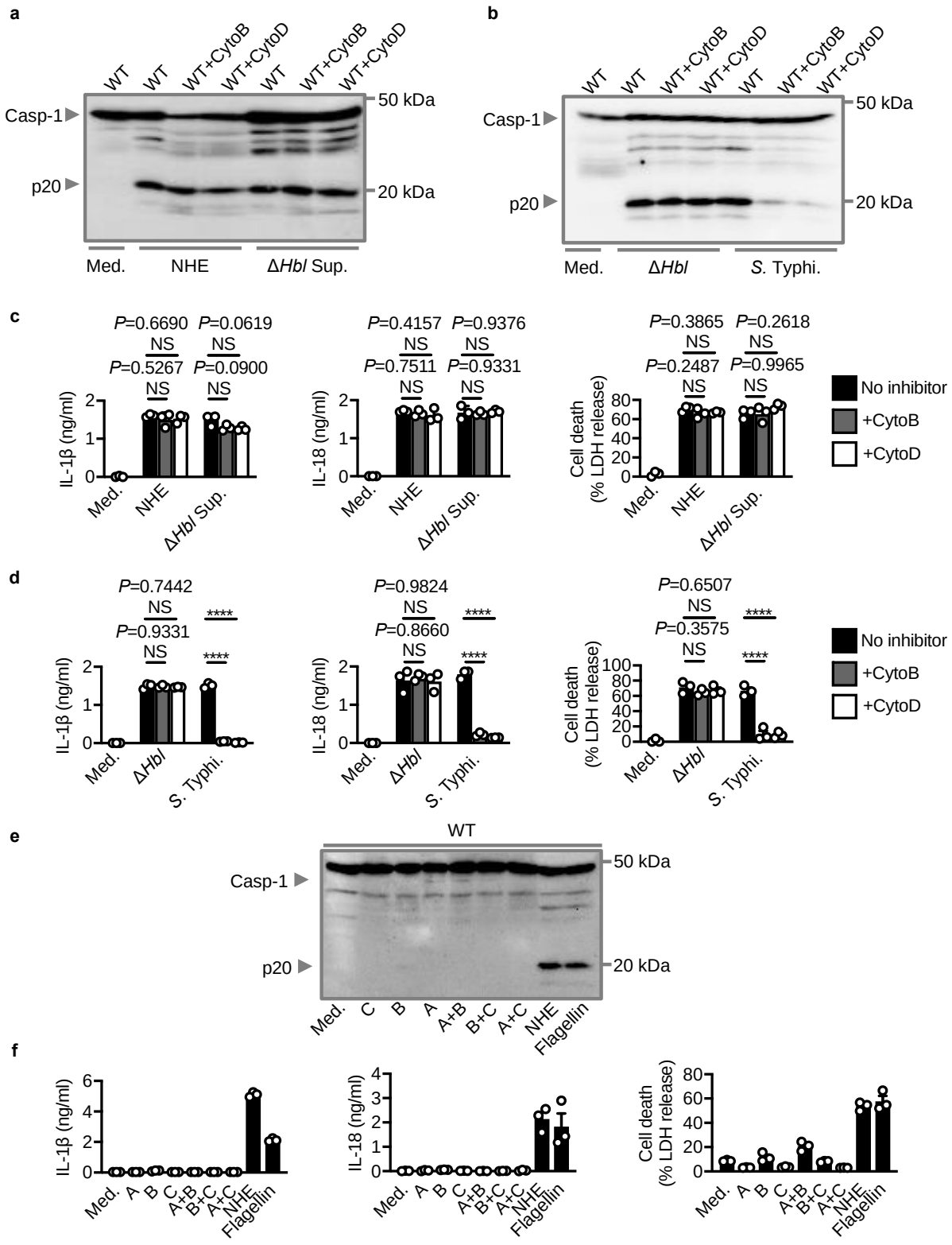
a
WT
WT
WT+CytoB
WT+CytoD
WT
WT+CytoB
WT+CytoD
Casp-1
p20
50 kDa
20 kDa
Med.
NHE
ΔHbl Sup.
b
WT
WT
WT+CytoB
WT+CytoD
WT
WT+CytoB
WT+CytoD
Casp-1
p20
50 kDa
20 kDa
Med.
ΔHbl
S. Typhi.
c
P=0.6690
P=0.0619
NS
NS
P=0.5267
P=0.0900
NS
NS
IL-1β (ng/ml)
Med.
NHE
ΔHbl Sup.
P=0.4157
P=0.9376
NS
NS
P=0.7511
P=0.9331
NS
NS
IL-18 (ng/ml)
Med.
NHE
ΔHbl Sup.
P=0.3865
P=0.2618
NS
NS
P=0.2487
P=0.9965
NS
NS
Cell death (% LDH release)
Med.
NHE
ΔHbl Sup.
No inhibitor
+CytoB
+CytoD
d
P=0.7442
NS
****
P=0.9331
NS
****
IL-1β (ng/ml)
Med.
ΔHbl
S. Typhi.
P=0.9824
NS
****
P=0.8660
NS
****
IL-18 (ng/ml)
Med.
ΔHbl
S. Typhi.
P=0.6507
NS
****
P=0.3575
NS
****
Cell death (% LDH release)
Med.
ΔHbl
S. Typhi.
No inhibitor
+CytoB
+CytoD
e
WT
Casp-1
p20
50 kDa
20 kDa
Med.
C
B
A
A+B
B+C
A+C
NHE
Flagellin
f
IL-1β (ng/ml)
IL-18 (ng/ml)
Cell death (% LDH release)
Med.
A
B
C
A+B
B+C
A+C
NHE
Flagellin

Figure 4.5 | Cytosolic entry of NHE is not required for inflammasome activation. (**a**) Immunoblot analysis of caspase-1 of WT BMDMs left untreated or LPS-primed and assessed 3 hr after treatment with NHE or the supernatant of Δ*hbl B. cereus*, in the absence or presence of cytochalasin B (CytoB; 50 μM) or cytochalasin D (CytoD; 50 μM). (**b**) Immunoblot analysis of caspase-1 of WT BMDMs left untreated or assessed 20 hr after infection with Δ*hbl B. cereus* (m.o.i. of 5) or *S.* Typhimurium (m.o.i. of 2), in the absence or presence of cytochalasin B (CytoB; 50 μM) or cytochalasin D (CytoD; 50 μM). **(c)** Release of IL-1β and IL-18, and cell death of BMDMs as treated in (a). (**d**) Release of IL-1β and IL-18, and cell death of BMDMs as treated in (b). (**e**) Immunoblot analysis of caspase-1 of WT BMDMs left untreated or LPS-primed and assessed 3 hr after transfection with one or two components of NHE or after stimulation with NHE or 5 hr after transfection with flagellin of *S*. Typhimurium. (**f**) Release of IL-1β and IL-18, and cell death of BMDMs as treated in (e). Each symbol represents an independent experiment (c, d and f). NS, not statistically significant. ****$P < 0.0001$ [one-way analysis of variance [ANOVA] with Dunnett's multiple-comparisons test (c and d)]. Data are representative of three independent experiments (a-f; mean and s.e.m. in c, d and f).

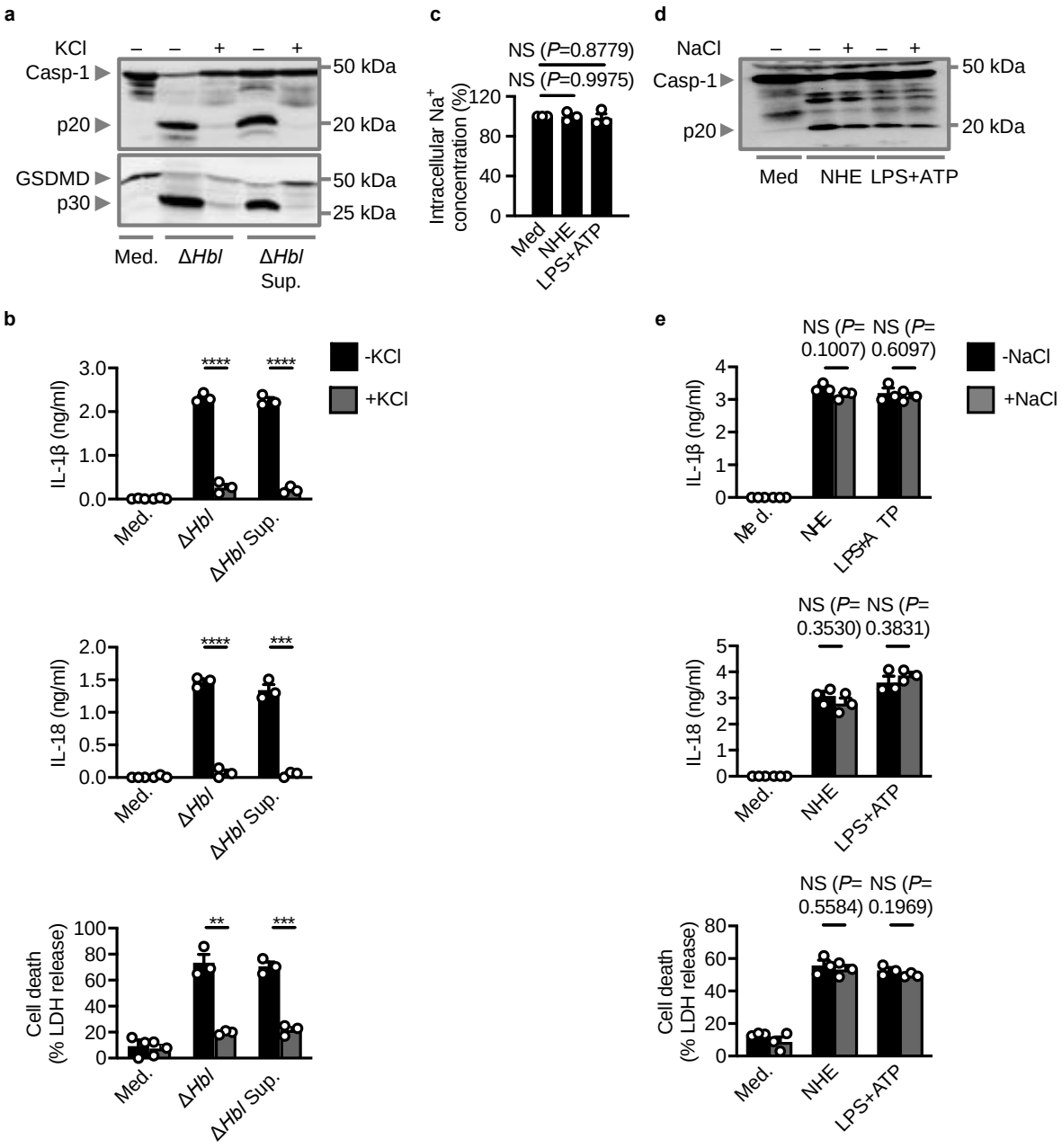
a
KCl – – + – +
Casp-1
p20
GSDMD
p30
50 kDa
20 kDa
50 kDa
25 kDa
Med. ΔHbl ΔHbl Sup.
c
NS (P=0.8779)
NS (P=0.9975)
Intracellular Na+ concentration (%)
Med
NHE
LPS+ATP
d
NaCl – – + – +
Casp-1
p20
50 kDa
20 kDa
Med NHE LPS+ATP
b
-KCl
+KCl
IL-1β (ng/ml)
IL-18 (ng/ml)
Cell death (% LDH release)
Med. ΔHbl ΔHbl Sup.
e
NS (P= 0.1007)
NS (P= 0.6097)
-NaCl
+NaCl
NS (P= 0.3530)
NS (P= 0.3831)
NS (P= 0.5584)
NS (P= 0.1969)
Med. NHE LPS+ATP

Figure 4.6 | Na^+ flux is not required for NLRP3 inflammasome activation. (**a**) Immunoblot analysis of caspase-1 and gasdermin D of WT BMDMs left untreated (Med.) or LPS-primed and assessed 20 hr after infection with Δ*hbl B. cereus* (m.o.i. of 5) or the supernatant of Δ*hbl B. cereus* in the absence (-) or presence (+; 50 mM) of extracellular KCl; (**b**) Release of IL-1β and IL-18, and death of WT BMDMs as in (a). (**c**) Inductively coupled plasma-optical emission spectrometry analysis of intracellular concentrations of Na^+ of BMDMs left untreated or assessed 2 hr after treatment with NHE or 30 mins after treatment with LPS+ATP. (**d**) Immunoblot analysis of caspase-1 of WT BMDMs left untreated or LPS-primed and assessed 2 hr after treatment with NHE or 30 mins after treatment with LPS+ATP in the absence (-) or presence (+; 50 mM) of extracellular NaCl; (**e**) Release of IL-1β and IL-18, and death of WT BMDMs as in (d). Each symbol represents an independent experiment (b, c and e). NS, not statistically significant. $^{**}P < 0.01$ and $^{***}P < 0.001$, $^{****}P < 0.0001$ [student's unpaired *t*-test (b and e) or one-way analysis of variance [ANOVA] with Dunnett's multiple-comparisons test (c)]. Data are representative of three independent experiments (a-e; mean and s.e.m. in b, c and e).

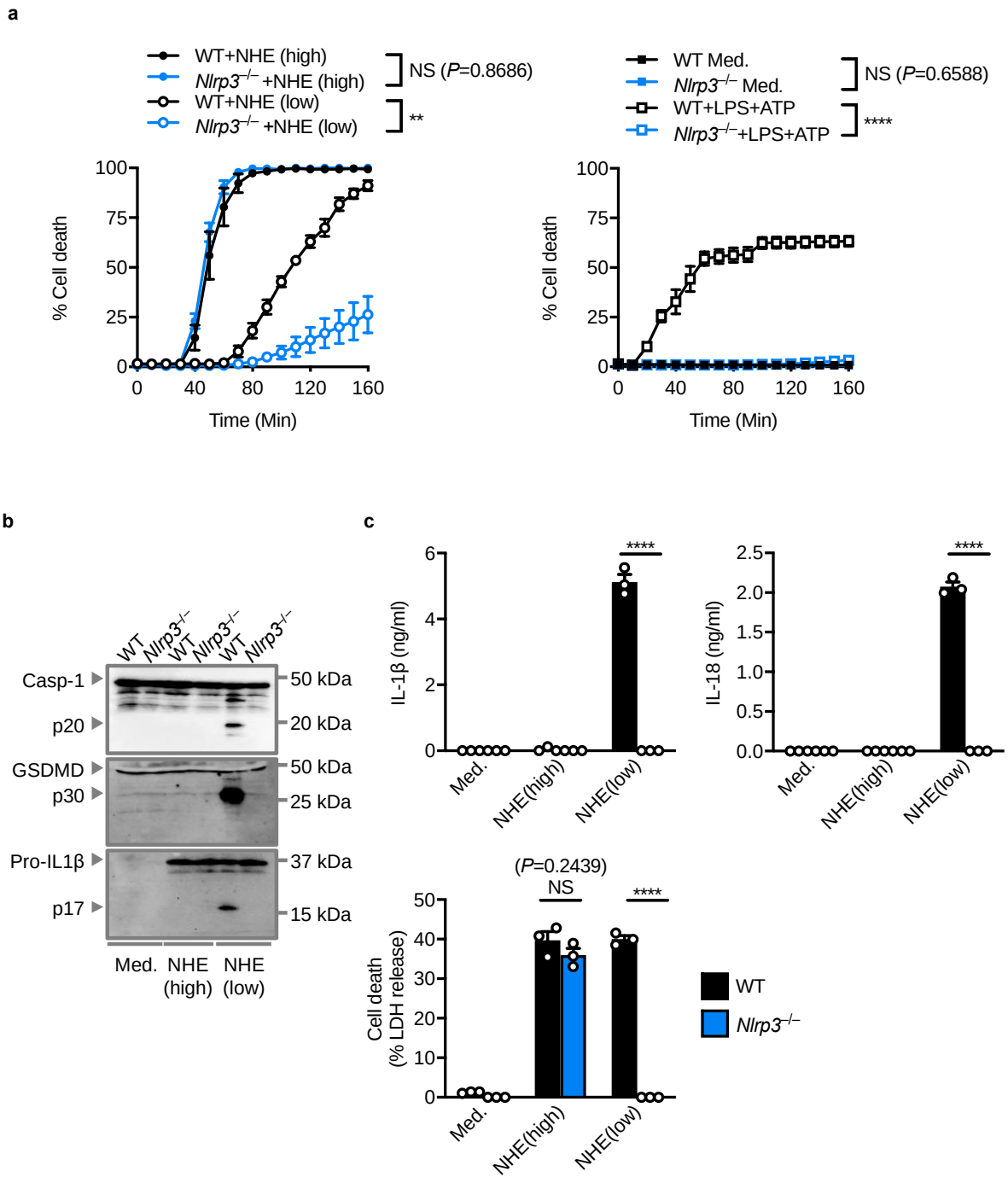
a
WT+NHE (high)
Nlrp3−/− +NHE (high)
WT+NHE (low)
Nlrp3−/− +NHE (low)
NS (P=0.8686)
**
% Cell death
Time (Min)
WT Med.
Nlrp3−/− Med.
WT+LPS+ATP
Nlrp3−/−+LPS+ATP
NS (P=0.6588)
****
b
WT
Nlrp3−/−
Casp-1
p20
GSDMD
p30
Pro-IL1β
p17
50 kDa
20 kDa
25 kDa
37 kDa
15 kDa
Med.
NHE (high)
NHE (low)
c
IL-1β (ng/ml)
IL-18 (ng/ml)
Cell death (% LDH release)
(P=0.2439)
NS
WT
Nlrp3−/−

Figure 4.7 | Bioavailability of NHE dictates cell death and activation of the NLRP3 inflammasome. (**a**) The viability of WT or *Nlrp3*$^{-/-}$ BMDMs left untreated (Med.) or after stimulation with 0.5 μM NHE (high) or 100 nM NHE (low) or with LPS+ATP, as determined by the IncuCyte live-imaging system. (**b**) Immunoblot analysis of caspase-1 (top), gasdermin D (middle) and IL-1β (bottom) of WT or *Nlrp3*$^{-/-}$ BMDMs left untreated or LPS-primed and assessed 3 hr after stimulation with 0.5 μM NHE or 100 nM NHE. (**c**) Release of IL- 1β and IL-18, and death of WT BMDMs after treatment as in (b). Each symbol represents an independent experiment (c). NS, not statistically significant. $^{**}P < 0.01$ and $^{****}P < 0.0001$ [Student's unpaired *t*-test (a and c)]. Data are representative of three independent experiments (a-c; mean and s.e.m. in a and c).

a

Protein NHE-C sequence

MQKRFYKKCLLTLMI AGVATSNAFPLHTFAAEQNVKIQQENANDYSLGPAGFQDVMAQTTSSIFAMDSYAKLIQN
QQETDLSKISSINGELKGNMIQHQRDAKMNAAYWLNSMKPQIMKTDQNIINYNNTFQSYYNDMLIAIDQKDSGKL
KADLEKLYADIVKNQNEVDGLLGNLKAFRDRMAKDTNSFKEDTNQLTAILASTNAGIPALEQQINTYNDSIKKSN
DM**VIAGGVLCVALITCLAGGPMIAV**AKKDIANAEREIANLKDRISGAQAEVAILTDVKNKTTNMTETIDAAITAL
QNISNQWYTVGAKYNNLLQNVKGITPEEFTFIKEDLHTAKDSWKDVKDYTEKLHEGVAK

b

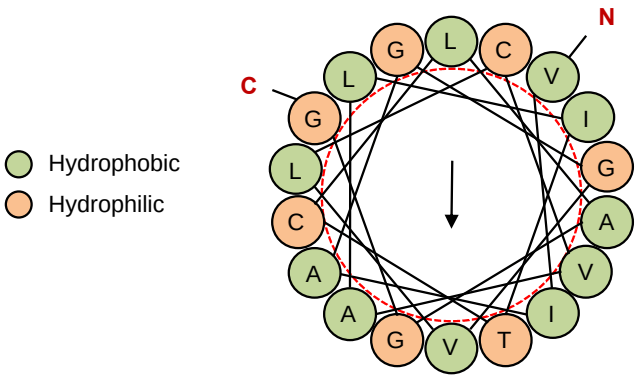

c

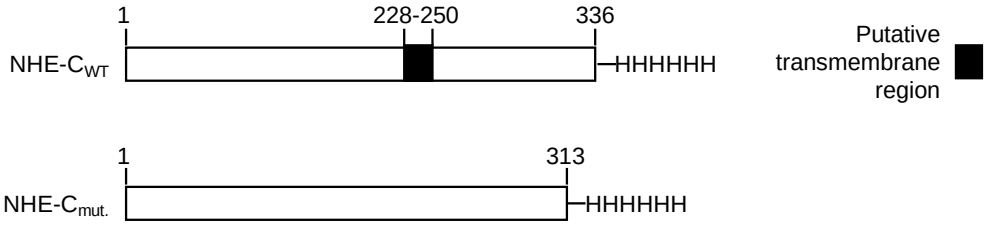

Protein NHE-C$_{mut.}$ sequence

MAEQNVKIQQENANDYSLGPAGFQDVMAQTTSSIFAMDSYAKLIQNQQETDLSKISSINGELKGNMIQHQRDAKM
NAAYWLNSMKPQIMKTDQNIINYNNTFQSYYNDMLIAIDQKDSGKLKADLEKLYADIVKNQNEVDGLLGNLKAFR
DRMAKDTNSFKEDTNQLTAILASTNAGIPALEQQINTYNDSIKKSNDMAKKDIANAEREIANLKDRISGAQAEVA
ILTDVKNKTTNMTETIDAAITALQNISNQWYTVGAKYNNLLQNVKGITPEEFTFIKEDLHTAKDSWKDVKDYTEK
LHEGVAK

Figure 4.8 | The putative transmembrane region of NHE. (**a**) Full-length amino acid sequence of NHE-C highlighting the putative signal-peptide sequence (blue) and putative transmembrane region (red) based on bioinformatic-assisted analysis using the Membrane Protein Explorer (MPEx) Application. (**b**) A standard helical wheel diagram showing the distribution of hydrophobic versus hydrophilic residues in the putative transmembrane region of the NHE-C drawn using the HELIQUEST server. Arrow in the helical wheel represents the direction of the hydrophobic moment. (**c**) Schematic of the sequences of NHE-C_{WT} and NHE-$C_{mut.}$ (top). Amino acid sequence of NHE-$C_{mut.}$ (bottom).

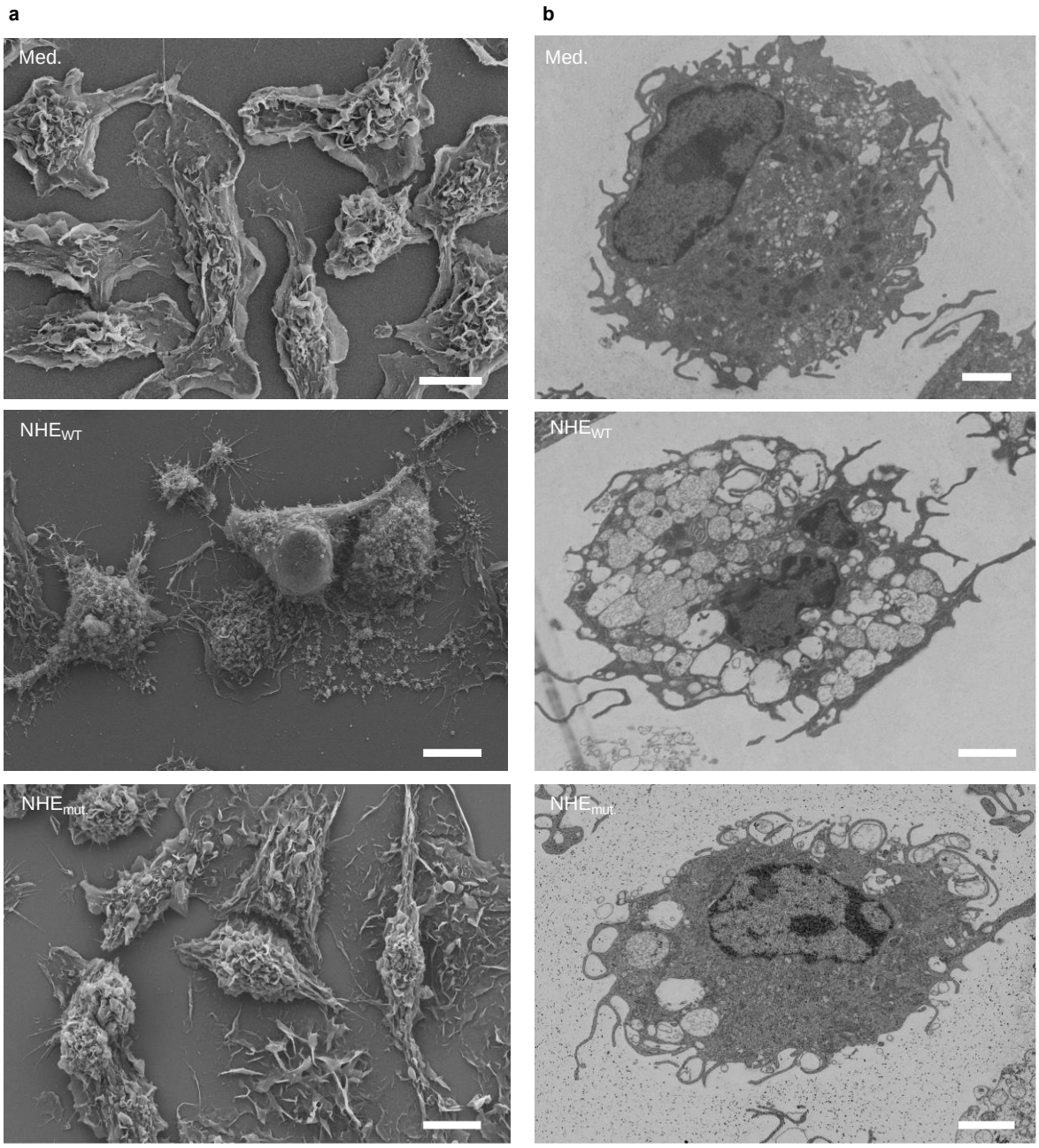

Figure 4.9 | The putative transmembrane region of NHE facilitates the induction of cell death. (**a**) Overview of scanning electron microscopy analysis of WT BMDMs left untreated (Med., top left) or LPS-primed and assessed 2 hr after stimulation with NHE_{WT} (middle left) and $NHE_{mut.}$ (bottom left). (**b**) Transmission electron microscopy analysis of WT BMDMs left untreated (top right) or LPS-primed and assessed 2 hr after stimulation with NHE_{WT} (middle right) and $NHE_{mut.}$ (bottom right). Scale bar, 10 µm (a), 2 µm (b). Data are representative of three independent experiments (a, b).

a

Protein HBL-B sequence

MGSEIEQTNNEDTALSANEVRMKETLQKAGLFAKSMNAYSYMLIKNPDVNFEGITINGYVDLPGRIVQDQKNARA
HAVTWDTKVKKQLLDTLNGIVEYDTTFDNYYETMIEAINTGDGETLKEGITDLRGEIQQNQKYAQQLIEELTKLR
DSIGHDVRAFGSNKELLQSILKNQGADVDADQKRLEEVLGSVNYYKQLESDG **FNVMKGAILGLPIIGGIIVGVA** R
DNLGKLEPLLAELRQTVDYKVTLNRVVGVAYSNINEMHKALDDAINALTYMSTQWHDLDSQYSGVLGHIENAAQK
ADQNKFKFLKPNLNAAKDSWKTLRTDAVTLKEGIKELKVETVTPQK

Protein HBL-$B_{mut.}$ sequence

MGSEIEQTNNEDTALSANEVRMKETLQKAGLFAKSMNAYSYMLIKNPDVNFEGITINGYVDLPGRIVQDQKNARA
HAVTWDTKVKKQLLDTLNGIVEYDTTFDNYYETMIEAINTGDGETLKEGITDLRGEIQQNQKYAQQLIEELTKLR
DSIGHDVRAFGSNKELLQSILKNQGADVDADQKRLEEVLGSVNYYKQLESDGGVARDNLGKLEPLLAELRQTVDY
KVTLNRVVGVAYSNINEMHKALDDAINALTYMSTQWHDLDSQYSGVLGHIENAAQKADQNKFKFLKPNLNAAKDS
WKTLRTDAVTLKEGIKELKVETVTPQK

b

c

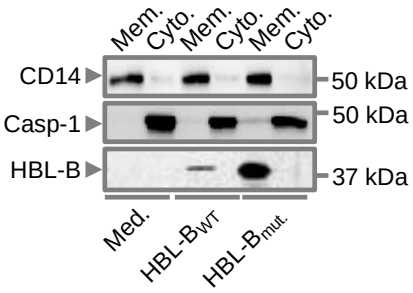

d

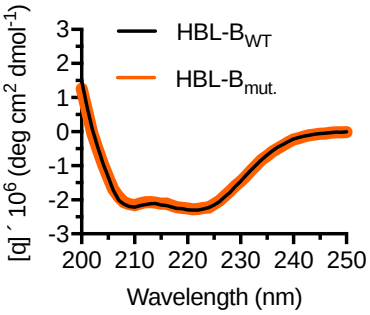

Figure 4.10 | The putative transmembrane region in HBL-B is not required for membrane binding. (**a**) Full-length amino acid sequences of HBL-B (top) and HBL-B_{mut} (below), highlighting the putative transmembrane region (red) based on bioinformatic-assisted analysis using the Membrane Protein Explorer (MPEx) Application. (**b**) Schematic of the sequences of HBL-B_{WT} and HBL-B_{mut}. (**c**) Immunoblot analysis of CD14, caspase-1, and HBL-B of WT BMDMs left untreated (Med.) or assessed 1 hr after treatment with HBL-B_{WT} or HBL-B_{mut}. Mem, membrane fraction; Cyto, cytosolic fraction. (**d**) Circular dichroism analysis of the secondary structures of HBL-B_{WT} or HBL-B_{mut}. Data are representative of three independent experiments (c) and one independent experiment (d).

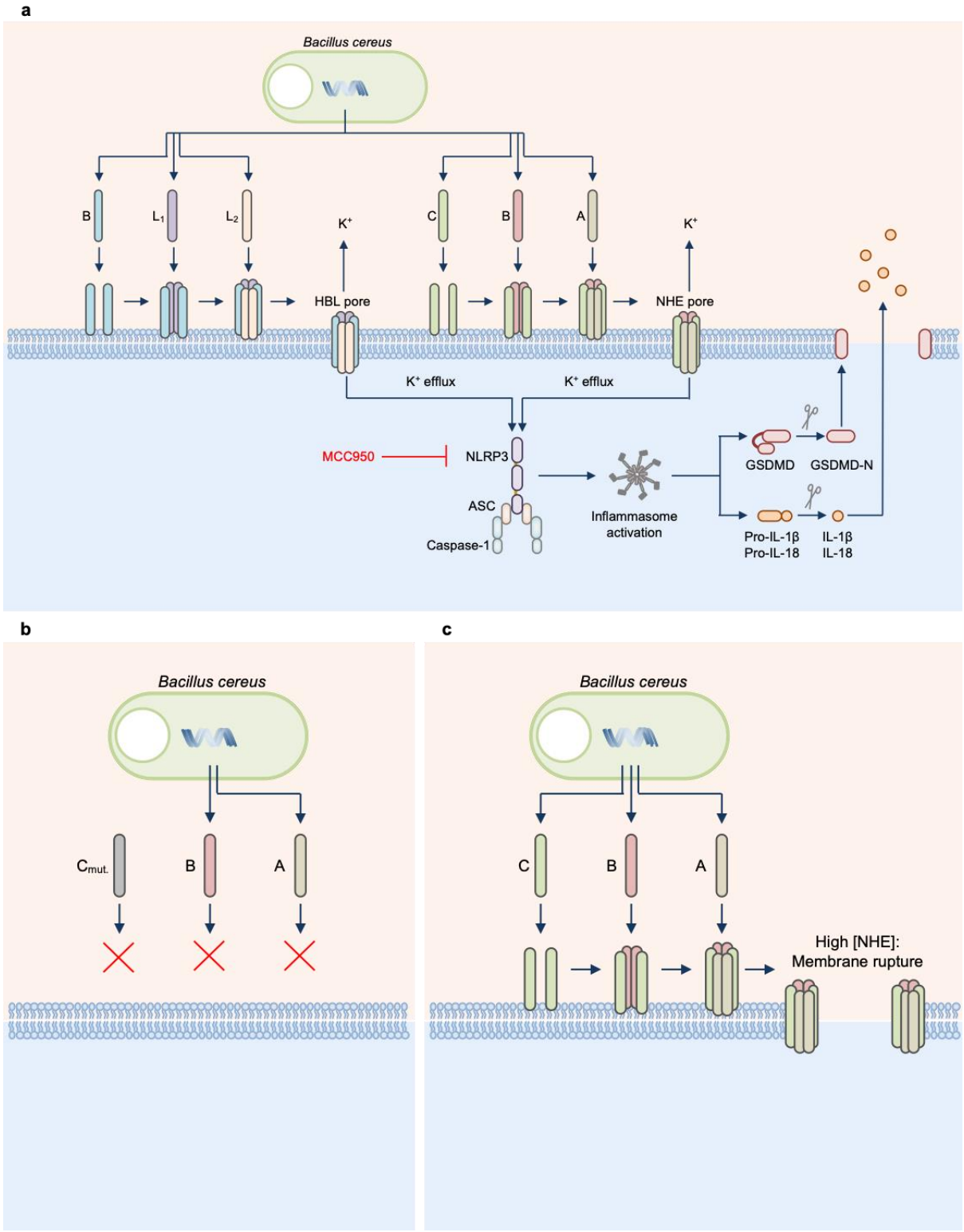
a
Bacillus cereus
B
L1
L2
K+
HBL pore
C
B
A
K+
NHE pore
K+ efflux
K+ efflux
MCC950
NLRP3
ASC
Caspase-1
Inflammasome activation
GSDMD
GSDMD-N
Pro-IL-1β
Pro-IL-18
IL-1β
IL-18
b
Bacillus cereus
Cmut
B
A
c
Bacillus cereus
C
B
A
High [NHE]:
Membrane rupture

Figure 4.11 | Model of *B. cereus*-induced activation of the NLRP3 inflammasome. (**a**) Model depicting the conserved mechanism of action of HBL and NHE exploited for sensing by the NLRP3 inflammasome. (**b**) Model showing the necessity of the putative transmembrane domain in NHE-C for driving assembly of the tripartite NHE toxin to the plasma membrane of BMDMs. (**c**) Model depicting cellular lysis and membrane rupture of BMDMs after treatment with high concentrations of NHE.

Appendices of Chapter 5: Phospholipase C of *Clostridium perfringens* disrupts lysosomal integrity and activates the NLRP3 inflammasome and pyroptosis

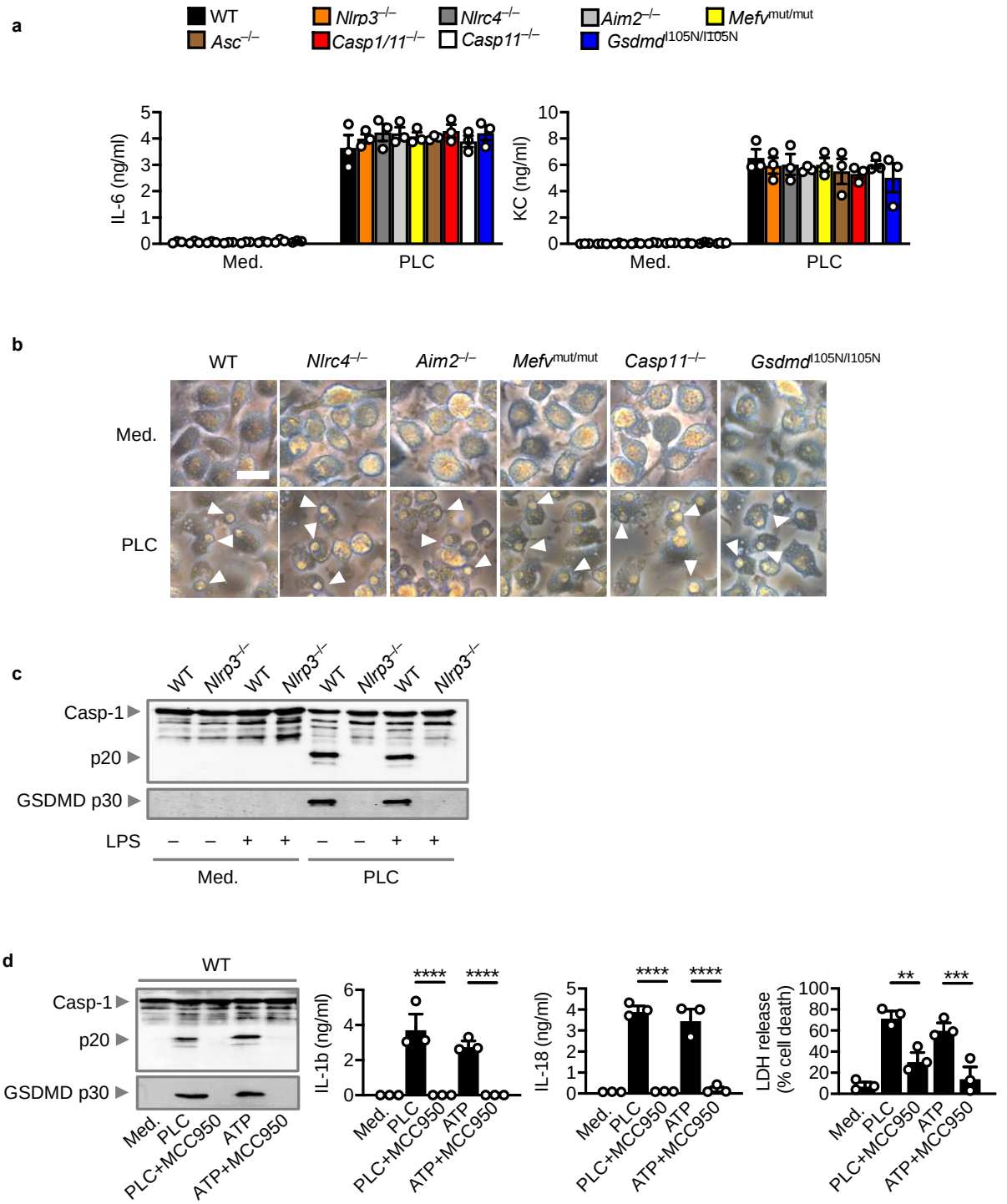
a
WT
Asc−/−
Nlrp3−/−
Casp1/11−/−
Nlrc4−/−
Casp11−/−
Aim2−/−
Gsdmdl105N/l105N
Mefvmut/mut
IL-6 (ng/ml)
KC (ng/ml)
Med.
PLC
b
WT
Nlrc4−/−
Aim2−/−
Mefvmut/mut
Casp11−/−
Gsdmdl105N/l105N
Med.
PLC
c
WT
Nlrp3−/−
Casp-1
p20
GSDMD p30
LPS
Med.
PLC
d
WT
Casp-1
p20
GSDMD p30
Med.
PLC
PLC+MCC950
ATP
ATP+MCC950
IL-1b (ng/ml)
IL-18 (ng/ml)
LDH release (% cell death)
****
**
***

Figure 5.1 | PLC-induced activation of the NLRP3 inflammasome in BMDMs is inhibited by MCC950. (**a**) Release of IL-6 and KC of BMDMs left untreated (Med.) or LPS-primed and assessed 3 hr after stimulation with PLC. (**b**) Microscopy analysis of death of BMDMs after treatment as in (a). (**c**) Immunoblot analysis of caspase-1 of WT or *Nlrp3*$^{-/-}$ BMDMs left untreated or LPS-primed and assessed 3 hr after stimulation with PLC. (**d**) Immunoblot analysis of caspase-1 and gasdermin D, release of IL-1β and IL-18, and death of WT BMDMs left untreated or LPS-primed and assessed 3 hr after stimulation with PLC or 30 min after stimulation with ATP in absence or presence of MCC950 (20 μM). Scale bars, 25 μm (b). Arrowheads indicate dead cells (b). Each symbol represents an independent experiment (a, c and d). NS, not statistically significant, $^{**}P < 0.01$, $^{***}P < 0.001$ and $^{****}P < 0.0001$ [two-tailed t test (c and d)]. Data are representative of three independent experiments (a-h; mean and s.e.m. in a, c and d).

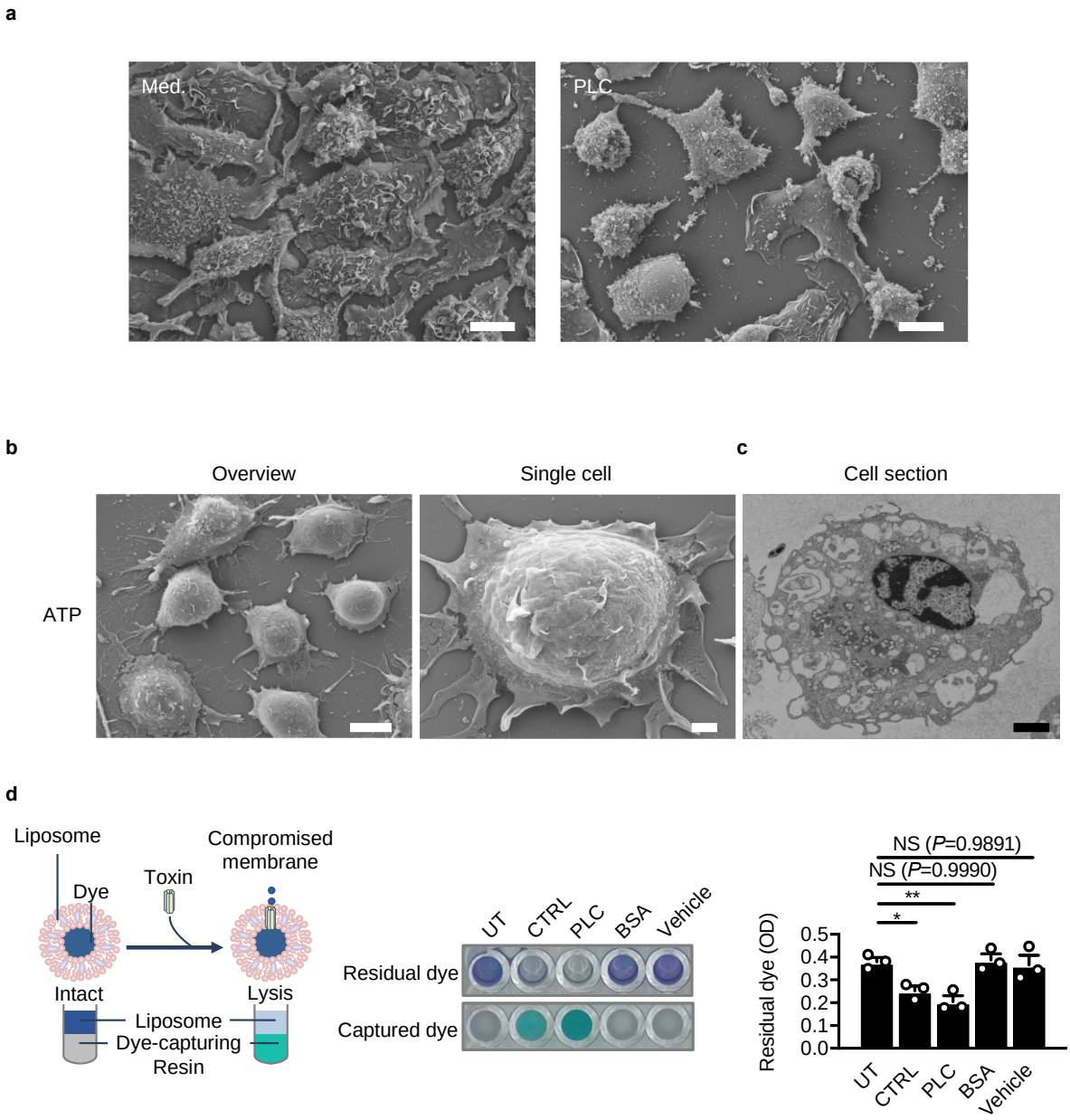

Figure 5.2 | PLC induces cell death in BMDMs. (**a**) Scanning electron microscopy analysis of WT BMDMs left untreated or LPS-primed and assessed 3 hr after treatment with PLC. (**b**) Scanning electron microscopy analysis of WT BMDMs left untreated or LPS-primed and assessed 30 min after treatment with ATP. (**c**) Transmission electron microscopy analysis of BMDMs after treatment as in (b). (**d**) Colorimetric analysis of liposomes left untreated (UT), sonicated for 5 min at 100 amplitude (CTRL), or assessed 5 min after stimulation with PLC, BSA or vehicle buffer. The absorbance (OD) of residual dye was measured at 595 nm. Scale bars: 10 μm (a) and (b, overview); 2 μm (b, single cell) and (c). Each symbol represents an

independent experiment (d). NS, not statistically significant, *P < 0.05, **P < 0.01 (one-way analysis of variance [ANOVA] with Dunnett's multiple-comparisons test [d]). Data are representative of one experiment (a-c) and three independent experiments (d; mean and s.e.m. in d).

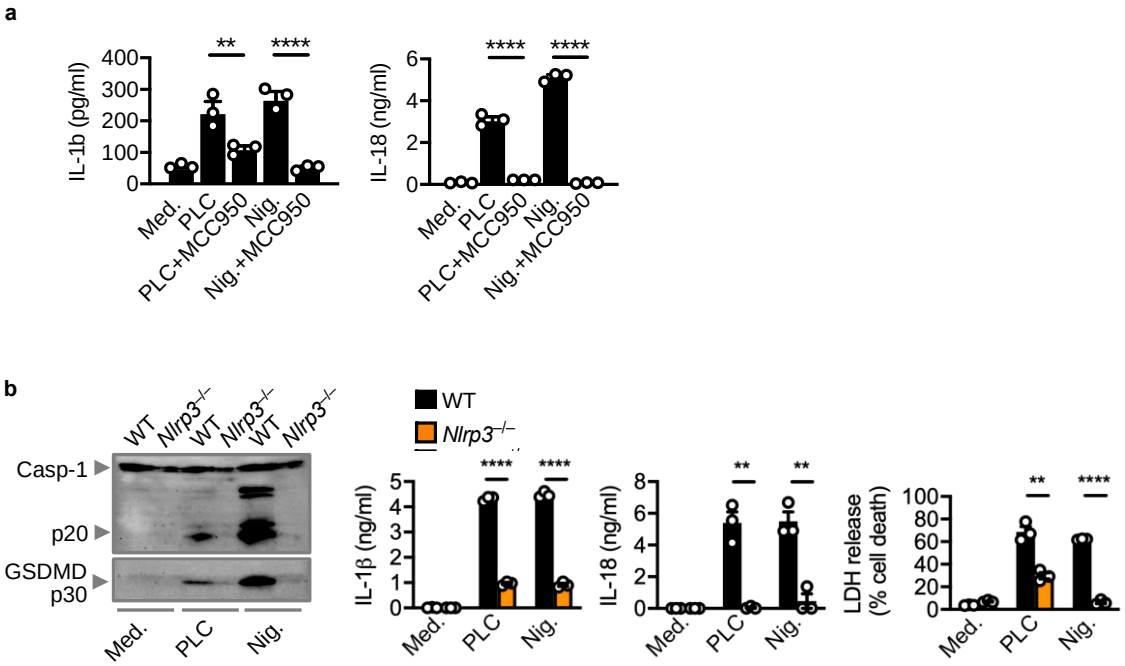

Figure 5.3 | PLC induces activation of the NLRP3 inflammasome in human monocytes and macrophages. (**a**) Release of IL-1β and IL-18 of WT THP-1 monocytes cells left 1untreated and assessed 3 hr after treatment with PLC or nigericin (Nig.) in absence or presence of MCC950 (20 μM). (**b**) Immunoblot analysis of caspase-1 and gasdermin D, release of IL-1β and IL-18, and death of WT or *Nlrp3*$^{-/-}$ THP1 macrophages left untreated or LPS-primed and assessed 3 hr after stimulation with PLC or 30 min after stimulation with ATP in absence or presence of MCC950 (20 μM).

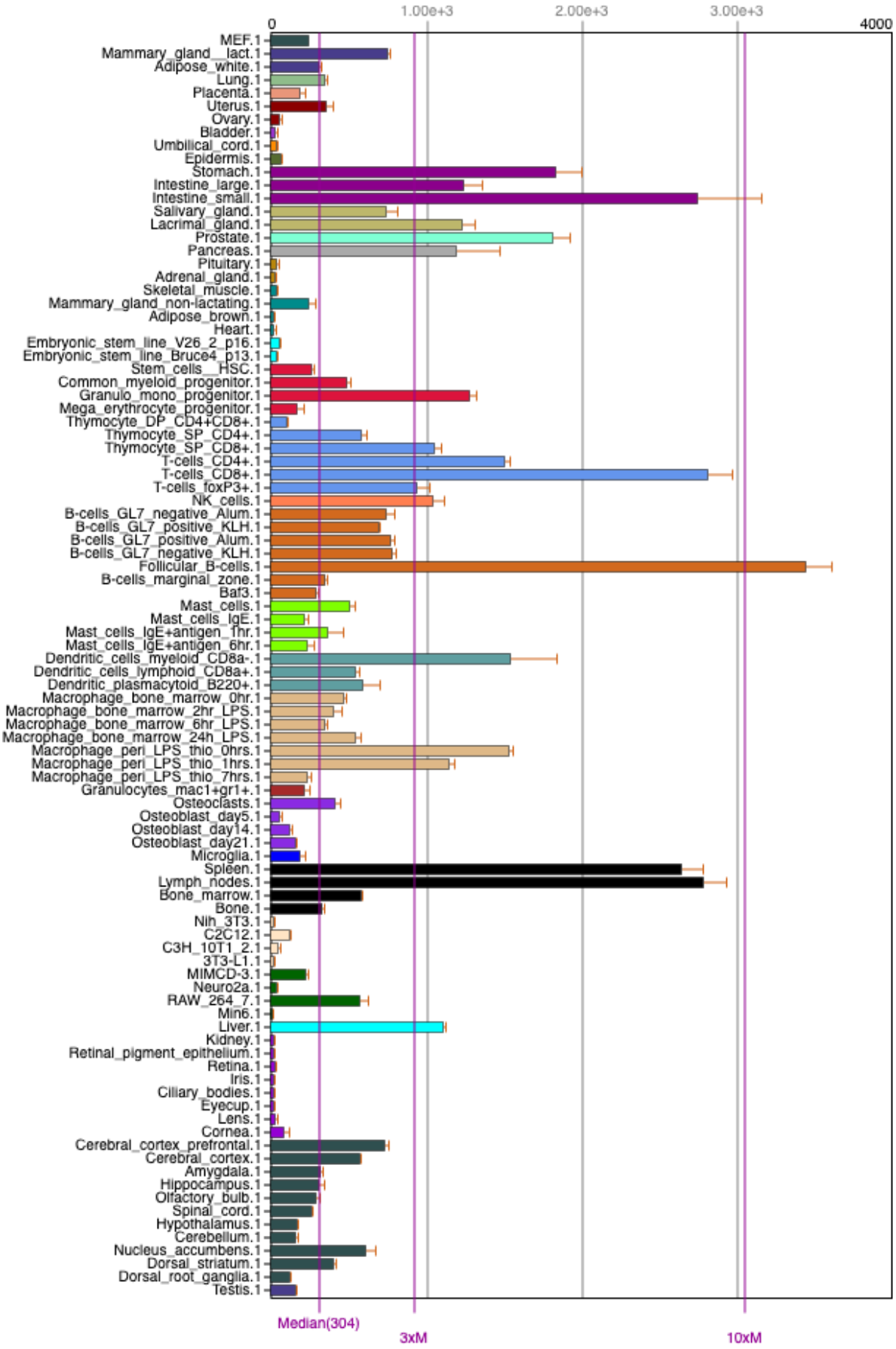
0
1.00e+3
2.00e+3
3.00e+3
4000
MEF.1
Mammary_gland__lact.1
Adipose_white.1
Lung.1
Placenta.1
Uterus.1
Ovary.1
Bladder.1
Umbilical_cord.1
Epidermis.1
Stomach.1
Intestine_large.1
Intestine_small.1
Salivary_gland.1
Lacrimal_gland.1
Prostate.1
Pancreas.1
Pituitary.1
Adrenal_gland.1
Skeletal_muscle.1
Mammary_gland_non-lactating.1
Adipose_brown.1
Heart.1
Embryonic_stem_line_V26_2_p16.1
Embryonic_stem_line_Bruce4_p13.1
Stem_cells__HSC.1
Common_myeloid_progenitor.1
Granulo_mono_progenitor.1
Mega_erythrocyte_progenitor.1
Thymocyte_DP_CD4+CD8+.1
Thymocyte_SP_CD4+.1
Thymocyte_SP_CD8+.1
T-cells_CD4+.1
T-cells_CD8+.1
T-cells_foxP3+.1
NK_cells.1
B-cells_GL7_negative_Alum.1
B-cells_GL7_positive_KLH.1
B-cells_GL7_positive_Alum.1
B-cells_GL7_negative_KLH.1
Follicular_B-cells.1
B-cells_marginal_zone.1
Baf3.1
Mast_cells.1
Mast_cells_IgE.1
Mast_cells_IgE+antigen_1hr.1
Mast_cells_IgE+antigen_6hr.1
Dendritic_cells_myeloid_CD8a-.1
Dendritic_cells_lymphoid_CD8a+.1
Dendritic_plasmacytoid_B220+.1
Macrophage_bone_marrow_0hr.1
Macrophage_bone_marrow_2hr_LPS.1
Macrophage_bone_marrow_6hr_LPS.1
Macrophage_bone_marrow_24h_LPS.1
Macrophage_peri_LPS_thio_0hrs.1
Macrophage_peri_LPS_thio_1hrs.1
Macrophage_peri_LPS_thio_7hrs.1
Granulocytes_mac1+gr1+.1
Osteoclasts.1
Osteoblast_day5.1
Osteoblast_day14.1
Osteoblast_day21.1
Microglia.1
Spleen.1
Lymph_nodes.1
Bone_marrow.1
Bone.1
Nih_3T3.1
C2C12.1
C3H_10T1_2.1
3T3-L1.1
MIMCD-3.1
Neuro2a.1
RAW_264_7.1
Min6.1
Liver.1
Kidney.1
Retinal_pigment_epithelium.1
Retina.1
Iris.1
Ciliary_bodies.1
Eyecup.1
Lens.1
Cornea.1
Cerebral_cortex_prefrontal.1
Cerebral_cortex.1
Amygdala.1
Hippocampus.1
Olfactory_bulb.1
Spinal_cord.1
Hypothalamus.1
Cerebellum.1
Nucleus_accumbens.1
Dorsal_striatum.1
Dorsal_root_ganglia.1
Testis.1
Median(304)
3xM
10xM

Figure 5.4 | Expression of *B4galnt1* in murine cells and tissues. The gene expression of mouse *B4galnt1* (encoding beta-1,4-N-acetyl-galactosaminyl transferase) from cells and tissues. *B4galnt1* encodes an enzyme involved in the biosynthesis of gangliosides, including the PLC receptor, GM1a. The graph is acquired from the BioGPS gene expression database [791] and curated using the dataset GeneAtlas MOE430, gcrma [792].

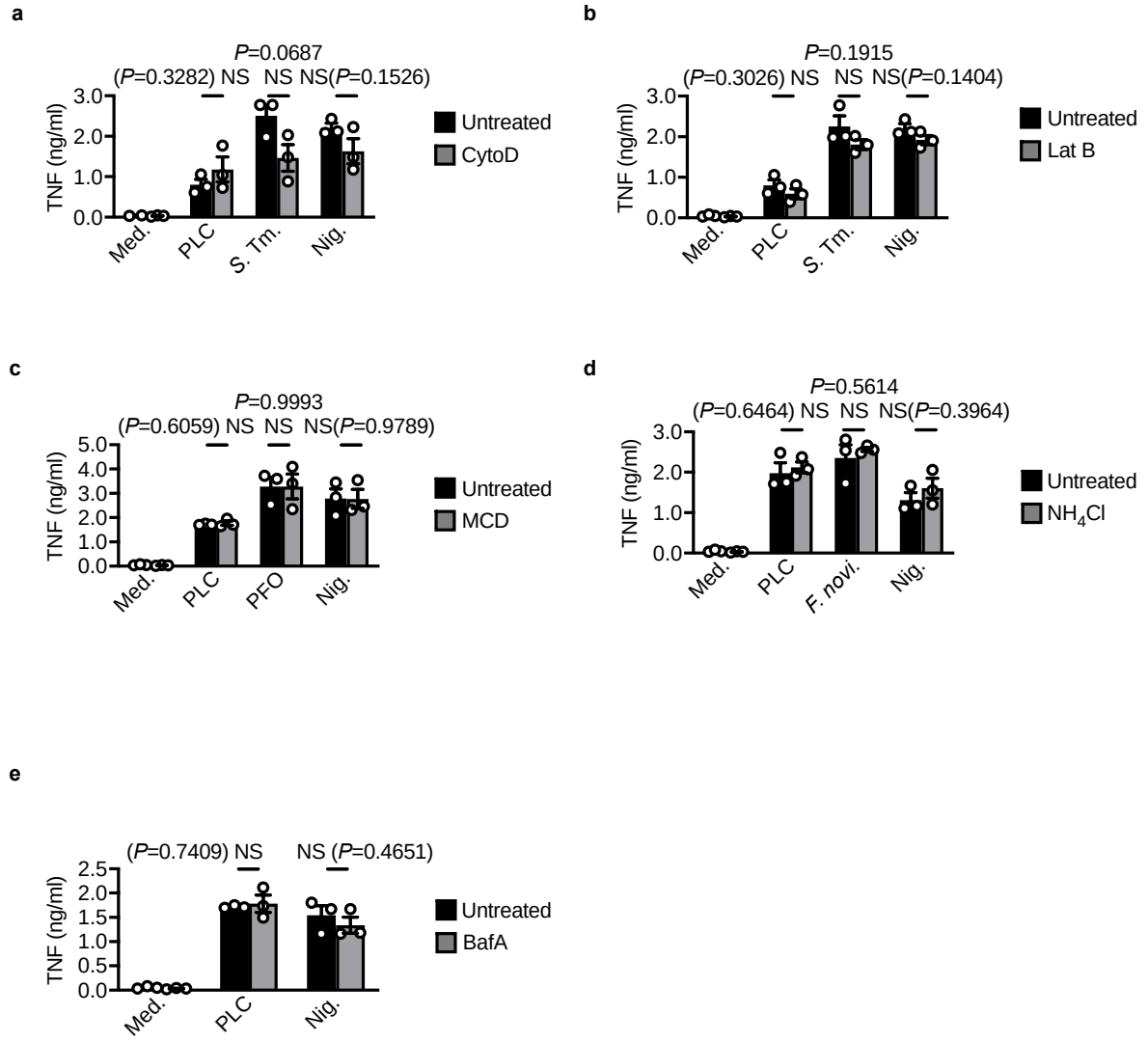

Figure 5.5 | Production of TNF by BMDMs is not affected by treatment of inhibitors. (**a-e**) Release of TNF from WT BMDMs left untreated (Med.) or LPS-primed and assessed 3 hr after treatment PLC or 30 min after treatment with nigericin in the absence or presence of inhibitors (Cytochalasin D [CytoD], 50μM; latrunculin B [LatB], 1 μg/ml; methyl-β-cyclodextrin [MCD], 5mM; ammonium chloride [Nh_4Cl], 20μM; bafilomycin A [Baf A], 100nM). Each symbol represents an independent experiment (a-e). NS, not statistically significant [two-tailed t test (a-e)]. Data are representative of three independent experiments (a-e; mean and s.e.m. in b, a-e).

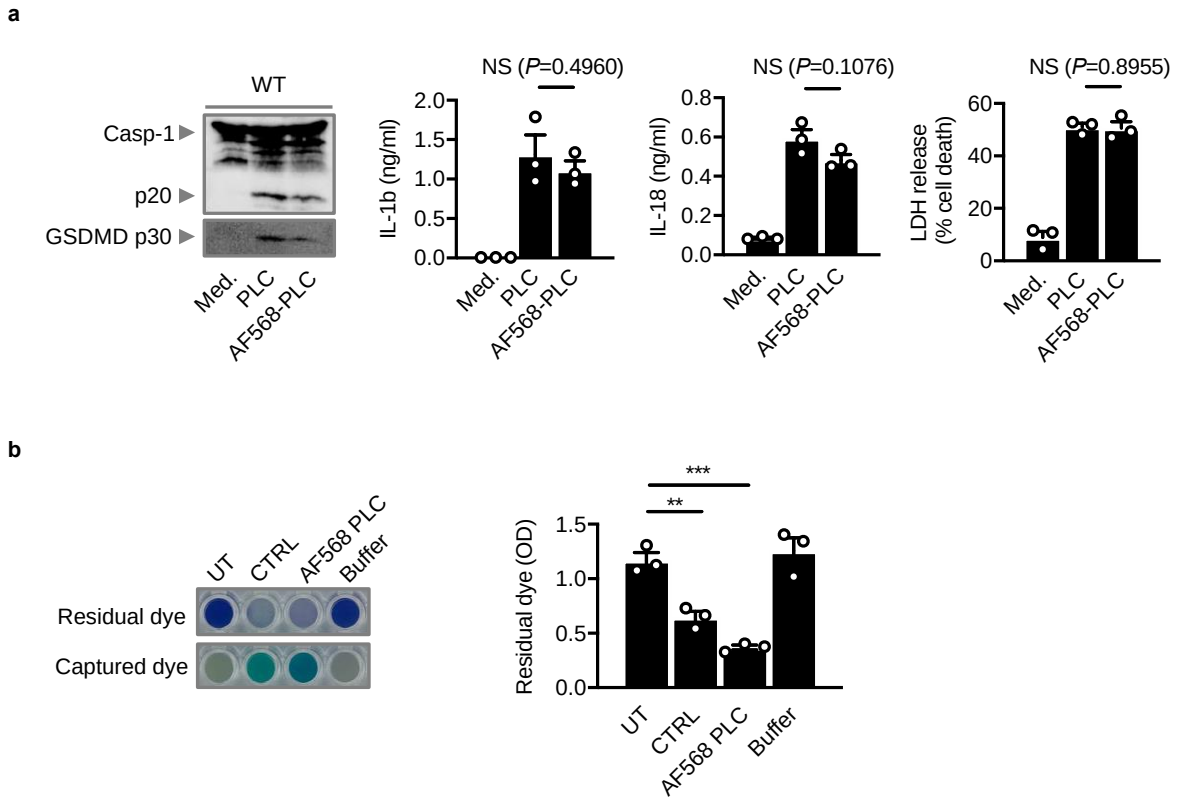

Figure 5.6 | AF568 labelling does not affect the ability of PLC to induce inflammasome activation in BMDMs. (**a**) Immunoblot analysis of caspase-1 and gasdermin D, release of IL-1β and IL-18, and cell death of WT BMDMs left untreated (Med.) or LPS-primed and assessed 4 hr after treatment with unlabelled or AF568-labelled PLC (AF568-PLC). (**b**) Colorimetric analysis of liposomes left untreated (UT), sonicated for 5 min at 100 amplitude (CTRL), or assessed 10 min after stimulation with AF568-PLC or vehicle buffer. The absorbance (OD) of residual dye was measured at 595 nm. Each symbol represents an independent experiment (a and b). NS, not statistically significant, $^{**}P < 0.01$ and $^{***}P < 0.001$ [two-tailed t test (a and b)]. Data are representative of three independent experiments (a and b; mean and s.e.m. in a and b).

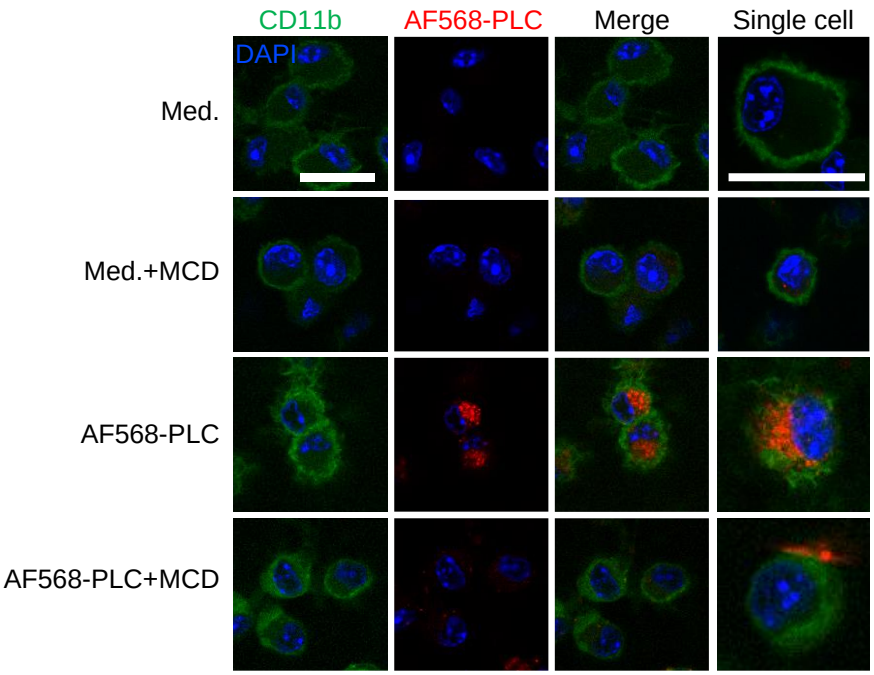

Figure 5.7 | Internalisation of PLC requires cholesterol. Confocal microscopy analysis of CD11b (green) and PLC (red) in unprimed WT BMDMs left untreated (Med.) or assessed 1 hr after stimulation with Alexa Fluor 568-labelled PLC (AF568-PLC) in the absence or presence of methyl-β-cyclodextrin (MCD; 5 mM). Scale bar, 25 μm. Data are representative of three independent experiments.

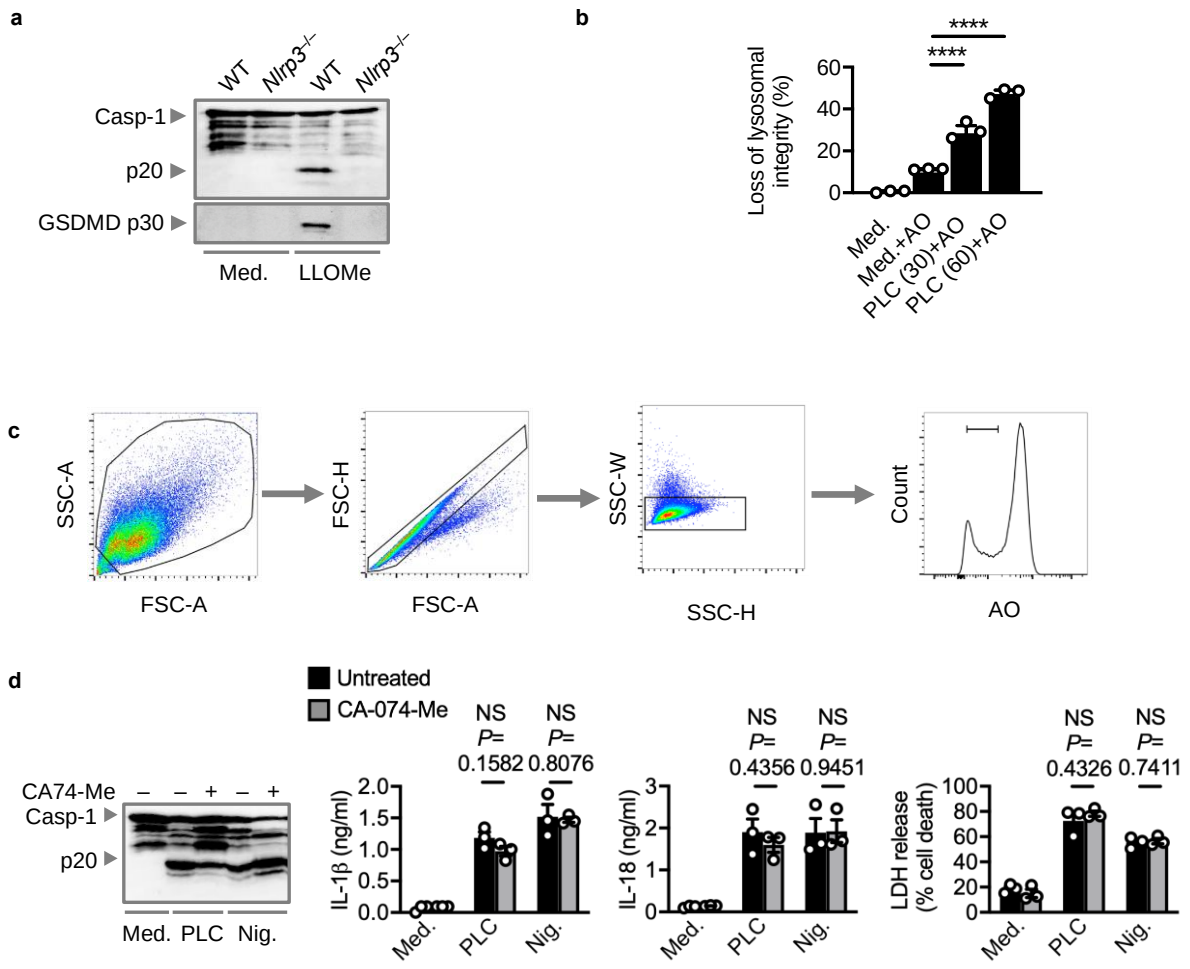

Figure 5.8 | Both LLOMe and PLC induce lysosomal rupture to activate the NLRP3 inflammasome. (**a**) Immunoblot analysis of caspase-1 and gasdermin D of LPS-primed WT or *Nlrp3*$^{-/-}$ BMDMs left untreated (Med.) or assessed 1 hr after treatment with LLOMe**.** (**b**) Flow cytometry analysis of *Nlrp3*$^{-/-}$ BMDMs stained with acridine orange (1μg/ml) and assessed 30 or 60 min after treatment with PLC. (**c**) Flow cytometry scatter plots illustrate the gating strategy used to detect a loss of acridine orange fluorescence. Single and viable cells were selected based on the side and forward scatter. From single cells, loss of acridine fluorescence was recorded at 600–650 nm. (**d**) Immunoblot analysis of caspase-1, release of IL-1β and IL-18, and cell death of LPS-primed WT BMDMs left untreated or assessed 3 hr after treatment with PLC or 30 mins after treatment with nigericin (Nig.) in absence or presence of 100 μM of a cathepsin B-specific inhibitor CA-074-Me. Each symbol represents an independent experiment (b,d). ****P < 0.0001 [one-way analysis of variance [ANOVA] with Dunnett's

multiple-comparisons test (a) or two-tailed t test (d)]. Data are representative of three independent experiments (a-d; mean and s.e.m. in b,d).

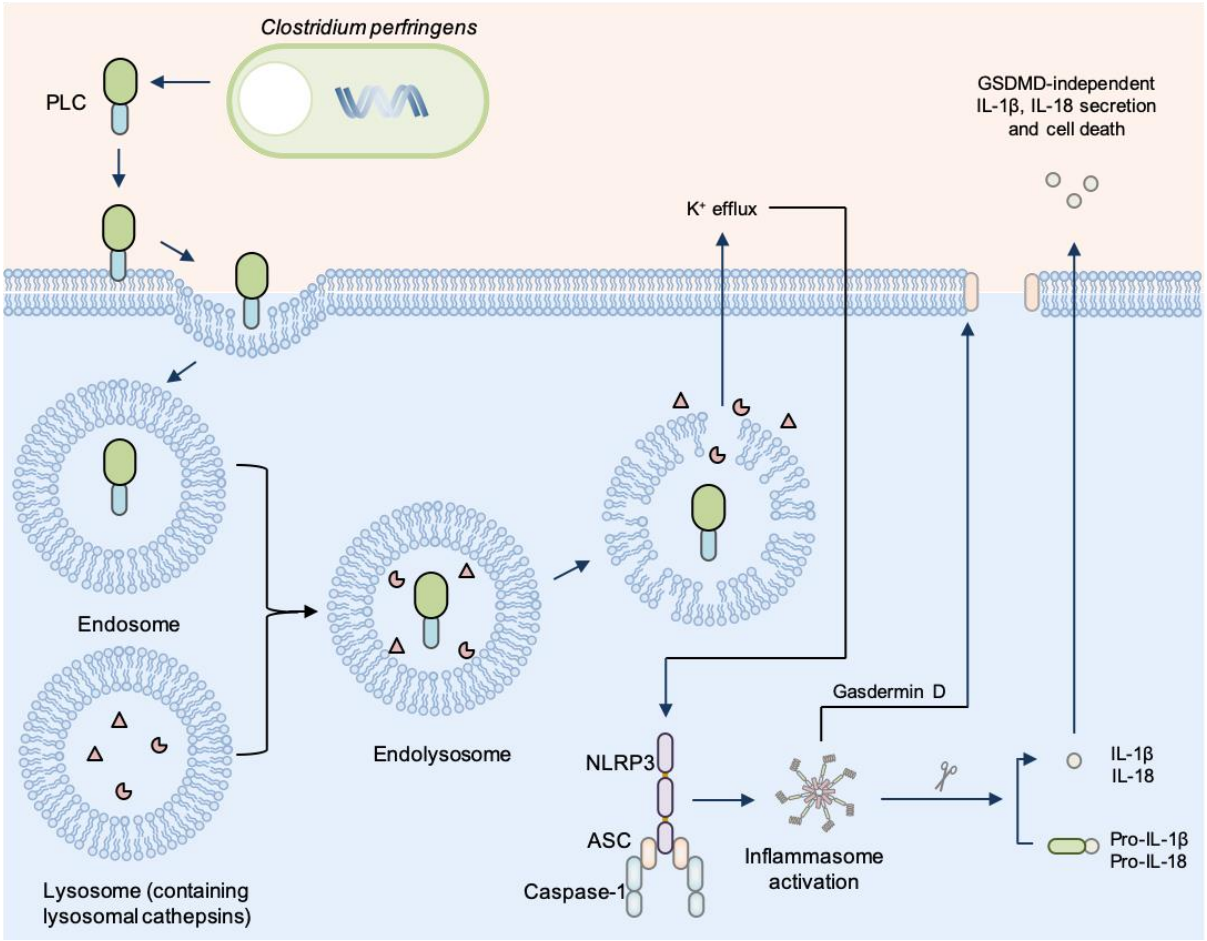

Figure 5.9 | Model of PLC-induced activation of the NLRP3 inflammasome.